Longitudinal analysis of brain networks by magnetic resonance imaging (MRI) in a murine model of neuropathic pain-induced depression

Meltem Karatas

UNIVERSITÉ DE STRASBOURG

ÉCOLE DOCTORALE DES SCIENCES DE LA VIE ET DE LA SANTÉ

UPR 3212

THÈSE

présentée par :

Meltem KARATAŞ

Soutenue le 05 septembre 2019

pour obtenir le grade de : **Docteur de l'Université de Strasbourg**

Discipline/ Spécialité : **Neurosciences**

Analyse longitudinale des réseaux cérébraux par Imagerie de Résonance Magnétique (IRM) dans un modèle murin de dépression induite par la douleur neuropathique

---

Longitudinal analysis of brain networks by magnetic resonance imaging (MRI) in a murine model of neuropathic pain-induced depression

---

THÈSE dirigée par :

Mme I. YALCIN — Chargée de Recherche, CNRS UPR 3212, Strasbourg

Mme I. DIESTER — Professeur, Albert Ludwig University of Freiburg

ENCADRANTE :

Mme LA. HARSAN — MCU-PH, ICube UMR 7357, Strasbourg

RAPPORTEURS :

Mme E. TZAVARA — Directeur de Recherche, INSERM UMR 8246, Paris

M C. FABER — Professeur, University of Münster, Münster

AUTRES MEMBRES DU JURY :

M J. FOUCHER — MCU-PH, ICube UMR 7357, Strasbourg

M D. von ELVERFELDT — PD, Albert Ludwig University of Freiburg

M. W. WEBER-FAHR — Directeur de Recherche, University of Heidelberg, Mannheim

Acknowledgements

First and foremost, I would like to thank my lovely supervisors İpek Yalçın and Laura Harsan. They were the nicest and kindest supervisors I could wish to have, and great academics. They supported and encouraged me, with a healthy dose of reprimanding if I was being particularly pessimistic. They always welcomed discussions and allowed me to express my opinions without fear of criticism. My PhD journey was rocky from the start, ending in unexpected hardships but they helped me every step of the way. When it came to worst, they treated me as if I were family, rather than a student. I'll be eternally grateful to them.

I would like to thank my thesis directors Ilka Diester and Jürgen Hennig at Freiburg University for taking the trouble of accepting me as their student; I also thank my team leaders Dominik von Elverfeldt in Freiburg and Jean-Paul Armspach in Strasbourg.

My special thanks go to Laetitia, with whom I spent hours on end at the scanner ('the batcave'), bursting into giggles at the end of the day from exhaustion, or really from too much isoflurane. We experienced the same difficulties, whether about a piece of code not working- 'Ça marche pas!' - or washing cages and getting wet all over. Thank you for all your help, understanding and great gossip. Thanks are in order for Eléna and Coralie, for your kindness and great friendship. I also thank Marion and Alix for welcoming the newbie to their office, helping in any way they could. Thanks to all members of our Stift club, Mary, Manon, Fabrice, Henrique and whomever I'm forgetting at the moment, it was a wonderful tradition. I thank all the people I had the privilege of collaborating- or rather pestering them for an analysis or code- Vincent Noblet, Céline Meillier, Julien Lamy, Lionel Landre, Dan Roquet and Argeesh Bhanot from ICube; Muris Humo from INCI and Taufiq Nasseef from Montreal. Thank you, Aude, Blandine and Cristina for all your help and compassion.

I would also like to thank Bahar, my free-spirited and extremely loyal friend; Han, an excellent person I met too late; Ewa, my partner in having fun complaining; Şehrazat and Müzeyyen- the Turkish team of emotional support for homesickness and Salma, the fun, warm and wise friend, all of whom made my life during the PhD much more colorful.

On Freiburg side, I would like to express my gratitude to Neele and Anna for being wonderful colleagues and friends. I wish we had more time working together but we made up for it in Hawaii. Thank you again for including me in your plans and thank you for your companionship. Thank you, Annette, it was so lovely to have those conversations every lunchtime with you and Neele, I really miss it. Thank you so much for all your help and support. Thanks to Tanzil, Thiago, Thomas, Katherina and Jochen for your assistance and friendship.

I have to extend my gratitude to my close friends Gülsüm, Duygu and Ayşegül for being always there for me to share all the joys and sorrows. Even though we had a continent between us and hardly saw each other once a year, I never felt we were in any way distant. Thank you so much for being in my life and showing unconditional love and support. I should also thank our little Defne for giving us constant amusement- however unintentionally. Ezgi, my professed 'sister', I thank you for the great conversations on anything and everything, and mutual commiserations on our neuroticism.

Last but not least, I would like to thank the members of my family, my parents and older brother, for all their love, care, and support. I'm incredibly lucky to have them. I should give my special thanks to my mother (I'll have to translate for her). Until last year, I didn't appreciate just how strong and resilient she was. In a strange place where she didn't speak the language or had any acquaintances, she took on the burden of caring for me, forgoing her own worries to give me strength. She managed everything admirably. Thank you so much!

Publications

Published articles

1. **Karatas, M.,** Noblet, V., Nasseef, M.T., Bienert, T., Reisert, M., Hennig, J., Yalcin, I., Kieffer, B.L., Elverfeldt, D. von, Harsan, L.-A., 2019. **Mapping the living mouse brain neural architecture: strain specific patterns of brain structural and functional connectivity.** bioRxiv 730366. https://doi.org/10.1101/730366

2. Grandjean, J., Canella, C., Anckaerts, C., Ayrancı, G., Bougacha, S., Bienert, T., Buehlmann, D., Coletta, L., Gallino, D., Gass, N., Garin, C.M., Nadkarni, N.A., Hübner, N., **Karatas, M.,** Komaki, Y., Kreitz, S., Mandino, F., Mechling, A.E., Sato, C., Sauer, K., Shah, D., Strobelt, S., Takata, N., Wank, I., Wu, T., Yahata, N., Yeow, L.Y., Yee, Y., Aoki, I., Chakravarty, M.M., Chang, W.-T., Dhenain, M., Elverfeldt, D. von, Harsan, L.-A., Hess, A., Jiang, T., Keliris, G.A., Lerch, J.P., Okano, H., Rudin, M., Sartorius, A., Linden, A.V. der, Verhoye, M., Weber-Fahr, W., Wenderoth, N., Zerbi, V., Gozzi, A., 2019. **Common functional networks in the mouse brain revealed by multi-centre resting-state fMRI analysis.** bioRxiv 541060. https://doi.org/10.1101/541060 (*In publication for NeuroImage*)

3. Nguyen, T.L., Duchon, A., Manousopoulou, A., Loaëc, N., Villiers, B., Pani, G., **Karatas, M.,** Mechling, A.E., Harsan, L.-A., Limanton, E., Bazureau, J.-P., Carreaux, F., Garbis, S.D., Meijer, L., Herault, Y., 2018. **Correction of cognitive deficits in mouse models of Down syndrome by a pharmacological inhibitor of DYRK1A.** Disease Models & Mechanisms dmm.035634. https://doi.org/10.1242/dmm.035634

4. Sellmeijer, J., Mathis, V., Hugel, S., Li, X.-H., Song, Q., Chen, Q.-Y., Barthas, F., Lutz, P.-E., **Karatas, M.,** Luthi, A., Veinante, P., Aertsen, A., Barrot, M., Zhuo, M., Yalcin, I., 2018. **Hyperactivity of Anterior Cingulate Cortex Areas 24a/24b Drives Chronic Pain-Induced Anxiodepressive-like Consequences.** J. Neurosci. 38, 3102–3115. https://doi.org/10.1523/JNEUROSCI.3195-17.2018

5. Barthas, F., Humo, M., Gilsbach, R., Waltisperger, E., **Karatas, M.,** Leman, S., Hein, L., Belzung, C., Boutillier, A.-L., Barrot, M., Yalcin, I., 2017. **Cingulate Overexpression of Mitogen-Activated Protein Kinase Phosphatase-1 as Key Factor for Depression.** Biological Psychiatry. https://doi.org/10.1016/j.biopsych.2017.01.019

In preparation

1. Time-dependent alterations in structural and functional brain networks in rodent neuropathic pain-induced depression.

2. Differential Effects of Anesthetics on Mouse Brain Connectivity and Function as Probed by Resting-State FMRI and [18] FDG-PET.

Oral Presentations

1. **Brain functional connectivity signatures of neuropathic pain-induced depression in a preclinical model.** Sixième Journées Scientifiques de la Fédération de Médicine Translationnelle de Strasbourg (FMTS) – 27 April 2018

2. **Analysis of Brain Networks in Murine Models of Depression with Different Imaging Modalities.** NeuroTime Annual Meeting, 7 April 2017, Amsterdam, Netherlands

3. **Mapping with MRI the functional and structural brain networks in the mouse: strain dependent signatures.** NeuroTime Annual Meeting, February 2016, Strasbourg

4. **Brain networks in stress- and pain- induced depression: insight into the structural and functional mechanisms in the anterior cingulate cortex.** NeuroTime Annual Meeting, January 2015, Basel, Switzerland

Poster presentations

1. **Meltem Karatas**, Muris Humo, Laetitia Degiorgis, Marion Sourty, Thomas Bienert, Céline Meillier, Jean-Paul Armspach, Dominik von Elverfeldt, Ipek Yalcin, and Laura-Adela Harsan. **Brain functional connectivity signatures of neuropathic pain-induced depression in a preclinical model.** Joint Annual Meeting ISMRM-ESMRMB, June 2018, Paris, FRANCE. Proc. Intl. Soc. Mag. Reson. Med. 26 (2018) Abstract number: 2341

2. Laetitia Degiorgis, **Meltem Karatas**, Marion Sourty, Thomas Bienert, Marco Reisert, Chantal Mathis, Anne-Laurence Boutillier, Frédéric Blanc, Jean-Paul Armspach, and Laura-Adela Harsan. **Longitudinal alterations of resting-state functional connectivity in Alzheimer's disease in a tauopathy mouse model.** Joint Annual Meeting ISMRM-ESMRMB, June 2018, Paris, FRANCE. Proc. Intl. Soc. Mag. Reson. Med. 26 (2018) Abstract number: 1214

3. **Meltem Karatas**, Laetitia Degiorgis, Marion Sourty, Daniel Roquet, Lionel Thomas, Patrice Marchand, Thomas Bienert, Lee Hsu-Lei, Julien Lamy, Chrystelle Po, Frédéric Boisson, David Brasse, Dominik von Elverfeldt, Izzie Jacques Namer, Jean-Paul Armspach, Ipek Yalcin, and Laura-Adela Harsan. **Differential Effects of Anesthetics on Mouse Brain Connectivity and Function as Probed by Resting-State FMRI and [18] FDG-PET.** ISMRM Annual Meeting, April 2017, Honolulu, Hawai'i, USA. Proc. Intl. Soc. Mag. Reson. Med. 25 (2017) Abstract number: 1678

4. Laura-Adela Harsan, **Meltem Karatas**, Thu Lan NGUYEN, Anna Mechling, Tanzil Arefin, Thomas Bienert, Hsu-Lei Lee, Dominik von Elverfeldt, and Yann Herault. **Mapping and modulation of Down Syndrome specific functional network in Dp(16)1yey mouse model.** ISMRM Annual Meeting, April 2017, Honolulu, Hawai'i, USA. Proc. Intl. Soc. Mag. Reson. Med. 25 (2017) Abstract number: 4086

5. Laetitia Degiorgis, **Meltem Karatas**, Marion Sourty, Chrystelle Po, Thomas Bienert, Hsu Lei Lee, Dominik von Elverfeldt, Chantal Mathis, Anne-Laurence Boutillier, Frédéric Blanc, Jean-Paul Armspach, and Laura-Adela Harsan**. Patterns of resting-state functional connectivity in the prodromal phase of Alzheimer's disease: insights from a tauopathy mouse model (Thy-Tau22).** ISMRM Annual Meeting, April 2017, Honolulu, Hawai'i, USA. Proc. Intl. Soc. Mag. Reson. Med. 25 (2017) Abstract number: 4082

Table of Contents

Table of Figures

Tables

List of Abbreviations

μl Microliter

18F-FDG, $_{18}$FDG 18F-fluorodeoxyglucose

5-HT 5-hydroxytryptamine; serotonin

AAA-CEA-MEA Anterior/Central /Medial Amygdala

ACB, NAc Nucleus accumbens

ACC, ACA Anterior cingulate cortex/area

ACh Acetylcholine

AD Axial diffusivity

ADC Apparent diffusion coefficient

AI Agranular insula

AIC Akaike information criterion

ALFF Amplitude of low frequency fluctuations

AMBA Allen Mouse Brain Atlas

AMPA α-amino-3-hydroxy-5-methyl-4-isoxazolepropionic acid receptor

AMY Amygdala

ANTs Advanced Normalization Tools

AP Action potential

ASD Autism spectrum disorders

ATP Adenosine triphosphate

AUD Auditory area

BDNF Brain-derived neurotrophic factor

BG Basal ganglia

BNST, BST Bed nucleus of stria terminalis

BOLD Blood oxygen level-dependent signal

BST, BNST Bed Nucleus of Stria Terminalis

CA Cornu ammonis, Ammon's horn

CBF Cerebral blood flow

CBP Chronic back pain

CBV Cerebral blood volume

CC Clustering coefficient

cc Corpus callosum

CCI Chronic constriction injury

CeA Central amygdala

ChR2 Channelrhodopsin-2

CLA Claustrum

cLH Congenital learned helplessness

$CMRO_2$ Cerebral metabolic rate of oxygen

CNS Central nervous system

COA-PAA-TR Cortical/Piriform Amygdala-Postpiriform Transition Area

cp Cerebral peduncle

CPL Characteristic path length

CPP Conditioned place preference

CPS Chronic psychosocial stress

CPu, CP Caudate-putamen

CRPS Complex regional pain syndrome

CUMS Chronic unpredictable mild stress

D Diffusion coefficient

D1, DR1 Dopamine receptor-1

D2, DR2 Dopamine receptor-2

DA Dopamine

dACC Dorsal anterior cingulate area

DBM Deformation-based morphometry

DCA Directional connectivity analysis

DG Dentate gyrus

dHIP/dhc Dorsal hippocampus

DKI Diffusion kurtosis imaging

dlPFC Dorsolateral prefrontal cortex

DMN Default-mode network

dPFC Dorsal prefrontal cortex

DRN Dorsal raphe nucleus

DSM-V Diagnostic and statistical manual of mental disorders-5th edition

DTI Diffusion tensor imaging

ECT Ectorhinal Area

EEG Electroencephalography

EFP Electrical field potential

ENT Entorhinal area

EP Endopiriform Nucleus

EPSP Excitatory post-synaptic potential

fa Anterior forceps

FA Fractional anisotropy

FC Functional connectivity

FD Fiber density

FDR False discovery rate

FMR1 Fragile X Mental Retardation gene

FMR1-KO Fragile X Mental Retardation gene

fMRI Functional Magnetic Resonance Imaging

FOV Field of view

fr Fasciculus retroflexus

FRP Frontal Pole

FWER Family-wise error correction

FWHM Full width at half maximum

GABA Gamma-aminobutyric acid
gcc Genu of corpus callosum
GCM Group comparison matrix
GE Gradient echo
GE-EPI Gradient echo-echo planar imaging
GM Gray matter
GU Gustatory Area
Hb Habenula
HIP Hippocampus
HR-MRI High resolution MRI
hrFM High resolution fiber mapping
HY Hypothalamus
IBS Irritable bowel syndrome
ICA Independent component analysis
IL Infralimbic area
IPSP Inhibitory post-synaptic potential
LA-BLA-BMA-PA Lateral/ Basolateral/Basomedial/Posterior Amygdala
LFP Local field potential
LH Learned helplessness
LHb Lateral habenula
LSX-MSC-TRS Lateral/Medial Septal Complex-Triangular Nucleus of Septum
LTD Long-term depression
LTP Long-term potentiation
LV Lateral ventricle
MBq Megabecquerel, unit of radioactivity
Mbsat Behavioral State Related Midbrain
MCC Mid-cingulate cortex
mcc Middle corpus callosum
MD_1 Medial dorsal nucleus
MD_2 Mean diffusivity
MD_3Medetomidine
MDD Major depressive disorder
MEG Magnetoencephalography
MEMRI Manganese-enhanced MRI
MFB, mfb Medial forebrain bundle
MH-LH Medial/Lateral Habenula
MK Mean kurtosis
MKP-1 Mitogen-activated protein kinase phosphatase-1
$MnCl_2$ Manganese chloride
MO Motor area
MOp Primary Motor Area
MOs Secondary Motor Area
mPFC Medial prefrontal cortex
MRI Magnetic resonance imaging
MRN Midbrain reticular nuclei
mRNA Messenger ribonucleic acid
MRS Magnetic resonance spectroscopy
MSN Medium spiny neurons
MUA Multiunit spiking activity
MVGC Multivariate Granger Causality toolbox
NAc, ACB Nucleus accumbens
NC Negative cognitive state
NMDA N-methyl-D-aspartate receptor
NP Neuropathic pain
OA Osteoarthritis
OFC Orbitofrontal cortex
ORB Orbital area
PAG Periaqueductal gray
PALd Dorsal Pallidum
PALv Ventral Pallidum
PAR-POST-PRE-SUB Para/ Post/Pre-Subiculum- Subiculum
PCA Principal component analysis
PCC Posterior cingulate cortex
PE Prediction error signal
PERI Perirhinal Area
PET Positron emission tomography
PF Parafascicular nucleus
PFC Prefrontal cortex
PIR Piriform area
PL Prelimbic area
PPT Pedunculopontine nucleus
PRN Pontine reticular nuclei
PSNL Partial sciatic nerve ligation
PTLp Posterior parietal association areas
RARE Rapid acquisition with refocused echoes
rCBV Regional cerebral blood volume
RD Radial diffusivity
RMTg Rostromedial tegmental area
ROI Region of interest
rs-fMRI Resting state functional magnetic resonance imaging
RSN Resting state network
RSP Retrosplenial area
RVM Rostral ventromedial medulla

SC Superior colliculus
sc, s.c. Subcutaneous
scc Splenium of corpus callosum
SCI Spinal cord injury
SEM Standard error of the mean
sgACC Subgenual anterior cingulate area
SI Substantia innominata
SMA Supplementary motor area
SN_1 Salience network
SN_2 Substantia nigra
SNc Substantia nigra pars compacta
SNI Spared nerve injury
SNL Spinal nerve ligation
SNr Substantia nigra pars reticulata
SPL Shortest path length
SPM Statistical Parametric Mapping
spO_2 Peripheral oxygen saturation
SS Somatosensory area
STN Subthalamic nucleus
SyN Symmetric normalization algorithm
T Tesla, unit of magnetic induction
tcp Thalamo-cortical pathways
TE Echo time
TeA Temporal association areas
TH Thalamus
TMD Temporo-mandibular disorder
TPN Task-positive network
TR Repetition time
VBM Voxel-based morphometry
VBQ Voxel-based quantification
vHIP Ventral hippocampus
VIS Visual area
VISC Visceral area
VM Ventromedial nucleus
vmPFC Ventromedial prefrontal cortex
VP Ventral pallidum
VPL Ventral posterolateral nucleus
VS Ventral striatum
VTA Ventral tegmental area
WM White matter
ZI Zona incerta

Summary

Introduction:

Neuropathic pain occurs as a result of an injury or disease affecting the somatosensory system, it is characterized by prolonged allodynia and hyperalgesia as well as spontaneous pain (Colloca et al., 2017). As of 2018, 6 to 8% of the European population suffers from neuropathic pain. Many patients with chronic pain also develop anxiety and/or depressive disorders, leading to a prevalence of around 50% for major depressive disorder (MDD) comorbidity with chronic pain conditions (Attal et al., 2011). Despite considerable clinical research, the mechanisms underlying this comorbidity remain largely unknown.

Recent studies in the field of neuroimaging have shown that neurological/ neuropsychiatric disorders influence the brain structural and functional networks, and thus, the way different brain areas communicate with each other (Fornito and Bullmore, 2010). Indeed, the study of the brain as an integrative system provides unique insights into large-scale neuronal communication. Study of brain networks and metabolism in preclinical settings is a crucial step for translational research.

In this context, we conducted a non-invasive brain imaging study to investigate changes in structural and functional connectivity in a mouse model of neuropathic pain-induced depression. We aimed to provide a fine-grained mapping of brain network architecture and the evolution of brain functional and structural connectivity in a longitudinal manner. This would allow us to understand the underlying mechanisms of pain-induced depression and develop novel diagnostic approaches and therapeutic strategies.

To achieve our goals, we used two methods of magnetic resonance imaging (MRI), currently the only non-invasive imaging technology that is capable of reconstructing the overall architecture of functional communication pathways (using resting state functional MRI- rs-fMRI) as well as their microstructural substrates (diffusion MRI).

Rs-fMRI is a method based on the analysis of spontaneous low frequency fluctuations (less than 0.1 Hz) of the BOLD (Blood Oxygen Level-Dependent) signal at rest (Biswal et al., 1995). It is now accepted that the synchronization of these fluctuations between distinct brain regions reflects a functional connectivity between them (Lee et al., 2013; Rosazza and Minati, 2011; van den Heuvel and Hulshoff Pol, 2010). On the other hand, diffusion MRI explores structures on a microscopic scale by mapping the displacements of water molecules in the context of the physical diffusion process (Le Bihan and Breton, 1985). It provides unique clues about the neural tissue microstructure and the changes associated with various physiological and pathological states. Since the diffusion directions reflect the underlying organization of white matter axons, diffusion MRI can also be used to map axonal fibers in the brain *in vivo* and non-invasively (Le Bihan, 2014, 2003).

Objectives:

Based on the published data and preliminary results, my thesis project serves **two main objectives**: **1)** to compare C57BL/ 6 and BALB/c strains in order to find the most suitable strain for the study of depression; **2)** to characterize brain functional and structural connectivity in chronic pain and depression comorbidity.

Results:

The neuropathic pain-induced depression model used in this project consists of placing a polyethylene "cuff" around the main branch of the right sciatic nerve in mice (Benbouzid et al., 2008; Yalcin et al., 2014b). This surgical procedure results in mechanical allodynia and anxio-depressive behaviors over time. As our first study demonstrated that C57BL/6 mice show less variability in their brain structure and function between individuals, we considered this strain more suitable for the study of depression. We performed a longitudinal investigation using brain resting state functional MRI (rs-fMRI) and structural MRI in this murine model of depression which enabled us to characterize the evolution of the pathology.

We first reproduced our team's previous results on cuff implantation inducing mechanical allodynia in the ipsilateral leg and the development of depression-like behaviors in splash test. Functional and structural MRI scans were performed in the same cohort of mice before surgery (baseline), at 2 weeks (the timepoint where animals develop mechanical allodynia, TP1) and at 8 weeks after surgery (the timepoint corresponding to animals displaying both mechanical allodynia and depressive phenotype, TP2).

Structural changes

We demonstrated differences in fractional anisotropy (FA) values in the anterior cingulate area (ACA), retrosplenial area (RSP), hypothalamus, ventral tegmental area (VTA), and thalamus at two weeks post-injury (TP1). By contrast, after 8 weeks (TP2), the only remaining changes were the ACA and the RSP, core regions of rodent default mode network (DMN).

Functional changes

Subsequently, using rs-fMRI, we performed a voxel-wise correlation study to identify changes in functional connectivity over time. Our most notable results indicate connectivity alterations in ACA and VTA for mice with neuropathic pain. Briefly, ACA had reduced connectivity towards insula, caudate-putamen (CP), dorsal hippocampus, habenula, and periaqueductal gray (PAG) in neuropathic mice at TP1. At TP2, in addition to this reduced connectivity, ACA had higher connectivity towards RSP, amygdala (AMY), and temporal association areas (TeA) in neuropathic animals with depressive phenotype. 2 weeks after surgery, VTA showed higher connectivity to somatosensory areas (SS), CP and RSP, whereas after 8 weeks this region had higher connectivity towards ACA, nucleus accumbens (ACB), CP, bed nucleus of stria terminalis (BST), habenula and thalamus in neuropathic group.

Discussion and perspectives:

The results obtained in this project demonstrate remarkable structural and functional modifications in the brain networks following the induction of neuropathic pain and the emergence of depressive phenotype. Combining a relevant preclinical model and *in vivo* brain MRI, we identified a brain connectivity signature of pain-induced depression and its evolution over time, involving alterations in reward circuits, with a major impact of the two centers: ACA and VTA.

The brain structural changes observed at 2 weeks post-surgery may be due to a glial activation process which subsides over time. Therefore, in the short-term, we are evaluating the changes in microglial activity using an immunohistochemistry approach, examining pertinent regions of interest.

The main results of functional imaging reveal considerable changes in the networks encompassing the reward circuit and DMN, which are known to be involved in both chronic pain pathologies (Borsook et al., 2016; DosSantos et al., 2017; Mitsi and Zachariou, 2016) and major depression (Bracht et al., 2015; Greicius et al., 2007; Russo and Nestler, 2013). Furthermore, we observed alterations in the interaction of these networks. The long-term perspective of this project is to investigate the causal relationship between pain and depression, reaching a mechanistic explanation for the comorbidity.

Résumé en français

Introduction :

Les douleurs neuropathiques, qui surviennent à la suite d'une lésion ou d'une maladie affectant le système somatosensoriel, sont caractérisées par une allodynie et une hyperalgésie prolongée ainsi que par des douleurs spontanées (Colloca et al., 2017). En 2018, 6 à 8 % de la population européenne est atteinte de douleur neuropathique. De nombreux patients douloureux chroniques développent également des troubles de l'anxiété ou/et des états dépressifs, conduisant à une prévalence d'environ 50% de trouble dépressif majeur (Attal, et al. 2011). Malgré la recherche clinique considérable, les mécanismes sous-jacents à cette comorbidité restent largement inconnus.

Les études récentes dans le domaine de la neuroimagerie ont montré que les troubles neurologiques/neuropsychiatriques influencent l'architecture structurale et fonctionnelle du réseau cérébral et, par conséquent, la façon dont différentes zones du cerveau communiquent entre elles (Fornito et Bullmore, 2010). En effet, l'étude du cerveau en tant que système intégratif fournit des informations uniques sur la communication neuronale à grande échelle. Étudier les réseaux et le métabolisme cérébral représente une étape cruciale pour la recherche translationnelle.

Dans ce contexte, nous avons mené une étude d'imagerie non-invasive - par Imagerie de Résonance Magnétique (IRM) du cerveau - pour étudier des changements dans la connectivité structurale et fonctionnelle dans un modèle murin de dépression induite par la douleur neuropathique. L'objectif principal de ce travail était de fournir une cartographie du réseau cérébral et de l'évolution de la connectivité fonctionnelle et structurelle du cerveau d'une manière longitudinale qui nous permettra d'une part de comprendre les mécanismes sous-jacents de la dépression induite par la douleur, d'autre part, de développer des nouvelles approches diagnostiques et des stratégies thérapeutiques.

Pour atteindre nos objectifs, nous avons utilisé deux méthodes d'imagerie par résonance magnétique (IRM), actuellement la seule technologie d'imagerie non invasive permettant de reconstruire l'architecture globale des voies fonctionnelles de communication (en utilisant l'imagerie fonctionnelle de repos- IRMfr) ainsi que leur substrat microstructural (imagerie du tenseur de diffusion – DTI et la tractographie des fibres).

L'IRMfr est une méthode basée sur l'analyse des fluctuations spontanées de basses fréquences (inférieures à 0,1 Hz) du signal BOLD (Blood Oxygen Level-Dependent) à l'état de repos (Biswal et al., 1995). Il est aujourd'hui admis que la synchronisation de ces fluctuations entre des régions cérébrales distinctes reflète une connexion fonctionnelle entre elles (Lee et al., 2013; Rosazza and Minati, 2011; van den Heuvel and Hulshoff Pol, 2010). D'autre part, l'IRM de diffusion permet d'étudier les structures à l'échelle microscopique en cartographiant les déplacements des molécules d'eau dans le cadre du processus de diffusion physique (Le Bihan and Breton, 1985). Il fournit des indices uniques sur l'architecture fine des tissus neuraux et sur les changements associés à divers états physiologiques et pathologiques. Comme la direction de diffusion reflète l'organisation sous-jacente des axones de la substance blanche, l'IRM de diffusion peut également être utilisée pour cartographier les fibres dans le cerveau de manière *in vivo* et non invasive (Le Bihan, 2014, 2003).

Objectifs :

Sur la base des données publiés et des résultats préliminaires, mon projet de thèse s'articule autour de **deux objectifs principaux : 1)** comparer les souches C57BL/6 et BALB/c afin de trouver la ligne plus adapter pour les études de la dépression ; **2)** caractériser les changements fonctionnelles et structurelles du cerveau dans la comorbidité douleur chronique et la dépression.

Résultats :

Le modèle d'animaux que nous avons utilisé pour induire la dépression consiste en poser un manchon de polyéthylène « cuff » autour de la branche principale du nerf sciatique (Benbouzid et al., 2008 ; Yalcin et al., 2014b). Cette procédure de chirurgie entraîne une allodynie mécanique et des comportements de type dépressifs au cours du temps. Comme notre première étude a démontré que les souris C57BL/6 sont plus adaptées pour étudier la dépression, nous avons utilisé celle-ci pour le reste de l'étude. En utilisant ce modèle, nous avons réalisé un suivi longitudinal par IRM fonctionnelle de repos et IRM structurelle du cerveau qui nous a permis de caractériser l'évolution de la pathologie.

Nous avons d'abord reproduit les résultats de l'équipe en démontrant que l'implantation du cuff induit l'allodynie mécanique dans la patte ipsilateral et le comportement de type dépressive mis en évidence avec le test de toilettage provoquée (splash test). Ensuite, des IRM fonctionnelle/structurelle ont été réalisée chez les mêmes animaux avant la chirurgie, à 2 semaines (le point temporal correspondant aux animaux montrant seulement l'allodynie mécanique) et à 8 semaines après la chirurgie (le point temporal correspondant aux animaux montrant à la fois l'allodynie mécanique et le phénotype dépressif).

Changements structurels

Nous avons démontré des différences de valeurs du facteur d'anisotropie tissulaire (FA) dans le cortex cingulaire antérieurs (CCA), le cortex rétrosplénial (RSP), de l'hypothalamus, de l'aire tegmentale ventrale (ATV) et du thalamus à deux semaines post-chirurgical. Par contre, à 8 semaines, ces changements restent détectables seulement dans le CCA et le RSP, les structures qui sont fortement impliquées dans le réseau du mode par défaut (MPD) chez le rongeur.

Changements fonctionnels

Par la suite, en utilisant l'IRMfr, nous avons réalisé une étude de corrélation « voxel-wise » pour identifier les changements de connectivité au cours du temps.

Brièvement, nos résultats ont montré que le CCA a une connectivité réduite vers l'insula, le caudé-putamen (CP), l'hippocampe dorsale, l'habénula et la substance grise périaqueducale (PAG) chez les souris neuropathiques. À huit semaines, en plus de cette connectivité réduite, le CCA présentait une connectivité plus élevée vers le RSP, l'amygdale (AMY), et les aires associatives temporales (TEa) chez les animaux neuropathiques présentant le phénotype dépressif. En outre, 2 semaines après la chirurgie, l'ATV (une des régions clés du réseau de la récompense et aversion – « reward-aversion ») montrait une connectivité élevée vers les aires somatosensorielles (SS), le CP et le RSP alors qu'à 8 semaines, il avait une connectivité plus

élevée vers le CCA, le noyau accumbens (NAc), le CP, le noyau de lit de la strie terminale (BST), l'habénula et le thalamus chez les neuropathiques.

Discussion et perspectives :

Les résultats obtenus dans le cadre de ce projet démontrent des modifications structurels et fonctionnels remarquables des réseaux cérébraux suite à l'induction de la douleur neuropathique et à l'émergence de comportements dépressifs. En combinant un modèle animal pertinent et l'IRM cérébrale in-vivo nous avons identifié la signature de la dépression induite par la douleur et son évaluation longitudinale sur la connectivité cérébrale, impliquant des altérations dans le cadre des circuits de la récompense, avec un impact majeur sur la connectivité des deux centres : le CCA et l'ATV.

A court terme, comme les changements structurels observés dans des structures corticales pourraient être due à un processus d'activation gliale, nous sommes en train d'évaluer les changements d'activité de microglie en utilisant une approche d'immunohistochimie dans des structures d'intérêts.

Les résultats principales d'IRLfr montrent une modification considérable dans les réseaux englobant le MPD et le circuit de récompense, qui sont impliqués à la fois dans les pathologies de la douleur chronique (Borsook et al., 2016; DosSantos et al., 2017; Mitsi and Zachariou, 2016) et de la dépression (Bracht et al., 2015; Greicius et al., 2007; Russo and Nestler, 2013). De plus, nous avons pu observer des changements d'interaction entre ces réseaux. Il est maintenant nécessaire d'étudier la relation causale entre la dépression induite par la douleur et ses changements fonctionnels qui font partie de la perspective long-termes de ce projet.

Preface

Neuropathic pain is caused by an injury or disease of the somatosensory system including peripheral fibers and central neurons (e.g. peripheral nerve damage, diabetic neuropathy, post-stroke pain, neurodegenerative diseases) and it is among the most frequent causes of chronic pain (Colloca et al., 2017). Neuropathic pain affects around 7 -10% of the population and its incidence is likely to increase due to ageing of the population. Comorbidities such as poor sleep, anxiety and depression are frequent in neuropathic pain and they greatly impair quality of life and has a high socioeconomic impact on society (von Hehn et al., 2012). Approximately 30% of patients with neuropathic pain develop major depression. Despite concerted efforts, the mechanisms underlying this comorbidity remain elusive.

In recent years, neuroimaging emerged as a method to non-invasively assess structural and functional architecture of brain networks and their modifications in various neurological/neuropsychiatric disease states (Fornito and Bullmore, 2010). Several different magnetic resonance imaging (MRI) methodologies provide tools for the study of the brain as an integrative system. MRI gives unique insights into large-scale neuronal communication and provides a platform to study and understand how neural networks can be modified or reorganized under pathological conditions.

In this thesis, my main objective was to shed light on the mechanisms underlying neuropathic pain and depression comorbidity by exploring the functional and structural brain connectivity features in a neuropathic pain-induced depression mouse model. For this, I applied non-invasive, *in vivo* MRI technology in a longitudinal experimental design, aimed at following the development of the anxio-depressive phenotype and brain network remodeling over time. Probing the brain networks in a mouse model is an important step for translational research as similar MRI techniques exist for clinical investigations and thus, animal findings can be transferable to humans. In addition, this research could pave the way for innovative diagnostic protocols and the development of targeted therapeutic intervention strategies.

Three MRI methods were used in this work: resting-state fMRI (rs-fMRI) to reconstruct the overall architecture of brain functional communication pathways, diffusion tensor imaging (DTI) to examine microstructural substrates underlying this communication, and anatomical imaging to track morphological alterations using deformation-based morphometry (DBM) methods.

In the **first** part of the introduction chapter, I give an overview of MRI methods that I utilized in my work or used in the literature that I'm discussing. **Second** part of my introduction is dedicated to neuropathic pain: including a part summarizing MRI literature in chronic pain conditions and the current knowledge on anxio-depressive consequences of pain.

Avant-propos

La douleur neuropathique résulte d'une lésion ou d'une maladie du système somatosensoriel; elle est l'une des causes les plus fréquentes de la douleur chronique. (Colloca et al., 2017). La douleur neuropathique touche environ 7 à 10% de la population et son incidence est susceptible d'augmenter en raison du vieillissement de la population. Les comorbidités telles que l'insomnie, l'anxiété et la dépression sont fréquentes dans les douleurs neuropathiques et compromettent grandement la qualité de vie. Elles ont également un impact socioéconomique important (von Hehn et al., 2012). Environ 30% des patients souffrant de douleurs neuropathiques développent également une dépression. Malgré des efforts concertés, les mécanismes sous-jacents à cette comorbidité restent inconnus.

Récemment, la neuroimagerie est apparue comme une méthode d'évaluation non-invasive de l'architecture structurelle et fonctionnelle des réseaux cérébraux et de leurs modifications dans divers états neurologiques/neuropsychiatriques (Fornito and Bullmore, 2010). Plusieurs méthodes différentes d'imagerie par résonance magnétique (IRM) donnent une possibilité d'étudier le cerveau en tant que système intégratif. Les méthodes de l'IRM, comme l'IRM fonctionnelle au repos et l'imagerie du tenseur de diffusion, donnent un aperçu unique de la communication neuronale à grande échelle et permet de comprendre comment les réseaux de neurones peuvent être modifiés ou réorganisés dans des conditions pathologiques.

Dans ce travail de thèse, mon objectif général était d'améliorer nos connaissances des mécanismes sous-jacents à la comorbidité entre douleur neuropathique et dépression en étudiant les altérations fonctionnelle et structurelle des réseaux cérébraux en utilisant un modèle de dépression e induite par la douleur neuropathique chez la souris. En effet, sonder les réseaux cérébraux dans un modèle de souris représente une étape cruciale pour la recherche translationnelle car des techniques similaires d'IRM existent pour les investigations cliniques ; par conséquent, les résultats obtenus chez la souris sont facilement transférables à l'homme. De plus, cela pourrait ouvrir une voie à des protocoles de diagnostic innovants et au développement de stratégies d'intervention thérapeutique ciblées.

Dans ce travail, trois méthodes d'IRM ont été utilisées : IRMf au repos (rs-IRM) pour reconstruire l'architecture globale des voies de communication fonctionnelles du cerveau, imagerie du tenseur de diffusion (DTI) pour examiner les substrats microstructuraux sous-jacents à cette communication et imagerie anatomique pour suivre les altérations morphologiques utilisant méthode de morphométrie déformation-basée (DBM).

Dans la **première** partie de l'introduction, je résume des méthodes d'IRM utilisées dans mon travail et des études précédentes que j'ai citées. La **deuxième** partie de l'introduction est consacrée à la douleur neuropathique, elle résume la littérature sur l'IRM dans les états douloureux chroniques et les connaissances actuelles sur les conséquences anxio-dépressives de la douleur.

1 Introduction

1.1 Functional and Structural Connectivity via Magnetic Resonance Imaging

In the following sections, I will introduce resting-state functional magnetic resonance imaging (rs-fMRI), diffusion MRI and fiber tracking methodologies as well as their use in mouse brain imaging.

1.1.1 Resting-state fMRI

Paramagnetic materials form internal, induced magnetizations in the direction of the externally applied magnetic fields (i.e. increasing the field strength in the surrounding area); thus, disrupt the homogeneity of the said external magnetic fields. Deoxyhemoglobin possesses paramagnetic properties which was first demonstrated by Pauling and Coryell in 1936. Later on, Ogawa and colleagues (1990) showed that the paramagnetic deoxyhemoglobin in venous blood can be utilized as a naturally occurring contrast agent for MRI through the use of gradient echo (GE) techniques in high fields. They recognized the fact that the MRI contrast they termed 'blood oxygen level dependent (BOLD)' can provide real-time maps of brain oxygenation *in vivo*. If blood flow increases suddenly with an increase in cellular activity and this increase is not accompanied by an increase in oxygen consumption of comparable magnitude, oxygenation in capillaries and veins is increased (Fox and Raichle, 1986). BOLD functional MRI (BOLD-fMRI) technique is based on the accentuated signal due to an increase in venous oxyhemoglobin levels resulting from overcompensation by the increased blood flow in response to neural activity.

Resting-state fMRI technique, based on the use of the BOLD signal, emerged following the seminal paper by Biswal and colleagues (1995). They discovered that the spontaneous low frequency (<0.1 Hz) fluctuations of the BOLD signal are not artefactual and the regions that are activated together during a task have correlated spontaneous BOLD fluctuations during rest. They concluded that correlation of low frequency BOLD signal fluctuations is a manifestation of *functional connectivity (FC)* of the brain. Functional connectivity is defined as the temporal dependence of neuronal activity patterns of anatomically separated brain regions (Friston et al., 1993).

BOLD-fMRI has gained immense popularity during the last three decades in the neuroscience field as the method of choice for non-invasively studying the entirety of brain with a high spatiotemporal resolution (Logothetis, 2008). However, the BOLD signal is not a direct measure of neuronal activity (Fox and Raichle, 2007); rather it is a surrogate signal that reflects neuronal mass activity via hemodynamic responses. As such, an understanding of what BOLD signal truly represents is a prerequisite to correctly interpret fMRI findings.

1.1.1.1 Origin of the BOLD signal

The BOLD signal does not directly measure the neuronal activity itself. Instead, the BOLD effect is sensitive to the changes in cerebral blood flow (CBF), cerebral metabolic rate of oxygen ($CMRO_2$), and cerebral blood volume (CBV): the set of physiological responses that are referred to collectively as the hemodynamic response to activation (Buxton et al., 2004). Based on numerous experimental studies of the BOLD responses to brain activation, certain characteristics of the BOLD signal were noted (Figure 1-1):

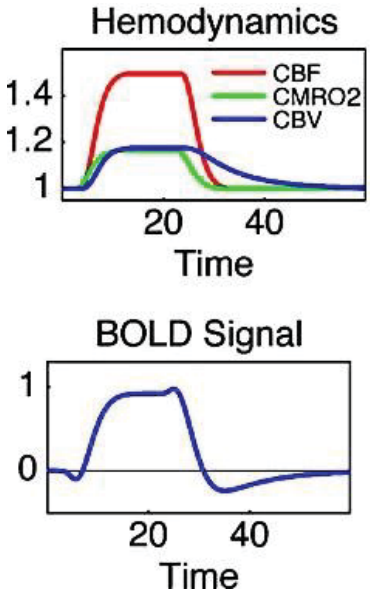

Figure 1-1 Schematic drawing of the BOLD response due to variations in the timing of responses of the physiological variables CBF, CBV, and $CMRO_2$.
(Adapted from Buxton, et al. 2004.)

BOLD responses to a brief stimulus are delayed by 1-2 s and have a temporal width on the order of 4-6 s. For a sustained stimulus of 20 s or longer, the response typically reaches a plateau. A post-stimulus undershoot of BOLD signal is common, with longer duration stimuli tend to have longer post-undershoots. This is thought to be related to CBV recovering slower than CBF and $CMRO_2$.

Some investigators have reported an initial dip of the BOLD signal lasting 1-2 s before the standard BOLD signal increase. This might reflect a rapid increase of $CMRO_2$ before the CBF increase, and this phenomenon may be better localized to the area of increased metabolism (Buxton et al., 2004).

Electrophysiological correlates of BOLD: Extracellular recording of field potentials bring information on different types of neural activity depending on the exact positioning of the electrodes and the recording sites (Logothetis, 2003). Single unit recording mainly gives information on the spiking activity of large principal cells. On the other hand, neural ensemble recordings can monitor electrical field potentials (EFP) related to both spikes and the integrative processes taking place mainly in dendrites by several hundred neurons. The two signal types can be distinguished by frequency band separation. Multiunit spiking activity (MUA) takes up the higher frequency band (500-1000 Hz) and it represents a weighted sum of extracellular action potentials (AP) of all neurons within a region. Local field potentials (LFP), low frequency range of the EFP signal (<250 Hz) mostly represent slow events reflecting cooperative activity in neuronal populations. These slow events include excitatory and inhibitory post-synaptic potentials (EPSP, IPSPs), after-potentials of somato-dendritic spikes, and voltage-gated membrane oscillations. To sum up, LFPs reflect the input of a given cortical area as well as its local intracortical processing, including the activity of excitatory and inhibitory interneurons.

Logothetis et al. (2001) have examined the relationship between BOLD fMRI signal and the underlying neural activity in simultaneous intracortical electrophysiology and imaging experiments in anesthetized monkeys. Their findings demonstrate a transient increase in power of all observed frequencies (i.e. both MUAs and LFPs) after stimulus presentation followed by a lower level of activation that was maintained during the entire stimulus presentation. However, the increase in LFPs during stimulation is significantly stronger than that of MUA. In addition, while MUA was often found to adapt, returning almost to baseline levels, LFP activity was always maintained throughout the stimulus presentation. These findings suggest that BOLD activation may actually reflect more the neural activity related to the input and the local processing in any given area, rather than the spiking activity commonly thought as the output of the data. Even though the output activity generally correlates with neurotransmitter release and pre- and post-synaptic currents; when input into a particular area has a primarily regulatory role, fMRI experiments may reveal activation in areas that single-unit activity is not detected (e.g. net inhibition of spiking in Purkinje cells is accompanied by LFPs and an increased blood flow) (Logothetis, 2003).

BOLD signal and brain energy metabolism: Activity-induced increases in the blood flow are not accompanied by proportional increases in oxygen consumption- a fact that forms the basis of BOLD imaging. Oxygen consumption does increase but this increase is much lower than that of blood flow and glucose consumption. In fact, the increase in blood flow is invariably accompanied by an augmented glucose consumption (Fox et al., 1988). Because this occurs in the presence of adequate tissue oxygenation, it is referred to as *aerobic glycolysis* (Raichle and Mintun, 2006).

The vast majority of the energy consumed by the brain is provided by the metabolism of glucose to carbon dioxide and water, a process that begins with glycolysis and ends with oxidative phosphorylation. But the two processes are not strictly linked. By far the largest amount of ATP is produced by the oxidative phosphorylation (~30 ATP per glucose molecule in contrast to net 2 ATP for glycolysis). An important advantage of glycolysis over oxidative phosphorylation, other than it can operate without oxygen, that it is much faster. Because glycolysis can make pyruvate much faster than it can be oxidized, ATP is made nearly twice as fast by converting glucose to lactate. In the case of sudden increases in neuronal activity, glycolysis can accommodate the metabolic needs, thus, its contribution to brain metabolism seems to be small but strategically important. The observed increase in glycolysis was found to be resulting from the uptake of glutamate into astrocytes from excitatory synapses along with Na_+. The intracellular glutamate is converted to glutamine and the resulting rise in intracellular sodium increases the activity of Na_+/K_+-ATPase. Both processes require the hydrolysis of ATP whose synthesis appears to be by glycolysis alone (Raichle and Mintun, 2006).

Astrocytic processes and the BOLD signal: Astrocytes have been considered to participate in BOLD signal generation in a passive way. They couple neuronal activity to the hemodynamic response to fulfill metabolic demand of neurons (Raichle and Mintun, 2006).

However, a recent study by Takata et al. (2018) demonstrated that astrocyte activation alone can evoke BOLD signal without neuronal activity. They used a transgenic mouse line carrying *channelrhodopsin-2 (ChR2)* in cortical astrocytes (Astrocyte-Chr2): transcranial illumination of the mouse cortex evoked BOLD response in awake fMRI. The absence of neuronal activation after astrocyte stimulation was detected using *c-fos* mRNA staining along with electrophysiological recordings (i.e. LFP and MUA). Optogenetic stimulation of astrocytes elicited oxygen consumption along with synthesis of acetyl-carnitine via oxidative glucose metabolism. In physiological conditions, astrocytes may be able to respond to neuromodulators released from axonal fibers of distant origin whereby activation of astrocytes is not accompanied by local neuronal activity. This study suggests BOLD signal fluctuations can reflect metabolic demands of astrocytes in addition to neurons.

1.1.1.2 Resting-state Functional Connectivity (FC)

Resting-state activity is a signature of neural oscillations synchronized across large-scale networks that occur in the absence of external inputs. The resting human brain represents only 2% of total body mass but consumes 20% of the body's energy, most of which used to support ongoing neuronal signaling. Task related increases in neuronal metabolism are usually small (<5%) when compared with this large resting energy consumption (Fox and Raichle, 2007). Biswal and colleagues (1995) proved that the resting-state BOLD fluctuations detected with fMRI are not artefactual by showing that BOLD fluctuations of left somatomotor cortex is specifically correlated with fluctuations in the right somatomotor cortex and medial motor areas in the absence of overt motor behavior. Later on, many other neuroanatomical systems have been shown to be coherent in their spontaneous activity (Fox and Raichle, 2007).

As a rule, regions that are similarly modulated by task paradigms tend to be correlated in their spontaneous BOLD activity. In addition, regions with apparently opposing functionality have been found to be negatively correlated (i.e. anticorrelated) in their spontaneous activity. These correlations and anticorrelations between segregated brain regions as shown by rs-fMRI form the basis of resting-state functional connectivity and resting-state networks. Resting-state networks were discovered in both humans (Fox et al., 2005; Greicius et al., 2003) and other mammalian species such as non-human primates, rats and mice (Belcher et al., 2013; Grandjean et al., 2014; Jonckers et al., 2011; Mantini et al., 2011; Mechling et al., 2014; Sforazzini et al., 2014).

Several resting-state networks were defined including: default-mode network (DMN), task-positive network (TPN), salience network (SN), somatomotor, visual, auditory and cerebellar networks (Fox and Raichle, 2007; Di and Biswal, 2015). Two of the major networks, DMN and TPN are described further below:

Default mode network (DMN): Among the discovered resting-state networks, DMN is unique in showing reductions in its activity in response to cognitive tasks. A 'default mode of brain function' was proposed by Raichle et al. (2001) following their observation using positron emission tomography (PET) that a set of brain regions- involving, among other areas, the medial prefrontal cortex (mPFC), posterior cingulate cortex (PCC), and precuneus shows ongoing activity during rest and deactivation during externally cued tasks. Further investigations using resting-state fMRI demonstrated the temporal coherence of BOLD fluctuations between regions comprising DMN as described previously in the PET study (Greicius et al., 2003). PCC was recognized as the central region whose connectivity displayed task deactivations in PET. Changes in DMN connectivity

were consistently demonstrated in major depression (Greicius et al., 2007; Zhou et al., 2010) and chronic pain conditions (Marwan N. Baliki et al., 2014; Kucyi et al., 2014; Alshelh et al., 2018).

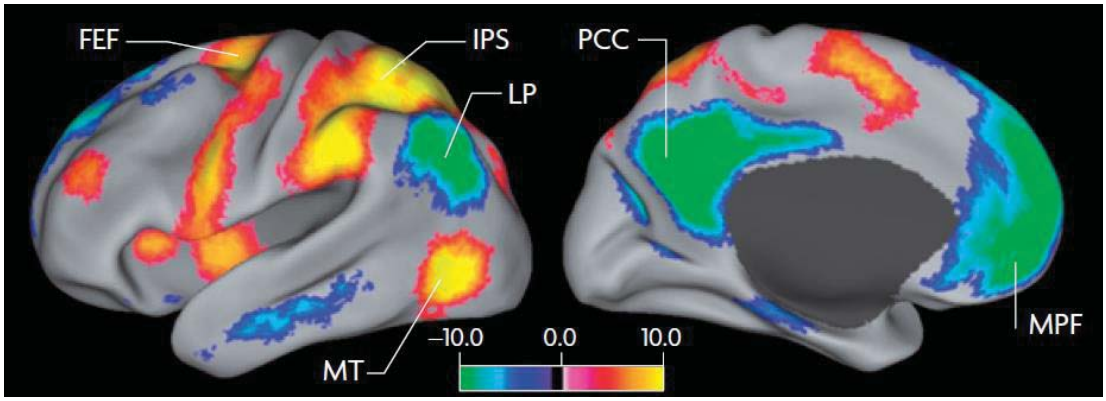

Figure 1-2 Anticorrelated networks in the human brain.
Task-positive network (TPN), shown in warm colours, is significantly correlated with regions involved in focused attention and working memory (intra-parietal sulcus (IPS), frontal eye field (FEF) and middle temporal (MT) area). DMN nodes (posterior cingulate/precuneus (PCC), lateral parietal cortex (LP) and medial prefrontal cortex (MPF)), shown in cool colours, are significantly correlated with task-negative areas and significantly anticorrelated with TPN. (Taken from Fox and Raichle, 2007.)

Fox et al. (2005) described a 'task-positive network (TPN)' that is diametrically opposite of DMN; these areas are routinely activated during goal-directed task performance (also called *dorsal attention system*) and they show anticorrelations with DMN regions at rest (Figure 1-2).

1.1.1.3 Methods for analysis of rs-fMRI data

Firstly, to separate spontaneous low frequency fluctuations from non-neuronal noise, certain steps can be followed (Fox and Raichle, 2007). A high sampling rate during data acquisition prevents aliasing by higher frequencies arising from cardiac or respiratory activity. Another method is the linear regression of physiological noise that was monitored during the experiments. Global signal regression or regression of ventricles/white matter can be included in the pre-processing pipeline of the acquired resting-state fMRI data.

Functional connectivity is defined as the temporal dependency of neuronal activation patterns of anatomically separated brain regions (Friston et al., 1993). In the context of resting-state fMRI experiments, functional connectivity is expressed as the level of correlated dynamics of fMRI time-series between brain areas (van den Heuvel and Hulshoff Pol, 2010).

Identification of spatial patterns of functional connectivity can be achieved with various analysis methods roughly classified into two: Model-dependent and model-free methods.

Model-dependent (seed) methods: The most straightforward way to examine the functional connections of a particular brain region is to correlate the resting-state time-series of the depicted brain region against the time-series of all other regions; resulting in a functional connectivity map (van den Heuvel and Hulshoff Pol, 2010). The advantage of seed analysis is the relative simplicity of the method and the ease with which to interpret the results. However, this type of analysis requires *a priori* assumptions on the data, necessary for the selection of the seed area (*see* Figure 1-3).

Model-free methods: In contrast to seed-based methods, model-free methods are designed to look for general patterns of connectivity across brain regions without *a priori* selected seeds (van den Heuvel and Hulshoff Pol, 2010). Independent component analysis (ICA) is the most commonly used method, providing a high level of consistency. ICA algorithms analyze the entire BOLD dataset and decompose it into components that are maximally independent in a statistical sense; each component is associated with a spatial component map (Fox and Raichle, 2007). Advantages of this method are that it is purely data-driven, and it automatically isolates the sources of noise. However, it requires a user-selected number of components, evaluation of resulting components is done by the user (i.e. neuronal vs. noise) and their interpretation is much more complex.

Taken together, seed-based and data-driven methods all tend to show strong overlap between their results; supporting the notion of robust formation of multiple functionally linked networks in the brain during resting-state (Fox and Raichle, 2007; van den Heuvel and Hulshoff Pol, 2010).

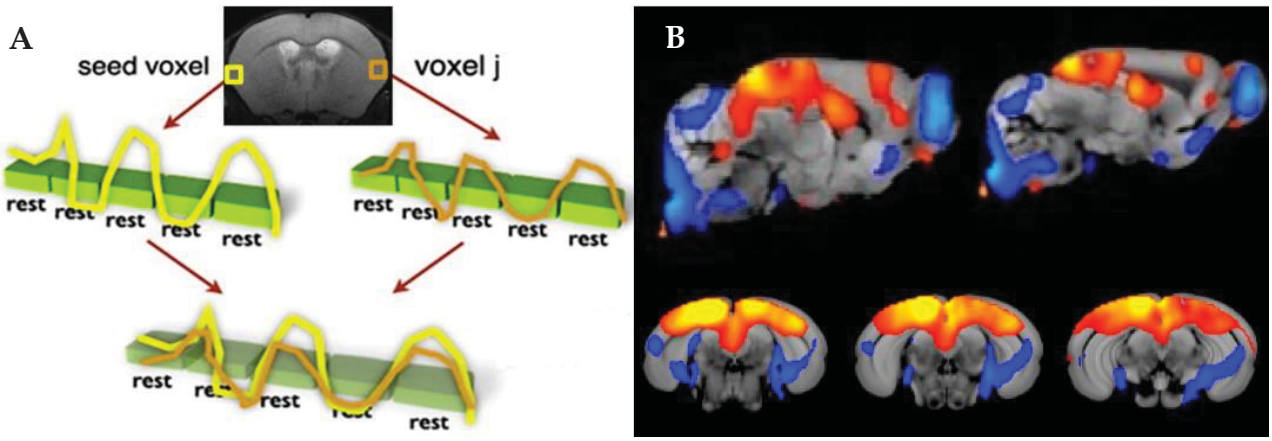

Figure 1-3 Simple schema of resting-state fMRI seed analysis and resulting resting-state functional connectivity maps.
A. High correlation between the time-series of seed voxel and the voxel j points to a functional connectivity between the two areas. (Adapted from van den Heuvel and Hulshoff Pol, 2010.) B. Warm colors represent positive correlations and cool colors represent anticorrelations with the seed area.

Graph analysis: Graph theory provides a theoretical framework in which the topology of complex networks is examined, revealing important information on both the local and global organization of functional brain networks. Graph analysis formulates brain networks as a collection of *nodes* representing brain regions and *edges*(also called *links*), the functional connections showing the correlation values between the time-series of the nodes (van den Heuvel and Hulshoff Pol, 2010). Graph analysis suggested that brain networks have an organization optimized towards a high level of local and global efficiency.

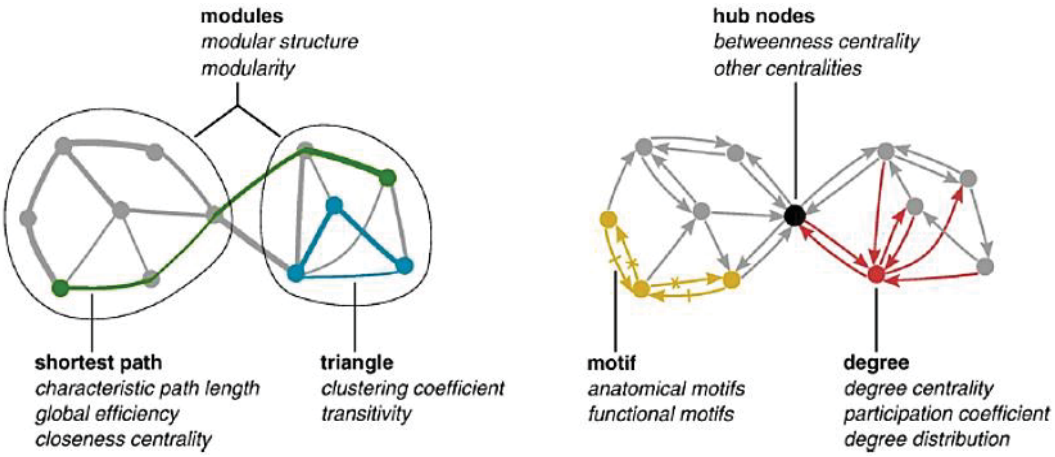

Figure 1-4 Certain metrics of network topology.
(Taken from Rubinov and Sporns, 2010.)

Graph theoretical measures commonly used in brain network analysis

Node *degree* is the number of links connected to the node.

Node *strength* is the sum of weights of links connected to the node.

The *clustering coefficient* (*CC*) is the fraction of triangles around a node and is equivalent to the fraction of node's neighbors that are neighbors of each other.

The characteristic path length (CPL) is the average shortest path length (SPL) in the network.

The *global efficiency* is the average inverse *shortest path length* (*SPL*) in the network and is inversely related to the *characteristic path length* (*CPL*).

The *local efficiency* is the global efficiency computed on the neighborhood of the node and is related to the clustering coefficient.

Node *betweenness centrality* is the fraction of all shortest paths in the network that contain a given node.

(Rubinov and Sporns, 2010)

1.1.2 Diffusion MRI and fiber tracking

Diffusion MRI allows probing of tissue structure on a microscopic scale by mapping displacements of water molecules as part of the physical diffusion process. It provides unique information on the fine architecture of neural tissues and to changes associated with various physiological and pathological states. Because the directedness of diffusion is associated with the underlying organization of white matter axonal bundles, diffusion MRI can also be used to map the fiber tracts in the brain in an in vivo and non-invasive manner (Le Bihan, 2003).

1.1.2.1 General information on diffusion MRI

Also known as 'Brownian motion', *diffusion* refers to the constant random microscopic molecular motion due to thermal energy. Einstein's equation (Einstein, 1905) gives the *diffusion coefficient (D)*- average displacement of a molecule over an area to the observation time (mm^2/s):

$$\langle r^2 \rangle = 6Dt$$

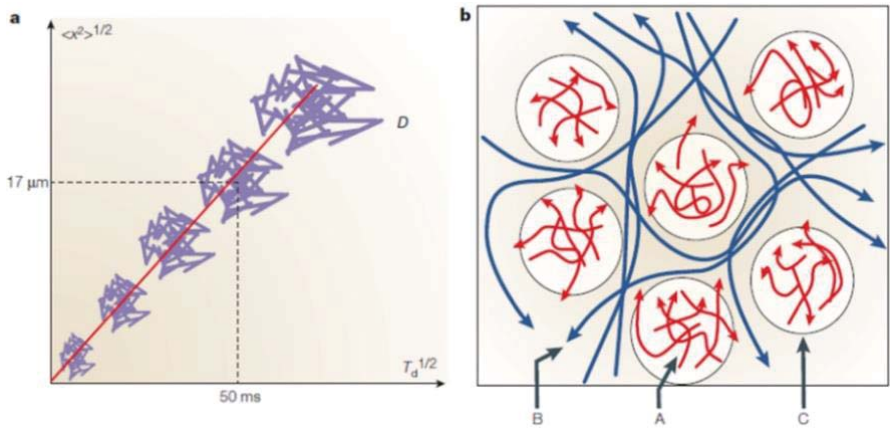

Figure 1-5 Water diffusion and tissue structure.
a. *The random displacements of molecules resulting from Brownian motion obey a statistical law formulated by Einstein (1905).* ***b.*** *In biological tissues, obstacles (i.e. cells, tortuous pathways, and exchange between compartments) modulate the free diffusion process. (Figure taken from Le Bihan, 2003.)*

In a free medium, molecular displacements obey a three-dimensional Gaussian distribution statistically described by diffusion coefficient (D). This constant depends on the size of the molecules, the temperature and the viscosity of the medium. Free water molecules at 37°C have a diffusion coefficient of 3×10^{-9} m^2/s. However, in biological tissues, diffusion is no longer 'free'; rather, molecules travel along the microscopic tissue structure. Water molecules bounce off, cross or interact with many tissue components, such as cell membranes, fibers and macromolecules. Because the movement is impeded by such obstacles, diffusion is restricted and displacement distribution is no longer Gaussian (Figure 1-5, above) (Le Bihan, 2003).

Diffusion weighted imaging: Diffusion weighted pulse sequence is constructed by the addition of a pair of diffusion sensitizing gradients (Stejskal and Tanner, 1965). Application of the first gradient pulse introduces a phase difference depending on the location of the molecules along the gradient axis. 10 to 100 ms after the first gradient pulse, another gradient along the same axis with opposite polarity is applied to refocus the phase differences. The refocusing is only perfect when the water molecules are immobile between the pulses. Because the signal at each voxel represents the sum of signals from all the water molecules in that voxel; the imperfect refocusing leads to a signal loss. Thus, MR signal is sensitized to the diffusion process; higher diffusion resulting in higher signal loss (Figure 1-6)(Le Bihan and Breton, 1985).

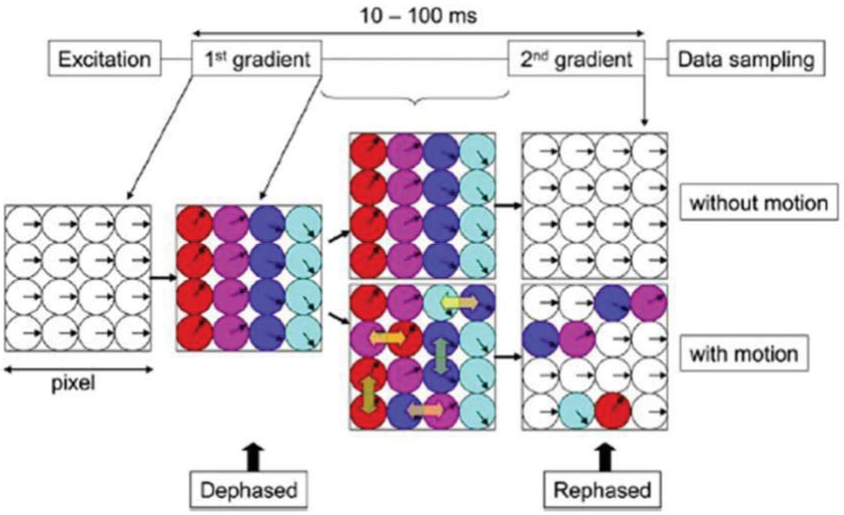

Figure 1-6 The relationship between the water motion and gradient applications.
(Figure taken from Mori and Zhang, 2006.)

b-factor is the measure of diffusion weighting that is a function of the strength, duration, and temporal spacing of the diffusion sensitizing gradients. Its unit is s/mm$_2$; the reciprocal to that of diffusion constant (Mukherjee et al., 2008). *Apparent diffusion coefficient (ADC)* is the diffusion constant measured with MRI, reflecting the fact that diffusion cannot be separated from other sources affecting water mobility. For instance, diffusion coefficient might be low due to viscosity of the environment directly related to diffusion process or due to many obstacles and barriers, diffusion might 'appear' slow (Mori and Zhang, 2006).

1.1.2.2 Quantifying diffusion anisotropy

Diffusion is said to be anisotropic when molecular mobility is not equal for all directions. In an ordered tissue, the measured apparent diffusion coefficient (ADC) will depend on the direction from which it is measured (Jones, 2008). White matter tracts with highly packed, coherently oriented fiber bundles hinder water displacement perpendicular to the direction of the fibers; resulting in larger ADC values parallel to the tracts rather than orthogonal to them. Hence, more than one diffusion-encoding direction is required to characterize regions of anisotropic diffusion (Moseley et al., 1990).

The model used to characterize diffusion anisotropy is the *diffusion tensor* which is a 3×3 symmetric matrix of numbers that characterizes three-dimensional water displacements. Diffusion tensor calculation requires at least six diffusion-encoded image sets along non-collinear directions in addition to at least one b=0 s/mm$_2$ image (Basser, et al. 1994). The diffusion tensor is often thought of in terms of an ellipsoid: a surface representing the distance that a molecule will diffuse to with equal probability from the origin. The principal axes of the ellipsoid are given by the eigenvectors, and the lengths are given by the diffusion distance at a given time. Ellipsoids are scaled according to square roots of diffusivities in each direction (i.e. eigenvalues) (Jones, 2008).

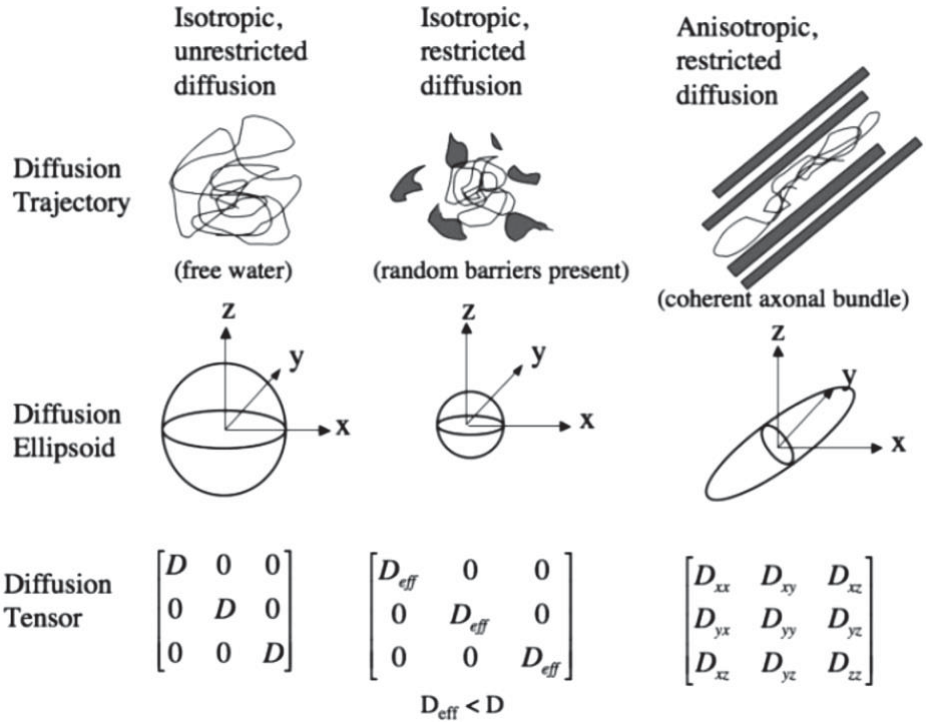

Figure 1-7 The diffusion ellipsoids and tensors for isotropic unrestricted diffusion, isotropic restricted diffusion, and anisotropic restricted diffusion.
(Figure taken from Mukherjee, et al. 2008.)

Degree of diffusion anisotropy determines the shape of the ellipsoid: in the case of isotropic diffusion where diffusion is equal in each direction, the ellipsoid would become a sphere. With a high degree of anisotropy, ellipsoid would become elongated or cigar-shaped (Mori and Zhang, 2006)(*see* Figure 1-7*,* above).

Diffusion tensor parameters: Three eigenvectors represent the three principal axes of the tensor and the three eigenvalues are the lengths of ellipsoid axes. The primary eigenvector with the largest eigenvalue gives the principal direction and magnitude of diffusion in the voxel. In white matter, this indicates the orientation of axonal fiber bundles. Parametric maps can be built from tensors to characterize the microstructure in a given voxel: *Axial diffusivity (AD)* maps show longitudinal diffusivity – along the main diffusion axis (λ_1); *radial diffusivity (R*D) maps show diffusivity perpendicular to the main axis (($\lambda_2 + \lambda_3$)/2), whereas *mean diffusivity (MD)* is a measure of rotationally invariant diffusion in a voxel (($\lambda_1+\lambda_2+\lambda_3$)/3) (Mukherjee et al., 2008).

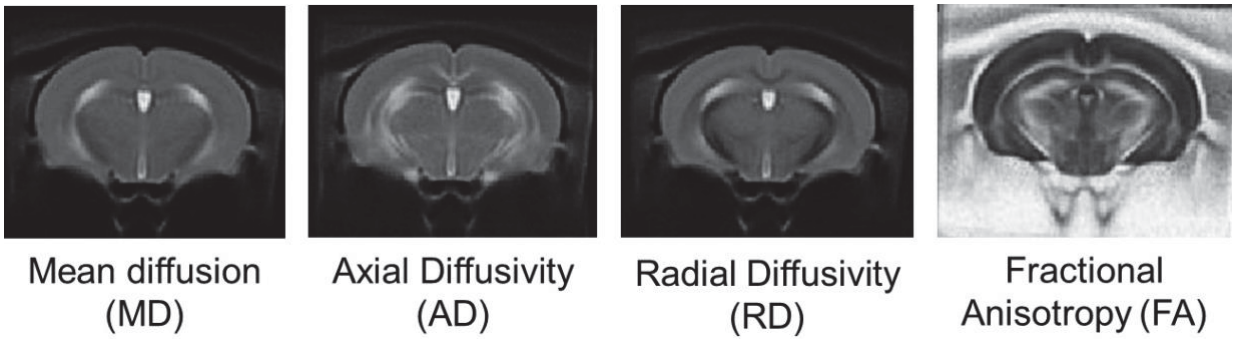

Figure 1-8 Parametric diffusion tensor maps of a mouse brain in coronal sections.

$$FA = \sqrt{\frac{3}{2}} \frac{(\lambda_1 - \langle\lambda\rangle)^2 + (\lambda_2 - \langle\lambda\rangle)^2 + (\lambda_3 - \langle\lambda\rangle)^2}{\lambda_1^2 + \lambda_2^2 + \lambda_3^2}$$

Fractional anisotropy (FA) is a normalized measure that expresses the directedness of diffusion in a scale ranging between 0 and 1. It takes the value 0 when diffusion is isotropic, and 1 when diffusion is constrained along one axis only (Basser and Pierpaoli, 1996).

Fiber orientation information inherent in the primary eigenvector can also be visualized on two dimensional images by assigning a color to each of three mutually orthogonal axes (Jones, 2008).

1.1.2.3 Fiber tracking

By the help of sophisticated computer algorithms, inter-voxel connectivity on the basis of anisotropic water diffusion can be calculated. In each brain voxel, the dominant direction of axonal tracts can be assumed to be parallel to the primary eigenvector of the diffusion tensor. Fiber tracking uses the diffusion tensor of each voxel to follow an axonal tract in three dimensions from voxel to voxel through the brain (Mukherjee et al., 2008).

Fiber tracking algorithms can be classified into two categories: *local* and *global* methods. Local methods construct fibers independently path-by-path. The reconstruction of long neuronal pathways is performed in small successive steps, either deterministically or probabilistically by following the local, voxel-wise defined distribution of fiber directions (Reisert et al., 2011). *Deterministic* fiber tracking algorithms calculate fiber trajectories by creating streamlines from the user-defined seed regions along the main diffusion directions in each voxel. Fiber construction halts when it reaches a voxel with low anisotropy value or the fiber exceeds a predefined turning angle (Mukherjee et al., 2008). *Probabilistic* algorithms, on the other hand, propagate a large number of pathways from each seed point rather than a single trajectory. Thus, a distribution of possible orientations is calculated. Stopping criterion for streamlines is the angular deviation between successive steps (Jones, 2008). Local methods have the advantage of being very fast; however, minor imperfections in the determination of local steps can accumulate and significantly affect the final result (Reisert et al., 2011).

Global methods try to reconstruct the fibers simultaneously by finding the configuration that describes best the measured data. Global tracking methods have better stability with respect to noise and imaging artefacts but the computation time is generally very long (Reisert et al., 2011). In this work, I used the global tracking method proposed by Reisert and colleagues (2011) and validated in the mouse brain (Harsan et al., 2013): Here the computational performance is greatly increased while the operator dependence is kept to a minimum. Briefly, the reconstructed fibers are built with small line segments that introduce the diffusion anisotropy. These elemental segments bind together during the optimization. Their orientation and numbers are adjusted simultaneously to match the data. In this method, there are no boundary conditions which minimize the necessary user interaction.

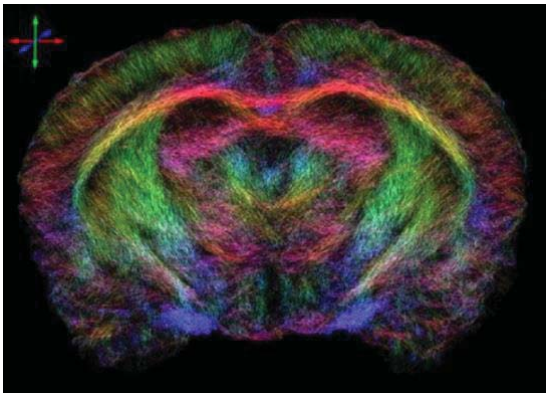

Figure 1-9 High resolution global fiber tracking map from a coronal section of the mouse brain.
Method proposed by Reisert, et al. 2011 was utilized for the creation of this image. (Colors denote fiber orientations: red, horizontal; green, dorso-ventral; blue, rostro-caudal.)

1.1.2.4 Applications of diffusion MRI

Diffusion MRI and fiber tracking methods are highly sensitive to microstructural changes in tissues; so that anomalies can be detected before changes appear in conventional T1 or T2-weighted images (Le Bihan, 2003). Tracking algorithms perform better in areas with high anisotropy; therefore, diffusion-based methods has found the largest application for the study of white matter disorders such as multiple sclerosis in literature (Fox, 2008).

In a preclinical model of cuprizone-induced demyelination (Sun et al. 2006), axonal damage was linked to decreased AD and demyelination lead to increased RD. Diffusion MRI could be exploited to monitor developing brain and myelination processes in fetuses, babies and during childhood (Schmithorst et al., 2002). Diffusion MRI can also be used to study more subtle, functional disorders related to dysconnectivity, such as psychiatric disorders (Le Bihan, 2003). In Figure 1-10 (below), some pathological processes that might result in changes in diffusion anisotropy and consequently the tensor representation are schematized.

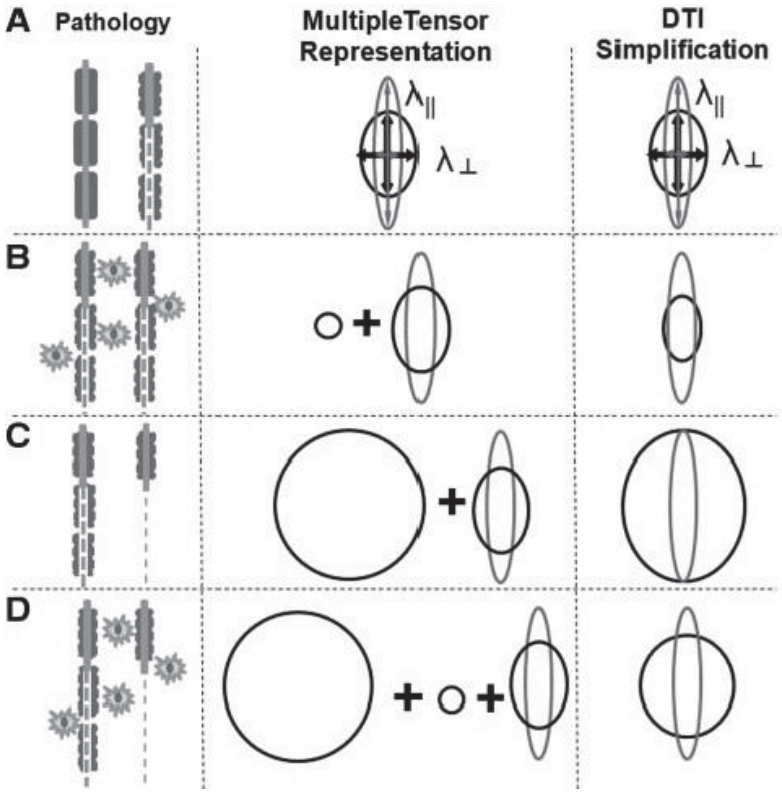

Figure 1-10 Different white matter pathologies associated multiple tensor representation and DTI simplification.
Grey ellipsoid represents the diffusion tensor profile for normal myelinated white matter. Black drawings represent the diffusion profiles for multiple tensor representation or DTI simplification: ***A.*** *co-existing axon and myelin injury of coherent pure myelinated axons;* ***B.*** *axon and myelin injury with cell infiltration;* ***C.*** *axon and myelin injury with axonal loss; and* ***D.*** *axon and myelin injury, cell infiltration or proliferation and axonal loss. (Figure taken from Wang, et al. 2011.)*

Limitations of diffusion MRI and tractography: Interpretation of both the diffusion tensor metrics and the fiber tracking maps can be difficult due to the inherent ambiguity of the data acquired with diffusion MRI (Mori and Zhang, 2006):

i. Firstly, there is no directionality information; whether the axons are oriented anterograde or retrograde cannot be determined by diffusion tensor imaging (DTI).

ii. Second issue arises from large voxel sizes; the effects of microscopic structures underlying diffusion anisotropy (i.e. protein filaments, cell membranes, and myelin) tend to be averaged over the voxel volume. Thus, the diffusion anisotropy can only be accurately detected with DTI when the microscopic sources of diffusion anisotropy are homogenously found in a macroscopic voxel (**Error! Reference source not found.**).

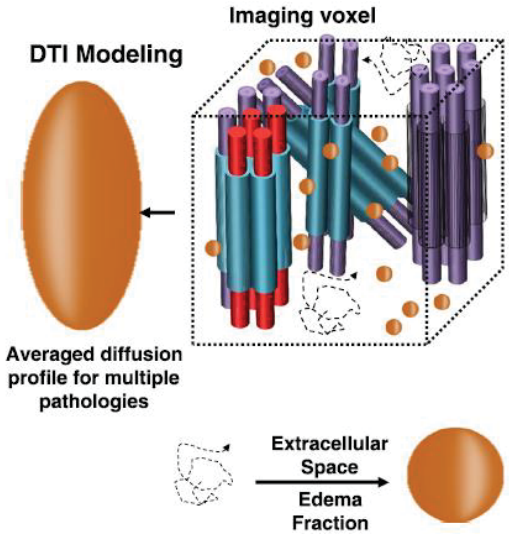

Figure 1-11 Averaging of diffusion anisotropy in a large imaging voxel in DTI.
(Figure adapted from Cross and Song, 2017.)

iii. Another crucial issue is the information reduction related to tensor modelling. For instance, there might be more than one fiber population within a voxel (i.e. crossing fibers, kissing fibers) and a single diffusion tensor cannot represent the orientations of these fibers (Jones, 2010; Jones et al., 2013). There are many proposals on alternative modelling approaches to simple tensors. Most of them are based on high angular resolution diffusion imaging (HARDI) (Tuch, 2004; Tuch et al., 2002) which uses acquisitions with tens to hundreds of diffusion gradient directions, allowing for a more complete description of the water displacements at the voxel level. Such approaches can provide the “orientation distribution function” within each voxel and therefore can resolve multiple fiber orientations within a single voxel.

iv. Finally, diffusion MRI is very sensitive to motion artefacts and together with long scan times required to acquire high resolution images, data quality might be compromised due to physiological motion.

1.1.3 Mouse brain connectome

Translational studies in the field of neuroscience can investigate hypotheses on the normal brain function as well as neuropsychiatric disease models in a well-controlled environment. In animal models- *rodents* in particular, it is possible to perform invasive recordings and stimulation along with genetic manipulations (e.g. optogenetics and chemogenetics), which are not feasible with human subjects. Rodent models can provide information on the fundamental neurophysiology and conserved biomarkers of disease which can pave the way for effective therapeutic interventions and can be translated into humans (Pan et al., 2015).

There is a considerable homology between human and rodent brains (Pan et al., 2015). Indeed, humans and rodents belong to the same subclass of placental mammals. Rostral to the brainstem and cerebellum common to all vertebrates, mammals share a common telencephalic organization consisting of basal ganglia, allocortex and neocortex. Placental mammals also have a large inter-cortical commissure; *corpus callosum*. All mammalian neocortices have primary and secondary representations of auditory, visual, somatosensory, multimodal association, and motor areas. Similar organization of brain structures in rodent and human is a strong rationale for translational studies focused on the rodent brain. Use of mouse as a model organism is further supported by the substantial number of genetically modified strains developed in the recent years as well as the ability to optogenetically (Boyden et al., 2005) and chemogenetically (Roth, 2016) manipulate specific neurons and circuits.

1.1.3.1 Resting-state fMRI in mice

Resting-state fMRI facilitates the study of brain function where task-based fMRI can be challenging (Pan et al., 2015). As no explicit task is needed, rs- fMRI method can be used both in rodents relatively easily. However, most rodent rs-fMRI studies require anesthesia to limit motion which might affect the results. Fortunately, resting-state networks including the default mode network (DMN) can also be detected in anesthetized rodent brain. This opens up opportunities for understanding the neurophysiological basis of the spontaneous BOLD fluctuations, the behavioral relevance of the network characteristics, connectomic deficits in diseases and treatment effects on brain connectivity in rodents (Chuang and Nasrallah, 2017).

Resting-state networks of the mouse brain: Although the very first resting-state fMRI studies in mice failed to show bilaterally symmetric connectivity between homotopic regions (Guilfoyle et al., 2013; Jonckers et al., 2011); further investigations demonstrated the existence of bilateral and distributed functional connectivity networks within the mouse brain, identifying both cortical and subcortical networks (Grandjean et al., 2014 ; Mechling et al., 2014 ; Nasrallah et al., 2014; Sforazzini et al., 2014). These findings underscore the presence of spontaneous interhemispheric homotopic fluctuations as a fundamental neuro-architectural trait of the mammalian brain (Gozzi and Schwarz, 2016).

Similarly, antero-posterior connectivity along the midline structures of the brain (i.e. *prefrontal and orbitofrontal cortices, cingulate and retrosplenial areas, peri-/ventro-hippocampal areas*) corresponding to an evolutionarily-conserved homologue of the DMN was detected with mouse rs-fMRI in several studies (Sforazzini et al., 2014; Shah et al., 2016b; Zerbi et al., 2015).

In addition, a network encompassing ventrolateral striatum, nucleus accumbens, anterior insula and cingulate, similar to human salience network was identified in mouse (Sforazzini et al.,

2014). Another feature of human resting-state networks, namely the anti-correlations, were found in mouse resting-state fMRI under different anesthetics (Grandjean et al., 2014; Liska et al., 2015; Sforazzini et al., 2014).

As described before, functional parcellation of the brain in resting-state can be achieved with different analysis methods. Mechling and colleagues (2014) used an ICA algorithm to parcellate mouse brain into more than ninety functional components including both cortical and subcortical structures. They were able to identify five bilaterally symmetric network modules (i.e. *sensorimotor and limbic, basal ganglia, cingulate area, visual processing and memory, hypothalamus modules*) under medetomidine (an α2-agonist commonly used in veterinary practice) sedation. Liska et al. (2015), on the other hand, used a voxel-wise correlation method in halothane-anesthetized mice and identified six modules: DMN, lateral cortical, hippocampus, basal forebrain, ventral midbrain and thalamic modules. Identification of functional network modules overlapping to a reasonable extent under different anesthetics and parcellation methods indicate reproducibility of mouse resting-state networks.

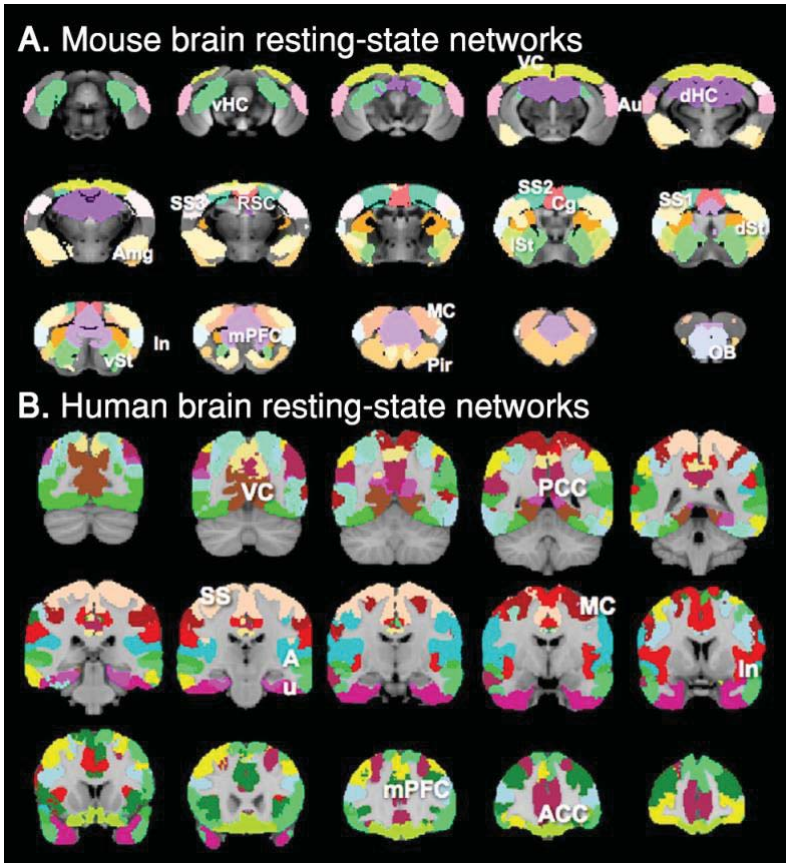

Figure 1-12 Resting-state networks (RSNs) of mouse and human brain.
A. *Mouse brain RSNs.* ***B.*** *Human brain RSNs. The labels indicate similar networks that can be identified among species. [ACC: anterior cingulate (equivalent to Cg in rodents); Amg: amygdala; Au: auditory cortex; Cg: cingulate cortex (equivalent to ACC in humans); dHC: dorsal hippocampus; dSt: dorsal striatum; In: insular cortex; lSt: lateral striatum; mPFC: medial prefrontal cortex; MC: motor cortex; PCC: posterior cingulate (equivalent to RSC in rodents); Pir: piriform cortex; RSC: retrosplenial cortex (equivalent to PCC in humans); SS1,2,3: somatosensory area 1,2,3; VC: visual cortex; vHC: ventral hippocampus.] From top to bottom: posterior to anterior. (Adapted from Chung and Nasrallah, 2017.)*

Effects of anesthesia on functional networks: Use of anesthesia in mouse resting-state fMRI is a prerequisite for obtaining reliable and interpretable data; anesthesia alleviates stress and prevents motion (Pan et al., 2015). However, anesthesia is known to elicit complicated effects on neural, metabolic and hemodynamic responses (Chuang and Nasrallah, 2017).

Anesthetics are a potential confound for rs-fMRI studies. Fortunately the influence of anesthesia appears to only modulate neurovascular coupling rather than completely abolishing it (Pan et al., 2013). Studies have demonstrated that rodent resting-state networks are highly reproducible and consistent across different anesthesia regimens at optimal doses (Chuang and Nasrallah, 2017). Interfering effect of anesthesia appears to be dose-dependent (Gozzi and Schwarz, 2016); neural effects of anesthesia mainly arises from sites of anesthetic action, associated downstream neural activities, and the regions related to unconsciousness and arousal (Chuang and Nasrallah, 2017). Anesthetics can also affect the cardiopulmonary and vascular functions, leading to systemic changes in blood oxygenation, basal cerebral blood flow (CBF), vascular reactivity, and neurovascular coupling. Certain anesthetics possess analgesic effects which would influence pain-related networks in the brain (Chuang and Nasrallah, 2017). Additionally, not only the dosage but also the route and timing of delivery can have an influence on the resting-state networks; as a rule, continuous delivery ensures more stable anesthesia depth and physiological states in comparison to bolus administration. Anesthetic effects are also animal species, gender, age, or disease-state dependent (Chuang and Nasrallah, 2017).

Methodological considerations for mouse rs-fMRI studies: Maintaining stable physiology is paramount for resting-state fMRI; constant monitoring and control of anesthetic dose, body temperature, blood oxygenation, respiratory and cardiac rates are crucial to obtain high quality data. Physiological recordings can also be used for removing nuisance signals later in the processing of data. Consistency in the use of strains, gender, age, weight, and housing conditions of animals are necessary to ensure reproducibility (Pan et al., 2015).

Most rodent rs-fMRI studies follow similar procedures to those designed for humans. However, due to very different brain size, shape, and tissue proportions, there are several aspects related to acquisition, pre-processing and analysis that need to be considered (Chuang and Nasrallah, 2017).

For the data acquisition, specialized high field scanners are used for rodent imaging: scanners with smaller bore size (20-30 cm) with field strengths 7, 9.4 or 11.7 T are common. Higher field strengths are necessary to increase the signal to noise ratios; in addition, strong gradients for higher spatial resolution and higher order shims for minimizing distortions are needed (Pan et al., 2015). These shims are additional electrical currents which are used to render the magnetic fields more uniform. Higher order shims have more complex geometrical configurations created by the electrical currents.

Table 1-1 Summary of anesthetics and their effects used commonly in rodent rs-fMRI studies.

(Taken from Chuang and Nasrallah, 2017.)

Anesthesia/Sedative	Neural effect	Vascular effect	Functional connectivity	Species and Reference
α-chloralose	• GABAergic	Minimal but increases CBF due to acidosis	• Reduces bilateral FC dose dependently	• Rat (Lu et al., 2007; Williams et al., 2010) • Mouse (Jonckers et al., 2014)
Isoflurane	• Glutamatergic, GABAergic • Burst-suppression activity	Vasodilation	• Increases FC at mid dose due to burst-suppression activity. • Abolishes FC at high dose.	• Rat (Bukhari et al., 2017; Hutchison et al., 2014; Kalthoff et al., 2013; Liu et al., 2011; Liu et al., 2013b; Nasrallah et al., 2014a; Williams et al., 2010) • Mouse (Grandjean et al., 2014a; Jonckers et al., 2014)
Medetomidine	• Adrenergic • Sedative • Potential epileptic effect	Vasoconstriction without affecting neurovascular coupling	• Reduces bilateral FC dose, region and time dependently	• Rat (Nasrallah et al., 2014a, 2012b; Pawela et al., 2008; Williams et al., 2010; Zhao et al., 2008) • Mouse (Grandjean et al., 2014a; Nasrallah et al., 2014c)
Medetomidine + isoflurane	• Stable sedation • Suppresses potential epileptic effect	Decreases pCO_2 after a long period	• Stable FC for up to 3 h	• Rat (Brynildsen et al., 2017; Fukuda et al., 2013; Lu et al., 2012) • Mouse (Grandjean et al., 2014a)
Propofol	• GABAergic • Hypnotic at low dose and deep anesthesia at high dose	Minimal but reduces CBF at high dose	• Cortical FC reduced with dose • Regions related to arousal do not change with dose	• Rat (Liu et al., 2013a) • Mouse (Grandjean et al., 2014a)
Urethane	• Glutamatergic, GABAergic • Induces sleep-like states	Minimal but could induce slow hemodynamic oscillation	• Reduces bilateral FC with dose • FC dependent on fast or slow wave state	• Rat (Wilson et al., 2011; Zhurakovskaya et al., 2016) • Mouse (Grandjean et al., 2014a; Jonckers et al., 2014)
Awake	• Potential chronic stress • Pain sensitivity	Minimal	• Generally stronger FC • Stronger anti-correlation	• Rat (Becerra et al., 2011; Liang et al., 2012a, 2011) • Mouse (Jonckers et al., 2014)

Pre-processing pipelines of acquired data are very similar to those of human data; they generally include motion correction, band-pass filtering, de-trending, removal of nuisance covariates (i.e. *global signal regression or white matter/cerebrospinal fluid regression*) and smoothing. Normalization of images into a common stereotaxic space is also required for group analysis in mice data. Allen Mouse Brain Atlas (Lein et al., 2007) is a high definition reference atlas accompanied by a systematic, hierarchically organized taxonomy of brain structures. It is frequently used as a reference space in mouse rs-fMRI studies. Further data analysis can be performed with seed-based or data-driven (i.e. *ICA, graph theory*) methods discussed above.

1.1.3.2 Integration of functional and structural connectivity

In the animal brain, anterograde (or retrograde) and monosynaptic tract tracers can be utilized to determine the direction and density of axonal tracts between brain regions to reveal the circuitry of the brain (Oh et al., 2014; Zingg et al., 2014). Good correspondence between regions with strong direct projections and functional connectivity strength have been found for DMN (Stafford et al., 2014) and other cortical networks (Bergmann et al., 2016; Grandjean et al., 2017). Grandjean and colleagues (2017) suggested that cortical functional connectivity is mostly associated with monosynaptic projections whereas subcortical connectivity tends to depend on polysynaptic projections.

Hübner et al. (2017) studied cuprizone model of demyelinating pathology using both rs-fMRI and DTI methods. Their findings suggest that with loss of myelin, the functional connectivity decreases globally and the normal relation between white matter fractional anisotropy (FA) and functional connectivity ceases to exist. Furthermore, in mice strains characteristically lacking corpus callosum (e.g. *I/LnJ; BTBR*), inter-hemispherical functional connectivity was found to be decreased. Similarly, complete callosotomy resulted in fully disturbed bilateral functional connectivity (Magnuson et al., 2014) whereas partial callosotomy was observed to recover partially, possibly indicating the plasticity mediated by remaining projections (Zhou et al., 2014).

These findings highlight the importance of axonal connectivity that subserves the resting-state network topology and activity; and the potential plasticity that may occur to maintain the networks and their associated functions (Chuang and Nasrallah, 2017).

1.2 Neuropathic pain

1.2.1 Definition and Pathophysiology

Pain is an unpleasant sensory and emotional experience associated with actual or potential tissue damage, or described in terms of such damage (IASP 2011). While acute pain is a survival mechanism that serves as a warning sign and promotes self-preservation; chronic pain confers no individual or evolutionary advantage (Cohen and Mao, 2014). During my thesis, I focused my attention on one specific type of chronic pain: Namely, neuropathic pain, which is caused by a lesion or disease affecting the somatosensory system including peripheral fibers (i.e. Aβ, Aδ and C fibers) and central neurons (Colloca et al., 2017). Neuropathic pain affects 7 to 10% of the population and its incidence is likely to increase owing to ageing global population. It is more common in females and after the age of 50 years (Colloca et al., 2017). Around 15-25% of people with chronic pain are currently thought to suffer from neuropathic pain (Cohen and Mao, 2014). Comorbidities such as poor sleep, anxiety and depression are frequent in neuropathic pain and it greatly impairs quality of life and has a high socioeconomic impact on society (von Hehn et al., 2012).

Symptoms of neuropathic pain include *spontaneous pain*- either continuous or paroxysmal- such as burning and electrical-like sensations or *evoked pain* resulting from non-painful stimulation (allodynia) as well as increased responses to painful stimuli (hyperalgesia) (von Hehn et al., 2012). Neuropathic pain can be classified into two: central and peripheral neuropathic pain (Colloca et al., 2017).

i. Central neuropathic pain arises due to spinal cord and brain disorders: for example, cerebrovascular diseases affecting the central somatosensory pathways (post-stroke pain), neurodegenerative disorders (notably Parkinson's), spinal cord injury, syringomyelia, demyelinating diseases (e.g. multiple sclerosis, transverse myelitis, neuromyelitis optica).

ii. Peripheral neuropathic pain can display generalized (usually symmetrical) or focal distribution. Causes of generalized peripheral neuropathic pain include diabetes or pre-diabetes, infections (e.g. HIV, leprosy), chemotherapy, immunological *(*Guillain-Barré) or inflammatory processes and inherited channelopathies. Focal neuropathic pain is caused by lesion of one or more peripheral nerves or nerve roots: for instance, post-herpetic neuralgia, post-traumatic neuropathy, trigeminal neuralgia, entrapment syndromes, HIV, leprosy, diabetes mellitus and complex regional pain syndrome (CRPS) type II.

Associated terms

Allodynia: Pain due to a stimulus that does not normally provoke pain.

Hyperalgesia: Increased pain from a stimulus that normally provokes pain.

Hypoesthesia: Decreased sensitivity to stimulation, excluding the special senses.

Windup: Progressive increase in the frequency and magnitude of firing of dorsal horn neurons produced by repetitive activation of C fibers above a critical threshold, leading to a perceived increase in pain intensity.

Nociceptor: A high-threshold sensory receptor of the peripheral somatosensory nervous system that is capable of transducing and encoding noxious stimuli.

Second-order nociceptive neurons: Nociceptive neurons in the central nervous system (CNS) that are activated by the Aβ, Aδ and C afferent fibers and convey sensory information from the spinal cord to other spinal circuits and the brain.

Central sensitization: Increased responsiveness of nociceptive neurons in the central nervous system to their normal or subthreshold afferent input.

Peripheral sensitization: Increased responsiveness and reduced threshold of nociceptive neurons in the periphery to the stimulation of their receptive fields.

(IASP 2011; Cohen and Mao 2014; Colloca et al. 2017)

Neuropathic pain appears as a result of pain signaling changes: peripheral neuropathy alters the electrical properties of sensory nerves, which then leads to imbalance between central excitatory and inhibitory signaling such that inhibitory interneurons and descending modulatory systems are impaired. In turn, transmission of sensory signals and disinhibition or facilitation mechanisms are altered at the level of spinal cord dorsal horn neurons (Colloca et al., 2017). Long-term plasticity changes in sensory pathways underlie the cellular mechanisms for behavioral sensitization in neuropathic pain (Zhuo et al., 2011). In the following sections, I will give a brief overview of the current state of knowledge on mechanisms underlying neuropathic pain.

1.2.1.1 Peripheral mechanisms

Peripheral processes for the generation of pain are the conversion of noxious stimuli to nociceptive signals, termed *transduction* and relay of nociceptive signals from the site of injury to the CNS, termed *transmission* (Cohen and Mao, 2014). Any disruption in these processes result in positive (i.e. gain of function) and negative (i.e. loss of function) sensory symptoms and signs, collectively named ‘pain fingerprint’ (von Hehn et al., 2012).

Peripheral sensitization: Once injury occurs, inflammation and reparatory processes ensue, leading to a hyperexcitable state known as peripheral sensitization. Inflammatory mediators (e.g. CGRP, substance P) induce increased vascular permeability, edema, and leakage of byproducts of injury such as prostaglandins, bradykinin, growth factors, and cytokines. These substances sensitize and excite nociceptors; lowering their firing thresholds and causing ectopic discharges (Cohen and Mao, 2014).

Ectopic activity: Ectopic discharges along the nociceptive pathways after nerve injury can generate spontaneous pain in the absence of any external stimuli (von Hehn et al., 2012). Most frequently, hyperexcitability of primary sensory neurons induce ectopic action potentials leading to paresthesia, dysthesia, and spontaneous pain of differing features (e.g. continuous vs. episodic; superficial vs. deep; burning vs. shock-like) depending on the fibers affected. Even uninjured neighboring fibers can give rise to spontaneous pain via non-synaptic cross-talk, termed *ephaptic transmission* (Cohen and Mao, 2014).

Nerve injury drastically changes the expression, distribution, and phosphorylation of several ion channels in sensory neurons leading to changes in intrinsic membrane properties and generation of membrane potential oscillations resulting in rhythmic firing bursts in the absence of a stimulus. Downregulation of potassium channels, spontaneous sodium currents, mixed cation current through hyperpolarization-activated cyclic nucleotide-gated channels (HCN), activation of low threshold T-type calcium channels, changes in the expression profile of voltage-gated sodium channels, and downregulation of voltage-gated potassium channels contribute to hyperexcitability and generation of ectopic discharges (von Hehn et al., 2012).

1.2.1.2 Spinal mechanisms

Central sensitization: Ongoing discharge of peripheral afferent fibers with concomitant release of excitatory amino acids and neuropeptides leads to postsynaptic changes in second-order nociceptive neurons in the dorsal horn resulting in an excess of signaling (Colloca et al., 2017) and long-lasting synaptic plasticity that facilitates nociceptive processing, called *central sensitization* (von Hehn et al., 2012). Central sensitization provides a mechanism where nociceptive neurons have reduced thresholds, increased receptive field sizes and altered firing temporal dynamics. All these changes contribute to the generation of dynamic mechanical allodynia, hyperalgesia, and temporal summation.

Central sensitization results from homo-synaptic - similar to long term potentiation (LTP) - and hetero-synaptic (i.e. by a spread of the change in synaptic strength from activated to neighboring non-activated synapses) facilitation mechanisms. For homo-synaptic facilitation, alterations in postsynaptic calcium levels, caused by calcium influx through ionotropic receptors and voltage-gated calcium channels or by release from intracellular stores on activation of metabotropic receptors or receptor tyrosine kinases, initiate change in synaptic strength. Calcium-dependent intracellular signaling pathways produce posttranslational and transcriptional changes in various effector proteins, altering their levels, distribution, and functional activity. Some of the major players of activity-dependent central sensitization are NMDA and AMPA glutamate receptors, substance P NK1 receptor, BDNF and its TrkB receptor, CaMKII, PKA and PKC (von Hehn et al., 2012).

In hetero-synaptic facilitation, nociceptor-derived input can enable subsequent long-lasting facilitation of responses to input from low threshold Aβ and C fibers, and to afferent inputs from topographically different locations (von Hehn et al., 2012).

Glutamatergic regulation: Persistent and enhanced activation of ionotropic (NMDA, AMPA) and metabotropic glutamate receptors along with downregulation of glutamate transporters reduce the activation thresholds of glutamate receptors, increase neuronal excitability, and cause neurotoxicity. For instance, the progressive increase in the frequency and magnitude of firing of dorsal horn neurons produced by repetitive activation of C fibers, called *windup*, requires NMDA receptor activity (Cohen and Mao, 2014).

Loss of inhibition: After nerve injury, there is a loss of inhibitory currents at the spinal level as a result of dysfunctional GABA production and release, impaired intracellular homeostasis from reduced activity of K^+Cl^- cotransporter or increased activity of Na^+K^+-Cl^- cotransporter, leading to increased Cl^- levels; and apoptosis of spinal inhibitory interneurons. Loss of inhibition provokes tactile allodynia, hyperalgesia, and transmission of non-painful stimuli through Aβ fibers to nociceptive second-order neurons in the dorsal horn.

Glial mechanisms: Glial cells comprise about 70% of the CNS and play an important role in maintenance and homeostasis. Microglia are activated within 24 hours of nerve injury, and astrocytes follow shortly thereafter, with activation persisting for up to 12 weeks (Cohen and Mao, 2014). While previous experiments hypothesis that microglia might be important for initiation while astrocytes are important for maintenance of neuropathic pain (Zhuo et al., 2011), our unpublished data showed increased microglial activity even after the 8 weeks of neuropathic pain.

1.2.1.3 Supraspinal mechanisms

Standard view of central sensitization as a peripherally initiated process must be supplemented with the supraspinal mechanisms of brain reorganization, in order to account for the long-term maintenance (i.e. chronicity) of central sensitization (Farmer et al., 2012). Descending pathways that modulate the transmission of nociceptive signals originate in periaqueductal gray (PAG), locus coeruleus, anterior cingulate cortex (ACC), amygdala, and hypothalamus, and are mostly relayed through brainstem nuclei in the PAG and medulla to the spinal cord; although direct connections from cortical structures to spinal cord do exist (Chen et al., 2018). Descending modulation can be both inhibitory and faciliatory, with conflicting signals often arising from the same regions. The balance between inhibition and facilitation is dynamic and influenced by context, behavior, emotions, timing, and pathology. The neurotransmitters involved in descending modulatory pathways include noradrenaline (norepinephrine), 5-hydroxytryptamine (5-HT or serotonin), dopamine, and endogenous opioids (Cohen and Mao, 2014).

After nerve injury, several processes take place that mitigate the normal pain attenuating pathways: tonic noradrenergic inhibition decreases, and serotonergic modulation becomes predominantly facilitative. The initial spike mediated by changes in the activation and expression of glutamatergic receptors after injury is followed by a decrease in the excitability of rostral ventromedial medulla (RVM); which results in both facilitation and inhibition (Cohen and Mao, 2014). Furthermore, supraspinal centers such as ACC, prefrontal cortex (PFC), amygdala and PAG have been implicated in central sensitization, pathological plasticity and comorbidities associated with neuropathic pain (e.g. anxiety, major depression, and sleep disturbances); with detected alterations in brain structure and function in neuroimaging studies.

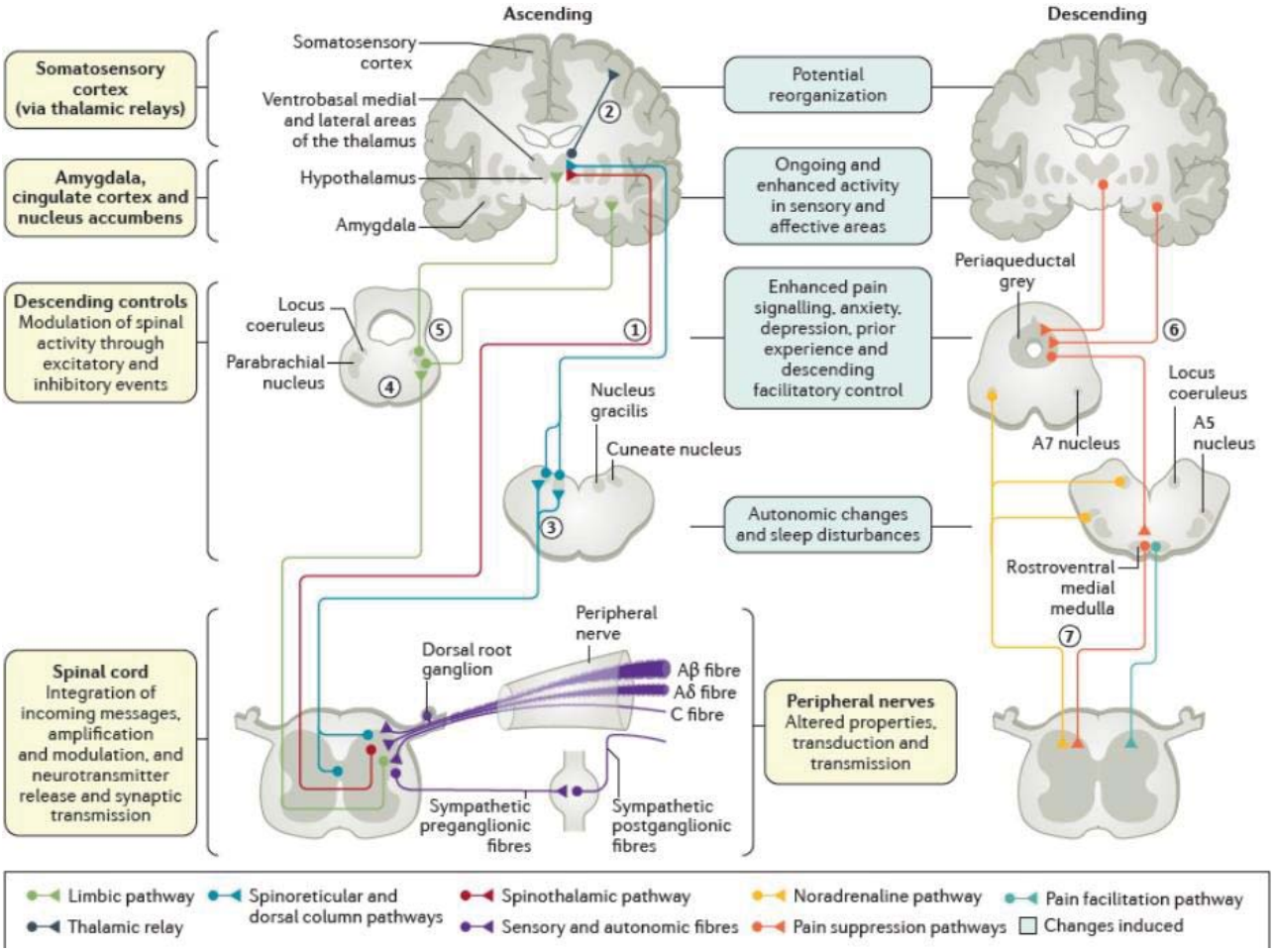

Figure 1-13 The peripheral and central changes induced by nerve injury or peripheral neuropathy.
(Schema taken from Colloca, et al. 2017.)

Neuroimaging techniques are especially well-suited for investigating brain mechanisms of chronic pain and comorbid conditions: in addition to relatively easy translation between animal models and patient populations; longitudinal experiments allow for surveying disease progression and treatment responsiveness in relation to brain function.

1.2.2 Magnetic resonance imaging of pain and chronic pain conditions

Neuroimaging can reveal the location and characteristics of brain responses to acute pain and plasticity associated with chronic pain (Davis and Moayedi, 2013). A variety of functional brain imaging techniques, including fMRI, PET, electroencephalography (EEG) and magnetoencephalography (MEG), have been utilized in the study of pain and in particular, chronic pain (Schmidt-Wilcke 2015). The most influential technique has been fMRI due to its fairly high spatial and temporal resolution, and the fact that no contrast agents or radioactive substances are required to image neural activation. In the next few sections, I will give an overview of the so-called 'pain matrix' (i.e. a set of areas sequentially activated in acute pain experience, as shown with functional neuroimaging); resuming with clinical imaging of chronic pain disorders, and finally, preclinical imaging of pain models.

1.2.2.1 Concept of a 'Pain matrix'

Pain experience is a multi-dimensional phenomenon with sensory-discriminative, affective-motivational, motor, and autonomic components (Seifert and Maihöfner, 2009); accordingly, functional neuroimaging studies have consistently identified several brain regions activated during nociceptive stimulation including thalamus, primary and secondary somatosensory areas, insula, ACC and PFC; collectively named the 'pain matrix'. The term originates from 'neuromatrix', first described by Melzack (1990, 2005), as a widespread ensemble of neurons integrating various sources of input - both nociceptive and non-nociceptive, processing information and generating patterns felt as a whole body possessing a sense of self. In this view, the pain matrix is composed of two parallel systems: *lateral* pain system responsible for perception of location and intensity of pain; and a *medial* pain system that includes ACC and parts of the insula related to affective-motivational processing of pain (Seifert and Maihöfner, 2009).

However, many of the regions belonging to pain matrix respond to stimuli other than nociception, there is no cortical area devoted exclusively to the initial processing of thalamo-cortical nociceptive input, and nociceptive specific neurons are sparsely distributed in space. Furthermore, the magnitude of the elicited brain responses in pain matrix can be dissociated from both the intensity of noxious stimulus and that of perceived pain. The brain responses to pain seem to be attentional context-dependent; novelty and unpredictability- that is to say *saliency* of stimuli determine the brain activation. These findings have led some researchers to characterize the aforementioned brain areas as a multimodal network related to the detection of saliency (Iannetti and Mouraux, 2010).

Nevertheless, pain matrix can be viewed as an interacting networks system: different orders of cortical networks, from cortical nociception to the conscious experience defined as pain. Pain itself is subject to reappraisal by internal states, feelings and beliefs before turning into memories (Garcia-Larrea and Peyron, 2013):

i. First-order processing (nociceptive matrix): Primate spinothalamic system, carrying nociceptive information, originates from spinal laminae I, V and VII and reaches posterior nuclei of thalamus. Nociceptive thalamo-cortical projections then reach posterior insula (~40%), medial parietal operculum (~30%-includes somatosensory areas) and midcingulate cortex (MCC, ~24%). Posterior insula and parietal operculum are the only areas where stimulation triggers acute pain, lesions cause selective pain deficits and injury causes neuropathic pain. However, transition from

nociception to conscious pain and its multiple attentional modulations requires the recruitment of a second set of areas.

ii. Second-order perceptual matrix: Other regions comprising the pain matrix, namely, mid-/anterior insula, ACC, PFC and posterior parietal areas are not direct targets of spinothalamic system, their direct stimulation does not evoke pain, or their selective destruction does not induce analgesia. These areas are also activated in contexts that are not related to pain and their contribution to pain experience depends on the context in which noxious stimuli are applied. The joint activity of the nociceptive and second order matrices is essential to ensure the modulation of vegetative reactions and internal feelings via anterior insular networks, the attentional modulation of sensory gain by top-down and bottom-up transactions and the conscious perception of pain via distributed brain activation.

iii. Third-order networks: High-level polymodal regions outside the classical pain matrix (i.e. pregenual cingulate, orbitofrontal cortex (OFC), temporal pole and anterolateral PFC) assign emotional significance, affective states and emotional responses to pain stimuli can enhance or attenuate subjective pain. Changes in the subjective pain require no adjustment of sensory gain but rather reappraisal of immediate pain perceptions. These areas have strong interconnections to subcortical descending pain control regions (e.g. PAG) and may also contribute to changes in the activity of ascending nociceptive systems (Garcia-Larrea and Peyron, 2013).

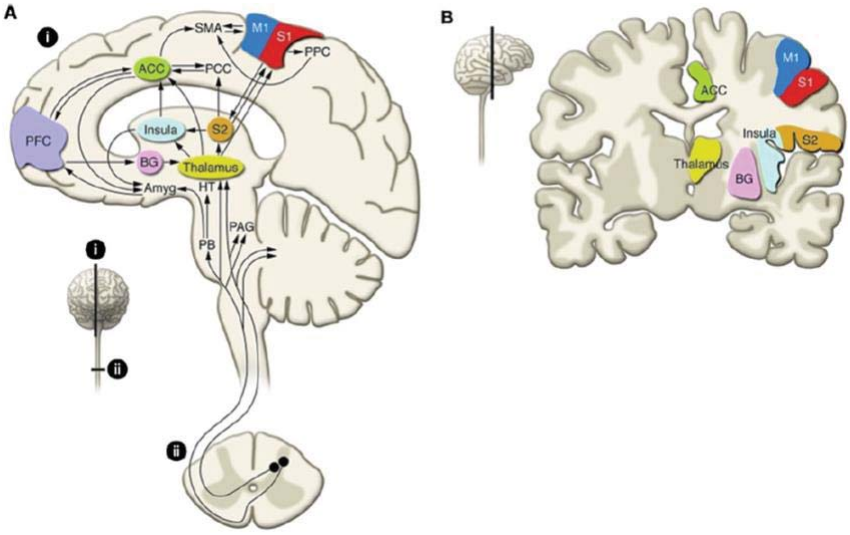

Figure 1-14 Graphical depiction of the 'pain matrix' of the human brain.
A. *sagittal;* ***B.*** *coronal views. (Adapted from Thompson and Bushnell, 2012.)*

In contrast to acute pain, chronic pain cannot be regarded as a state of continuous nociceptive inputs to an otherwise normally functioning brain. Neuroplastic remodeling occurs on various levels of nervous system ranging from synaptic plasticity to reorganization of large scale neural networks, which can lead to the maintenance of pain even in the absence of nociceptive stimuli (Schmidt-Wilcke 2015). In a chronic pain state, there may be abnormal pain and/or salience/attention-related activity, disturbances in connectivity and/or morphology of the pain, attention and descending pain control networks (Davis and Moayedi, 2013). These abnormalities may represent pre-existing vulnerabilities or arise from disease/pain-driven plasticity.

1.2.2.2 Structural MRI in chronic pain conditions

In chronic pain, the brain regions commonly showing gray matter abnormalities are as follows: prefrontal cortex (PFC), insula, anterior cingulate cortex (ACC), mid-cingulate cortex (MCC), posterior cingulate cortex (PCC), thalamus, basal ganglia, somatosensory areas, supplementary motor area (SMA), temporal lobe, and brainstem (Davis and Moayedi, 2013). Most of the studies report a decrease in gray matter density/volume or a decrease in cortical thickness (Schmidt-Wilcke 2015) with the exceptions of basal ganglia, thalamus and brainstem. Volumetric alterations were described for neuropathic pain conditions: trigeminal neuralgia was linked with reductions in primary sensory cortex, anterior insula, putamen, NAc and thalamus volumes as well as increases in posterior insular area (Gustin et al., 2011). Yoon et al. (2013) found decreases in the gray matter volume of left dorsolateral PFC, bilateral insula, and subgenual ACC in patients with neuropathic pain following spinal cord injury.

Furthermore, voxel-based morphometry (VBM) study of a chronic back pain (CBP) population (Apkarian et al. 2004) showed decreases in the volume of dorsolateral PFC and right thalamus. In another study in this disorder (Schmidt-Wilcke et al. 2006), bilateral basal ganglia and left thalamus volumes were found to be increased. Patients with tension-type headache displayed reductions in dorsolateral prefrontal, somatosensory areas, and pons volumes (Schmidt-Wilcke et al. 2005). Kuchinad and colleagues (2007) have shown decreases in left hippocampus, bilateral MCC and PCC, left insula, and medial prefrontal cortex (mPFC) volumes in fibromyalgia; whereas Lutz et al. (2008) demonstrated volume reductions in postcentral gyrus, amygdala, superior frontal gyrus, ACC, and hippocampus in patients with the same pathology. Complex regional pain syndrome (CRPS) was found to be associated with gray matter atrophy in right insula, ventromedial PFC, nucleus accumbens (NAc) (Geha et al., 2008), and hippocampus (Mutso et al. 2013); hippocampal volume loss was also detected in chronic back pain patients.

DTI studies performed in various chronic pain conditions found white matter changes in several brain areas. DaSilva and colleagues (2007) reported for instance decreased fractional anisotropy (FA) for tracts connecting brainstem-thalamus and thalamus-primary somatosensory areas in migraine sufferers. In fibromyalgia, there were decreases in FA values in thalamus and insula; together with increases in postcentral gyrus (Lutz et al., 2008). Geha et al. (2008) showed white matter connectivity changes along ventromedial PFC, anterior insula, and NAc in CRPS patients. In temporo-mandibular disorder (TMD), decreases in FA was accompanied by increases in mean diffusivity (MD) and radial diffusivity (RD) values in corpus callosum and internal/external capsule related to sensory thalamocortical communication (Moayedi et al., 2012); tractography revealed reduced fiber density in genu of corpus callosum and dorsolateral PFC in addition to fiber increases in other parts of corpus callosum and frontal poles. There were also conflicting findings for the same pathologies in different studies. Chen et al. (2011) found increases in FA in anterior insula, thalamus (i.e. ventral posterolateral nuclei), fornix, and external capsule in irritable bowel syndrome (IBS); whereas another group reported FA decreases in thalamus, basal ganglia, sensory-motor association areas along with increased FA in frontal lobe and corpus callosum (Ellingson et al., 2013).

1.2.2.3 Functional MRI in chronic pain conditions

fMRI technique has been extensively used to study brain function and connectivity across various chronic pain conditions. In a cohort with diabetic neuropathic pain, Cauda et al. (2010)

reported increased connectivity between DMN and the dorsal ACC and primary motor/somatosensory cortices bilaterally and decreased connectivity between DMN and the dorsolateral PFC, frontopolar cortex, insula, and thalamus bilaterally. Napadow et al.,(2011) have shown that intrinsic brain connectivity is associated with pain intensity in fibromyalgia since functional connectivity within the DMN, within right executive attention network (i.e. a resting state network involved with cognitive processing of working memory and attention comprising fronto-parietal regions: namely dorsolateral PFC, superior parietal lobule, and intraparietal sulcus), and between DMN-insula were found to be increased. This increase was also correlated with spontaneous pain intensity.

Moreover, in several studies by Baliki and colleagues (Baliki et al., 2006; 2008a; 2008b; 2010) chronic back pain (CBP) was found to be associated with increased activation in mPFC and rostral ACC during sustained pain, with reduced deactivation in default mode network (DMN) regions in response to an attention task, and with changes in NAc responses to noxious stimuli. The same research group demonstrated an increase in the high frequency oscillations of the BOLD signal in mPFC and DMN regions which was related to spontaneous pain in CBP patients (Baliki et al., 2011). With longitudinal rs-fMRI, they were able to show that the transition from sub-acute to chronic back pain could be predicted by the enhanced functional connectivity between NAc and PFC (Baliki et al., 2012) and decreased functional connectivity between hippocampus and mPFC (Mutso et al., 2013). In another study where patients with CBP, complex regional pain syndrome (CRPS), and osteoarthritis (OA) were investigated with rs-fMRI, all chronic pain groups demonstrated an attenuated functional connectivity between mPFC and more posterior parts of DMN, namely the precuneus, and enhanced insula-mPFC connectivity (Baliki et al., 2014) along with increased high frequency BOLD oscillations in mPFC and DMN. Moreover, ongoing pain in OA patients were found to be linked with activations in prefrontal and limbic regions (Parks et al. 2011).

Taken together, brain networks involved in chronic pain at least partially differ from those seen in acute pain perception (pain matrix); as chronic pain involves brain regions critical for cognitive and emotional processing/assessment (Schmidt-Wilcke, 2015). Chronic pain seems to reflect a shift from nociceptive to meso-corticolimbic circuitry overtime with conditions exhibiting distinct patterns of brain network reorganization (Farmer et al., 2012).

1.2.2.4 Structural and functional MRI of rodent pain models

Several different chronic pain models have been investigated with rodent MRI techniques, sometimes in a longitudinal fashion to allow examining the progression of the pathology (Seminowicz et al. 2012; Baliki et al. 2014; Buehlmann et al. 2018; Bilbao et al. 2018). When compared with clinical studies in chronic pain, preclinical studies give remarkably similar results. For instance, volumetric changes have been observed in prefrontal, somatosensory and limbic areas both in humans (Apkarian et al., 2004; Geha et al., 2008; Gustin et al., 2011; Kuchinad et al., 2007; Yoon et al., 2013) and in rodents (Bilbao et al., 2018; Seminowicz et al., 2009).

Functional connectivity studies in chronic pain also highlight similar areas in humans (Baliki et al., 2011, 2012; Mutso et al., 2013) and rodents (Chang et al., 2014; M. N. Baliki et al., 2014; Morris et al., 2017; Bilbao et al., 2018; Buehlmann et al., 2018) including mPFC/ACC, VS/NAc, and hippocampus in which connectivity changes across different pathologies and preclinical

models were demonstrated. Following table gives a summary of brain structural and functional MRI studies in rodent chronic pain models (Table 1-2).

Table 1-2 Preclinical imaging studies in rodent chronic pain models.
Abbreviations: *DBM: Deformation-based morphometry; VBM: Voxel-based morphometry; MRS: Magnetic resonance spectroscopy; MEMRI: manganese-enhanced MRI; FC: Functional connectivity; CC: Clustering coefficient; DR2: Dopamine receptor-2; PFC: Prefrontal cortex; RSP: Retrosplenial area; SS: Somatosensory area; MO: Motor area; TH: Thalamus; HY: Hypothalamus; PAG: Periaqueductal gray; HIP: Hippocampus; NAc: Nucleus accumbens; CPu: Caudate-putamen; VP: Ventral pallidum; AMY: Amygdala; CeA: Central amygdala; ACC: Anterior cingulate cortex; ORB: Orbital area; VS: Ventral striatum; VPL: Ventral posterolateral nucleus of thalamus; PL: Prelimbic area; BG: Basal ganglia; BNST: Bed nucleus of stria terminalis; ZI: Zona incerta.*

Study	Species	Model	Imaging modality	Findings
Seminowicz et al., 2009	Rat	Spared nerve injury (SNI)	T1-weighted MRI/ DBM	Age-related volume decreases in both shams and SNI animals. Lower PFC, RSP, entorhinal cortex, SS, and insula volumes in SNI group at 4 months after injury-coincides with *anxiety phenotype*.
Seminowicz et al., 2012	Rat	Spinal cord injury (SCI)	Rs-fMRI	FC of TH contralateral to injury was increased with ipsilateral TH, PAG, and HIP; decreased with SS areas 1w after injury. Asynchrony between thalamus and cortex was thought to be due to enhanced thalamic activity resulting in neuropathic pain.
Chang et al., 2014	Rat	Spared nerve injury (SNI)	Rs-fMRI	FC decreases in subregions of NAc towards CPu, insula, and SS areas at 28d after injury. Decreases correlated with mechanical allodynia and reduced *DR2* expression in NAc contralateral to injury. DR2 is engaged in indirect striatopallidal pathway; whose inactivation results in *aversive learning*.

Study	Species	Model	Imaging modality	Findings
Hubbard et al., 2015	Rat	Spared nerve injury (SNI)	Task-fMRI (acetone application induced cold allodynia)	At 4w, SNI animals showed *larger activations* in contralateral SS, VPL, and dorsal striatum; *larger deactivations* in contralateral insula, midline TH, ipsilateral ACC, PAG, and pons. At 20w, SNI animals showed *larger activations* in ACC, PL, insula, BG, and SS; *larger deactivations* in midline TH and PAG. Cold allodynia was correlated with ACC and PL activation levels.
Komaki et al., 2016	Mouse	L4 spinal nerve root injury	Rs-fMRI	7d after surgery, contralateral primary SS had lower degree and eigenvector centrality, ACC had higher CC and local efficiency, and VPL had higher betweenness centrality in graph theoretical analysis.
Morris et al., 2017	Rat	Inflammatory arthritis	Rs-fMRI	At 3w, with the establishment of pain behaviors, ACC FC towards dorsal striatum and SS areas were increased. FC of ACC towards HY, preoptic area, and BNST negatively correlated with *burrowing* (a behavioral measure of motivation).
Matsubayashi et al., 2018	Mouse	Spinal cord injury (SCI)	Awake rs-fMRI	FC between MO-upper limb SS increased at 1w; decreased later on; lower limb FC consistently decreased. FC between MO-ORB increased. MO-ACC and SS-ACC FC decreased at 3-7w; increased at 14w. SS-CPu FC increased over time
Buehlmann et al., 2018	Mouse	Metastatic bone cancer	Rs-fMRI	Loss of coherence in ACC, PFC, NAc, piriform area, and dorsal HIP intra-regionally. Reduced FC of ACC/PFC to NAc and ventral HIP; ACC to dorsal HIP, and striatum to SS/MO/parietal areas/TH.

Study	Species	Model	Imaging modality	Findings
Apkarian et al., 2018	Rat	Spared nerve injury (SNI)	Awake fMRI/ Chemogenetics	Both glutamate-mediated and chemogenetic activation of dorsal HIP reversed *allodynia*. FC of dorsal HIP with cortical (i.e. primary SS, MO, RSP, insula, and mPFC) and dorsolateral TH predicted *pain relief.* FC of dorsal HIP with ZI, pallidum, barrel field and posterior HIP predicted *pain exacerbation.*
Bilbao et al., 2018	Mouse	Spared nerve injury (SNI)	T2-weighted MRI/ VBM, Rs-fMRI, MRS	VBM: Arrest of normal brain growth trajectory at 1w after surgery. At 12w, SNI mice caught up to shams excepting the reduced volumes of BNST, PFC, NAc, and dorsal striatum. Rs-fMRI: At 1w, lower local efficiency, CC, and small worldness in SNI brains. SC showed lower strength, PAG showed lower local efficiency, and NAc- CPu showed higher betweenness centrality. At 12w, NAc showed higher strength, mammillary bodies showed lower strength and local efficiency in SNI group. At both time points, PFC-HIP FC was lower in SNI mice. MRS: HIP dopamine levels were decreased at 1w; increased at 12w.

Even though the studies mentioned in the next few pages mostly found alterations in similar brain regions, there were also discrepancies between study results. It is important to bear in mind that each research group used either distinct species/strains or pain models (i.e. neuropathic vs. inflammatory pain); or simply conduct experiments at different time points. Experimental protocols, especially the selection of anesthesia for functional imaging might also influence the results.

1.2.3 Affective consequences of chronic pain

Chronic pain and neuropsychiatric conditions such as stress, anxiety, sleep disturbances, and depression are significantly comorbid (DosSantos et al., 2017). Indeed, a wealth of clinical data suggests a high degree of comorbidity between chronic pain and depression, with an incidence of approximately 50% (Doan et al., 2015). Both animal models and human brain imaging studies show strong similarities between chronic pain and mood disorders; both conditions critically involve limbic brain circuits (Baliki and Apkarian, 2015) related to reward and motivational behaviors. Significant overlap between affected brain regions in chronic pain and mood disorders might explain their comorbidity based on 'shared substrate hypothesis' which defines the comorbidity of pain and depression as the plasticity of specific brain regions processing both the emotional aspect of pain and mood-related information (Yalcin et al., 2014a). Transition from acute to chronic pain has been associated with a gradual shift from sensory neural activity toward a limbic representation of spontaneous pain (Vachon-Presseau et al., 2016); possibly achieved by reorganization of cortex by corticolimbic learning mechanisms. Functional, chemical, and anatomical changes from chronic pain can, in time, alter the sensory, emotional and motivational systems and result in comorbidities such as depression (Shelton et al., 2012). Another view in the field regards nociception, pain and negative mood states a single continuum of aversion in the framework of behavioral selection (Baliki and Apkarian, 2015), which explains the overlap between structures affected by each condition.

In the following sections, I give a brief overview of brain regions implicated in both depression and chronic pain; stating their role in reward and aversive behaviors and discussing their dysfunction - *with an emphasis on imaging findings*. Gaining insight into each pathology might pave the way for reaching an understanding of their comorbidity.

1.2.3.1 Reward/aversion system and its dysfunction in chronic pain and depression

The reward circuit comprises several cortical and subcortical regions forming a complex network that mediates different aspects of incentive-based learning, leading to adaptive behaviors (Haber and Knutson, 2010). In mammals, encoding reward and directing motivated behaviors require the coordination of multiple brain regions including nucleus accumbens (NAc), amygdala, prefrontal cortex (PFC), substantia nigra (SN), ventral tegmental area (VTA), dorsal raphe nucleus (DRN), and lateral habenula (LHb).

The connections between these regions and others define the reward circuitry and they appear to be conserved between rodents and primates (Scaplen and Kaun, 2016). Brain reward circuitry is responsible for reinforcing behaviors that are rewarding and preventing behaviors that lead to punishment (Proulx et al., 2014) and it is involved in incentive salience, learning, and memory of rewards; ensuring survival of the organism (Arias-Carrión et al., 2010).

Dopamine (DA) is recognized as the main neurotransmitter in reward circuitry. Evidence for differential dopamine-dependent positive and negative reinforcement learning exists in both rodents and humans via different receptor subtypes (i.e. DR1/DR2). Furthermore, gamma aminobutryric acid (GABA), noradrenaline, opioid peptides, serotonin, acetylcholine (ACh), endocannabinoids, and glutamate are also implicated in acute reinforcing properties in mammals, mainly through modulatory processes (Scaplen and Kaun, 2016).

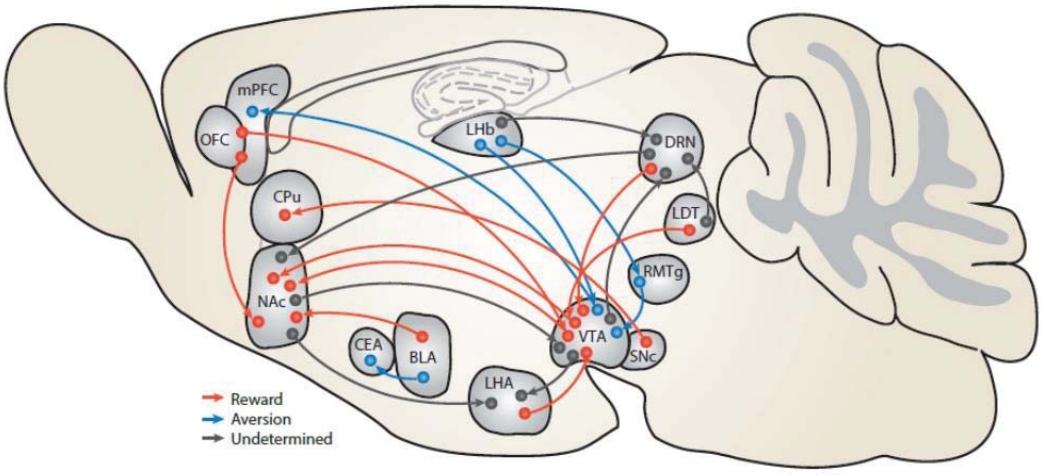

Figure 1-15 Simplified schema of reward-mediating and aversion-mediating pathways in rodents.
(Figure taken from Hu 2016.)

Reward dysfunction is a prominent feature of major depression: DSM-V classifies anhedonia (i.e. inability to feel pleasure in normally pleasurable activities) and lack of motivation as the cardinal symptoms of the disease. Abnormalities in the perception and interpretation of reward valence, motivation to acquire rewards, and decision-making as well as increased responses to aversion underlie reward dysfunction in depression (Russo and Nestler, 2013).

Pain is an aversive stimulus which can act as punishment; whereas pain relief is associated with reward. Pain relief itself can induce reward-based operant learning (e.g. conditioned placed preference - CPP) (Nees and Becker, 2018). Motivation-decision model of pain (Fields, 2004, 2007) states that in situations in which reward consumption is more important for an organism than pain avoidance, endogenously mediated pain inhibition occurs; while in situations in which pain avoidance is more important, pain facilitation occurs to ensure best outcomes for the survival of the organism. In the case of chronic pain (Nees and Becker, 2018), pain avoidance and/or achieving pain relief becomes an all-dominate goal which can result in an imbalance between the valuation of pain and reward. Furthermore, the rewarding properties of pain relief might diminish over time and averseness of uncontrolled pain and negative events becomes more overwhelming (Borsook et al., 2016). Thus, reward deficiency and anti-reward (i.e. negative affective states) are major components of chronic pain. Decreased reward responsivity may underlie a key system mediating the anhedonia and depression common with chronic pain (Taylor et al., 2016).

In addition, involvement of dopaminergic systems in both pain and depression are evidenced by chronic pain and mood disorders frequently resulting from malfunction of dopaminergic areas (e.g. Parkinson's disease) (Mitsi and Zachariou, 2016).

Ventral striatum (VS)/Nucleus accumbens (NAc): Ventral striatum (VS) region encompasses NAc, caudate-putamen ventral to rostral internal capsule and olfactory tubercle (Haber and Knutson, 2010). The link between NAc activity and reward had been first established by the self-stimulation circuit originally described by Olds and Milner (1954). VS constitutes a critical element of mesocorticolimbic system responsible for reward, motivation, and salience attribution (Borsook et al., 2016). Afferent and efferent connections of the VS are schematized in the Figure 1-16 (below).

Striatal regions are recruited during reward processing (Haber and Knutson, 2010): both for primary (e.g. sensory) and secondary (e.g. monetary) rewards. It has been shown that the dopamine release after amphetamine injection into the VS correlates with positive and arousing affective experience (i.e. euphoria).

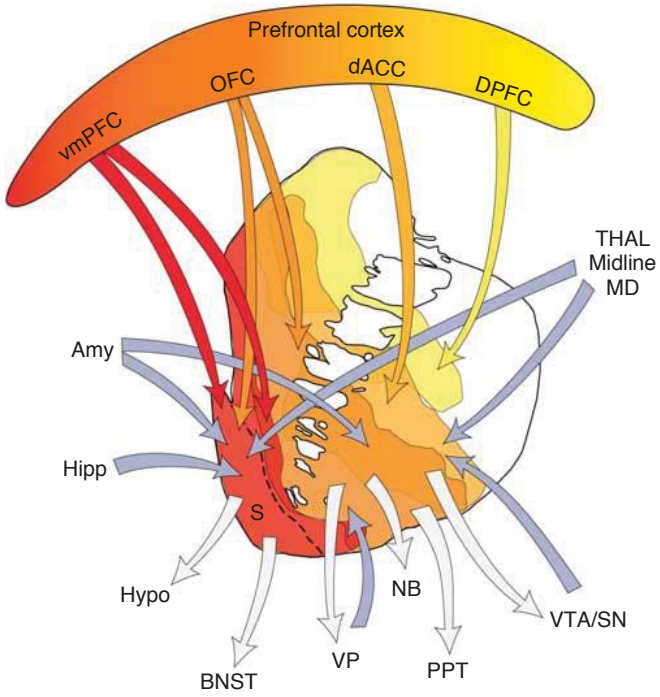

Figure 1-16 Schema illustrating the connections of the VS.
Blue arrows: inputs; gray arrows: outputs; Amy: amygdala; BNST:bed nucleus stria terminalis; dACC: dorsal anterior cingulate cortex; Hipp: hippocampus; hypo: hypothalamus; MD: medio-dorsal nucleus of the thalamus; OFC: orbital frontal cortex; PPT: pedunculopontine nucleus; S: shell; SNc: substantia nigra, pars compacta; STN: subthalamic nucleus; Thal: thalamus; VP: ventral pallidum; VS: ventral striatum; VTA: ventral tegmental area; vmPFC: ventral medial prefrontal cortex. (Taken from Haber and Knutson, 2010.)

Anticipated reward magnitude consistently increases the NAc and medial caudate activation; other aspects of anticipated value (e.g. probability and effort) may elicit more pronounced activation in the rostroventral putamen. Rewarding outcomes elicit activation in the medial caudate portion of the VS, a region which might integrate information from reward and cognitive cortical areas in the development of strategic action planning. Reward omission reliably decreases VS activation (Haber and Knutson, 2010).

NAc activity in response to reward is decreased in major depression (Russo and Nestler, 2013). Several brain functional imaging studies have shown reduced activation in VS in response to gain outcomes (Pizzagalli et al., 2009; Redlich et al., 2015; Satterthwaite et al., 2015; Stoy et al., 2012), during reward anticipation (Hägele et al., 2015; Segarra et al., 2015; Smoski et al., 2009), during reward selection and feedback (Smoski et al., 2009) in major depressive disorder (MDD). Hypoactivity of VS was also seen in response to positive-valance words (Epstein et al., 2006) and enjoyable music (Lepping et al., 2016; Osuch et al., 2009) in MDD. Depressed individuals failed to sustain NAc activity while trying to upregulate their positive affect (Heller et al., 2009). Reduced NAc volume was found to be correlated with anhedonia in depressed patients (Wacker et al., 2009) and with social avoidance scores in stress-susceptible mice (Anacker et al., 2016).

In pain studies, termination of a brief noxious stimulus (Becerra et al., 2013) was associated with increased NAc activation in fMRI both in humans and rats. However, this effect was negative in polarity for chronic back pain (CBP) patients (Baliki et al., 2010): termination of acute pain stimulus decreased NAc activation, suggesting that the acute pain alleviates the ongoing back pain. Reduction in NAc volume was reported for trigeminal neuralgia (Gustin et al., 2011), complex regional pain syndrome (CRPS) (Geha et al., 2008) and in a mouse model of spared nerve injury (SNI) (Bilbao et al., 2018). Functional connectivity (FC) of NAc with mPFC was shown to be predictive of pain chronicity (Baliki et al., 2012) in clinical populations. Preclinical chronic pain studies also demonstrated FC changes of NAc against several brain regions and changes in dopamine receptor expression in this area (Chang et al., 2014). Peripheral nerve injury has been shown to disturb glutamatergic information processing and long-term depression (LTD) of NAc neurons, resulting in decreased motivated behaviors (Schwartz et al., 2014).

Ventral tegmental area (VTA)/ Substantia nigra (SN): Midbrain dopamine neurons form two functional divisions: dorsal tier associated with limbic circuitry including VTA and dorsal parts of SN pars compacta (SNc), and ventral tier including ventral SNc and SN pars reticulata (SNr) associated with motor functions (Haber and Knutson, 2010). Dorsal tier dopaminergic neurons receive input from VS, bed nucleus of stria terminalis (BNST), substantia innominate, amygdala, ventral pallidum (VP), pedunculopontine nucleus (PPT), dorsal raphe nucleus (DRN), and superior colliculus (SC). Direct sensory input from SC is thought to be responsible from short latency burst firing of dopaminergic cells to salient and rewarding stimuli. Dorsal tier of dopaminergic neurons sends projections primarily to VS (via medial forebrain bundle-MFB) and to midline structures such as hypothalamus, PAG, BNST, amygdala, hippocampus. Dorsal tier also diffusely innervates cortical areas.

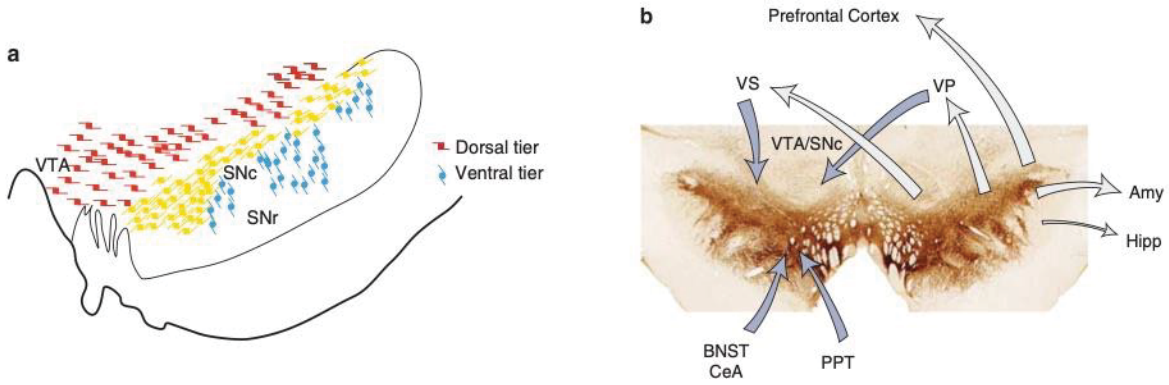

Figure 1-17 Schematic illustration of a. the organization and b. the connections of the midbrain dopamine cells.
Red cells: connections with VS regions; yellow cells: connections with dorsal caudate nucleus; blue cells: connections with motor control striatal areas. BNST: bed nucleus stria terminalis; CeA: central amygdala nucleus; Amy: amygdala; Hipp: hippocampus; PPT: Pedunculopontine nucleus; SNc: substantia nigra, pars compacta; VP: ventral pallidum; VTA: ventral tegmental area.(Taken from Haber and Knutson, 2010.)

Dorsal tier dopaminergic neurons respond to unexpected reward by phasic bursts and to reward omission by phasic inhibition; encoding prediction error (PE) signals- the discrepancy between the expected and actual reward. VTA innervates NAc medium spiny neurons (MSNs) via two pathways : direct (D1 type receptor-mediated) which causes excitation and positive affect and indirect (D2 type receptor-mediated) which inhibits MSNs and results in negative affect (DosSantos et al., 2017).

Human fMRI studies has shown that dorsal tier dopaminergic neurons increase their activity in response to stimuli that predict reward (Haber and Knutson, 2010). Additionally, a small percentage of dopaminergic neurons (mostly found in dorsolateral SN with projections to NAc core) fire preferentially during aversive stimuli (e.g. noxious stimuli) or during both aversive and rewarding stimuli. Neurons activated by both rewarding and punishing stimuli are likely to code motivational salience independent of valence (Taylor et al., 2016). Dopamine modulates the salience of pain stimuli and thereby mediates the motivation to avoid or endure pain depending on the situational context explained in motivation-decision model of pain (Fields, 2007).

Different rodent models of stress-induced depression reveal differences in VTA and mesolimbic reward pathway modulation. Mouse model of social defeat stress was associated with increased activity in VTA dopaminergic neurons and higher brain-derived neurotrophic factor (BDNF) levels in NAc (Berton et al., 2006). Optogenetic activation of VTA-NAc pathway in this model resulted in even higher BDNF levels in NAc which was absent for stress-naïve mice (Walsh et al., 2014). Imaging in this model (Anacker et al., 2016) demonstrated that larger VTA volume was correlated with social avoidance scores. In addition, stress-susceptible mice tended to have larger VTA and smaller cingulate volumes.

However, chronic unpredictable mild stress (CUMS) model showed decreased activity in VTA-mPFC pathway but not in VTA-NAc pathway (Liu et al., 2018) and injection of BDNF into mPFC reversed depression-like behaviors. In clinical imaging, VS and VTA functional connectivity was higher in depression group (Redlich et al., 2015). Gradin et al. (2011) have shown lower prediction-error (PE) signals in both striatum and midbrain during reward learning and this signal reduction was correlated with anhedonia scores. Moreover, weaker memory for positive material along with lower activation in dopaminergic midbrain were found in depressed patients (Dillon et al., 2014).

Chronic pain models in rodents also show discrepancies in dopaminergic system alterations: In a rat model of peripheral nerve injury, microglial activation in VTA has been shown to result in disruption of dopaminergic signaling and reward behavior (Taylor et al., 2015); these effects were mediated by microglia-regulated activation of chloride channels in GABAergic VTA interneurons. Ko et al (2018) showed increased GABAergic and decreased dopaminergic neuronal activity in a rat model of spinal cord injury (SCI). Inflammatory pain in rats (Hipólito et al., 2015) resulted in lower levels of mu-opioid receptors in VTA along with a loss of opioid-induced dopamine release in NAc. In the spared nerve injury (SNI) model, spontaneous spiking of VTA and extracellular dopamine in NAc were reduced together with increased cell-specific excitability of NAc shell indirect pathway neurons; which was shown to be responsible from amplification of tactile allodynia (Ren et al., 2015). In a study using manganese-enhanced MRI (MEMRI) in a rat model of knee-joint pain, $MnCl_2$ accumulation was decreased in VTA (i.e. *showing lower activity*) in line with hyperalgesia (Devonshire et al., 2017). Watanabe and colleagues (2018) used both nerve injury and cancer pain models in mice and replicated the findings of reduced neuronal excitability of VTA dopaminergic neurons projecting to NAc; moreover, optogenetic stimulation of VTA dopamine neurons or their terminals in NAc reversed pathological allodynia.

On the other hand, a study using SNI reported an *increase* in bursting activity and dopamine release in VTA along with higher serotonergic activity in dorsal raphe (Sagheddu et al., 2015); yet, another study in SNI model showed increased firing rate but not *burst firing* of VTA

dopaminergic neurons (Fu et al., 2018). In a chronic constriction injury (CCI) model (Zhang et al., 2017), an increased dopaminergic signaling in VTA-NAc pathway- dependent on BDNF release from VTA - was detected; inhibition of VTA or BNDF signaling attenuated thermal hyperalgesia.

The conflicting findings for VTA in chronic pain might be partially explained by the heterogeneity of this region with respect to cell-types, firing patterns, and projections; as well as the use of different preclinical models and experimental protocols.

Lateral habenula (LHb): LHb is another important center in reward circuitry that encodes negative value/aversion relevant to avoidance or escape behaviors. LHb receives inputs from forebrain limbic circuits (via stria medullaris) and sends outputs to aminergic brainstem nuclei (via fasciculus retroflexus). See a summary of LHb circuitry on Figure 1-18:

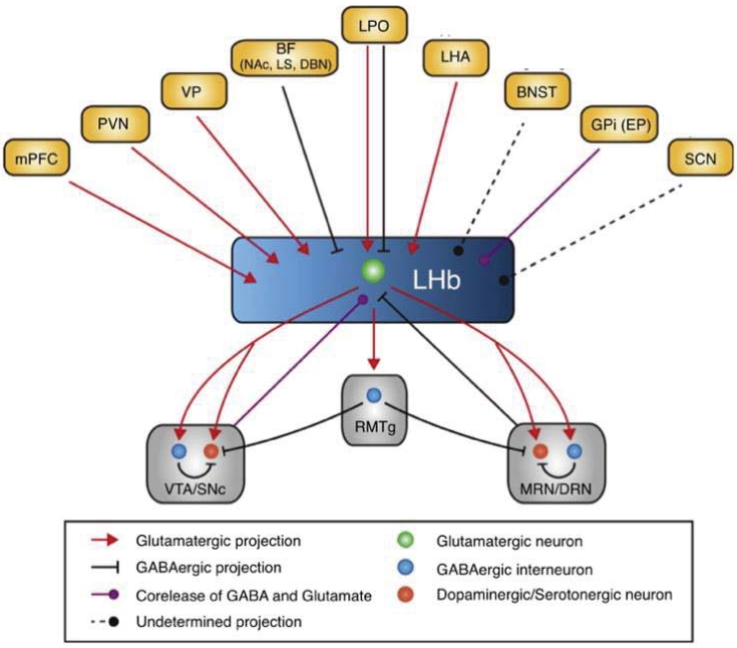

Figure 1-18 Summary of the input and output circuitry of the LHb.
Projections to the lateral habenula (LHb), shown in brown, include the paraventricular nucleus (PVN), basal forebrain (BF, including the nucleus accumbens (NAc), lateral septum, and diagonal band nuclei (DBN)), lateral hypothalamic area (LHA), lateral preoptic area (LPO), ventral pallidum (VP), globus pallidus (GPi), medial prefrontal cortex (mPFC), suprachiasmatic nucleus (SCN), and bed nucleus of the stria terminalis (BNST). (Taken from Yang, et al. 2018b.)

LHb encodes also negative reward prediction error (PE) signals which is induced by unexpected non-rewarding or unpleasant events (i.e. pain) and inhibited by unexpected rewards. LHb sends glutamatergic projections either directly to VTA inhibitory GABAergic neurons or indirectly via rostromedial tegmental area (RMTg) which in turn inhibits VTA. LHb also innervates serotonergic raphe nuclei of brainstem (Proulx et al., 2014).

fMRI studies in depressed patients and rodent depression models have shown LHb hyperactivity while LHb lesions abolished depressive phenotypes in rodents: In a rat model of congenital learned helplessness (cLH)(Gass et al., 2014b), regional cerebral blood volume (rCBV) was found to be increased in LHb and optogenetic perturbation of LHb (Clemm von Hohenberg et al., 2018) eliminated DMN hyperconnectivity related to cLH phenotype. Enhanced burst activity of LHb was found to be driving depressive behaviors and anhedonia; this phenotype was reversed by the suppression of bursting activity using NMDA-receptor antagonist ketamine (Yang et al., 2018a). Cui et al. (2018) has discovered that the LHb bursting pattern in depression

was due to the upregulation of an astrocytic potassium channel, Kir4.1. Overactive LHb neurons may produce an unpleasant state of constant disappointment or sense of doom, which may contribute to human depression (Proulx et al., 2014). In a case study where the habenula was inactivated by deep brain stimulation (DBS) resulted in a full remission of major depression in a treatment-resistant patient (Sartorius et al., 2010).

Habenula is modulated or directly modulates systems or pathways involved in pain processing, including opioidergic, serotoninergic and dopaminergic and noradrenergic systems (Shelton et al., 2012). LHb is part of a pain modulation loop consisting of NAc, PAG, and LHb and morphine injection at these sites promotes analgesia. In a study conducted in pediatric CRPS (Erpelding et al., 2013), patients exhibited an overall FC reduction of habenula with the rest of the brain; specifically, with the anterior midcingulate cortex (MCC), dorsolateral prefrontal cortex (dlPFC), and motor cortices.

For an understanding of depression and pain comorbidity, a research group has devised a set of experiments studying their reciprocal interactions (Li et al., 2016, 2017). Firstly, they have shown that CUMS model of depression results in pain hypersensitivity and significant enhancement of LHb firing rates, especially for pain-activated neurons. Indeed, the percentage of c-fos positive cells in LHb was increased for rats submitted to the CUMS or pain stimulation; this percentage was even higher in rats receiving both. Lesioning LHb was able to overcome both depressive behaviors and pain hypersensitivity. Later on, they used a chronic constriction injury (CCI) model of pain in rats (Li et al., 2017) where they showed emergence of depressive-like behaviors 28 days after surgery. In neuropathic pain group, LHb activity and βCaMKII expression were increased along with decreases in dorsal raphe activity and serotonin levels. LHb lesions in this model also improved pain thresholds and depressive-like behaviors. They came to the conclusion that increased activity in LHb may be a common neurobiological mechanism underlying pain and depression coexistence.

Medial prefrontal cortex (mPFC)/ Anterior cingulate cortex (ACC): The main cortical areas associated with reward are orbitofrontal cortex (OFC-areas 11,12,13,14 in humans) and anterior cingulate cortex (ACC- areas 24, 25, and 32). In imaging studies, distinguishing these cortical divisions are difficult; therefore, more broad definitions are used. Prefrontal regions include a caudal sensory region (i.e. parts of OFC and insula), a rostral OFC region, ventromedial PFC (vmPFC-including areas 11,10,32), and dorsal ACC (area 24). Medial PFC is a subregion of vmPFC; includes areas 10/32 (Haber and Knutson, 2010).

vmPFC is implicated in reward processing, including diverse and abstract rewards. Rewarding outcomes by sensory cues activate vmPFC; however, abstract rewards (i.e. money) mainly activate the mPFC region. mPFC activation may also integrate value across different stimulus dimensions (e.g. *magnitude, probability, benefits, costs,* and *immediacy*) or different stimuli (Haber and Knutson, 2010). The overall function of dACC seems to involve monitoring motivation, cognition, and motor control functions in potential conflict situations (Vogt, 2005). dPFC (areas 9 and 46) is engaged when working memory is required for monitoring incentive-based behavioral responses (Haber and Knutson, 2010).

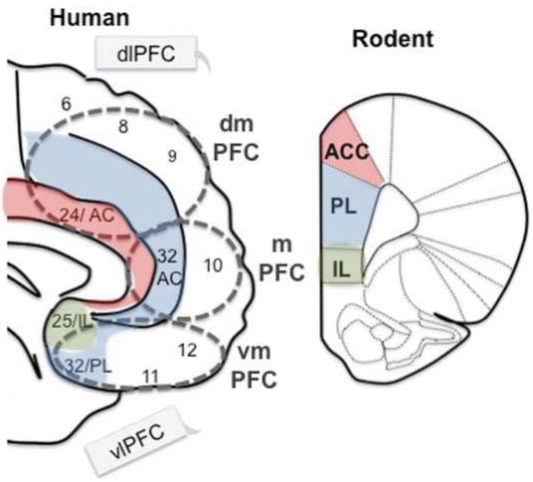

Figure 1-19 Medial prefrontal regions in human and mouse.
ACC: anterior cingulate cortex; PL: prelimbic area; IL: infralimbic area; dl:dorsolateral, dm:dorsomedial, m:medial, vm:ventromedial, vl:ventrolateral PFC: prefrontal cortex. (Taken from Bicks, et al. 2015.)

In major depressive disorder (MDD), ACC demonstrates reduced volume, related to both glial and neuronal loss, and hyperactivity in subgenual part (Drevets et al., 1997; Rajkowska, 2000; Uranova et al., 2004; Mayberg, 2009; Russo and Nestler, 2013). In addition to ACC, gray matter loss was also observed in dorsolateral PFC and OFC in depressed individuals (Bora et al., 2012; Du et al., 2012; Lai, 2013). The involvement of ACC (Knutson et al., 2008) and mPFC (Kumar et al., 2015) in reward processing was more pronounced in MDD. For instance, MDD patients showed reduced recruitment of vmPFC and lateral OFC during punishment and changes in reward contingencies (Hall et al., 2014). Reduced fronto-striatal connectivity during anticipation of high magnitude gains and losses (Ubl et al., 2015) and during rest (Anand et al., 2009, 2005) were documented in major depression. Subgenual ACC connectivity with DMN regions during rest were greater in MDD and sgACC functional connectivity correlated positively with the length of the current depressive episode (Greicius et al., 2007).

Representation of reward in OFC and pain-related activity in insula were found to be positively associated (Talmi et al., 2009) so that the increased activation in insula prioritizes pain avoidance over obtaining a reward with increased activation in OFC. Activations in both NAc and ACC towards rewards were attenuated as a function of anticipated pain levels. OFC also seems to mediate reward-induced pain inhibition via increased anti-correlations with anterior insula, dACC, and primary sensory cortex (Becker et al., 2017). Patients with neuropathic pain following spinal cord injury showed dorsolateral PFC(dlPFC) and subgenual ACC gray matter loss (Yoon et al., 2013); volumetric losses were also reported in chronic back pain for dlPFC (Apkarian et al., 2004); in fibromyalgia for mPFC (Kuchinad et al., 2007) and ACC (Lutz et al., 2008); in CRPS for vmPFC (Geha et al., 2008). Diabetic neuropathic pain (Cauda et al., 2010) was associated with increased FC between dACC-DMN and decreased FC between dlPFC-DMN. Chronic back pain(CBP) patients showed increased activation of mPFC and ACC during sustained pain (Baliki et al., 2006) and an attenuated FC between mPFC-precuneus was reported for CBP, CRPS, and osteoarthritis (Baliki et al., 2014).

The ACC is an integration center that interconnects neurons from the frontal cortex, the thalamus and the amygdala, processing cognitive, emotional and autonomic functions (Yalcin et al., 2014a). ACC is implicated in the processing of pain, anticipation of pain, and avoidance

learning; this region shows synaptic changes and increased activity in various chronic pain models along with volume decrease associated with emergence of anxiety behaviors (Seminowicz et al., 2009; Yalcin et al., 2014a). ACC is thought to play an important role in pain-depression comorbidity: Hyperactivity of this region (comprising areas 24a/24b in mice) was associated with anxio-depressive consequences in a cuff model of neuropathic pain in mice (Sellmeijer et al., 2018) and optogenetic inhibition of the area provided relief from pain aversion and anxio-depressive phenotype without affecting mechanical hypersensitivity in this model. Another study (Barthas et al., 2017) showed ACC overexpression of mitogen-activated protein kinase phosphatase-1 (MKP-1) in chronic pain-induced depression, CUMS model and ACC optogenetic stimulation in mice which was reversed by antidepressant use; knockout, local silencing and pharmacological inhibition of MKP-1 alleviated depressive behaviors. In addition, lesion or optogenetic activation of prelimbic area (PL), part of rodent mPFC, induced both analgesic and anxiolytic effects; GABAergic activation in the region decreased pain responses and anxiety, and activation of PL projections to the NAc produced relief from chronic pain (Lee et al., 2015; Vachon-Presseau et al., 2016; Wang et al., 2015; Z. Zhang et al., 2015).

Amygdala: Amygdala is responsible from emotional coding of environmental stimuli and providing contextual information used for adjusting motivational level. Imaging studies show that amygdala activates both in contexts of potential reward and punishment, thus it responds more to stimulus arousal than value. Amygdala is prominently implicated in fear learning in animal studies; in addition, amygdala deactivates in response to devaluation of previously rewarding stimuli (Haber and Knutson, 2010).

Amygdala hyperactivity, especially seen in basolateral amygdala (BLA) excitatory tone, was demonstrated in MDD (Russo and Nestler, 2013). In functional neuroimaging, depressed patients showed enhanced activity in the amygdala and bilateral caudate-putamen (CPu) in response to individualized self-critical words compared to controls (Doerig et al., 2016). Moreover, amygdala was coupled positively with bilateral medial temporal, ventral occipital regions and negatively with the ACC in depressed individuals in an implicit sad affect processing task (Chen et al., 2008) and chronic antidepressant use induced higher functional coupling of amygdala with right frontal cortex, ACC, striatum, and thalamus. During viewing of negative pictures, depression severity correlated with left amygdala, bilateral OFC and left insula activity (Lee et al., 2007). In addition, bilateral amygdala volume reduction was detected in patients with depression (Hickie et al., 2007; Sheline et al., 1998).

Amygdala is also another candidate for an important player in affective consequences of pain. In addition to fear processing, amygdala (i.e. central amygdala) has connections to pain centers and contains nociceptive neurons (Yalcin et al., 2014a). Amygdala hyperactivity and volume increase (Gonçalves et al., 2008), along with signaling changes in several neurotransmitter systems have been observed in chronic pain models. Amygdala involvement in spinal cord central sensitization processes and influence on PFC (Baliki and Apkarian, 2015) further highlights the role of amygdala in chronic pain.

Hippocampus: Hippocampal regions are anatomically and functionally connected to reward circuitry (Haber and Knutson, 2010). Reward processes modulate memory formation and reward learning informs goal-directed behaviors (Adcock et al., 2006; Kahn and Shohamy, 2013; Le Merre et al., 2018).

Hippocampus dysfunction had long been observed in major depressive disorder (MDD) (Belzung et al., 2015; Wingenfeld and Wolf, 2014) including reduced hippocampal volume associated with synaptic and glial loss (Russo and Nestler, 2013). In addition, neuroimaging research featuring reward tasks in major depression discovered various hippocampal abnormalities: Reward learning signals in many regions including VS, ACC, retrosplenial cortex (RSP), midbrain, and hippocampus were reduced for depressed patients (Kumar et al., 2008). Dorsal raphe, PAG and hippocampus were hyperactive during unsuccessful loss-avoidance, whereas median raphe was hypoactive (Johnston et al., 2015); during loss events, hippocampus failed to deactivate. Healthy subjects demonstrated a stronger encoding response in the right parahippocampus and dopaminergic midbrain for reward-paired drawings versus non-rewards (Dillon et al., 2014) while depressed individuals showed the opposite pattern.

Furthermore, hippocampus likely plays a role in cognitive and affective consequences of chronic pain: deficits in working memory and short/long-term memory have been detected in chronic pain models (Yalcin et al., 2014a). Neurogenesis and synaptic plasticity were shown to be impaired in preclinical pain models (Mutso et al., 2012). In a rat spared nerve injury (SNI) model, increased HIP connectivity towards VS and sensorimotor areas inversely correlated with mechanical pain thresholds (Baliki et al., 2014) and activation of dorsal HIP reversed allodynia in the same model (Apkarian et al., 2018). Hippocampus volume was found to be reduced in chronic pain patients with fibromyalgia (Kuchinad et al., 2007; Lutz et al., 2008), CRPS, and CBP (Mutso et al., 2013). Moreover, decreased FC between hippocampus and mPFC (Mutso et al., 2013) predicted chronification of back pain.

Ventral pallidum (VP): In rats, the term VP was first used to describe the forebrain region below the anterior commissure, extending into anterior perforated space that contained pallidal-like cells. Substantia innominata (SI) is also an extension of the reward-related striato-pallidal complex. VP receives inputs from VS, subthalamic nucleus (STN), and midbrain dopaminergic neurons and projects to STN, hypothalamus, SN/VTA, PPT, MD nucleus of thalamus, striatum, and LHb (Haber and Knutson, 2010). Glutamatergic VP neurons seems to play a role in aversion processing, while canonical GABAergic VP neurons promote reinforcement and encode the hedonic value of reward (Wulff et al., 2018) via their influence on VTA and LHb.

Thalamus: Mediodorsal nucleus (MD) of thalamus projects to PFC and is the final link in the reward circuit; it completes the reward circuit back to cortex. MD receives reciprocal and non-reciprocal inputs from the cortex. Thalamic relay nuclei from the basal ganglia seem to integrate information flow from reward and higher cortical association areas of the PFC (Haber and Knutson, 2010).

1.2.3.2 Rodent models of chronic pain and its affective consequences

Although the reciprocal interaction between pain and depression is well documented, clinical pain conditions and depressive outcomes are very heterogenous; rendering the study of underlying neurobiological mechanisms challenging. Preclinical animal research is uniquely positioned to address this issue; as the experimental conditions can be carefully controlled and pain variables can be precisely measured (Li, 2015). Moreover, preclinical studies allow for more invasive methodologies; the effects of novel pharmacological and non-pharmacological analgesics can be tested in animals (Thompson and Bushnell, 2012).

Chronic pain models: Many animal models have been developed that are designed to model different aspects and/or origins of sensory pain and have good construct, face and predictive validity (e.g. inflammatory, nerve injury or cancer pain) (Li, 2015). Since trauma is one of the leading causes of neuropathic pain and it can be easily applied in animal models, most chronic pain models are based on nerve injury. Commonly used nerve injury-induced chronic pain models in rodents are as follows (Doan et al., 2015; Li, 2015; Yalcin et al., 2014a): Chronic constriction injury (CCI), partial sciatic nerve ligation (PSNL), spinal nerve ligation (SNL), common peroneal nerve ligation, spared nerve injury (SNI), and cuff model. Several of these rodent pain models have been used to study the anxiety and depression-like comorbidity.(Doan et al., 2015). Previous studies showed that it is possible to model the relation between chronic pain and anxiety and depressive-like consequences by taking into consideration the time factor (Gonçalves et al., 2008; Suzuki et al., 2007; Yalcin et al., 2014a). Indeed, in chronic pain models, while the hypersensitivity to pain develops quickly, anxio-depressive behaviors are time dependent and develop much slower; usually weeks after primary injury (Li, 2015). Time-dependence of affective consequences of pain points to a reorganization of brain circuits or neuroplasticity in the interim.

Behavioral tests for anxio-depressive phenotype: There are several renowned and well-validated behavioral tests which could be employed to demonstrate anxio-depressive consequences of chronic pain in rodents (Yalcin et al., 2014a). They are summarized in Table 1-3. Depression also includes homeostatic, neurovegetative (abnormalities in sleep, appetite, weight), or cognitive symptoms; however these symptoms are much less studied in chronic pain paradigms (Yalcin et al., 2014a).

Table 1-3 Commonly used behavioral tests for anxiety and depression related phenotypes.

Anxiety-related	Depression-related
Exploratory-based approach-avoidance conflict tests • Elevated plus maze (EPM) • Open field (OF) • Light-dark exploration (LD)	Exposure to stressful situations and the measure of time spent in active versus passive stress coping • Forced swimming test (FST) • Tail suspension test (TST) • Learned helplessness Interest in pleasurable activities • Sucrose preference test (SP) • Social interaction measures (SI) Motivation Marble burying (MB)
Both anxiety and depression related	
Novelty suppressed feeding test (NSF)	

Table 1-4 Selected studies on the affective consequences of neuropathic pain.
(Table taken from Yalcin, Barthas, and Barrot (2014).) ALB: anxiety-like behavior, DLB: depression-like behavior, BB: burrowing behavior)

Pain models	Species	Tests	Results	References
PSNL	Rat	BT	BB deficits	Andrews et al. (2012)
	Mouse	OF, EPM, TST	No effect	Hasnie et al. (2007b)
	Mouse	OF	No effect	Kodama et al. (2011)
	Mouse	LD, EPM	ALB	Narita et al. (2006a,b)
	Mouse	LD, EPM	ALB	Matsuzawa-Yanagida et al. (2008)
SNL	Rat	OF, EPM, LD, FST	No effect	Kontinen et al. (1999)
	Mouse	OF, EPM, LD, FST	ALB, DLB	Suzuki et al. (2007)
CCI	Rat	FST, SP	No effect	Bravo et al. (2012)
	Rat	FST, OF	DLB	Zeng et al. (2008)
	Rat	EPM	ALB	Roeska et al. (2009)
	Rat	FST	DLB	Fukuhara et al. (2012)
	Mouse	EZM, FST, OF	No effect	Urban et al. (2011)
SNI	Rat	OF, EPM, FST	No ALB, DLB	Goncalves et al. (2008)
	Rat	OF, EPM, FST	ALB, DLB	Leite-Almeida et al. (2009)
	Rat	OF, EPM	ALB	Seminowicz et al. (2009)
	Rat	FST, SP	DLB	Wang et al. (2011)
	Mouse	OF, FST	No ALB, DLB	Norman et al. (2010)
	Mouse	EZM, FST, OF	No effect	Urban et al. (2011)
	Mouse	DL, NSF	ALB	Mutso et al. (2012)
Cuff	Mouse	EPM, MB, SI, TST	ALB	Benbouzid et al. (2008)
	Mouse	LD, MB, NSF, Splash, FST	ALB, DLB	Yalcin et al. (2011)
SNT	Rat	FST	DLB	Hu et al. (2010)
	Rat	BT	BB deficits	Andrews et al. (2012)
Antiretroviral	Rat	OF, BT	ALB, BB deficits	Huang et al. (2013)

1.2.3.3 Structural and functional MRI of preclinical depression models

Although the comorbidity of chronic pain and depression is well-established; there is a scarcity of research on this topic in the MRI field, both in clinical and preclinical settings. *To the best of our knowledge, there is no animal MR imaging study focusing on depression induced by neuropathic pain.* However, in order to see whether the brain mechanisms underlying pain-induced and stress-induced depression are similar or distinct and develop targeted therapies for each individual pathology; it is paramount to study and compare the two conditions. The following table (Table 1-5) offers an overview on animal imaging studies of depression induced by other models, mainly stress-related mechanisms. As discussed earlier, several brain regions pertaining to reward circuitry show dysfunction in depression models.

Table 1-5 Preclinical imaging studies in rodent depression models.
Abbreviations: *DKI: Diffusion kurtosis imaging; HR-MRI: high resolution MRI; rCBV: regional cerebral blood volume; MEMRI: manganese enhanced MRI; MK: mean kurtosis; AD: axial diffusivity; RD: radial diffusivity; ALFF: amplitude of low frequency fluctuations; CPu: caudate-putamen; AMY: amygdala; BLA: basolateral amygdala; PFC: prefrontal cortex; DG: dentate gyrus; FC: functional connectivity; DRN: dorsal raphe nucleus; BNST: bed nucleus of stria terminalis; DMN: default mode network; TH: thalamus; HY: hypothalamus; HIP: hippocampus; vHIP: ventral hippocampus; BDNF: brain-derived neurotrophic factor.*

Study	Species	Model	Imaging modality	Findings
Delgado y Palacios et al. 2014	Rat	Chronic mild stress	DKI, HR-MRI	MK reduced; AD increased at CPu for *stress susceptible animals*: RD at AMY increased; CPu/brain volume ratio increased
Gass et al. 2014	Rat	Congenital learned helplessness (cLH)	rCBV, rs-fMRI	rCBV bilaterally increased in LHb, DG, subiculum; decreased in BNST for *cLH* FC increased for DRN-forebrain serotonergic connections, hippocampo-frontal network and BNST-lateral frontal connection in *cLH*
Henckens et al. 2015	Rat	Immobilization stress	rs-fMRI, DKI, HR-MRI	FC in somatosensory, visual and DMN areas increased in *chronic stress* Volume and diffusivity of lateral ventricles increased in *stress*
Gass et al. 2016	Rat	Congenital learned helplessness (cLH) – *negative cognitive state rats*	rs-fMRI	Increased internodal role, decreased local clustering/efficiency in ACC and PL for *negative cognitive state* Enhancement of long-range connections (AMY, DMN)

Study	Species	Model	Imaging modality	Findings
Grandjean et al. 2016	Mouse	Chronic psychosocial stress (CPS)	rs-fMRI, DTI	Overall increased FC including PFC and cingulate networks (mouse DMN) in *stressed mice:* increased between network FC for AMY-PFC and AMY-cingulate networks Increased FA in cingulum bundle
Laine et al. 2017	Mouse	Chronic psychosocial stress (CPS)	MEMRI	Increased activity in PFC, BNST, vHIP, and PAG for *stressed mice*
Clemm von Hohenberg et al. 2018	Rat	Negative cognitive state (NC/cLH)	rs-fMRI	Optogenetic perturbation of LHb decreased DMN FC in NC rats
Huang et al., 2018	Mouse	Chronic unpredictable mild stress (CUMS)	rs-fMRI	ALFF was increased in HIP and PFC; decreased in BLA; BDNF levels were inversely correlated with ALFF; increased in BLA and decreased in HIP, PFC for CUMS.

2 Hypothesis and Objectives

My **main objective** in this thesis work is to map functional and structural brain connectivity alterations in neuropathic pain and depression comorbidity using preclinical MRI in a mouse model. Probing the brain networks in a mouse model is an important step for translational research as similar MRI techniques exist for clinical investigations and therefore, animal findings can be transferable to humans. Such characterization of the network fluctuations underlying depression development would bring essential information regarding the mechanisms of the disease, paving the way towards targeted therapeutic interventions. In addition, such altered circuitry patterns might constitute specific biomarkers of the disease, relating with the causality (i.e. pain) or the severity and specificity of the mood disorder.

I conducted **a preliminary study** to inform the choice of **mouse strain** to be used in the neuropathic pain-induced depression model: Many inbred strains of mice are commercially available and C57BL/6N and BALB/cJ are the two strains most commonly used for depression studies. However, important strain differences as well as intra-strain variability were reported in the literature regarding both the behavioral outcomes and neuroanatomy (Fairless et al., 2013, 2012; Kim et al., 2012). Therefore, an important aspect in my project was to compare the brain connectivity between C57BL/6N and BALB/cJ mice using structural and functional MRI, with the aim of determining more adapted strain for modelling depression. (*see* section 3.1, page 47)

Subsequently, I applied non-invasive, *in vivo* MRI methods in a longitudinal experimental design in **neuropathic pain-induced depression** model, **aimed** at following the development of the anxio-depressive phenotype and brain network remodeling over time.

My **hypothesis** is that neuropathic pain and subsequent anxio-depressive phenotype are associated with time-dependent changes in brain structure and connectivity at functional and structural levels. Based on the previous literature discussed in the **Introduction** section; I predict alterations in brain regions linked to both pain processing and reward circuitry. The alterations likely mirror human counterparts of modifications in the brain structure and connectivity for these pathological processes and could be useful for developing novel treatments for patients. (*see* section 3.2, page 74).

3 Results

3.1 Mapping the living mouse brain neural architecture: strain specific patterns of brain structural and functional connectivity.

Meltem Karatas[a,b,c], Vincent Noblet[b,d], Taufiq Nasseef[e], Thomas Bienert[a], Marco Reisert[a], Jürgen Hennig[a], Ipek Yalcin[c], Brigitte Lina Kieffer[e], Dominik von Elverfeldt[a] and Laura-Adela Harsan[a,b,f*]

[a] Department of Radiology, Medical Physics, Medical Center – University of Freiburg, Faculty of Medicine, Breisacher Strasse 60a, 79106 Freiburg, Germany,

[b] Laboratory of Engineering, Informatics and Imaging (ICube), Integrative multimodal imaging in healthcare (IMIS), UMR 7357, University of Strasbourg, 4 Rue Kirschleger, 67000 Strasbourg, France

[c] Institut Neurosciences Cellulaires et Intégratives (INCI), CNRS UPR 3212, University of Strasbourg, 8 allée du Général Rouvillois, 67000, Strasbourg, France

[d] Laboratory of Engineering, Informatics and Imaging (ICube), Images-Modelling-Learning-Geometry and Statistics (IMAGeS), UMR 7357, University of Strasbourg, 300 Bd Sébastien Brant, BP 10413, 67412, Illkirch Cedex, France

[e] Department of Psychiatry, School of Medicine, Douglas Hospital Research Center, McGill University, Montreal, QC, Canada

[f] Department of Biophysics and Nuclear Medicine, Hautepierre Hospital, University Hospitals of Strasbourg, 1, Avenue Molière, 67098 Strasbourg Cedex, France

Corresponding author:

Laura-Adela Harsan

Email: harsan@unistra.fr

Keywords:

mouse brain connectivity, resting state functional magnetic resonance imaging, diffusion tensor imaging, BALB/cJ, C57BL6/N, inbred strains

3.1.1 Introduction

Animal models of disease - essential for neuroscience research, are gaining huge importance in the recent years with the development of genetically modified mice and novel methods to investigate brain function. However, the diversity in the genetic background of the organisms used for modelling pathology raises questions of the impact of genetic confound on findings (Crawley et al., 1997; Keane et al., 2011). Indeed, each strain of mice display distinct sets of behavioral, neurochemical and neuroanatomical features (Grubb et al., 2004). Among these strains, C57BL/6 and BALB/cJ the commonly used inbred mouse strains, are prime examples of such divergent phenotypes (Anderzhanova et al., 2013; Belzung and Griebel, 2001; Calcagno et al., 2007).

At behavioral level, BALB/cJ strain displays neophobia (i.e. reluctance to engage with novel stimuli) and elevated anxiety (Anderzhanova et al., 2013; Ohl et al., 2001), in contrast to C57BL/6 mice. At young ages, social proximity is not rewarding for BALB/cJ mice (Panksepp and Lahvis, 2007) and they typically show reduced sociability towards conspecifics (Brodkin, 2007; Brodkin et al., 2004; Jacome et al., 2011; Moy et al., 2007; Sankoorikal et al., 2006). Such differences in social behavior are accompanied by differences in early maternal care (Lassi and Tucci, 2017) as BALB/cJ mice present a weaker maternal attachment to offspring compared to C57BL/6 mice. To divulge the underlying mechanisms of different behavioral phenotypes in C57BL/6 and BALB/cJ mice, neurochemical and neuroanatomical studies are indeed necessary (Belzung and Griebel, 2001). For instance, it has been previously demonstrated that serotonergic and dopaminergic neurotransmitter systems show strain-dependent variations in the brain (Calcagno et al., 2007; Guzzetti et al., 2008). At anatomical and microstructural level, longitudinal in-vivo diffusion tensor imaging (DTI) (Le Bihan, 2014; Le Bihan and Breton, 1985) of BALB/cJ and C57BL/6J mouse brains (Kumar et al., 2012) showed as well differences in developmental trajectories along major white matter (WM) tracts, such as the corpus callosum, as well as of gray matter (GM) regions including thalamic areas and frontal motor cortices.

Besides inter-strain differences, within strain inter-individual variations were also reported, especially concerning the BALB/cJ animals. Neuroanatomical studies using histological methods revealed variability of the size - even complete absence - of the corpus callosum (cc) in BALB/cJ mice (Wahlsten, 1974). The size of this structure (Fairless et al., 2008) and whole brain size (Fairless et al., 2012) were correlated with social measures in 30-day-old BALB/cJ mice. In addition to histology, anatomical magnetic resonance imaging (MRI) and DTI of the brain, evaluating morphology and microstructural features (Kim et al., 2012; Kumar et al., 2012), further revealed associations between sociability and DTI-derived parameters in several brain regions (Kim et al., 2012), including gray matter, of BALB/cJ male mice. For instance, positive regression between fractional anisotropy (FA) - an index of water diffusion orientation and indirectly of tissue organization – and social sniffing times was found in regions located in thalamic nuclei, zona incerta, substantia nigra, visual/orbital/ somatosensory cortices, and entorhinal cortex of BALB/cJ strain (Kumar et al., 2012).

In clinics, alterations in the corpus callosum region has also been detected in subgroups of autism spectrum disorders (ASD) patients (Alexander et al., 2007; Just et al., 2006). Indeed, behavioral phenotype of BALB/cJ mice also share similarities with certain aspects of ASD, namely the low sociability, higher anxiety and aggression (Brodkin, 2007; Liska and Gozzi, 2016). Such behavioral phenotypes might stem from the underlying architecture of neural circuitries and

established patterns of brain communication. Therefore, mapping the brain connectivity blueprints is an essential field of study in neurology and experimental neuroscience.

A detailed non-invasive insight into the whole brain axonal connectivity in vivo has become possible with the development of diffusion based tractography (Horsfield and Jones, 2002) and high-resolution fiber mapping (hrFM) (Calamante et al., 2011; Harsan et al., 2013). In mice, non-invasive DTI based fiber mapping revealed the spatial organization of axonal and dendritic networks in brain WM regions, in good agreement with the spatial projection patterns visualized using viral axonal tracer data (Wu and Zhang, 2016).

Meanwhile, the functional brain communication or connectivity (FC) can be deciphered non-invasively via resting-state functional MRI, detecting low frequency fluctuations in the blood oxygen level-dependent (BOLD) fMRI signals and their temporal correlations (Chuang and Nasrallah, 2017). Baseline BOLD signals manifest correlations between distinct brain areas that are co-activated during a task; thus, said to be functionally connected (Biswal et al., 1995).

In mouse models, deciphering strain-related patterns in the brain structural and functional connectivity or intra-strain variations of the brain wiring schemes have a tremendous importance, since these animals are used to answer questions relating to human neurological or neuropsychiatric disorders. In this context, the principal goal of our study was to bridge this gap by systematically probing the brain connectivity patterns of two mouse strains extensively used in preclinical neuroscience, including brain connectivity studies: C57BL/6N and BALB/cJ (Grandjean et al., 2017; Grubb et al., 2004; Hübner et al., 2017; Liska et al., 2015; Mechling et al., 2016; Shah et al., 2016a). We thus performed comparative MRI exploration of brain structure and function via a combination of brain deformation-based morphometry (DBM), DTI and hrFM and resting state functional MRI (rs-fMRI) in female animals.

3.1.2 Materials and Methods

3.1.2.1 Ethics statement

All procedures were conducted in compliance with the European Directive 2010/63/EU on the protection of animals used for scientific purposes, national guidelines of the German animal protective law for the use of laboratory animals and with permission of the responsible local authorities for the University Medical Center Freiburg (Regierungspräsidium Freiburg, permit numbers: G-08/15).

3.1.2.2 Animal setup

8-9 weeks old female C57BL/6N (n=11) and BALB/cJ (n=14) mice, purchased from Charles River Laboratories (Sulzfeld, Germany) were used for the MRI experiments. Animals were housed under standard animal room conditions (temperature 21°C, humidity 55-60%, food and water were given ad libitum).

For the rs-fMRI scans, the animals were initially anesthetized moderately using a subcutaneous (s.c.) medetomidine (MD, Domitor, Pfizer, Karlsruhe, Germany) bolus injection of 0.3 mg per kg body weight in 100 µl 0.9% sodium chloride solution. Preparation for the imaging session included the placement of the animal into the adapted imaging bed, stereotactic fixation of the head and attachment of physiological monitoring devices (pulse oximeter clipped to the hind paw, rectal temperature probe and pressure sensitive respiration pad placed underneath the abdomen). 15 minutes after the MD bolus injection, a continuous s.c. MD infusion of 0.6 mg per kg body weight in 200 µl per hour was applied to the animals throughout the rs-fMRI exams. Animals were monitored strictly for optimal physiological conditions (spO2: 97-99%, body temperature: 35.5±1.5°C, respiratory rates: 100-130 breaths/min). For the morphological T2-weighted and diffusion MRI acquisitions, anesthesia was switched to 1.5% isoflurane (Forene; Abbvie Deutschland GmbH & Co. KG, Wiesbaden, Germany) in 1.2 l/min oxygen and respiratory gating was performed. At the end of experiments the mice spontaneously recovered.

3.1.2.3 Data acquisition

All scans were performed using a 7T small bore animal scanner (Biospec 70/20, Bruker, Ettlingen, Germany), a cryogenically cooled quadrature mouse brain resonator (MRI CryoProbe, Bruker, Ettlingen, Germany) and the ParaVision software version 5.1 (Bruker, Ettlingen, Germany).

Resting-state fMRI data was acquired with T2*-weighted single shot Gradient Echo-echo planar imaging (GE-EPI) sequence using an echo time (TE) of 10 ms and repetition time (TR) of 1700 ms. 12 axial slices of 0.7 mm thickness were positioned on the mouse brain excluding olfactory bulb and cerebellum, field of view (FOV) and acquisition matrix were 19 × 12 mm^2 and 128 × 80, respectively. A resolution of 0.15 × 0.15 × 0.7 mm^3 was achieved and 200 volumes were recorded in an interlaced fashion for each run.

High resolution T2-weighted anatomical images (resolution of 0.051 × 0.051 × 0.3 mm^3) were acquired with a RARE sequence using the following parameters: TE/TR = 50 ms/6514 ms; 48 slices, 0.3 mm slice thickness, interlaced sampling, RARE factor of 4, 2 averages; an acquisition matrix of 256 × 196 and FOV of 1.3×1 cm^2.

Structural connectivity was investigated based on DTI data. Acquisitions were carried-out using a 4-shot DT-EPI sequence (TE/TR = 26 ms / 7750 ms; gradient duration (δ) = 4 ms and gradient separation (Δ) = 14 ms), with diffusion gradients applied along 30 nonlinear directions (Jones, 2004) and a b-factor of 1000 s/mm^2. 25 axial slices with 0.5 mm thickness were acquired with a FOV of 1.5 x 1.2 cm² and an acquisition matrix of 160 x 128 resulting in an image resolution of 0.094 x 0.094 x 0.5 mm^3.

3.1.2.4 Data processing

Anatomical MRI analysis

T2-weighted images were compared across groups using a DBM framework. First, each image was corrected for bias field inhomogeneity using N4ITK (Tustison et al., 2010). Then, all images were jointly registered in a deformable way using the group-wise registration procedure implemented in the ANTs registration toolbox (http://stnava.github.io/ANTs/) (Avants et al., 2011). Jacobian maps were computed for each estimated deformation field and a logarithmic transformation was applied on them so that dilation (i.e. jacobian greater than one) and contraction (i.e. jacobian between 0 and 1) are mapped on [0; +∞ [and]-∞; 0], respectively. These maps were finally smoothed using a Gaussian kernel (FWHM: 0.2 mm). Intergroup comparisons were conducted at the voxel level using the general linear model implemented in SPM12 (http://www.fil.ion.ucl.ac.uk/spm/). Statistical maps were thresholded at $P < 0.05$ after false discovery rate (FDR) p-value correction. Results were superimposed on the average morphological image built from the group-wise registration procedure.

Diffusion Tensor MRI data analysis and high-resolution fiber mapping (hrFM)

Post-processing of the diffusion data was performed using an in-house developed DTI and FiberTool software package for SPM (Harsan et al., 2013; Reisert et al., 2011). Diffusion based parameter maps were generated, including FA, mean diffusivity (MD), radial (RD) and axial diffusivities (AD). We further performed diffusion tractography using a global fiber tracking algorithm (Harsan et al., 2013; Reisert et al., 2011). With this family of tractography algorithms, the reconstructed fibers are built with small line segments (particle) described by a spatial position and orientation. These segments are the basic building blocks of a fiber model, bounding together to form the individual fibers. Their orientation and number are adjusted simultaneously and the connections between segments are formed based on a probabilistic procedure (Reisert et al., 2011). To generate fiber density (FD) maps, the number of tracts in each element of a grid was calculated from whole-mouse brain fibers in a manner very similar to previously published methodology (Calamante et al., 2011; Harsan et al., 2013). Further, the method used the continuity information contained in the fibers reconstructed during the global tracking procedure, to introduce sub-voxel information based on supporting information from neighboring voxels. After the generation of sufficient number of fibers passing a voxel at different spatial locations, their density was used as intravoxel information to construct highly resolved spatial histograms of diffusion orientations referred to as hrFM. The directionality of the fibers was therefore incorporated into the hrFM by assigning red/green/blue color to different spatial directions: red: mediolateral, green: dorsoventral and blue: rostro-caudal orientation.

The grid size was tailored to generate maps of 12 x 12 x 50 μm^3 of resolution, 8 times the resolution of the acquired data. hrFM allowed individual assessment of the connectivity features, highlighting fine details of the structural brain scaffolding.

Diffusion MRI parametric maps were also compared across groups using a voxel-based analysis. The FA and FD maps were jointly registered using the multimodal group-wise registration procedure implemented in the ANTs registration toolbox (Avants et al., 2011). The analysis was then conducted using the voxel-based quantification (VBQ) method (Draganski et al., 2011) which implements a combined weighting/smoothing procedure, avoiding parameter value changes by Gaussian smoothing applied in standardized space. Furthermore, we conducted voxel-wise analysis on FD maps modulated by jacobian values - in a similar way to the modulated grey matter probability map used in DBM (Good et al., 2001)- in order to quantify the amount of fibers in the standardized space which accurately reflects that of the native space. A Gaussian kernel with a FWHM of 0.5 mm was applied here. Intergroup comparisons were conducted at the voxel level using the general linear model in SPM12. Statistical maps were thresholded at $p< 0.05$ after false discovery rate (FDR) p-value correction. Results showing higher statistical values for each group were superimposed on the average FD or FA images built from the corresponding group images.

Resting-state fMRI analysis

Each of the resting-state fMRI image volumes were first realigned on the corresponding first scan, using a least square approach and a 6-parameter rigid body transformation in space. The rs-fMRI data was next registered to a morphological template created from individual T2*-weighted scans with ANTs software using deformable SyN algorithm (Avants et al., 2011). Spatially normalized images were smoothed using a Gaussian kernel with FWHM of 0.3×0.3×0.7 mm^3 on SPM8 and a zero-phase band-pass filter was applied to extract frequencies between 0.01-0.1 Hz, representatives of the low rs-fMRI Blood Oxygen Level Dependent (BOLD) signal. The signal from ventricles was regressed out using a least square approach in order to reduce non-neural correlations from the cerebrospinal fluid. Several analysis approaches were applied on this data as following:

Graph theory-based analysis of functional connectivity

To evaluate direct correlations between spatially separated regions of interest (ROIs), Partial Correlation (PC) analysis was performed (Hübner et al., 2017) between the mean time courses of the resting-state BOLD signal of included ROIs. 37 ROIs covering the major mouse brain cortical and subcortical areas were extracted from the Allen Brain Atlas (AMBA) (http://mouse.brain-map.org/static/atlas) (Lein et al., 2007) and registered on morphological template using an in-house built MATLAB tool.

The following analysis steps were carried out:

i. Groups specific average FC matrices of 37x37 ROIs (corresponding to each experimental group: C57BL/6N and BALB/cJ mice) were generated and the matrices were arranged according to the most similar pattern of connectivity across ROIs. The matrices were Fisher transformed to obtain the z scores associated to the connection strength – the edges - between pairs of ROIs. A one-sample t-test ($p<0.05$, FDR corrected) was applied to identify the statistically significant pairs of connections (edges). The resulting significant FC matrices were used to as inputs for graph theory measures. For each group, the most influent nodes of the network were identified using as parameters the weighted hubness (presented as the size of the node in the graph) and the Stouffer coefficients (color coded).

ii. Direct intergroup (C57BL/6N vs. BALB/cJ) statistical comparison of connectivity matrices ($P<0.05$, uncorrected) was performed to identify the most different "nodes" and "edges". A group comparison matrix (GCM) was generated and graphically represented (e.g. Figure 4G) with a color-scale, displaying statistically significant inter-group differences of connectivity. A method to identify most different network nodes among the FC matrices of the two strains was implemented. The following information was taken in account for ranking the most different nodes: the number of significantly changed connections for each node, the strength of the connection difference between pair of nodes and the number of statistically different connections of the neighboring nodes. This information is graphically represented in the GCM in relationship with the node's size and ranked in Figure 4H. Additionally, the group comparison matrix was used for calculating the Stouffer coefficients (Stouffer et al., 1949) for each node. A single p-value was computed for each region based on the combination of the p-values derived from the statistical tests made on the correlations with all other regions. The results were color-coded for most significantly different nodes (e.g. nodes color in the Figure 4B, E, G).

Seed-based functional connectivity analysis was further performed with a MATLAB tool developed in-house. Several ROIs (extracted from AMBA) were selected for this analysis based on the DTI and DBM results, as well as based on the previously published reports (Anderzhanova et al., 2013; Fairless et al., 2012; Kim et al., 2012; Kumar et al., 2012; Ohl et al., 2001, p. 6; Sankoorikal et al., 2006; Wahlsten, 1974) on the behavior of C57BL/6N and BALB/cJ mice. These ROIs were:

i. Right and left somatosensory cortex (SSr and SSl) and right and left motor cortex (MOr and MOl). These ROIs were used to check the inter-hemispherical connectivity.

ii. Anterior cingulate area (ACA) and retrosplenial cortex (RSP), to derive information about the default mode patterns in the two mouse strains. c) Key players of the known reward aversion circuitry: accumbens nuclei (ACB), hippocampus (hc).

iii. Partial correlation coefficients (Spearman correlation) were computed between the mean rs-fMRI time course of each ROI and the time courses from each voxel of the brain while excluding the effect of all the remaining voxels. Functional connectivity maps for each ROI were constructed at the individual level and also at the group level. Voxel-wise group based statistical analysis was performed using a two-sample t-test via SPM8 and the statistical results were cluster corrected at the $P<0.05$, FDR cluster corrected.

Directional connectivity analysis (DCA)

To probe dominant asymmetric information flow alterations within small network, population level directionality analysis using MVGC toolbox was performed (Barnett and Seth, 2014). A small network was constructed via selection of six regions of interest that showed structural/function strain differences in previous analysis: nucleus accumbens (ACB), anterior cingulate area (ACA), amygdala (AMY), caudate-putamen (CP), hippocampus (hc) and ventral tegmental area (VTA) (Figure 9 A). Briefly, the pre-processed resting state functional data was deconvolved (Wu et al., 2013) and pairwise unconditional Granger causality (completely data driven approach) (Barnett and Seth, 2014; Roebroeck et al., 2005) was carried-out on all possible seed pairs included in the constructed network, for each subject. Akaike information criterion (AIC) was engaged to find the best stable model order. Statistical analysis was implemented following t-test with multiple hypothesis testing (FDR correction, $p<0.05$).

3.1.3 Results

3.1.3.1 DTI reveals strain differences in structural connectivity

Diffusion tensor imaging data obtained from the BALB/cJ and C57BL/6N cohorts were used for global mouse brain fiber tracking, generation of hrFM as well as mapping of FA, RA, AD and trace values. These maps were assessed at individual and group levels. hrFM, displaying color-coded fiber orientations, were used as a first step to explore the whole brain structural connectome. Figure 3-1 (*on the next page*) presents exemplary hrFMs, representative for each strain (Figure 3-1-A for BALB/cJ strain and B for C57BL/6N strain). These maps are highlighting the variability of inter-hemispherical connectivity through corpus callosum (cc) within the BALB/cJ strain (Figure 3-1-A and B). Certain individuals from BALB/cJ group had visibly shorter cc; the variability along this major inter-hemispherical pathway is clearly identified at different callosal levels; namely the genu (gcc), body or middle part (mcc), and splenium (scc) parts (Figure 3-1). Additionally, statistical tests on fiber density maps showed higher variability within the BALB/cJ population (data not shown). C57BL/6N strain, in contrast, showed homogenous and well-defined structure of this region (Figure 3-1-B).

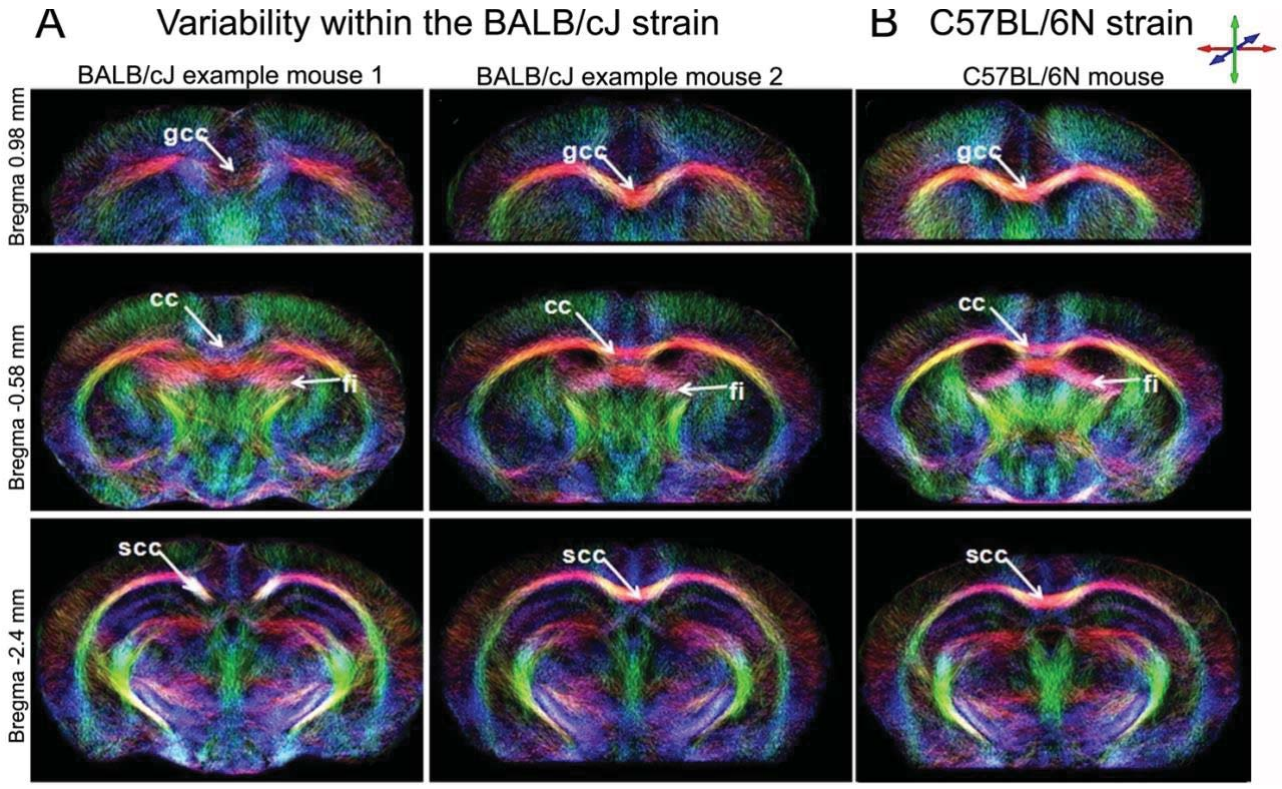

Figure 3-1 Living mouse brain connectional anatomy in BALB/cJ and C57BL/6N mouse brains.

Representative high-resolution fiber maps (hrFM) were generated from the global fiber tracking data and were reconstructed with a resolution of 12×12×50 µm3, at different bregma levels (bregma -0.6; -0.7 and -0.9). ***(A and B)****: Variability within the BALB/cJ mice population along the patterns of callosal (cc) connectivity. Reduced inter-hemispherical connectivity is seed in BALB/cJ mouse 1 compared to BALB/cJ mouse 2, at the levels of genu of the corpus callosum (gcc), body of the corpus callosum (bcc) and splenium of the corpus callosum (scc), suggestive of shorter callosal size in mouse 1.* ***(C)*** *Overall view of the connectional architecture in a C57BL/6N individual. The color-coding indicates the local fiber orientation: red, mediolateral; green, dorso-ventral; blue, rostro-caudal.*

To further assess the inter-strain differences, group-specific mean FD maps were generated (Figure 3-2-A and B) illustrating strain FD differences along the length of the cc. Individual FD maps were further used for voxel-wise statistical group comparison (C57BL/6N vs. BALB/cJ) (Figure 3-2-C and D). The C57BL/6N strain shows higher FD than BALB/cJ mice ($p<0.05$, FDR corrected; Figure 3-2-C) at the level of WM structures such as gcc and scc, fasciculus retroflexus (fr) or cerebral peduncle (cp). Significant differences are demonstrated in GM regions including prelimbic and anterior cingulate areas (PL and ACA), caudate putamen (CP) and dorsal hippocampus (dhc), temporal association areas (TEa), thalamus (TH), periaqueductal gray (PAG), and midbrain nuclei (MB). The shape of the areas is suggestive of FD differences along striato-cortical pathways (scp), reaching notably the ACA. By contrast, the statistics indicate higher FD values in BALB/cJ strain compared to C57BL/6N (Figure 3-2-C, $p<0.05$, FDR corrected) in motor areas (MO). The lateral ventricle (LV) area is marked in the statistics (Figure 3-2-D) as a result of morphological differences at the ventricular level in-between two strains, which is taken into account in the VBQ statistical method (Draganski et al., 2011).

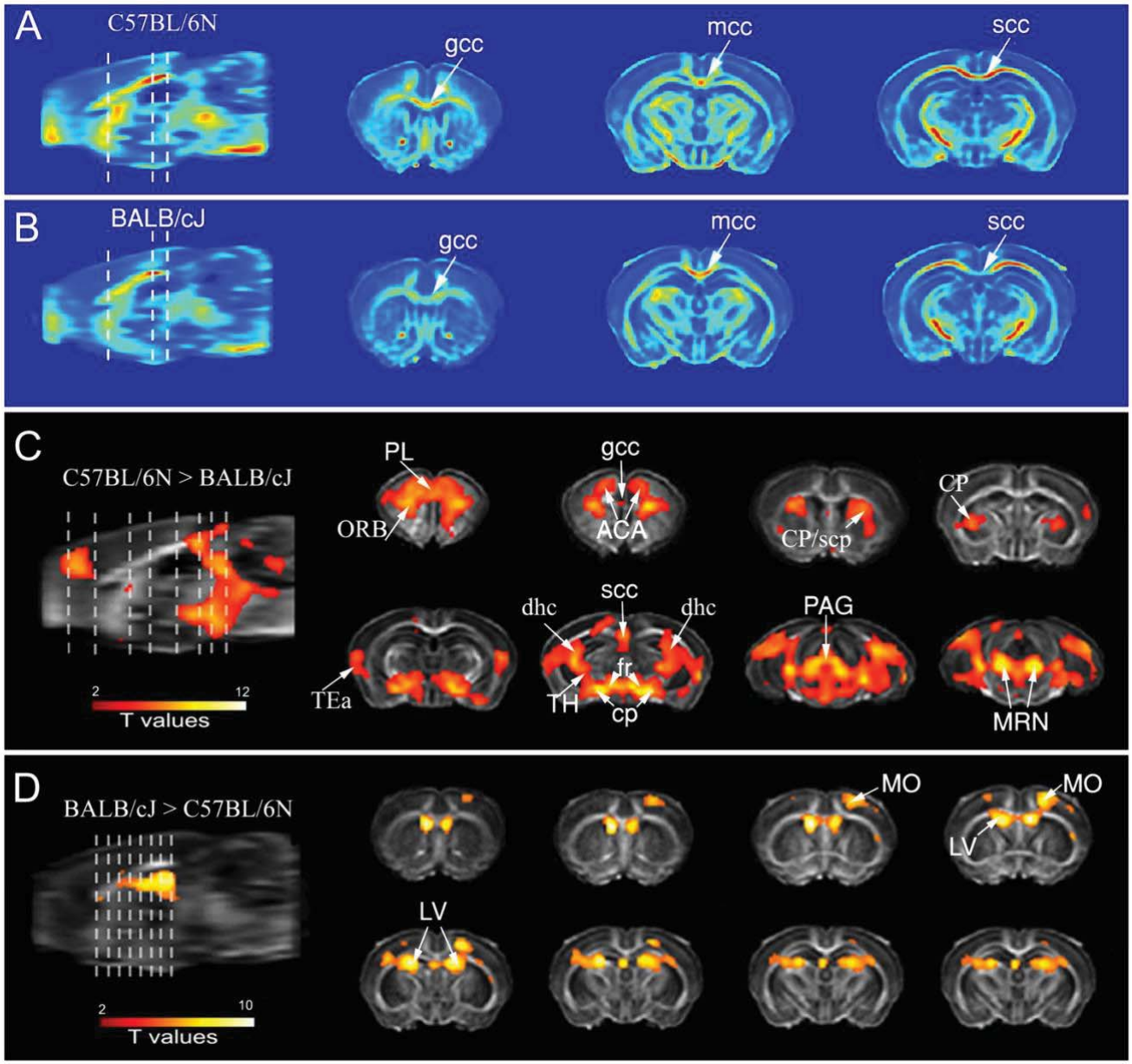

Figure 3-2 Group-specific fiber density (FD) maps reveal structural strain differences. ***(A)*** *Mean FD for C57BL/6N group.* ***(B)*** *Mean FD for BALB/cJ group.* ***(C-D)*** *Voxel-wise statistical group comparison of FD maps ($p < 0.05$, after false discovery rate (FDR) p-value correction; color scales represent t-values) indicate areas of differences* ***(C)*** *Contrast C57BL/6N > BALB/cJ: higher fiber density in C57BL/6N mice vs. BALB/cJ group.* ***(D)*** *Contrast BALB/cJ > C57BL/6N: higher fiber density in BALB/cJ mice vs. C57BL/6N group.[**Abbreviations:** Genu (gcc), middle (mcc) and splenium (scc) of corpus callosum(cc); fasciculus retroflexus(fr), cerebral peduncle(cp), striato-cortical pathways (scp), prelimbic area (PL), anterior cingulate area (ACA), caudate-putamen (CP), temporal association areas (TeA), thalamus (TH), periaqueductal gray (PAG), midbrain reticular nucleus (MRN), motor areas (MO), lateral ventricle(LV).]*

Statistical analysis of FA maps at the group level showed comparable differences between strains: cc, including anterior forceps (fa), cingulum (cg), gcc and scc, internal capsule (int), medial forebrain bundle (mfb) and cp as well as gray matter or mixed gray/white matter regions: PL/ACA, TEa, CP, dhc, TH, midbrain and pontine reticular nuclei (MRN; PRN, respectively) demonstrated significantly higher FA values in C57BL/6N strain ($p<0.05$, FDR corrected, Figure 3-3-A). The patterns are also indicative of increased FA along striato-cortical pathways. BALB/cJ mice, on the other hand, showed higher FA in ventral CP, as well as along caudal thalamo-cortical pathways (tcp), reaching somatosensory (SS) and auditory cortices (AUD) ($p<0.05$, FDR corrected, (Figure 3-3-B).

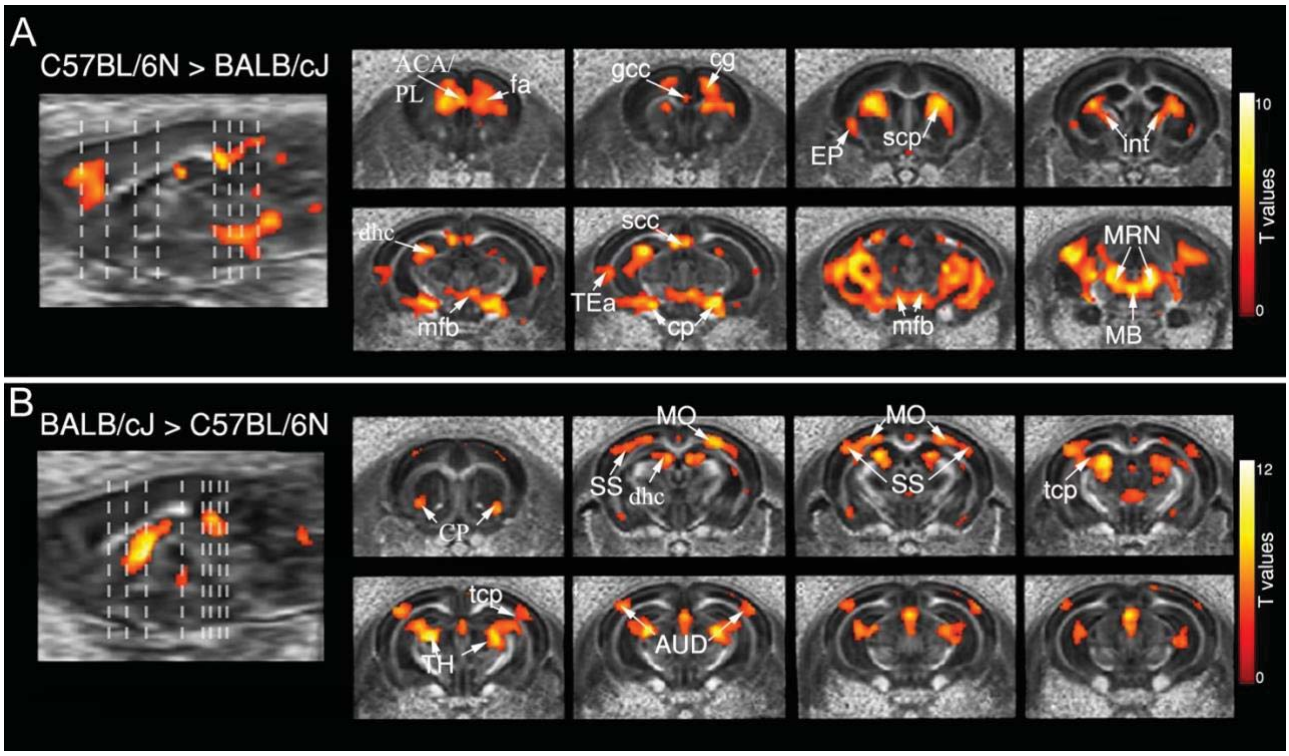

Figure 3-3 Fractional anisotropy (FA) maps reveal differences between strains.
(A-B) *Voxel-wise statistical group comparison of FA maps ($p< 0.05$, after false discovery rate (FDR) p-value correction; color scales represent t-values) indicate areas of differences* ***(C)*** *Contrast C57BL/6N > BALB/cJ: higher FA in C57BL/6N mice vs. BALB/cJ group.* ***(D)*** *Contrast BALB/cJ > C57BL/6N: higher FA in BALB/cJ mice vs. C57BL/6N group. [**Abbreviations:** Corpus callosum (cc), anterior forceps (fa), genu and splenium of cc (gcc and scc), internal capsule (int), medial forebrain bundle (mfb), cerebral peduncle (cp), prelimbic area (PL), caudate-putamen (CP), Ammon's horn (CA), temporal association areas (TeA), thalamus (TH), midbrain and pontine reticular nuclei (MRN; PRN, respectively) dentate gyrus (DG), thalamo-cortical pathways (tcp), somatosensory (SS) and auditory cortices (AUD).]*

3.1.3.2 Inter-strain regional volumetric differences uncovered by DBM

Figure 3-4 shows statistically significant brain volume differences in-between strains. C57BL/6N mice had significantly bigger ($p<0.05$, FDR corrected; Figure 3-4-A) frontal cortical areas, including ACA, MO and SS as well as TEa and entorhinal areas (ENT). At subcortical levels, the analysis revealed bigger septal areas in C57BL/6N mice and increased size at the level of thalamic nuclei (TH) (i.e. ventral group of the dorsal thalamus). The results also indicate larger lateral ventricles (LV) in the C57BL/6N strain. For BALB/cJ mice, volumes were significantly bigger ($p<0.05$, FDR corrected; Figure 3-4-B) in piriform area (PIR), CP, certain hippocampal areas, medial hypothalamus (HY), substantia nigra (SN), VTA, and PAG. Intriguingly, the body of cc had larger volume in BALB/cJ, suggesting a different inter-hemispherical connectivity in comparison to C57BL/6N strain, which might be a compensatory mechanism for shorter length of cc.

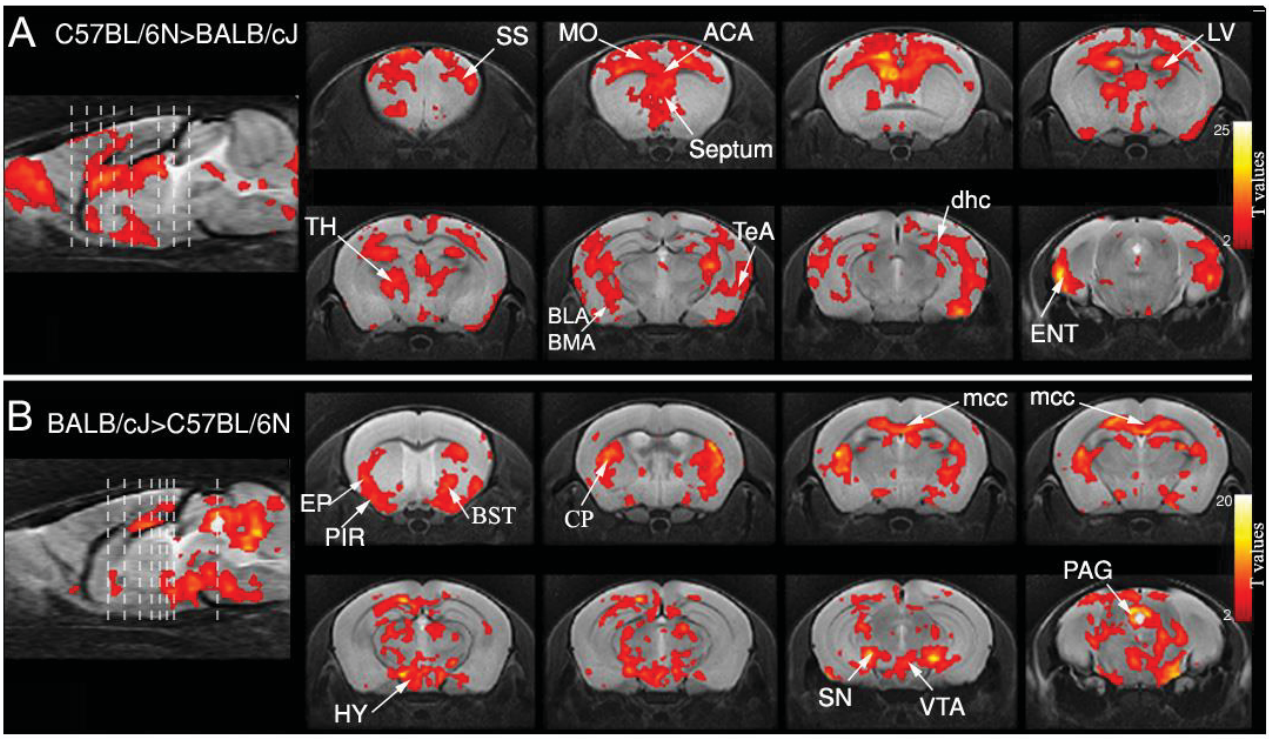

Figure 3-4 Inter-group statistical comparison for deformation-based morphometry (DBM).
(Threshold at P< 0.05 after false discovery rate (FDR) p-value correction; color scales represent t-values). ***(A)*** *Contrast C57BL/6N > BALB/cJ.* ***(B)*** *Contrast BALB/cJ > C57BL/6N. [Abbreviations: Anterior cingulate area (ACA), motor areas (MO), sensory areas (SS), temporal association areas (TeA), entorhinal areas (ENT), thalamus (TH), lateral ventricles (LV), piriform area (PIR), caudate-putamen (CP), Ammon's Horn (CA), hypothalamus (HY), substantia nigra (SN), ventral tegmental area (VTA), periaqueductal gray (PAG), corpus callosum (cc).]*

3.1.3.3 Functional connectivity patterns in C57BL/6N and BALB/cJ mice

To complete the picture of the brain connectome in the two investigated strains we further mapped the large-scale FC patterns via rs-fMRI, to determine whether their different brain structural architectures are accompanied by functional discrepancies.

Global FC features of C57BL/6N and BALB/6J brains

We applied graph network analysis at group level and mapped the topological organization of the FC, by modeling the 37×37 ROI PC matrices (Figure 3-5-A and D). The nodes were defined by the 37 ROIs extracted from AMBA, covering major cortical and subcortical brain areas. The selection of nodes was also guided by the structural results. For instance, certain nuclei, such as EP were included because differences in this area were observed in the voxel-wise FA analysis. Prominent inter-strain differences were obtained in the "hubness" characteristics (Figure 3-5-B, C vs. E, F). In the C57BL/6N group a dominance of basal forebrain subcortical areas was revealed (Figure 3-5-C – blue labels), encompassing the major limbic centers modulating reward (ACB, CP, ventral pallidum - PALv), stress and anxiety (bed nuclei of stria terminalis - BST) but also integrative centers for sensory information (Claustrum – CLA and EP). Cortical hubs included frontal areas; namely, insula (AI), piriform (PIR) cortex and orbito-frontal cortex (ORB), but also primary motor (MOp). The key player of the default mode network - the retrosplenial cortex (RSP) – was one of the C57BL/6N FC hubs.

The "hubness" patterns in the BALB/6J mice was dominated by cortical areas (see Figure 3-5-F), including associative (TEa) and sensory areas (visual - VIS, auditory - AUD, PIR). A marked difference when compared to the C57BL/6N was the absence of striatal/reward-related regions among the identified relay centers of the FC (i.e. ACB, CP).

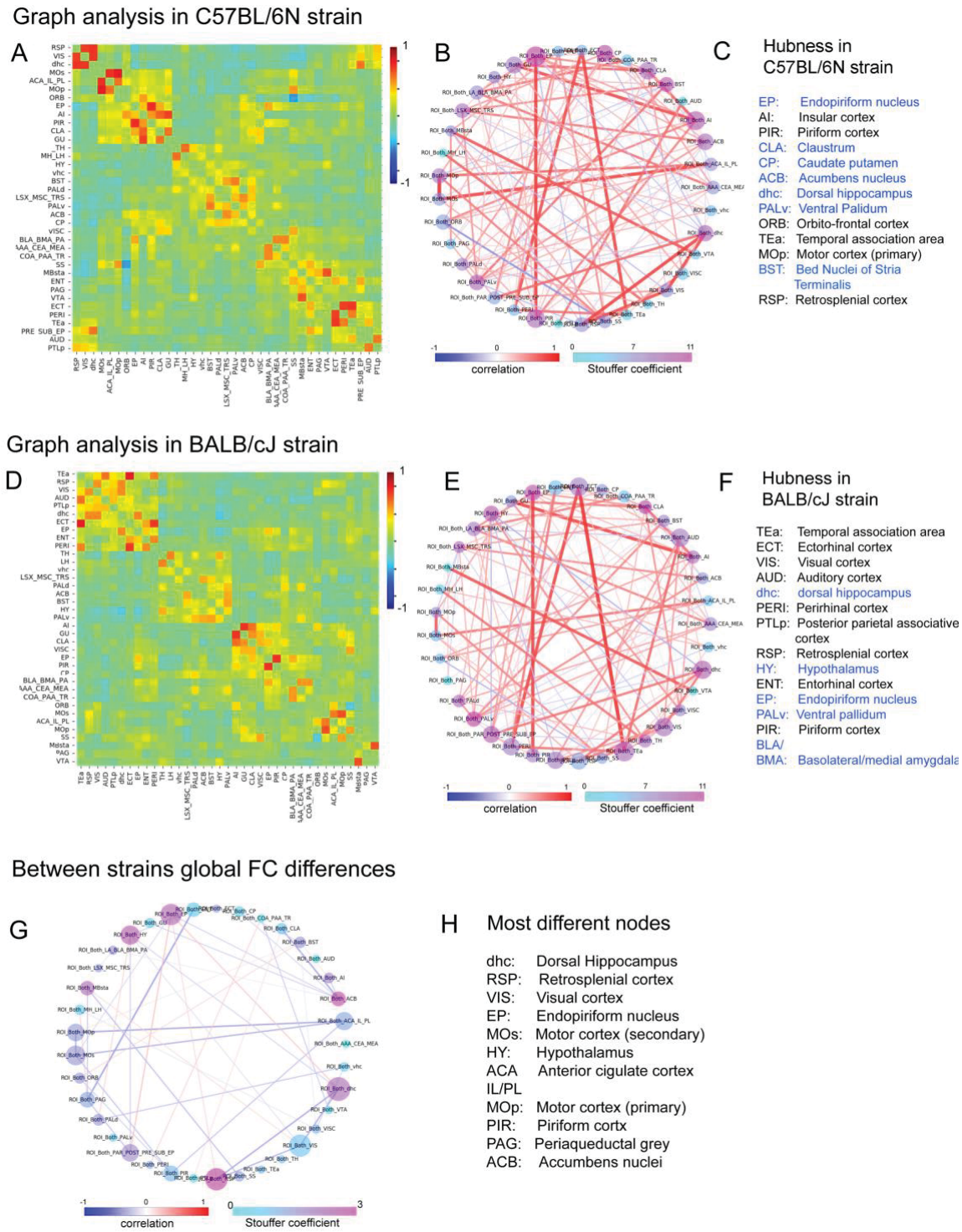

Figure 3-5 Functional connectivity matrices and related graph theoretical measures for C57BL/6N and BALB/cJ mice.

(A and D) *Functional connectivity matrices created with 37 bilateral brain areas (nodes) are represented for* ***(A)*** *C57BL/6N and* ***(D)*** *BALB/cJ. Color scale denotes correlation coefficients.* ***(B and E)*** *Statistically significant connections presented on a scale of correlation coefficients and matrix nodes color coded on a scale of Stouffer coefficients (one sample t-test, p<0.05, FDR corrected) for* ***(B)*** *C57BL/6N and* ***(E)*** *BALB/cJ matrices. (Node sizes correspond to hubness ranking.)* ***(C)*** *C57BL/6N and* ***(F)*** *BALB/cJ brains have distinct hub regions (List is ordered according to ranking, highest to lowest).* ***(G)*** *Differences between C57BL/6N and BALB/cJ brain FC are shown (Two sample t-test, p<0.05, uncorrected.). Connection strength differences are depicted on a scale of correlation coefficients and nodes are color coded to depict differences according to Stouffer coefficients; node sizes correspond to most different areas.* ***(H)*** *Ranking of most different nodes between C57BL/6N and BALB/cJ.*

Direct inter-group comparison of the global FC matrices identified the brain areas with divergent patterns of connectivity (Figure 3-5-G, H). ACB showed highest number of different connections (see color coding – magenta). However, when normalized for the strength of the connectivity difference with other nodes, dorsal hippocampus emerged as the most dissimilar area in terms of FC (Figure 3-5-H and Figure 3-5-G – size of the nodes). Furthermore, our global analysis suggested strain variations in the DMN features, as two of the main DMN nodes (ACA and RSP) appeared among the nodes with variant FC (Figure 3-5-H). Several sensory processing areas (VIS, PIR, EP) as well as MO suggest also strain specific connectivity patterns.

Most of the areas indicated as divergent in the graph resting state network analysis (Figure 3-5-G and H) were also highlighted in the inter-strain comparison of the structural data (i.e FA voxel vise analysis from Figure 3-3). Therefore, the next group level seed analysis of FC was guided both by the structural results and the brain-wide graph theoretical resting state results.

Inter-hemispherical FC

Given the structural differences observed at callosal level in between the two strains, we first evaluated the inter-hemispherical FC, largely mediated through cc connections. The connectivity between the right and left hemispheric SS and MO cortical areas were therefore investigated. We selected successively right and left-lateral SS (SSr and SSl) as seed regions for mapping their connectivity patterns across the whole brain; subsequently, group comparisons were performed (two-sample t-tests, $p<0.05$, FDR cluster corrected). Despite the group differences observed at the level of gcc and scc after group comparison for structural FD and FA maps, the FC of the SS cortices with the same anatomical areas of the contralateral hemisphere (homotopic areas) does not show statistically significant inter-group differences (Figure 3-6-A and B). Interestingly, the results indicate greater synchrony of the BOLD signal ipsilaterally, within the cortical areas of the same hemisphere for the BALB/cJ mice (Fig. Figure 3-6-A and B, blue areas). The feature was reproducible for both right and left SS seeds. SS cortex also showed stronger correlation with RSP and VIS area in C57BL/6N strain (Figure 3-6-A, red areas).

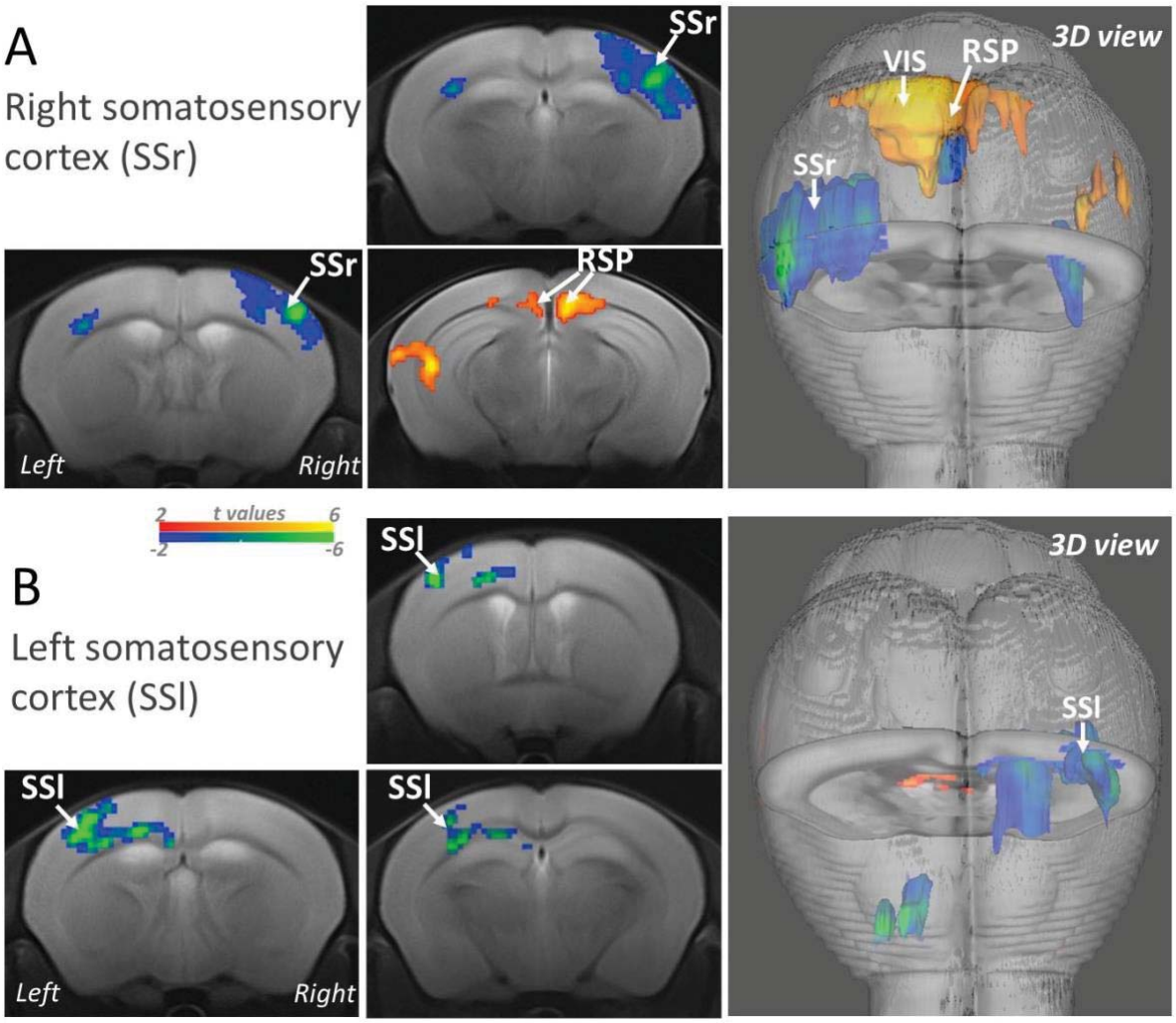

Figure 3-6 Inter-group differences in somatosensory cortex functional connectivity for C57BL/6N and BALB/cJ.

*Inter-group statistical comparison results of seed-based connectivity maps for **(A)** Right SS; **(B)** Left SS regions of interest (ROI). (FWER correction applied at cluster level for p<0.05); Scales represent t-values for contrast C57BL/6N > BALB/cJ in red or BALB/cJ > C57BL/6N in blue). [Abbreviations: somatosensory area right and left (SSr and SSl); posterior parietal association areas (PTLp), retrosplenial cortex (RSP), visual area (VIS).]*

Inter-group statistical analysis carried-out for MO areas - right (MOr) - and left (MOl), indicated more complex differences of FC in two strains. First reproducible feature for both right and left MO was the stronger FC connectivity with frontal cortical areas (ACA but also within rostral MO – ipsilateral and contralateral to the seed) and frontal subcortical areas (including ACB, CP, BST) in C57BL/6N. However - along the rostro-medial-caudal axis, the medial brain regions - MO (right and left) displayed higher intra- and inter-hemispherical synchrony of the BOLD resting state signal in the BALB/cJ group (Figure 3-7, blue patterns), notably within the sensory-motor cortex (SS and MO).

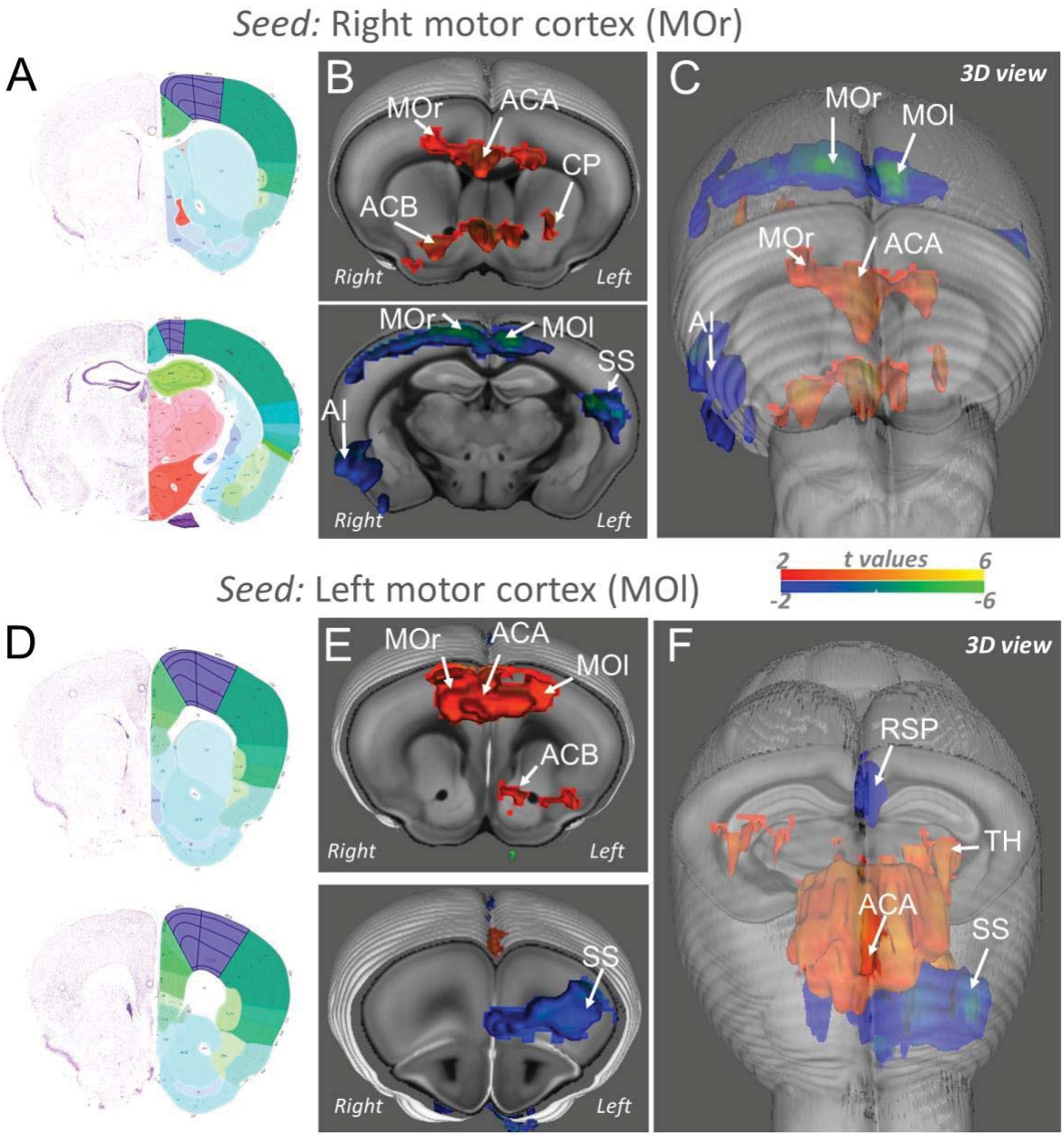

Figure 3-7 Inter-group differences in motor cortex functional connectivity for C57BL/6N and BALB/cJ.

*Inter-group statistical comparison results of seed-based connectivity maps for **(A)** Right MO; **(B)** Left MO regions of interest (ROI). (FWER correction applied at cluster level for p<0.05; Scales represent t-values for contrast C57BL/6N > BALB/cJ in red or BALB/cJ > C57BL/6N in blue). [Abbreviations: motor area right and left (MOr and MOl), anterior cingulate area (ACA), caudate-putamen (CP), nucleus accumbens (ACB), agranular insula (AI), somatosensory area (SS), retrosplenial area (RSP).]*

DMN patterns in C57BL/6N and BALB/cJ strains

The significant strain-specific features measured with structural MRI (Figure 3-3 and Figure 3-4) in the frontal brain areas including ACA - that is part of DMN- and along frontal part of cg bundle (Figure 3-3-A) suggested that DMN patterns might also have strain-specific characteristics. Therefore, we probed the topological patterns of DMN using seed analysis.

ACA and RSP were previously described as the key DMN nodes in rodents, showing synchronous rs-fMRI activity. We used the RSP as seed and mapped the spatial extent of DMN network, shown comparatively in Figure 3-8 for the two strains. A prominent pattern of BOLD rs-fMRI signal synchrony is noted along top cortical areas in both groups, encompassing the RSP and ACA cortices. Two main features are relevant: larger cortical extent along the caudal to rostral axis of the BALB/cJ DMN and RSP-subcortical connectivity (towards CP, hc and TH) patterns in C57BL/6N mice. Inter-group comparative evaluation (Figure 3-8-B, $p<0.05$, FDR cluster corrected) confirmed significantly stronger connectivity of RSP towards dhc and TH areas in C57BL/6N group. Further inter-group analysis of ACA FC (Figure 3-8-C) unmasked major differences in the topology of ACA network: (i) stronger patterns of synchrony within rostral ACA and with neighboring cortical areas (MO) in C57Bl/6N mice and (ii) stronger ACA connectivity with RSP and dhc in the BALB/cJ group.

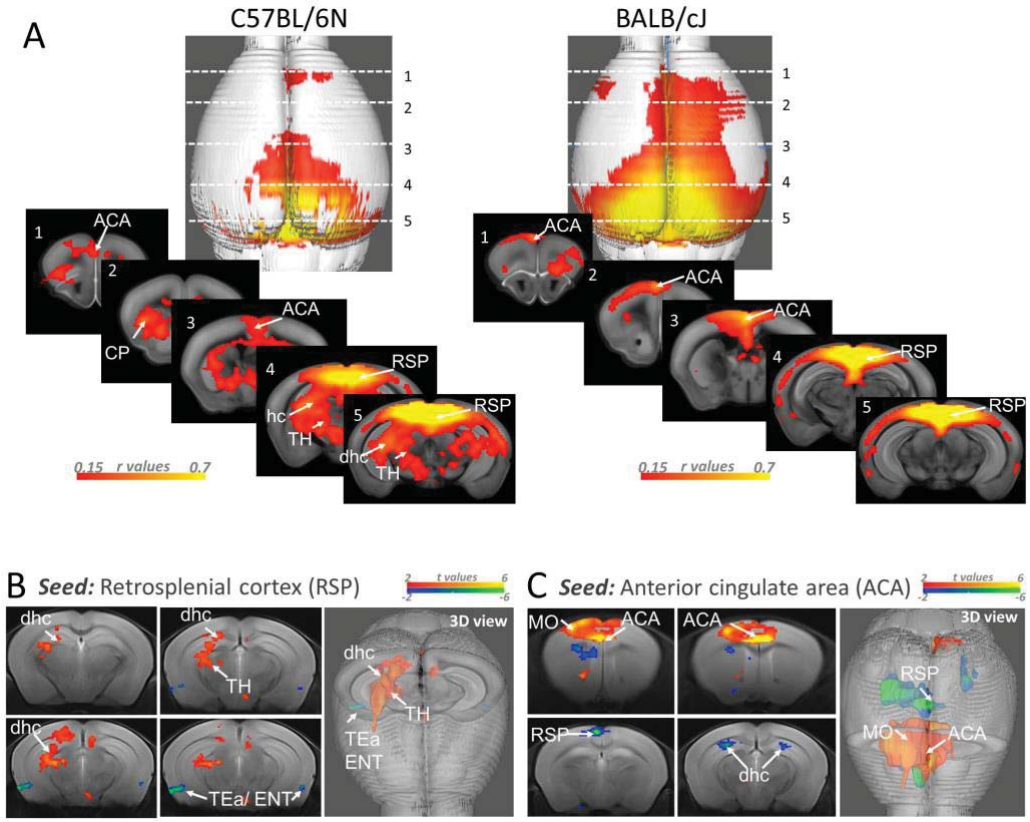

Figure 3-8 Default mode network (DMN)-like patterns in C57BL/6N and BALB/cJ. ***(A)*** *Default mode network as mapped using retrosplenial area (RSP) as seed in the C57BL/6N and BALB/cJ strains. (Correlation values were scaled between 0.15 and 0.7.)* ***(B and C)*** *Inter-group statistical comparison of functional connectivity in (B) Retrosplenial area (RSP) and (C) Anterior cingulate area (ACA); (FWER correction applied at cluster level for p<0.05; Scales represent t-values for contrast C57BL/6N > BALB/cJ in red or BALB/cJ > C57BL/6N in blue) [Abbreviations: motor area (MO), dorsal hippocampus (dhc), thalamus (TH), temporal association area (TEa), entorhinal area (ENT).]*

Functional connectivity of the reward/aversion centers

We next performed fine-grain connectivity mapping of ACB and hc using seed analysis and carried-out inter-group statistical analysis (Figure 3-9-A and B). These two areas are among key nodes of the limbic and/or reward-aversion system. This choice was motivated by reported behavioral results in the two strains, indicating different sociability and anxiety-related behaviors, possibly reflecting strain-specific patterns of the limbic FC. FC modifications of the limbic subcortical areas may emerge as well on the basis of the structural differences observed in the striatum (i.e greater FA and FD along C57BL/6N striatal-cortical pathways –Figure 3-3-A) or dhc (Figure 3-3-A and B), as shown in our study. Additionally, graph-based network analysis identified dhc and ACB as major nodes with divergent FC features in the two experimental groups (Figure 3-5-G and H). Seed correlation approach – in agreement with FA increase along striato-cortical pathways in C57BL/6N mice - revealed better rsfMRI signal synchrony between ACB and frontal cortex, encompassing ORB, ACA and MO in this strain (Figure 3-9-A), but also more caudally with RSP. Subcortically, ACB showed locally stronger FC with other centers of the reward circuitry, notably CP and ventral tegmental areas VTA (Figure 3-9-A) for C57BL/6N strain. Seed-based cartography of the hc network showed a better synchrony of the hc rs-fMRI signal with medial ACA, AI, SS, TEa as well as RSP in C57BL/6N brains, while better correlating with TH nuclei in BALB/cJ strain (Figure 3-9-B).

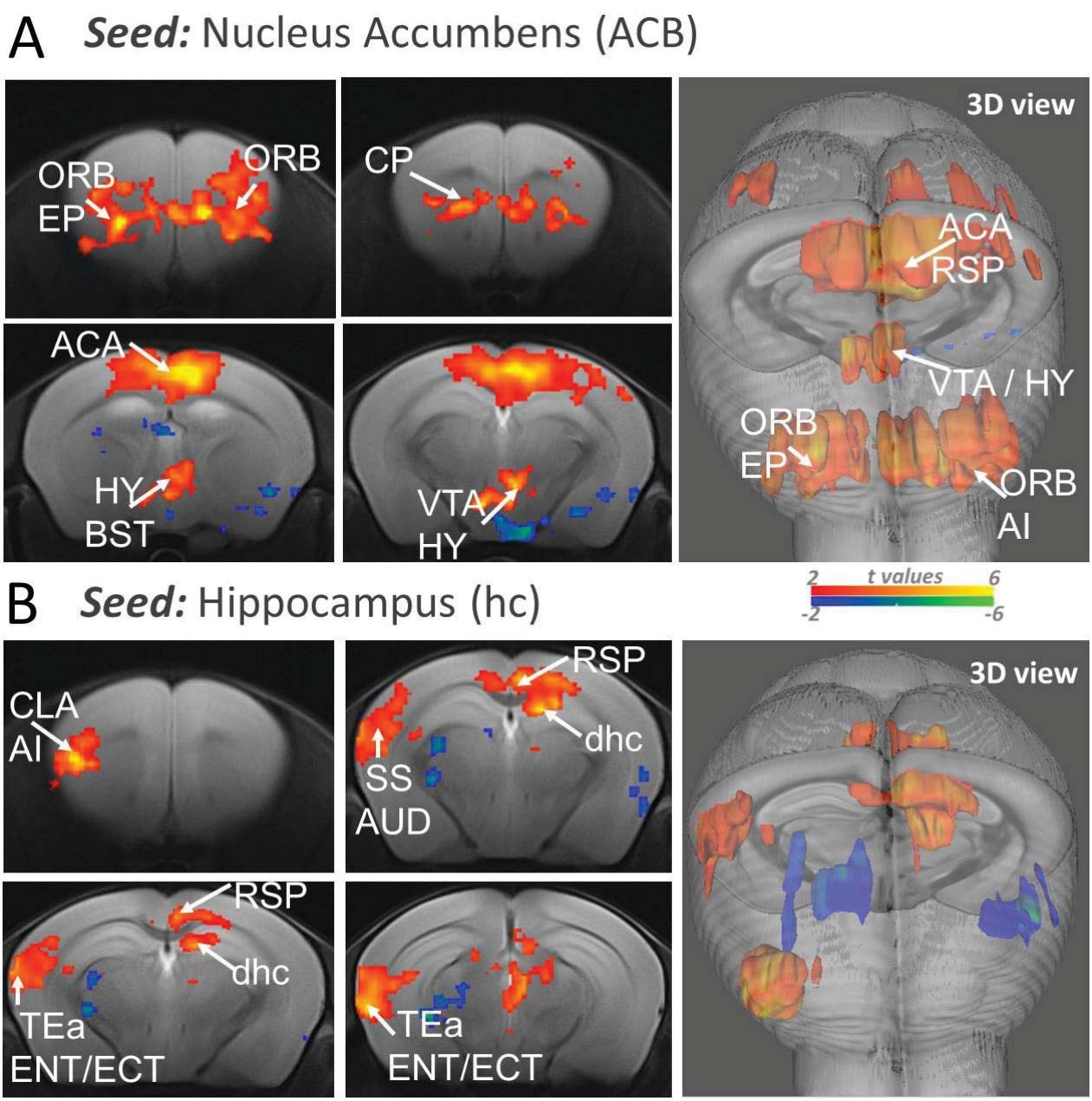

Figure 3-9 Inter-group statistical comparison of seed-based connectivity maps for nucleus accumbens and hippocampus.

(A) *Nucleus accumbens (ACB) and* ***(B)*** *Hippocampus (hc) functional connectivity differences between C57BL/6N and BALAB/cJ. (FWER correction applied at cluster level for p<0.05; Scales represent t-values for contrast C57BL/6N > BALB/cJ in red or BALB/cJ > C57BL/6N in blue) [Abbreviations: orbital area (ORB), anterior cingulate(ACA), endopiriform nucleus (EP), caudate-puatamen (CP), hypothalamus (HY), bed nucleus of stria terminalis (BST), ventral tegmental area (VTA), retrosplenial area (RSP), agranular insula (AI), claustrum (CLA), somatosensory area (SS), auditory area (AUD), temporal association area (TEa), entorhinal (ENT) and ectorhinal areas (ECT), dorsal hippocampus (dhc).]*

Directional communication analysis among key nodes of the reward/aversion network

To investigate the direction of information flow between pairs of nodes of the reward-aversion circuitry we conducted pairwise Granger Causality analysis. We constructed a network by selecting six relevant regions showing group differences in structural or seed-based FC analysis: ACB, hc, CP, ACA, amygdala (AMY) and VTA (Figure 3-10-A). These regions are core players of the reward circuitry and known to be involved in regulating -among others- the affective/social behaviors. For each set of ROIs, we computed pairwise Granger Causality extracting bidirectional information between pairs of nodes (Figure 3-10-B and D) and established dominant directionality ($p<0.05$; FDR corrected). Overall, the information flow directionality was similar in both groups with the exception of the ACA. This node was found to be dominantly receiving information from hc, AMY and CP only in C57BL/6N group and sending information towards ACB only in BALB/cJ strain; clearly providing evidence of group directional information differences in ACA region (Figure 3-10-C and E). Indeed, these findings again highlight the strain-specific communication patterns of ACA region, in accordance with seed-based FC analysis and microstructural and morphological (DTI and DBM) results.

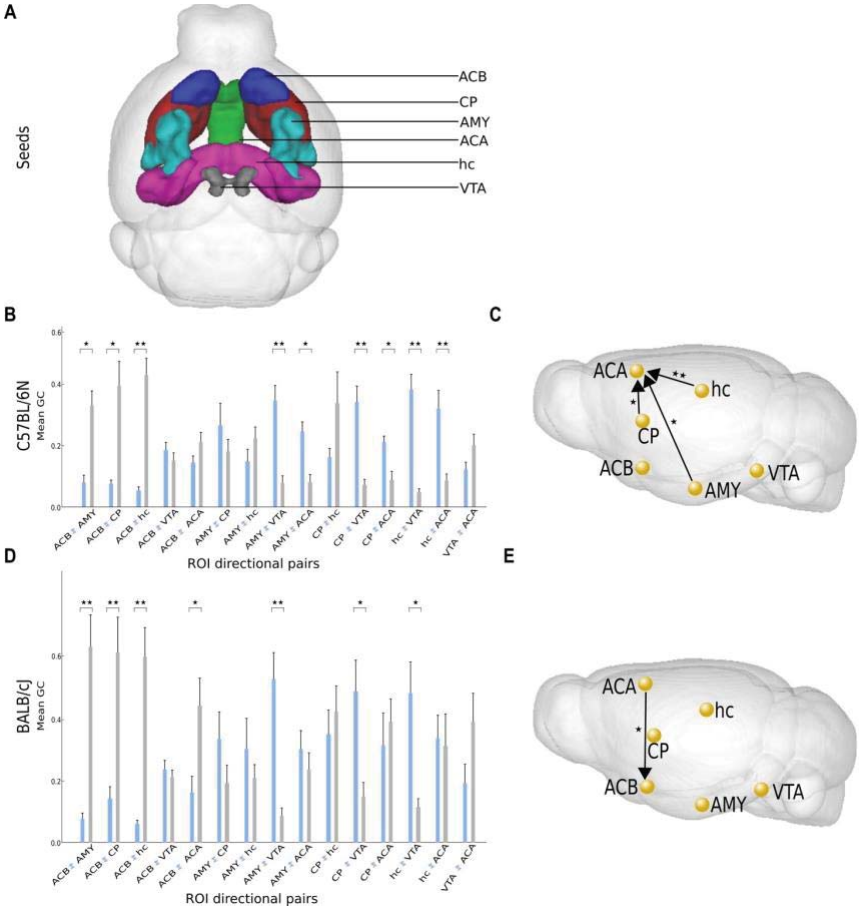

Figure 3-10 Directional connectivity between reward/aversion centers.
(A) *3D individual color-coded representation of 6 selected seeds over mouse brain template with identification;* ***(B-D)*** *Mean (+SEM) of Granger Causality results with t-test (*p<0.05,**p<0.01,***p<0.001, FDR corrected).* ***(C-E)*** *Graphical illustration of dominant directionality difference between the two strains (C57BL/6N and BALB/cJ) with black directional arrows including black stars to represent level of significance. [**Abbreviations:** Nucleus Accumbens (ACB), anterior cingulate area (ACA), Hippocampus (hc), Amygdala (AMY), Caudate-putamen (CP) and ventral tegmental area (VTA)].*

3.1.4 Discussion

In the recent years, huge effort has been dedicated for the characterization of the mouse brain connectome - at micro and mesoscale (Bardella et al., 2016; Grandjean et al., 2017; Grange, 2018; Ingalhalikar et al., 2014; Knox et al., 2018; Oh et al., 2014; Pervolaraki et al., 2019), as this species remains the principal animal model used in neuroscience research. Most of these studies were carried-out in the C57BL/6 strain, which remains the primary "genetic background" for modelling of human disease. However, C57BL/6 has many behavioral characteristics that make it useful for some work and inappropriate for others (Clipperton-Allen et al., 2015, p. 6; Fairless et al., 2013; Fontaine and Davis, 2016; Ohl et al., 2001; Pilz et al., 2015; Sankoorikal et al., 2006; Yoshida et al., 2016). Therefore, the uncovering the large-scale brain circuitry configurations in a strain-specific manner represents a first step towards a better understanding of modifications in brain networks under the influence of various genetic factors, pharmacological interventions and pathological conditions. In this study, we systematically characterized the brain morphological patterns along with the structural and functional connectivity profiles of two commonly used mouse strains, C57BL/6N and BALB/cJ, via non-invasive *in vivo* MRI techniques. We show brain-wide morphological and functional differences encompassing cortical and subcortical structures as well as WM tracts. We further provide exemplary high-resolution fiber tractography maps demonstrating the inter-individual variability across inter-hemispherical callosal pathways in the BALB/cJ strain.

3.1.4.1 Strain specific morphological and structural brain connectivity patterns

Multiple previous histological and MRI studies captured the impact of genetic variability on the morphology of the brain (Fairless et al., 2012, 2008; Fontaine and Davis, 2016; Kim et al., 2012; Kumar et al., 2012; X. Zhang et al., 2015). Mice on different genetic backgrounds have stable yet distinct behavioral phenotypes that may lead to unique gene-strain interactions on brain structure. One classical example is observed with Fragile X Mental Retardation 1 knock-out (FMR1-KO) mice in which Fragile X Syndrome and related phenotypic manifestations of autism spectrum disorder (ASD) are induced. Indeed, while FMR1-KO in C57BL/6 strain show very few differences in brain morphology compared to wild-type mice (Ellegood et al., 2010) FMR1-KO mice on an FVB background displayed multiple neuroanatomical differences, including modifications of major white matter structures throughout the brain and changes in areas associated with fronto-striatal circuitry (Lai et al., 2016). White matter changes, including prominent reduction of callosal fibers are also reported with BTBR mouse, another ASD mouse model (Dodero et al., 2013; Ellegood et al., 2013; McFarlane et al., 2008; Miller et al., 2013) In our study, we produced highly resolved fiber maps that depict striking inter-individual differences along callosal commissure in the BALB/cJ female mice, with significant inter-hemispherical under-connectivity in the rostral and caudal cc in some individuals. These *in vivo* brain tractograms are in agreement with previous histological (Fairless et al., 2012; Moy et al., 2007; Wahlsten, 1974) and diffusion MRI findings in BALB/cJ males (Kim et al., 2012; Kumar et al., 2012) that reported variability in the size of cc, including the complete absence, in 30-40% of this strain (Wahlsten, 1974). This variability was suggested to be possibly due to a variable delay in formation of an interhemispheric bridge of tissue in the dorsal septal region during prenatal development (Wahlsten, 1974).

In some ASD-relevant rodent models, this callosal underconnectivity normalizes overtime (Frazier et al., 2012), especially in the rostral regions of the cc - suggesting developmental

trajectories that might influence behavioral outcome overtime. The BALB/cJ inbred strain was long been discussed as relevant for certain aspects of ASD (Brodkin, 2007), showing low sociability, high anxiety and aggressive behaviors. However, compared to C57BL/6J mice, only juvenile BALB/6J animals demonstrated lower sociability scores (Fairless et al., 2012) that positively correlated with mean diffusivity values along the external capsule of the WM (Kumar et al., 2012).

Although in our study, we cannot establish a direct link between behavioral features and strain-specific brain structural modifications, we provide a refined, high resolution evidence about fiber density and tissue anisotropy dissimilarities at the level of callosal structures (gcc, mcc and scc) and alongside other WM bundles (fi, fx, cg) in female C57BL/6N and BALB/cJ mice. GM regions, likewise, showed distinct microstructural patterns in the two mice populations, prominent differences appearing in frontal cortices (ORB, IL, PL, ACA); along the fronto-striatal pathways (within CP) and within thalamic and caudal midbrain nuclei, including dopaminergic VTA and substantia nigra areas. For all these areas BALB/cJ mice show lower fiber densities and FA. Changes in fronto-striatal circuitry have been often implicated in the fragile X syndrome (FXS) with autistic-like features (Dennis and Thompson, 2013a, 2013b) as well as other brain disorders (Qiu et al., 2011; Shepherd, 2013), including attention deficit disorders. In FXS patients, the lack of response inhibition and conscious regulation of anxiety are among the phenotypes that relate to the functions of these regions (Bonelli and Cummings, 2007; Eagle et al., 2008; Fox et al., 2010), so it might be relevant that fronto-striatal fiber pathways are less dense in BALB/cJ animals, that are known to show high anxiety levels.

Furthermore, we observed large volumetric variations between two strains in the prefrontal, rostral MO, SS and temporal association cortices along with septal, hc and TH areas displaying bigger volumes in C57BL/6N. Intriguingly, mcc region was found to be larger in BALB/cJ; perhaps compensating for shorter rostro-caudal cc length to ensure unperturbed inter-hemispherical information transfer. In an *ex-vivo* study comparing several mouse strains (Ellegood et al., 2015) for brain morphometry, BALB/cJ mice were found to have smaller frontal and parieto-temporal lobes, similar to our findings. Such regional brain volume changes were correlated with functional impairments in ASD patients. For example, changes in superior and medial prefrontal gyri volumes correlate with cognitive outcomes in spatial relations and verbal fluency scores in ASD adolescents (Bray et al., 2011). In addition, larger CP volumes– as seen in BALB/cJ mice - is a recurrent finding in ASD patients and are associated with repetitive behaviors and cognitive deficits (Peng et al., 2014).

3.1.4.2 From structure to function: divergent functional connectivity in C57BL/6N and BALB/cJ mice

To discover whether differences in the brain structural scaffolding of the two strains also give rise to functional variations, we first performed a global assessment of the topological features of the rs-fMRI FC in both strains via graph analysis. The “brain hubs” - a set of highly connected regions serving as integrators of distributed neuronal activity were defined for each strain. These FC nodes have an integrative role and are therefore susceptible points to dysfunction in brain disorders. Strain differences in cerebral network “hubness” may impose strain-specific regional dominance in processing of the functional information. The circuitry vulnerability to stressors might be divergent, as well as the circuitry response in terms of mal-adaptations or compensatory remodeling.

Based on the anatomical selections of the FC network nodes, our analysis revealed that the dominant players in the C57BL/6N strain were subcortical forebrain limbic areas, including endopiriform nucleus, claustrum, along with centers controlling reward and motivation (ACB, CP, dhc, PALv). The endopiriform nuclei as well as claustrum are intriguing brain structures, featuring the highest connectivity per regional volume in the brain. Their connectivity patterns were dissimilar, both in structural and functional analysis. Enclosed between the striatum and the insular cortex, with widespread reciprocal connections with the sensory modalities and prefrontal cortices, these nuclei seem to perform functions in processing limbic and sensorimotor information (Watson et al., 2017). The “hubness” in BALB/cJ strain is dominated by cortical areas with associative and sensory valence (Tea, VIS, AUD, PERI, PTLp, PIR) but also includes aversive centers, such as amygdala (BLA/BMA).

In both strains, the RSP seem to appear as a hub, emphasizing the importance of this DMN node in the FC of the mouse brain. Inter-group comparison highlighted FC differences in brain areas showing variations in either the FA or FD maps or the morphometry measures. Dhc, the most different node in terms of FC showed higher FA and FD values, but also bigger volumes in the C57BL/6N strain. This is coherent with previous studies (de Sá-Calçada et al., 2015) that found smaller dendritic lengths and fewer ramifications in dentate granular neurons of BALB/cJ hippocampus compared to C57BL/6 strain. Differences in the hippocampal functioning and contextual memory formation in between the two strains were among the earliest demonstrated features (Chen et al., 1996) as hippocampal lesions impact less on contextual fear conditioning in BALB/c mice than C57BL/6 animals. In another study hippocampus related cognitive deficits – poor learning and memory performance in both the open field and passive avoidance inhibitory tasks - were assessed in stressed BALB/c, but not C57Bl/6 mice (Palumbo et al., 2010). This feature can be also mediated by distinct FC between dhc and frontal cortex (including ACA) and more dominant flow of information passing from the dhc to the ACA in C57Bl/6N strain. Previous studies demonstrated a role for the ACA-dhc pathway in recall of remote memory and its involvement in attention in both novel situations as well as during performance of well-learned tasks (Weible, 2013).

We further examined if inter-hemispherical FC of homotopic cortical areas, known to be largely mediated by callosal commissure show strain-specific features. FC between SS and MO homotopic areas did not show clearly a stronger inter-hemispherical connectivity in the C57BL/6N mice, as one might expect on the basis of the structural findings. Rather, a very specific pattern of FC differences was observed, along the rostro-caudal axis. For SS cortex, ipsilateral

connectivity was stronger in the BALB/cJ mice, displaying a greater intra-hemispherical synchrony of the BOLD rs-fMRI signal. These results could be reproduced for the MO cortex in the medial brain areas, where better inter-hemispherical FC was also noticed for BALB/cJ. These results reinforced the observed higher intra cortical FD and FA values of the motor cortex in the BALB/cJ strain and bigger volume of the cc in the medial region, eventually favoring the functional brain communication locally. The pattern is reversed however in more rostral regions where seed analysis of MO cortex shows stronger intra and inter-hemispherical FC in the C57BL/6N animals. Higher density of fibers and bigger brain volumes measured in the C57BL/6N strain for the ACA, ORB regions and along gcc, might facilitate the FC in this strain locally.

In a study comparing inter-hemispherical FC in different strains, comprising acallosal mouse strain I/LnJ, C57BL/6 and BALB/cJ (Schroeter et al., 2017), all strains demonstrated bilateral stimulus-evoked fMRI responses to unilateral hind paw stimulation, thus ruling out minimizing the contribution of transcallosal structural communication as a reason for bilateral FC. Emergence of inter-hemispherical homotopic cortical as well as striato-cortical connectivity was shown to be primarily due to monosynaptic connections (Grandjean et al., 2017); whereas, certain distributed cortical (e.g. default mode network) and subcortical networks emerge through polysynaptic connections in C57BL/6 brains. In BALB/cJ strain, compensation for inter-hemispherical cross-talk could be achieved through the thicker middle portion of cc or possibly through polysynaptic routes. In a rodent model of partial callosotomy (Zhou et al., 2014), initial decrease in inter-hemispherical connectivity was reversed over time, likely due to compensation by remaining axonal pathways. In this study, similar to our findings, an increased intra-hemispherical connectivity was also noted.

Default mode-like network

FC differences were also found in the DMN-like patterns of two mice populations. The DMN maps highlighted larger patterns of connectivity between RSP and parts of TH, CP and dhc areas in the C57BL/6N animals, while the ACA and RSP connect better along the top cortical line and TEa in BALB/cJ. Stronger local connectivity of ACA was noted in the frontal regions of C57Bl/6N brains, in agreement with locally increased density of fibers and higher FA in these areas. Weaker synchrony of the BOLD rsfMRI signal within DMN was previously reported in the C57BL/6 animals (Shah et al., 2016b), when compared to BALB/c and SJL mice. In the present work, we didn't reproduce the lower C57BL/6N functional connectivity features for DMN when compared with the BALB/cJ strain. We rather observed variance in the spatial organization of this network, with stronger cortico-subcortical communication in C57BL/6N and less functionally connected ACA-RSP.

Strain-dependent impact of the medetomidine anesthesia cannot be excluded in this context and depends – among other factors - on the expression levels of alpha-2 adrenoreceptors across the brain.

Functional connectivity signatures of reward aversion pathways

Reward system has consistently been implicated in several pathologies especially ASD and mood disorders (Hägele et al., 2015; Russo and Nestler, 2013) and is relevant for the behavioral phenotypes previously described in the C57BL/6N and BALB/c strains. For instance, BALB/c genetic background seems to favor strong response to stress conditions, show high anxiety and reduced social interaction (Anderzhanova et al., 2013; Brodkin, 2007; Moy et al., 2007; Ohl et al., 2001; Panksepp and Lahvis, 2007). Such phenotypes might stem from vulnerability of specific connectional pathways between key nodes of the reward-aversion system in which ACB is one of the major players. Our results thus demonstrated large patterns of stronger ACB FC in the C57BL/6N mice, including reinforced ACB - VTA dopaminergic pathways and stronger ACB – prefrontal cortical subcortical septal regions.

Activity dynamics of VTA - ACB projection encodes and predicts key features of social interaction in mice. Optogenetic control of cells specifically contributing to this projection is sufficient to modulate social behavior, mediated by dopamine receptor type 1 signaling downstream from VTA to ACB (Gunaydin et al., 2014). Weaker ACB-VTA communication might therefore form the neural substrate of the social reward deficiency previously described in the BALB/c mice. Similarly, differences of directional connectivity of the frontal cingulate (ACA) and striatal limbic network (CP, ACB and AMY) could account for behavioral differences in rewarding effects of addictive substances such as cocaine (Belzung and Barreau, 2000; Crawley et al., 1997). In light of distinct FC patterns we observed in the BALB/cJ mice, it could be argued that specific functioning of reward system determines the atypical behavioral phenotype in this strain.

3.1.5 Conclusion

Taken together, our findings demonstrate distinct structural and functional brain architectures in two frequently used mouse strains: C57BL/6N and BALB/cJ. In particular, BALB/cJ strain was characterized by marked intra-strain variability; thus, this variability should be taken into account while interpreting results from studies using BALB/cJ. C57BL/6N and BALB/cJ further show divergent brain wide FC diagrams; an essential aspect to be considered in experimental disease models that would also reflect inherent strain differences.

3.2 Time-dependent alterations in structural and functional brain networks in rodent neuropathic pain-induced depression

3.2.1 Introduction

Neuropathic pain is a neurological syndrome that associates both sensory nociceptive and aversive emotional components. It can also lead to anxio-depressive consequences, which increases the pain burden. The existence of neuropathic pain-induced affective disorders is further supported by preclinical studies showing that neuropathic pain models can induce anxiety- and/or depression-like behaviors in a time dependent manner (Yalcin et al., 2014a, 2011).

Previous imaging studies frequently focused on the transition from an acute to chronic pain state and demonstrated that the nucleus accumbens (ACB), hippocampus (HIP), prefrontal cortex (PFC)(M. N. Baliki et al., 2014; Bilbao et al., 2018; Chang et al., 2014), somatosensory and insular cortices (Baliki et al., 2012; Hubbard et al., 2015) are involved in the pain chronicity. However, we still do not know how the brain reorganizes functional connectivity when chronic pain comorbid with anxiety and depressive-like behaviors, which may stem from the fact that experiments in humans are generally cross-sectional in nature. Longitudinal experimental designs are thus the unique tool to study how changes occur overtime.

Longitudinal neuroimaging studies in rodent neuropathic pain models (M. N. Baliki et al., 2014; Bilbao et al., 2018; Hubbard et al., 2015; Seminowicz et al., 2009) demonstrated time-dependent changes in brain morphology, metabolism and functional connectivity. For instance, volume abnormalities in medial PFC and limbic brain regions (Bilbao et al., 2018; Seminowicz et al., 2009), altered glutamatergic transmission in the anterior cingulate area (ACA) and HIP (Bilbao et al., 2018; Hubbard et al., 2015) and an overall reorganization of corticolimbic system functional connectivity highlighting ACB, PFC and hippocampus connectivity changes (M. N. Baliki et al., 2014; Bilbao et al., 2018; Chang et al., 2014) were reported at different time points. However, the main focus of these aforementioned studies once again was nociception-related behaviors and pain chronicity.

Affective consequences of pain can be attributed to plasticity changes caused by chronic pain conditions in brain regions processing both pain and emotional/motivational information (Shelton et al., 2012; Yalcin et al., 2014a). In this framework, mesocortico-limbic circuits, encompassing reward/aversion areas such as ACB and ventral tegmental area (VTA) (Borsook et al., 2016; Mitsi and Zachariou, 2016), mPFC, ACA (Barthas et al., 2015; Wang et al., 2015; Z. Zhang et al., 2015; Zhuo, 2013) and limbic regions (e.g. amygdala, HIP) (Gonçalves et al., 2008; Mutso et al., 2013) have been shown to play important roles in negative moods associated with pain conditions. Rodent brain imaging studies using stress-based animal models of depression also highlighted the role of mesocortico-limbic areas (Anacker et al., 2016; Clemm von Hohenberg et al., 2018; Gass et al., 2014a) in particular, the major role of reward/aversion system comprising ACB, VTA, and lateral habenula (LHb). Moreover, hyperactivity of default mode network (DMN)- a large scale network of interacting brain regions that are activated during rest and deactivated during task performance- and its increased connectivity with subgenual cingulate characterizes major depressive disorder (MDD) in clinics. This hyper-connectivity is often interpreted as rumination, where depressed subjects persevere on negative, self-referential thoughts (Berman et al., 2011; Greicius et al., 2007). Similarly, these DMN alterations were also reported in rodent with stress-induced depression models (Grandjean et al., 2016; Henckens et al., 2015). Whether

the brain network alterations in stress-induced and pain-induced depression overlap or diverge is an important research question that needs to be answered for a better understanding of pain-depression comorbidity.

In this study, we combined neuroimaging methods with behavioral measurements for a global characterization of structural and functional brain changes in the neuropathic pain and depression comorbidity. For this purpose, we used the cuff model of neuropathic pain in mice (Benbouzid et al., 2008; Yalcin et al., 2014b), inducing mechanical allodynia and anxio-depressive phenotype in a time-dependent manner. We evaluated mechanical allodynia weekly and tested depressive-like behaviors at 8 weeks after cuff surgery, timepoint that animals develop the phenotype (Sellmeijer et al., 2018; Yalcin et al., 2011). We longitudinally followed brain functional and structural connectivity changes along with morphology at different time points by using resting-state fMRI (rs-fMRI), high angular resolution diffusion MRI (HARDI) and fiber tractography and anatomical imaging. Our objective was to identify brain structural and functional network signatures of pain-induced depression and to define specific imaging-related biomarkers for this condition.

Our main results showed that the cingulate area displays significant structural alterations over time with diffusion MRI. Furthermore, resting-state fMRI revealed the reorganization of the functional connectivity of brain structures involved in reward, DMN and salience pathways in a time-dependent manner.

3.2.2 Material and Methods

3.2.2.1 Animals

14 adult male C57BL/6J mice (Charles River Laboratories, L'Arbresle, France) were used for the MRI experiments. Mice were housed under standard animal facility conditions (4-5 per cage, temperature 21°C, humidity 55-60%, food and water were given ad libitum, 12h/12h light-dark cycle). All experiments were conducted in accordance with the European Directive 2010/63/EU on the protection of animals used for scientific purposes and approved by the local ethical committee of the University of Strasbourg (CREMEAS, No: 2016072818151694).

3.2.2.2 Neuropathic pain model and relevant behavioral tests

We used the cuff model to induce neuropathic pain in mice (Barthas et al., 2017). Cuff surgery was performed as described in the previous literature (Yalcin et al., 2014b). Briefly, mice were anesthetized with ketamine/xylazine (80/10 mg/kg) and then a polyethylene cuff was placed around right main branch of the sciatic nerve (cuff group, n=7). The nerve was simply exposed for the controls (sham surgery group, n=7).

Since mechanical allodynia is one of the main symptoms of neuropathic pain, we used von Frey filaments (Bioseb, Vitrolles, France) to evaluate the mechanical hypersensitivity weekly. For this, mice were placed in Plexiglas® boxes (7 cm x 9 cm x 7 cm) on an elevated mesh screen. After a 15-minute habituation, animals were tested by applying a series of ascending forces (0.6 to 8 grams) on the plantar surface of each hind paw. Each filament was tested 5 times per paw, applied until it just bent (Barthas et al., 2017; Yalcin et al., 2014b). The threshold was defined as 3 or more withdrawals observed out of the 5 trials. In order to characterize changes in mechanical thresholds during an extended period, we tested animals before and at given time points after sciatic nerve surgery.

Depressive-like phenotype was assessed eight weeks after the surgery using splash test. This test was used to measure grooming behavior indirectly (Barthas et al., 2017; Yalcin et al., 2011), as decreased grooming can be related to the loss of interest in performing self-relevant tasks. This behavior was measured for 5 minutes after spraying a 10% sucrose solution on the coat of the animals.

3.2.2.3 Experimental design

After baseline MRI acquisition, we separated animals into two groups (i.e. Control and Cuff) on the basis of baseline mechanical hypersensitivity. Second MRI acquisition was performed 2 weeks after the peripheral nerve injury (timepoint 1-TP1). The development of depressive-like phenotype was confirmed using the splash test 7 weeks after the neuropathic pain induction. The last MRI acquisition was conducted at 8-9 weeks post-surgery (timepoint 2-TP2). Mechanical threshold was checked once a week throughout the whole procedure (*see* Figure 3-11).

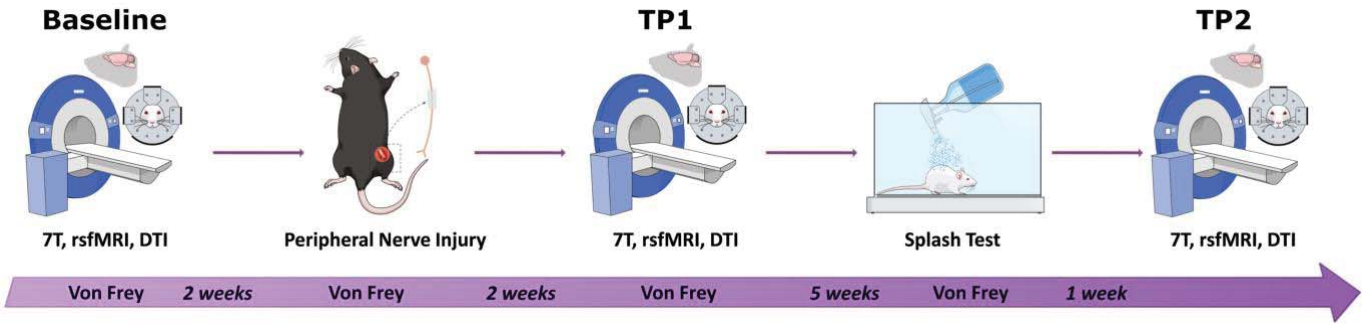

Figure 3-11 Experimental timeline.
After baseline resting state functional magnetic resonance imaging (rs-fMRI) and diffusion MRI acquisition, we separated animals into two groups, cuff and sham surgery groups (neuropathic pain and control mice, respectively) based on their mechanical hypersensitivity. Second MRI acquisition was performed 2 weeks after the peripheral nerve injury (TP1). The development of depressive-like phenotype was confirmed using the splash test 7 weeks after the neuropathic pain induction. Last MRI acquisition was conducted at 8-9 weeks post-surgery (TP2). Mechanical threshold was checked once a week throughout the entire procedure.

3.2.2.4 MRI data acquisition

All scans were performed with a 7T Bruker BioSpec 70/30 USR animal scanner, room temperature surface coil for the acquisition of the MRI signal and ParaVision software version 6.1 (Bruker, Ettlingen, Germany) at baseline and at 2 (TP1) and 8 weeks (TP2) after cuff surgery.

Animal preparation and placement were done under 2% isoflurane; a bolus of medetomidine (0.15 mg/kg body weight sc) was administered during preparation. 10 minutes after the bolus injection, isoflurane was discontinued, and animal bed was placed in the scanner. Medetomidine infusion was started (0.3 mg/kg bw /h sc) right before the rs-fMRI scans, within 35 minutes of bolus injection. Respiration and body temperature were monitored throughout the imaging session. Acquisition parameters for rs-fMRI were: single shot GE-EPI sequence, 31 axial slices of 0.5 mm thickness, FOV=2.12×1.8 cm, matrix=147× 59, TE/TR= 15 ms /2000 ms, 500 image volumes, 0.14× 0.23× 0.5 mm^3 resolution. Acquisition time was 16 minutes.

Morphological T2-weighted brain images (resolution of 0.08 × 0.08 × 0.4 mm_3) were acquired with a RARE sequence using the following parameters: TE/TR =40 ms/4591 ms; 48 slices, 0.4 mm slice thickness, interlaced sampling, RARE factor of 8, 4 averages; an acquisition matrix of 256 × 256 and FOV of 2.12×2 cm_2. For the diffusion MRI, medetomidine infusion was replaced with 1.5% isoflurane anesthesia. HARDI (High Angular Resolution Diffusion Imaging) acquisitions were carried out using a single shot DTI-EPI sequence, 27 axial slices, 0.1×0.1×0.5 mm^3 resolution, TE/TR= 28.9 ms/3000 ms, 4 averages, diffusion gradients applied along 30 non-collinear directions, 2 b-values (1000/2000 s/mm_2), gradient duration (δ)/separation(Δ)= 5 ms/10.6 ms for an acquisition time of 1 hour 13 minutes.

3.2.2.5 Statistical analysis of behavioral parameters

Data are presented as mean± SEM. For behavioral data, statistical analyses were performed with Statistica 7.1 software (StatSoft, Tulsa, OK) by using multifactor analysis of variance (ANOVA) with repeated measures and Duncan post hoc analyses for von Frey test and unpaired Student's t tests for splash test. Significance level was set to $p<0.05$.

3.2.2.6 MRI data processing

Resting-state fMRI data

Rs-fMRI images were spatially normalized into a template using Advanced Normalization Tools (ANTs) software (Avants et al., 2011) using SyN algorithm and smoothed (FWHM=0.28×0.46×1 mm_3) with SPM8.

Seed-based functional connectivity analysis was performed with a MATLAB tool developed in-house. Regions of interest (ROI) were extracted from Allen Mouse Brain Atlas (Lein et al., 2007) which were later normalized into the template space. Resting-state time series were de-trended, band-pass filtered (0.01-0.1 Hz) and regressed for cerebrospinal fluid signal from the ventricles. Principal component analysis (PCA) of the BOLD time courses across voxels within a given ROI was performed and first principal component accounting for the largest variability was selected as the representative time course for further analysis.

Partial correlation (PC) between the representative time courses of selected ROIs were computed to construct individual connectivity matrices for each mouse (76 pre-selected regions comprising limbic, cortical, reward, and nociceptive areas and covering the entire isocortex and major subcortical areas). Fisher's r-to-z transformation was applied to individual matrices and average PC matrices were computed by pooling the two groups at baseline, and for each group at TP1 and T2. Connections surviving $p<0.001$ (uncorrected) threshold for one sample t-test were selected for graph theoretical analysis using NetworkX software package for Python (https://networkx.github.io). A ranking of hub regions (nodes) are reported for each timepoint. For statistical comparison between the two groups, individual baseline matrices were subtracted from those belonging to TP1 and TP2, and two sample t-test was applied for subtraction matrices at each post-injury time point. Most changed connections (edges, expressed as degrees) and most changed nodes (expressed as Stouffer coefficients) were ranked among connections surviving $p<0.05$ (uncorrected) threshold. Briefly, Stouffer method uses a single p-value computed for each region based on the combination of the p-values derived from the statistical tests made on the correlations with all other regions, highlighting the regions with major changes in the inter-group comparison (Stouffer et al., 1949).

Furthermore, Spearman correlations between the PCA time course of single ROIs and each voxel of the brain was computed at the group and individual levels and r values were converted to z using Fisher's r-to-z transformation. Individual connectivity maps for baseline rs-fMRI acquisitions were subtracted from TP1 and TP2 counterparts for each subject. Baseline subtracted TP1 and TP2 connectivity maps were subsequently used for two sample t-test with SPM8 to perform group comparison at two post-injury timepoints. Family-wise error rate (FWER) correction was applied at the cluster level ($p<0.05$) for each statistical image. Additionally, statistical analysis of baseline-subtracted connectivity maps was performed using SPM full factorial ANOVA of the two factors group and time point, associated with two levels respectively (Neuropathic and control for the group factor; TP1 and TP2 for the time point factor) to compare longitudinal evolution of functional modifications between groups. The group effect results on the evolution functional connectivity of several ROIs from TP1 to TP2 in mice were reported ($p<0.05$, FWER cluster corrected).

Diffusion MRI data

Post-processing of the diffusion data was performed using an in-house developed DTI and FiberTool software package (*see* www.uniklinik-freiburg.de/mr-en/research-groups/diffperf/fibertools.html) for SPM on MATLAB. Diffusion-based parameter maps were generated, including fractional anisotropy (FA), mean diffusivity (MD), radial (RD) and axial diffusivities (AD). Mouse brain diffusion tractograpy using a global fiber tracking algorithm (Harsan et al., 2013) was also performed and fiber density (FD) maps were generated (Reisert et al., 2011). Diffusion MRI parametric maps were also compared across groups using a voxel-based analysis. The FA and FD maps were jointly registered using the multimodal group-wise registration procedure implemented in the ANTs; the analysis was then conducted using the voxel-based quantification (VBQ) method (Draganski et al., 2011). This method implements a combined weighting/smoothing procedure, which avoids parameter value changes by Gaussian smoothing applied in standardized space. Furthermore, we conducted voxel-wise analysis on FD maps modulated by jacobian values in order to quantify the amount of fibers in the standardized space which accurately reflects that of the native space. A Gaussian kernel with a FWHM of 0.5 mm was applied here. Baseline VBQ images were subtracted from images for later time points. Intergroup comparisons were conducted at the voxel level using the general linear model in SPM8. Statistical maps were corrected with family-wise error rate (FWER) applied at the cluster level for $p<0.05$.

3.2.3 Results

3.2.3.1 Behavioral results

von Frey and splash tests were carried-out as shown in Figure 3-11 at timepoints selected in correlation with MRI experiments to assess mechanical allodynia and emergence of depressive phenotype, respectively. The mechanical allodynia was evaluated at baseline (before surgery) and overtime (after cuff or sham surgeries). Mice were then scanned at 2 weeks, the time point corresponding to animals displaying only mechanical hypersensitivity (TP1) (Figure 3-12-A, $F_{(6,72)}$=6.26 p=0.000025; post-hoc: Neuropathic vs. Control from 1 to 7 weeks, p<0.00001) but not depressive-like behaviors, and at 8 weeks, the time point corresponding to cuff animals displaying both mechanical hypersensitivity and depressive-like behaviors as demonstrated by decreased grooming behavior in the splash test (TP2) (Figure 3-12-B, p<0.00001).

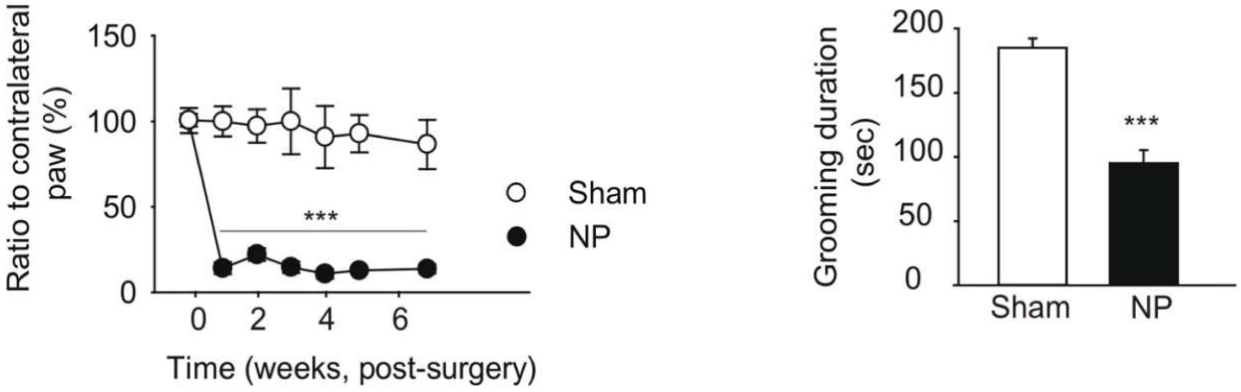

Figure 3-12 Nerve injury induces mechanical hypersensitivity and depressive-like behavior.
(A) *In C57BL/6J mice, unilateral sciatic nerve compression induces an ipsilateral long-lasting mechanical hypersensitivity. Results are presented as a ratio to contralateral paw (%).* ***(B)*** *Splash test at 7 weeks after the peripheral nerve injury illustrating decreased grooming behavior in neuropathic (NP) animals compared to sham-operated littermates. ***p<0.0001.*

3.2.3.2 HARDI measures of structural connectivity

Fractional anisotropy (FA) is a measure of water diffusion directedness within the tissue where values approach 0 for free unrestricted diffusion (i.e. isotropic) and 1 for oriented diffusion direction (i.e. anisotropy, such as seen in muscle and axonal fibers). FA could be an indicator of brain microstructural integrity, fiber organization and density, myelination, and axon diameters as well as other tissue characteristics unrelated to white matter (e.g. glial processes) (Scholz et al., 2009). We used voxel-based quantification (VBQ, *see* Material and Methods section) method for the inter-group analysis (TP1/TP2 neuropathic group vs. control group) of FA parametric maps. VBQ comparisons were performed after the subtraction of the baseline VBQ images from TP1 and TP2 counterparts.

Our results showed lower FA values in the neuropathic group in several areas involved in pain processing, including ACA, thalamus (TH), hypothalamus (HY), HIP and retrosplenial area (RSP) at TP1 (Figure 3-13-A). However, at TP2 these differences persist only for ACA and RSP (Figure 3-13-B) - core areas of rodent default mode network (DMN).

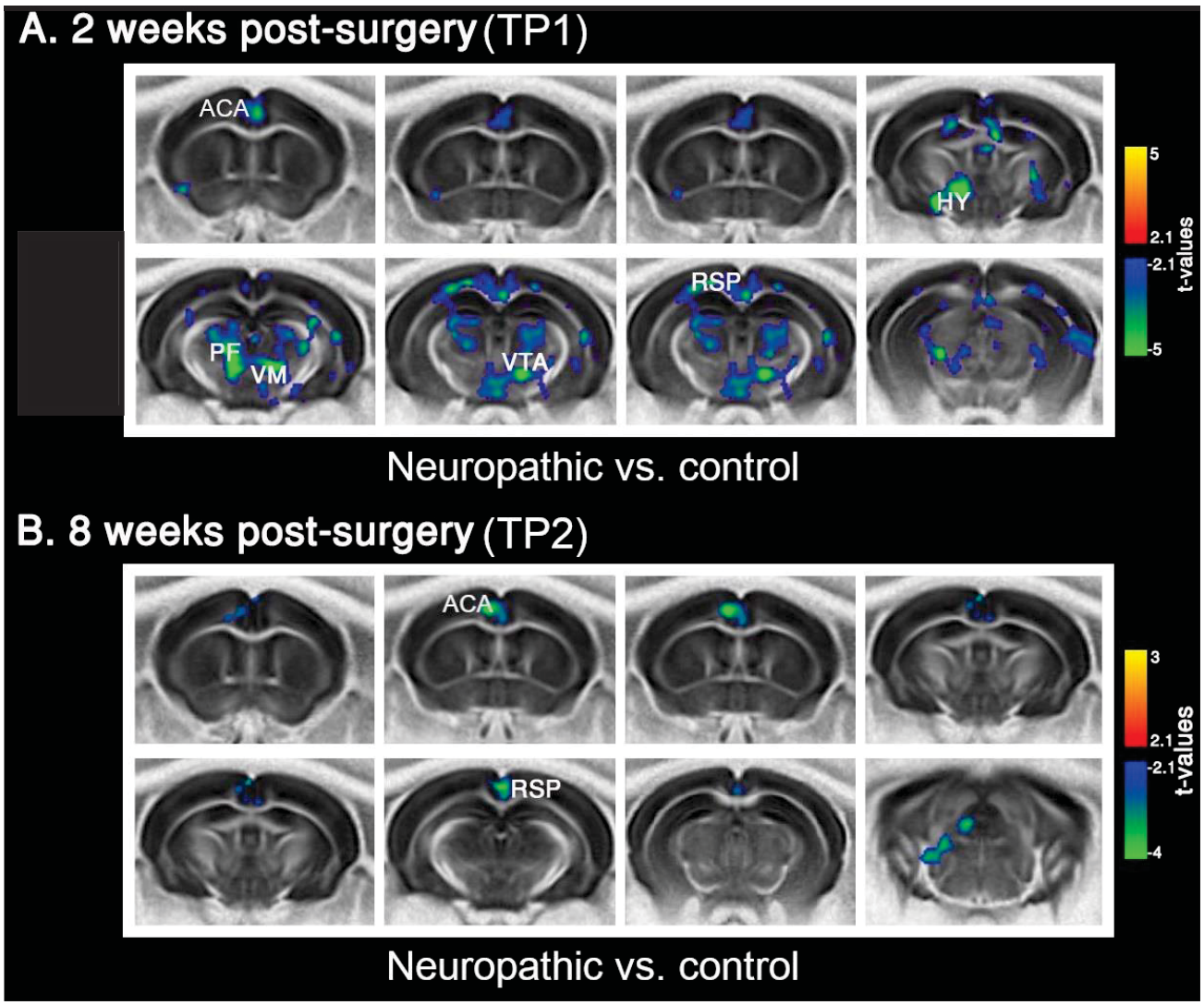

Figure 3-13 Fractional anisotropy (FA) differences between groups at 2 weeks (TP1) and 8 weeks (TP2) after peripheral nerve injury.
(A) *At TP1, neuropathic group displayed lower FA values than controls in the anterior cingulate (ACA) and hypothalamus, ventral tegmental area (VTA), parafascicular (PF) and ventromedial (VM) nuclei of thalamus (TH), and retrosplenial area (RSP).* ***(B)*** *At TP2, neuropathic mice showed lower FA than controls only in ACA and RSP. FWER correction used at cluster level for $p<0.05$ for statistical images.*

3.2.3.3 Functional connectivity (FC) via resting-state fMRI

Next, we created functional connectivity matrices for each timepoint to obtain a global view of the potential functional changes associated with neuropathic pain and subsequent depressive behaviors. We selected 76 unilateral ROIs which cover the entire isocortex and major subcortical areas including limbic, cortical, reward, and nociceptive areas. Figure 3-14 demonstrates the significant connectivity changes between neuropathic and control group matrices (Figure 3-14-A and D, $p<0.05$, uncorrected) overlaid on the mouse brain. We then calculated the connections (edges) and regions (nodes) showing most changes between the two groups at TP1 (Figure 3-14-A shows edge strength changes as correlation coefficients and node degree changes as Stouffer coefficients, node sizes correspond to ranking of most changed nodes; Figure 3-14-B, C list the most changed edges and nodes, respectively) and TP2 (Figure 3-14-D, E, F). At TP1, most changed nodes consisted of areas related to pain processing (e.g. TH and agranular insula-AI), and areas associated with aversion (e.g. amygdala, septum, ACB, hypothalamus, hippocampal formation and thalamus), highlighting pain-related functional alterations in the mouse brain (Figure 3-14-C). At TP2, however, the emergence of depressive phenotype coincided with functional changes mainly in reward/aversion areas (e.g. ACB, pallidum (PAL), ventral tegmental area (VTA), hippocampal formation, bed nucleus of stria terminalis (BST), and septum) and areas of rodent DMN (e.g. RSP, hippocampus, midbrain) which are known to be involved in major depression (Figure 3-14-F).

In light of the Stouffer analysis results determining the nodes with the most significant FC changes (Figure 3-14-C, F) and the structural connectivity results previously presented (Figure 3-13), we chose ACA, VTA, habenula (Hb), HIP, ACB, insula and periaqueductal gray (PAG) as regions of interest for inter-group analysis.

Intergroup comparison at TP1 : Neuropathic vs. control

A

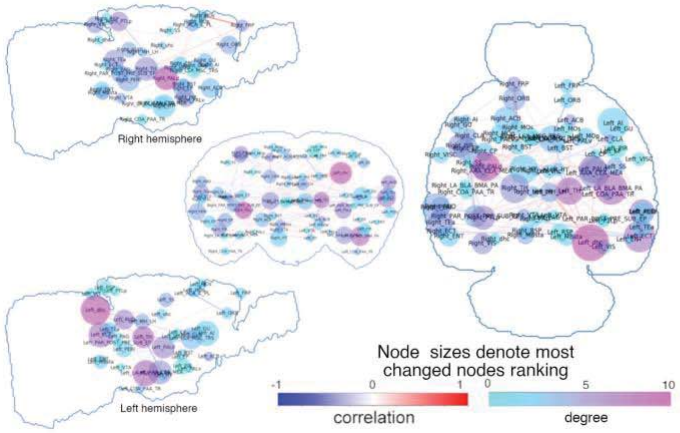

B **Most changed connections**

Right PALd <-> Left HY
Left TEa <-> Left ECT
Right PAG <-> Left ACB
Left ECT <-> Left AUD
Right PIR <-> Left HY
Left dhc <-> Left MH-LH
Right vhc <-> Left dhc
Right LA-BMA-BLA-PA <-> Left MH-LH
Right EP <-> Left PALd
Right PTLp <-> Right PIR
Right TH <-> Right FRP
Right ECT <-> Left ECT
Right GU <-> Right FRP
Right MBsts <-> Left AI

C **Most changed nodes**

Left dhc
Left LA-BLA-BMA-PA
Left ECT
Left AI
Left AAA-CEA-MEA
Right TH
Right HY
Right PALd
Right PERI
Left PALd
Left TH
Left LSX-MSC-TRS
Right TEa
Left AUD
Right ACB

Intergroup comparison at TP2 : Neuropathic vs. control

D

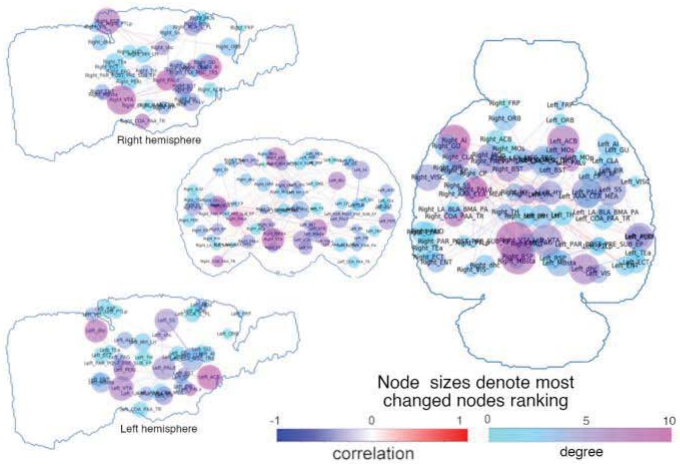

E **Most changed connections**

Right RSP <-> Left MH-LH
Right PAR-POST-PRE-SUB <-> Left PALv
Right VTA <-> Right AI
Right VTA-> Right PALv
Right MBsta <-> Left ACB
Right COA-PAA-TR <-> Left PALd
Right MBsta <-> Left BST
Right AI <-> Left ENT
Left SS <-> Left CLA
Right MBsta <-> Left PALv
Left RSP <-> Left PTLp
Right RSP <-> Left AAA-CEA-MEA
Right COA-PAA-TR <->Left MOp

F **Most changed nodes**

Right VTA
Right RSP
Left ACB
Right AI
Left VTA
Left SS
Left dhc
Left PALd
Left LSX-MSC-TRS
Left PERI
Right VISC
Left MBsta
Right PALd
Right BST
Right ORB

Figure 3-14 Graph theoretical analysis for functional connectivity matrices.
(A and D) *Significant changes between neuropathic and control groups for connection (edge) strengths and nodes are shown as mouse brain overlays at TP1* ***(A)*** *and TP2* ***(D).*** *Edge strength changes are displayed on a scale of correlation coefficients. The relevance of FC chances for each node was assessed using two measures: the degree (color coded) denoting the number of significantly changed connections / node; and the Stouffer coefficient (node size) that is also introducing the weight of the changes for each connection. Stouffer coefficients and therefore the node sizes correspond to ranking of most changed nodes****. (B and E)*** *List of most changed edges (according to the p value) are ranked for TP1* ***(B)*** *and TP2* ***(E)****.* ***(C and F)*** *List of most changed nodes from Stouffer analysis are ranked for the two post-injury timepoints.* ***(C)*** *At TP1, most changed nodes are areas related to pain processing (e.g. thalamus [TH] and agranular insula [AI]) and aversion (e.g. amygdala, septum, nucleus accumbens [ACB], hypothalamus [HY], hippocampal formation and thalamus [TH]).* ***(F)*** *At TP2, mainly reward/aversion areas (e.g. ACB, pallidum (PAL), ventral tegmental area (VTA), hippocampal formation, bed nucleus of stria terminalis (BST), and septum) and areas of rodent default-mode network (DMN) (e.g. RSP, hippocampus, midbrain) are listed as the nodes with most changes. All results are p<0.05, uncorrected.*

*(****Abbreviations:*** *AAA-CEA-MEA: Anterior-central-medial amygdala; ACB: Nucleus accumbens; AI: Agranular insula; AUD: Auditory areas; BST: Bed nucleus of stria terminalis; CLA: Claustrum; COA-PAA-TR: Cortical-piriform amygdalar areas, post-piriform transition area; dhc: Dorsal hippocampus; ECT: Ectorhinal area; ENT: Entorhinal area; EP: Endopiriform nucleus; FRP: Frontal pole; GU: Gustatory area; HY: Hypothalamus; LA-BMA-BLA-PA: Lateral-basomedial-basolateral-posterior amygdala; LSX-MSC-TRS: Lateral-medial septum, triangular nucleus; MBsta: Behavioral state-related midbrain; MH-LH: Medial-lateral habenula; MOp: Primary motor area; ORB: Orbital area; PAG: Periaqueductal gray; PALd: Dorsal pallidum; PALv: Ventral pallidum; PAR-POST-PRE-SUB: Para-/post-/pre-/subiculum; PERI: Perirhinal area; PIR: Piriform area; PTLp: Posterior parietal association area; RSP: Retrosplenial area; SS: Somatosensory area; TEa: Temporal association area; TH: Thalamus; vhc: Ventral hippocampus; VISC: Visceral area; VTA: Ventral tegmental area.)*

Functional connectivity of cingulate area, a region showing structural alterations in the neuropathic group, was assessed at both TP1 and TP2 (Figure 3-15, FWER corrected at cluster level for p<0.05). At TP1, ACA FC towards AI, caudate-putamen (CP), dorsal hippocampus (dHIP), Hb, and PAG was decreased in the neuropathic mice; whereas a stronger ACA-hypothalamus connectivity was observed in this group compared with control (Figure 3-15-A). At TP2, when neuropathic mice display depressive-like behaviors, ACA was found more connected to RSP, amygdala (AMY), and temporal association areas (TeA) in neuropathic mice, while the ACA connectivity with CP, dHIP, Hb, and PAG was lower in neuropathic animals than controls, similar to TP1 results in this seed (Figure 3-15-B).

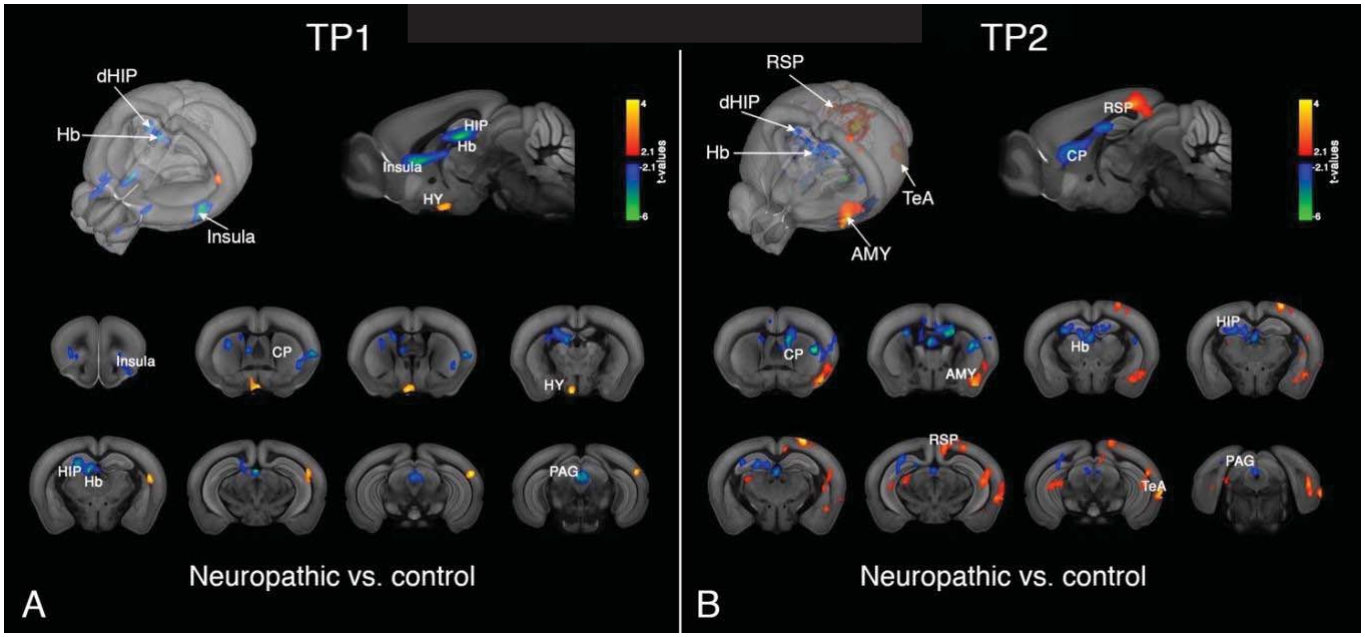

Figure 3-15 Inter-group differences in anterior cingulate area (ACA) functional connectivity at TP1 and TP2.
(A) *At TP1, ACA connectivity towards agranular insula (AI), caudate-putamen (CP), dorsal hippocampus (dHIP), habenula (Hb), periaqueductal gray (PAG) was lower and ACA-hypothalamus connectivity was higher in the neuropathic group.* ***(B)*** *At TP2 weeks, ACA was more connected to retrosplenial area (RSP), amygdala (AMY), and temporal association areas (TeA) for neuropathic mice whereas ACA connectivity with CP, dHIP, Hb, and PAG was reduced. FWER corrected at cluster level for p<0.05.*

Inter-group statistical comparisons suggest strong remodeling of the VTA functional connectivity in the neuropathic animals. Indeed, at TP1, neuropathic animals showed higher synchrony of the BOLD rs-fMRI signal towards somatosensory cortex (SS), CP, and RSP areas (Figure 3-16, FWER corrected at cluster level for p<0.05; Figure 3-16-A) while at TP2, the VTA FC changes detected towards ACA, ACB, CP, BST, Hb, PF and medial dorsal (MD) nuclei of thalamus, as well as higher intra-region connectivity within VTA (Figure 3-16-B). Many of these areas belong to the reward circuitry, a system concerned with incentive salience, motivated behaviors, and reward learning (Borsook et al., 2016; Hu, 2016; Russo and Nestler, 2013). Figure 3-17 shows 3D reconstruction of inter-group statistical differences in longitudinal evolution of VTA FC from T1 to T2 (Figure 3-17, FWER correction applied at cluster level for p<0.05).

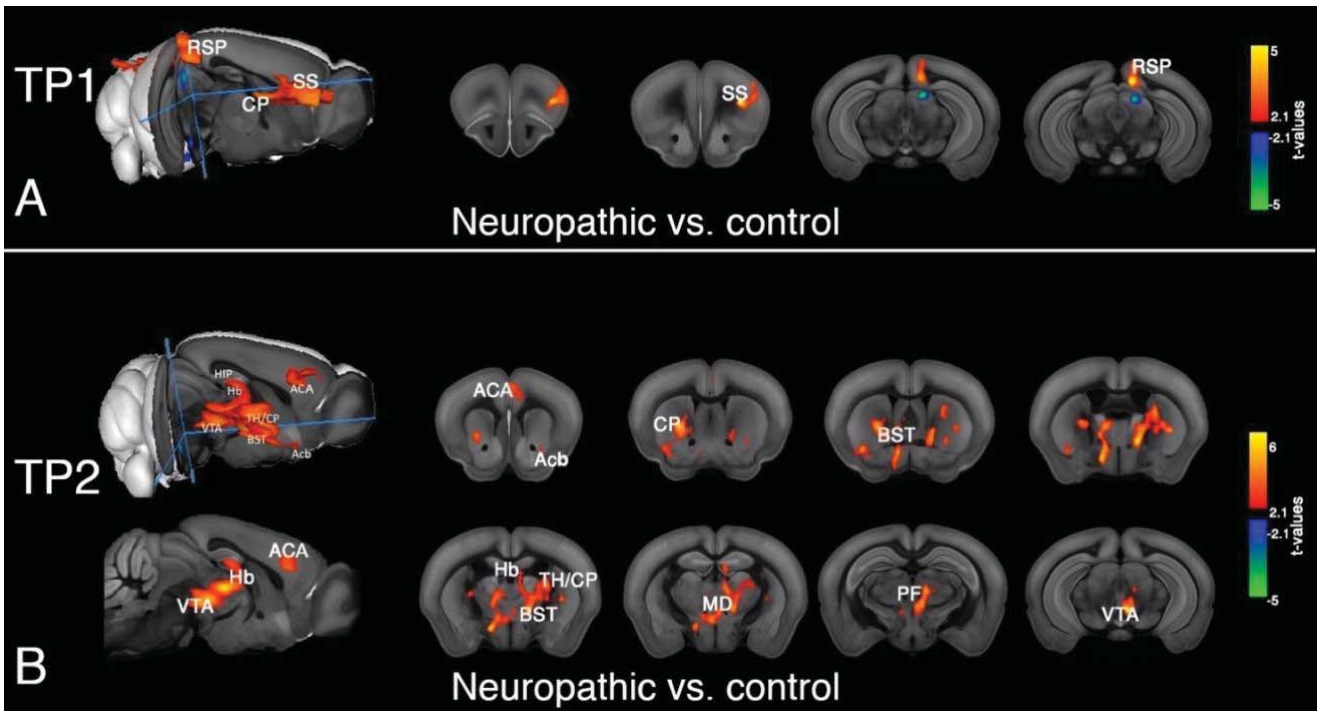

Figure 3-16 Inter-group differences in ventral tegmental area (VTA) functional connectivity at TP1 and TP2.
(A) *At TP1, somatosensory (SS), caudate-putamen (CP) and retrosplenial area (RSP) connectivity towards VTA was higher in neuropathic mice than in controls.* ***(B)*** *At TP2, neuropathic group showed greater VTA synchrony towards anterior cingulate (ACA), nucleus accumbens (ACB), CP, bed nucleus of stria terminalis (BST), habenula (Hb), parafascicular (PF) and medial dorsal (MD) nuclei of thalamus and higher intra-region connectivity at VTA. FWER corrected at cluster level for p<0.05.*

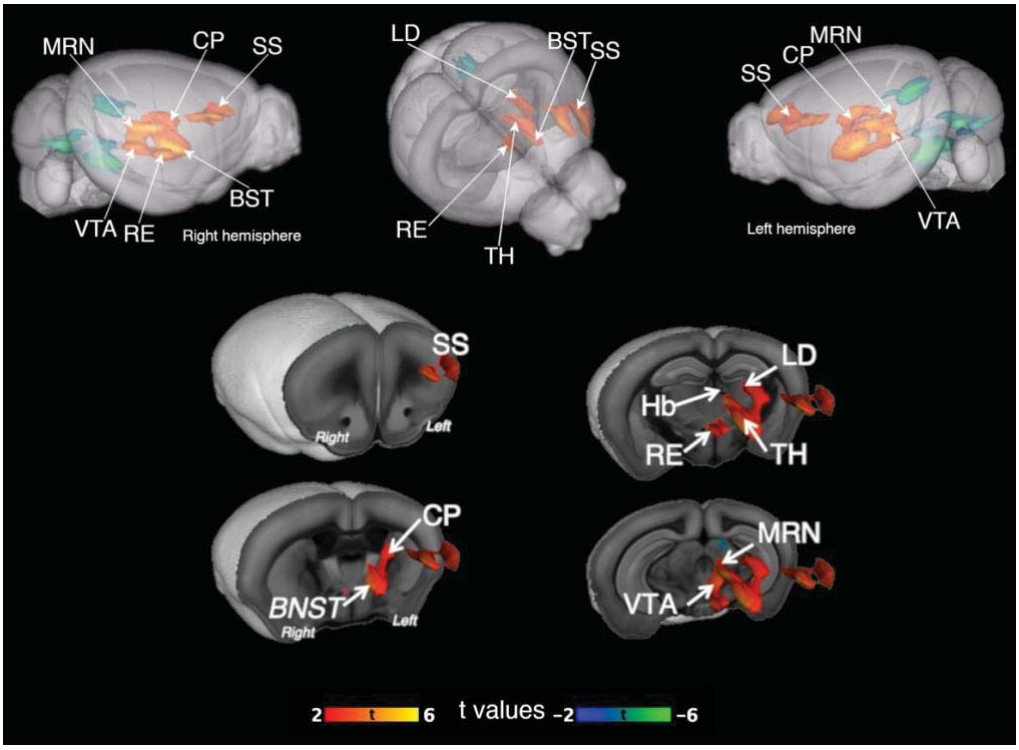

Figure 3-17 3D reconstruction of inter-group statistical differences in longitudinal evolution of VTA functional connectivity from T1 to T2.
Full factorial ANOVA results, FWER correction applied at cluster level for p<0.05.

Lateral habenula (LHb) is an important brain region encoding negative value/ aversion and inhibition of reward signals via its extensive connections to limbic forebrain and aminergic brainstem centers. At TP1, LHb connectivity towards amygdala, TeA, midbrain reticular nucleus (MRN) and ventral hippocampus (vHIP) were increased in neuropathic animals compared to controls (Figure 3-18-A, FWER cluster correction at p<0.05). At TP2, higher connectivity of LHb with thalamus, HY, VTA, and MRN and lower connectivity with AI and secondary motor area (MOs) were observed for neuropathic group (Figure 3-18-B, FWER correction at cluster level at p<0.05).

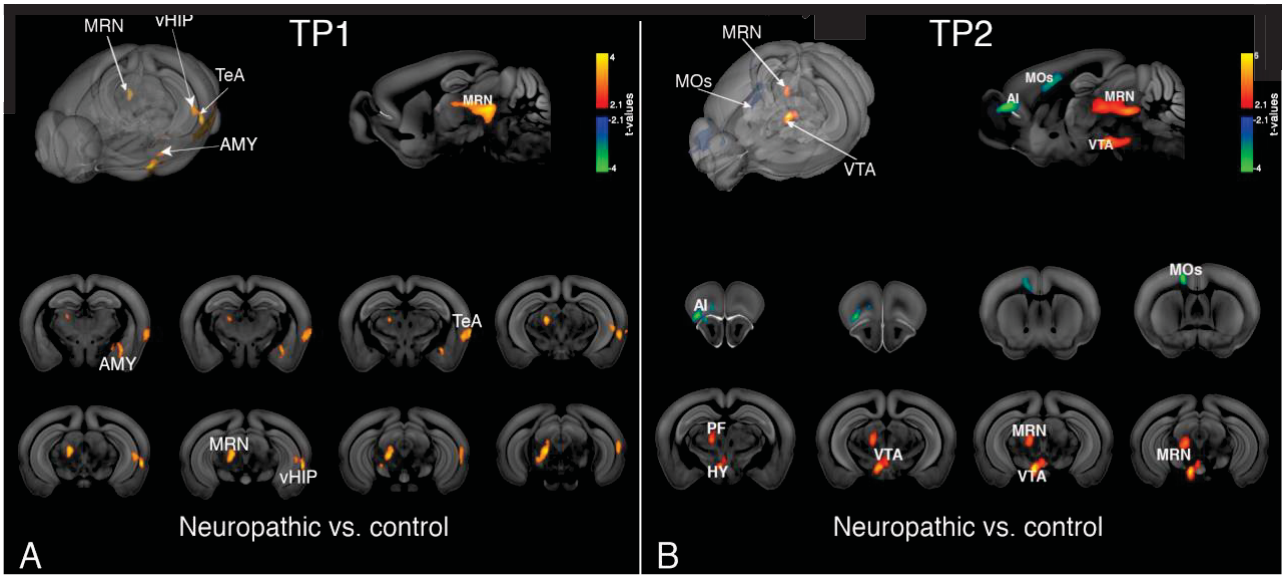

Figure 3-18 Inter-group differences in lateral habenula (LHb) functional connectivity at TP1 and TP2.
(A) *At TP1, LHb connectivity towards amygdala (AMY), temporal association area (TeA), ventral hippocampus (vHIP) and midbrain reticular nucleus (MRN) were increased in neuropathic mice.* ***(B)*** *At TP2, neuropathic animals displayed higher connectivity of LHb with parafascicular (PF) nucleus of thalamus, hypothalamus (HY), ventral tegmental area (VTA), and MRN; lower connectivity with agranular insula (AI) and secondary motor area (MOs). FWER correction at cluster level was applied for p<0.05.*

Based on the graph analysis results that highlighted important inter-group differences of FC involving pain and reward/aversion areas, we further performed fine-grained mapping of FC using ACB, dorsal HIP (dHIP), insula (AI), and PAG as seeds. Figure 3-19 presents the functional connectivity alterations of these ROIs in the neuropathic pain group compared with controls at TP1 and TP2 (All statistical results are FWER corrected at cluster level for p<0.05). At TP1, ACB displays reduced connectivity towards CP, SS, lateral geniculate nucleus (LGN) of thalamus and vHIP in neuropathic mice (Figure 3-19-A). At TP2, reduced ACB connectivity to CP, SS, and primary MO (MOp) areas were accompanied with greater connectivity towards zona incerta (ZI), TeA, vHIP, and substantia nigra (SN) for neuropathic animals (Figure 3-19-B).

dHIP connectivity at TP1 was higher towards AMY, RSP, superior colliculus (SC), and LGN and lower towards CP in neuropathic pain group (Figure 3-19-C). dHIP demonstrated increased connectivity with AMY and posterior parietal association areas (PTLp) and decreased connectivity with ACA and septum in neuropathic animals with depressive phenotype at TP2 (Figure 3-19-D).

Insula and PAG, areas known to be involved in pain processing, also showed connectivity alterations in the neuropathic pain group. Insular connectivity towards RSP and PAG was greater and its connectivity towards MOs, TH and vHIP was lower in neuropathic mice at TP1 (Figure 3-19-E). At TP2, neuropathic pain group presenting depressive behaviors showed insular connectivity patterns increased towards HY, LGN, and entorhinal areas (ENT) and decreased towards CP, PF nucleus, TeA, and MRN (Figure 3-19-F). PAG connectivity at TP1 (Figure 3-19-G) was higher towards ACB, CP and HY and lower towards Hb, PTLp and SS areas in neuropathic mice compared to controls. At TP2, connectivity of PAG with ACB, piriform area (PIR), olfactory tubercle (OT), and LGN was stronger and PAG-SS connections were weaker for neuropathic pain-induced depression group (Figure 3-19-H).

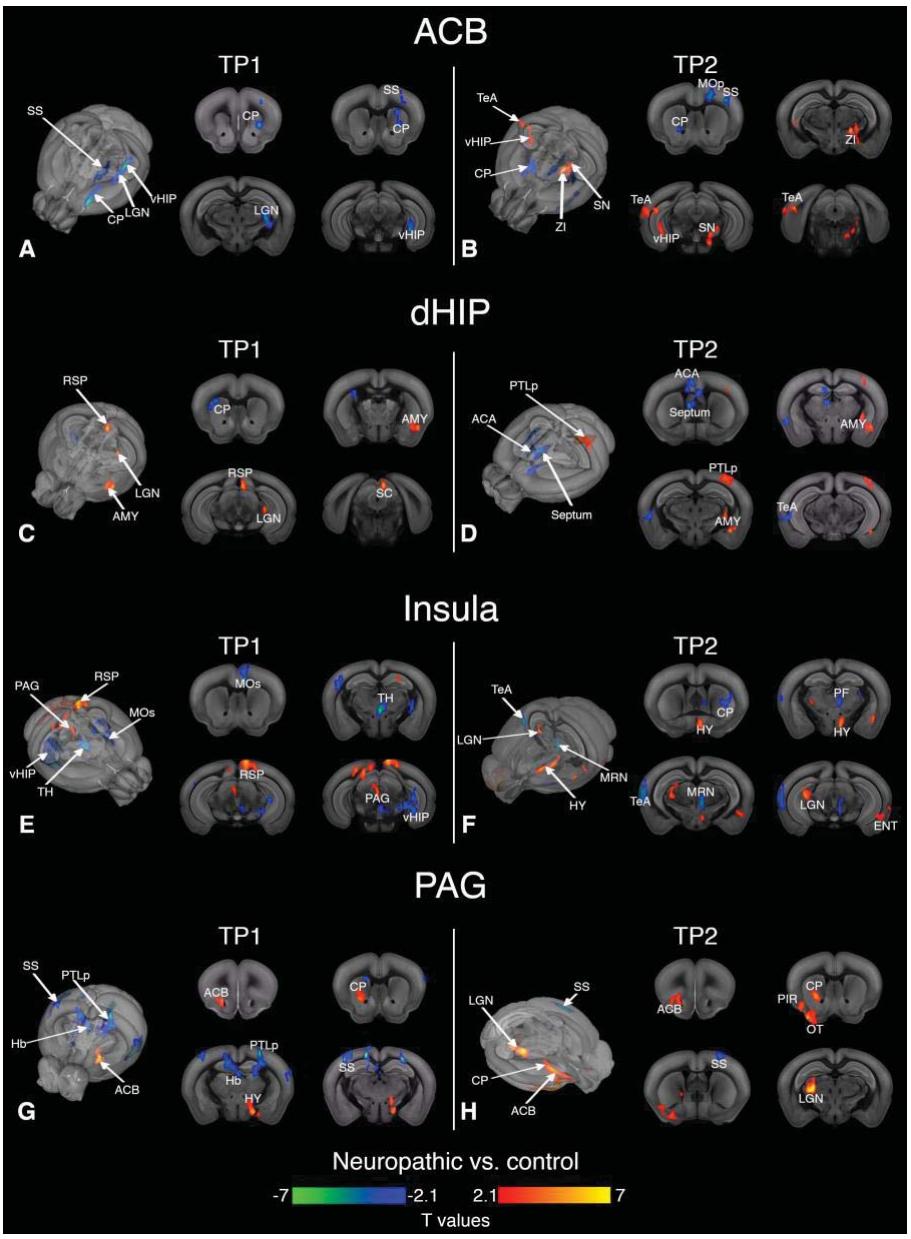

Figure 3-19 Inter-group differences in the nucleus accumbens (ACB), dorsal hippocampus (dHIP), agranular insula (AI), and periaqueductal gray (PAG) functional connectivity at TP1 and TP2.

(A) *ACB displays reduced connectivity towards caudate-putamen (CP), somatosensory areas (SS), lateral geniculate nucleus (LGN) of the thalamus and ventral HIP (vHIP) in neuropathic mice at TP1.* ***(B)*** *At TP2, reduced ACB connectivity to CP, SS, and primary MO (MOp) areas and greater connectivity towards zona incerta (ZI), temporal association area (TeA), vHIP, and substantia nigra (SN) were shown for neuropathic animals.* ***(C)*** *dHIP connectivity at TP1 was higher towards amygdala (AMY), retrosplenial area (RSP), superior colliculus (SC), and LGN and lower towards CP in neuropathic pain group.* ***(D)*** *dHIP demonstrated increased connectivity with AMY and posterior parietal association areas (PTLp) and decreased connectivity with anterior cingulate (ACA) and septum in neuropathic animals with depressive phenotype at TP2.* ***(E)*** *Insular connectivity towards RSP and periaqueductal gray (PAG) was greater and its connectivity towards secondary motor (MOs), thalamus (TH) and ventral hippocampus (vHIP) was lower in neuropathic mice at TP1.* ***(F)*** *At TP2, neuropathic pain group showed increased insular connectivity patterns towards hypothalamus (HY), LGN, and entorhinal areas (ENT) and decreased towards CP, parafascicular (PF) nucleus, TeA, and MRN.* ***(G)*** *PAG connectivity at TP1 was higher towards ACB, CP and HY and lower towards Hb, PTLp and SS areas in neuropathic mice compared to controls.* ***(H)*** *At TP2, connectivity of PAG with ACB, piriform area (PIR), olfactory tubercle (OT), and LGN was stronger and PAG-SS connections were weaker for neuropathic pain-induced depression group. All statistical results were FWER corrected at cluster level for $p<0.05$.*

Longitudinal evolution:

Additionally, we performed full factorial ANOVA to highlight group-differences in the evolution of the FC patterns from TP1 to TP2 (Figure 3-20, FWER corrected at cluster level for $p<0.05$). Overall, neuropathic mice showed stronger connectivity modifications of the ACA FC with basolateral amygdala (BLA), RSP, and VTA and reduced variations towards claustrum (CLA), insula, Hb, and dHIP when compared to the control animals (Figure 3-20-A). Overtime, RSP functional connectivity was reduced towards thalamus and dHIP in neuropathic group in comparison to controls (Figure 3-20-B). In neuropathic mice, insular cortex displayed greater FC modifications towards RSP and PAG areas and lower variations towards SS and thalamus compared to controls overtime (Figure 3-20-C). These time-dependent changes were also observed for PAG which exhibited stronger FC modifications towards ACB, CP, thalamus and dHIP in the neuropathic group while modifications towards SS were reduced compared to controls (Figure 3-20-D).

Aside from structures implicated in pain processing, structures involved in reward-aversion processes showed a distinct evolution profile of FC in neuropathic animals with depressive-like behaviors in comparison with controls. For instance, ACB connectivity changes became dominant towards vHIP and VTA in neuropathic animals (Figure 3-21-A). In regard to LHb, we observed stronger FC changes with amygdala, VTA, and midbrain reticular nuclei (MRN) and weaker FC alterations with dHIP (Figure 3-21-B). The main changes of the VTA FC were observed with SS, CP, BST, and thalamus in neuropathic animals (Figure 3-21-C).

Hippocampus, a structure implicated in both pain and depression also showed time-dependent changes in neuropathic animals compared to controls. The vHIP (Figure 3-21-D) displayed stronger FC alterations with infralimbic (IL), prelimbic (PL), SS, insula and dHIP in animals displaying depressive-like behaviors while dHIP (Figure 3-21-E) revealed stronger changes towards insula and amygdala and reduced connectivity alterations towards ACA, Hb and within dHIP in neuropathic mice with depressive phenotype compared to controls.

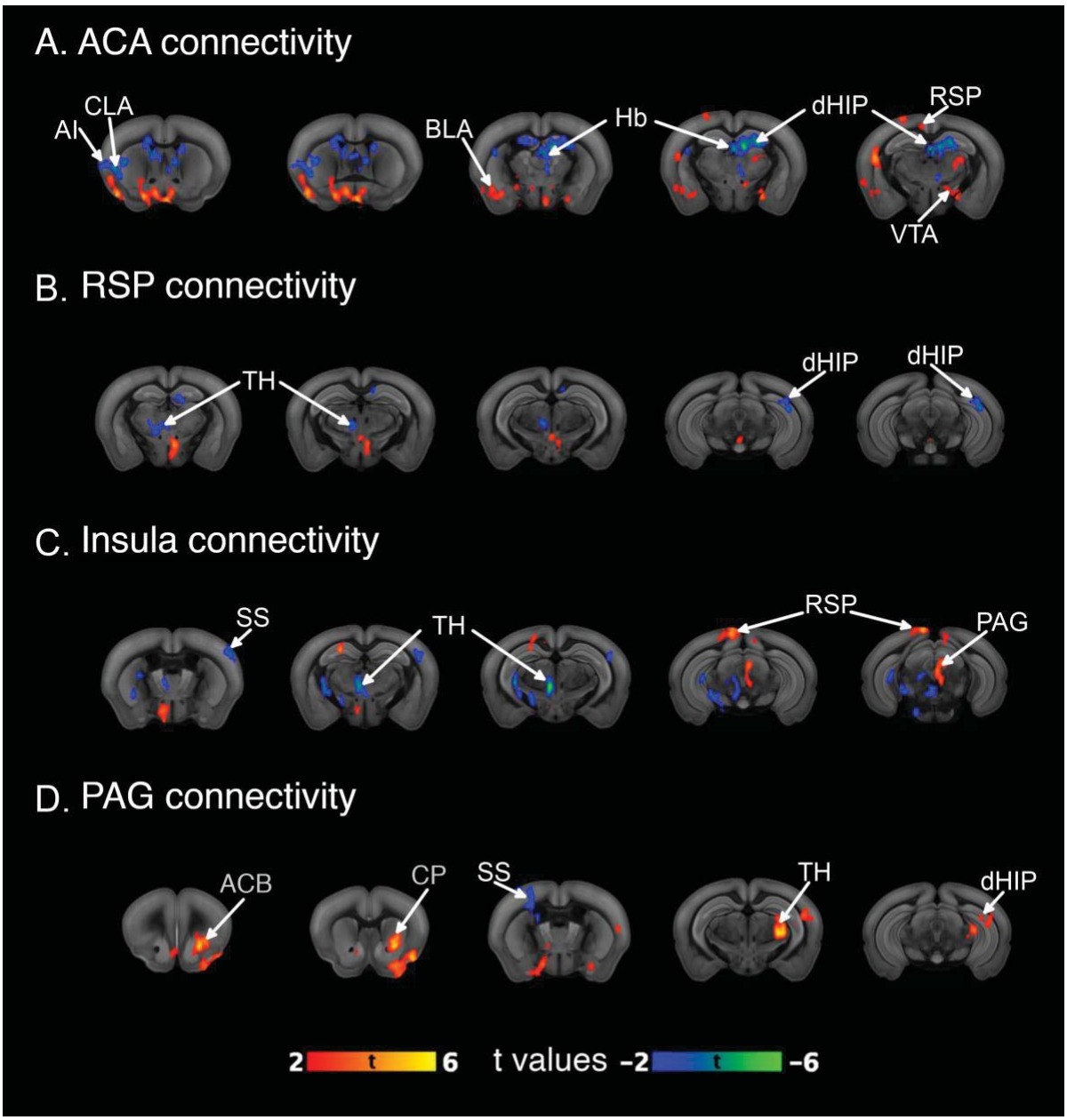

Figure 3-20 Group-differences in the evolution of the FC patterns from TP1 to TP2 for anterior cingulate (ACA), retrosplenial area (RSP), agranular insula (AI) and periaqueductal gray (PAG).

(A) *Stronger modifications of the ACA connectivity towards basolateral amygdala (BLA), RSP, and ventral tegmental area (VTA) were found neuropathic animals (red). ACA had reduced connectivity modifications towards claustrum (CLA), insula, habenula (Hb), and dorsal hippocampus (dHIP) in neuropathic mice as compared to control group (blue).* ***(B)*** *RSP connectivity showed stronger modifications towards thalamus and dHIP in neuropathic group than in controls.* ***(C)*** *Neuropathic mice showed greater insula-RSP and insula-PAG connectivity alterations ovetime when compared to the sham group, while insula-SS and insula - thalamus connectivity showed lower variations from TP1 to TP2****(D)*** *Connectivity modifications between PAG and ACB, CP, thalamus, and dHIP were higher in neuropathic mice as compared to sham; SS connectivity showed less changes to PAG in this group. FWER corrected at cluster level for p<0.05.*

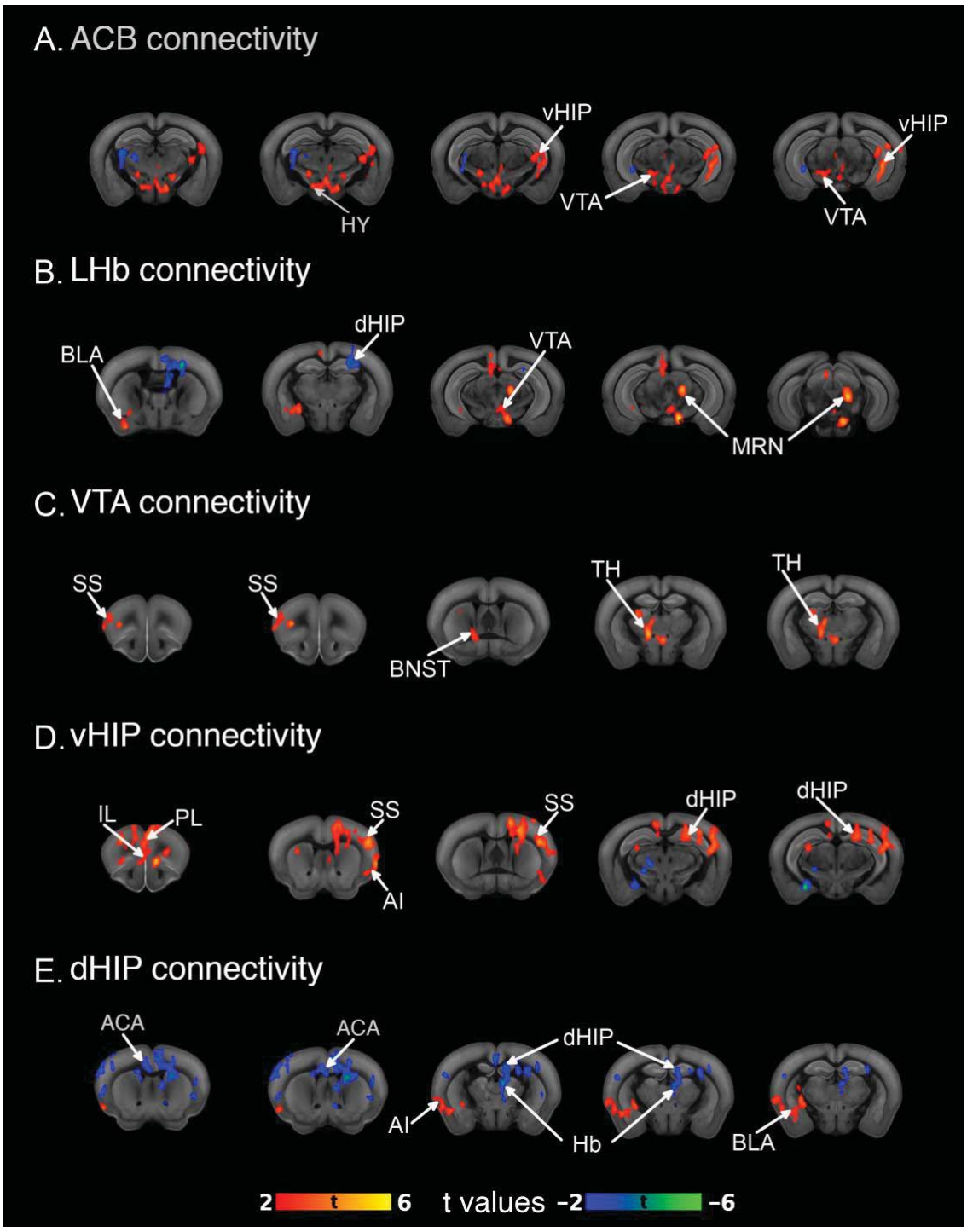

Figure 3-21 Group-differences in the evolution of the FC patterns for nucleus accumbens (ACB), ventral tegmental area (VTA), lateral habenula (LHb) and two main hippocampal divisions (dorsal and ventral hippocampus (dHIP and vHIP, respectively) from TP1 to TP2. ***(A)*** *ACB connectivity with vHIP and VTA showed stronger overtime modifications for neuropathic animals in comparison with controls.* ***(B)*** *LHb area displayed greater connectivity changes towards BLA, VTA, and midbrain reticular nuclei (MRN) in neuropathic pain group; they also had lower connectivity changes between LHb-dHIP.* ***(C)*** *VTA revealed stronger than control modifications in neuropathic mice towards somatosensory area (SS), bed nucleus of stria terminalis (BST), and thalamus.* ***(D)*** *Ventral part of the hippocampus (vHIP) displayed in neuropathic animals greater connectivity changes towards infralimbic (IL), prelimbic (PL), and SS areas, insula, dHIP than in controls.* ***(E)*** *Dorsal part of hippocampal area (dHIP) exhibited in neuropathic animals greater than control connectivity variations from TP1 to TP2 towards insula and BLA and reduced connectivity changes with ACA, Hb, and within dHIP when compared to the sham group. FWER corrected at cluster level for $p<0.05$.*

3.2.4 Discussion

In this study, we aimed to uncover the evolution of the brain structural and functional connectivity associated with the establishment of chronic pain and later, the emergence of depressive behaviors in a mouse model of neuropathic pain. For this purpose, we used diffusion MRI and resting state fMRI in parallel with behavioral measures in a longitudinal design. We were able to show structural differences at two post-injury timepoints for neuropathic mice. ACA and RSP displayed lower FA values at both 2 weeks and 8 weeks following cuff surgery while TH, HY, and hippocampus had reduced FA values only at 2 weeks post-surgery.

Brain functional connectivity networks had also undergone a substantial remodeling throughout the period of neuropathic pain. As expected, following cuff surgery, mice developed long lasting mechanical allodynia (Yalcin et al., 2011). Thus at 2 weeks, corresponding to the early stages of the neuropathy, we observed regions involved in pain processing and aversion taking predominant roles in neuropathic mouse brain networks determined from graph theoretical analysis. At 8 weeks when animals display not only mechanical allodynia but also depressive-like behavior, we demonstrated alterations in the reward circuitry and default mode network (DMN).

Further, we investigated functional connectivity profiles of brain areas showing structural changes or changes in graph measures between groups in more detail. Several regions exhibited connectivity changes for neuropathic pain group at 2-week (TP1) and 8-week (TP2) time points. Most notable results were obtained in ACA, VTA, and LHb nodes along with other reward areas and DMN components.

3.2.4.1 Neuropathic pain leads to brain structural modifications

Our results revealed that FA values are reduced at the early stages of neuropathy (2 weeks) in ACA and RSP, core regions of mouse DMN, along with TH, HY and hippocampus in neuropathic mice. Moreover, ACA and RSP changes persisted at TP2, where a depressive phenotype manifests in behavioral tests.

Preclinical and clinical studies focusing on pain research showed several structural alterations which support the results of our present study. Indeed, reduced volumes of prefrontal cortex (PFC) and RSP were reported in a rat spared nerve injury (SNI) model, coinciding with anxious behavior (Seminowicz et al., 2009). Prefrontal volume reduction was also described in the SNI model using mice (Bilbao et al., 2018). In addition, patients with neuropathic pain following spinal cord injury (Yoon et al., 2013) displayed gray matter decrease in subgenual ACC while decreased FA in thalamic areas was reported for patients with migraine (DaSilva et al., 2007), fibromyalgia(Lutz et al., 2008) and temporomandibular disorder (Moayedi et al., 2012). In addition, gray matter atrophy in ventromedial prefrontal cortex (vmPFC) along with lower FA in cingulum and decreased vmPFC-basal ganglia connectivity were found in complex regional pain syndrome (CRPS) (Geha et al., 2008)

Furthermore, studies in major depressive disorder (MDD) showed reduced volume of anterior cingulate, related to both glial and neuronal losses (Drevets et al., 1997; Mayberg, 2009; Rajkowska, 2000; Russo and Nestler, 2013; Uranova et al., 2004). Structural changes found in the same brain region for chronic pain and MDD suggest a contribution of anterior cingulate in their comorbidity. Indeed, ACA is thought to play an important role in pain-induced depression. Previous research from our group showed that the hyperactivity of this region is associated with anxio-depressive consequences of the cuff model (Sellmeijer et al., 2018) and the optogenetic inhibition of this area abolishes aversion to pain without affecting mechanical hypersensitivity.

Longitudinal nature of our experimental design enabled us to assess time-dependent evolution of brain connectivity, which is difficult to capture with cross-sectional designs often used in clinical settings. We thus could detect the disappearance of FA alterations in TH, HY, and hippocampal areas at TP2, which points to an early but short-lasting reaction to cuff surgery. TH, HY, and hippocampus were identified as parts of aversion circuitry (Hayes and Northoff, 2011) and thalamus is well-known to be involved in pain processing (Garcia-Larrea and Peyron, 2013) thus, transient structural changes in these areas might correspond to initiation of chronic pain and related aversive behaviors. Concerning the long-lasting changes that we observed in ACA and RSP might be associated with steady neuroplastic changes resulting from activity-dependent or inflammatory and glial processes, leading to depressive behavior. In line with this, ACA shows long term potentiation (LTP) of glutamatergic synapses following nerve injury in mice (Xu et al., 2008). Astrocytic processes in ACA were also shown to be involved in the establishment of LTP and pain hypersensitivity (Ikeda et al., 2013) in an inflammatory injury model. Chemotherapy-induced neuropathic pain resulted in a significant increase in ACA astrocytes in rats (Mannelli et al., 2013) and Narita Minoru et al. (2006) reported role of the cortical δ-opioid receptor dysfunction in ACA astrogliosis, potentially leading to anxiety state. Putative role of glial processes in depression were also investigated. Postmortem brains of depressed patients showed increased microglial quinolinic acid, an NMDA agonist which is considered to modulate the link between immune and neurotransmitter staple changes, in subgenual ACC and mid-cingulate areas (Steiner et al., 2011). Impairment of gap junction-mediated communication between astrocytes and oligodendrocytes in ACA was discovered in postmortem brain tissues from depressed suicides (Tanti et al., 2019), emphasizing the importance of glia in normal brain function.

RSP is a principal area of rodent DMN (Stafford et al., 2014; Upadhyay et al., 2011) together with ACA. Default mode network (DMN) is a set of regions that show synchronous activity at rest and deactivate during task performance (Greicius et al., 2003; Raichle et al., 2001). DMN alterations are found across several neurologic and psychiatric disorders (Baliki et al., 2014; Berman et al., 2011; Broyd et al., 2009; Buckner et al., 2008). Deactivation of DMN was reduced while switching from rest to attentional task in patients suffering from chronic back pain (Marwan N Baliki et al., 2008). In a diabetic neuropathy cohort, DMN connectivity was increased towards dorsal ACA and MO/SS cortices and decreased towards dlPFC, insula and TH (Cauda et al., 2010), whereas in fibromyalgia, DMN-insula connectivity and coherence within DMN were increased (Napadow et al., 2011). In three distinct pain conditions, mPFC connectivity with posterior part of DMN was found to be decreased and mPFC-insula FC was increased (Baliki et al., 2014). In short, while the DMN connectivity changes are not consistent across conditions, DMN dysfunction seems to be important maladaptation in chronic pain.

DMN modifications in major depression are also well-documented(Wang et al., 2012; Zhu et al., 2012). For instance, Greicius et al. (2007) has shown greater subgenual ACC connectivity towards DMN regions which is correlated with the length of current depressive episode in MDD. On the preclinical side, DMN connectivity was enhanced with chronic stress (Henckens et al., 2015) in a model of depression in mice (Grandjean et al., 2016) and in rats. In rats with genetic predisposition for major depression, enhancement of DMN connectivity (Gass et al., 2016) was observed while the optogenetic perturbation of LHb in this model resulted in diminished DMN connectivity and rescued the rats from depressive phenotype (Clemm von Hohenberg et al., 2018). Hence, RSP structural modifications might be giving rise to network-level functional connectivity reorganization, promoting aversive and anxio-depressive behaviors.

3.2.4.2 Functional connectivity remodeling in limbic circuitry

To obtain a global perspective on brain functional connectivity in neuropathic pain, we generated large connectivity matrices. We extracted ROIs from anatomical segmentation of Allen mouse brain atlas (Lein et al., 2007), covering isocortex and subcortical regions. The connectivity matrices were constructed with partial correlation, which computes correlation between any two nodes while excluding the influence of all others. Difference between neuropathic and control groups were analyzed for TP1 and TP2, graph theoretical parameters were assessed and most changed connections (edges) and regions (nodes) were ranked. In this manner, we were able to evaluate the longitudinal evolution of brain-wide FC.

At TP1, the point where mechanical hypersensitivity is established, the most prominent changes appeared in pain and aversion-related regions such as thalamus and insula (Iannetti and Mouraux, 2010) along with amygdala, hypothalamus, and parts of hippocampal formation. These areas were shown to be parts of aversion circuitry (Hayes and Northoff, 2011) in humans and in animals. Chronic pain is thought to reflect a shift from pain-related circuitry to meso-corticolimbic circuitry over time (Farmer et al., 2012), different pain conditions displaying divergent patterns of network reorganization. Transition from subacute to chronic back pain, as followed by rs-fMRI over time, could be predicted from initial cortico-striatal FC patterns (Baliki et al., 2012). Here, we observed limbic/reward areas and DMN components as most changed nodes at TP2 for neuropathic animals. These areas included VTA, ACB, pallidum, hippocampus, midbrain, septum, BST as well as SS, insula and RSP- implicating them in the development of anxiety and depression as a consequence of neuropathic pain.

On the basis of the nodes with most marked changes determined from graph theoretical approach and the areas showing structural alterations, we chose several ROIs to perform fine-grained seed analyses.

ACA functional connectivity presented major changes at both timepoints: At TP1, lower connectivity of ACA towards nociceptive areas (insula, PAG) might reflect the loss of descending pain modulation from this area, exacerbating pain. FC reductions towards CP, dHIP, and Hb also imply deficits in top-down control, allowing negative affect to prevail. At TP2, along with the changes observed at TP1, ACA displayed stronger connectivity towards RSP; thus, enhanced within-DMN connectivity patterns coinciding with depressive phenotype. ACA-AMY FC also showed enhancements, denoting an amplification of aversive inputs from amygdala into ACA or alterations of the negative loop between ACA and AMY. As mentioned earlier, ACA structural and functional connectivity changes are quite prevalent in depression and chronic pain conditions in

their comorbidity. Combined with our observations, ACA emerges as a crucial node taking part in brain network reconstruction prompted by nerve injury and bringing out the behavioral signatures of depressive pathology.

VTA, a dopaminergic midbrain center encoding reward and coordinating meso-corticolimbic pathway, was one of the most changed areas at TP2 in the graph analysis. At this time point, VTA demonstrated stronger connectivity towards several other limbic areas, namely, ACA, ACB, CP, BST, Hb, PF and MD nuclei of thalamus in neuropathic mice with depressive phenotype. VTA connectivity increases both within reward circuitry and towards ACA, a DMN node which position VTA and ACA at the intersection of two important networks, possibly regulating their interactions. VTA takes part in both reward and aversion (Lammel et al., 2014), pain processing (Ezzatpanah et al., 2016; Hipólito et al., 2015; Ko et al., 2018; Sotres-Bayón et al., 2001; Watanabe et al., 2018), stress- and pain-induced depressive behaviors (Fu et al., 2018; Isingrini et al., 2017; Ji et al., 2018). In rodent chronic pain models, VTA activity and reward behaviors are shown to be disrupted since rats with peripheral nerve injury had reduced dopaminergic signaling due to microglia-regulated activation of GABAergic VTA interneurons (Taylor et al., 2015) and increased GABAergic and decreased dopaminergic signaling was also reported for spinal cord injury in rats (Ko et al., 2018). In a spared nerve injury model, VTA activity and dopamine concentration in ACB were reduced (Ren et al., 2015). Both nerve injury and cancer pain models resulted in reduced neuronal excitability in VTA (Devonshire et al., 2017; Watanabe et al., 2018), while optogenetic stimulation of VTA dopaminergic neurons projecting to ACB alleviated allodynia (Watanabe et al., 2018). While preclinical studies such as chronic unpredictable mild stress (CUMS) model of depression reported lower VTA activity in VTA-mPFC pathway (Liu et al., 2018; Redlich et al., 2015) showed higher functional connectivity of ventral striatum (VS) and VTA in depressed patients. However, contradicting findings of increased VTA activity were reported in social defeat stress model (Berton et al., 2006; Walsh et al., 2014) and in chronic constriction injury (CCI) model (Liu et al., 2018). These contradictions might stem from VTA heterogeneity with respect to projections, activity patterns, and neurotransmitter types. Although we cannot determine activity levels in VTA with rs-fMRI, we might conjecture the increased connectivity towards reward/aversion areas as either compensatory mechanisms counteracting reward deficit or increased signaling for anti-reward, or a combination of both mechanisms.

LHb is another key reward/aversion structure which presents with connectivity alterations in neuropathic mice. LHb encodes aversion relevant to avoidance and escape behaviors and inhibits reward signals. At TP1, LHb connectivity towards AMY, TeA, vHIP and MRN were increased in neuropathic animals, which point to an augmented aversive signaling. The higher connectivity of LHb with PF nucleus of thalamus, HY, VTA, and MRN and lower connectivity with AI and MOs at TP2 can be interpreted as the enhancement of the inhibitory influence of LHb over reward areas. This effect can likely cause reward deficits associated with depressive phenotype. Longitudinal evolution of LHb FC in neuropathic animals identified stronger connections towards amygdala, VTA, and MRN and weaker connections to dHIP, indicating heightened LHb influence over reward areas promoting aversion and reward deficiency in a time dependent manner.

LHb is implicated in pain modulation (Shelton et al., 2012) via its connections to monoaminergic and opioidergic centers. Similar to our results, LHb connectivity towards PFC divisions and MO cortices were decreased in pediatric CRPS patients (Erpelding et al., 2013).

LHb is also involved in depressive pathologies (Proulx et al., 2014). For instance, increased blood flow to LHb (Gass et al., 2014a) and LHb hyperactivity (Gass et al., 2016) was reported in rodent models of depression model while the lesion of the LHb diminish depressive behaviors. In addition, increased LHb burst activity drives depressive phenotype and rapid antidepressant ketamine acts to suppress this hyperactivity, reversing depressive behaviors and anhedonia (Yang et al., 2018b) and inactivation of habenula with deep brain stimulation (DBS) in treatment resistant depression resulted in full remission in a patient (Sartorius et al., 2010). Even more relevant, some recent studies showed the involvement of the LHb in depression-pain comorbidity. Indeed, it has been shown that CUMS model in rats induces pain hypersensitivity and LHb hyperactivity, and its lesion relieves both the pain hypersensitivity and depressive phenotype (Li et al., 2016). Moreover, chronic constriction injury in rats also caused increased LHb activity and depressive behaviors which were eliminated by lesioning the LHb (Li et al., 2017). To conclude, increased LHb activity might be the common denominator in pain and depression comorbidity, regardless of initial pathology.

Moreover, functional connectivity of dorsal hippocampus (dHIP) showed higher connectivity towards RSP, SC, and LGN at TP1 which might be associated with amplified nociceptive inputs or compensation for lower dHIP activation in chronic pain. Indeed, impaired neurogenesis and synaptic plasticity were detected in hippocampus, which contribute to memory deficits commonly observed in chronic pain (Mutso et al., 2013). At TP2, dHIP connectivity towards ACA and septum was lower and its connectivity towards AMY and PTLp was greater in neuropathic mice. Reduced ACA-dHIP connectivity was also shown in a mouse model of metastatic bone cancer pain (Buehlmann et al., 2018). Decreased hippocampal connectivity towards mPFC was predictive of chronification of back pain in patients (Mutso et al., 2013) and may correlate with reduced reward learning signals in depressive disorder (Kumar et al., 2008). Overall, dHIP FC was higher with insula and amygdala, pain and aversion areas, and reduced towards ACA, Hb, and within itself in neuropathic pain-induced depression model.

On the other hand, ventral HIP showed stronger overall connectivity to mPFC, SS and insular area, and dHIP underlining their distinct functionalities. In fact, dorsal hippocampus engages in cognitive functions whereas vHIP is related to stress and emotional processing (Fanselow and Dong, 2010) and the two hippocampal divisions show differential gene expression patterns (Lee et al., 2017). Taken together, hippocampal FC patterns we observe might correspond to cognitive deficits and heightened emotional processing encountered in chronic pain (Simons et al., 2014) and depression.

While our study brought valuable information concerning the functional and structural reorganization of the brain in pain and depression comorbidity, it has some methodological limitations. Even though we started with the bigger animal cohort, due to a variation in the prevalence of relevant behavioral phenotype our sample size became smaller. Reproduction of our findings in a larger cohort would confirm their biological significance. Another caveat was the use of male subjects only. Recently, the stance on higher hormonal variability in female subjects was abandoned (Shansky, 2019) citing similar variability in males as well as the effects of male social hierarchy. There is a pronounced gender bias in basic research (Alderton, 2019) which might lead to false generalizations and public health problems. As depression prevalence is higher in women (Abate, 2013) and pain responses might differ between sexes (Fillingim et al., 2009), it is especially important to use female subjects in pain-induced depression results.

3.2.5 Conclusion

To recapitulate, we assessed the longitudinal evolution of the brain structural and functional connectivity coinciding with pain- and depression-related phenotypes. We observed time-dependent brain structural alterations and functional connectivity remodeling in several relevant brain areas for neuropathic mice in comparison to controls. Predominance of pain and aversion circuitries in the earlier post-injury time point accounted for the establishment of pain hypersensitivity. Development of depressive behaviors were accompanied by reorganization of reward system and DMN delineating causal relations between pain and depression. A prominent role of ACA, LHb, and VTA regions was discovered in pain-induced depression.

4 General Discussion

My thesis work consisted of the investigation of brain structural and functional connectivity signatures of neuropathic pain-induced depression in a relevant mouse model. In particular, I studied the **evolution** of brain networks to identify alterations occurring at different stages of the pathology in a longitudinal experimental design. Prospective studies on this subject are rather difficult to perform in clinical settings. Not only the transition periods of injury to chronic pain and then to depressive disorder are much longer in patients, but also the variability in the type of injury, genetic disposition, environmental factors, and other comorbid conditions renders the interpretation of findings complex (Burma et al., 2017). In preclinical research, we have the advantage of precisely controlling these factors: a standard injury procedure, use of inbred organisms, and a strict regulation of housing conditions and experimental variables ensure more consistent results. The ability to employ more invasive methods is another crucial advantage of animal experiments.

The inbred strains used for most rodent experiments are created for the purpose of reducing genetic variability, as mating of siblings over 20 generations are expected to produce an identical genotype for all members of an inbred strain (Padmanabhan, 2014). There are more than 400 mouse and 150 rat inbred strains commercially available. Each strain has specific phenotypic features which might be useful for addressing different research questions. In neuroscience field, inbred rodents are chosen to lower variability in nervous system structure and function, consequently the behavioral phenotype. This way, the results of an experiment can be attributed to its design and studied parameters, not the inherent variability of the test subjects.

C57BL/6N and BALB/cJ mouse strains are two most often used strains for depression research. BALB/cJ is especially preferred for its vulnerability to develop anxiety and depressive behaviors. However, there were previous reports on the intra-strain variability for BALB/cJ mice concerning their brain anatomy and behaviors (Fairless et al., 2012; Kim et al., 2012; Wahlsten, 1974). Thus, I performed a brain connectivity study in C57BL/6N and BALB/cJ to describe potential inter-strain differences and within-strain variability, utilizing MRI methods. The main aim was to determine the particular strain of mice to use for further experiments on neuropathic pain-induced depression.

4.1 Comparison of strains C57BL/6N and BALB/cJ

Investigation of brain structure and connectivity in the two strains was performed via anatomical T2 imaging, diffusion MRI and resting state-fMRI.

4.1.1 Structural connectivity

Diffusion imaging and further implementation of high-resolution fiber mapping was employed to demonstrate brain structural connectivity. C57BL/6N and BALB/cJ mice exhibited divergent white matter architectures, showing differences in corpus callosum (genu, splenium and parts) and other axonal bundles (e.g. cingulum, fimbria). Several gray matter regions also showed microstructural differences, including prefrontal areas, striatum, thalamus and midbrain. There was a general under-connectivity in BALB/cJ strain, shorter average corpus callosum and lower density of fronto-striatal communication fibers. Notably, BALB/cJ mice displayed great variation in the length and fiber density of corpus callosum within the strain. The specific patterns of under-connectivity in BALB/cJ strain might account for the specific behavioral phenotypes they exhibit, such as decreased social interaction and increased anxiety.

In addition, we performed a volumetric analysis of T2 anatomical images and found extensive volume differences in several brain regions between C57BL/6N and BALB/cJ. C57BL/6N had larger volumes for cortical (e.g. PFC, motor and somatosensory areas, association areas) and subcortical areas (e.g. septum, thalamus, and hippocampus) whereas, BALB/cJ showed a thicker corpus callosum around the middle part which can be interpreted as a compensation mechanism for its shorter length to ascertain adequate communication between hemispheres.

4.1.2 Functional connectivity

We further analyzed resting-state fMRI data to discover putative variations in functional connectivity arising from discrepancies in brain structures of the two strains. First, we investigated global functional connectivity by creating large connectivity matrices and identifying *hubs*, dominant regions within functional brain networks serving to establish effective information transfer. Hub regions in the C57BL/6N strain were subcortical forebrain limbic areas (e.g. endopiriform nucleus, claustrum) and parts of reward circuity (e.g. ACB, CP, dhc, PALv) along with RSP, the core region of mouse DMN. Densely connected endopiriform nucleus and claustrum have roles in the integration of limbic and somatomotor information. For BALB/cJ strains, sensory (e.g. visual and auditory) and associative (e.g. TEa, PTLp) cortices as well as regions implicated in aversion (e.g. BLA, BMA) assumed hub roles. Statistically, dorsal hippocampus was the most different area between strains, falling in line with memory impairments documented in BALB/cJ (Chen et al., 1996) associated with fear conditioning.

Next, we examined seed connectivity differences between strains using voxel-wise correlation analysis. We found that the structural under-connectivity of corpus callosum does not preclude inter-hemispherical cross-talk for the BALB/cJ strain; yet, functional connectivity of homotopic cortical areas exhibits a strain-specific configuration. Ipsilateral somatosensory areas show more coherence in BALB/cJ. For somatomotor areas, this coherence was observed only for caudal regions, connected through middle division of corpus callosum. Rostral motor areas, however, were more inter-connected in the C57BL/6N mice around the genu of corpus callosum; previously mentioned to have higher density of fibers. In short, structural connectivity of BALB/cJ

strain shapes functional connectivity; yet, inter-hemispherical connectivity is preserved, either through thicker middle part of callosal fibers or through polysynaptic routes. This shows the immense capacity of mouse brains to compensate for connectivity deficits.

Core regions of rodent default mode network are the ACA and RSP areas. Functional connectivity of these regions was also dissimilar for the two strains. BALB/cJ connectivity was higher between ACA-RSP cortical areas, while C57BL/6N showed higher RSP connectivity towards subcortical areas and higher intra-regional synchrony in ACA, where fibers are more densely packed.

Specific behavioral phenotype of BALB/cJ mice, exhibiting neophobia, anxiety, lower sociability and strong predisposition to depression (Anderzhanova et al., 2013; Brodkin, 2007; Moy et al., 2004; Ohl et al., 2001; Panksepp and Lahvis, 2007) suggest a role of reward/aversion circuitry. C57BL/6N mice displayed stronger ACB connectivity towards VTA, prefrontal, and septal regions compared to BALB/cJ. Weaker ACB-VTA connectivity, the principal reward pathway, might give rise to social reward deficits previously described in the BALB/cJ strain. Directional communication of ACA and limbic areas (i.e. ventral and dorsal striatum, amygdala) also showed differences between strains. Distinct behavioral phenotype of BALB/cJ mice might arise from the specific connectivity patterns we observed here, especially involving reward system function.

To conclude, C57BL/6N and BALB/cJ strains demonstrate intrinsic differences in brain structural connectivity with dissimilarities in white matter tracts and gray matter areas, volumetric differences in several regions, as well as divergent functional network architecture. Furthermore, the variability of white matter structures in BALB/cJ strain, seen in the dimensions of corpus callosum, is of great importance. Intra-strain variability in BALB/cJ might lead to inconsistent and contradictory results in experiments with different cohorts of animals. To prevent this, it might be possible to control corpus callosum size of BALB/cJ brains with histology or imaging for research in the neuroscience field. However, variability in smaller structures might still bias the experimental findings. Thus, for my future experiments in the neuropathic pain model, I decided to use C57BL/6 strain.

The results of this study do show some consistency with behavior results described in the literature for the BALB/cJ strain, especially the connectivity in fronto-striatal and reward pathways, proposing reward deficits as the basis of social impairments and anxio-depressive behaviors in this strain. Moreover, FC shows flexibility and exceeds the confines of anatomically defined networks, as synchronous activity between two regions might exist due to polysynaptic connections or driven by a third region (Park and Friston, 2013).

4.2 Brain connectivity signatures of neuropathic pain-induced depression in mice

Chronic pain is an important public health problem, affecting a large proportion of the population (Attal et al., 2011; Pitcher et al., 2019). Anxiety and depression frequently accompany chronic pain and worsen the disease burden (von Hehn et al., 2012). To shed light on the elusive pathophysiological mechanisms underlying depressive comorbidity in chronic pain, we investigated brain structural and functional connectivity in a mouse model of neuropathic pain, using diffusion MRI and resting state fMRI in parallel with behavioral assessments in a longitudinal manner. Neuropathic pain was induced by placing a polyethylene cuff around the right sciatic nerve; von Frey filaments were used to assess allodynia weekly and splash test- measuring grooming behaviors, was used to demonstrate depressive behaviors. Imaging sessions were scheduled at baseline, prior to cuff surgery; at 2 weeks following surgery (TP1) coinciding with mechanical hypersensitivity; and at 8 weeks after surgery where the depressive phenotype appears (TP2).

4.2.1 Structural connectivity

We detected modifications of the DTI-derived parameter maps, probably accounting for microstructural changes for neuropathic mice at post-injury time points (TP1 and TP2). TH, HY, and hippocampus had reduced FA values at TP1 while ACA and RSP, centers of rodent DMN, displayed lower FA values at both TP1 and TP2. We interpreted these findings as an initial reactive process involving pain (Garcia-Larrea and Peyron, 2013) and aversion (Hayes and Northoff, 2011) in order to respond to elevated nociceptive inputs.

ACA and RSP, on the other hand show persistent modifications over time. The principal role of ACA in pain-induced depression was reported previously by our group (Barthas et al., 2015; Sellmeijer et al., 2018). ACA hyperactivity drives anxio-depressive phenotype and inhibition of this area removes this phenotype and pain aversion without affecting pain hypersensitivity in the cuff model. Structural modifications of ACA and larger mPFC region was also reported in preclinical (Bilbao et al., 2018; Seminowicz et al., 2009) and clinical (DaSilva et al., 2007; Geha et al., 2008; Lutz et al., 2008; Moayedi et al., 2012; Yoon et al., 2013) chronic pain studies. In addition, structural alterations in this region were documented in major depressive disorder (MDD) (Drevets et al., 1997; Mayberg, 2009; Rajkowska, 2000; Russo and Nestler, 2013; Uranova et al., 2004). Seed connectivity of RSP is often used for detection of DMN in rodents. Distinct modifications in DMN connectivity was found for several chronic pain conditions (Marwan N. Baliki et al., 2014; Marwan N Baliki et al., 2008; Cauda et al., 2010; Napadow et al., 2011) as well as major depression (Greicius et al., 2007; Wang et al., 2012; Zhu et al., 2012) and preclinical stress-based depression models (Clemm von Hohenberg et al., 2018; Gass et al., 2016; Grandjean et al., 2016; Henckens et al., 2015). Long-lasting structural modifications of ACA and RSP might thus be associated with stable neuroplastic changes leading to depressive behavior. Activity-dependent (Xu et al., 2008) and glia-mediated (Ikeda et al., 2013; Mannelli et al., 2013; Narita et al., 2004) neuroplasticity occurs in ACA as a result of chronic pain. Glial abnormalities were also shown for anterior cingulate in postmortem depression studies (Steiner et al., 2011; Tanti et al., 2019) which can underlie the structural modifications observed in these structures.

In short, transient changes in TH, HY, and HIP regions are likely due to pain and aversive processes while ACA and RSP are strong candidates for mechanistic basis of pain-depression

comorbidity. Their structural alterations might give rise to extensive functional brain network reorganization, promoting aversive and depressive behaviors.

4.2.2 Functional connectivity

Neuropathic mice exhibited a substantial remodeling of brain functional networks over the experimental period. To assess brain-wide functional connectivity, we created matrices using seed areas covering the entire isocortex and subcortical areas. At TP1, major changes were discovered in pain (e.g. TH and insula) and aversion-related regions (e.g. amygdala, hypothalamus, and hippocampal formation). In line with mechanical hypersensitivity seen at this time point, nociceptive and aversive circuits displayed the most changes. At TP2 limbic/reward areas (e.g. VTA, ACB, pallidum, hippocampus, midbrain, septum, BST) and DMN (RSP) components showed the most changes in neuropathic animals along with SS and insula. Development of depressive-like behavior might stem from changes in the dominant nodes of brain networks. Initiated by neuropathic pain, alterations in reward/aversion circuitry may cause reward deficits and heightened aversive behaviors. DMN connectivity differences might also lead to depressive behaviors (Greicius et al., 2007; Wang et al., 2012; Zhu et al., 2012). Changes in SS and insular areas could be explained by continued existence of neuropathic state at TP2. Thus, the transition from chronic pain to associated depressive phenotype seems to involve a shift in predominant networks of the brain from nociceptive to affective circuitries.

The nodes with most marked changes from graph theoretical analysis and areas with structural alterations were chosen as regions of interest (ROIs) for correlation analyses. At TP1, ACA showed reduced connectivity towards nociceptive areas (e.g. insula, PAG) and limbic areas (e.g. CP, dorsal hippocampus and habenula). ACA is an important center of descending pain modulation; therefore, lower connectivity with pain areas suggests a loss of pain modulation. Decreased connectivity towards subcortical limbic regions might point to a top-down control deficit, causing negative affect. At TP2, along with the changes observed at TP1, ACA displayed larger DMN connectivity and an enhanced connectivity to AMY-a major aversive center, concurrent with the depressive phenotype. Our results further support the idea that the ACA is a critical region in the remodeling of brain networks following nerve injury at both structural and functional levels.

VTA, implicated in in reward and aversion (Lammel et al., 2014), nociceptive processes (Ezzatpanah et al., 2016; Hipólito et al., 2015; Ko et al., 2018; Sotres-Bayón et al., 2001; Watanabe et al., 2018) and depressive behaviors (Fu et al., 2018; Isingrini et al., 2017; Ji et al., 2018) was one of the most changed areas in the graph analysis at TP2. Indeed, VTA showed higher connectivity towards many limbic areas (e.g. ACA, ACB, CP, BST, Hb, PF and MD nuclei of thalamus) in neuropathic mice with depressive phenotype. VTA connectivity increased both within reward circuitry and towards ACA, a DMN node which points out to potential implication of DMN in pain-depression comorbidity. The increased connectivity towards reward/aversion areas might either be compensation for reward deficits or increased anti-reward signaling, or a combination of both mechanisms.

LHb, an important part of the reward system, encodes aversion relevant to avoidance and escape behaviors and inhibits reward signals. At TP1, LHb connectivity towards aversive areas (e.g. AMY, TeA, vHIP and MRN) was increased in neuropathic animals. At TP2, stronger connectivity of LHb with thalamus, HY, VTA, and MRN and weaker connectivity with AI and MOs

were observed. Enhanced LHb inhibition of reward areas might be the cause of reward deficits and negative affect associated with depressive phenotype. LHb is implicated in pain processing (Erpelding et al., 2013; Shelton et al., 2012; Taylor et al., 2015) and in depression (Clemm von Hohenberg et al., 2018; Cui et al., 2018; Gass et al., 2014a; Proulx et al., 2014; Sartorius et al., 2010; Yang et al., 2018a). LHb is also shown to be involved in depression-pain comorbidity as shown by Li et al., 2016. A stress-based rat depression model led to pain hypersensitivity and LHb hyperactivity (Li et al., 2016), and LHb lesion relieved both the pain hypersensitivity and depressive phenotype. In addition, chronic constriction injury in rats also caused increased LHb activity and depressive behaviors (Li et al., 2017) which were eliminated by lesioning the LHb. Increased LHb activity might be a common mechanism underlying pain-depression comorbidity.

Our study had certain caveats. Due to a variation in the prevalence of relevant behavioral phenotype in neuropathic mice, our sample size was rather small. In the future, an investigation into neuropathic mice without anxio-depressive behaviors may be warranted to find out resiliency-related factors in brain connectivity. Further reproduction of our findings in neuropathic pain-induced depression with a larger cohort would confirm their biological significance. Another caveat was the use of male subjects only. Recently, the stance on higher hormonal variability in female subjects was abandoned (Shansky, 2019) citing similar variability in males as well as the effects of male social hierarchy. There is a pronounced gender bias in basic research (Alderton, 2019) which might lead to false generalizations and public health problems. As depression prevalence is higher in women (Abate, 2013) and pain responses might differ between sexes (Fillingim et al., 2009), it is especially important to use female subjects in pain-induced depression results.

Nonetheless, we obtained important findings on the contribution of different brain areas to neuropathic pain-induced pain and their temporal evolution. Further work on underlying cellular and molecular mechanisms, and the role of specific projections in highlighted regions are needed to provide a mechanistic explanation of pain-depression comorbidity.

4.3 Conclusion

My investigations into of the evolution of the brain structural and functional networks underlying pain- and depression-related phenotypes showed a dominant role of pain/ aversion areas immediately following nerve injury. Depressive phenotype was established pursuant to reward system and DMN remodeling; highlighting a causal relationship in pain-depression comorbidity. ACA, LHb, and VTA were highlighted as strongly core brain areas implicated involved in the development of neuropathic pain-induced depression in mice.

5 Perspectives

By describing pain and depression-related brain connectivity architecture in this the “cuff” preclinical model, we were able to indicate putative brain areas and pathways responsible from for the emergence of pain-depression comorbidity. The longitudinal experimental design in the present work enabled us to explore time-dependent evolution of brain functional and structural remodeling. Detailed work into the highlighted areas, using further molecular and histological methods as well as cutting-edge technologies such as optogenetic and chemogenetic manipulations designed to alter the activity the highlighted areas, might offer mechanistic explanations into the pathophysiology of pain-induced depression. Moreover, brain MR imaging in this model might be used to monitor therapy responses to new pharmaceutical agents or alternative approaches such as repetitive transcranial magnetic stimulation (rTMS), transcranial direct current stimulation (tDCS), and deep brain stimulation (DBS). Therapeutical strategies tested in this animal model can be transferred to clinical settings, translating the treatments from bench to bedside.

6 References

Abate, K.H., 2013. Gender Disparity in Prevalence of Depression Among Patient Population: A Systematic Review. Ethiop. J. Health Sci. 23, 283–288.

Adcock, R.A., Thangavel, A., Whitfield-Gabrieli, S., Knutson, B., Gabrieli, J.D.E., 2006. Reward-Motivated Learning: Mesolimbic Activation Precedes Memory Formation. Neuron 50, 507–517. https://doi.org/10.1016/j.neuron.2006.03.036

Alderton, G., 2019. Sex bias in research animals. Science 364, 846–848. https://doi.org/10.1126/science.364.6443.846-p

Alexander, A.L., Lee, J.E., Lazar, M., Boudos, R., DuBray, M.B., Oakes, T.R., Miller, J.N., Lu, J., Jeong, E.-K., McMahon, W.M., Bigler, E.D., Lainhart, J.E., 2007. Diffusion tensor imaging of the corpus callosum in Autism. NeuroImage 34, 61–73. https://doi.org/10.1016/j.neuroimage.2006.08.032

Alshelh, Z., Marciszewski, K.K., Akhter, R., Di Pietro, F., Mills, E.P., Vickers, E.R., Peck, C.C., Murray, G.M., Henderson, L.A., 2018. Disruption of default mode network dynamics in acute and chronic pain states. NeuroImage Clin. 17, 222–231. https://doi.org/10.1016/j.nicl.2017.10.019

Anacker, C., Scholz, J., O'Donnell, K.J., Allemang-Grand, R., Diorio, J., Bagot, R.C., Nestler, E.J., Hen, R., Lerch, J.P., Meaney, M.J., 2016. Neuroanatomic Differences Associated With Stress Susceptibility and Resilience. Biol. Psychiatry, Mechanisms of Resilience to Stress Effects 79, 840–849. https://doi.org/10.1016/j.biopsych.2015.08.009

Anand, A., Li, Y., Wang, Y., Lowe, M.J., Dzemidzic, M., 2009. Resting state corticolimbic connectivity abnormalities in unmedicated bipolar disorder and unipolar depression. Psychiatry Res. Neuroimaging 171, 189–198. https://doi.org/10.1016/j.pscychresns.2008.03.012

Anand, A., Li, Y., Wang, Y., Wu, J., Gao, S., Bukhari, L., Mathews, V.P., Kalnin, A., Lowe, M.J., 2005. Antidepressant Effect on Connectivity of the Mood-Regulating Circuit: An fMRI Study. Neuropsychopharmacology. https://doi.org/10.1038/sj.npp.1300725

Anderzhanova, E.A., Bächli, H., Buneeva, O.A., Narkevich, V.B., Medvedev, A.E., Thoeringer, C.K., Wotjak, C.T., Kudrin, V.S., 2013. Strain differences in profiles of dopaminergic neurotransmission in the prefrontal cortex of the BALB/C vs. C57Bl/6 mice: Consequences of stress and afobazole. Eur. J. Pharmacol. 708, 95–104. https://doi.org/10.1016/j.ejphar.2013.03.015

Apkarian, A.V., Sosa, Y., Sonty, S., Levy, R.M., Harden, R.N., Parrish, T.B., Gitelman, D.R., 2004. Chronic Back Pain Is Associated with Decreased Prefrontal and Thalamic Gray Matter Density. J. Neurosci. 24, 10410–10415. https://doi.org/10.1523/JNEUROSCI.2541-04.2004

Apkarian, A.V., Wei, X., Ren, W., Centeno, M., Procissi, D., Xu, T., Jabakhanji, R., Martina, M., Radulovic, J., Surmeier, D., Liu, X., 2018. Dorsal Hippocampal Activation Suppresses Neuropathic Pain Behaviors: Chronic pain as extinction-resistant pain-related memory traces. bioRxiv 292094. https://doi.org/10.1101/292094

Arias-Carrión, O., Stamelou, M., Murillo-Rodríguez, E., Menéndez-González, M., Pöppel, E., 2010. Dopaminergic reward system: a short integrative review. Int. Arch. Med. 3, 24. https://doi.org/10.1186/1755-7682-3-24

Attal, N., Lanteri-Minet, M., Laurent, B., Fermanian, J., Bouhassira, D., 2011. The specific disease burden of neuropathic pain: Results of a French nationwide survey. PAIN 152, 2836. https://doi.org/10.1016/j.pain.2011.09.014

Avants, B.B., Tustison, N.J., Song, G., Cook, P.A., Klein, A., Gee, J.C., 2011. A reproducible evaluation of ANTs similarity metric performance in brain image registration. Neuroimage 54, 2033–2044. https://doi.org/10.1016/j.neuroimage.2010.09.025

Baliki, M.M., Baria, A., Apkarian, A.V., 2011. The cortical rhythms of chronic back pain. J. Neurosci. Off. J. Soc. Neurosci. 31, 13981–13990. https://doi.org/10.1523/JNEUROSCI.1984-11.2011

Baliki, M.N., Apkarian, A.V., 2015. Nociception, Pain, Negative Moods, and Behavior Selection. Neuron 87, 474–491. https://doi.org/10.1016/j.neuron.2015.06.005

Baliki, M. N., Chang, P.C., Baria, A.T., Centeno, M.V., Apkarian, A.V., 2014. Resting-sate functional reorganization of the rat limbic system following neuropathic injury. Sci. Rep. 4, 6186. https://doi.org/10.1038/srep06186

Baliki, M.N., Chialvo, D.R., Geha, P.Y., Levy, R.M., Harden, R.N., Parrish, T.B., Apkarian, A.V., 2006. Chronic Pain and the Emotional Brain: Specific Brain Activity Associated with Spontaneous Fluctuations of Intensity of Chronic Back Pain. J. Neurosci. Off. J. Soc. Neurosci. 26, 12165–12173. https://doi.org/10.1523/JNEUROSCI.3576-06.2006

Baliki, Marwan N., Geha, P.Y., Apkarian, A.V., Chialvo, D.R., 2008. Beyond Feeling: Chronic Pain Hurts the Brain, Disrupting the Default-Mode Network Dynamics. J. Neurosci. 28, 1398–1403. https://doi.org/10.1523/JNEUROSCI.4123-07.2008

Baliki, M.N., Geha, P.Y., Fields, H.L., Apkarian, A.V., 2010. Predicting Value of Pain and Analgesia: Nucleus Accumbens Response to Noxious Stimuli Changes in the Presence of Chronic Pain. Neuron 66, 149–160. https://doi.org/10.1016/j.neuron.2010.03.002

Baliki, Marwan N, Geha, P.Y., Jabakhanji, R., Harden, N., Schnitzer, T.J., Apkarian, A.V., 2008. A Preliminary fMRI Study of Analgesic Treatment in Chronic Back Pain and Knee Osteoarthritis. Mol. Pain 4, 1744-8069-4–47. https://doi.org/10.1186/1744-8069-4-47

Baliki, Marwan N., Mansour, A.R., Baria, A.T., Apkarian, A.V., 2014. Functional reorganization of the default mode network across chronic pain conditions. PloS One 9, e106133. https://doi.org/10.1371/journal.pone.0106133

Baliki, M.N., Petre, B., Torbey, S., Herrmann, K.M., Huang, L., Schnitzer, T.J., Fields, H.L., Apkarian, A.V., 2012. Corticostriatal functional connectivity predicts transition to chronic back pain. Nat. Neurosci. 15, 1117–1119. https://doi.org/10.1038/nn.3153

Bardella, G., Bifone, A., Gabrielli, A., Gozzi, A., Squartini, T., 2016. Hierarchical organization of functional connectivity in the mouse brain: a complex network approach. Sci. Rep. 6, 32060. https://doi.org/10.1038/srep32060

Barnett, L., Seth, A.K., 2014. The MVGC multivariate Granger causality toolbox: A new approach to Granger-causal inference. J. Neurosci. Methods 223, 50–68. https://doi.org/10.1016/j.jneumeth.2013.10.018

Barthas, F., Humo, M., Gilsbach, R., Waltisperger, E., Karatas, M., Leman, S., Hein, L., Belzung, C., Boutillier, A.-L., Barrot, M., Yalcin, I., 2017. Cingulate Overexpression of Mitogen-Activated Protein Kinase Phosphatase-1 as a Key Factor for Depression. Biol. Psychiatry 82, 370–379. https://doi.org/10.1016/j.biopsych.2017.01.019

Barthas, F., Sellmeijer, J., Hugel, S., Waltisperger, E., Barrot, M., Yalcin, I., 2015. The anterior cingulate cortex is a critical hub for pain-induced depression. Biol. Psychiatry 77, 236–245. https://doi.org/10.1016/j.biopsych.2014.08.004

Basser, P.J., Mattiello, J., LeBihan, D., 1994. MR diffusion tensor spectroscopy and imaging. Biophys. J. 66, 259–267. https://doi.org/10.1016/S0006-3495(94)80775-1

Basser, P.J., Pierpaoli, C., 1996. Microstructural and physiological features of tissues elucidated by quantitative-diffusion-tensor MRI. J. Magn. Reson. B 111, 209–219.

Becerra, L., Navratilova, E., Porreca, F., Borsook, D., 2013. Analogous responses in the nucleus accumbens and cingulate cortex to pain onset (aversion) and offset (relief) in rats and humans. J. Neurophysiol. 110, 1221–1226. https://doi.org/10.1152/jn.00284.2013

Becker, S., Gandhi, W., Pomares, F., Wager, T.D., Schweinhardt, P., 2017. Orbitofrontal cortex mediates pain inhibition by monetary reward. Soc. Cogn. Affect. Neurosci. 12, 651–661. https://doi.org/10.1093/scan/nsw173

Belcher, A.M., Yen, C.C., Stepp, H., Gu, H., Lu, H., Yang, Y., Silva, A.C., Stein, E.A., 2013. Large-Scale Brain Networks in the Awake, Truly Resting Marmoset Monkey. J. Neurosci. 33, 16796–16804. https://doi.org/10.1523/JNEUROSCI.3146-13.2013

Belzung, C., Barreau, S., 2000. Differences in drug-induced place conditioning between BALB/c and C57B1/6 mice. Pharmacol. Biochem. Behav. 65, 419–423. https://doi.org/10.1016/S0091-3057(99)00212-9

Belzung, C., Griebel, G., 2001. Measuring normal and pathological anxiety-like behaviour in mice: a review. Behav. Brain Res. 125, 141–149.

Belzung, C., Willner, P., Philippot, P., 2015. Depression: from psychopathology to pathophysiology. Curr. Opin. Neurobiol. 30, 24–30. https://doi.org/10.1016/j.conb.2014.08.013

Benbouzid, M., Pallage, V., Rajalu, M., Waltisperger, E., Doridot, S., Poisbeau, P., Freund-Mercier, M.J., Barrot, M., 2008. Sciatic nerve cuffing in mice: A model of sustained neuropathic pain. Eur. J. Pain 12, 591–599. https://doi.org/10.1016/j.ejpain.2007.10.002

Bergmann, E., Zur, G., Bershadsky, G., Kahn, I., 2016. The Organization of Mouse and Human Cortico-Hippocampal Networks Estimated by Intrinsic Functional Connectivity. Cereb. Cortex 26, 4497–4512. https://doi.org/10.1093/cercor/bhw327

Berman, M.G., Peltier, S., Nee, D.E., Kross, E., Deldin, P.J., Jonides, J., 2011. Depression, rumination and the default network. Soc. Cogn. Affect. Neurosci. 6, 548–555. https://doi.org/10.1093/scan/nsq080

Berton, O., McClung, C.A., DiLeone, R.J., Krishnan, V., Renthal, W., Russo, S.J., Graham, D., Tsankova, N.M., Bolanos, C.A., Rios, M., Monteggia, L.M., Self, D.W., Nestler, E.J., 2006. Essential Role of BDNF in the Mesolimbic Dopamine Pathway in Social Defeat Stress. Science 311, 864–868. https://doi.org/10.1126/science.1120972

Bilbao, A., Falfán-Melgoza, C., Leixner, S., Becker, R., Singaravelu, S.K., Sack, M., Sartorius, A., Spanagel, R., Weber-Fahr, W., 2018. Longitudinal Structural and Functional Brain Network Alterations in a Mouse Model of Neuropathic Pain. Neuroscience. https://doi.org/10.1016/j.neuroscience.2018.04.020

Biswal, B., Zerrin Yetkin, F., Haughton, V.M., Hyde, J.S., 1995. Functional connectivity in the motor cortex of resting human brain using echo-planar mri. Magn. Reson. Med. 34, 537–541.

Bonelli, R.M., Cummings, J.L., 2007. Frontal-subcortical circuitry and behavior. Dialogues Clin. Neurosci. 9, 141–151.

Bora, E., Fornito, A., Pantelis, C., Yücel, M., 2012. Gray matter abnormalities in Major Depressive Disorder: a meta-analysis of voxel based morphometry studies. J. Affect. Disord. 138, 9–18. https://doi.org/10.1016/j.jad.2011.03.049

Borsook, D., Linnman, C., Faria, V., Strassman, A.M., Becerra, L., Elman, I., 2016. Reward deficiency and anti-reward in pain chronification. Neurosci. Biobehav. Rev. 68, 282–297. https://doi.org/10.1016/j.neubiorev.2016.05.033

Boyden, E.S., Zhang, F., Bamberg, E., Nagel, G., Deisseroth, K., 2005. Millisecond-timescale, genetically targeted optical control of neural activity. Nat. Neurosci. 8, 1263–1268. https://doi.org/10.1038/nn1525

Bracht, T., Linden, D., Keedwell, P., 2015. A review of white matter microstructure alterations of pathways of the reward circuit in depression. J. Affect. Disord. 187, 45–53. https://doi.org/10.1016/j.jad.2015.06.041

Bray, S., Hirt, M., Jo, B., Hall, S.S., Lightbody, A.A., Walter, E., Chen, K., Patnaik, S., Reiss, A.L., 2011. Aberrant Frontal Lobe Maturation in Adolescents with Fragile X Syndrome is Related to Delayed Cognitive Maturation. Biol. Psychiatry, Genetic and Environmental Contributors to Disturbed Cortical Development in Developmental Disorders 70, 852–858. https://doi.org/10.1016/j.biopsych.2011.05.038

Brodkin, E.S., 2007. BALB/c mice: Low sociability and other phenotypes that may be relevant to autism. Behav. Brain Res., Animal Models for Autism 176, 53–65. https://doi.org/10.1016/j.bbr.2006.06.025

Brodkin, E.S., Hagemann, A., Nemetski, S.M., Silver, L.M., 2004. Social approach–avoidance behavior of inbred mouse strains towards DBA/2 mice. Brain Res. 1002, 151–157. https://doi.org/10.1016/j.brainres.2003.12.013

Broyd, S.J., Demanuele, C., Debener, S., Helps, S.K., James, C.J., Sonuga-Barke, E.J.S., 2009. Default-mode brain dysfunction in mental disorders: A systematic review. Neurosci. Biobehav. Rev. 33, 279–296. https://doi.org/10.1016/j.neubiorev.2008.09.002

Buckner, R.L., Andrews-Hanna, J.R., Schacter, D.L., 2008. The Brain's Default Network: Anatomy, Function, and Relevance to Disease. Ann. N. Y. Acad. Sci. 1124, 1–38. https://doi.org/10.1196/annals.1440.011

Buehlmann, D., Grandjeanc, J., Xandryd, J., Rudin, M., 2018. Longitudinal resting-state fmri in a mouse model of metastatic bone cancer reveals distinct functional reorganizations along a developing chronic pain state. Pain Publish Ahead of Print. https://doi.org/10.1097/j.pain.0000000000001148

Burma, N.E., Leduc-Pessah, H., Fan, C.Y., Trang, T., 2017. Animal models of chronic pain: Advances and challenges for clinical translation: Animal Models of Chronic Pain. J. Neurosci. Res. 95, 1242–1256. https://doi.org/10.1002/jnr.23768

Buxton, R.B., Uludağ, K., Dubowitz, D.J., Liu, T.T., 2004. Modeling the hemodynamic response to brain activation. NeuroImage, Mathematics in Brain Imaging 23, S220–S233. https://doi.org/10.1016/j.neuroimage.2004.07.013

Calamante, F., Tournier, J.-D., Heidemann, R.M., Anwander, A., Jackson, G.D., Connelly, A., 2011. Track density imaging (TDI): Validation of super resolution property. NeuroImage 56, 1259–1266. https://doi.org/10.1016/j.neuroimage.2011.02.059

Calcagno, E., Canetta, A., Guzzetti, S., Cervo, L., Invernizzi, R.W., 2007. Strain differences in basal and post-citalopram extracellular 5-HT in the mouse medial prefrontal cortex and dorsal hippocampus: relation with tryptophan hydroxylase-2 activity. J. Neurochem. 103, 1111–1120. https://doi.org/10.1111/j.1471-4159.2007.04806.x

Cauda, F., D'Agata, F., Sacco, K., Duca, S., Cocito, D., Paolasso, I., Isoardo, G., Geminiani, G., 2010. Altered resting state attentional networks in diabetic neuropathic pain. J. Neurol. Neurosurg. Psychiatry 81, 806–811. https://doi.org/10.1136/jnnp.2009.188631

Chang, P.-C., Pollema-Mays, S.L., Centeno, M.V., Procissi, D., Contini, M., Baria, A.T., Martina, M., Apkarian, A.V., 2014. Role of nucleus accumbens in neuropathic pain: Linked multi-scale evidence in the rat transitioning to neuropathic pain: Pain 155, 1128–1139. https://doi.org/10.1016/j.pain.2014.02.019

Chen, C., Kim, J.J., Thompson, R.F., Tonegawa, S., 1996. Hippocampal lesions impair contextual fear conditioning in two strains of mice. Behav. Neurosci. 110, 1177–1180. https://doi.org/10.1037/0735-7044.110.5.1177

Chen, C.-H., Suckling, J., Ooi, C., Fu, C.H., Williams, S.C., Walsh, N.D., Mitterschiffthaler, M.T., Pich, E.M., Bullmore, E., 2008. Functional coupling of the amygdala in depressed patients treated with antidepressant medication. Neuropsychopharmacology 33, 1909–1918.

Chen, J.Y.-W., Blankstein, U., Diamant, N.E., Davis, K.D., 2011. White matter abnormalities in irritable bowel syndrome and relation to individual factors. Brain Res. 1392, 121–131. https://doi.org/10.1016/j.brainres.2011.03.069

Chen, T., Taniguchi, W., Chen, Q.-Y., Tozaki-Saitoh, H., Song, Q., Liu, R.-H., Koga, K., Matsuda, T., Kaito-Sugimura, Y., Wang, J., Li, Z.-H., Lu, Y.-C., Inoue, K., Tsuda, M., Li, Y.-Q., Nakatsuka, T., Zhuo, M., 2018. Top-down descending facilitation of spinal sensory excitatory transmission from the anterior cingulate cortex. Nat. Commun. 9. https://doi.org/10.1038/s41467-018-04309-2

Chuang, K.-H., Nasrallah, F.A., 2017. Functional networks and network perturbations in rodents. NeuroImage 163, 419–436. https://doi.org/10.1016/j.neuroimage.2017.09.038

Classification of Chronic Pain, Second Edition (Revised) - IASP [WWW Document], n.d. URL https://www.iasp-pain.org/PublicationsNews/Content.aspx?ItemNumber=1673 (accessed 5.14.18).

Clemm von Hohenberg, C., Weber-Fahr, W., Lebhardt, P., Ravi, N., Braun, U., Gass, N., Becker, R., Sack, M., Cosa Linan, A., Gerchen, M.F., Reinwald, J.R., Oettl, L.-L., Meyer-Lindenberg, A., Vollmayr, B., Kelsch, W., Sartorius, A., 2018. Lateral habenula perturbation reduces default-mode network connectivity in a rat model of depression. Transl. Psychiatry 8, 68. https://doi.org/10.1038/s41398-018-0121-y

Clipperton-Allen, A.E., Ingrao, J.C., Ruggiero, L., Batista, L., Ovari, J., Hammermueller, J., Armstrong, J.N., Bienzle, D., Choleris, E., Turner, P.V., 2015. Long-Term Provision of Environmental Resources Alters Behavior but not Physiology or Neuroanatomy of Male and Female BALB/c and C57BL/6 Mice. J. Am. Assoc. Lab. Anim. Sci. 54, 718–730.

Cohen, S.P., Mao, J., 2014. Neuropathic pain: mechanisms and their clinical implications. BMJ 348, f7656.

Colloca, L., Ludman, T., Bouhassira, D., Baron, R., Dickenson, A.H., Yarnitsky, D., Freeman, R., Truini, A., Attal, N., Finnerup, N.B., Eccleston, C., Kalso, E., Bennett, D.L., Dworkin, R.H., Raja, S.N., 2017. Neuropathic pain. Nat. Rev. Dis. Primer 3, 17002. https://doi.org/10.1038/nrdp.2017.2

Crawley, J.N., Belknap, J.K., Collins, A., Crabbe, J.C., Frankel, W., Henderson, N., Hitzemann, R.J., Maxson, S.C., Miner, L.L., Silva, A.J., 1997. Behavioral phenotypes of inbred mouse strains: implications and recommendations for molecular studies. Psychopharmacology (Berl.) 132, 107–124.

Cui, Y., Yang, Y., Ni, Z., Dong, Y., Cai, G., Foncelle, A., Ma, S., Sang, K., Tang, S., Li, Y., Shen, Y., Berry, H., Wu, S., Hu, H., 2018. Astroglial Kir4.1 in the lateral habenula drives neuronal bursts in depression. Nature 554, 323–327. https://doi.org/10.1038/nature25752

DaSilva, A.F.M., Granziera, C., Tuch, D.S., Snyder, J., Vincent, M., Hadjikhani, N., 2007. Interictal alterations of the trigeminal somatosensory pathway and PAG in migraine. Neuroreport 18, 301–305. https://doi.org/10.1097/WNR.0b013e32801776bb

Davis, K.D., Moayedi, M., 2013. Central mechanisms of pain revealed through functional and structural MRI. J. Neuroimmune Pharmacol. Off. J. Soc. NeuroImmune Pharmacol. 8, 518–534. https://doi.org/10.1007/s11481-012-9386-8

de Sá-Calçada, D., Roque, S., Branco, C., Monteiro, S., Cerqueira-Rodrigues, B., Sousa, N., Palha, J.A., Correia-Neves, M., 2015. Exploring Female Mice Interstrain Differences Relevant for Models of Depression. Front. Behav. Neurosci. 9. https://doi.org/10.3389/fnbeh.2015.00335

Delgado y Palacios, R., Verhoye, M., Henningsen, K., Wiborg, O., Van der Linden, A., 2014. Diffusion Kurtosis Imaging and High-Resolution MRI Demonstrate Structural Aberrations of Caudate Putamen and Amygdala after Chronic Mild Stress. PLoS ONE 9, e95077. https://doi.org/10.1371/journal.pone.0095077

Dennis, E.L., Thompson, P.M., 2013a. Mapping connectivity in the developing brain. Int. J. Dev. Neurosci. 31, 525–542. https://doi.org/10.1016/j.ijdevneu.2013.05.007

Dennis, E.L., Thompson, P.M., 2013b. Typical and atypical brain development: a review of neuroimaging studies. Dialogues Clin. Neurosci. 15, 359–384.

Devonshire, I.M., Burston, J.J., Xu, L., Lillywhite, A., Prior, M.J., Watson, D.J.G., Greenspon, C.M., Iwabuchi, S.J., Auer, D.P., Chapman, V., 2017. Manganese-enhanced magnetic resonance imaging depicts brain activity in models of acute and chronic pain: A new window to study experimental spontaneous pain? NeuroImage 157, 500–510. https://doi.org/10.1016/j.neuroimage.2017.06.034

Di, X., Biswal, B.B., 2015. Dynamic Brain Functional Connectivity Modulated by Resting-State Networks. Brain Struct. Funct. 220, 37–46. https://doi.org/10.1007/s00429-013-0634-3

Dillon, D.G., Dobbins, I.G., Pizzagalli, D.A., 2014. Weak reward source memory in depression reflects blunted activation of VTA/SN and parahippocampus. Soc. Cogn. Affect. Neurosci. 9, 1576–1583. https://doi.org/10.1093/scan/nst155

Doan, L., Manders, T., Wang, J., 2015. Neuroplasticity underlying the comorbidity of pain and depression. Neural Plast. 2015, 504691. https://doi.org/10.1155/2015/504691

Dodero, L., Damiano, M., Galbusera, A., Bifone, A., Tsaftsaris, S.A., Scattoni, M.L., Gozzi, A., 2013. Neuroimaging Evidence of Major Morpho-Anatomical and Functional Abnormalities in the BTBR T+TF/J Mouse Model of Autism. PLOS ONE 8, e76655. https://doi.org/10.1371/journal.pone.0076655

Doerig, N., Krieger, T., Altenstein, D., Schlumpf, Y., Spinelli, S., Spa ti, J., Brakowski, J., Quednow, B.B., Seifritz, E., Holtforth, M. g., 2016. Amygdala response to self-critical stimuli and symptom improvement in psychotherapy for depression. Br. J. Psychiatry 208, 175–181. https://doi.org/10.1192/bjp.bp.114.149971

DosSantos, M.F., Moura, B. de S., DaSilva, A.F., 2017. Reward Circuitry Plasticity in Pain Perception and Modulation. Front. Pharmacol. 8. https://doi.org/10.3389/fphar.2017.00790

Draganski, B., Ashburner, J., Hutton, C., Kherif, F., Frackowiak, R.S.J., Helms, G., Weiskopf, N., 2011. Regional specificity of MRI contrast parameter changes in normal ageing revealed by voxel-based quantification (VBQ). NeuroImage 55, 1423–1434. https://doi.org/10.1016/j.neuroimage.2011.01.052

Drevets, W.C., Price, J.L., Jr, J.R.S., Todd, R.D., Reich, T., Vannier, M., Raichle, M.E., 1997. Subgenual prefrontal cortex abnormalities in mood disorders. Nature 386, 824–827. https://doi.org/10.1038/386824a0

Du, M.-Y., Wu, Q.-Z., Yue, Q., Li, J., Liao, Y., Kuang, W.-H., Huang, X.-Q., Chan, R.C.K., Mechelli, A., Gong, Q.-Y., 2012. Voxelwise meta-analysis of gray matter reduction in major depressive disorder. Prog. Neuropsychopharmacol. Biol. Psychiatry 36, 11–16. https://doi.org/10.1016/j.pnpbp.2011.09.014

Eagle, D.M., Baunez, C., Hutcheson, D.M., Lehmann, O., Shah, A.P., Robbins, T.W., 2008. Stop-Signal Reaction-Time Task Performance: Role of Prefrontal Cortex and Subthalamic Nucleus. Cereb. Cortex 18, 178–188. https://doi.org/10.1093/cercor/bhm044

Einstein, A., 1905. Über die von der molekularkinetischen Theorie der Wärme geforderte Bewegung von in ruhenden Flüssigkeiten suspendierten Teilchen. Ann. Phys. 322, 549–560. https://doi.org/10.1002/andp.19053220806

Ellegood, J., Anagnostou, E., Babineau, B.A., Crawley, J.N., Lin, L., Genestine, M., DiCicco-Bloom, E., Lai, J.K.Y., Foster, J.A., Peñagarikano, O., Geschwind, D.H., Pacey, L.K., Hampson, D.R., Laliberté, C.L., Mills, A.A., Tam, E., Osborne, L.R., Kouser, M., Espinosa-Becerra, F., Xuan, Z., Powell, C.M.,

Raznahan, A., Robins, D.M., Nakai, N., Nakatani, J., Takumi, T., van Eede, M.C., Kerr, T.M., Muller, C., Blakely, R.D., Veenstra-VanderWeele, J., Henkelman, R.M., Lerch, J.P., 2015. Clustering autism: using neuroanatomical differences in 26 mouse models to gain insight into the heterogeneity. Mol. Psychiatry 20, 118–125. https://doi.org/10.1038/mp.2014.98

Ellegood, J., Babineau, B.A., Henkelman, R.M., Lerch, J.P., Crawley, J.N., 2013. Neuroanatomical analysis of the BTBR mouse model of autism using magnetic resonance imaging and diffusion tensor imaging. NeuroImage 70, 288–300. https://doi.org/10.1016/j.neuroimage.2012.12.029

Ellegood, J., Pacey, L.K., Hampson, D.R., Lerch, J.P., Henkelman, R.M., 2010. Anatomical phenotyping in a mouse model of fragile X syndrome with magnetic resonance imaging. NeuroImage, Imaging Genetics 53, 1023–1029. https://doi.org/10.1016/j.neuroimage.2010.03.038

Ellingson, B.M., Mayer, E., Harris, R.J., Ashe-mcnally, C., Naliboff, B.D., Labus, J.S., Tillisch, K., 2013. Diffusion tensor imaging detects microstructural reorganization in the brain associated with chronic irritable bowel syndrome. Pain 154, 1528–1541. https://doi.org/10.1016/j.pain.2013.04.010

Epstein, J., Pan, H., Kocsis, J.H., Yang, Y., Butler, T., Chusid, J., Hochberg, H., Murrough, J., Strohmayer, E., Stern, E., others, 2006. Lack of ventral striatal response to positive stimuli in depressed versus normal subjects. Am. J. Psychiatry.

Erpelding, N., Sava, S., Simons, L.E., Lebel, A., Serrano, P., Becerra, L., Borsook, D., 2013. Habenula functional resting-state connectivity in pediatric CRPS. J. Neurophysiol. 111, 239–247. https://doi.org/10.1152/jn.00405.2013

Ezzatpanah, S., Babapour, V., Haghparast, A., 2016. Differential contribution of orexin receptors within the ventral tegmental area to modulation of persistent inflammatory pain. Eur. J. Pain 20, 1090–1101. https://doi.org/10.1002/ejp.833

Fairless, A.H., Dow, H.C., Kreibich, A.S., Torre, M., Kuruvilla, M., Gordon, E., Morton, E.A., Tan, J., Berrettini, W.H., Li, H., Abel, T., Brodkin, E.S., 2012. Sociability and brain development in BALB/cJ and C57BL/6J mice. Behav. Brain Res. 228, 299–310. https://doi.org/10.1016/j.bbr.2011.12.001

Fairless, A.H., Dow, H.C., Toledo, M.M., Malkus, K.A., Edelmann, M., Li, H., Talbot, K., Arnold, S.E., Abel, T., Brodkin, E.S., 2008. Low sociability is associated with reduced size of the corpus callosum in the BALB/cJ inbred mouse strain. Brain Res. 1230, 211–217. https://doi.org/10.1016/j.brainres.2008.07.025

Fairless, A.H., Katz, J.M., Vijayvargiya, N., Dow, H.C., Kreibich, A.S., Berrettini, W.H., Abel, T., Brodkin, E.S., 2013. Development of home cage social behaviors in BALB/cJ vs. C57BL/6J mice. Behav. Brain Res. 237, 338–347. https://doi.org/10.1016/j.bbr.2012.08.051

Fanselow, M.S., Dong, H.-W., 2010. Are the Dorsal and Ventral Hippocampus Functionally Distinct Structures? Neuron 65, 7–19. https://doi.org/10.1016/j.neuron.2009.11.031

Farmer, M.A., Baliki, M.N., Apkarian, A.V., 2012. A dynamic network perspective of chronic pain. Neurosci. Lett. 520, 197–203. https://doi.org/10.1016/j.neulet.2012.05.001

Fields, H., 2004. State-dependent opioid control of pain. Nat. Rev. Neurosci. 5, 565–575. https://doi.org/10.1038/nrn1431

Fields, H.L., 2007. Understanding How Opioids Contribute to Reward and Analgesia 32, 242–246. https://doi.org/10.1016/j.rapm.2007.01.001

Fillingim, R.B., King, C.D., Ribeiro-Dasilva, M.C., Rahim-Williams, B., Riley, J.L., 2009. Sex, Gender, and Pain: A Review of Recent Clinical and Experimental Findings. J. Pain Off. J. Am. Pain Soc. 10, 447–485. https://doi.org/10.1016/j.jpain.2008.12.001

Fontaine, D.A., Davis, D.B., 2016. Attention to Background Strain Is Essential for Metabolic Research: C57BL/6 and the International Knockout Mouse Consortium. Diabetes 65, 25–33. https://doi.org/10.2337/db15-0982

Fornito, A., Bullmore, E.T., 2010. What can spontaneous fluctuations of the blood oxygenation-level-dependent signal tell us about psychiatric disorders? Curr. Opin. Psychiatry 23, 239–249. https://doi.org/10.1097/YCO.0b013e328337d78d

Fox, A.S., Shelton, S.E., Oakes, T.R., Converse, A.K., Davidson, R.J., Kalin, N.H., 2010. Orbitofrontal Cortex Lesions Alter Anxiety-Related Activity in the Primate Bed Nucleus of Stria Terminalis. J. Neurosci. 30, 7023–7027. https://doi.org/10.1523/JNEUROSCI.5952-09.2010

Fox, M.D., Raichle, M.E., 2007. Spontaneous fluctuations in brain activity observed with functional magnetic resonance imaging. Nat. Rev. Neurosci. 8, 700–711. https://doi.org/10.1038/nrn2201

Fox, M.D., Snyder, A.Z., Vincent, J.L., Corbetta, M., Van Essen, D.C., Raichle, M.E., 2005. The human brain is intrinsically organized into dynamic, anticorrelated functional networks. Proc. Natl. Acad. Sci. U. S. A. 102, 9673–9678.

Fox, P.T., Raichle, M.E., 1986. Focal physiological uncoupling of cerebral blood flow and oxidative metabolism during somatosensory stimulation in human subjects. Proc. Natl. Acad. Sci. 83, 1140–1144. https://doi.org/10.1073/pnas.83.4.1140

Fox, P.T., Raichle, M.E., Mintun, M.A., Dence, C., 1988. Nonoxidative glucose consumption during focal physiologic neural activity. Science 241, 462–464. https://doi.org/10.1126/science.3260686

Fox, R.J., 2008. Picturing Multiple Sclerosis: Conventional and Diffusion Tensor Imaging. Semin. Neurol. 28, 453–466. https://doi.org/10.1055/s-0028-1083689

Frazier, T.W., Youngstrom, E.A., Speer, L., Embacher, R., Law, P., Constantino, J., Findling, R.L., Hardan, A.Y., Eng, C., 2012. Validation of Proposed DSM-5 Criteria for Autism Spectrum Disorder. J. Am. Acad. Child Adolesc. Psychiatry 51, 28-40.e3. https://doi.org/10.1016/j.jaac.2011.09.021

Friston, K.J., Frith, C.D., Liddle, P.F., Frackowiak, R.S.J., 1993. Functional Connectivity: The Principal-Component Analysis of Large (PET) Data Sets. J. Cereb. Blood Flow Metab. 13, 5–14. https://doi.org/10.1038/jcbfm.1993.4

Fu, B., Wen, S.-N., Wang, B., Wang, K., Zhang, J.-Y., Weng, X.-C., Liu, S.-J., 2018. Gabapentin regulates dopaminergic neuron firing and theta oscillation in the ventral tegmental area to reverse depression-like behavior in chronic neuropathic pain state [WWW Document]. J. Pain Res. https://doi.org/10.2147/JPR.S170167

Garcia-Larrea, L., Peyron, R., 2013. Pain matrices and neuropathic pain matrices: a review. Pain 154 Suppl 1, S29-43. https://doi.org/10.1016/j.pain.2013.09.001

Gass, N., Becker, R., Schwarz, A.J., Weber-Fahr, W., Clemm von Hohenberg, C., Vollmayr, B., Sartorius, A., 2016. Brain network reorganization differs in response to stress in rats genetically predisposed to depression and stress-resilient rats. Transl. Psychiatry 6, e970–e970. https://doi.org/10.1038/tp.2016.233

Gass, N., Cleppien, D., Zheng, L., Schwarz, A.J., Meyer-Lindenberg, A., Vollmayr, B., Weber-Fahr, W., Sartorius, A., 2014a. Functionally altered neurocircuits in a rat model of treatment-resistant depression show prominent role of the habenula. Eur. Neuropsychopharmacol. 24, 381–390. https://doi.org/10.1016/j.euroneuro.2013.12.004

Gass, N., Schwarz, A.J., Sartorius, A., Schenker, E., Risterucci, C., Spedding, M., Zheng, L., Meyer-Lindenberg, A., Weber-Fahr, W., 2014b. Sub-Anesthetic Ketamine Modulates Intrinsic BOLD Connectivity Within the Hippocampal-Prefrontal Circuit in the Rat. Neuropsychopharmacology 39, 895–906. https://doi.org/10.1038/npp.2013.290

Geha, P.Y., Baliki, M.N., Harden, R.N., Bauer, W.R., Parrish, T.B., Apkarian, A.V., 2008. The Brain in Chronic CRPS Pain: Abnormal Gray-White Matter Interactions in Emotional and Autonomic Regions. Neuron 60, 570–581. https://doi.org/10.1016/j.neuron.2008.08.022

Gonçalves, L., Silva, R., Pinto-Ribeiro, F., Pêgo, J.M., Bessa, J.M., Pertovaara, A., Sousa, N., Almeida, A., 2008. Neuropathic pain is associated with depressive behaviour and induces neuroplasticity in the amygdala of the rat. Exp. Neurol. 213, 48–56. https://doi.org/10.1016/j.expneurol.2008.04.043

Good, C.D., Johnsrude, I.S., Ashburner, J., Henson, R.N.A., Friston, K.J., Frackowiak, R.S.J., 2001. A Voxel-Based Morphometric Study of Ageing in 465 Normal Adult Human Brains. NeuroImage 14, 21–36. https://doi.org/10.1006/nimg.2001.0786

Gozzi, A., Schwarz, A.J., 2016. Large-scale functional connectivity networks in the rodent brain. NeuroImage 127, 496–509. https://doi.org/10.1016/j.neuroimage.2015.12.017

Gradin, V.B., Kumar, P., Waiter, G., Ahearn, T., Stickle, C., Milders, M., Reid, I., Hall, J., Steele, J.D., 2011. Expected value and prediction error abnormalities in depression and schizophrenia. Brain 134, 1751–1764. https://doi.org/10.1093/brain/awr059

Grandjean, J., Azzinnari, D., Seuwen, A., Sigrist, H., Seifritz, E., Pryce, C.R., Rudin, M., 2016. Chronic psychosocial stress in mice leads to changes in brain functional connectivity and metabolite levels

comparable to human depression. NeuroImage 142, 544–552. https://doi.org/10.1016/j.neuroimage.2016.08.013

Grandjean, J., Schroeter, A., Batata, I., Rudin, M., 2014. Optimization of anesthesia protocol for resting-state fMRI in mice based on differential effects of anesthetics on functional connectivity patterns. NeuroImage 102, 838–847. https://doi.org/10.1016/j.neuroimage.2014.08.043

Grandjean, J., Zerbi, V., Balsters, J., Wenderoth, N., Rudina, M., 2017. The structural basis of large-scale functional connectivity in the mouse. J. Neurosci. 0438–17. https://doi.org/10.1523/JNEUROSCI.0438-17.2017

Grange, P., 2018. Topology of the mesoscale connectome of the mouse brain. ArXiv181104698 Q-Bio.

Greicius, M.D., Flores, B.H., Menon, V., Glover, G.H., Solvason, H.B., Kenna, H., Reiss, A.L., Schatzberg, A.F., 2007. Resting-State Functional Connectivity in Major Depression: Abnormally Increased Contributions from Subgenual Cingulate Cortex and Thalamus. Biol. Psychiatry 62, 429–437. https://doi.org/10.1016/j.biopsych.2006.09.020

Greicius, M.D., Krasnow, B., Reiss, A.L., Menon, V., 2003. Functional connectivity in the resting brain: a network analysis of the default mode hypothesis. Proc. Natl. Acad. Sci. 100, 253–258.

Grubb, S.C., Churchill, G.A., Bogue, M.A., 2004. A collaborative database of inbred mouse strain characteristics. Bioinformatics 20, 2857–2859. https://doi.org/10.1093/bioinformatics/bth299

Guilfoyle, D.N., Gerum, S.V., Sanchez, J.L., Balla, A., Sershen, H., Javitt, D.C., Hoptman, M.J., 2013. Functional connectivity fMRI in mouse brain at 7 T using isoflurane. J. Neurosci. Methods 214, 144–148. https://doi.org/10.1016/j.jneumeth.2013.01.019

Gunaydin, L.A., Grosenick, L., Finkelstein, J.C., Kauvar, I.V., Fenno, L.E., Adhikari, A., Lammel, S., Mirzabekov, J.J., Airan, R.D., Zalocusky, K.A., Tye, K.M., Anikeeva, P., Malenka, R.C., Deisseroth, K., 2014. Natural Neural Projection Dynamics Underlying Social Behavior. Cell 157, 1535–1551. https://doi.org/10.1016/j.cell.2014.05.017

Gustin, S.M., Peck, C.C., Wilcox, S.L., Nash, P.G., Murray, G.M., Henderson, L.A., 2011. Different Pain, Different Brain: Thalamic Anatomy in Neuropathic and Non-Neuropathic Chronic Pain Syndromes. J. Neurosci. 31, 5956–5964. https://doi.org/10.1523/JNEUROSCI.5980-10.2011

Guzzetti, S., Calcagno, E., Canetta, A., Sacchetti, G., Fracasso, C., Caccia, S., Cervo, L., Invernizzi, R.W., 2008. Strain differences in paroxetine-induced reduction of immobility time in the forced swimming test in mice: role of serotonin. Eur. J. Pharmacol. 594, 117–124. https://doi.org/10.1016/j.ejphar.2008.07.031

Haber, S.N., Knutson, B., 2010. The Reward Circuit: Linking Primate Anatomy and Human Imaging. Neuropsychopharmacology 35, 4–26. https://doi.org/10.1038/npp.2009.129

Hägele, C., Schlagenhauf, F., Rapp, M., Sterzer, P., Beck, A., Bermpohl, F., Stoy, M., Ströhle, A., Wittchen, H.-U., Dolan, R.J., Heinz, A., 2015. Dimensional psychiatry: reward dysfunction and depressive mood across psychiatric disorders. Psychopharmacology (Berl.) 232, 331–341. https://doi.org/10.1007/s00213-014-3662-7

Hall, G.B.C., Milne, A.M.B., MacQueen, G.M., 2014. An fMRI study of reward circuitry in patients with minimal or extensive history of major depression. Eur. Arch. Psychiatry Clin. Neurosci. 264, 187–198. https://doi.org/10.1007/s00406-013-0437-9

Harsan, L.-A., Dávid, C., Reisert, M., Schnell, S., Hennig, J., von Elverfeldt, D., Staiger, J.F., 2013. Mapping remodeling of thalamocortical projections in the living reeler mouse brain by diffusion tractography. Proc. Natl. Acad. Sci. U. S. A. 110, E1797-1806. https://doi.org/10.1073/pnas.1218330110

Hayes, D.J., Northoff, G., 2011. Identifying a Network of Brain Regions Involved in Aversion-Related Processing: A Cross-Species Translational Investigation. Front. Integr. Neurosci. 5. https://doi.org/10.3389/fnint.2011.00049

Heller, A.S., Johnstone, T., Shackman, A.J., Light, S.N., Peterson, M.J., Kolden, G.G., Kalin, N.H., Davidson, R.J., 2009. Reduced capacity to sustain positive emotion in major depression reflects diminished maintenance of fronto-striatal brain activation. Proc. Natl. Acad. Sci. 106, 22445–22450.

Henckens, M.J.A.G., van der Marel, K., van der Toorn, A., Pillai, A.G., Fernández, G., Dijkhuizen, R.M., Joëls, M., 2015. Stress-induced alterations in large-scale functional networks of the rodent brain. NeuroImage 105, 312–322. https://doi.org/10.1016/j.neuroimage.2014.10.037

Hickie, I.B., Naismith, S.L., Ward, P.B., Scott, E.M., Mitchell, P.B., Schofield, P.R., Scimone, A., Wilhelm, K., Parker, G., 2007. Serotonin transporter gene status predicts caudate nucleus but not amygdala or hippocampal volumes in older persons with major depression. J. Affect. Disord. 98, 137–142. https://doi.org/10.1016/j.jad.2006.07.010

Hipólito, L., Wilson-Poe, A., Campos-Jurado, Y., Zhong, E., Gonzalez-Romero, J., Virag, L., Whittington, R., Comer, S.D., Carlton, S.M., Walker, B.M., Bruchas, M.R., Morón, J.A., 2015. Inflammatory Pain Promotes Increased Opioid Self-Administration: Role of Dysregulated Ventral Tegmental Area μ Opioid Receptors. J. Neurosci. 35, 12217–12231. https://doi.org/10.1523/JNEUROSCI.1053-15.2015

Horsfield, M.A., Jones, D.K., 2002. Applications of diffusion-weighted and diffusion tensor MRI to white matter diseases – a review. NMR Biomed. 15, 570–577. https://doi.org/10.1002/nbm.787

Huang, P., Gao, T., Dong, Z., Zhou, C., Lai, Y., Pan, T., Liu, Y., Zhao, X., Sun, X., Hua, H., Wen, G., Gao, L., Lv, Z., 2018. Neural circuitry among connecting the hippocampus, prefrontal cortex and basolateral amygdala in a mouse depression model: Associations correlations between BDNF levels and BOLD – fMRI signals. Brain Res. Bull. 142, 107–115. https://doi.org/10.1016/j.brainresbull.2018.06.019

Hubbard, C.S., Khan, S.A., Xu, S., Cha, M., Masri, R., Seminowicz, D.A., 2015. Behavioral, metabolic and functional brain changes in a rat model of chronic neuropathic pain: A longitudinal MRI study. NeuroImage 107, 333–344. https://doi.org/10.1016/j.neuroimage.2014.12.024

Hübner, N.S., Mechling, A.E., Lee, H.-L., Reisert, M., Bienert, T., Hennig, J., von Elverfeldt, D., Harsan, L.-A., 2017. The connectomics of brain demyelination: Functional and structural patterns in the cuprizone mouse model. NeuroImage 146, 1–18. https://doi.org/10.1016/j.neuroimage.2016.11.008

Iannetti, G.D., Mouraux, A., 2010. From the neuromatrix to the pain matrix (and back). Exp. Brain Res. 205, 1–12. https://doi.org/10.1007/s00221-010-2340-1

Ikeda, H., Mochizuki, K., Murase, K., 2013. Astrocytes are involved in long-term facilitation of neuronal excitation in the anterior cingulate cortex of mice with inflammatory pain: Pain 154, 2836–2843. https://doi.org/10.1016/j.pain.2013.08.023

Ingalhalikar, M., Smith, A., Parker, D., Satterthwaite, T.D., Elliott, M.A., Ruparel, K., Hakonarson, H., Gur, R.E., Gur, R.C., Verma, R., 2014. Sex differences in the structural connectome of the human brain. Proc. Natl. Acad. Sci. 111, 823–828. https://doi.org/10.1073/pnas.1316909110

Isingrini, E., Perret, L., Rainer, Q., Amilhon, B., Guma, E., Tanti, A., Martin, G., Robinson, J., Moquin, L., Marti, F., 2017. 695. Resilience against Chronic Stress is Mediated by Noradrenergic Regulation of the Ventral Tegmental Area. Biol. Psychiatry 81, S282.

Jacome, L.F., Burket, J.A., Herndon, A.L., Deutsch, S.I., 2011. Genetically inbred Balb/c mice differ from outbred Swiss Webster mice on discrete measures of sociability: relevance to a genetic mouse model of autism spectrum disorders. Autism Res. 4, 393–400. https://doi.org/10.1002/aur.218

Ji, N.-N., Kang, J., Hua, R., Zhang, Y.-M., 2018. Involvement of dopamine system in the regulation of the brain corticotropin-releasing hormone in paraventricular nucleus in a rat model of chronic visceral pain. Neurol. Res. 0, 1–8. https://doi.org/10.1080/01616412.2018.1460702

Johnston, B.A., Tolomeo, S., Gradin, V., Christmas, D., Matthews, K., Douglas Steele, J., 2015. Failure of hippocampal deactivation during loss events in treatment-resistant depression. Brain 138, 2766–2776. https://doi.org/10.1093/brain/awv177

Jonckers, E., Van Audekerke, J., De Visscher, G., Van der Linden, A., Verhoye, M., 2011. Functional Connectivity fMRI of the Rodent Brain: Comparison of Functional Connectivity Networks in Rat and Mouse. PLoS ONE 6, e18876. https://doi.org/10.1371/journal.pone.0018876

Jones, D., 2008. Studying connections in the living human brain with diffusion MRI. Cortex 44, 936–952. https://doi.org/10.1016/j.cortex.2008.05.002

Jones, D.K., 2004. The effect of gradient sampling schemes on measures derived from diffusion tensor MRI: A Monte Carlo study. Magn. Reson. Med. 51, 807–815. https://doi.org/10.1002/mrm.20033

Just, M.A., Cherkassky, V.L., Keller, T.A., Kana, R.K., Minshew, N.J., 2006. Functional and Anatomical Cortical Underconnectivity in Autism: Evidence from an fMRI Study of an Executive Function Task and Corpus Callosum Morphometry. Cereb. Cortex 17, 951–961. https://doi.org/10.1093/cercor/bhl006

Kahn, I., Shohamy, D., 2013. Intrinsic connectivity between the hippocampus, nucleus accumbens, and ventral tegmental area in humans. Hippocampus 23, 187–192. https://doi.org/10.1002/hipo.22077

Keane, T.M., Goodstadt, L., Danecek, P., White, M.A., Wong, K., Yalcin, B., Heger, A., Agam, A., Slater, G., Goodson, M., Furlotte, N.A., Eskin, E., Nellåker, C., Whitley, H., Cleak, J., Janowitz, D., Hernandez-Pliego, P., Edwards, A., Belgard, T.G., Oliver, P.L., McIntyre, R.E., Bhomra, A., Nicod, J., Gan, X., Yuan, W., Weyden, L. van der, Steward, C.A., Bala, S., Stalker, J., Mott, R., Durbin, R., Jackson, I.J., Czechanski, A., Guerra-Assunção, J.A., Donahue, L.R., Reinholdt, L.G., Payseur, B.A., Ponting, C.P., Birney, E., Flint, J., Adams, D.J., 2011. Mouse genomic variation and its effect on phenotypes and gene regulation. Nature 477, 289. https://doi.org/10.1038/nature10413

Kim, S., Pickup, S., Fairless, A.H., Ittyerah, R., Dow, H.C., Abel, T., Brodkin, E.S., Poptani, H., 2012. Association between sociability and diffusion tensor imaging in BALB/cJ mice: DIFFUSION TENSOR IMAGING AND SOCIABILITY. NMR Biomed. 25, 104–112. https://doi.org/10.1002/nbm.1722

Knox, J.E., Harris, K.D., Graddis, N., Whitesell, J.D., Zeng, H., Harris, J.A., Shea-Brown, E., Mihalas, S., 2018. High resolution data-driven model of the mouse connectome. bioRxiv 293019. https://doi.org/10.1101/293019

Knutson, B., Bhanji, J.P., Cooney, R.E., Atlas, L.Y., Gotlib, I.H., 2008. Neural Responses to Monetary Incentives in Major Depression. Biol. Psychiatry 63, 686–692. https://doi.org/10.1016/j.biopsych.2007.07.023

Ko, M.Y., Jang, E.Y., Lee, J.Y., Kim, S.P., Whang, S.H., Lee, B.H., Kim, H.Y., Yang, C.H., Cho, H.J., Gwak, Y.S., 2018. The Role of Ventral Tegmental Area Gamma-Aminobutyric Acid in Chronic Neuropathic Pain after Spinal Cord Injury in Rats. J. Neurotrauma 35, 1755–1764. https://doi.org/10.1089/neu.2017.5381

Komaki, Y., Hikishima, K., Shibata, S., Konomi, T., Seki, F., Yamada, M., Miyasaka, N., Fujiyoshi, K., Okano, H.J., Nakamura, M., Okano, H., 2016. Functional brain mapping using specific sensory-circuit stimulation and a theoretical graph network analysis in mice with neuropathic allodynia. Sci. Rep. 6, 37802. https://doi.org/10.1038/srep37802

Kuchinad, A., Schweinhardt, P., Seminowicz, D.A., Wood, P.B., Chizh, B.A., Bushnell, M.C., 2007. Accelerated Brain Gray Matter Loss in Fibromyalgia Patients: Premature Aging of the Brain? J. Neurosci. 27, 4004–4007. https://doi.org/10.1523/JNEUROSCI.0098-07.2007

Kucyi, A., Moayedi, M., Weissman-Fogel, I., Goldberg, M.B., Freeman, B.V., Tenenbaum, H.C., Davis, K.D., 2014. Enhanced medial prefrontal-default mode network functional connectivity in chronic pain and its association with pain rumination. J. Neurosci. Off. J. Soc. Neurosci. 34, 3969–3975. https://doi.org/10.1523/JNEUROSCI.5055-13.2014

Kumar, M., Kim, S., Pickup, S., Chen, R., Fairless, A.H., Ittyerah, R., Abel, T., Brodkin, E.S., Poptani, H., 2012. Longitudinal in-vivo diffusion tensor imaging for assessing brain developmental changes in BALB/cJ mice, a model of reduced sociability relevant to autism. Brain Res. 1455, 56–67. https://doi.org/10.1016/j.brainres.2012.03.041

Kumar, P., Slavich, G.M., Berghorst, L.H., Treadway, M.T., Brooks, N.H., Dutra, S.J., Greve, D.N., O'Donovan, A., Bleil, M.E., Maninger, N., Pizzagalli, D.A., 2015. Perceived life stress exposure modulates reward-related medial prefrontal cortex responses to acute stress in depression. J. Affect. Disord. 180, 104–111. https://doi.org/10.1016/j.jad.2015.03.035

Kumar, P., Waiter, G., Ahearn, T., Milders, M., Reid, I., Steele, J.D., 2008. Abnormal temporal difference reward-learning signals in major depression. Brain 131, 2084–2093. https://doi.org/10.1093/brain/awn136

Lai, C.-H., 2013. Gray matter volume in major depressive disorder: a meta-analysis of voxel-based morphometry studies. Psychiatry Res. 211, 37–46. https://doi.org/10.1016/j.pscychresns.2012.06.006

Lai, J.K.Y., Lerch, J.P., Doering, L.C., Foster, J.A., Ellegood, J., 2016. Regional brain volumes changes in adult male FMR1-KO mouse on the FVB strain. Neuroscience 318, 12–21. https://doi.org/10.1016/j.neuroscience.2016.01.021

Laine, M.A., Sokolowska, E., Dudek, M., Callan, S.-A., Hyytiä, P., Hovatta, I., 2017. Brain activation induced by chronic psychosocial stress in mice. Sci. Rep. 7. https://doi.org/10.1038/s41598-017-15422-5

Lammel, S., Lim, B.K., Malenka, R.C., 2014. Reward and aversion in a heterogeneous midbrain dopamine system. Neuropharmacology 76, 351–359. https://doi.org/10.1016/j.neuropharm.2013.03.019

Lassi, G., Tucci, V., 2017. Gene-environment interaction influences attachment-like style in mice. Genes Brain Behav. 16, 612–618. https://doi.org/10.1111/gbb.12385

Le Bihan, D., 2014. Diffusion MRI: what water tells us about the brain. EMBO Mol. Med. 6, 569–573. https://doi.org/10.1002/emmm.201404055

Le Bihan, D., 2003. Looking into the functional architecture of the brain with diffusion MRI. Nat. Rev. Neurosci. 4, 469–480. https://doi.org/10.1038/nrn1119

Le Bihan, D., Breton, E., 1985. Imagerie de diffusion in-vivo par résonance magnétique nucléaire. Comptes-Rendus Académie Sci. 93, 27–34.

Le Merre, P., Esmaeili, V., Charrière, E., Galan, K., Salin, P.-A., Petersen, C.C.H., Crochet, S., 2018. Reward-Based Learning Drives Rapid Sensory Signals in Medial Prefrontal Cortex and Dorsal Hippocampus Necessary for Goal-Directed Behavior. Neuron 97, 83-91.e5. https://doi.org/10.1016/j.neuron.2017.11.031

Lee, A.-R., Kim, J.-H., Cho, E., Kim, M., Park, M., 2017. Dorsal and Ventral Hippocampus Differentiate in Functional Pathways and Differentially Associate with Neurological Disease-Related Genes during Postnatal Development. Front. Mol. Neurosci. 10. https://doi.org/10.3389/fnmol.2017.00331

Lee, B.-T., Seong Whi Cho, Hyung Soo Khang, Lee, B.-C., Choi, I.-G., In Kyoon Lyoo, Ham, B.-J., 2007. The neural substrates of affective processing toward positive and negative affective pictures in patients with major depressive disorder. Prog. Neuropsychopharmacol. Biol. Psychiatry 31, 1487–1492. https://doi.org/10.1016/j.pnpbp.2007.06.030

Lee, M., Manders, T.R., Eberle, S.E., Su, C., D'amour, J., Yang, R., Lin, H.Y., Deisseroth, K., Froemke, R.C., Wang, J., 2015. Activation of corticostriatal circuitry relieves chronic neuropathic pain. J. Neurosci. Off. J. Soc. Neurosci. 35, 5247–5259. https://doi.org/10.1523/JNEUROSCI.3494-14.2015

Lee, M.H., Smyser, C.D., Shimony, J.S., 2013. Resting-State fMRI: A Review of Methods and Clinical Applications. Am. J. Neuroradiol. 34, 1866–1872. https://doi.org/10.3174/ajnr.A3263

Lein, E.S., Hawrylycz, M.J., Ao, N., Ayres, M., Bensinger, A., Bernard, A., Boe, A.F., Boguski, M.S., Brockway, K.S., Byrnes, E.J., Chen, Lin, Chen, Li, Chen, T.-M., Chi Chin, M., Chong, J., Crook, B.E., Czaplinska, A., Dang, C.N., Datta, S., Dee, N.R., Desaki, A.L., Desta, T., Diep, E., Dolbeare, T.A., Donelan, M.J., Dong, H.-W., Dougherty, J.G., Duncan, B.J., Ebbert, A.J., Eichele, G., Estin, L.K., Faber, C., Facer, B.A., Fields, R., Fischer, S.R., Fliss, T.P., Frensley, C., Gates, S.N., Glattfelder, K.J., Halverson, K.R., Hart, M.R., Hohmann, J.G., Howell, M.P., Jeung, D.P., Johnson, R.A., Karr, P.T., Kawal, R., Kidney, J.M., Knapik, R.H., Kuan, C.L., Lake, J.H., Laramee, A.R., Larsen, K.D., Lau, C., Lemon, T.A., Liang, A.J., Liu, Y., Luong, L.T., Michaels, J., Morgan, J.J., Morgan, R.J., Mortrud, M.T., Mosqueda, N.F., Ng, L.L., Ng, R., Orta, G.J., Overly, C.C., Pak, T.H., Parry, S.E., Pathak, S.D., Pearson, O.C., Puchalski, R.B., Riley, Z.L., Rockett, H.R., Rowland, S.A., Royall, J.J., Ruiz, M.J., Sarno, N.R., Schaffnit, K., Shapovalova, N.V., Sivisay, T., Slaughterbeck, C.R., Smith, S.C., Smith, K.A., Smith, B.I., Sodt, A.J., Stewart, N.N., Stumpf, K.-R., Sunkin, S.M., Sutram, M., Tam, A., Teemer, C.D., Thaller, C., Thompson, C.L., Varnam, L.R., Visel, A., Whitlock, R.M., Wohnoutka, P.E., Wolkey, C.K., Wong, V.Y., Wood, M., Yaylaoglu, M.B., Young, R.C., Youngstrom, B.L., Feng Yuan, X., Zhang, B., Zwingman, T.A., Jones, A.R., 2007. Genome-wide atlas of gene expression in the adult mouse brain. Nature 445, 168–176. https://doi.org/10.1038/nature05453

Lepping, R.J., Atchley, R.A., Chrysikou, E., Martin, L.E., Clair, A.A., Ingram, R.E., Simmons, W.K., Savage, C.R., 2016. Neural Processing of Emotional Musical and Nonmusical Stimuli in Depression. PLOS ONE 11, e0156859. https://doi.org/10.1371/journal.pone.0156859

Li, J., Li, Y., Zhang, B., Shen, X., Zhao, H., 2016. Why depression and pain often coexist and mutually reinforce: Role of the lateral habenula. Exp. Neurol. 284, 106–113. https://doi.org/10.1016/j.expneurol.2016.08.010

Li, J.-X., 2015. Pain and depression comorbidity: a preclinical perspective. Behav. Brain Res. 276, 92–98. https://doi.org/10.1016/j.bbr.2014.04.042

Li, Yanhui, Wang, Y., Xuan, C., Li, Yang, Piao, L., Li, J., Zhao, H., 2017. Role of the Lateral Habenula in Pain-Associated Depression. Front. Behav. Neurosci. 11. https://doi.org/10.3389/fnbeh.2017.00031

Liska, A., Galbusera, A., Schwarz, A.J., Gozzi, A., 2015. Functional connectivity hubs of the mouse brain. NeuroImage 115, 281–291. https://doi.org/10.1016/j.neuroimage.2015.04.033

Liska, A., Gozzi, A., 2016. Can Mouse Imaging Studies Bring Order to Autism Connectivity Chaos? Front. Neurosci. 10. https://doi.org/10.3389/fnins.2016.00484

Liu, D., Tang, Q.-Q., Yin, C., Song, Yu, Liu, Y., Yang, J.-X., Liu, H., Zhang, Y.-M., Wu, S.-Y., Song, Ying, Juarez, B., Ding, H.-L., Han, M.-H., Zhang, H., Cao, J.-L., 2018. Brain-derived neurotrophic factor–mediated projection-specific regulation of depressive-like and nociceptive behaviors in the mesolimbic reward circuitry: PAIN 159, 175. https://doi.org/10.1097/j.pain.0000000000001083

Logothetis, N.K., 2008. What we can do and what we cannot do with fMRI. Nature 453, 869–878. https://doi.org/10.1038/nature06976

Logothetis, N.K., 2003. The underpinnings of the BOLD functional magnetic resonance imaging signal. J. Neurosci. 23, 3963–3971.

Logothetis, N.K., Pauls, J., Augath, M., Trinath, T., Oeltermann, A., 2001. Neurophysiological investigation of the basis of the fMRI signal. Nature 412, 150–157. https://doi.org/10.1038/35084005

Lutz, J., Jäger, L., Quervain, D. de, Krauseneck, T., Padberg, F., Wichnalek, M., Beyer, A., Stahl, R., Zirngibl, B., Morhard, D., Reiser, M., Schelling, G., 2008. White and gray matter abnormalities in the brain of patients with fibromyalgia: A diffusion-tensor and volumetric imaging study. Arthritis Rheum. 58, 3960–3969. https://doi.org/10.1002/art.24070

Magnuson, M.E., Thompson, G.J., Pan, W.-J., Keilholz, S.D., 2014. Effects of Severing the Corpus Callosum on Electrical and BOLD Functional Connectivity and Spontaneous Dynamic Activity in the Rat Brain. Brain Connect. 4, 15–29. https://doi.org/10.1089/brain.2013.0167

Mannelli, L.D.C., Pacini, A., Bonaccini, L., Zanardelli, M., Mello, T., Ghelardini, C., 2013. Morphologic Features and Glial Activation in Rat Oxaliplatin-Dependent Neuropathic Pain. J. Pain 14, 1585–1600. https://doi.org/10.1016/j.jpain.2013.08.002

Mantini, D., Gerits, A., Nelissen, K., Durand, J.-B., Joly, O., Simone, L., Sawamura, H., Wardak, C., Orban, G.A., Buckner, R.L., Vanduffel, W., 2011. Default Mode of Brain Function in Monkeys. J. Neurosci. Off. J. Soc. Neurosci. 31, 12954–12962. https://doi.org/10.1523/JNEUROSCI.2318-11.2011

Matsubayashi, K., Nagoshi, N., Komaki, Y., Kojima, K., Shinozaki, M., Tsuji, O., Iwanami, A., Ishihara, R., Takata, N., Matsumoto, M., Mimura, M., Okano, H., Nakamura, M., 2018. Assessing cortical plasticity after spinal cord injury by using resting-state functional magnetic resonance imaging in awake adult mice. Sci. Rep. 8, 14406. https://doi.org/10.1038/s41598-018-32766-8

Mayberg, H.S., 2009. Targeted electrode-based modulation of neural circuits for depression. J. Clin. Invest. 119, 717–725. https://doi.org/10.1172/JCI38454

McFarlane, H.G., Kusek, G.K., Yang, M., Phoenix, J.L., Bolivar, V.J., Crawley, J.N., 2008. Autism-like behavioral phenotypes in BTBR T+tf/J mice. Genes Brain Behav. 7, 152–163. https://doi.org/10.1111/j.1601-183X.2007.00330.x

Mechling, A.E., Arefin, T., Lee, H.-L., Bienert, T., Reisert, M., Ben Hamida, S., Darcq, E., Ehrlich, A., Gaveriaux-Ruff, C., Parent, M.J., Rosa-Neto, P., Hennig, J., von Elverfeldt, D., Kieffer, B.L., Harsan, L.-A., 2016. Deletion of the mu opioid receptor gene in mice reshapes the reward–aversion connectome. Proc. Natl. Acad. Sci. 201601640. https://doi.org/10.1073/pnas.1601640113

Mechling, A.E., Hübner, N.S., Lee, H.-L., Hennig, J., von Elverfeldt, D., Harsan, L.-A., 2014. Fine-grained mapping of mouse brain functional connectivity with resting-state fMRI. NeuroImage 96, 203–215. https://doi.org/10.1016/j.neuroimage.2014.03.078

Melzack, R., 2005. Evolution of the Neuromatrix Theory of Pain. The Prithvi Raj Lecture: Presented at the Third World Congress of World Institute of Pain, Barcelona 2004. Pain Pract. 5, 85–94. https://doi.org/10.1111/j.1533-2500.2005.05203.x

Melzack, R., 1990. Phantom limbs and the concept of a neuromatrix. Trends Neurosci. 13, 88–92. https://doi.org/10.1016/0166-2236(90)90179-E

Miller, V.M., Gupta, D., Neu, N., Cotroneo, A., Boulay, C.B., Seegal, R.F., 2013. Novel inter-hemispheric white matter connectivity in the BTBR mouse model of autism. Brain Res. 1513, 26–33. https://doi.org/10.1016/j.brainres.2013.04.001

Mitsi, V., Zachariou, V., 2016. Modulation of pain, nociception, and analgesia by the brain reward center. Neuroscience. https://doi.org/10.1016/j.neuroscience.2016.05.017

Moayedi, M., Weissman-Fogel, I., Salomons, T.V., Crawley, A.P., Goldberg, M.B., Freeman, B.V., Tenenbaum, H.C., Davis, K.D., 2012. White matter brain and trigeminal nerve abnormalities in temporomandibular disorder. Pain 153, 1467–1477. https://doi.org/10.1016/j.pain.2012.04.003

Mori, S., Zhang, J., 2006. Principles of Diffusion Tensor Imaging and Its Applications to Basic Neuroscience Research. Neuron 51, 527–539. https://doi.org/10.1016/j.neuron.2006.08.012

Morris, L.S., Sprenger, C., Koda, K., de la Mora, D.M., Yamada, T., Mano, H., Kashiwagi, Y., Yoshioka, Y., Morioka, Y., Seymour, B., 2017. Anterior cingulate cortex connectivity is associated with suppression of behavior in a rat model of chronic pain. https://doi.org/10.1101/225482

Moseley, M.E., Cohen, Y., Kucharczyk, J., Mintorovitch, J., Asgari, H.S., Wendland, M.F., Tsuruda, J., Norman, D., 1990. Diffusion-weighted MR imaging of anisotropic water diffusion in cat central nervous system. Radiology 176, 439–445. https://doi.org/10.1148/radiology.176.2.2367658

Moy, S.S., Nadler, J.J., Perez, A., Barbaro, R.P., Johns, J.M., Magnuson, T.R., Piven, J., Crawley, J.N., 2004. Sociability and preference for social novelty in five inbred strains: an approach to assess autistic-like behavior in mice. Genes Brain Behav. 3, 287–302.

Moy, S.S., Nadler, J.J., Young, N.B., Perez, A., Holloway, L.P., Barbaro, R.P., Barbaro, J.R., Wilson, L.M., Threadgill, D.W., Lauder, J.M., Magnuson, T.R., Crawley, J.N., 2007. Mouse behavioral tasks relevant to autism: Phenotypes of 10 inbred strains. Behav. Brain Res., Animal Models for Autism 176, 4–20. https://doi.org/10.1016/j.bbr.2006.07.030

Mukherjee, P., Berman, J.I., Chung, S.W., Hess, C.P., Henry, R.G., 2008. Diffusion Tensor MR Imaging and Fiber Tractography: Theoretic Underpinnings. Am. J. Neuroradiol. 29, 632–641. https://doi.org/10.3174/ajnr.A1051

Mutso, A.A., Petre, B., Huang, L., Baliki, M.N., Torbey, S., Herrmann, K.M., Schnitzer, T.J., Apkarian, A.V., 2013. Reorganization of hippocampal functional connectivity with transition to chronic back pain. J. Neurophysiol. 111, 1065–1076. https://doi.org/10.1152/jn.00611.2013

Mutso, A.A., Radzicki, D., Baliki, M.N., Huang, L., Banisadr, G., Centeno, M.V., Radulovic, J., Martina, M., Miller, R.J., Apkarian, A.V., 2012. Abnormalities in Hippocampal Functioning with Persistent Pain. J. Neurosci. 32, 5747–5756. https://doi.org/10.1523/JNEUROSCI.0587-12.2012

Napadow, V., LaCount, L., Park, K., As-Sanie, S., Clauw, D.J., Harris, R.E., 2011. Intrinsic brain connectivity in fibromyalgia is associated with chronic pain intensity. Arthritis Rheum. 62, 2545–2555. https://doi.org/10.1002/art.27497

Narita Minoru, Kuzumaki Naoko, Narita Michiko, Kaneko Chihiro, Hareyama Nana, Miyatake Mayumi, Shindo Keiko, Miyoshi Kan, Nakajima Mayumi, Nagumo Yasuyuki, Sato Fumiaki, Wachi Hiroshi, Seyama Yoshiyuki, Suzuki Tsutomu, 2006. Chronic pain-induced emotional dysfunction is associated with astrogliosis due to cortical δ-opioid receptor dysfunction. J. Neurochem. 97, 1369–1378. https://doi.org/10.1111/j.1471-4159.2006.03824.x

Narita, Minoru, Suzuki, M., Imai, S., Narita, Michiko, Ozaki, S., Kishimoto, Y., Oe, K., Yajima, Y., Yamazaki, M., Suzuki, T., 2004. Molecular mechanism of changes in the morphine-induced pharmacological actions under chronic pain-like state: Suppression of dopaminergic transmission in the brain. Life Sci., The First International Pfizer Science and Research Symposium: Key Topic 2003: Central Mechanism of Neuropathic Pain 74, 2655–2673. https://doi.org/10.1016/j.lfs.2004.01.006

Nasrallah, F.A., Tay, H.-C., Chuang, K.-H., 2014. Detection of functional connectivity in the resting mouse brain. NeuroImage 86, 417–424. https://doi.org/10.1016/j.neuroimage.2013.10.025

Nees, F., Becker, S., 2018. Psychological Processes in Chronic Pain: Influences of Reward and Fear Learning as Key Mechanisms – Behavioral Evidence, Neural Circuits, and Maladaptive Changes. Neuroscience 387, 72–84. https://doi.org/10.1016/j.neuroscience.2017.08.051

Ogawa, S., Lee, T.-M., Kay, A.R., Tank, D.W., 1990. Brain magnetic resonance imaging with contrast dependent on blood oxygenation. Proc. Natl. Acad. Sci. 87, 9868–9872.

Oh, S.W., Harris, J.A., Ng, L., Winslow, B., Cain, N., Mihalas, S., Wang, Q., Lau, C., Kuan, L., Henry, A.M., Mortrud, M.T., Ouellette, B., Nguyen, T.N., Sorensen, S.A., Slaughterbeck, C.R., Wakeman, W., Li, Y., Feng, D., Ho, A., Nicholas, E., Hirokawa, K.E., Bohn, P., Joines, K.M., Peng, H., Hawrylycz, M.J., Phillips, J.W., Hohmann, J.G., Wohnoutka, P., Gerfen, C.R., Koch, C., Bernard, A., Dang, C., Jones, A.R., Zeng, H., 2014. A mesoscale connectome of the mouse brain. Nature 508, 207–214. https://doi.org/10.1038/nature13186

Ohl, F., Sillaber, I., Binder, E., Keck, M.E., Holsboer, F., 2001. Differential analysis of behavior and diazepam-induced alterations in C57BL/6N and BALB/c mice using the modified hole board test. J. Psychiatr. Res. 35, 147–154. https://doi.org/10.1016/S0022-3956(01)00017-6

Olds, J., Milner, P., 1954. Positive reinforcement produced by electrical stimulation of septal area and other regions of rat brain. J. Comp. Physiol. Psychol. 47, 419–427. https://doi.org/10.1037/h0058775

Osuch, E.A., Bluhm, R.L., Williamson, P.C., Théberge, J., Densmore, M., Neufeld, R.W.J., 2009. Brain activation to favorite music in healthy controls and depressed patients: NeuroReport 20, 1204–1208. https://doi.org/10.1097/WNR.0b013e32832f4da3

Padmanabhan, S. (Ed.), 2014. Handbook of Pharmacogenomics and Stratified Medicine, in: Handbook of Pharmacogenomics and Stratified Medicine. Academic Press, San Diego, p. i. https://doi.org/10.1016/B978-0-12-386882-4.00047-5

Palumbo, M.L., Canzobre, M.C., Pascuan, C.G., Ríos, H., Wald, M., Genaro, A.M., 2010. Stress induced cognitive deficit is differentially modulated in BALB/c and C57Bl/6 mice: Correlation with Th1/Th2 balance after stress exposure. J. Neuroimmunol. 218, 12–20. https://doi.org/10.1016/j.jneuroim.2009.11.005

Pan, W.-J., Billings, J.C.W., Grooms, J.K., Shakil, S., Keilholz, S.D., 2015. Considerations for resting state functional MRI and functional connectivity studies in rodents. Front. Neurosci. 9. https://doi.org/10.3389/fnins.2015.00269

Pan, W.-J., Thompson, G.J., Magnuson, M.E., Jaeger, D., Keilholz, S., 2013. Infraslow LFP correlates to resting-state fMRI BOLD signals. NeuroImage 74, 288–297. https://doi.org/10.1016/j.neuroimage.2013.02.035

Panksepp, J.B., Lahvis, G.P., 2007. Social reward among juvenile mice. Genes Brain Behav. 6, 661–671.

Parksl, E.L., Gehal, P.Y., Balikil, M.N., Katzl, J., Schnitzerl, T.J., Apkarianl, A.V., 2011. Brain activity for chronic knee osteoarthritis: Dissociating evoked pain from spontaneous pain. Eur. J. Pain 15, 843.e1-843.e14. https://doi.org/10.1016/j.ejpain.2010.12.007

Pauling, L., Coryell, C.D., 1936. The Magnetic Properties and Structure of Hemoglobin, Oxyhemoglobin and Carbonmonoxyhemoglobin. Proc. Natl. Acad. Sci. U. S. A. 22, 210–216.

Peng, D.X., Kelley, R.G., Quintin, E.-M., Raman, M., Thompson, P.M., Reiss, A.L., 2014. Cognitive and behavioral correlates of caudate subregion shape variation in fragile X syndrome. Hum. Brain Mapp. 35, 2861–2868. https://doi.org/10.1002/hbm.22376

Pervolaraki, E., Tyson, A.L., Pibiri, F., Poulter, S.L., Reichelt, A.C., Rodgers, R.J., Clapcote, S.J., Lever, C., Andreae, L.C., Dachtler, J., 2019. The within-subject application of diffusion tensor MRI and CLARITY reveals brain structural changes in Nrxn2 deletion mice. Mol. Autism 10, 8. https://doi.org/10.1186/s13229-019-0261-9

Pilz, L.K., Quiles, C.L., Dallegrave, E., Levandovski, R., Hidalgo, M.P.L., Elisabetsky, E., Pilz, L.K., Quiles, C.L., Dallegrave, E., Levandovski, R., Hidalgo, M.P.L., Elisabetsky, E., 2015. Differential susceptibility of BALB/c, C57BL/6N, and CF1 mice to photoperiod changes. Rev. Bras. Psiquiatr. 37, 185–190. https://doi.org/10.1590/1516-4446-2014-1454

Pitcher, M.H., Korff, M.V., Bushnell, M.C., Porter, L., 2019. Prevalence and Profile of High-Impact Chronic Pain in the United States. J. Pain 20, 146–160. https://doi.org/10.1016/j.jpain.2018.07.006

Pizzagalli, D.A., Holmes, A.J., Dillon, D.G., Goetz, E.L., Birk, J.L., Bogdan, R., Dougherty, D.D., Iosifescu, D.V., Rauch, S.L., Fava, M., 2009. Reduced caudate and nucleus accumbens response to rewards in unmedicated individuals with major depressive disorder. Am. J. Psychiatry 166, 702–710.

Proulx, C.D., Hikosaka, O., Malinow, R., 2014. Reward processing by the lateral habenula in normal and depressive behaviors. Nat. Neurosci. 17, 1146–1152. https://doi.org/10.1038/nn.3779

Qiu, M., Ye, Z., Li, Q., Liu, G., Xie, B., Wang, J., 2011. Changes of Brain Structure and Function in ADHD Children. Brain Topogr. 24, 243–252. https://doi.org/10.1007/s10548-010-0168-4

Raichle, M.E., MacLeod, A.M., Snyder, A.Z., Powers, W.J., Gusnard, D.A., Shulman, G.L., 2001. A default mode of brain function. Proc. Natl. Acad. Sci. 98, 676–682.

Raichle, M.E., Mintun, M.A., 2006. Brain work and brain imaging. Annu Rev Neurosci 29, 449–476.

Rajkowska, G., 2000. Postmortem studies in mood disorders indicate altered numbers of neurons and glial cells. Biol. Psychiatry 48, 766–777. https://doi.org/10.1016/S0006-3223(00)00950-1

Redlich, R., Dohm, K., Grotegerd, D., Opel, N., Zwitserlood, P., Heindel, W., Arolt, V., Kugel, H., Dannlowski, U., 2015. Reward Processing in Unipolar and Bipolar Depression: A Functional MRI Study. Neuropsychopharmacology 40, 2623–2631. https://doi.org/10.1038/npp.2015.110

Reisert, M., Mader, I., Anastasopoulos, C., Weigel, M., Schnell, S., Kiselev, V., 2011. Global fiber reconstruction becomes practical. NeuroImage 54, 955–962. https://doi.org/10.1016/j.neuroimage.2010.09.016

Ren, W., Centeno, M.V., Berger, S., Wu, Y., Na, X., Liu, X., Kondapalli, J., Apkarian, A.V., Martina, M., Surmeier, D.J., 2015. The indirect pathway of the nucleus accumbens shell amplifies neuropathic pain. Nat. Neurosci. 19, 220–222. https://doi.org/10.1038/nn.4199

Roebroeck, A., Formisano, E., Goebel, R., 2005. Mapping directed influence over the brain using Granger causality and fMRI. NeuroImage 25, 230–242. https://doi.org/10.1016/j.neuroimage.2004.11.017

Rosazza, C., Minati, L., 2011. Resting-state brain networks: literature review and clinical applications. Neurol. Sci. 32, 773–785. https://doi.org/10.1007/s10072-011-0636-y

Roth, B.L., 2016. DREADDs for Neuroscientists. Neuron 89, 683–694. https://doi.org/10.1016/j.neuron.2016.01.040

Rubinov, M., Sporns, O., 2010. Complex network measures of brain connectivity: uses and interpretations. Neuroimage 52, 1059–1069.

Russo, S.J., Nestler, E.J., 2013. The brain reward circuitry in mood disorders. Nat. Rev. Neurosci. 14, 609–625. https://doi.org/10.1038/nrn3381

Sagheddu, C., Aroni, S., De Felice, M., Lecca, S., Luchicchi, A., Melis, M., Muntoni, A.L., Romano, R., Palazzo, E., Guida, F., Maione, S., Pistis, M., 2015. Enhanced serotonin and mesolimbic dopamine transmissions in a rat model of neuropathic pain. Neuropharmacology 97, 383–393. https://doi.org/10.1016/j.neuropharm.2015.06.003

Sankoorikal, G.M.V., Kaercher, K.A., Boon, C.J., Lee, J.K., Brodkin, E.S., 2006. A Mouse Model System for Genetic Analysis of Sociability: C57BL/6J Versus BALB/cJ Inbred Mouse Strains. Biol. Psychiatry 59, 415–423. https://doi.org/10.1016/j.biopsych.2005.07.026

Sartorius, A., Kiening, K.L., Kirsch, P., Gall, C.C. von, Haberkorn, U., Unterberg, A.W., Henn, F.A., Meyer-Lindenberg, A., 2010. Remission of Major Depression Under Deep Brain Stimulation of the Lateral Habenula in a Therapy-Refractory Patient. Biol. Psychiatry 67, e9–e11. https://doi.org/10.1016/j.biopsych.2009.08.027

Satterthwaite, T.D., Kable, J.W., Vandekar, L., Katchmar, N., Bassett, D.S., Baldassano, C.F., Ruparel, K., Elliott, M.A., Sheline, Y.I., Gur, R.C., others, 2015. Common and dissociable dysfunction of the reward system in bipolar and unipolar depression. Neuropsychopharmacology 40, 2258–2268.

Scaplen, K.M., Kaun, K.R., 2016. Reward from bugs to bipeds: a comparative approach to understanding how reward circuits function. J. Neurogenet. 30, 133–148. https://doi.org/10.1080/01677063.2016.1180385

Schmidt-Wilcke, T., 2015. Neuroimaging of chronic pain. Best Pract. Res. Clin. Rheumatol. 29, 29–41. https://doi.org/10.1016/j.berh.2015.04.030

Schmidt-Wilcke, T., Leinisch, E., Gänbauer, S., Draganski, B., Bogdahn, U., Altmeppen, J., May, A., 2006. Affective components and intensity of pain correlate with structural differences in gray matter in chronic back pain patients: Pain 125, 89–97. https://doi.org/10.1016/j.pain.2006.05.004

Schmidt-Wilcke, T., Leinisch, E., Straube, A., Kämpfe, N., Draganski, B., Diener, H.C., Bogdahn, U., May, A., 2005. Gray matter decrease in patients with chronic tension type headache. Neurology 65, 1483–1486. https://doi.org/10.1212/01.wnl.0000183067.94400.80

Schmithorst, V.J., Wilke, M., Dardzinski, B.J., Holland, S.K., 2002. Correlation of White Matter Diffusivity and Anisotropy with Age during Childhood and Adolescence: A Cross-sectional Diffusion-Tensor MR Imaging Study. Radiology 222, 212–218. https://doi.org/10.1148/radiol.2221010626

Scholz, J., Tomassini, V., Johansen-Berg, H., 2009. Chapter 11 - Individual Differences in White Matter Microstructure in the Healthy Brain, in: Johansen-Berg, H., Behrens, T.E.J. (Eds.), Diffusion MRI. Academic Press, San Diego, pp. 237–249. https://doi.org/10.1016/B978-0-12-374709-9.00011-0

Schroeter, A., Grandjean, J., Schlegel, F., Saab, B.J., Rudin, M., 2017. Contributions of structural connectivity and cerebrovascular parameters to functional magnetic resonance imaging signals in mice at rest and during sensory paw stimulation. J. Cereb. Blood Flow Metab. 37, 2368–2382. https://doi.org/10.1177/0271678X16666292

Schwartz, N., Temkin, P., Jurado, S., Lim, B.K., Heifets, B.D., Polepalli, J.S., Malenka, R.C., 2014. Decreased motivation during chronic pain requires long-term depression in the nucleus accumbens. Science 345, 535–542. https://doi.org/10.1126/science.1253994

Segarra, N., Metastasio, A., Ziauddeen, H., Spencer, J., Reinders, N.R., Dudas, R.B., Arrondo, G., Robbins, T.W., Clark, L., Fletcher, P.C., others, 2015. Abnormal Frontostriatal Activity During Unexpected Reward Receipt in Depression and Schizophrenia: Relationship to Anhedonia. Neuropsychopharmacology.

Seifert, F., Maihöfner, C., 2009. Central mechanisms of experimental and chronic neuropathic pain: Findings from functional imaging studies. Cell. Mol. Life Sci. 66, 375. https://doi.org/10.1007/s00018-008-8428-0

Sellmeijer, J., Mathis, V., Hugel, S., Li, X.-H., Song, Q., Chen, Q.-Y., Barthas, F., Lutz, P.-E., Karatas, M., Luthi, A., Veinante, P., Aertsen, A., Barrot, M., Zhuo, M., Yalcin, I., 2018. Hyperactivity of Anterior Cingulate Cortex Areas 24a/24b Drives Chronic Pain-Induced Anxiodepressive-like Consequences. J. Neurosci. 38, 3102–3115. https://doi.org/10.1523/JNEUROSCI.3195-17.2018

Seminowicz, D.A., Jiang, L., Ji, Y., Xu, S., Gullapalli, R.P., Masri, R., 2012. Thalamocortical asynchrony in conditions of spinal cord injury pain in rats. J. Neurosci. Off. J. Soc. Neurosci. 32, 15843–15848. https://doi.org/10.1523/JNEUROSCI.2927-12.2012

Seminowicz, D.A., Laferriere, A.L., Millecamps, M., Yu, J.S.C., Coderre, T.J., Bushnell, M.C., 2009. MRI structural brain changes associated with sensory and emotional function in a rat model of long-term neuropathic pain. NeuroImage, Brain Body Medicine 47, 1007–1014. https://doi.org/10.1016/j.neuroimage.2009.05.068

Sforazzini, F., Schwarz, A.J., Galbusera, A., Bifone, A., Gozzi, A., 2014. Distributed BOLD and CBV-weighted resting-state networks in the mouse brain. NeuroImage 87, 403–415. https://doi.org/10.1016/j.neuroimage.2013.09.050

Shah, D., Blockx, I., Keliris, G.A., Kara, F., Jonckers, E., Verhoye, M., Van der Linden, A., 2016a. Cholinergic and serotonergic modulations differentially affect large-scale functional networks in the mouse brain. Brain Struct. Funct. 221, 3067–3079. https://doi.org/10.1007/s00429-015-1087-7

Shah, D., Deleye, S., Verhoye, M., Staelens, S., Van der Linden, A., 2016b. Resting-state functional MRI and [18F]-FDG PET demonstrate differences in neuronal activity between commonly used mouse strains. NeuroImage 125, 571–577. https://doi.org/10.1016/j.neuroimage.2015.10.073

Shansky, R.M., 2019. Are hormones a “female problem” for animal research? Science 364, 825–826. https://doi.org/10.1126/science.aaw7570

Sheline, Y.I., Gado, M.H., Price, J.L., 1998. Amygdala core nuclei volumes are decreased in recurrent major depression. Neuroreport Int. J. Rapid Commun. Res. Neurosci. 9, 2023–2028. https://doi.org/10.1097/00001756-199806220-00021

Shelton, L., Becerra, L., Borsook, D., 2012. Unmasking the mysteries of the habenula in pain and analgesia. Prog. Neurobiol. 96, 208–219. https://doi.org/10.1016/j.pneurobio.2012.01.004

Shepherd, G.M.G., 2013. Corticostriatal connectivity and its role in disease. Nat. Rev. Neurosci. 14, 278–291. https://doi.org/10.1038/nrn3469

Simons, L.E., Elman, I., Borsook, D., 2014. Psychological processing in chronic pain: a neural systems approach. Neurosci. Biobehav. Rev. 39, 61–78. https://doi.org/10.1016/j.neubiorev.2013.12.006

Smoski, M.J., Felder, J., Bizzell, J., Green, S.R., Ernst, M., Lynch, T.R., Dichter, G.S., 2009. fMRI of alterations in reward selection, anticipation, and feedback in major depressive disorder. J. Affect. Disord. 118, 69–78. https://doi.org/10.1016/j.jad.2009.01.034

Sotres-Bayón, F., Torres-López, E., López-Ávila, A., del Ángel, R., Pellicer, F., 2001. Lesion and electrical stimulation of the ventral tegmental area modify persistent nociceptive behavior in the rat. Brain Res. 898, 342–349. https://doi.org/10.1016/S0006-8993(01)02213-2

Stafford, J.M., Jarrett, B.R., Miranda-Dominguez, O., Mills, B.D., Cain, N., Mihalas, S., Lahvis, G.P., Lattal, K.M., Mitchell, S.H., David, S.V., Fryer, J.D., Nigg, J.T., Fair, D.A., 2014. Large-scale topology and the default mode network in the mouse connectome. Proc. Natl. Acad. Sci. 111, 18745–18750. https://doi.org/10.1073/pnas.1404346111

Steiner, J., Walter, M., Gos, T., Guillemin, G.J., Bernstein, H.-G., Sarnyai, Z., Mawrin, C., Brisch, R., Bielau, H., zu Schwabedissen, L.M., Bogerts, B., Myint, A.-M., 2011. Severe depression is associated with increased microglial quinolinic acid in subregions of the anterior cingulate gyrus: Evidence for an immune-modulated glutamatergic neurotransmission? J. Neuroinflammation 8, 94. https://doi.org/10.1186/1742-2094-8-94

Stejskal, E.O., Tanner, J.E., 1965. Spin Diffusion Measurements: Spin Echoes in the Presence of a Time-Dependent Field Gradient. J. Chem. Phys. 42, 288–292. https://doi.org/10.1063/1.1695690

Stouffer, S.A., Suchman, E.A., DeVinney, L.C., Star, S.A., Williams, R.M.J., 1949. Adjustment During Army Life. Princet. NJ Princet. Univ. Press.

Stoy, M., Schlagenhauf, F., Sterzer, P., Bermpohl, F., Hagele, C., Suchotzki, K., Schmack, K., Wrase, J., Ricken, R., Knutson, B., Adli, M., Bauer, M., Heinz, A., Strohle, A., 2012. Hyporeactivity of ventral striatum towards incentive stimuli in unmedicated depressed patients normalizes after treatment with escitalopram. J. Psychopharmacol. (Oxf.) 26, 677–688. https://doi.org/10.1177/0269881111416686

Sun Shu-Wei, Liang Hsiao-Fang, Trinkaus Kathryn, Cross Anne H., Armstrong Regina C., Song Sheng-Kwei, 2006. Noninvasive detection of cuprizone induced axonal damage and demyelination in the mouse corpus callosum. Magn. Reson. Med. 55, 302–308. https://doi.org/10.1002/mrm.20774

Suzuki, T., Amata, M., Sakaue, G., Nishimura, S., Inoue, T., Shibata, M., Mashimo, T., 2007. Experimental Neuropathy in Mice Is Associated with Delayed Behavioral Changes Related to Anxiety and Depression. Anesth. Analg. 104, 1570. https://doi.org/10.1213/01.ane.0000261514.19946.66

Takata, N., Sugiura, Y., Yoshida, K., Koizumi, M., Hiroshi, N., Honda, K., Yano, R., Komaki, Y., Matsui, K., Suematsu, M., Mimura, M., Okano, H., Tanaka, K.F., n.d. Optogenetic astrocyte activation evokes BOLD fMRI response with oxygen consumption without neuronal activity modulation. Glia 0. https://doi.org/10.1002/glia.23454

Talmi, D., Dayan, P., Kiebel, S.J., Frith, C.D., Dolan, R.J., 2009. How Humans Integrate the Prospects of Pain and Reward during Choice. J. Neurosci. 29, 14617–14626. https://doi.org/10.1523/JNEUROSCI.2026-09.2009

Tanti, A., Lutz, P.-E., Kim, J., O'Leary, L., Turecki, G., Mechawar, N., 2019. Evidence of decreased gap junction coupling between astrocytes and oligodendrocytes in the anterior cingulate cortex of depressed suicides. bioRxiv 578807. https://doi.org/10.1101/578807

Taylor, A.M.W., Becker, S., Schweinhardt, P., Cahill, C., 2016. Mesolimbic dopamine signaling in acute and chronic pain: implications for motivation, analgesia, and addiction. PAIN 157, 1194. https://doi.org/10.1097/j.pain.0000000000000494

Taylor, A.M.W., Castonguay, A., Taylor, A.J., Murphy, N.P., Ghogha, A., Cook, C., Xue, L., Olmstead, M.C., De Koninck, Y., Evans, C.J., Cahill, C.M., 2015. Microglia Disrupt Mesolimbic Reward Circuitry in Chronic Pain. J. Neurosci. 35, 8442–8450. https://doi.org/10.1523/JNEUROSCI.4036-14.2015

Thompson, S.J., Bushnell, M.C., 2012. Rodent functional and anatomical imaging of pain. Neurosci. Lett. 520, 131–139. https://doi.org/10.1016/j.neulet.2012.03.015

Tuch, D.S., 2004. Q-ball imaging. Magn. Reson. Med. 52, 1358–1372. https://doi.org/10.1002/mrm.20279

Tuch, D.S., Reese, T.G., Wiegell, M.R., Makris, N., Belliveau, J.W., Wedeen, V.J., 2002. High angular resolution diffusion imaging reveals intravoxel white matter fiber heterogeneity. Magn. Reson. Med. 48, 577–582. https://doi.org/10.1002/mrm.10268

Tustison, N.J., Avants, B.B., Cook, P.A., Yuanjie Zheng, Egan, A., Yushkevich, P.A., Gee, J.C., 2010. N4ITK: Improved N3 Bias Correction. IEEE Trans. Med. Imaging 29, 1310–1320. https://doi.org/10.1109/TMI.2010.2046908

Ubl, B., Kuehner, C., Kirsch, P., Ruttorf, M., Flor, H., Diener, C., 2015. Neural reward processing in individuals remitted from major depression. Psychol. Med. 45, 3549–3558. https://doi.org/10.1017/S0033291715001452

Upadhyay, J., Baker, S.J., Chandran, P., Miller, L., Lee, Y., Marek, G.J., Sakoglu, U., Chin, C.-L., Luo, F., Fox, G.B., Day, M., 2011. Default-mode-like network activation in awake rodents. PloS One 6, e27839. https://doi.org/10.1371/journal.pone.0027839

Uranova, N.A., Vostrikov, V.M., Orlovskaya, D.D., Rachmanova, V.I., 2004. Oligodendroglial density in the prefrontal cortex in schizophrenia and mood disorders: a study from the Stanley Neuropathology Consortium. Schizophr. Res. 67, 269–275. https://doi.org/10.1016/S0920-9964(03)00181-6

Vachon-Presseau, E., Centeno, M.V., Ren, W., Berger, S.E., Tétreault, P., Ghantous, M., Baria, A., Farmer, M., Baliki, M.N., Schnitzer, T.J., others, 2016. The emotional brain as a predictor and amplifier of chronic pain. J. Dent. Res. 95, 605–612.

van den Heuvel, M.P., Hulshoff Pol, H.E., 2010. Exploring the brain network: A review on resting-state fMRI functional connectivity. Eur. Neuropsychopharmacol. 20, 519–534. https://doi.org/10.1016/j.euroneuro.2010.03.008

Vogt, B.A., 2005. Pain and emotion interactions in subregions of the cingulate gyrus. Nat. Rev. Neurosci. 6, 533–544. https://doi.org/10.1038/nrn1704

von Hehn, C.A., Baron, R., Woolf, C.J., 2012. Deconstructing the Neuropathic Pain Phenotype to Reveal Neural Mechanisms. Neuron 73, 638–652. https://doi.org/10.1016/j.neuron.2012.02.008

Wacker, J., Dillon, D.G., Pizzagalli, D.A., 2009. The role of the nucleus accumbens and rostral anterior cingulate cortex in anhedonia: Integration of resting EEG, fMRI, and volumetric techniques. NeuroImage 46, 327–337. https://doi.org/10.1016/j.neuroimage.2009.01.058

Wahlsten, D., 1974. Heritable aspects of anomalous myelinated fibre tracts in the forebrain of the laboratory mouse. Brain Res. 68, 1–18. https://doi.org/10.1016/0006-8993(74)90530-7

Walsh, J.J., Friedman, A.K., Sun, H., Heller, E.A., Ku, S.M., Juarez, B., Burnham, V.L., Mazei-Robison, M.S., Ferguson, D., Golden, S.A., Koo, J.W., Chaudhury, D., Christoffel, D.J., Pomeranz, L., Friedman, J.M., Russo, S.J., Nestler, E.J., Han, M.-H., 2014. Stress and CRF gate neural activation of BDNF in the mesolimbic reward pathway. Nat. Neurosci. 17, 27–29. https://doi.org/10.1038/nn.3591

Wang, G.-Q., Cen, C., Li, C., Cao, S., Wang, N., Zhou, Z., Liu, X.-M., Xu, Y., Tian, N.-X., Zhang, Y., Wang, J., Wang, L.-P., Wang, Y., 2015. Deactivation of excitatory neurons in the prelimbic cortex via Cdk5 promotes pain sensation and anxiety. Nat. Commun. 6, 7660. https://doi.org/10.1038/ncomms8660

Wang, L., Hermens, D.F., Hickie, I.B., Lagopoulos, J., 2012. A systematic review of resting-state functional-MRI studies in major depression. J. Affect. Disord. 142, 6–12. https://doi.org/10.1016/j.jad.2012.04.013

Watanabe, M., Narita, Michiko, Hamada, Y., Yamashita, A., Tamura, H., Ikegami, D., Kondo, T., Shinzato, T., Shimizu, T., Fukuchi, Y., Muto, A., Okano, H., Yamanaka, A., Tawfik, V.L., Kuzumaki, N., Navratilova, E., Porreca, F., Narita, Minoru, 2018. Activation of ventral tegmental area dopaminergic neurons reverses pathological allodynia resulting from nerve injury or bone cancer. Mol. Pain 14, 1744806918756406. https://doi.org/10.1177/1744806918756406

Watson, G.D.R., Smith, J.B., Alloway, K.D., 2017. Interhemispheric connections between the infralimbic and entorhinal cortices: The endopiriform nucleus has limbic connections that parallel the sensory and motor connections of the claustrum. J. Comp. Neurol. 525, 1363–1380. https://doi.org/10.1002/cne.23981

Weible, A.P., 2013. Remembering to attend: The anterior cingulate cortex and remote memory. Behav. Brain Res. 245, 63–75. https://doi.org/10.1016/j.bbr.2013.02.010

Wingenfeld, K., Wolf, O.T., 2014. Stress, Memory, and the Hippocampus. Hippocampus Clin. Neurosci. 34, 109–120. https://doi.org/10.1159/000356423

Wu, D., Zhang, J., 2016. In vivo mapping of macroscopic neuronal projections in the mouse hippocampus using high-resolution diffusion MRI. NeuroImage 125, 84–93. https://doi.org/10.1016/j.neuroimage.2015.10.051

Wu, G.-R., Liao, W., Stramaglia, S., Ding, J.-R., Chen, H., Marinazzo, D., 2013. A blind deconvolution approach to recover effective connectivity brain networks from resting state fMRI data. Med. Image Anal. 17, 365–374. https://doi.org/10.1016/j.media.2013.01.003

Wulff, A.B., Tooley, J., Marconi, L.J., Creed, M.C., 2018. Ventral pallidal modulation of aversion processing. Brain Res. https://doi.org/10.1016/j.brainres.2018.10.010

Xu, H., Wu, L.-J., Wang, H., Zhang, X., Vadakkan, K.I., Kim, S.S., Steenland, H.W., Zhuo, M., 2008. Presynaptic and Postsynaptic Amplifications of Neuropathic Pain in the Anterior Cingulate Cortex. J. Neurosci. 28, 7445–7453. https://doi.org/10.1523/JNEUROSCI.1812-08.2008

Yalcin, I., Barthas, F., Barrot, M., 2014a. Emotional consequences of neuropathic pain: Insight from preclinical studies. Neurosci. Biobehav. Rev. 47, 154–164. https://doi.org/10.1016/j.neubiorev.2014.08.002

Yalcin, I., Bohren, Y., Waltisperger, E., Sage-Ciocca, D., Yin, J.C., Freund-Mercier, M.-J., Barrot, M., 2011. A time-dependent history of mood disorders in a murine model of neuropathic pain. Biol. Psychiatry 70, 946–953. https://doi.org/10.1016/j.biopsych.2011.07.017

Yalcin, I., Megat, S., Barthas, F., Waltisperger, E., Kremer, M., Salvat, E., Barrot, M., 2014b. The Sciatic Nerve Cuffing Model of Neuropathic Pain in Mice. J. Vis. Exp. https://doi.org/10.3791/51608

Yang, Y., Cui, Y., Sang, K., Dong, Y., Ni, Z., Ma, S., Hu, H., 2018a. Ketamine blocks bursting in the lateral habenula to rapidly relieve depression. Nature 554, 317–322. https://doi.org/10.1038/nature25509

Yang, Y., Wang, H., Hu, J., Hu, H., 2018b. Lateral habenula in the pathophysiology of depression. Curr. Opin. Neurobiol., Neurobiology of Disease 48, 90–96. https://doi.org/10.1016/j.conb.2017.10.024

Yoon, E.J., Kim, Y.K., Shin, H.I., Lee, Y., Kim, S.E., 2013. Cortical and white matter alterations in patients with neuropathic pain after spinal cord injury. Brain Res. 1540, 64–73. https://doi.org/10.1016/j.brainres.2013.10.007

Yoshida, K., Mimura, Y., Ishihara, R., Nishida, H., Komaki, Y., Minakuchi, T., Tsurugizawa, T., Mimura, M., Okano, H., Tanaka, K.F., Takata, N., 2016. Physiological effects of a habituation procedure for functional MRI in awake mice using a cryogenic radiofrequency probe. J. Neurosci. Methods 274, 38–48. https://doi.org/10.1016/j.jneumeth.2016.09.013

Zerbi, V., Grandjean, J., Rudin, M., Wenderoth, N., 2015. Mapping the mouse brain with rs-fMRI: An optimized pipeline for functional network identification. NeuroImage 123, 11–21. https://doi.org/10.1016/j.neuroimage.2015.07.090

Zhang, H., Qian, Y.-L., Li, C., Liu, D., Wang, L., Wang, X.-Y., Liu, M.-J., Liu, H., Zhang, S., Guo, X.-Y., Yang, J.-X., Ding, H.-L., Koo, J.W., Mouzon, E., Deisseroth, K., Nestler, E.J., Zachariou, V., Han, M.-H., Cao, J.-L., 2017. Brain-Derived Neurotrophic Factor in the Mesolimbic Reward Circuitry Mediates Nociception in Chronic Neuropathic Pain. Biol. Psychiatry 82, 608–618. https://doi.org/10.1016/j.biopsych.2017.02.1180

Zhang, X., Li, Q., Wong, N., Zhang, M., Wang, W., Bu, B., McAlonan, G.M., 2015. Behaviour and prefrontal protein differences in C57BL/6N and 129 X1/SvJ mice. Brain Res. Bull. 116, 16–24. https://doi.org/10.1016/j.brainresbull.2015.05.003

Zhang, Z., Gadotti, V.M., Chen, L., Souza, I.A., Stemkowski, P.L., Zamponi, G.W., 2015. Role of Prelimbic GABAergic Circuits in Sensory and Emotional Aspects of Neuropathic Pain. Cell Rep. 12, 752–759. https://doi.org/10.1016/j.celrep.2015.07.001

Zhou, I.Y., Liang, Y.-X., Chan, R.W., Gao, P.P., Cheng, J.S., Hu, Y., So, K.-F., Wu, E.X., 2014. Brain resting-state functional MRI connectivity: Morphological foundation and plasticity. NeuroImage 84, 1–10. https://doi.org/10.1016/j.neuroimage.2013.08.037

Zhou, Y., Yu, C., Zheng, H., Liu, Y., Song, M., Qin, W., Li, K., Jiang, T., 2010. Increased neural resources recruitment in the intrinsic organization in major depression. J. Affect. Disord. 121, 220–230. https://doi.org/10.1016/j.jad.2009.05.029

Zhu, X., Wang, X., Xiao, J., Liao, J., Zhong, M., Wang, W., Yao, S., 2012. Evidence of a Dissociation Pattern in Resting-State Default Mode Network Connectivity in First-Episode, Treatment-Naive Major Depression Patients. Biol. Psychiatry 71, 611–617. https://doi.org/10.1016/j.biopsych.2011.10.035

Zhuo, M., 2013. Long-term potentiation in the anterior cingulate cortex and chronic pain. Philos. Trans. R. Soc. B Biol. Sci. 369, 20130146–20130146. https://doi.org/10.1098/rstb.2013.0146

Zhuo, M., Wu, G., Wu, L.-J., 2011. Neuronal and microglial mechanisms of neuropathic pain. Mol. Brain 4, 31. https://doi.org/10.1186/1756-6606-4-31

Zingg, B., Hintiryan, H., Gou, L., Song, M.Y., Bay, M., Bienkowski, M.S., Foster, N.N., Yamashita, S., Bowman, I., Toga, A.W., Dong, H.-W., 2014. Neural Networks of the Mouse Neocortex. Cell 156, 1096–1111. https://doi.org/10.1016/j.cell.2014.02.023

7 Annex

7.1 Published Manuscripts

1. Cingulate Overexpression of Mitogen-Activated Protein Kinase Phosphatase-1 as Key Factor for Depression.

2. Hyperactivity of Anterior Cingulate Cortex Areas 24a/24b Drives Chronic Pain-Induced Anxiodepressive-like Consequences.

3. Correction of cognitive deficits in mouse models of Down syndrome by a pharmacological inhibitor of DYRK1A.

4. Common functional networks in the mouse brain revealed by multi-centre resting-state fMRI analysis.

Archival Report

Biological Psychiatry

Cingulate Overexpression of Mitogen-Activated Protein Kinase Phosphatase-1 as a Key Factor for Depression

Florent Barthas, Muris Humo, Ralf Gilsbach, Elisabeth Waltisperger, Meltem Karatas, Samuel Leman, Lutz Hein, Catherine Belzung, Anne-Laurence Boutillier, Michel Barrot, and Ipek Yalcin

ABSTRACT

BACKGROUND: Depression is frequently associated with chronic pain or chronic stress. Among cortical areas, the anterior cingulate cortex (ACC, areas 24a and 24b) appears to be important for mood disorders and constitutes a neuroanatomical substrate for investigating the underlying molecular mechanisms. The current work aimed at identifying ACC molecular factors subserving depression.

METHODS: Anxiodepressive-like behaviors in C57BL/6J male mice were induced by neuropathic pain, unpredictable chronic mild stress, and optogenetic ACC stimulation and were evaluated using novelty suppressed feeding, splash, and forced swim tests. ACC molecular changes in chronic pain–induced depression were uncovered through whole-genome expression analysis. Further mechanistic insights were provided by chromatin immunoprecipitation, Western blot, and immunostaining. The causal link between molecular changes and depression was studied using knockout, pharmacological antagonism, and local viral-mediated gene knockdown.

RESULTS: Under chronic pain–induced depression, gene expression changes in the ACC highlighted the overexpression of a regulator of the mitogen-activated protein kinase pathway, mitogen-activated protein kinase phosphatase-1 (MKP-1). This upregulation is associated with the presence of transcriptionally active chromatin marks (acetylation) at its proximal promoter region as well as increased cyclic adenosine monophosphate response element–mediated transcriptional activity and phosphorylation of cyclic adenosine monophosphate response element binding protein and activating transcription factor. MKP-1 overexpression is also observed with unpredictable chronic mild stress and repeated ACC optogenetic stimulation and is reversed by fluoxetine. A knockout, an antagonist, or a local silencing of MKP-1 attenuates depressive-like behaviors, pointing to an important role of this phosphatase in depression.

CONCLUSIONS: These data point to ACC MKP-1 as a key factor in the pathophysiology of depression and a potential target for treatment development.

Keywords: Anterior cingulate cortex, Chronic pain, Chronic stress, Depression, MAPK, MKP-1

http://dx.doi.org/10.1016/j.biopsych.2017.01.019

Besides chronic stress (1), chronic pain is also clinically associated with the development of mood disorders (2). Epidemiological studies report a mean prevalence rate of around 50% for major depressive disorder in patients with chronic pain (3). Preclinical research further revealed that the anxiodepressive consequences of chronic pain can be studied in murine models (4,5) and highlighted the time dependency of these affective phenotypes (6). These models now offer a reliable tool to explore original mechanisms leading to depression.

A conceptualized view of depression relates this pathology to specific structural and functional changes in the brain neurocircuitry. Among the candidate regions, the anterior cingulate cortex (ACC) appears to be critical because it is known to display functional and morphological alterations in depressed patients (7) such as decreased connectivity to the amygdala (8), altered glucose metabolism (9), and reduced gray matter volume (10). Preclinical studies also showed functional and morphological alterations in the ACC following chronic stress exposure (11,12). Recently, we reported that the optogenetic activation of pyramidal neurons within the ACC is sufficient to induce anxiety and depressive-like behaviors in naïve animals (13). Furthermore, the lesion of the ACC prevents chronic pain–induced depressive-like behaviors and the aversiveness of spontaneous pain without affecting the sensory mechanical sensitivity (13). Thus, the ACC is a critical hub for mood disorders, including anxiodepressive consequences observed in chronic pain, and for studying their underlying molecular aspects.

In this context, open approaches such as genome-wide studies can be powerful to identify molecular blueprints of

SEE COMMENTARY ON PAGE e33

 ISSN: 0006-3223

depression. Here, we first performed a whole microarray analysis within the ACC in both sham and sciatic nerve–injured animals. Based on this genome expression analysis, the current study then focused on one critical regulator of the mitogen-activated protein kinase (MAPK) pathway, MAPK phosphatase-1 (MKP-1), in chronic pain–induced depression. Namely, our microarray results indicate that *Mkp-1* is significantly upregulated in the ACC of sciatic nerve–injured animals. Reports of MKP-1 overexpression in the hippocampus of stressed animals (14,15), as well as in patients with major depressive disorder (14), supported our interest to further investigate MKP-1 in chronic pain and mood disorder comorbidity.

MKP-1, also known as dual specificity phosphatase 1, is the main negative regulator of the MAPK signaling cascade (14,16). Cell culture studies showed that the expression of MKP-1 can be induced by a wide variety of extracellular factors such as growth factors, lipopolysaccharides, heat shock, and hydrogen peroxide (17). Studies focusing on the mechanisms of MKP-1 expression suggest that its transcription can be preceded by chromatin remodeling at the promoter region. External stressors (e.g., arsenite or ultraviolet C) can initiate phosphorylation and acetylation of histone H3 at the *Mkp-1* promoter region (17) and/or activate several transcription factors such as cyclic adenosine monophosphate response element binding protein (CREB), activating transcription factors 1 and 2 (ATF1 and -2), and activator protein 1 (18,19), which leads to the induction of *Mkp-1*.

These data raise questions about whether ACC MKP-1 is a key factor in depression pathophysiology, particularly for chronic pain–induced depression. Thus, using animal models, we studied the link between MKP-1 and anxiodepressive-like behaviors, identified molecular upstream mechanisms leading to its increased expression in the ACC, and tested the therapeutic potential of targeting this phosphatase. We show that neuropathic pain (NP)–induced depressive-like behaviors are associated with an increase in c-Fos expression, an increase in phosphorylated CREB and phosphorylated ATF levels in the ACC, and increased histone H3 lysine 9/lysine 14 (H3K9/K14) acetylation at the promoter regions of *C-fos* and *Mkp-1*. We further demonstrate that ACC MKP-1 overexpression is present in several animal models of depression, suggesting a general link between depression and increased level of ACC MKP-1. We also show that chronic treatment with a classical antidepressant drug, fluoxetine, suppresses the increase in MKP-1 levels within the ACC. Moreover, knocking out, antagonizing, or locally silencing its presence in the ACC attenuates depressive-like behaviors induced by NP, pointing to an essential role of MKP-1.

METHODS AND MATERIALS

Animals

Approximately 350 adult male C57BL/6J mice (Charles River, L'Arbresle, France) were used in all experiments. For the optogenetic experiments, we used Thy1-ChR2-YFP mice (13,20). The cyclic adenosine monophosphate response element (CRE)–related activity was examined by using CRE-LacZ mice (21) (see Supplement). Protocols were approved by the local ethical committee of the University of Strasbourg (No. 2015012909428166) and Comité d'expérimentation animale du Val de Loire (No. 19).

Surgical Procedures

All surgical procedures were done under general anesthesia (ketamine/xylazine, 68/10 mg/kg, intraperitoneally; Centravet, Taden, France). Viral transfection and optogenetic procedures used standard in vivo stereotaxic procedures, and coordinates for the ACC (areas 24a and 24b) were 0.7 mm anterior and 0.3 lateral to the bregma, based on the Mouse Brain Atlas (22).

NP Model and Nociceptive Testing

Chronic NP was induced by placing a polyethylene cuff around the right common sciatic nerve of the animal (23). The control group (sham) underwent the same procedure without cuff implantation. The mechanical sensitivity was scored using von Frey filaments (Bioseb, Vitrolles, France) (see Supplement).

Unpredictable Chronic Mild Stress Model

Mice were subjected to a variety of stressors several times a day/night for 8 weeks, including altered cage and bedding, altered light/dark cycle, cage tilting (45°), and predator smell exposure (24,25). At the end of 8 weeks, the novelty suppressed feeding (NSF) test was performed and the ACC was harvested for protein analyses (see Supplement and Supplemental Table S3).

Anxiodepressive-Related Behaviors

Behavioral phenotyping was performed by using the NSF, splash, and forced swim tests (FST) (see Supplement).

Optogenetic

Independent sets of Thy1-ChR2-YFP mice implanted with optic fibers were tested either 5 minutes and 1 day after a single stimulation or 1 day and 2 weeks after four consecutive (30 min/day) stimulations. Animals were stimulated with a blue light–emitting diode (peak wavelength: 460 nm; intensity: 4–6 mW) (see Supplement).

Viral-Mediated Gene Knockdown

Three weeks after sciatic nerve surgery, NP- or sham-operated animals received either lentiviral vectors expressing a set of *Mkp-1* small interfering RNA (siRNA)/short hairpin RNA/RNA-mediated interference and green fluorescent protein under the cytomegalovirus promoter (Applied Biological Materials, Richmond, BC, Canada) or a scrambled version of the virus, bilaterally (2 μL/site) into the ACC. Four weeks after transfection, behavioral tests were conducted on three groups: 1) sham-operated (control for NP) mice that express siRNA (sham/siRNA), 2) mice displaying NP-induced anxiodepressive-like behaviors administered with scramble virus (NP/control), and 3) mice displaying NP-induced anxiodepressive-like behaviors expressing siRNA (NP/siRNA). In a separate experiment, the impact of local deletion of ACC MKP-1 was assessed in naïve animals. Details are shown in the Supplement.

Pharmacological Agents

The selective serotonin reuptake inhibitor fluoxetine (20 mg/kg/day) mixed with 0.2% saccharine was administered in drinking water for 3 weeks (starting 5 weeks after the sciatic nerve injury), while the control group drank 0.2% saccharine. The MKP antagonist dusp-(*E*)-2-benzylidene-3-(cyclohexylamino)-2,3-dihydro-1*H*-inden-1-one (BCI) dissolved in 2% dimethyl sulfoxide was administered systemically (10 mg/kg, intraperitoneally, twice a day) for 4 days, followed by a behavioral test 1 hour after the last injection. Control animals received 2% dimethyl sulfoxide. All drugs were purchased from Sigma-Aldrich (Saint-Quentin-Fallavier, France) (see Supplement).

Tissue Harvesting and Analysis

For genomic analysis, chromatin immunoprecipitation (26), and Western blot, all animals were killed by cervical dislocation and the ACC, primary somatosensory cortex, and whole hippocampus were harvested and stored at −80°C. For detailed procedures of the microarray analysis, chromatin immunoprecipitation, Western blot, and immunostaining, see the Supplement.

Statistical Analysis

Results are expressed as mean ± SEM. Statistical analyses were performed with Statistica 7.1 (StatSoft, Tulsa, OK) by using unpaired Student's *t* tests or multifactor analysis of variance with independent or repeated measures and Duncan post hoc analyses. Immunoblotting experiments were analyzed with the nonparametric Kruskal-Wallis test, followed by multiple comparisons with the Wilcoxon or Mann-Whitney *U* test when data did not fit with the rules of parametric analyses. The significance level was set at $p \leq .05$. For detailed information, see Supplemental Table S4.

RESULTS

Mkp-1 Messenger RNA and Protein Levels Increase in the ACC of NP Mice Displaying Depressive-like Behaviors

To characterize molecular changes within the ACC, we conducted a whole-genome expression analysis in NP-induced depressed-like animals. The ACC tissues were collected at 8 weeks after sciatic nerve surgery, which corresponds to the presence of both nociceptive and anxiodepressive-like phenotypes, as illustrated by decreased mechanical thresholds in the von Frey test (Figure 1A; $F_{7,70} = 6.04$, $p \leq .001$; post hoc: weeks 1–7, $p \leq .001$) and increased latency to feed in the NSF test (Figure 1B; $p \leq .01$), respectively. At this time point, no change in food intake or in spontaneous locomotor activity was present in NP mice (Supplemental Figure S1A). The microarray data revealed several changes in gene expression within the ACC (Figure 1C and Supplemental Table S1). A Kyoto Encyclopedia of Genes and Genomes signaling pathway analysis from WebGestalt highlighted a major alteration in the MAPK pathway (Figure 1D; $p = 1.40e\text{-}06$), in particular concerning its negative regulator *Mkp-1*, whose expression was robustly upregulated in the ACC of animals displaying anxiodepressive-like behaviors (1.7-fold) (Figure 1E; $p \leq .01$). This finding was then confirmed by Western blot analysis, showing that the increase was also present at protein level in NP mice within the ACC (Figure 1F; $p \leq .001$; see also Supplemental Figure S1B) but not in the primary somatosensory cortex and whole hippocampus (Supplemental Figure S2). Interestingly, microarray data showed that *Mkp-1* was already upregulated at the messenger RNA (mRNA) level 2 weeks after sciatic nerve surgery in animals displaying nociceptive hypersensitivity but not yet detectable anxiodepressive-like behaviors (Supplemental Figure S3A; $p \leq .001$; see also Supplemental Table S2). However, this upregulation was not significant at the protein level at this 2-week early time point (Supplemental Figure S3B), but it slightly increased at 5 weeks postsurgery (Supplemental Figure S3C; $p = .10$), when animals displayed anxiety-like behavior (6) in the light/dark box (Supplemental Figure S3C; $p \leq .001$).

NP-Induced Depressive-like Behaviors Are Associated With Transcription Factors' Recruitment

To identify potential upstream factors responsible for *Mkp-1* overexpression, we looked at the involvement of relevant transcription factors within the genomic data. Based on transcription factor target analyses from WebGestalt, we focused on CREB (Figure 2A; $p = 2.55e\text{-}08$) and ATF-1 (Figure 2A; $p = 4.76e\text{-}12$) as well as on Fos proteins (Figure 2A; $p = 5.02e\text{-}10$, serum response factor) that displayed significant changes in the microarray data (for *C-fos* and *Fosb*: 1.94- and 1.47-fold increases in NP animals, respectively). CREB and ATF are known to bind CREs at the *Mkp-1* promoter region (27), and functional activator protein 1 binding sites are also present within this promoter region (18).

Western blot analyses confirmed that both phosphorylated forms of CREB (Figure 2B; $p \leq .05$) and ATF-1 (Figure 2B; $p \leq .01$) increased in the ACC of NP animals. To have a functional assessment of CREB/ATF activity, we used CRE-LacZ transgenic reporter mice. By using a line of CRE-LacZ mice displaying very high basal reporter activity in the cortex, we previously reported no alteration in ACC CRE-mediated transcription (6). However, this could have been related to a ceiling effect preventing effective detection of increased activity in this brain region. Thus, here we used another CRE-LacZ line with lower basal reporter activity. In this line, β-galactosidase immunostaining showed a significant increase in the presence of CRE-positive cells in the ACC of NP animals (Figure 2C, D; $F_{16,48} = 3.98$, $p < .001$; post hoc: −0.47 to +1.41 from the bregma; $p \leq .05$) but not in the prelimbic (A32) and infralimbic cortices (Supplemental Figure S4). Because *Fos* expression was upregulated by NP in our microarray analysis (Figure 1C and Supplemental Table S1; $p < .05$), we also confirmed increased c-Fos protein levels in the ACC of NP animals (Figure 2E, F; $F_{14,48} = 5.75$, $p < .001$; post hoc: −0.47 to +1.33 from the bregma; $p \leq .001$). This alteration was also observed in the rostal part of the infralimbic cortex (A25) ($F_{1,5} = 2.47$, $p < .05$; Supplemental Figure S4) but not in the prelimbic cortex.

NP-Induced Depressive-like Behaviors Are Associated With Epigenetic Changes at *Mkp-1* and *C-fos* Promoters in the ACC

As immediate early genes, it is intriguing that *C-fos* and *Mkp-1* are still present at high levels in the ACC 8 weeks after NP induction,

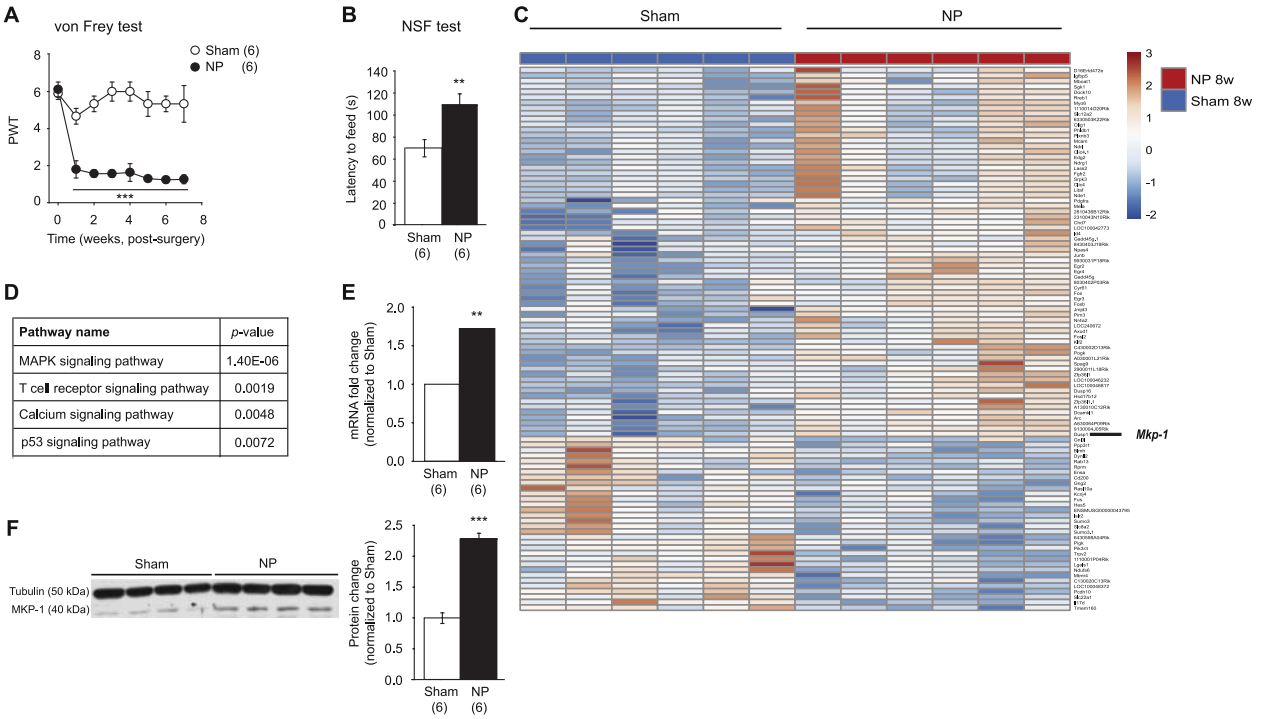

Figure 1. After 8 weeks of sciatic nerve compression, mitogen-activated protein kinase (MAPK) phosphatase-1 (MKP-1) messenger RNA (mRNA) and protein levels increase in the anterior cingulate cortex (ACC) of neuropathic pain (NP) animals displaying depressive-like behaviors. **(A)** von Frey test shows long-lasting ipsilateral allodynia, as evidenced by decreased mechanical thresholds of the right paw of NP animals. **(B)** NP animals display an anxiodepressive-like behavior, as shown by an increased latency to feed compared with their sham-operated littermates in the novelty suppressed feeding (NSF) test 8 weeks after surgery. **(C)** Heatmap representing dysregulated genes in the ACC 8 weeks after the surgery. **(D)** Results of Kyoto Encyclopedia of Genes and Genomes signaling pathway analysis showing that the MAPK pathway was most significantly enriched. **(E)** Microarray result showing an overexpression of *Mkp-1* (1.7-fold) in the ACC of NP animals compared with controls. **(F)** Western blot results illustrating an upregulation of ACC MKP-1 protein levels in animals displaying NP-induced depressive-like behaviors. Data are expressed as mean ± SEM; $^{**}p \leq .01$, $^{***}p \leq .001$. PWT, paw withdrawal thresholds.

and we tested whether specific epigenetic alterations relevant for active gene transcription could be found at their promoters. We used chromatin immunoprecipitation followed by quantitative polymerase chain reaction to look for induction of specific acetylated marks on H3K9/K14ac, a marker of transcriptionally active chromatin found mainly in the proximal promoter/transcription start site (TSS) regions, and histone H3 lysine 27 (H3K27ac), a mark of both active enhancers and TSS regions (28,29). We controlled immunoprecipitation enrichment and specificity for H3K9/K14ac and H3K27ac on *Gapdh* as ubiquitously expressed positive control and *Tsh2b* as negative control (i.e., not expressed in the brain) (Supplemental Figure S5). Both histone marks were enriched on *Mkp-1* and *C-fos* promoter/TSS regions, with H3K9/K14ac (Figure 2G), but not H3K27ac (Figure 2H), showing a significant increased enrichment on these promoters in the NP group ($p \leq .05$). Together, these data show that 8 weeks after the surgery, NP maintains active epigenetic regulations on the *Mkp-1* gene.

MKP-1 Level Increases in Other Models of Depression

We then assessed whether NP-induced alterations in ACC MKP-1 levels could be generalized to other models of depression. Hence, mice were subjected to unpredictable chronic mild stress (UCMS) during 8 weeks (see Supplemental Table S3) (25). Similarly to what was observed in NP animals, mice that underwent the UCMS procedure displayed an increase in both anxiodepressive-like behavior in the NSF test (Figure 3A; $p \leq .001$) and MKP-1 protein level in the ACC (Figure 3B; $p \leq .01$). Moreover, we previously showed that sustained activation of pyramidal neurons of the ACC leads to anxiodepressive-like behavior in naïve Thy1-ChR2-YFP mice (13). By using the same protocol, we determined the influence of ACC activation on MKP-1 levels. Repeated, but not single (Supplemental Figure S6A), optogenetic activation of the ACC of naïve Thy1-ChR2-YFP mice (Figure 3C) induced depressive-like behavior 1 day after the last stimulation, as shown by the increased latency to eat in the NSF test (Figure 3D; $p \leq .01$). More notably, this repeated optogenetic stimulation of the ACC also increased local MKP-1 levels (Figure 3E, F; $p \leq .05$). The anxiodepressive-like behaviors totally disappeared 2 weeks after the last stimulation (Supplemental Figure S6B), while MKP-1 levels still remained significantly high (Supplemental Figure S6C). However, this upregulation was lower than that obtained on day 1 following the last consecutive stimulation (1.54 ± 0.15-fold vs. 2.29 ± 0.63-fold; $p = .06$) (Figure 3E).

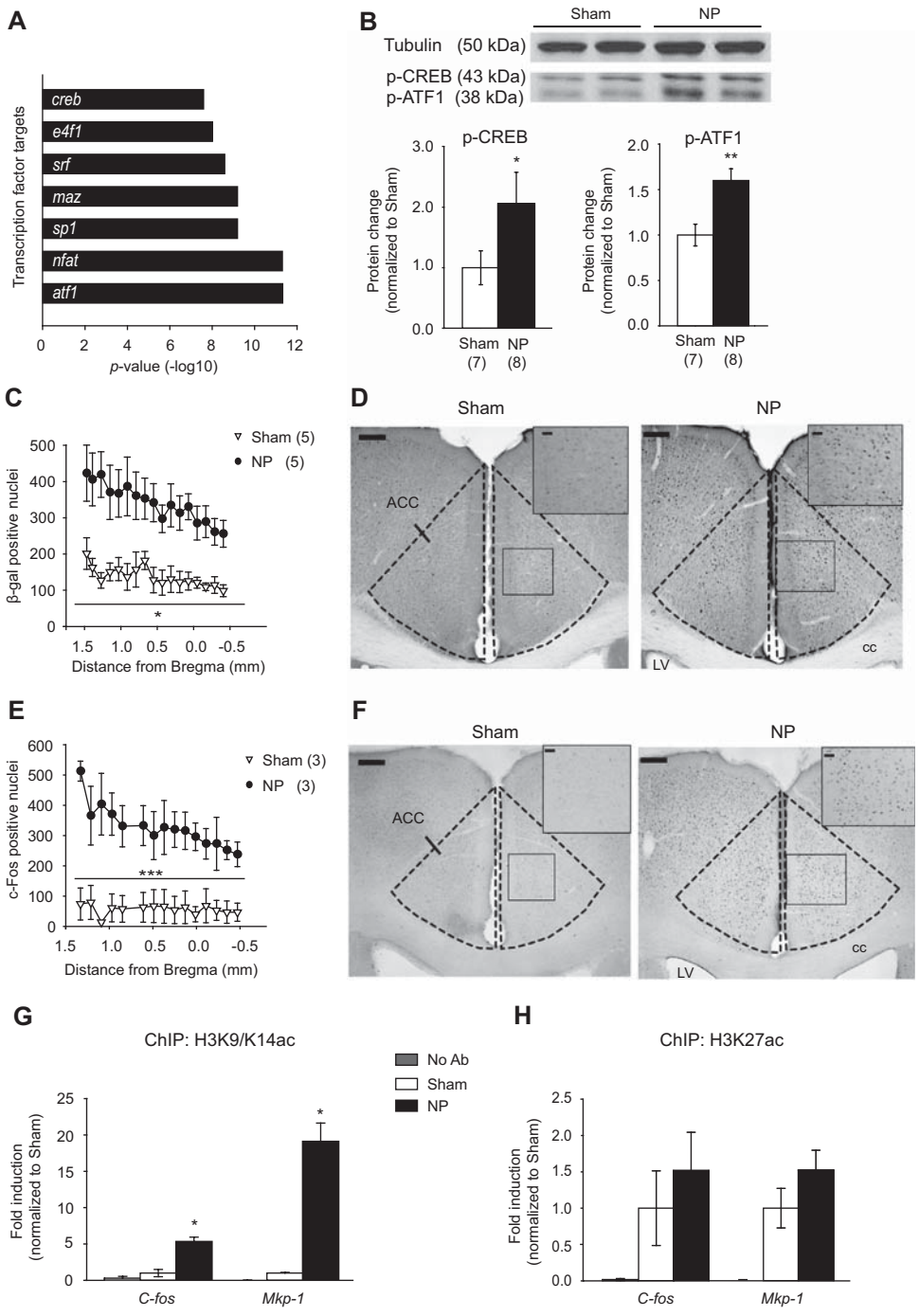

Figure 2. Neuropathic pain (NP)–induced depressed animals display enhanced cyclic adenosine monophosphate (cAMP)–driven transcriptional activity and H3 acetylation at the promoter of *C-fos* and *Mkp-1* in the anterior cingulate cortex (ACC). **(A)** Microarray-based transcription factor target analysis showing the 7 most probable transcription factors regulating the prominently changed genes in the ACC of animals displaying NP-induced depressive-like behaviors. **(B)** Western blot analysis showing an increase in phosphorylated cAMP response element binding protein (p-CREB) and phosphorylated activating transcription factor (p-ATF) in the ACC of the NP group. **(C)** Quantitative representation of β-galactosidase (β-gal)-positive nuclei in the ACC of sham and NP animals at various distances from the bregma, showing a higher presence of CRE positive cells in the ACC of NP animals after 8 weeks of sciatic nerve compression. **(D)** Representative pictures comparing the expression and distribution of β-gal labeling in the ACC of sham and NP CRE-LacZ mice. Large scale bar = 300 μm, inset scale bar = 30 μm. **(E)** Increased c-Fos expression in NP animals compared with sham animals after 8 weeks of sciatic nerve compression. **(F)** Representative pictures comparing the expression and distribution of c-Fos-positive cells in the ACC of sham and NP animals. Large scale bar = 300 μm, inset scale bar = 30 μm. **(G, H)** Quantitative polymerase chain reaction results from chromatin immunoprecipitation (ChIP) experiments performed in the ACC of NP animals compared with sham, demonstrating the presence of histone H3 lysine 27 acetylation (H3K27ac) at the proximal promoter/transcription start site regions of *C-fos* and *Mkp-1* and a significant increase in histone H3 lysine 9/lysine 14 acetylation (H3K9/K14ac) binding on both genes in the NP group. No Ab, no antibody. Data are expressed as mean ± SEM; $^{*}p \leq .05$, $^{**}p \leq .01$, $^{***}p \leq .001$. cc, corpus callosum; LV, lateral ventricle.

Fluoxetine Decreases ACC MKP-1 Levels

Chronic oral treatment (3 weeks) with the selective serotonin reuptake inhibitor fluoxetine did not affect mechanical hypersensitivity (Figure 4A; $F_{1,44} = 0.65$, $p = .42$), but it blocked the anxiodepressive-like behavior in the NSF test (Figure 4B; $F_{3,42} = 14.10$, $p \leq .001$; post hoc: NP vehicle > sham vehicle, $p \leq .001$; NP fluoxetine < NP vehicle, $p \leq .001$). Interestingly, fluoxetine treatment also significantly decreased the ACC MKP-1 in the NP and sham groups (Figure 4C; $H = 13.93$, $p \leq .01$; post hoc: sham vehicle < NP vehicle, NP vehicle > NP fluoxetine, sham vehicle > sham fluoxetine, $p \leq .01$).

MKP-1-Deficient Mice Are Resistant to NP-Induced Depression

To investigate the causal link between MKP-1 and depression, we obtained *Mkp-1*$^{-/-}$ mice from the laboratory of Andrew

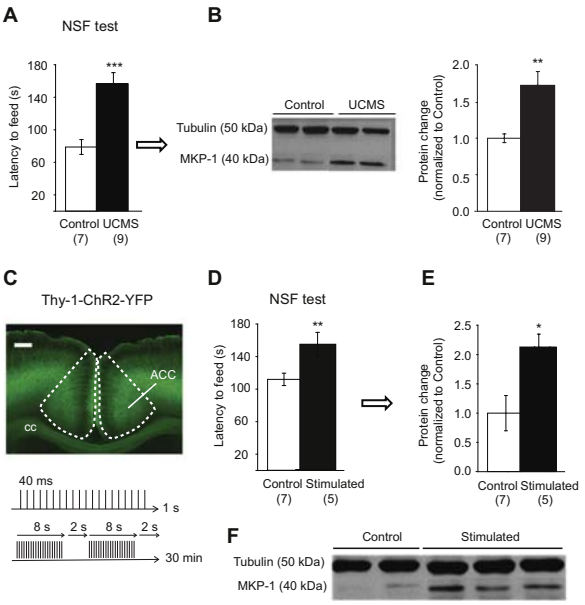

Figure 3. Anterior cingulate cortex (ACC) mitogen-activated protein kinase phosphatase-1 (MKP-1) levels increase in other models of depression. **(A)** Novelty suppressed feeding (NSF) test performed after unpredictable chronic mild stress (UCMS) procedure illustrating an anxiodepressive-like behavior in stressed animals compared with nonstressed animals, as shown by an increased latency to feed. **(B)** Western blot analysis showing increased levels of ACC MKP-1 in stressed animals compared with nonstressed animals. **(C)** Representative picture of the ACC in the Thy-1-ChR2-YFP mice (top) and a scheme of the stimulation protocol used (20 Hz; 4 days; 30 min/day; 8 seconds stimulation; 40-ms pulses; 2 seconds no stimulation) (bottom). Scale bar = 300 μm. **(D)** NSF test at day 5 after ACC stimulation showing that stimulated animals display an anxiodepressive-like behavior, as shown by an increased latency to feed. **(E, F)** Western blot results illustrating an upregulation of ACC MKP-1 in stimulated animals compared with controls. Data are expressed as mean ± SEM; $^{*}p \leq .05$, $^{**}p \leq .01$, $^{***}p \leq .001$. cc, corpus callosum.

Cato (30) and bred them in our animal facilities. We characterized the nociceptive sensitivity and anxiodepressive-like behavior in *Mkp-1*$^{-/-}$ and *Mkp-1*$^{+/+}$ animals before and after NP induction. It is important to note that we did not observe any alteration in the mechanical paw withdrawal thresholds in *Mkp-1*$^{-/-}$ mice compared with *Mkp-1*$^{+/+}$ mice before surgery (Figure 5A; $F_{1,43} = 3.33$, $p > .05$). After surgery, NP animals developed mechanical allodynia regardless of their genetic background (Figure 5B; $F_{3,123} = 50.25$, $p \leq .001$), showing that the loss of MKP-1 expression did not modify the NP somatosensory component. However, by using the NSF and splash tests, we showed that *Mkp-1*$^{-/-}$ mice did not display the anxiodepressive-like behaviors normally induced by NP. Indeed, the loss of MKP-1 suppressed the NP-induced increased latency to feed in the NSF test (Figure 5C; $F_{1,41} = 4.09$, $p \leq .05$, sham < NP in *Mkp-1*$^{+/+}$, sham = NP in *Mkp-1*$^{-/-}$). Similarly, *Mkp-1*$^{-/-}$ NP animals did not display decreased grooming behavior in the splash test (Figure 5D; $F_{1,41} = 12.60$, $p \leq .001$, sham < NP in *Mkp-1*$^{+/+}$, sham = NP *Mkp-1*$^{-/-}$). Interestingly, *Mkp-1* deficiency had no effect per se on behavioral tests in sham *Mkp-1*$^{-/-}$ mice (Figure 5C, D).

BCI, an MKP Antagonist, Reduces NP-Induced Depressive-like Behavior

Beyond constitutive depletion of MKP-1, we assessed whether a reversible pharmacological blockade of this phosphatase could also lead to antidepressant-like effects by testing a systemic subchronic treatment (4 days, intraperitoneally) with MKP-1/6 antagonist BCI (31). Before treatment, NP animals showed an increased latency to feed in the NSF test (Figure 5E; $F_{1,20} = 10.34$, $p \leq .001$; post hoc: NP > sham, $p \leq .001$), thereby confirming the presence of an anxiodepressive-like state. Subsequent BCI treatment increased the grooming time of NP animals in the splash test (Figure 5E; $F_{1,19} = 3.72$, $p \leq .05$; post hoc: NP saline < NP BCI, $p \leq .01$) without affecting their mechanical sensitivity threshold (Figure 5F; $F_{2,23} = 92.2$, $p \leq .001$; post hoc: NP BCI right < sham right, $p \leq .001$; NP saline right < sham right, $p \leq .001$).

Local Suppression of MKP-1 Within the ACC Blocks NP-Induced Depression

While constitutive MKP-1 depletion and pharmacological antagonism brought information for evaluating the link between MKP-1 and depression, they lack neuroanatomical selectivity. Thus, we performed a local viral-mediated manipulation (Figure 5G) of *Mkp-1* to identify its role in the ACC.

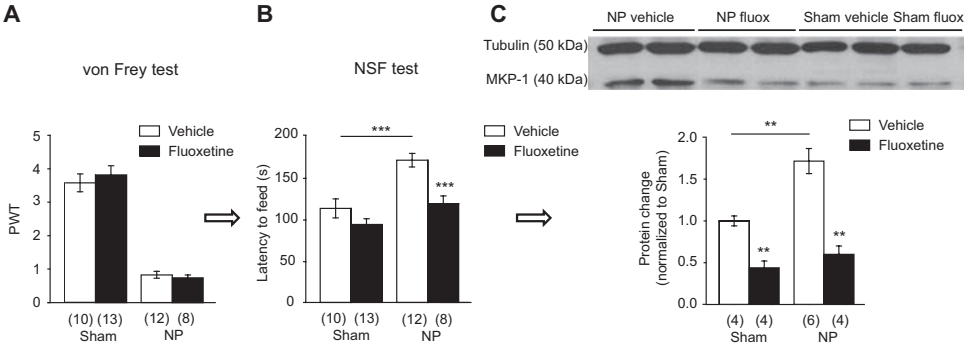

Figure 4. Prolonged fluoxetine treatment blocks anterior cingulate cortex (ACC) mitogen-activated protein kinase phosphatase-1 (MKP-1) upregulation. **(A)** von Frey results for the right hind paw showing that fluoxetine treatment (3 weeks) did not affect the development of allodynia after neuropathy induction. **(B)** Novelty suppressed feeding (NSF) test results illustrating that fluoxetine treatment decreases the anxiodepressive-like behavior in neuropathic pain (NP) animals, as shown by a lowered latency to feed. **(C)** Western blot results demonstrating a decrease in MKP-1 in the ACC of both sham and NP animals after fluoxetine treatment. Data are expressed as mean ± SEM; $^{**}p \leq .01$, $^{***}p < .001$. PWT, paw withdrawal thresholds.

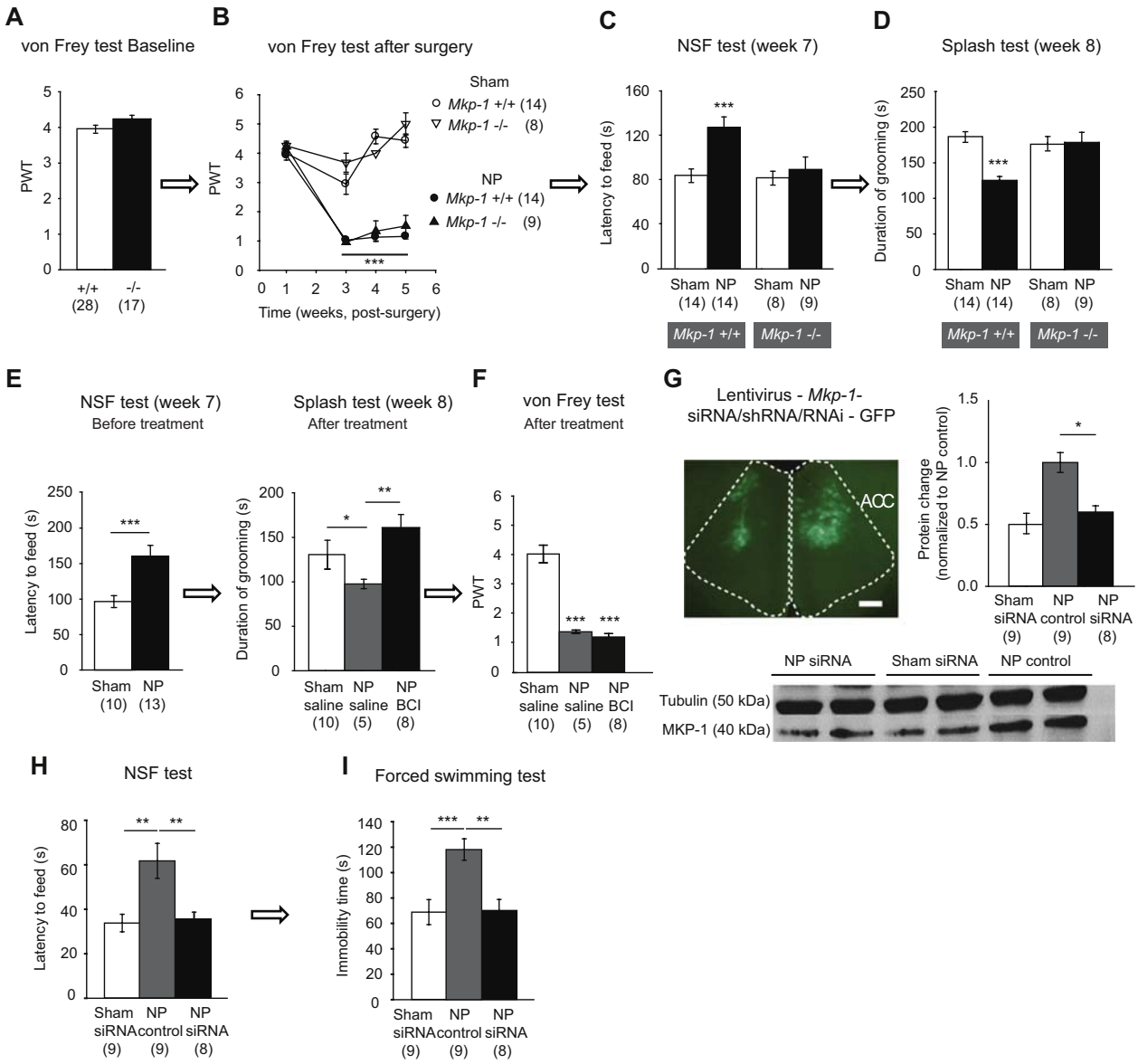

Figure 5. Total, systemic, and local suppression or blockade of mitogen-activated protein kinase phosphatase-1 (MKP-1) prevents and/or blocks neuropathic pain (NP)–induced depression. **(A)** Baseline von Frey results (right paw) illustrating that *Mkp-1*$^{-/-}$ mice show no initial difference in mechanical sensitivity compared with *Mkp-1*$^{+/+}$ animals before surgery. **(B)** von Frey results showing that both *Mkp-1*$^{+/+}$ and *Mkp-1*$^{-/-}$ mice develop mechanical allodynia after cuff surgery. **(C, D)** Behavioral tests demonstrating that there is no difference in the latency to feed in the novelty suppressed feeding (NSF) test or duration of grooming in the splash test between *Mkp-1*$^{-/-}$ sham and NP animals, suggesting an absence of development of depressive-like behaviors 8 weeks after NP induction, contrary to that normally observed in *Mkp-1*$^{+/+}$ cuff mice. **(E)** NSF test before BCI treatment demonstrating that NP animals display anxiodepressive-like behaviors 8 weeks after surgery. Splash test results showing that the NP group treated with BCI spent more time grooming compared with the nontreated group, suggesting a decrease in depressive-like behavior. **(F)** von Frey results demonstrating that BCI treatment did not affect the NP-induced mechanical allodynia in the right hind paw. **(G)** Representative picture of the anterior cingulate cortex (ACC) after bilateral injections of lentiviruses (Lentivirus-*MkP-1*-small interfering RNA (siRNA)/short hairpin RNA (shRNA)/RNA-mediated interference (RNAi)-GFP, 2 μL/site) (top left) and Western blot results showing a decrease in ACC MKP-1 after *Mkp-1* silencing (top right and bottom). Scale bars = 300 μm. **(H)** NSF test illustrating that NP animals with *Mkp-1* silencing have shorter latency to feed compared with NP animals that received the control virus, suggesting a decrease in anxiodepressive-like behavior. **(I)** Forced swim test data showing a decreased immobility time in NP animals with *Mkp-1* silencing compared with NP control animals, suggesting a reduction in depressive-like behavior. Data are expressed as mean ± SEM; $^{**}p \leq .01$, $^{***}p \leq .001$. PWT, paw withdrawal thresholds.

In naïve animals, the local deletion of the MKP-1 within the ACC did not affect behaviors (Supplemental Figure S7). In NP mice, the local *Mkp-1* suppression had a prominent global effect on both the NSF test (Figure 5H; $F_{2,23} = 7.280$, $p \leq .01$) and the FST (Figure 5I; $F_{2,23} = 8.35$, $p \leq .01$). Indeed, this silencing lowered both the latency to feed in the NSF test

(Figure 5H; $p \leq .01$) and the immobility time in the FST (Figure 5I; $p \leq .01$) compared with the scramble-injected NP group. This suggests that silencing ACC *Mkp-1* leads to a decrease in anxiodepressive-like behaviors and further reinforces the causal link between ACC MKP-1 and depression.

DISCUSSION

Here we show that anxiodepressive-like behaviors in mice are associated with an upregulation of ACC MKP-1, which is reversed by fluoxetine. This upregulation is accompanied by increased phosphorylated CREB/ATF-1 levels and Fos expression as well as increased enrichment of H3K9/K14ac at *Mkp-1* promoter in animals displaying depressive-like behaviors. Antidepressant-like effects produced by experimentally preventing, blocking, or decreasing MKP-1 activity within the ACC further reinforce its crucial role in depression.

While depression is the most prevalent lifetime disorder, our limited knowledge of its etiology, alongside the lack of efficient treatment strategies, points to an obvious need for objectively quantifiable abnormalities at the molecular, cellular, or circuit level. Because the ACC is an integration center interconnecting neurons from brain regions implicated in pain and affective-related processing, this study mainly focused on identifying molecular alterations within this structure. Through genomic analyses, we identified *Mkp-1* as one of the most prominently upregulated genes in the ACC, extending previous studies showing increased expression of *Mkp-1* in other brain regions in animal models of depression and in depressed patients (14,15).

By exploring the expression dynamics of MKP-1, we observed that its mRNA, but not the protein, starts being overexpressed after 2 weeks of NP, when mice display mechanical hypersensitivity without anxiodepressive-like behaviors. This delay between gene expression and protein synthesis might involve negative feedback mechanisms controlling MKP-1 degradation (32,33) and/or synthesis (34,35). Furthermore, MKP-1 protein shows a tendency for overexpression at 5 weeks of NP, when anxiety-like behaviors are present, and significant overexpression after 8 weeks, when animals fully display anxiodepressive-like behaviors. Because *Mkp-1* deletion or local downregulation suppresses these behaviors, MKP-1 overexpression appears to be necessary to anxiodepressive phenotypes. However, it might not be sufficient. Indeed, following optogenetic stimulation of the ACC, the increase in MKP-1 levels lasted longer than the anxiodepressive phenotype. Together, these results suggest that other molecular actors (which still remain to be identified) should also be critical and/or that the increase in MKP-1 levels should reach a certain threshold in order to translate into a behavioral outcome.

Various studies (16,36,37) focused on the downstream targets of MKP-1, showing that its main functional role is to modulate MAPK-CREB signaling pathways by inactivating several downstream targets, such as extracellular signal-regulated kinases, c-Jun N-terminal kinases, and P38 (16,36), which further affects the expression of various genes implicated in depression (14,38). However, the molecular events triggering MKP-1 upregulation remain unknown. Previous studies showed that *Mkp-1* mRNA has a short half-life of 1 to 2 hours (17,39); however, our genomic analysis at 8 weeks of NP points out a sustained expression of ACC *Mkp-1*. Increased presence of activated transcription factors thus could be responsible for such prolonged transcription given that microarray results revealed significant modifications in several of these factors, including mRNA coding ATF-1, CREB, and Fos proteins, which are known to target *Mkp-1* (40).

Besides changes in transcription factors, a prolonged expression of relatively short half-life mRNA, such as *Mkp-1* and *C-fos* mRNAs, might also require sustained changes in chromatin structure. Thus, we looked for epigenetic regulation by testing H3ac at the *Mkp-1* and *C-fos* promoters, which has been previously reported to be altered in response to various stimuli (17,41–43). Interestingly, while both H3K9/K14ac and H3K27ac are present at the promoter/TSS region of *C-fos* and *Mkp-1*, only H3K9/K14ac was increased in response to NP. H3K27ac is generally associated with active enhancers (44), whereas H3K9/K14ac, which is more particularly present at the promoter/TSS region of highly transcribed genes (45), is a highly inducible mark that has been shown to be modulated by behavior at the global and locus-specific levels (46,47). The enrichment of H3K27ac and increased NP-induced enrichment of H3K9/K14ac observed at both genes, demonstrating a favorable chromatin conformation for transcription that may be relevant, possibly with other modifications, for the sustained upregulation of MKP-1. Such epigenetic alterations in the ACC could contribute to the emergence of depressive-like behaviors during NP by modulating *Mkp-1* (and other genes) in the long term.

We further demonstrate that ACC MKP-1 is overexpressed not only in NP-induced depression but also in other models such as sustained optogenetic stimulation of the ACC and UCMS, one of the most valid and relevant models of depression (48), suggesting that this pattern is consistent regardless to the cause of depression and could be a common marker. Interestingly, Duric *et al.* (14) did not report alterations of *Mkp-1* in the whole cortex after chronic stress, whereas they demonstrated an increased level of this gene in the dentate gyrus and the cornu ammonis 1 of animals submitted to UCMS and in patients with major depressive disorder. Likewise, we did not observe any change in the primary somatosensory cortex, suggesting that the overexpression is not a general cortical effect but rather may be selective for the ACC. Conversely, we did not observe alteration in MKP-1 protein level when we studied the whole hippocampus, which may reflect that reported changes (14) affect specific subregions of this structure.

To leap from a correlative analysis to a causal analysis for understanding the link between MKP-1 and depression, we combined several approaches. Knocking out and systemic antagonism of MKP-1 blocks the development as well as the maintenance of depressive-like behaviors without affecting the nociceptive hypersensitivity component of NP, suggesting that the presence of MKP-1 at the systemic level may be crucial for depression. Interestingly, local silencing of *Mkp-1* within the ACC is sufficient to suppress depressive-like behaviors after NP. Besides systemic and local suppression of MKP-1, fluoxetine also induces antidepressant-like effects in our model and decreases the ACC MKP-1 levels. The latter is in

line with studies showing a decrease in MKP-1 in the frontal cortex and hippocampus of rats after chronic fluoxetine treatment (49,50). Unlike tricyclic antidepressants that are successful in treating the nociceptive hypersensitivity component, such as mechanical allodynia, observed in NP (51), selective serotonin reuptake inhibitors, and particularly fluoxetine, show limited to no analgesic efficacy in NP (52). Accordingly, the antidepressant-like effect of fluoxetine that we observed was also independent of its impact on the mechanical hypersensitivity.

In conclusion, our results indicate that the upregulation of ACC MKP-1 is necessary for the expression of depressive symptoms induced by chronic pain, chronic stress, and optogenetic activation of the ACC. From a drug discovery perspective, dual specificity phosphatase family members are promising drug targets given that several MAPK inhibitors are already in different states of development for inflammatory disease and cancer (53). Our results further provide a preclinical target validation for potential treatment of depression given that systemic pharmacological blockade and local suppression of the MKP-1 display antidepressant-like effects.

ACKNOWLEDGMENTS AND DISCLOSURES

This work was supported by the Centre National de la Recherche Scientifique (Contract No. UPR3212) (to IY and MB), the University of Strasbourg (to FB and MH), the Neurotime Erasmus Mundus Joint Doctorate (to MK), the Institut UPSA de la Douleur (to IY and MB), and a National Alliance for Research on Schizophrenia and Depression Young Investigator Grant from the Brain & Behavior Research Foundation (to IY).

We thank Stephane Doridot for assistance in breeding and genotyping *Mkp-1*$^{-/-}$ mice. We are grateful to Andrew Cato and Bristol-Myers Squibb for providing *Mkp-1*$^{-/-}$ mice. We thank the Core Facility Genomics of the Medical Faculty Münster, especially Anika Witten and Monika Stoll, for excellent gene expression analysis using Illumina microarrays.

The authors report no biomedical financial interests or potential conflicts of interest.

ARTICLE INFORMATION

From the Institute of Cellular and Integrative Neuroscience (FB, MH, EW, MK, MB, IY), Centre National de la Recherche Scientifique, Laboratory of Cognitive and Adaptive Neuroscience (A-LB), Centre National de la Recherche Scientifique, University of Strasbourg (FB, MH, MK), Strasbourg, and University François Rabelais (SL, CB), Institut National de la Santé et de la Recherche Médicale, Tours, France; and Institute of Pharmacology and Toxicology (RG, LH), University of Freiburg, and BIOSS Centre for Biological Signalling Studies, Freiburg, Germany.

FB and MH contributed equally to this work.

Address correspondence to Ipek Yalcin, Ph.D., Pharm.D., Institut des Neurosciences Cellulaires et Intégratives, UPR 3212 CNRS, 5 rue Blaise Pascal, 67084 Strasbourg cedex, France; E-mail: yalcin@inci-cnrs.unistra.fr.

Received Jul 25, 2016; revised Jan 11, 2017; accepted Feb 2, 2017.

Supplementary material cited in this article is available online at http://dx.doi.org/10.1016/j.biopsych.2017.01.019.

REFERENCES

1. Pittenger C, Duman RS (2008): Stress, depression, and neuroplasticity: A convergence of mechanisms. Neuropsychopharmacology 33: 88–109.
2. Attal N, Lanteri-Minet M, Laurent B, Fermanian J, Bouhassira D (2011): The specific disease burden of neuropathic pain: Results of a French nationwide survey. Pain 152:2836–2843.
3. Maletic V, Raison CL (2009): Neurobiology of depression, fibromyalgia, and neuropathic pain. Front Biosci (Landmark Ed) 14: 5291–5338.
4. Suzuki T, Amata M, Sakaue G, Nishimura S, Inoue T, Shibata M, *et al*. (2007): Experimental neuropathy in mice is associated with delayed behavioral changes related to anxiety and depression. Anesth Analg 104:1570–1577.
5. Alba-Delgado C, Llorca-Torralba M, Horrillo I, Ortega JE, Mico JA, Sanchez-Blazquez P, *et al*. (2013): Chronic pain leads to concomitant noradrenergic impairment and mood disorders. Biol Psychiatry 73: 54–62.
6. Yalcin I, Bohren Y, Waltisperger E, Sage-Ciocca D, Yin JC, Freund-Mercier MJ, *et al*. (2011): A time-dependent history of mood disorders in a murine model of neuropathic pain. Biol Psychiatry 70: 946–953.
7. Pizzagalli DA (2011): Frontocingulate dysfunction in depression: Toward biomarkers of treatment response. Neuropsychopharmacology 36:183–206.
8. Matthews SC, Strigo IA, Simmons AN, Yang TT, Paulus MP (2008): Decreased functional coupling of the amygdala and supragenual cingulate is related to increased depression in unmedicated individuals with current major depressive disorder. J Affect Disord 111:13–20.
9. Drevets WC (2001): Neuroimaging and neuropathological studies of depression: Implications for the cognitive-emotional features of mood disorders. Curr Opin Neurobiol 11:240–249.
10. Drevets WC, Ongur D, Price JL (1998): Neuroimaging abnormalities in the subgenual prefrontal cortex: Implications for the pathophysiology of familial mood disorders. Mol Psychiatry 3:190–191, 220–226.
11. Radley JJ, Sisti HM, Hao J, Rocher AB, McCall T, Hof PR, *et al*. (2004): Chronic behavioral stress induces apical dendritic reorganization in pyramidal neurons of the medial prefrontal cortex. Neuroscience 125: 1–6.
12. Ito H, Nagano M, Suzuki H, Murakoshi T (2010): Chronic stress enhances synaptic plasticity due to disinhibition in the anterior cingulate cortex and induces hyper-locomotion in mice. Neuropharmacology 58:746–757.
13. Barthas F, Sellmeijer J, Hugel S, Waltisperger E, Barrot M, Yalcin I (2015): The anterior cingulate cortex is a critical hub for pain-induced depression. Biol Psychiatry 77:236–245.
14. Duric V, Banasr M, Licznerski P, Schmidt HD, Stockmeier CA, Simen AA, *et al*. (2010): A negative regulator of MAP kinase causes depressive behavior. Nat Med 16:1328–1332.
15. Iio W, Matsukawa N, Tsukahara T, Kohari D, Toyoda A (2011): Effects of chronic social defeat stress on MAP kinase cascade. Neurosci Lett 504:281–284.
16. Boutros T, Chevet E, Metrakos P (2008): Mitogen-activated protein (MAP) kinase/MAP kinase phosphatase regulation: Roles in cell growth, death, and cancer. Pharmacol Rev 60:261–310.
17. Li J, Gorospe M, Hutter D, Barnes J, Keyse SM, Liu Y (2001): Transcriptional induction of MKP-1 in response to stress is associated with histone H3 phosphorylation-acetylation. Mol Cell Biol 21: 8213–8224.
18. Casals-Casas C, Alvarez E, Serra M, de la Torre C, Farrera C, Sanchez-Tillo E, *et al*. (2009): CREB and AP-1 activation regulates MKP-1 induction by LPS or M-CSF and their kinetics correlate with macrophage activation versus proliferation. Eur J Immunol 39: 1902–1913.
19. Boulle F, Massart R, Stragier E, Paizanis E, Zaidan L, Marday S, *et al*. (2014): Hippocampal and behavioral dysfunctions in a mouse model of environmental stress: Normalization by agomelatine. Transl Psychiatry 4:e485.
20. Chaumont J, Guyon N, Valera AM, Dugue GP, Popa D, Marcaggi P, *et al*. (2013): Clusters of cerebellar Purkinje cells control their afferent climbing fiber discharge. Proc Natl Acad Sci U S A 110:16223–16228.
21. Impey S, Mark M, Villacres EC, Poser S, Chavkin C, Storm DR (1996): Induction of CRE-mediated gene expression by stimuli that generate long-lasting LTP in area CA1 of the hippocampus. Neuron 16: 973–982.

22. Paxinos G, Franklin K (2012): Paxinos and Franklin's the Mouse Brain in Stereotaxic Coordinates, 4th ed. New York: Academic Press.
23. Yalcin I, Megat S, Barthas F, Waltisperger E, Kremer M, Salvat E, Barrot M (2014): The sciatic nerve cuffing model of neuropathic pain in mice. J Vis Exp (89). http://dx.doi.org/10.3791/51608.
24. Yalcin I, Coubard S, Bodard S, Chalon S, Belzung C (2008): Effects of 5,7-dihydroxytryptamine lesion of the dorsal raphe nucleus on the antidepressant-like action of tramadol in the unpredictable chronic mild stress in mice. Psychopharmacology (Berl) 200:497–507.
25. Nollet M, Le Guisquet AM, Belzung C (2013): Models of depression: Unpredictable chronic mild stress in mice. Curr Protoc Pharmacol chapter 5:unit 5.65.
26. Neidl R, Schneider A, Bousiges O, Majchrzak M, Barbelivien A, de Vasconcelos AP, *et al*. (2016): Late-life environmental enrichment induces acetylation events and nuclear factor κB-dependent regulations in the hippocampus of aged rats showing improved plasticity and learning. J Neurosci 36:4351–4361.
27. Rastogi R, Jiang Z, Ahmad N, Rosati R, Liu Y, Beuret L, *et al*. (2013): Rapamycin induces mitogen-activated protein (MAP) kinase phosphatase-1 (MKP-1) expression through activation of protein kinase B and mitogen-activated protein kinase kinase pathways. J Biol Chem 288:33966–33977.
28. Wang Z, Zang C, Rosenfeld JA, Schones DE, Barski A, Cuddapah S, *et al*. (2008): Combinatorial patterns of histone acetylations and methylations in the human genome. Nat Genet 40:897–903.
29. Karmodiya K, Krebs AR, Oulad-Abdelghani M, Kimura H, Tora L (2012): H3K9 and H3K14 acetylation co-occur at many gene regulatory elements, while H3K14ac marks a subset of inactive inducible promoters in mouse embryonic stem cells. BMC Genomics 13:424.
30. Maier JV, Brema S, Tuckermann J, Herzer U, Klein M, Stassen M, *et al*. (2007): Dual specificity phosphatase 1 knockout mice show enhanced susceptibility to anaphylaxis but are sensitive to glucocorticoids. Mol Endocrinol 21:2663–2671.
31. Molina G, Vogt A, Bakan A, Dai W, Queiroz de Oliveira P, Znosko W, *et al*. (2009): Zebrafish chemical screening reveals an inhibitor of Dusp6 that expands cardiac cell lineages. Nat Chem Biol 5:680–687.
32. Lin YW, Chuang SM, Yang JL (2003): ERK1/2 achieves sustained activation by stimulating MAPK phosphatase-1 degradation via the ubiquitin-proteasome pathway. J Biol Chem 278:21534–21541.
33. Choi BH, Hur EM, Lee JH, Jun DJ, Kim KT (2006): Protein kinase Cδ-mediated proteasomal degradation of MAP kinase phosphatase-1 contributes to glutamate-induced neuronal cell death. J Cell Sci 119:1329–1340.
34. Lin YW, Yang JL (2006): Cooperation of ERK and SCFSkp2 for MKP-1 destruction provides a positive feedback regulation of proliferating signaling. J Biol Chem 281:915–926.
35. Korhonen R, Moilanen E (2014): Mitogen-activated protein kinase phosphatase 1 as an inflammatory factor and drug target. Basic Clin Pharmacol Toxicol 114:24–36.
36. Sun H, Charles CH, Lau LF, Tonks NK (1993): MKP-1 (3CH134), an immediate early gene product, is a dual specificity phosphatase that dephosphorylates MAP kinase in vivo. Cell 75:487–493.
37. Lawan A, Shi H, Gatzke F, Bennett AM (2013): Diversity and specificity of the mitogen-activated protein kinase phosphatase-1 functions. Cell Mol Life Sci 70:223–237.
38. Licznerski P, Duman RS (2013): Remodeling of axo-spinous synapses in the pathophysiology and treatment of depression. Neuroscience 251:33–50.
39. Kuwano Y, Kim HH, Abdelmohsen K, Pullmann R Jr, Martindale JL, Yang X, *et al*. (2008): MKP-1 mRNA stabilization and translational control by RNA-binding proteins HuR and NF90. Mol Cell Biol 28:4562–4575.
40. Ananieva O, Darragh J, Johansen C, Carr JM, McIlrath J, Park JM, *et al*. (2008): The kinases MSK1 and MSK2 act as negative regulators of Toll-like receptor signaling. Nat Immunol 9:1028–1036.
41. Tsankova NM, Kumar A, Nestler EJ (2004): Histone modifications at gene promoter regions in rat hippocampus after acute and chronic electroconvulsive seizures. J Neurosci 24:5603–5610.
42. Pollack BP, Sapkota B, Boss JM (2009): Ultraviolet radiation-induced transcription is associated with gene-specific histone acetylation. Photochem Photobiol 85:652–662.
43. Sharma AK, Mansukh A, Varma A, Gadewal N, Gupta S (2013): Molecular modeling of differentially phosphorylated serine 10 and acetylated lysine 9/14 of histone H3 regulates their interactions with 14-3-3ζ, MSK1, and MKP1. Bioinform Biol Insights 7:271–288.
44. Creyghton MP, Cheng AW, Welstead GG, Kooistra T, Carey BW, Steine EJ, *et al*. (2010): Histone H3K27ac separates active from poised enhancers and predicts developmental state. Proc Natl Acad Sci U S A 107:21931–21936.
45. Lopez-Atalaya JP, Ito S, Valor LM, Benito E, Barco A (2013): Genomic targets, and histone acetylation and gene expression profiling of neural HDAC inhibition. Nucleic Acids Res 41:8072–8084.
46. Bousiges O, Vasconcelos AP, Neidl R, Cosquer B, Herbeaux K, Panteleeva I, *et al*. (2010): Spatial memory consolidation is associated with induction of several lysine-acetyltransferase (histone acetyltransferase) expression levels and H2B/H4 acetylation-dependent transcriptional events in the rat hippocampus. Neuropsychopharmacology 35:2521–2537.
47. Bousiges O, Neidl R, Majchrzak M, Muller MA, Barbelivien A, Pereira de Vasconcelos A, *et al*. (2013): Detection of histone acetylation levels in the dorsal hippocampus reveals early tagging on specific residues of H2B and H4 histones in response to learning. PLoS One 8:e57816.
48. Willner P (2005): Chronic mild stress (CMS) revisited: Consistency and behavioural-neurobiological concordance in the effects of CMS. Neuropsychobiology 52:90–110.
49. Kodama M, Russell DS, Duman RS (2005): Electroconvulsive seizures increase the expression of MAP kinase phosphatases in limbic regions of rat brain. Neuropsychopharmacology 30:360–371.
50. Sun YR, Wang XY, Li SS, Dong HY, Zhang XJ (2015): β-Asarone from *Acorus gramineus* alleviates depression by modulating MKP-1. Genet Mol Res 14:4495–4504.
51. Jackson KC 2nd, St Onge EL (2003): Antidepressant pharmacotherapy: Considerations for the pain clinician. Pain Pract 3:135–143.
52. Max MB, Lynch SA, Muir J, Shoaf SE, Smoller B, Dubner R (1992): Effects of desipramine, amitriptyline, and fluoxetine on pain in diabetic neuropathy. N Engl J Med 326:1250–1256.
53. Jeffrey KL, Camps M, Rommel C, Mackay CR (2007): Targeting dual-specificity phosphatases: Manipulating MAP kinase signalling and immune responses. Nat Rev Drug Discov 6:391–403.

Neurobiology of Disease

Hyperactivity of Anterior Cingulate Cortex Areas 24a/24b Drives Chronic Pain-Induced Anxiodepressive-like Consequences

Jim Sellmeijer,[1,2,3] Victor Mathis,[1] Sylvain Hugel,[1] Xu-Hui Li,[5] Qian Song,[5] Qi-Yu Chen,[5] Florent Barthas,[1] Pierre-Eric Lutz,[1] Meltem Karatas,[1] Andreas Luthi,[2] Pierre Veinante,[1] Ad Aertsen,[3] Michel Barrot,[1] Min Zhuo,[4,5] and Ipek Yalcin[1]

[1]Centre National de la Recherche Scientifique, Université de Strasbourg, Institut des Neurosciences Cellulaires et Intégratives, 67000 Strasbourg, France, [2]Friedrich Miescher Institute for Biomedical Research, 4058 Basel, Switzerland, [3]Faculty of Biology and Bernstein Center Freiburg, University of Freiburg, D-79104 Freiburg, Germany, [4]Department of Physiology, Faculty of Medicine, University of Toronto, Toronto, Ontario M5S 1A8, Canada, and [5]Center for Neuron and Brain Disease, Frontier Institutes of Science and Technology, Xi'an Jiaotong University, Xi'an, 710049, China

Pain associates both sensory and emotional aversive components, and often leads to anxiety and depression when it becomes chronic. Here, we characterized, in a mouse model, the long-term development of these sensory and aversive components as well as anxiodepressive-like consequences of neuropathic pain and determined their electrophysiological impact on the anterior cingulate cortex (ACC, cortical areas 24a/24b). We show that these symptoms of neuropathic pain evolve and recover in different time courses following nerve injury in male mice. *In vivo* electrophysiological recordings evidence an increased firing rate and bursting activity within the ACC when anxiodepressive-like consequences developed, and this hyperactivity persists beyond the period of mechanical hypersensitivity. Whole-cell patch-clamp recordings also support ACC hyperactivity, as shown by increased excitatory postsynaptic transmission and contribution of NMDA receptors. Optogenetic inhibition of the ACC hyperactivity was sufficient to alleviate the aversive and anxiodepressive-like consequences of neuropathic pain, indicating that these consequences are underpinned by ACC hyperactivity.

Key words: anterior cingulate cortex; anxiety; depression; electrophysiology; neuropathic pain; optogenetics

Significance Statement

Chronic pain is frequently comorbid with mood disorders, such as anxiety and depression. It has been shown that it is possible to model this comorbidity in animal models by taking into consideration the time factor. In this study, we aimed at determining the dynamic of different components and consequences of chronic pain, and correlated them with electrophysiological alterations. By combining electrophysiological, optogenetic, and behavioral analyses in a mouse model of neuropathic pain, we show that the mechanical hypersensitivity, ongoing pain, anxiodepressive consequences, and their recoveries do not necessarily exhibit temporal synchrony during chronic pain processing, and that the hyperactivity of the anterior cingulate cortex is essential for driving the emotional impact of neuropathic pain.

Introduction

Mood disorders, such as anxiety and depression, are frequently observed in patients suffering from chronic pain, which adds dramatically to the patients' pain burden (Radat et al., 2013). Preclinical studies have shown that the anxiodepressive-like consequences of chronic pain, as in neuropathic pain condition, can be studied in murine models (Narita et al., 2006; Yalcin et al., 2011; Alba-Delgado et al., 2013) and further highlight the im-

Received Nov. 7, 2017; revised Jan. 10, 2018; accepted Feb. 10, 2018.

Author contributions: A.L., A.A., M.B., M.Z., and I.Y. designed research; J.S., V.M., S.H., X.-H.L., Q.S., Q.-Y.C., F.B., M.K., and I.Y. performed research; J.S., S.H., X.-H.L., Q.S., Q.-Y.C., F.B., P.-E.L., P.V., A.A., M.Z., and I.Y. analyzed data; J.S. and I.Y. wrote the paper.

This work was supported by the Centre National de la Recherche Scientifique Contract UPR3212, the University of Strasbourg, the NeuroTime Erasmus Mundus Joint doctorate, and Brain & Behavior Research Foundation National Alliance for Research on Schizophrenia and Depression Young Investigator Grant 18893 to I.Y. P.-E.L. was supported by Fondation pour la Recherche Médicale and Fondation Deniker fellowships. M.Z. was supported by Canada Research Chair, Canadian Institutes of Health Research Operating Grant MOP-124807, and Azrieli Neurodevelopmental Research Program and Brain Canada. We thank Stéphane Doridot for assistance in breeding mice and in genotyping; Elaine Gravel for technical support; and Dr. Modesto R. Peralta for English editing.

The authors declare no competing financial interests.

Correspondence should be addressed to Dr. Ipek Yalcin, Centre National de la Recherche Scientifique, Université de Strasbourg, Institut des Neurosciences Cellulaires et Intégratives, 67000 Strasbourg. E-mail: yalcin@inci-cnrs.unistra.fr.

DOI:10.1523/JNEUROSCI.3195-17.2018

 0270-6474/18/383102-14$15.00/0

portance of the time factor in the development of these consequences (Yalcin et al., 2011; Barthas et al., 2015). It has been recently shown that depressive-like behaviors are still present 2 weeks after recovery from mechanical hypersensitivity in an animal model of neuropathic pain (Dimitrov et al., 2014), raising the question of whether these consequences of chronic pain might be maintained in the long-term independently from sensory aspects.

The anterior cingulate cortex (ACC) is involved in the processing of both pain and mood-related information (Shackman et al., 2011; Bliss et al., 2016). The implication of the ACC in depression is supported by a hyperactivity of the ACC in depressed patients (Mayberg et al., 1999; Drevets et al., 2002; Yoshimura et al., 2010), and by changes in the mouse ACC transcriptome that are correlated with depressive-like behaviors in the chronic stress model (Surget et al., 2009). Clinical imaging studies also show the recruitment of the ACC in pain processing (Peyron et al., 2000), and preclinical studies more precisely associate the activation of ACC neurons with pain-like aversive (Johansen et al., 2001; Barthas et al., 2015) or fearful (Tang et al., 2005) behaviors. Potentiation of synaptic responses (Xu et al., 2008; Chen et al., 2014), disinhibition (Blom et al., 2014), and increased excitability (Li et al., 2010; Cordeiro Matos et al., 2015) are also observed *ex vivo* in the ACC in rodent models of chronic pain. *In vivo* studies further show that a lesion of the ACC prevents both chronic pain-induced anxiodepressive-like behaviors (Barthas et al., 2015) and the aversiveness of ongoing pain (Johansen et al., 2001; King et al., 2009; Qu et al., 2011; Barthas et al., 2015). In addition, it has been reported that (1) optogenetic activation of pyramidal neurons within the ACC is sufficient to induce anxiodepressive-like behaviors in naive mice (Barthas et al., 2015) and that (2) these behaviors are associated with transcriptomic changes in the ACC (Barthas et al., 2017). Finally, presynaptic LTP in the ACC has been linked to pain-related anxiety (Koga et al., 2015).

Accordingly, the ACC seems to be a critical brain region implicated in different symptoms of chronic pain, and especially in its anxiodepressive-like consequences (Barthas et al., 2015; Koga et al., 2015).

In the present study, we first aimed at characterizing the long-term evolution, over 6 months, of mechanical hypersensivity, of the aversive state induced by ongoing pain, and of the anxiodepressive-like consequences of neuropathic pain in mice using the "cuff" model. This model, based on sciatic nerve cuffing, has the advantage of displaying spontaneous recovery from mechanical allodynia (Yalcin et al., 2014b), which allows studying the behavioral consequences of neuropathic pain in the presence and absence of hypersensitivity. We also determined the time course of *in vivo* electrophysiological alterations accompanying these various symptoms within the ACC (cortical areas 24a/24b) (Fillinger et al., 2017b), and correlated them to the different stages of the pathology.

This long-term characterization evidenced that the mechanical hypersensitivity, aversiveness of ongoing pain, and anxiety/depressive-like consequences of neuropathic pain evolve in distinct time courses. The *in vivo* electrophysiological recordings further showed a correlation between ACC hyperactivity and the aversive and anxiodepressive-like consequences. These results are reinforced by whole-cell patch-clamp recordings highlighting a facilitation of excitatory synaptic transmission onto ACC pyramidal neurons in cuff-implanted animals showing depressive-like consequences. Moreover, we showed that optogenetic inhibition of the ACC was sufficient to counteract the chronic pain-induced emotional consequences, which supports a causal link between ACC hyperactivity and the emotional aspects of neuropathic pain.

Materials and Methods

Animals

Experiments were conducted using male adult C57BL/6J (RRID:IMSR_JAX:000664) mice (Charles River), group-housed with a maximum of 5 animals per cage and kept under a reversed 12 h light/dark cycle. Only the animals used for optogenetic experiments were single housed after the optic fiber implantation to avoid possible damage to the implant. Behavioral tests were conducted during the dark phase under red light. The Chronobiotron animal facilities are registered for animal experimentation (Agreement A67-2018-38), and protocols were approved by the local ethical committee of the University of Strasbourg (CREMEAS, #02015021314412082).

Surgical procedures

Surgical procedures were performed under ketamine/xylazine anesthesia (ketamine 17 mg/ml, xylazine 2.5 mg/ml; i.p., 4 ml/kg) (Centravet).

Neuropathic pain model. Neuropathic pain was induced by implanting a 2 mm section of PE-20 polyethylene tubing (Harvard Apparatus) around the main branch of the right sciatic nerve (Benbouzid et al., 2008; Barrot, 2012; Yalcin et al., 2014b). Before surgery, animals were assigned to experimental groups according to their initial mechanical nociceptive threshold, to even out the average mechanical threshold among groups. Animals in the sham condition underwent the same procedure without cuff implantation.

Virus injection. After anesthesia, C57BL/6J mice were placed in a stereotaxic frame (Kopf). The 0.5 μl of AAV5-CaMKIIa-eArchT3.0-EYFP (UNC Vector core) was injected bilaterally in the ACC (areas 24a/24b) using a 5 μl Hamilton syringe (0.05 μl/min, coordinates for the ACC: 0.7 mm from bregma, lateral: $\pm$0.3 mm, dorsoventral: $-$1.5 mm from the skull). After injection, the 32 gauge needle remained in place for 10 min and then the skin was sutured.

Optic fiber cannula implantation. Four weeks after virus injection, the animals underwent optic fiber cannula implantation. The mice were implanted unilaterally over the site of virus injection. Cannulas were implanted in the left hemisphere in half of each experimental group, whereas the other half received the implant in the right hemisphere. The optic fiber cannula was 1.7 mm long and 220 μm in diameter. The cannula was inserted 1.5 mm deep in the brain (MFC_220/250–0.66_1.7mm_RM3_FLT, Doric Lenses) (Barthas et al., 2015).

Optogenetic procedures

After a 3 to 7 d recovery period, we performed behavioral experiments. Green laser light (custom assembly, Green 520 nm, 16 mW, Miniature Fiber Coupled Laser Diode Module, Doric Lenses) was delivered through a 0.75-m-long monofiber optic patch chord (MFP_240/250/2000–0.63_0.75m_FC-CM3, Doric Lenses) that was mounted to the optic fiber implant on the skull. Optogenetic inhibition was performed either before or during behavioral testing, by continuous light for 5 min with a power of 16 mW. Control animals underwent the same procedures but the light was turned off during stimulation protocols.

Behavioral analysis

Behavioral testing was performed during the dark phase, under red light. While each mouse went through different tests, those were conducted according to the following rules: excepted for the von Frey results, no mouse went twice through the same test (i.e., the different time points (TPs) for a given test were performed on independent sets of animals); the forced swim test was always considered as terminal (i.e., no other test was done on mice after they went through forced swimming). Each graph displayed in Figure 2 is from a given (single) batch of animals, with Sham and Cuff mice from this batch tested on the same day(s) to always ensure internal control, and with von Frey data always available the same week for these mice. Thus, for this general characterization, we did not mix results from different batches within a given graph of Figure 2, and we always had the hypersensitivity status of the animals to justify the hyper-

sensitivity component of the TP clustering. Mechanical threshold and anxiodepressive-like behaviors of animals used for electrophysiology studies were determined before recordings.

Nociceptive testing. von Frey filaments were used to determine the mechanical threshold of hindpaw withdrawal (Bioseb). Mice were placed in Plexiglas boxes (7 cm × 9 cm × 7 cm) on an elevated mesh screen. After 15 min habituation, animals were tested by applying a series of ascending forces (0.16–8 g) on the plantar surface of each hindpaw. Each filament was tested 5 times per paw, applied until it just bent (Yalcin et al., 2014b; Barthas et al., 2015). The threshold was defined as 3 or more withdrawals observed out of the 5 trials. To characterize changes in mechanical thresholds during an extended period, we tested animals before and at given TPs after sciatic nerve surgery. The animals used for optogenetic inhibition of the ACC were tested before sciatic nerve surgery and before the behavioral tests. Finally, we tested the animals during light stimulation to see whether optogenetic inhibition affected mechanical thresholds.

Conditioned place preference (CPP). To test the motivational drives resulting from the aversive state induced by ongoing pain and from its relief by clonidine, a single-trial CPP paradigm was used (King et al., 2009). In this test, animals develop a preference to a clonidine-paired chamber due to both pain relief in this environment and avoidance for the saline-paired chamber associated with ongoing pain. The apparatus consisted of 3 Plexiglas chambers separated by manually operated doors (Imetronic). Two chambers (15 cm × 24 cm × 33 cm), distinguished by the texture of the floor and by the wall patterns, were connected by a central chamber (15 cm × 11 cm × 33 cm). Animals went through a 3 d preconditioning period during which they had access to all chambers for 30 min each day. Time spent in each chamber was analyzed to control for the lack of preference for one of the chambers. Animals spending >75% or <25% of the total time in one of the chambers were excluded from the study. On the conditioning day (day 4), mice first received intrathecal saline (10 μl) and were placed in a conditioning chamber. Four hours later, mice received clonidine (10 μg/10 μl), an α2-adrenoceptor agonist inducing analgesia after intrathecal administration, and were placed in the opposite chamber. Conditioning lasted 15 min per chamber, without allowing the animal to access the other chambers. On the fifth day, mice were placed in the center chamber, with free access to both conditioning chambers, and the time spent in each chamber was recorded for 30 min. CPP was assessed in separate sets of mice corresponding to 8 weeks (TP2), 14 weeks (TP3), and 22 weeks (TP4) after cuff implantation. The exact TP status of the animals was each time determined using the von Frey test for mechanical hypersensitivity and by using the novelty suppressed feeding test for the anxiodepressive-like state.

To study whether optogenetic inhibition of the ACC caused a preference, we used another version of the CPP test, with a custom-made box with 2 chambers (23 cm × 22 cm × 16 cm), distinguishable by different wall patterns, and connected to each other by a single sliding door. The test lasted 4 d. On the first day, animals were habituated to the testing box by allowing them full access to both compartments for 5 min. During the second and third days, animals went through a conditioning period. For this purpose, during the mornings, the animals were placed in the compartment where they received no-light stimulation, whereas during the afternoon sessions the animals were light-stimulated following the above-mentioned protocol. Control animals underwent the same procedures, but during the afternoon session the laser light remained off. On the fourth day, we placed the animal at the level of the sliding door and measured the time spent in each compartment during 5 min.

Dark-light test. To measure anxiety-like behavior, we performed the dark-light test (Vogt et al., 2016), with a two compartment testing box (18 cm × 18 cm × 14.5 cm) connected by a dark tunnel (8.5 cm × 7 cm × 6 cm). One compartment was brightly illuminated (1500 lux), whereas the other was dark. Mice were placed in the dark compartment at the beginning of the test, and the time spent in the lit compartment was recorded for 5 min. This test was performed 2, 8, 11, and 15 weeks after sciatic nerve surgery in different sets of animals.

Novelty suppressed feeding (NSF) test. The NSF test was used to assess anxiodepressive-like behavior as it induces a conflict between the drive to eat and the fear of venturing into the center of the box (Yalcin et al., 2011; Barthas et al., 2015, 2017). For this test, we used a plastic box with the floor covered with 2 cm of sawdust. Animals were food deprived for 24 h. At the time of testing, a single pellet of food was placed in the middle of the testing chamber under 7 lux, and the latency to eat the pellet was recorded within a 5 min period. The NSF test was performed 2, 8, 11, 16, 18, and 21 weeks after sciatic nerve surgery in independent sets of animals. For the optogenetic experiment, the NSF test was performed immediately after the inhibition procedure.

Splash test. This test was used to measure grooming behavior indirectly (Yalcin et al., 2011; Barthas et al., 2015) because decreased grooming can be related to the loss of interest in performing self-relevant tasks. This behavior was measured for 5 min after spraying a 10% sucrose solution on the coat of the animals. The splash test was performed on animals 3, 9, 12, 14, and 16 weeks after the peripheral nerve injury in independent sets of animals. For the optogenetic experiment, the splash test was performed during the inhibition procedure.

Forced swimming test. This test was performed to evaluate despair-like behavior (Porsolt et al., 1977). We lowered the mouse into a glass cylinder (height 17.5 cm, diameter 12.5 cm) containing 11.5 cm of water (23°C–25°C). The test duration was 6 min; but because only little immobility was observed during the first 2 min, we only quantified the duration of immobility during the last 4 min of the test. We considered the mouse to be immobile when it floated upright in the water, with only minor movements to keep its head above the water. This test was performed 7, 14, 17, 18, and 21 weeks after the sciatic nerve surgery in different sets of animals.

Locomotor activity. At three different TPs, locomotor activity was monitored in both sham and cuff-implanted mice. Mice were individually placed in activity cages with photocell beams. The number of beam breaks was recorded over 1 h.

Ex vivo *electrophysiological recordings*

We performed whole-cell patch-clamp recordings of neurons from the layer II/III of the ACC. Local electrical stimulation was delivered by a bipolar stimulation electrode placed in layer V/VI of the ACC. For these experiments, mice were killed by decapitation and the brain was removed, then immediately immersed in cold (0°C-4°C) sucrose-based ACSF containing the following (in mM): 2 kynurenic acid, 248 sucrose, 11 glucose, 26 $NaHCO_3$, 2 KCl, 1.25 KH_2PO_4, 2 $CaCl_2$, and 1.3 $MgSO_4$ (bubbled with 95% O_2 and 5% CO_2). Transverse slices (300 μm thick) were cut with a vibratome (VT1000S, Leica). Slices were maintained at room temperature in a chamber filled with ACSF containing the following (in mM): 126 NaCl, 26 $NaHCO_3$, 2.5 KCl, 1.25 NaH_2PO_4, 2 $CaCl_2$, 2 $MgCl_2$, and 10 glucose (bubbled with 95% O_2 and 5% CO_2; pH 7.3; 310 mOsm measured). Slices were transferred to a recording chamber and continuously superfused with ACSF saturated with 95% O_2 and 5% CO_2. Pyramidal ACC neurons were recorded in the whole-cell patch configuration. Patch pipettes were pulled from borosilicate glass capillaries (Harvard Apparatus) using a P-1000 puller (Sutter Instruments). For optogenetic experiments performed in AAV5-CaMKIIa-eArchT3.0-EYFP-injected animals, pipettes were filled with a solution containing the following (in mM): 145 KCl, 10 HEPES, and 2 $MgCl_2$. For mEPSCs recordings, pipettes were filled with a solution containing the following (in mM): 75 Cs_2SO_4, 10 CsCl, 10 HEPES, and 2 $MgCl_2$. The pH of intrapipette solutions was adjusted to 7.3 with KOH, and osmolarity to 310 mOsm with sucrose. With this solution, the patch pipettes had an open tip resistance from 3.5 to 4.5 MΩ. Recordings were performed in the presence of CNQX (10 μM) and bicuculline (10 μM) for optogenetic experiments, whereas mEPSCs were recorded with TTX (0.5 μM) in the recording solution. For optogenetic experiments, the ACC was illuminated with the same system used for the *in vivo* experiments (see below) triggered with WinWCP 4.3.5, the optic fiber being localized in the recording chamber at 3 mm from the recorded neuron. In voltage-clamp mode, the holding potential was fixed at −60 mV, and in current-clamp mode at a holding current allowing maintaining the resting neuron at ~−60 mV. Recordings were acquired with WinWCP 4.3.5 (courtesy of

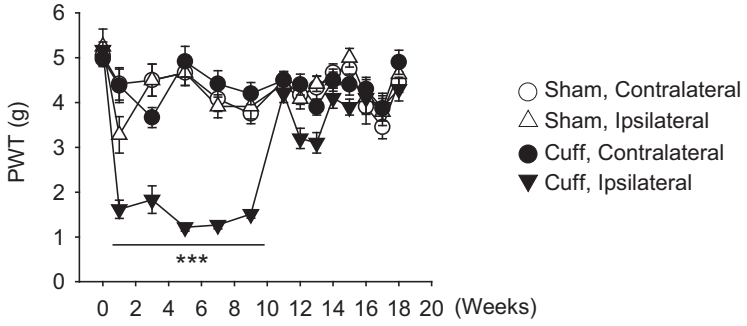

Figure 1. Nerve injury induces mechanical hypersensitivity. In C57BL/6J mice, unilateral sciatic nerve compression induces an ipsilateral long-lasting mechanical hypersensitivity which lasts ~11 weeks. After this period, mechanical thresholds return back to sham levels spontaneously. Sham, $n = 24$; Cuff, $n = 24$. Data are mean ± SEM. ***$p < 0.001$. PWT, Paw withdrawal threshold.

Dr. J. Dempster, University of Strathclyde, Glasgow, United Kingdom). All recordings were performed at 34°C.

In vivo *electrophysiological recordings*

Animals were anesthetized in an induction box with a 2% isoflurane/air mixture (Vetflurane, Virbac) and then placed in a Kopf stereotaxic frame (KOPF 1730) equipped with a tight nose mask to continuously deliver the anesthesia.

A 1 × 1.4 mm cranial window was prepared directly anterior to the bregma, ranging from −0.7 to 0.7 mm lateral from the midline. The dura was opened to lower the glass electrode into the brain. Recordings of spontaneous activity were performed using sharp electrodes pulled from borosilicate micropipettes (1.2 mm outer and 0.69 mm inner diameters, Harvard Apparatus, 30–0044), with a Narashige pipette puller (tip diameter < 1 μm, resistance ±25 MΩ). The glass electrodes were filled with 0.5 M potassium acetate solution. The signal from the electrode was recorded by a silver wire, amplified using an operational amplifier (Neurodata IR-183A, Cygnus Technology; gain × 10), and then amplified further and filtered using a differential amplifier (Model 440, Brownlee Precision; gain × 100; bandpass filter 0.1–10 kHz). The signal was then digitized with a CED digitizer (sampling rate: 20 kHz) and recorded with Spike2 software (version 7.12b, Cambridge Electronic Design). Raw data files were exported into MATLAB (The MathWorks) and analyzed with custom-made MATLAB scripts, which are available in a bitbucket repository entitled Sellmeijer, 2016.

During the recording procedure, isoflurane anesthesia was lowered to 0.5%–0.75% and was monitored by regular paw pinching. The glass pipette was slowly lowered using a Scientifica one-dimensional micromanipulator, and recordings were made between 0.2 and 1.0 mm anterior to the bregma ranging from −0.5 to 0.5 mm from the midline, which corresponds to layers II/III of the cortex. Neurons were recorded from the brain surface until 1500 μm deep. Once stable cell activity was detected, a 5 min segment of spontaneous activity was recorded. Recording sites were marked by iontophoretically injecting a 4% Pontamine Sky blue dye (Sigma-Aldrich) in 0.5 M sodium-acetate solution (Sigma-Aldrich). At the end of the recording, the mice were perfused, the brain was collected, and 40 μm sections were cut on a cryostat. The position of recorded cells was registered using the microdrive reference point with respect to the Pontamine Sky blue dye deposit.

Firing rate and bursting activity were calculated. Bursting activity, defined as ≥3 spikes within a 50 ms time window, was analyzed by calculating the total number of bursting events within a 90 s data segment. Neurons in which >20% of action potentials occurred in a bursting event were considered bursting neurons. The average number of spikes within a bursting event was also calculated.

Experimental design and statistical analysis

Before starting experiments, based on our previous behavioral studies, we estimated the sample size by using power analysis. All behavioral tests, *in vivo* electrophysiological recordings, and experiments using optogenetic approach were replicated several times. For each group, the mechanical sensitivity and anxiodepressive-like behaviors were analyzed before recordings and optogenetic manipulation. The number of animals per group is indicated in each behavioral graph; and both the number of recorded cells and of animals per group is indicated in each electrophysiology graph. Data are mean ± SEM. When data were not normally distributed, the Kruskal–Wallis test was performed followed by Mann–Whitney *U post hoc* tests to compare the means. When data were normally distributed, groups were compared with ANOVA multiple group comparisons followed by Duncan *post hoc* analysis, or with the Student's *t* test. For the von Frey results, we used a multifactorial ANOVA, considering paws (ipsilateral vs contralateral) and TPs as two levels of dependent data, and surgery (sham vs cuff) as independent groups. Significance level was set to $p < 0.05$. Statistical analyses were performed with MATLAB 2014a (The MathWorks) and Statistica version 7.1 (Statsoft).

Results

Long-term characterization of different symptoms of neuropathic pain

It has been previously shown that the anxiodepressive-like consequences of neuropathic pain evolve over time (Suzuki et al., 2007; Gonçalves et al., 2008; Yalcin et al., 2011). Indeed, whereas mechanical hypersensitivity is immediately present following nerve injury in the cuff model, mice develop anxiety-related behaviors 3–4 weeks later, while depression-related behaviors are observed after 6–8 weeks (Yalcin et al., 2011). On the longer term, cuff-implanted animals recover spontaneously from mechanical hypersensitivity (example from one batch of mice: $F_{(13,260)} = 5.54$, $p = 6.9 \times 10^{-9}$; cuff<sham: first $p = 2.7 \times 10^{-6}$; week 3, $p = 8.8 \times 10^{-7}$; week 5, $p = 1 \times 10^{-6}$; week 7, $p = 1.8 \times 10^{-6}$; week 9, $p = 1.5 \times 10^{-6}$; Fig. 1). Depending on the considered batch of animals, this recovery happened between the 11th and 14th weeks after operation. However, it is to be noted that all mice displayed mechanical hypersensitivity up to the 10th weeks after operation, and that no mice was hypersensitive at 15 weeks after operation. This recovery from mechanical hypersensitivity raises the question of whether the aversiveness of ongoing pain and/or the anxiodepressive-like consequences of chronic pain also disappear or remain present.

As reported previously (Yalcin et al., 2011), the nerve-injured animals did not show anxiodepressive-like behaviors yet at 2 weeks after operation (dark-light test, Fig. 2*A*; NSF test, Fig. 2*C*) or at 3 weeks after operation (splash test, Fig. 2*B*), even though mechanical hypersensitivity was already present (VF: $p = 0.01$, Fig. 2*A*; $p = 0.0001$, Fig. 2*B*; $p = 0.001$, Fig. 2*C*). In the dark-light test, nerve-injured animals displayed increased anxiety-like behavior at 8 weeks after operation, as shown by the reduced time spent in the lit compartment ($p = 6.17 \times 10^{-4}$; Fig. 2*A*). This behavior disappeared at 11 and 15 weeks after operation, coinciding with the recovery from mechanical hypersensitivity in the same animals (Fig. 1). In contrast, in the splash test, decreased grooming behavior was present at 9 weeks after operation ($p = 0.01$), but also at 12 weeks ($p = 0.003$) and 14 weeks after operation ($p = 0.0011$) (Fig. 2*B*) despite that mechanical hypersensitivity was no longer present in these sets of animals at these last 2 TPs. The deficit in grooming behavior, however, disappeared at 16 weeks after operation (Fig. 2*B*). Recovery was even more delayed in the NSF test, for which an increased latency to feed was present at 8 ($p = 3.3 \times 10^{-4}$), 11 ($p = 0.0437$), and 16 weeks after operation ($p = 0.0016$) (with no mechanical hypersensitivity at

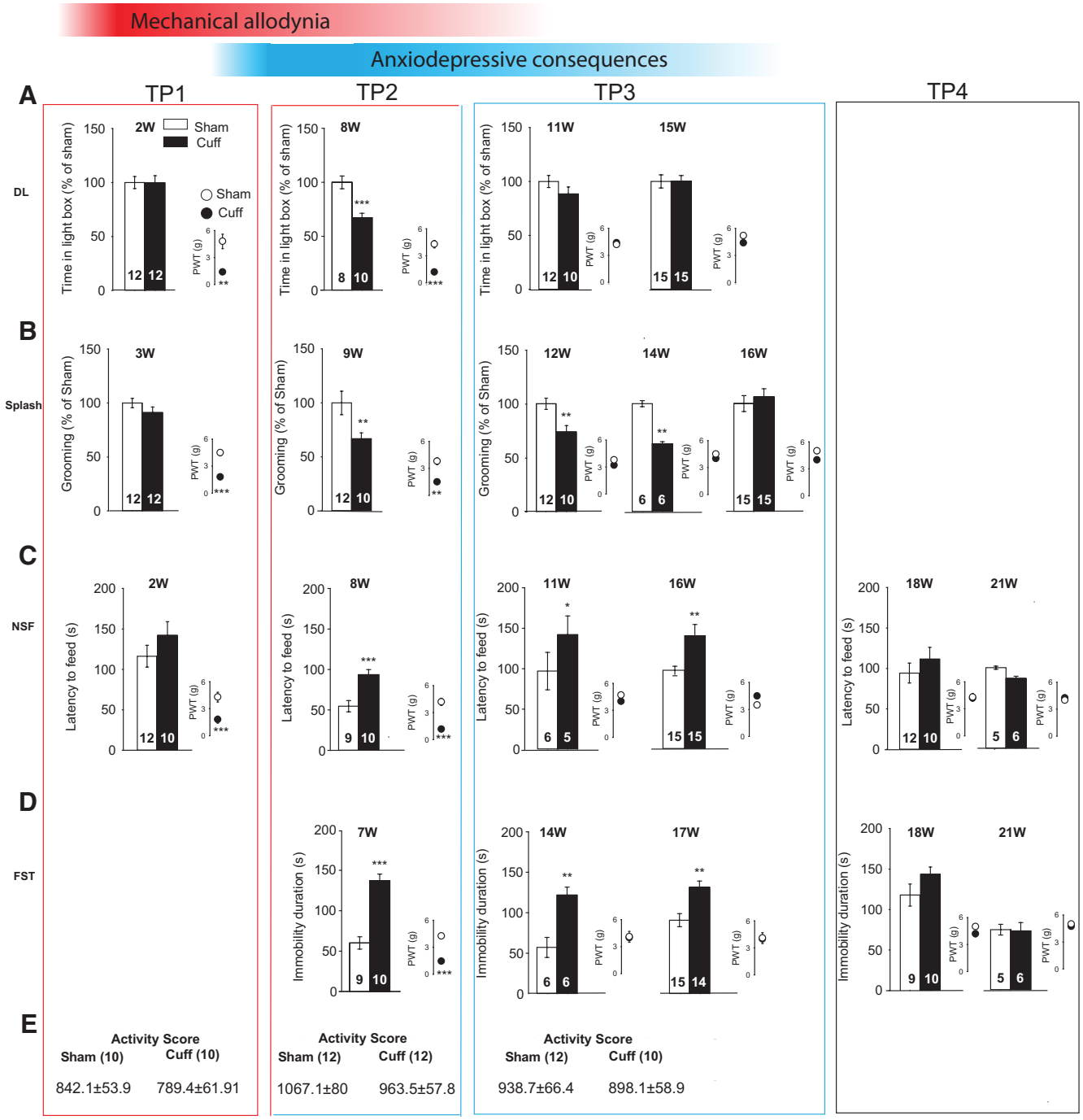

Figure 2. Long-term anxiodepressive-like consequences of neuropathic pain. Neuropathic pain induces anxiodepressive-like consequences, which disappear in a time-dependent manner. Sciatic nerve injury significantly: decreases the time spent in the lit compartment of the dark-light (DL) box at 8 but not at 2, 11, and 15 weeks (W) after operation (***A***), decreases grooming behavior in the splash test at 9, 12, and 14 but not at 3 and16 weeks after operation (***B***), increases the latency to feed in the NSF at 8, 11, 16 but not at 2, 18, 21 weeks after operation (***C***), increases immobility time at 7, 14, 17 but not at 18, 21 weeks after operation in the forced swimming test (FST) (***D***). Cuff-implanted animals did not show any locomotor activity deficits at TP1, TP2, and TP3 (***E***). For a given test, each TP was obtained in an independent set of mice and their corresponding von Frey results are presented nearby (***A–D***). TP1 corresponds to animals displaying mechanical hypersensitivity but not yet anxiodepressive-like consequences, TP2 corresponds to animals displaying both mechanical hypersensitivity and anxiodepressive-like consequences, TP3 corresponds to animals that recovered from mechanical hypersensitivity but still displayed depressive-like consequences, TP4 corresponds to animals that recovered from both mechanical hypersensitivity and anxiodepressive-like consequences. Data are mean ± SEM. Numbers in the bars or nearby activity scores indicate the number of animals. *$p < 0.05$, **$p < 0.01$, ***$p < 0.001$. For other TP data between 2 weeks and 9 weeks after operation, see Yalcin et al. (2011).

these last 2 TPs), with recovery at 18 and 21 weeks after operation (Fig. 2*C*). The presence of depressive-like behavior as assessed using the forced swimming test was also long-lasting. Indeed, nerve-injured mice spent more time immobile at 7 ($p = 4.33 \times 10^{-5}$), 14 ($p = 0.0043$), and 17 weeks after operation ($p = 0.0023$) (with no mechanical hypersensitivity at these last 2 TPs) (Fig. 2*D*), and returned back to sham level only at 18 and 21 weeks after operation (Fig. 2*D*). Each von Frey result obtained the same week as the anxiodepressive behavioral tests is presented near the anxiodepressive behavioral graph (Fig. 2*A–D*).

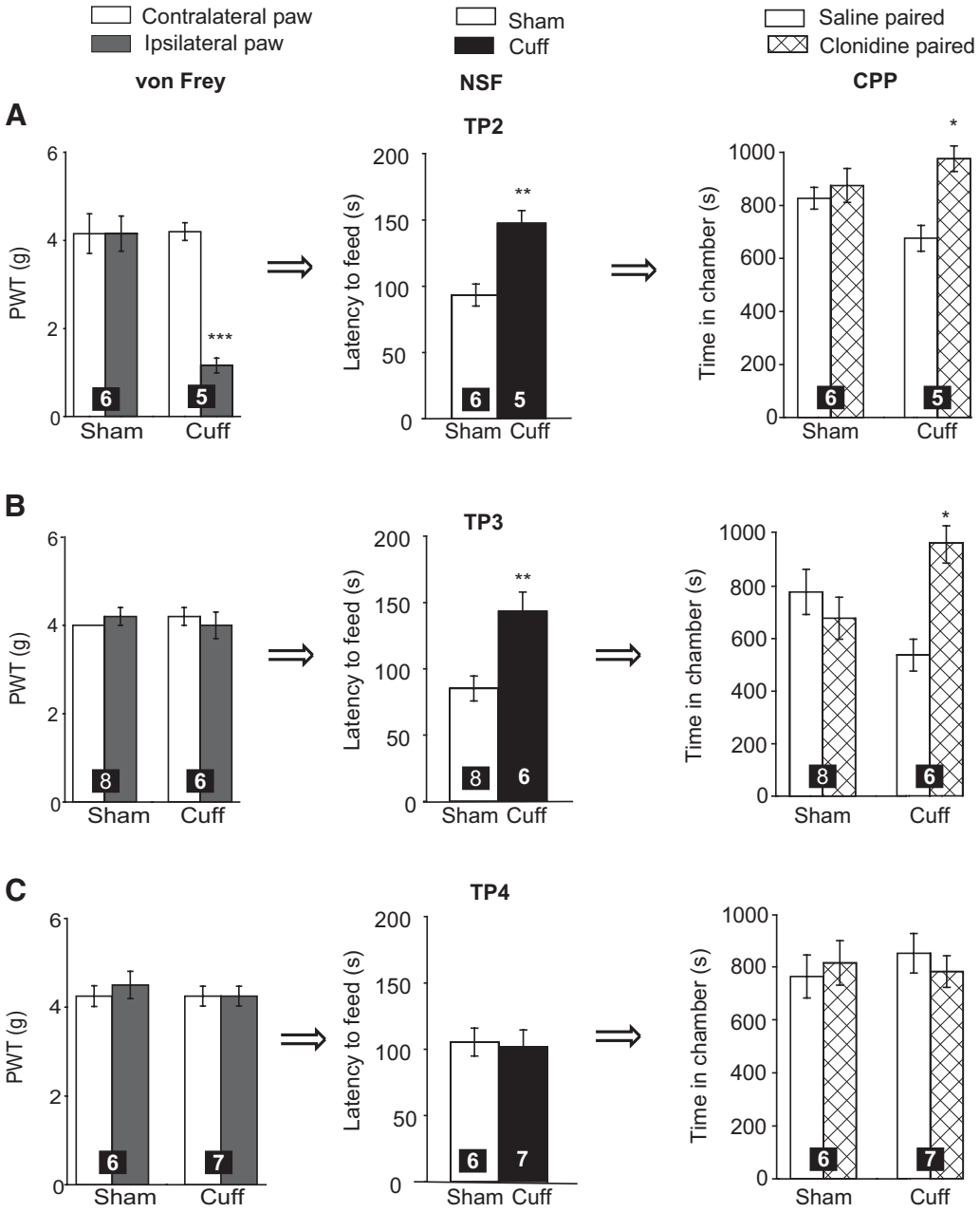

Figure 3. Nerve injury induces ongoing pain. ***A***, At TP2, animals displayed mechanical hypersensitivity, anxiodepressive-like behavior, and place preference for ongoing pain relief (10 μg clonidine, intrathecal). ***B***, At TP3, animals recovered from mechanical hypersensitivity but still displayed anxiodepressive-like consequences and place preference for ongoing pain relief. ***C***, At TP4, animals recovered from mechanical hypersensitivity and anxiodepressive-like behavior, and ongoing pain is no longer detected. Each TP corresponds to an independent experiment performed in separate sets of mice. Data are mean ± SEM. Numbers in the bars indicate the number of animals. *$p < 0.05$, **$p < 0.01$, ***$p < 0.001$. ** PWT, Paw withdrawal threshold.

Because the time course of recovery from mechanical hypersensitivity could slightly differ between batches of experiments, the results are presented according to 4 representative TPs for the rest of this study. TP1 corresponds to animals displaying mechanical hypersensitivity but not yet anxiodepressive-like consequences. TP2 corresponds to animals displaying both mechanical hypersensitivity and anxiodepressive-like consequences. TP3 corresponds to animals that recovered from mechanical hypersensitivity but still displayed depressive-like consequences. TP4 corresponds to animals that recovered from both mechanical hypersensitivity and anxiodepressive-like consequences.

As a control for behavioral tests, we checked the locomotor activity of animals over 1 h at different TPs and confirmed our previous reports (Barthas et al., 2015, 2017) by showing that locomotor activity was not significantly affected in cuff-implanted animals at the representative TP1, TP2, and TP3 (Fig. 2*E*).

We then tested the aversiveness of ongoing pain by using a CPP test. Clonidine was delivered intrathecally at lumbar level, which inhibits ascending inputs and leads to pain relief. Nerve-injured animals displayed a significant preference for the compartment associated with clonidine analgesia at TP2 ($F_{(1,9)} = 5.36$, $p = 0.04$; cuff saline vs cuff clonidine, $p = 0.017$; Figure 3*A*) but also at TP3 ($F_{(1,12)} = 5.219$, $p = 0.04$; cuff saline vs cuff clonidine, $p = 0.03$; Fig. 3*B*), despite the absence of mechanical hypersensitivity at this TP. Interestingly, this preference was no longer present at TP4 ($F_{(1,11)} = 0.36$, $p = 0.55$; Fig. 3*C*), suggesting a recovery from

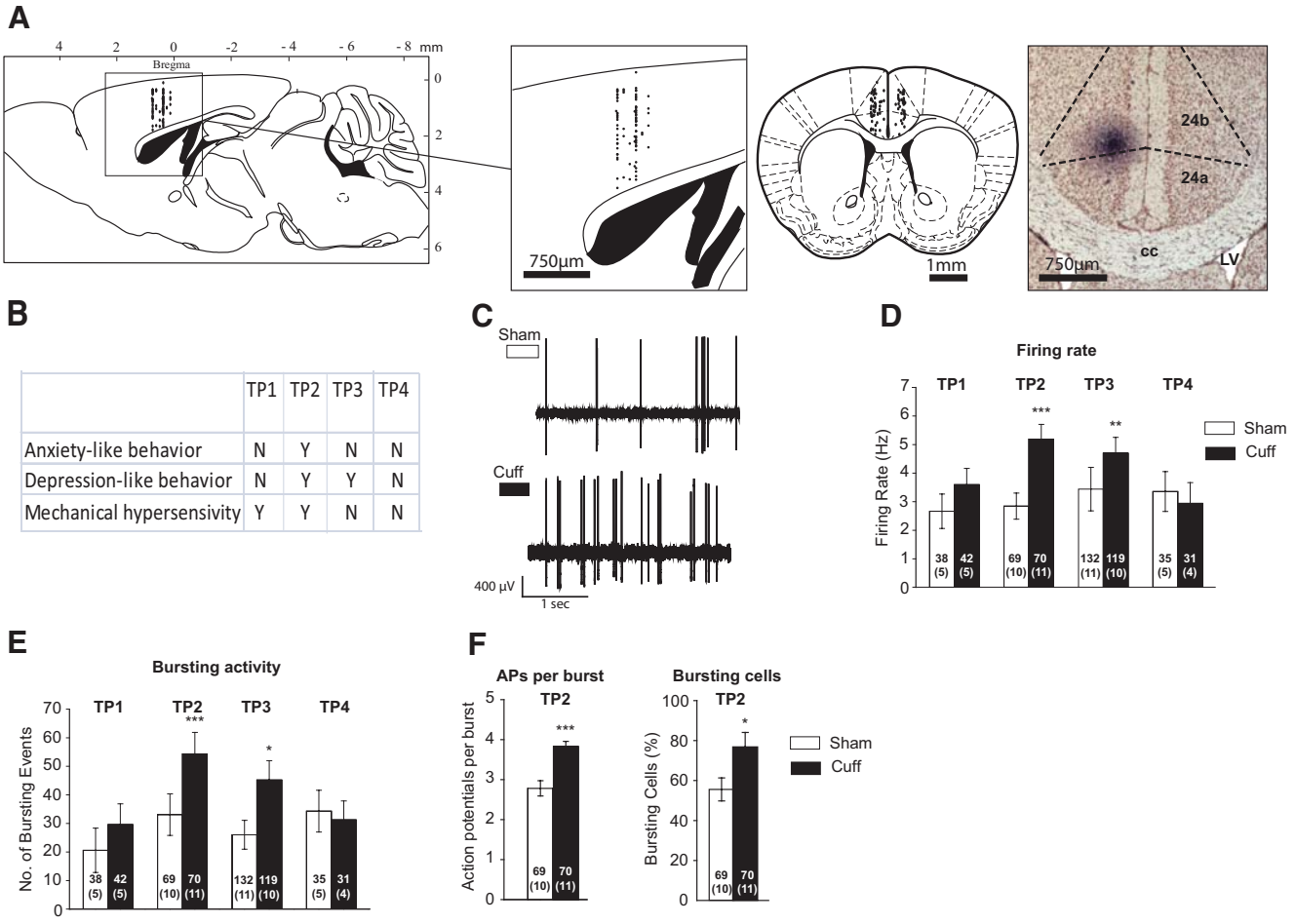

	TP1	TP2	TP3	TP4
Anxiety-like behavior	N	Y	N	N
Depression-like behavior	N	Y	Y	N
Mechanical hypersensivity	Y	Y	N	N

Figure 4. Increased ACC single-unit activity. ***A***, Illustration of the recording sites in the ACC (dots) on a sagittal and on a frontal plane. Right, Pontamine Sky blue dye deposit at the end of the recording. ***B***, Overview of the development and recovery of different aspects of neuropathic pain. Time frames of recorded animals correspond to 4 phenotypical TPs defined based on previous experiments (Fig. 2) and corresponding to the presence or absence of given behaviors. Each recorded animal was tested for mechanical hypersensitivity and anxiodepressive consequences. ***C***, Example of representative recordings from sham and nerve-injured animals at TP2. Single-unit firing rate (***D***) and bursting activity (***E***) are increased at TP2 and TP3 but not at TP1 and TP4. ***F***, Increased number of action potentials per burst and increased number of bursting cells at TP2. TP1 corresponds to animals displaying mechanical hypersensitivity but not yet anxiodepressive-like consequences. TP2 corresponds to animals displaying both mechanical hypersensitivity and anxiodepressive-like consequences. TP3 corresponds to animals that recovered from mechanical hypersensitivity but still displayed depressive-like consequences. TP4 corresponds to animals that recovered from both mechanical hypersensitivity and anxiodepressive-like consequences. Data are mean ± SEM. Numbers in the bars indicate the number of cells and animals. *$p < 0.05$, **$p < 0.01$, ***$p < 0.001$. cc, Corpus callosum; LV, Lateral ventricle.

ongoing pain. See also Figure 3*A–C* for the state of mechanical hypersensitivity (TP2, $p = 6.2 \times 10^{-5}$; TP3, $p = 0.34$; TP 4, $p = 0.58$) and of anxiodepressive-like consequences (TP2, $p = 0.0028$; TP3, $p = 0.0014$; TP4, $p = 0.83$) in the same mice.

Together, these data show that ongoing pain and the depressive-like consequences of neuropathic pain can persist for weeks after the recovery from mechanical hypersensitivity.

ACC hyperactivity coincides with anxiodepressive-like consequences of neuropathic pain

To understand whether the spontaneous activity of the ACC is affected along the time-dependent evolution of neuropathic pain symptoms, we performed *in vivo* single-unit electrophysiological recording (Fig. 4*A*) at 4 different TPs (Fig. 4*B*). ACC neurons from nerve-injured animals had a significantly higher *in vivo* spontaneous firing rate at TP2 ($p = 3.52 \times 10^{-7}$) and TP3 ($p = 0.0022$; Fig. 4*C*,*D*), which was associated with an increase in bursting activity (TP2: $p = 5.50 \times 10^{-5}$, TP3: $p = 0.017$; Fig. 4*E*), in the number of action potentials per burst ($p = 3.42 \times 10^{-5}$, Fig. 4*F*) and in the number of bursting cells ($p = 0.034$; Fig. 4*F*) in nerve-injured animals at TP2. In the absence of anxiodepressive-like behaviors (i.e., at TP1, before affective symptoms developed; and at TP4, after affective symptoms recovered), the firing rate and bursting activity remained similar between sham and nerve-injured animals (Fig. 4*D*,*E*). No significant lateralization effect was measured for firing rate and bursting activity in cuff-implanted animals (data not shown).

Enhancement of excitatory synaptic transmission in the ACC coincides with anxiodepressive-like consequences of neuropathic pain

To assess the impact of neuropathic pain on synaptic transmission of pyramidal neurons, we recorded both paired-pulse ratio and miniature synaptic currents at TP2, when nerve-injured animals displayed depressive-like behavior. There was a significant reduction in the paired-pulse ratio of electrically evoked EPSCs, which provides support for presynaptic changes in nerve-injured mice ($F_{(1,120)} = 30.8$, $p < 0.001$; Fig. 5*A*). Both the amplitude and frequency of mEPSCs (amplitude: sham mice 7.8 ± 0.4 pA, cuff mice 9.8 ± 0.6 pA, $p < 0.05$; frequency: sham mice 1.2 ± 0.1 Hz, cuff mice 2.2 ± 0.2 Hz, $p < 0.01$; Fig. 5*B*) were significantly increased in nerve-injured mice, indicating that the facilitation of

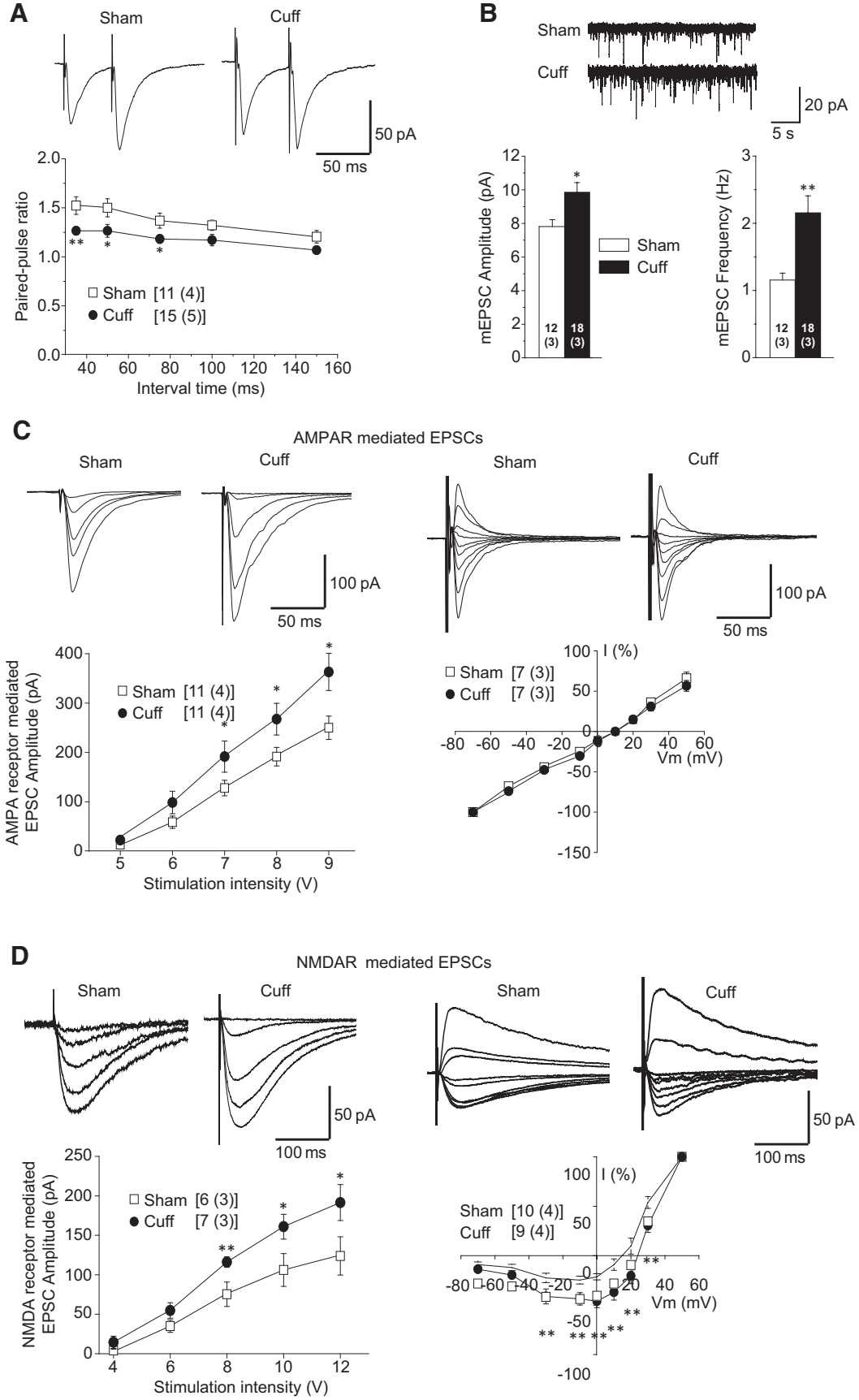

Figure 5. Facilitated presynaptic and postsynaptic ACC transmission in nerve-injured animals displaying depressive-like behaviors. ***A***, Samples (top) and summarized results (bottom) showed that the paired-pulse ratios, with recorded intervals of 35, 50, 75, 100, and 150 ms, were decreased in the cuff group compared with the sham group. ***B***, Samples (top) and summarized results (bottom) of the amplitude and frequency of mEPSCs. Both amplitude and frequency were increased in the cuff group compared with the sham group. (*Figure legend continues.*)

excitatory synaptic transmission onto pyramidal ACC neurons involved presynaptic and postsynaptic changes. Interestingly, both the slopes of the AMPAR-mediated input–output curve ($F_{(1,97)} = 17.1$, $p < 0.001$; Fig. 5*C*, left) and NMDAR-mediated input–output curve ($F_{(1,55)} = 7.7$, $p < 0.01$; Fig. 5*D*, left) were shifted to the left in nerve-injured mice, suggesting that an upregulation of AMPA and NMDA receptors could contribute to excitatory facilitation. We then tested the AMPAR and NMDAR-mediated *I–V* relationship and found that there was no difference in the AMPAR-mediated *I–V* between sham and nerve-injured mice ($F_{(1,108)} = 2.0$, $p = 0.15$; Fig. 5*C*, right). However, the NMDAR-mediated *I–V* curve differed between groups ($F_{(1,153)} = 61.3$, $p < 0.01$; Fig. 5*D*). When the same experiments were performed at TP3, which corresponds to animals still displaying depressive-like behaviors after recovery from mechanical hypersensitivity, we observed that the mEPSC frequency was still increased ($F_{(1,19)} = 8.974$; $p = 0.008$; Fig. 6), but not the paired-pulse ratio of evoked EPSCs. This finding indicates that the spontaneous release of glutamate was still enhanced in the ACC after the recovery from mechanical hypersensitivity. Neither the AMPAR nor the NMDAR-mediated input and output curves were altered. Interestingly, the NMDAR *I–V* curve remained different in the cuff group ($F_{(1,108)} = 15.54$; $p = 0.001$; Fig. 6).

Inhibition of the ACC relieves the emotional consequences of neuropathic pain

Based on our results demonstrating ACC hyperactivity in mice displaying anxiodepressive-like behaviors, we studied whether optogenetic inhibition of the ACC may counteract these consequences.

The delivery of AAV5-CaMKIIa-eArchT3.0-EYFP resulted in reliable virus transfection in the ACC, which was confirmed by EYFP fluorescence (Fig. 7*A*). To characterize the effect of green laser light illumination on transfected ACC neurons, we performed *ex vivo* electrophysiological recordings. Patch-clamp recordings showed that illumination with green light reliably inhibited spontaneous action potential firing in the current-clamp mode, and induced an outward current in the voltage-clamp mode (Fig. 7*B*).

In vivo, mechanical hypersensitivity was not affected by the ACC inhibition at either TP2 ($F_{(1,26)} = 60.29$, $p = 0.3 \times 10^{-8}$, cuff right < sham right, $p = 0.0001$) or TP3 ($F_{(1,20)} = 0.0032$, $p = 0.95$) (Fig. 7*C*). However, inhibition of the targeted ACC neurons induced a place preference in nerve-injured animals at both TPs (i.e., when mechanical hypersensitivity was still present) (TP2, $F_{(1,18)} = 5.42$, $p = 0.031$, cuff stimulated [light on] vs cuff control, $p = 0.006$) (Fig. 7*D*) or after it recovered (TP3, $F_{(1,8)} = 8.66$, $p = 0.018$, cuff stimulated [light on] vs cuff control, $p = 0.039$; Figure 7*D*), without having any effect in sham animals. These findings indicate that the inhibition of the CaMKIIa ACC neurons relieved the aversiveness of ongoing pain in nerve-injured mice.

Finally, we showed that optogenetic inhibition of the ACC also suppressed the anxiodepressive-like behaviors in nerve-injured animals, as observed by a normalization of grooming behavior in the splash test (Fig. 7*E*) at both TP2 ($p = 0.0033$, cuff no-light vs cuff light on) and TP3 ($p = 0.03$, cuff no-light vs cuff light on), and of the feeding latency in the NSF test at TP2 ($p = 0.0013$) (Fig. 7*F*). "No-light delivered" nerve-injured animals, however, still displayed characteristic chronic pain induced-behaviors (sham no-light vs cuff no-light grooming duration: $p = 0.03$, TP2; $p = 0.01$, TP3; Fig. 7*E*; sham no-light vs cuff no-light latency to feed: $p = 0.015$, TP2; $p = 0.015$, TP3; Fig. 7*F*). Together, our results show that a selective inhibition of ACC excitatory neurons is sufficient to alleviate the long-lasting consequences of neuropathic pain.

Discussion

We show here that different symptoms of neuropathic pain, including mechanical hypersensitivity, aversiveness of ongoing pain, and anxiodepressive-like consequences, display different time courses following nerve injury. The *in vivo* electrophysiological recordings showed an ACC hyperactivity coinciding with the time window of pain aversiveness and of anxiodepressive-like behaviors. *Ex vivo* patch-clamp recordings further supported ACC hyperactivity, as shown by increased excitatory postsynaptic transmission and increased contribution of NMDA receptors. Finally, our results show that optogenetic inhibition of the ACC can alleviate the aversiveness and anxiodepressive-like consequences of neuropathic pain.

A growing number of preclinical studies shows that the anxiodepressive-like consequences of chronic pain evolve over time (Yalcin et al., 2011; Alba-Delgado et al., 2013), raising the question of whether the various symptoms of neuropathic pain are interdependent or whether they develop separately. With the model and species used in this study, animals develop mechanical hypersensitivity immediately after nerve injury and spontaneously recover ~3 months later, which allows studying the behavioral consequences of neuropathic pain in the presence and absence of mechanical hypersensitivity. Patients with chronic pain also experience ongoing pain, which is rarely evaluated in preclinical studies. In animals, this symptom can be unmasked by alleviating the pain-related tonic aversive state in a CPP procedure (King et al., 2009; Barthas et al., 2015). For instance, lidocaine injected into the rostral ventromedial medulla, the brain area mediating descending modulation of pain (Wang et al., 2013), or spinal injection of clonidine (King et al., 2009; Barthas et al., 2015), induces place preference only in nerve-injured animals. In the present study, we also detected the presence of ongoing pain at TP3 (i.e., when mechanical hypersensitivity is no longer present), a finding that represents, to our knowledge, the first evidence in an animal model for a naturally occurring temporal dichotomy between evoked and ongoing pain. The hypersensitivity and ongoing pain that follow nerve injury have been proposed to share some mechanistic features. Indeed, both may imply an upregulation of voltage-gated Nav1.8 channels in primary afferent neurons (Yang et al., 2014), an alteration of descending pathways (Wang et al., 2013). and of spinal NK-1-positive ascending projections (King et al., 2011). Studies also pointed out that they can be distinguished mechanistically as well as neuroanatomically. An ACC lesion can block the aversiveness of ongoing pain in both neuropathic (Qu et al., 2011; Barthas et al., 2015) and inflammatory pain models without affecting mechanical hypersensitivity (Johansen et al., 2001; Chen et al., 2014; Barthas et al., 2015), whereas lesioning the posterior insular cortex can suppress the maintenance of mechanical hypersensitivity

←

(*Figure legend continued.*) ***C***, Samples (top) and summarized results (bottom) showed that the input– output curve of AMPARs-mediated EPSCs was steeper in the cuff group. However, the *I–V* curves were not changed. ***D***, Samples (top) and summarized results (bottom) showed that the input– output curve of NMDARs-mediated EPSCs was steeper in the cuff group. The *I–V* curve in the cuff group differed from that of the sham group. All experiments were performed at TP2 (8–9 weeks after surgery), which corresponds to animals displaying both mechanical hypersensitivity and anxiodepressive-like consequences. $*p < 0.05$, $**p < 0.01$. Numbers in bars or near group names indicate the numbers of cells and animals.

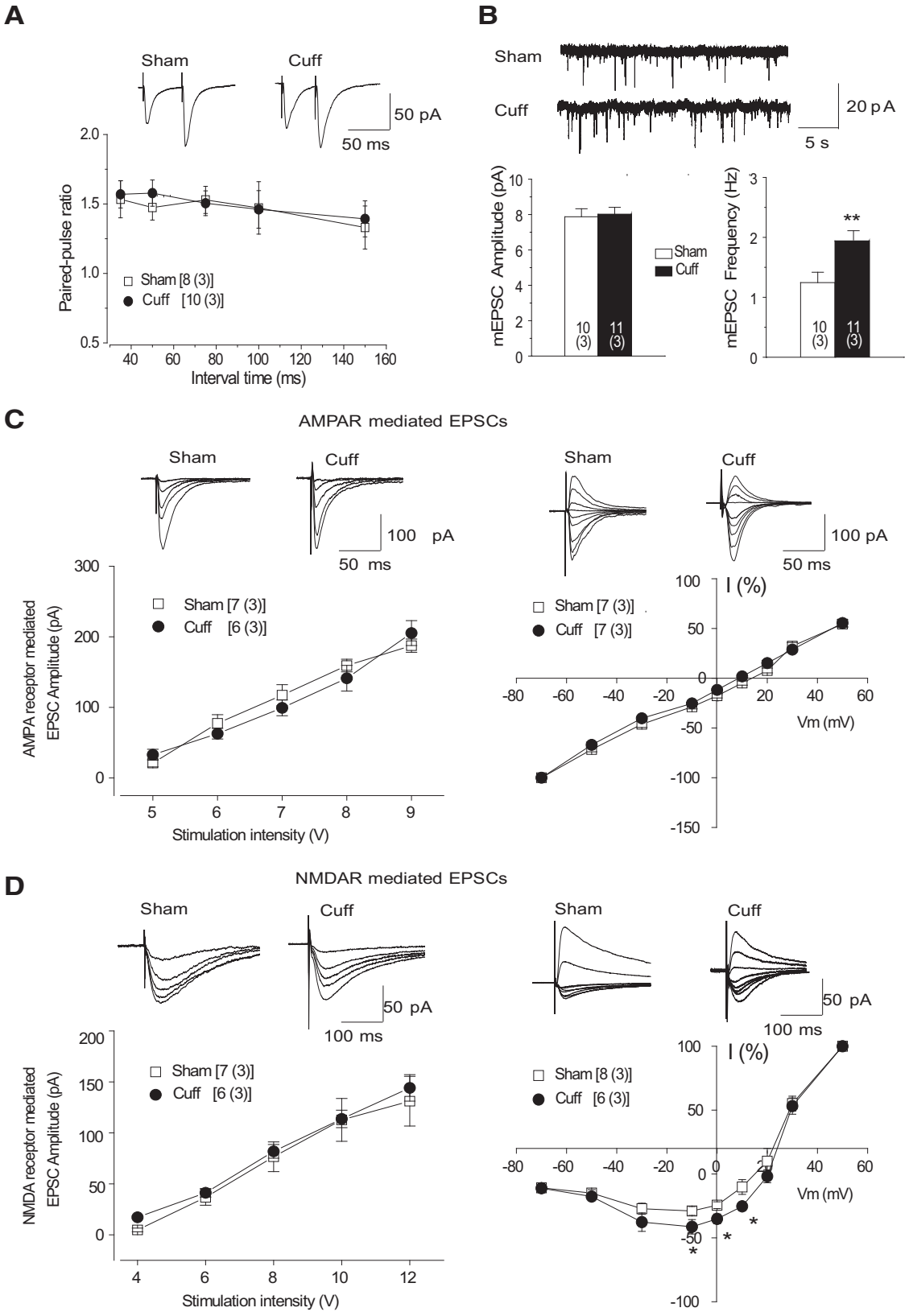

Figure 6. Facilitated presynaptic but nonpostsynaptic ACC transmission in nerve-injured animals, which recovered from mechanical hypersensitivity. ***A***, Samples (top) and summarized results (bottom) showed that the paired-pulse ratios, with recorded intervals of 35, 50, 75, 100, and 150 ms, were not changed in the cuff group compared with the sham group. ***B***, Samples (top) and summarized results (bottom) of the amplitude and frequency of mEPSCs. Frequency was increased in cuff group compared with the sham group. ***C***, Samples (top) and summarized results (bottom) showed that the input– output and *I–V* curves of AMPAR-mediated EPSCs were not changed in the cuff group. ***D***, Samples (top) and summarized results (bottom) showed that the input– output curve of NMDAR-mediated EPSCs was not different in the cuff group. The *I–V* curve in the cuff group differed from that of the sham group. All experiments were performed at TP3 (14–16 weeks after surgery), which corresponds to animals that recovered from mechanical hypersensitivity but still displayed depressive-like consequences. *$p < 0.05$, **$p < 0.01$. ** Numbers in bars or near group names indicate the number of cells and animals.

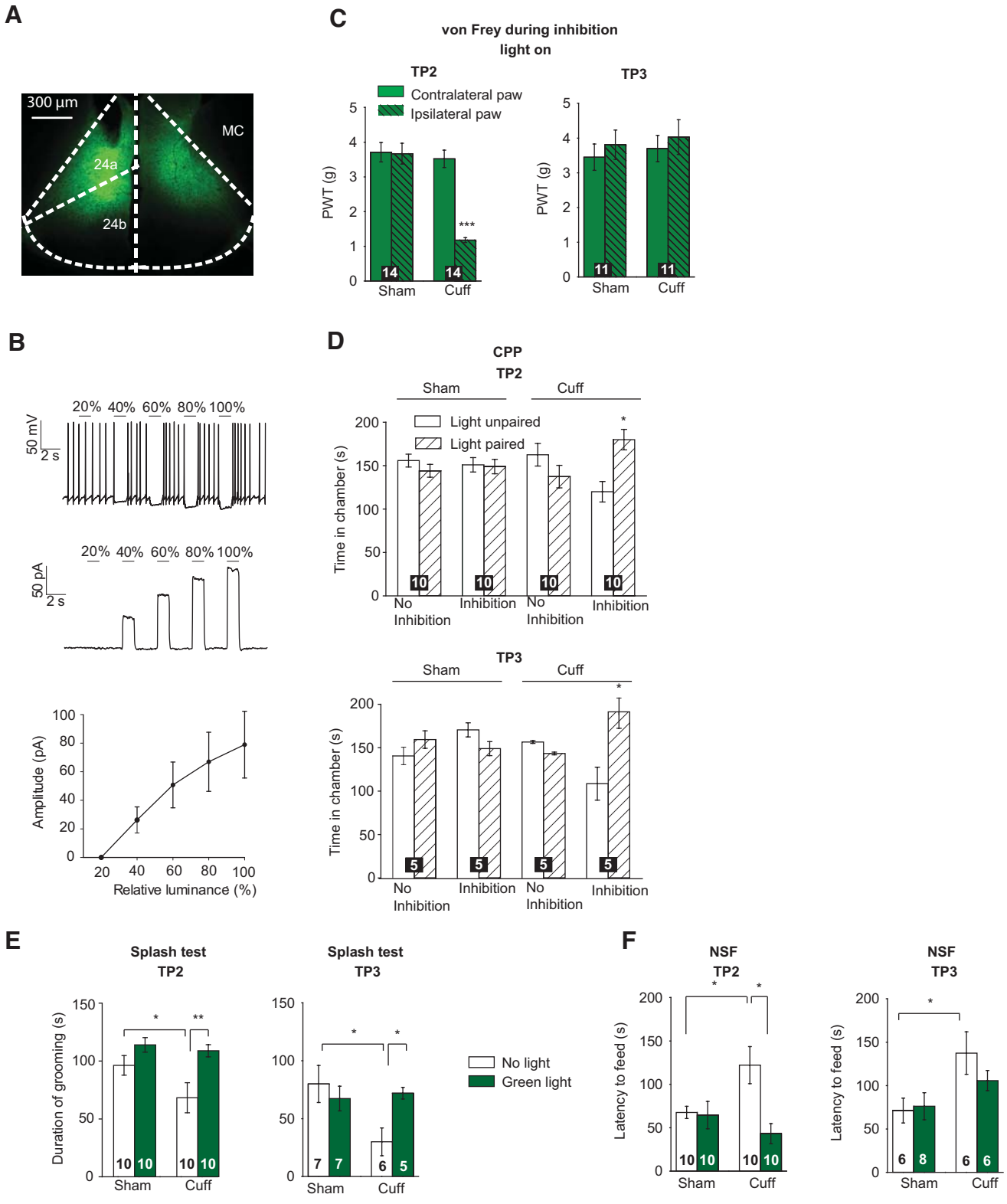

Figure 7. Optogenetic ACC inhibition blocks the aversiveness of ongoing pain and the anxiodepressive-like consequences of neuropathic pain. ***A***, Representative picture of an AAV5-CaMKII-eArchT3.0-EYFP site 5 weeks after transfection. ***B***, Light-evoked effects recorded in the ACC pyramidal neurons of AAV5-CaMKIIa-eArchT3.0-EYFP-injected mice. Top, Representative trace recorded in the current-clamp mode (note the full inhibition of spikes at all tested luminances). Middle, Representative trace of light-evoked currents recorded in the voltage-clamp mode. Bottom, Luminance-response curve of light-evoked currents ($n = 6$). The maximal luminance corresponds to 16 mW. ***C***, Mechanical hypersensitivity is not affected by ACC inhibition at both TP2 and TP3. PWT, Paw withdrawal threshold. ***D***, Optogenetic inhibition of the ACC induces a place preference at TP2 and TP3 in nerve-injured animals (but not in Sham animals) for the chamber in which light was delivered. ***E***, ACC optogenetic inhibition during the splash test reverses the decreased grooming behavior observed in nerve-injured nonstimulated animals at both TP2 and TP3. ***F***, ACC optogenetic inhibition 5 min before NSF test blocks the cuff-induced increased latency to feed at TP2. TP2 corresponds to animals displaying both mechanical hypersensitivity and anxiodepressive-like consequences. TP3 corresponds to animals that recovered from mechanical hypersensitivity but still displayed depressive-like consequences. For the CPP, Splash, and NSF experiments, the laser stimulation used was continuous green light (520 nm) for 5 min at 16 mW. Data are mean ± SEM. Numbers in the bars indicate the number of animals. $^{*}p < 0.05$, $^{**}p < 0.01$, $^{***}p < 0.001$. MC, Motor cortex.

(Benison et al., 2011; Barthas et al., 2015) without affecting ongoing pain (Barthas et al., 2015). In addition, large-diameter fibers of the dorsal column were proposed to mediate mechanical hypersensitivity but not ongoing pain (King et al., 2011). This dichotomy should thus be taken into consideration for drug development because mechanical hypersensitivity, rather than ongoing pain, is presently used for target validation. As it is more often ongoing pain that leads patients to seek treatment, this may in part explain why the development of new treatments has not always provided translational satisfaction.

While mechanical hypersensitivity is no longer present ~3 months after operation, we still observed depressive-like behaviors. Previously, it has been reported in mice that anxiodepressive-like behaviors can persist at least 10 d after normalization of mechanical sensitivity following cuff removal (Dimitrov et al., 2014). Our results confirm and further extend this hypersensitivity/affective dichotomy by showing that aversiveness and depressive-like symptoms persist at least 3–6 weeks after cessation of hypersensitivity. We also show that recovery from anxiety-like behaviors is faster, happening almost 6 weeks before the loss of depressive-like consequences, and that it coincides with the disappearance of mechanical hypersensitivity. It is important to consider that the detailed time courses for the various behavioral consequences of neuropathic pain likely depend on the considered species, strain, and pain model or etiology, as already suggested by published reports (Yalcin et al., 2014a).

The prolonged emotional consequences point out the presence of long-term plastic changes in the brain, secondary to a peripheral nerve injury. One of the cortical regions where such morphological (Blom et al., 2014; Yalcin et al., 2014b), molecular (Barthas et al., 2017), and functional plasticity (Li et al., 2010; Koga et al., 2015) has been reported is the ACC. Our *in vivo* single-unit extracellular recordings showed an increased firing rate and bursting activity in the ACC at TP2 and TP3, coinciding with aversive and depressive-like behaviors. Interestingly, the ACC hyperactivity persists even after anxiety-like behaviors disappeared, suggesting that this hyperactivity may be important but not sufficient for the anxiety-like behavior. In humans, fMRI studies have shown that the ventral part of the ACC, which is involved in emotional processing (Kanske and Kotz, 2012), is hyperactive in depressed patients (Mayberg et al., 1999; Yoshimura et al., 2010), and that activity patterns in ACC subregions correlated with symptom clusters, such as sadness and depressed mood (Mayberg et al., 1999). This possible role of ACC is further supported by animal studies showing increased cingulate cortex activity accompanying depressive-like behaviors in a social-defeat paradigm, as evidenced by c-Fos overexpression (Yu et al., 2011), and in the present model of nerve-injured mice, as evidenced by enhanced phosphorylation of the transcription factors cAMP response element binding protein and activating transcription factor as well as by enhanced cAMP responsive element-driven transcriptional activity and by c-Fos expression (Barthas et al., 2017). While it has been hypothesized that the abnormal ACC activity in depression can be associated with changes in GABA interneurons because levels of somatostatin (Seney et al., 2015) and parvalbumin (Tripp et al., 2012) are low in patients with major depressive disorders (Northoff and Sibille, 2014), 80% of ACC neurons are pyramidal ones, and the optogenetic inhibition of CaMKII-expressing ACC neurons blocks the anxiodepressive-like behaviors induced by chronic pain. Moreover, we previously showed that optogenetic activation of pyramidal neurons was sufficient to drive anxiodepressive-like behaviors in naive mice (Barthas et al., 2015, 2017). While these data indirectly support an implication of pyramidal neurons in ACC hyperactivity, the shape of spikes did not allow differentiating neuronal subtypes responsible for the *in vivo* increased firing activity. However, our *ex vivo* recordings further show that ACC might also be linked to a long-term increase in excitatory synaptic transmission. This hyperactivity could be supported by long-term alterations in functional connections onto pyramidal neurons, which may be initiated at an early stage of the neuropathy (Koga et al., 2015) and participate in the long-lasting presence of affective symptoms. Here, all the recordings were performed in layers II-III because these neurons receive both sensory inputs from the thalamus and inputs from the basal forebrain, including amygdala ones; and we previously reported that synapses in layers II-III undergo plastic changes after LTP induction or peripheral nerve injury (Koga et al., 2015; Song et al., 2017).

To leap from correlative analyses to a causal link between ACC hyperactivity and the behavioral outputs of neuropathic pain, we performed optogenetic inhibition of the ACC. We showed that the inhibition of the ACC suppressed the aversiveness of ongoing pain and the depressive-like consequences of neuropathic pain without affecting mechanical hypersensitivity at TP2 and TP3. These results further reinforce the links between pain aversiveness and depressive-like consequences on the one hand, and between ACC hyperactivity and these emotional aspects of chronic pain on the other. Together with our recent data showing that optogenetic recapitulation of the ACC hyperactivity by using channelrhodopsin 2 (Barthas et al., 2015, 2017) is sufficient to drive anxiodepressive-like behaviors in naive animals, the present data with archaerhodopsin further support the hypothesis that ACC hyperactivity is critical to anxiodepressive-like behaviors. Conversely, it has been shown that inhibiting ACC pyramidal neurons (Kang et al., 2015) or activating inhibitory neurons (Gu et al., 2015) can acutely reduce the hypersensitivity induced by Freund's complete adjuvant or formalin respectively, as also observed with pharmacological manipulation at early stages of neuropathic pain (Li et al., 2010). It suggests that ACC manipulation might also affect nociceptive hypersensitivity in given conditions.

In conclusion, our results emphasize that anxiodepressive-like consequences of chronic pain can experimentally be segregated from mechanical hypersensitivity in a time-dependent manner, whereas they follow the same time course as the aversiveness of ongoing pain. This time dependency between symptoms should be taken into consideration to improve the translational features of preclinical models, and for preclinical target validation of relevant potential therapies. The fact that the emotional consequences of chronic pain are driven by ACC hyperactivity further highlights the ACC and its circuitry as critical neuroanatomical substrates to further explore mood disorder mechanisms. Such circuitry analysis requires a precise knowledge of the ACC connectome, which was recently detailed in mice (Fillinger et al., 2017a, b). Together with present behavioral characterization and electrophysiological data, this information should now allow reaching circuit-level of analysis, including concerning the question of critical input(s) required to induce ACC hyperactivity, and of whether maintaining ACC hyperactivity requires or not input(s) hyperactivity.

Note Added in Proof: The 12th author was left out of the author line in the early release version of this article that was published online on February 20, 2018. The author line has since been corrected.

References

Alba-Delgado C, Llorca-Torralba M, Horrillo I, Ortega JE, Mico JA, Sánchez-Blázquez P, Meana JJ, Berrocoso E (2013) Chronic pain leads to con-

comitant noradrenergic impairment and mood disorders. Biol Psychiatry 73:54–62. CrossRef Medline

Barrot M (2012) Tests and models of nociception and pain in rodents. Neuroscience 211:39–50. CrossRef Medline

Barthas F, Sellmeijer J, Hugel S, Waltisperger E, Barrot M, Yalcin I (2015) The anterior cingulate cortex is a critical hub for pain-induced depression. Biol Psychiatry 77:236–245. CrossRef Medline

Barthas F, Humo M, Gilsbach R, Waltisperger E, Karatas M, Leman S, Hein L, Belzung C, Boutillier AL, Barrot M, Yalcin I (2017) Cingulate overexpression of mitogen-activated protein kinase phosphatase-1 as a key factor for depression. Biol Psychiatry 82:370–379. CrossRef Medline

Benbouzid M, Choucair-Jaafar N, Yalcin I, Waltisperger E, Muller A, Freund-Mercier MJ, Barrot M (2008) Chronic, but not acute, tricyclic antidepressant treatment alleviates neuropathic allodynia after sciatic nerve cuffing in mice. Eur J Pain 12:1008–1017. CrossRef Medline

Benison AM, Chumachenko S, Harrison JA, Maier SF, Falci SP, Watkins LR, Barth DS (2011) Caudal granular insular cortex is sufficient and necessary for the long-term maintenance of allodynic behavior in the rat attributable to mononeuropathy. J Neurosci 31:6317–6328. CrossRef Medline

Bliss TV, Collingridge GL, Kaang BK, Zhuo M (2016) Synaptic plasticity in the anterior cingulate cortex in acute and chronic pain. Nat Rev Neurosci 17:485–496. CrossRef Medline

Blom SM, Pfister JP, Santello M, Senn weeks, Nevian T (2014) Nerve injury-induced neuropathic pain causes disinhibition of the anterior cingulate cortex. J Neurosci 34:5754–5764. CrossRef Medline

Chen T, Koga K, Descalzi G, Qiu S, Wang J, Zhang LS, Zhang ZJ, He XB, Qin X, Xu FQ, Hu J, Wei F, Huganir RL, Li YQ, Zhuo M (2014) Postsynaptic potentiation of corticospinal projecting neurons in the anterior cingulate cortex after nerve injury. Mol Pain 10:33. CrossRef Medline

Cordeiro Matos S, Zhang Z, Séguéla P (2015) Peripheral neuropathy induces HCN channel dysfunction in pyramidal neurons of the medial prefrontal cortex. J Neurosci 35:13244–13256. CrossRef Medline

Dimitrov EL, Tsuda MC, Cameron HA, Usdin TB (2014) Anxiety- and depression-like behavior and impaired neurogenesis evoked by peripheral neuropathy persist following resolution of prolonged tactile hypersensitivity. J Neurosci 34:12304–12312. CrossRef Medline

Drevets WC, Bogers weeks, Raichle ME (2002) Functional anatomical correlates of antidepressant drug treatment assessed using PET measures of regional glucose metabolism. Eur Neuropsychopharmacol 12:527–544. CrossRef Medline

Fillinger C, Yalcin I, Barrot M, Veinante P (2017a) Efferents of anterior cingulate areas 24a and 24b and midcingulate areas 24a′ and 24b′ in the mouse. Brain Struct Funct. Advance online publication. Retrieved Dec. 6, 2017. doi: 10.1007/s00429–017-1585-x. CrossRef Medline

Fillinger C, Yalcin I, Barrot M, Veinante P (2017b) Afferents to anterior cingulate areas 24a and 24b and midcingulate areas 24a′ and 24b′ in the mouse. Brain Struct Funct 222:1509–1532. CrossRef Medline

Gonçalves L, Silva R, Pinto-Ribeiro F, Pêgo JM, Bessa JM, Pertovaara A, Sousa N, Almeida A (2008) Neuropathic pain is associated with depressive behaviour and induces neuroplasticity in the amygdala of the rat. Exp Neurol 213:48–56. CrossRef Medline

Gu L, Uhelski ML, Anand S, Romero-Ortega M, Kim YT, Fuchs PN, Mohanty SK (2015) Pain inhibition by optogenetic activation of specific anterior cingulate cortical neurons. PLoS One 10:e0117746. CrossRef Medline

Johansen JP, Fields HL, Manning BH (2001) The affective component of pain in rodents: direct evidence for a contribution of the anterior cingulate cortex. Proc Natl Acad Sci U S A 98:8077–8082. CrossRef Medline

Kang SJ, Kwak C, Lee J, Sim SE, Shim J, Choi T, Collingridge GL, Zhuo M, Kaang BK (2015) Bidirectional modulation of hyperalgesia via the specific control of excitatory and inhibitory neuronal activity in the ACC. Mol Brain 8:81. CrossRef Medline

Kanske P, Kotz SA (2012) Effortful control, depression, and anxiety correlate with the influence of emotion on executive attentional control. Biol Psychol 91:88–95. CrossRef Medline

King T, Vera-Portocarrero L, Gutierrez T, Vanderah TW, Dussor G, Lai J, Fields HL, Porreca F (2009) Unmasking the tonic-aversive state in neuropathic pain. Nat Neurosci 12:1364–1366. CrossRef Medline

King T, Qu C, Okun A, Mercado R, Ren J, Brion T, Lai J, Porreca F (2011) Contribution of afferent pathways to nerve injury-induced spontaneous pain and evoked hypersensitivity. Pain 152:1997–2005. CrossRef Medline

Koga K, Descalzi G, Chen T, Ko HG, Lu J, Li S, Son J, Kim T, Kwak C, Huganir RL, Zhao MG, Kaang BK, Collingridge GL, Zhuo M (2015) Coexistence of two forms of LTP in ACC provides a synaptic mechanism for the interactions between anxiety and chronic pain. Neuron 85:377–389. CrossRef Medline

Li XY, Ko HG, Chen T, Descalzi G, Koga K, Wang H, Kim SS, Shang Y, Kwak C, Park SW, Shim J, Lee K, Collingridge GL, Kaang BK, Zhuo M (2010) Alleviating neuropathic pain hypersensitivity by inhibiting PKMzeta in the anterior cingulate cortex. Science 330:1400–1404. CrossRef Medline

Mayberg HS, Liotti M, Brannan SK, McGinnis S, Mahurin RK, Jerabek PA, Silva JA, Tekell JL, Martin CC, Lancaster JL, Fox PT (1999) Reciprocal limbic-cortical function and negative mood: converging PET findings in depression and normal sadness. Am J Psychiatry 156:675–682. CrossRef Medline

Narita M, Kaneko C, Miyoshi K, Nagumo Y, Kuzumaki N, Nakajima M, Nanjo K, Matsuzawa K, Yamazaki M, Suzuki T (2006) Chronic pain induces anxiety with concomitant changes in opioidergic function in the amygdala. Neuropsychopharmacology 31:739–750. CrossRef Medline

Northoff G, Sibille E (2014) Why are cortical GABA neurons relevant to internal focus in depression[quest] A cross-level model linking cellular, biochemical and neural network findings. Mol Psychiatry 19:966–977. CrossRef Medline

Peyron R, García-Larrea L, Grégoire MC, Convers P, Richard A, Lavenne F, Barral FG, Mauguière F, Michel D, Laurent B (2000) Parietal and cingulate processes in central pain: a combined positron emission tomography (PET) and functional magnetic resonance imaging (fMRI) study of an unusual case. Pain 84:77–87. CrossRef Medline

Porsolt RD, Le Pichon M, Jalfre M (1977) Depression: a new animal model sensitive to antidepressant treatments. Nature 266:730–732. CrossRef Medline

Qu C, King T, Okun A, Lai J, Fields HL, Porreca F (2011) Lesion of the rostral anterior cingulate cortex eliminates the aversiveness of spontaneous neuropathic pain following partial or complete axotomy. Pain 152:1641–1648. CrossRef Medline

Radat F, Margot-Duclot A, Attal N (2013) Psychiatric co-morbidities in patients with chronic peripheral neuropathic pain: a multicentre cohort study. Eur J Pain 17:1547–1557. CrossRef Medline

Sellmeijer J (2016) Analysis electrophys. Available at https://bitbucket.org/jsellmeijer/analysis_electrophys/commits/7c2d9026c770c42211c2fd34b44328dbc25b4666?at=master

Seney ML, Tripp A, McCune S, Lewis DA, Sibille E (2015) Laminar and cellular analyses of reduced somatostatin gene expression in the subgenual anterior cingulate cortex in major depression. Neurobiol Dis 73:213–219. CrossRef Medline

Shackman AJ, Salomons TV, Slagter HA, Fox AS, Winter JJ, Davidson RJ (2011) The integration of negative affect, pain and cognitive control in the cingulate cortex. Nat Rev Neurosci 12:154–167. CrossRef Medline

Song Q, Zheng HW, Li XH, Huganir RL, Kuner T, Zhuo M, Chen T (2017) Selective phosphorylation of AMPA receptor contributes to the network of long-term potentiation in the anterior cingulate cortex. J Neurosci 37:8534–8548. Medline

Surget A, Wang Y, Leman S, Ibarguen-Vargas Y, Edgar N, Griebel G, Belzung C, Sibille E (2009) Corticolimbic transcriptome changes are state-dependent and region-specific in a rodent model of depression and of antidepressant reversal. Neuropsychopharmacology 34:1363–1380. CrossRef Medline

Suzuki T, Amata M, Sakaue G, Nishimura S, Inoue T, Shibata M, Mashimo T (2007) Experimental neuropathy in mice is associated with delayed behavioral changes related to anxiety and depression. Anesth Analg 104:1570–1577. CrossRef Medline

Tang J, Ko S, Ding HK, Qiu CS, Calejesan AA, Zhuo M (2005) Pavlovian fear memory induced by activation in the anterior cingulate cortex. Mol Pain 1:6. CrossRef Medline

Tripp A, Oh H, Guilloux JP, Martinowich K, Lewis DA, Sibille E (2012) Brain-derived neurotrophic factor signaling and subgenual anterior cingulate cortex dysfunction in major depressive disorder. Am J Psychiatry 169:1194–1202. CrossRef Medline

Vogt MA, Mallien AS, Pfeiffer N, Inta I, Gass P, Inta D (2016) Minocycline

does not evoke anxiolytic and antidepressant-like effects in C57BL/6 mice. Behav Brain Res 301:96–101. CrossRef Medline

Wang R, King T, De Felice M, Guo weeks, Ossipov MH, Porreca F (2013) Descending facilitation maintains long-term spontaneous neuropathic pain. J Pain 14:845–853. CrossRef Medline

Xu H, Wu LJ, Wang H, Zhang X, Vadakkan KI, Kim SS, Steenland HW, Zhuo M (2008) Presynaptic and postsynaptic amplifications of neuropathic pain in the anterior cingulate cortex. J Neurosci 28:7445–7453. CrossRef Medline

Yalcin I, Bohren Y, Waltisperger E, Sage-Ciocca D, Yin JC, Freund-Mercier MJ, Barrot M (2011) A time-dependent history of mood disorders in a murine model of neuropathic pain. Biol Psychiatry 70:946–953. CrossRef Medline

Yalcin I, Barthas F, Barrot M (2014a) Emotional consequences of neuropathic pain: insight from preclinical studies. Neurosci Biobehav Rev 47:154–164. CrossRef Medline

Yalcin I, Megat S, Barthas F, Waltisperger E, Kremer M, Salvat E, Barrot M (2014b) The sciatic nerve cuffing model of neuropathic pain in mice. J Vis Exp 16:89. CrossRef Medline

Yang Q, Wu Z, Hadden JK, Odem MA, Zuo Y, Crook RJ, Frost JA, Walters ET (2014) Persistent pain after spinal cord injury is maintained by primary afferent activity. J Neurosci 34:10765–10769. CrossRef Medline

Yoshimura S, Okamoto Y, Onoda K, Matsunaga M, Ueda K, Suzuki S, Shigetoyamawaki (2010) Rostral anterior cingulate cortex activity mediates the relationship between the depressive symptoms and the medial prefrontal cortex activity. J Affect Disord 122:76–85. CrossRef Medline

Yu T, Guo M, Garza J, Rendon S, Sun XL, Zhang weeks, Lu XY (2011) Cognitive and neural correlates of depression-like behaviour in socially defeated mice: an animal model of depression with cognitive dysfunction. Int J Neuropsychopharmacol 14:303–317. CrossRef Medline

© 2018. Published by The Company of Biologists Ltd | Disease Models & Mechanisms (2018) 11, dmm035634. doi:10.1242/dmm.035634

RESEARCH ARTICLE

Correction of cognitive deficits in mouse models of Down syndrome by a pharmacological inhibitor of DYRK1A

Thu Lan Nguyen[1,2,3,4,5], Arnaud Duchon[1,2,3,4], Antigoni Manousopoulou[6], Nadège Loaëc[5], Benoît Villiers[5], Guillaume Pani[1,2,3,4], Meltem Karatas[7,8], Anna E. Mechling[8], Laura-Adela Harsan[7,8], Emmanuelle Limanton[9], Jean-Pierre Bazureau[9], François Carreaux[9], Spiros D. Garbis[6,*,‡], Laurent Meijer[5,‡] and Yann Herault[1,2,3,4,‡]

ABSTRACT

Growing evidence supports the implication of DYRK1A in the development of cognitive deficits seen in Down syndrome (DS) and Alzheimer's disease (AD). We here demonstrate that pharmacological inhibition of brain DYRK1A is able to correct recognition memory deficits in three DS mouse models with increasing genetic complexity [Tg(*Dyrk1a*), Ts65Dn, Dp1Yey], all expressing an extra copy of *Dyrk1a*. Overexpressed DYRK1A accumulates in the cytoplasm and at the synapse. Treatment of the three DS models with the pharmacological DYRK1A inhibitor leucettine L41 leads to normalization of DYRK1A activity and corrects the novel object cognitive impairment observed in these models. Brain functional magnetic resonance imaging reveals that this cognitive improvement is paralleled by functional connectivity remodelling of core brain areas involved in learning/memory processes. The impact of *Dyrk1a* trisomy and L41 treatment on brain phosphoproteins was investigated by a quantitative phosphoproteomics method, revealing the implication of synaptic (synapsin 1) and cytoskeletal components involved in synaptic response and axonal organization. These results encourage the development of DYRK1A inhibitors as drug candidates to treat cognitive deficits associated with DS and AD.

KEY WORDS: DYRK1A, Kinase inhibitor, Leucettine, Down syndrome, Synapsin

[1]Institut de Génétique et de Biologie Moléculaire et Cellulaire, Department of Translational Medicine and Neurogenetics, 67400 Illkirch, France. [2]Centre National de la Recherche Scientifique, UMR7104, 67400 Illkirch, France. [3]Institut National de la Santé et de la Recherche Médicale, U964, 67400 Illkirch, France. [4]Université de Strasbourg, 67400 Illkirch, France. [5]ManRos Therapeutics, Perharidy Research Center, 29680 Roscoff, Bretagne, France. [6]Faculty of Medicine/Cancer Sciences & Clinical and Experimental Medicine, University of Southampton, Center for Proteomic Research, Life Sciences Building 85, Highfield, Southampton SO17 1BJ, UK. [7]Laboratory of Engineering, Informatics and Imaging (ICube), Integrative multimodal imaging in healthcare (IMIS), UMR 7357, and University Hospital Strasbourg, Department of Biophysics and Nuclear Medicine, University of Strasbourg, 67400 Illkirch, France. [8]Department of Radiology, Medical Physics, Medical Center – University of Freiburg, Breisacher Strasse 60a, 79106 Freiburg, Germany. [9]Université de Rennes 1, ISCR (Institut des sciences chimiques de Rennes)-UMR, 6226, 35000 Rennes, France.
*Present address: Proteome Exploration Laboratory, Division of Biology and Biological Engineering, Beckman Institute, California Institute of Technology, Pasadena, CA 91125, USA.

‡Authors for correspondence (sgarbis@caltech.edu; meijer@manros-therapeutics.com; herault@igbmc.fr)

S.D.G., 0000-0002-1050-0805; L.M., 0000-0003-3511-4916; Y.H., 0000-0001-7049-6900

Received 11 May 2018; Accepted 1 August 2018

INTRODUCTION

Down syndrome (DS) results from the trisomy of human chromosome 21 (HSA21). It is still the most frequent intellectual disability, affecting 1 newborn per 700 births. Among the most common DS features are hypotonia, dysmorphic features and intellectual disability (Sureshbabu et al., 2011; Morris et al., 1982). Although children with DS show good socialization skills – encompassing social relations, friendship and leisure activities – they exhibit difficulties in communication abilities, i.e. the daily use of receptive, expressive and written language (Marchal et al., 2016). They experience troubles in daily life skills, such as self-caring, eating, toileting, dressing, behaving safely, and conceptualizing time and money. Improving the intellectual quotient of DS people would allow them to achieve more independence, increase their vigilance and globally improve their quality of life.

Among candidate genes explaining intellectual disabilities in DS people, the dual specificity tyrosine-phosphorylation-regulated kinase 1A, *DYRK1A*, is located in the DS chromosome 21 critical region (Walte et al., 2013; Duchon and Herault, 2016). It encodes a serine/threonine kinase which has numerous substrates. Two nuclear localization signals confer nuclear activity to this kinase (Alvarez et al., 2007), through interactions with transcription factors including GLI1 (Mao et al., 2002), RNA POL II (Di Vona et al., 2015) or splicing factors like cyclin L2 (Graaf et al., 2004). In the cytoplasm, DYRK1A phosphorylates cytoskeletal substrates such as β-tubulin, MAP1A or MAP1B (Ori-McKenney et al., 2016; Murakami et al., 2012; Scales et al., 2009). DYRK1A plays a role in cell cycle regulation by phosphorylating the cyclin-dependent kinase (CDK) inhibitor KIP1 (also known as CDKN1B) in cultured hippocampal neurons and in embryonic mouse brain (Soppa et al., 2014) and LIN52 *in vitro* (Litovchick et al., 2011). Through its 'priming' activity for glycogen synthase kinase 3β (GSK-3β)-dependent phosphorylation, DYRK1A regulates the nuclear/cytoplasmic localization of the NFAT transcription factors (Arron et al., 2006). At the synaptic level, DYRK1A binds to N-methyl-D-aspartate receptor subunit 2A (GLUN2A; also known as GRIN2A) and synaptojanin 1 (SYNJ1) (Chen et al., 2014; Grau et al., 2014) and phosphorylates amphyphysin 1 (Murakami et al., 2012) and GLUN2A (Grau et al., 2014). These are examples of different biological brain functions controlled by DYRK1A which are probably dysregulated when DYRK1A is overexpressed in DS, leading to cognitive impairments.

Several mouse models overexpressing DYRK1A have been described. The first one, Tg(CEPHY152F7)12Hgc, carries a single copy of a yeast artificial chromosome (YAC) containing a 570 kb fragment of human DNA encompassing *TTC3*, *DYRK1A* and *KCNJ6*. This model shows no strong defect in spatial learning and memory, but displays less crossing of the site where the platform was during the probe test in the Morris water maze (MWM) task

Disease Models & Mechanisms (2018) 11, dmm035634. doi:10.1242/dmm.035634

(Smith et al., 1997). Another model, Tg(MT1A-*Dyrk1a*)#Xest (#=9 or 33), was produced by expressing the *Dyrk1a* rat complementary DNA (cDNA) under the control of the metallothionein 1a exogenous promoter (Altafaj et al., 2001). These mice demonstrated impairments in neuromotor development and hyperactivity evaluated in treadmill performance and rotarod tests (Martínez de Lagrán et al., 2004). They also display defects in visuospatial learning and memory in the MWM task (Martínez de Lagrán et al., 2004; Pons-Espinal et al., 2013), as well as in recognition memory revealed in the novel object recognition (NOR) task (de la Torre et al., 2014). A third model, Tg(*DYRK1A*)36Wjs, was generated using a bacterial artificial chromosome (BAC) containing the human *DYRK1A* gene. *DYRK1A* triplication leads to alterations in synaptic transmission with an increase in long-term potentiation (LTP) and a decrease in long-term depression (LTD). The transgenic mice are also deficient in the MWM task, suggesting spatial learning and memorization disabilities (Ahn et al., 2006). Although the human YAC and BAC transgenic mice exhibit features similar to those seen in DS patients, they carry an extra copy of human/rat *DYRK1A* gene, which could lead to biased phenotypes, as optimal expression and functionality of the human/rat protein cannot be ensured in a mouse background. Therefore, a BAC transgenic model with the entire *Dyrk1a* murine gene, Tg(*Dyrk1a*)189N3Yah [hereafter referred to as Tg(*Dyrk1a*)], was created (Guedj et al., 2012). This model shows alterations in short-term memory in the Y-maze task, and in spatial memory in the MWM task (Souchet et al., 2014). Deficits in cortical synaptic plasticity were also observed (Thomazeau et al., 2014). Comparable impairments were seen in the Ts(17^{16})65Dn model (hereafter referred to as Ts65Dn), a mouse model trisomic for almost 13.4 Mb, homologous to HSA21 and containing *DYRK1A* (Reeves et al., 1995). Spatial memory, especially reversal learning reflecting cognitive flexibility, was altered in the Water T-maze test and in the reversal version of the MWM (Olmos-Serrano et al., 2016). Although the Ts65Dn model has been widely used to study DS features, it carries a triplication of genes located in a subcentromeric region of mouse chromosome 17 (MMU17) which are not syntenic to any HSA21 genes (Duchon et al., 2011). A complete DS model, Dp1Yey, was thus produced, which is trisomic for 22.9 Mb, spanning the entire HSA21 region on MMU16 (Li et al., 2007). Dp1Yey mice are less well performing than control mice in the MWM task and display context-associated learning deficits in the fear conditioning test (Yu et al., 2010).

Reducing DYRK1A overdosage leads to correction of several DS traits, demonstrating the major implication of this kinase in DS. Indeed, normalization of DYRK1A expression attenuates spatial learning as well as associative memory defects, and rescues LTP in the Ts65Dn model (García-Cerro et al., 2014; Altafaj et al., 2013). In addition, reversal to two DYRK1A copies in Dp1Yey mice enhances working and associative learning performance assessed in the T-maze and contextual fear-conditioning tests, respectively (Jiang et al., 2015). Furthermore, epigallocatechin gallate (EGCG), a natural polyphenol found in coffee, cocoa and green tea, reported to inhibit DYRK1A, restores intellectual capacities of trisomic mice (Guedj et al., 2009; de la Torre et al., 2014). EGCG has undergone a phase 2 clinical trial (de la Torre et al., 2016). However, EGCG also interacts with the cannabinoid receptor 1 (CNR1) (Korte et al., 2010). This receptor modulates the release of neurotransmitters in various brain areas, such as the prefrontal cortex and hippocampus, thereby controlling memory, cognition processes and mood. Interaction of EGCG with CNR1 might thus affect memory, cognition and pain perception, leading to psychiatric disorders (Freund et al., 2003; Wilson and Nicoll, 2002), compromising its therapeutic use. Furthermore, DYRK1A is less sensitive to EGCG [half-maximal inhibitory concentration (IC_{50}), 0.33 µM] than vimentin (IC_{50}, 0.003 µM) and the laminin receptor (IC_{50}, 0.04 µM) (Khan et al., 2006; Yang et al., 2009). Cognitive restoration in trisomic mice by EGCG might thus be due to inhibition of targets other than DYRK1A. Consequently, alternative pharmacological inhibitors have started to emerge (Kim et al., 2016; Nakano-Kobayashi et al., 2017; Nguyen et al., 2017). Nevertheless, all available results clearly demonstrate the implication of DYRK1A in DS intellectual deficiencies and the beneficial effects of its inhibition on the correction of cognitive deficits.

DYRK1A has become a major screening target for the development of selective and potent pharmacological inhibitors (Smith et al., 2012; Stotani et al., 2016; Nguyen et al., 2017). We here investigated the effects of a relatively selective DYRK1A inhibitor, leucettine L41 (hereafter referred to as L41) in three different trisomic mouse models with increasing genetic complexity: Tg(*Dyrk1a*), Ts65Dn and Dp1Yey. Leucettines are derived from the marine sponge alkaloid Leucettamine B (Debdab et al., 2011; Tahtouh et al., 2012). The chemically synthesized L41 displays a high selectivity for DYRK1A but also DYRK1B, DYRK2 and some Cdc2-like kinases (CLKs) (Fig. 1). It acts by competing with ATP binding to the kinase catalytic site. We here establish a proof of concept that pharmacological inhibition of brain DYRK1A is able to correct NOR cognitive impairment in three DS models with increasing genetic complexity. We show, via brain functional magnetic resonance imaging (fMRI) in Dp1Yey, the most complete mouse model of DS, that such cognitive improvement is paralleled by significant functional connectivity remodelling of core brain areas involved in learning and memory processes. Furthermore, phosphoproteomic analyses in the Tg(*Dyrk1a*) model unravelled brain DYRK1A targets for which phosphorylation increases with DYRK1A overdosage and decreases following L41 treatment. These novel substrates, such as synapsin 1 (SYN1), also found in the phosphoproteomic analyses of Ts65Dn, the most used DS model, bring new insight into the role of DYRK1A, and allow us to propose some dysregulated biological processes related to axonal organization and synaptic response which are responsible for cognitive deficits associated with DS.

RESULTS

Leucettines restore cognitive function, assessed in the NOR test, through kinase inhibition in three DS mouse models overexpressing DYRK1A

To investigate the importance of DYRK1A in cognitive deficits shown by transgenic mouse models of DS, we used a series of low molecular weight pharmacological inhibitors, collectively known as leucettines (Debdab et al., 2011; Tahtouh et al., 2012; T. Tahtouh, unpublished). We selected the well-characterized leucettine L41 as an archetype of this inhibitor family (Fig. 1) and L43, a closely related analogue which displays little kinase inhibitory action. Because both compounds were found to inhibit CNR1 (T. Tahtouh, unpublished), we also used L99, a DYRK1A inhibitor lacking activity on CNR1 (Fig. 1). To ensure its brain bioavailability, L41 was dosed following acute intraperitoneal (i.p.) injection in Tg(*Dyrk1a*) and wild-type (wt) mice. Plasma half-life was ∼45 min, and the inhibitor reached a maximum brain concentration at 20 min, and was eliminated 2 h later. No differences in L41 pharmacokinetics or biodistribution were observed between transgenic and wt mice (Fig. S1).

Disease Models & Mechanisms (2018) 11, dmm035634. doi:10.1242/dmm.035634

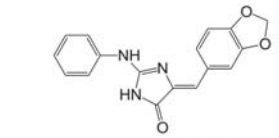

Leucettine **L41**

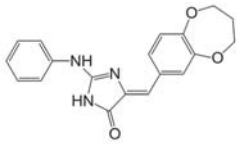

Leucettine **L43**

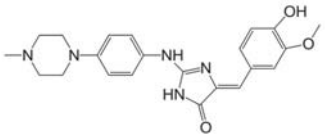

Leucettine **L99**

Kinase	L41	L43	L99
CDK1/cyclin B	>10	>10	>10
CDK2/cyclin A	>10	>10	>10
CDK5/p25	>10	>10	>10
CDK9/cyclin T	>10	>10	0.32
CK1	>10	>10	0.78
CLK1	0.023	>10	0.012
CLK2	0.130	-	0.030
CLK3	1.2	-	0.7
CLK4	0.023	>10	0.012
DYRK1A	0.024	7.4	0.014
DYRK1B	0.062	>10	0.020
DYRK2	0.014	>10	0.015
DYRK3	0.230	-	0.010
GSK3	0.6	-	0.2
CK2	0.510	-	-
PIM1	1.2	>10	0.21
CB1 arrestin	0.314	0.890	-

Fig. 1. Chemical structure and selectivity of the leucettines used in this study. Selectivity of leucettines L41, L43 and L99 was assessed *in vitro* on 16 recombinant kinases, and in a cellular CB1 annexin assay. Dose-response curves provided IC_{50} values (reported in µM). –, no inhibition at 10 µM.

We used three mouse models of DS: Tg(*Dyrk1a*), which expresses a single additional copy of DYRK1A (Guedj et al., 2012); and Ts65Dn (Reeves et al., 1995) and Dp1Yey (Li et al., 2007), which carry MMU16 segments encompassing *Dyrk1a*, with 89 and 101 genes homologous to HSA21, respectively (Gupta et al., 2016).

Using the NOR test, we first evaluated the effects on Tg(*Dyrk1a*) animals following daily i.p. treatment with L41 (20 mg/kg) for 5, 12 or 19 days (Fig. 2A). As expected, untreated wt mice discriminated the novel over the familiar object. L41 treatment for 5, 12 or 19 days had no effect on the performance of wt animals. Untreated Tg(*Dyrk1a*) mice were unable to discriminate the novel over the familiar object (de la Torre et al., 2014) (Fig. 2A). In contrast, L41-treated Tg(*Dyrk1a*) mice preferentially explored the novel object, thus reverting to the behaviour of wt animals. This recovery was fully observed following 19 days of treatment, but was consistently or only marginally seen following 12 and 5 days of treatment, respectively (Fig. 2A). In other words, a minimum of 12 days of daily L41 treatment was necessary for full recovery in the NOR test.

These experiments were repeated (daily i.p. treatment for 19 days) with the kinase-inactive/CNR1-active L43 and the kinase-active/CNR1-inactive L99 leucettines (Fig. 2B). Results clearly showed the beneficial behavioural effects of L99 (Fig. 2B, right) and the lack of effects of L43 (Fig. 2B, left), demonstrating that the rescuing activity of leucettines derives from kinase inhibition rather than CNR1 antagonism.

We next ran the same experiments in Ts65Dn and Dp1Yey animals (Fig. 2C). Daily i.p. treatment with L41 for 19 days led to rescue in the NOR test. Intriguingly, L41 treatment had no restoring effect on working memory (Fig. S2A), nor on place memory in Tg(*Dyrk1a*) mice (Fig. S2B), as assessed in the Y-maze and place object location paradigms, respectively.

L41 treatment has a global effect on brain functional connectivity measured by resting state fMRI

To noninvasively investigate whether DYRK1A kinase activity alters the brain functional connectivity (FC) and to reveal possible circuitry-based mechanisms underlying cognitive improvements induced by L41, we performed brain resting state fMRI (rsfMRI) experiments in vehicle or L41-treated Dp1Yey and wt mice. The brain connectivity patterns associated with default mode network (DMN) – the main functional circuitry describing the brain's intrinsic activity at rest (Raichle, 2015) – were mapped comparatively for each experimental group (Fig. 3A-a,b,B-a,b) via seed-based analysis. The seed used for generating DMN was the retrosplenial cortex (RSP), considered as the mouse DMN core area. DMN configuration obtained for the wt vehicle-treated group (Fig. 3A-a) served as a control pattern and encompassed the midline cortical areas [RSP, posterior parietal association areas (PTLp), temporal association areas, visual areas] as well as the rostral and medial anterior cingulate cortex (ACA) and hippocampal formation (HF) as previously described in mice (Sforazzini et al., 2014; Stafford et al., 2014). This DMN-like configuration was only minimally impacted by L41 treatment in wt animals (Fig. 3A-c,d), by decreasing the RSP connectivity with limited hippocampal (HF) areas.

In Dp1Yey mice, trisomy strongly influenced DMN architecture (Fig. 3B-a) by altering its pattern along midline cortical areas, highlighting the pathological features of Dp1Yey brain, as compared with wt brains (Fig. 3A-a). Notably, Dp1Yey mice show reversed connectivity features of RSP (the core area of DMN) towards the rostrofrontal cortical regions, including ACA [Fig. 3A-a versus B-a; switch from positive correlations (red/yellow scale) to negative correlations (blue scale)]. Intergroup statistics (vehicle-treated wt versus vehicle-treated Dp1Yey; Fig. S3) revealed diminished RSP-ACA connectivity in Dp1Yey animals compared with controls (Fig. S3A), while strengthening the local connectivity around the RSP seed (Fig. S3B). Concurrently, the RSP of Dp1Yey vehicle animals showed increased connectivity to limbic areas of basal forebrain [i.e. pallidum (PAL)] when compared with that of the wt vehicle group (Fig. S3B).

L41 treatment of Dp1Yey mice rescued this altered DMN pattern (Fig. 3B-b), prominently acting to significantly increase the FC of the RSP with the ACA, prefrontal cortex (PFC) and ventral HF (group statistics in Fig. 3B-d, orange/red) and to reduce FC with subcortical regions including the thalamus (TH) and PAL (Fig. 3B-d, green/blue).

To further reveal FC signatures of L41 action in Dp1Yey mice we evaluated the connectivity, across the whole brain, for several key brain areas involved in learning and memory [hippocampal CA1 and dentate gyrus (DG) areas, perirhinal cortex (PERI) and ACA]. Group statistical analysis of FC maps highlighted overall restricted

Disease Models & Mechanisms (2018) 11, dmm035634. doi:10.1242/dmm.035634

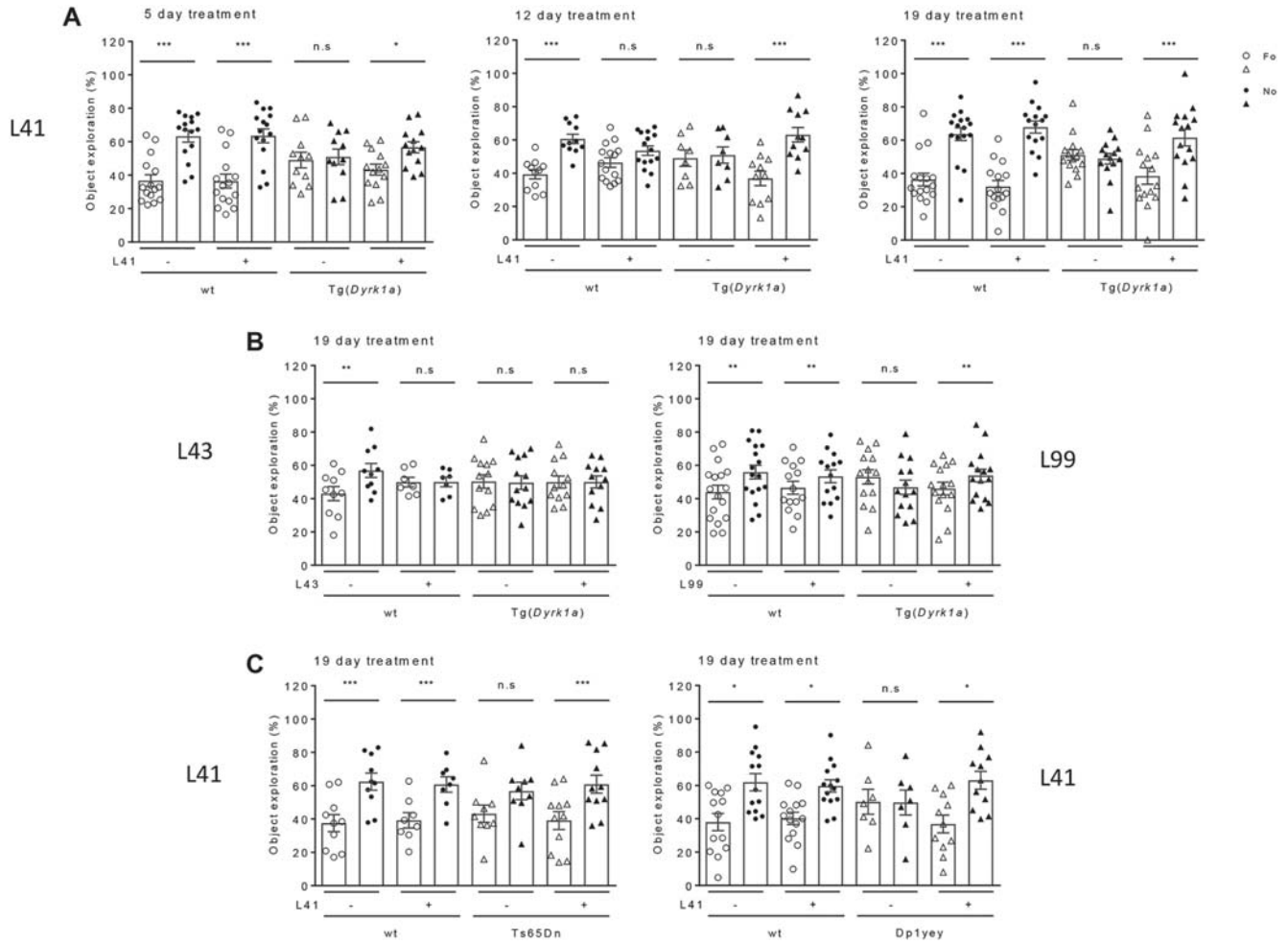

Fig. 2. DYRK1A-specific inhibitors rescue NOR deficits induced in Tg(*Dyrk1a*), Ts65Dn and Dp1yey trisomic mice. (A) Duration of treatment. NOR test results for Tg(*Dyrk1a*) mice treated with L41 or vehicle for 5, 12 or 19 days. Percentage object exploration by sniffing was determined for each object after a 24 h retention delay (familiar object, open symbol; novel object, filled symbol). NOR results of three Tg(*Dyrk1a*) cohorts treated with L41 for 5 (left), 12 (centre) or 19 (right) days. Tg(*Dyrk1a*) and Ts65Dn treated animals spent more time exploring the novel object compared with control mice, showing a rescue of their recognition memory. Left: 5 days treatment induced a NOR rescue in Tg(*Dyrk1a*) animals [wt: n=15, P<0.001; treated wt: n=15, P<0.001; untreated Tg(*Dyrk1a*): n=11, P=0.8; treated Tg(*Dyrk1a*): n=13, P=0.02]. Centre: a more consistent rescue was obtained after 12 days of L41 treatment [not treated wt: n=12, P<0.001; treated wt: n=15, P=0.11; untreated Tg(*Dyrk1a*): n=8, P=0.76; treated Tg(*Dyrk1a*): n=11, P<0.001]. Right: rescue obtained after 19 days of L41 treatment: the exploration was significantly different for wt (n=15, P<0.001), treated wt (n=15, P<0.001) and treated Tg(*Dyrk1a*) (n=15b, P<0.001) mice, but not for nontreated transgenic mice (n=13, P=0.64). (B) Treatment with L43 (left) and L99 (right). L99 treatment induced a cognitive rescue in the Tg(*Dyrk1a*) mice, whereas L43 treatment had no effect. L99 (right): [wt: n=10, P=0.02; treated wt: n=12, P=0.003; Tg(*Dyrk1a*): n=12, P=0.01; treated Tg(*Dyrk1a*): n=9, P<0.001]. L43 (left): [wt: n=12, P=0.008; treated wt: n=7, P=0.9; Tg(*Dyrk1a*): n=13, P=0.91; treated Tg(*Dyrk1a*): n=12, P=0.71]. (C) Ts65Dn and Dp1yey models. Left: in the Ts65Dn study, a significant statistical difference was observed for untreated wt (n=10, P<0.001), treated wt (n=8, P=0.009) and treated Ts65Dn (n=11, P=0.002), but not for untreated Ts65Dn animals (n=9, P=0.08). Right: L41 also normalizes the recognition memory of Dp1Yey mice (wt: n=13, P=0.04; treated wt: n=14, P=0.02; Dp1Yey: n=7, P=0.98; treated Dp1Yey: n=11, P=0.03). Data are represented as mean±s.e.m. with individual points per animal. Statistical analysis was performed with the two-way ANOVA test, Tukey post hoc. n.s., not significant. *P<0.05, **P<0.01, ***P<0.001.

effects of L41 on brain FC of wt animals (Fig. 3C-a-d) but robust L41-dependent brain FC modifications in the DS model (Fig. 3D-a-d). Acting at the hippocampal level, L41 treatment triggered robust changes in CA1 and DG connectivity in Dp1Yey mice (Fig. 3D-a,b). The CA1 strengthened its FC with the PFC and ACA (Fig. 3D-a, orange/red) and decreased its functional communication with the ventral HF (subiculum) and thalamic nuclei (Fig. 3D-a, green/blue). The strongest L41-triggered DG connectivity modifications were identified along the DG-RSP functional pathway in Dp1Yey mice (Fig. 3D-b). A divergent and limited effect of decreased CA1-ACA connectivity was measured in wt mice, after L41 treatment (Fig. 3C-a, green/blue), and the DG altered its connectivity towards the TH and superior colliculus (SC) in wt animals.

Furthermore, L41 treatment triggered remodelling of functional cross-talk between the PERI and the HF, RSP and PTLp in Dp1Yey animals (Fig. 3D-c), while acting primarily on PERI-TH connectivity in wt animals (Fig. 3C-c). Group statistics additionally revealed a selective impact of L41 on ACA connectivity in Dp1Yey mice (Fig. 3D-d), significantly modifying its patterns towards the PFC (decrease), RSP (increase), SC (increase) and hypothalamic (HY) areas (decrease). Meanwhile, L41 induced limited effects in wt mice, by decreasing ACA-PFC connectivity (Fig. 3C-d). Overall, these results indicate the potential of L41 to act at a circuitry level, modifying the global brain FC in Dp1Yey mice, which are strongly susceptible to its effects.

Disease Models & Mechanisms (2018) 11, dmm035634. doi:10.1242/dmm.035634

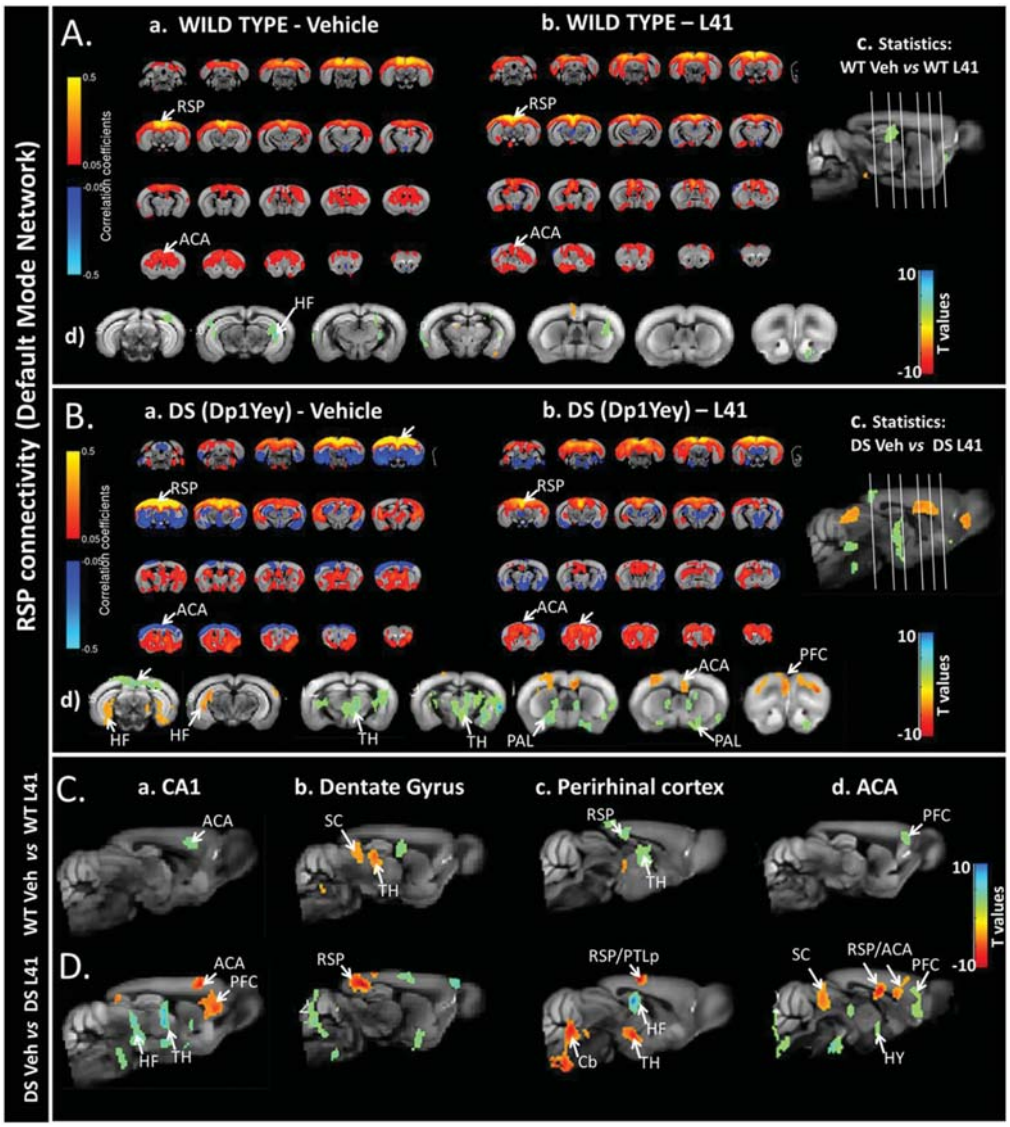

Fig. 3. Influence of L41 on mouse brain functional connectivity (FC) patterns mapped via rsfMRI. (A,B) Default mode network (DMN) pattern in wt (a) and Dp1Yey (b) animals, mapped using the RSP cortex (core hub of DMN) as a seed region. A-a shows the typical DMN-like pattern observed in mice, spatially covering the middle rostrocaudal cortical axis of wt animals treated with vehicle, connecting the RSP and ACA. As shown in B-b, L41 treatment in wt animals slightly modifies the DMN patterns compared with wt-vehicle (see also statistics in A-c, sagittal view and A-d, coronal view; two-tailed Student's *t*-test, $P<0.01$). Red-orange scale quantifies the areas in which L41 treatment results in increased FC of wt-L41 compared with wt-vehicle. Blue-green scale indicates areas with decreased RSP connectivity after L41 treatment, compared with vehicle-treated wt mice. B-a demonstrates strongly altered DMN in vehicle-treated Dp1Yey compared with wt vehicle-treated animals (A-a, wt-vehicle), highlighting the pathological connectivity features of the mutant animals. As shown in B-b, L41 treatment in mutant Dp1Yey animals (DP16-L41) strongly modifies the DMN, restoring the positive correlations (red) of the RSP with the frontal brain areas (arrows, B-b). Voxel-wise statistics shown in B-c and B-d indicate, in red-orange, the areas in which L41 treatment results in increased FC of the DP16-L41 group compared with the DP16-vehicle group. Blue-green scale indicates areas with decreased RSP connectivity after L41 treatment, compared with the vehicle-treated group mutant mice. In A-a,b and B-a,b, red indicates the positively correlated areas (0.1 to 0.5 correlation coefficients); blue indicates negatively correlated areas (–0.1 to –0.5 correlation coefficients). (C,D) FC patterns in wt (C) and Dp1Yey (D) animals after L41 treatment: C-a, CA1 FC; C-b, dentate gyrus FC; C-c, perirhinal cortex FC; C-d, ACA FC (two-tailed Student's *t*-test, $P<0.01$). Red-orange shows the brain areas in which L41 treatment results in increased FC; blue-green indicates areas with decreased connectivity after L41 treatment, compared with vehicle-treated mice. ACA, rostral and medial anterior cingulate cortex; Cb, cerebellum; HF, hippocampal formation; HY, hypothalamus; PAL, pallidum; PFC, prefrontal cortex; PTLp, posterior parietal association areas; RSP, retrosplenial cortex; SC, superior colliculus; TH, thalamus.

Increased DYRK1A expression and catalytic activity in DS models: leucettines normalize DYRK1A activity

To validate the Tg(*Dyrk1a*) and Ts65Dn models in terms of DYRK1A expression and function, we first verified the expression levels of *Dyrk1a* mRNA (Fig. 4A) and DYRK1A protein (Fig. 4B) in brains derived from control or L41-treated animals (19 days, daily i.p.). Total mRNAs were extracted from brains and *Dyrk1a*, *Gsk-3b* and *Rplp0* mRNAs were quantified by quantitative polymerase chain reaction (qPCR) with specific primers. Results showed the expected ∼1.5-fold increase in *Dyrk1a* mRNA levels (normalized with respect to *Gsk-3b* and *Rplp0*) in both transgenic models compared with their wt littermates. L41 treatment for 19 days did not modify *Dyrk1a* mRNA levels (Fig. 4A). DYRK1A protein levels were also increased in transgenic mice models

Disease Models & Mechanisms (2018) 11, dmm035634. doi:10.1242/dmm.035634

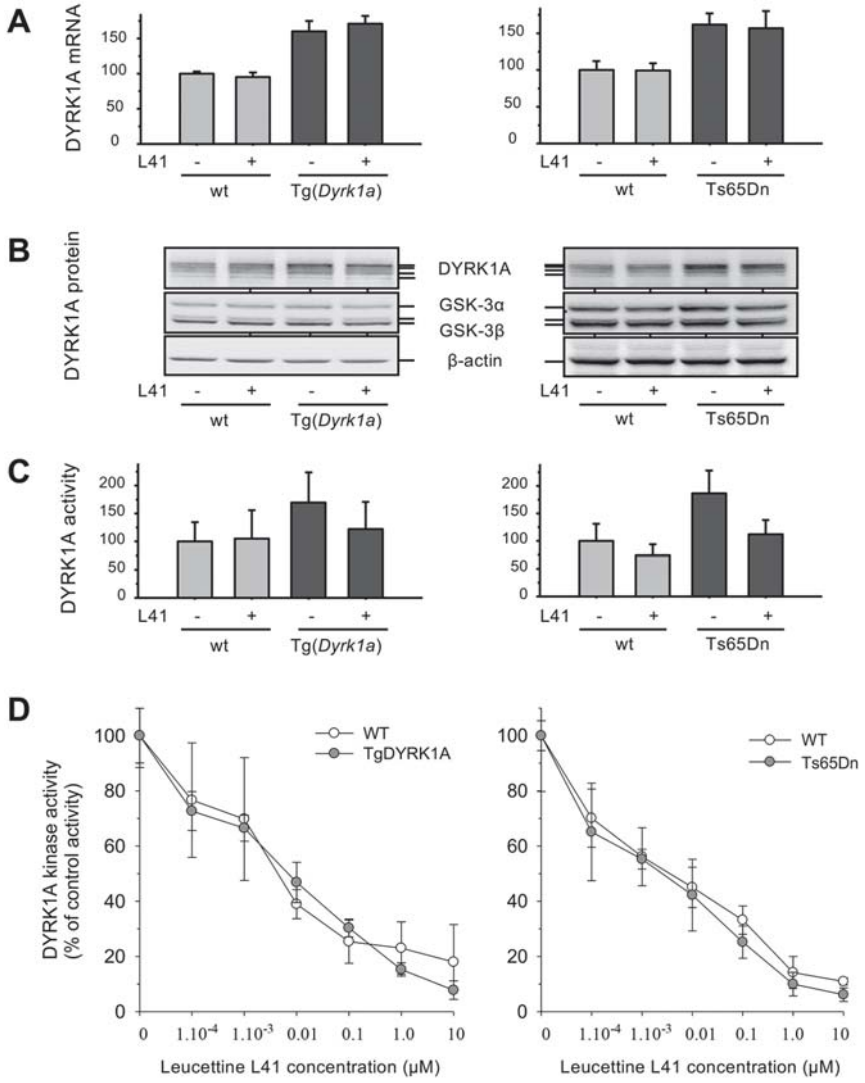

Fig. 4. *Dyrk1a* mRNA and DYRK1A protein expression, and catalytic activity in Tg(*Dyrk1a*) and corresponding wt mice brains, and in Ts65Dn and corresponding wt mice brains. (A) mRNA expression. Total RNA was extracted, purified and reverse transcribed into cDNA. mRNA expression of *Dyrk1a*, *Gsk-3b* and reference *Rplp0* was quantified by qPCR from the amplification of cDNA with specific primers (one primer annealing to an exon-exon junction). Results are presented as mean±s.e. of four to six measurements and are shown relative to *Rplp0* expression, normalized to wt *Gsk-3b* expression. (B) Protein expression. Total proteins were extracted, resolved by SDS-PAGE and analysed by WB using antibodies directed against DYRK1A, GSK-3α/β and actin (loading control). (C) DYRK1A catalytic activity. DYRK1A was purified from brain extracts by immunoprecipitation and GSK-3α/β was purified by affinity chromatography on axin-agarose beads. Activities of the purified kinases were assayed in triplicate in a radioactive kinase assay using specific peptide substrates, and are reported after normalization with wt GSK-3α/β activities (mean±s.e.). (D) *In vitro* DYRK1A kinase activity. The catalytic activity of DYRK1A immunoprecipitated from the brains of Tg(*Dyrk1a*) and Ts65Dn mice and their respective controls was assayed in the presence of a range of L41 concentrations.

compared with control wt animals, as shown by western blotting (WB) of total brain proteins, whereas GSK-3α/β and β-actin levels remained at identical levels in transgenic and wt mice brains (Fig. 4B). L41 treatment had no effect on the expression of DYRK1A and GSK-3α/β. We next measured DYRK1A catalytic activities from transgenic and wt brain protein extracts (Fig. 4C). After 19 days of L41 or vehicle treatment, GSK-3α/β activity remained identical in the brains of transgenic and wt mice (data not shown), and was thus used to normalize the DYRK1A kinase activity. As expected, DYRK1A activity was elevated by ∼1.5- to 1.8-fold in transgenic brains compared with wt brains (Fig. 4C). L41 treatment did not reduce DYRK1A activity in wt mice brains, but reduced DYRK1A activity by ∼30% in the brains of Tg(*Dyrk1a*) and Ts65Dn animals, essentially down to the level of control counterparts. DYRK1A kinase activity was thus normalized by L41 treatment (Fig. 4C). In other words, although basal DYRK1A activity in trisomic and disomic mice brains was insensitive to L41, only excess DYRK1A activity in trisomic mice brains appeared to be sensitive to L41. To verify that all brain DYRK1A activity can, in principle, be inhibited by L41, DYRK1A was extracted and immunopurified from the brains of untreated wt and both transgenic animals. DYRK1A kinase activities were assayed *in vitro* in the presence of increasing concentrations of L41. Results showed that the DYRK1A of wt and transgenic animal brains can be almost fully inhibited *in vitro* with essentially identical dose-response curves (Fig. 4D).

DYRK1A activity was measured following immunoprecipitation (and normalization on the basis of GSK-3α/β activity measured in the same samples) from brain extracts of wt and Tg(*Dyrk1a*) animals treated daily for 5, 12 or 19 days (Fig. 5A-C) with L41, or for 19 days with kinase-inactive L43 (Fig. 5D). As expected, DYRK1A activity was increased in Tg(*Dyrk1a*) versus wt brains. Tg(*Dyrk1a*) brain DYRK1A activity was normalized after treatment with L41 for 12 and 19 days, but not after 5 days of L41 treatment, nor after 19 days of L43 treatment. These results correlate with L41-induced DYRK1A activity normalization (Fig. 5) and cognitive rescue (Fig. 2).

In all previous experiments, brains were collected 1 h after the last leucettine treatment. We wondered about the persistence of the effects of L41 after the last injection (Fig. 6). Tg(*Dyrk1a*) and wt animals were treated with L41/vehicle daily for 19 days. NOR tests were run and brains collected 24 h or 48 h after the last L41 treatment. DYRK1A catalytic activity was dosed in Tg(*Dyrk1a*) and wt mice brains. As expected, wt brain DYRK1A activity was insensitive to L41 treatment. Tg(*Dyrk1a*) brain DYRK1A activity was increased compared with control wt brain DYRK1A activity (Fig. 6A,C), and normalized to wt levels 24 h after the last L41

Disease Models & Mechanisms (2018) 11, dmm035634. doi:10.1242/dmm.035634

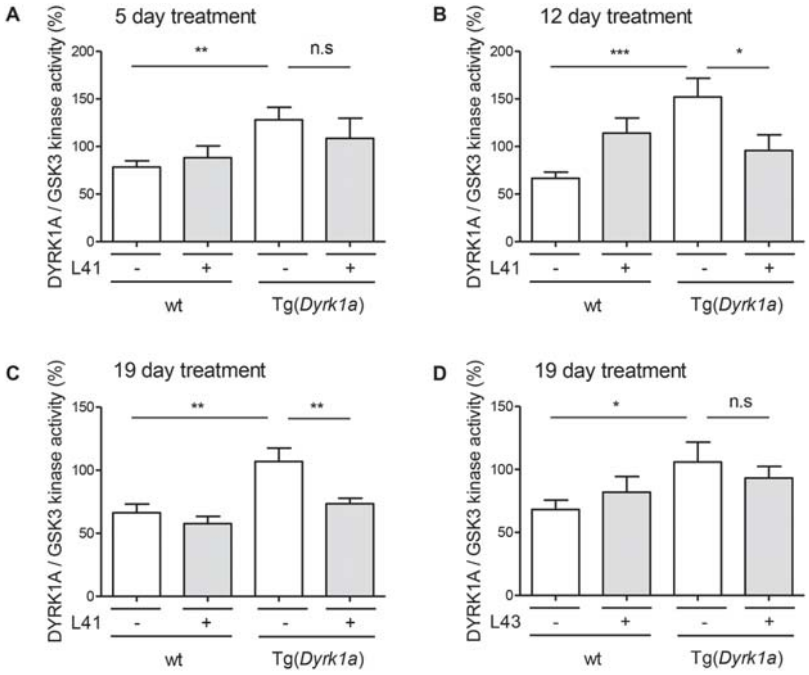

Fig. 5. Effects of L41 treatment duration and treatment with L43. (A-D) Wt and Tg(*Dyrk1a*) mice were treated with L41 or vehicle for 5 (A), 12 (B) or 19 (C) days or L43 or vehicle for 19 days (D). Brains were recovered and extracted, and then DYRK1A and GSK-3α/β were immunopurified and affinity purified, respectively, and assayed for their catalytic activities. DYRK1A kinase activity was normalized with GSK-3α/β activities in each extract (mean±s.e.). DYRK1A inhibition in Tg(*Dyrk1a*) mice brains was not significant after 5 days of L41 treatment (P=0.42), but was increasingly significant after 12 (P=0.04) and 19 (P=0.01) days of L41 treatment. 19 days treatment with kinase-inactive L43 did not reduce DYRK1A activity in Tg(*Dyrk1a*) mice (P=0.5). n.s., not significant. *P<0.05, **P<0.01, ***P<0.001.

treatment (Fig. 6A). In contrast, L41 had no more effects 48 h after the last treatment (Fig. 6C). In terms of restoration of cognitive abilities, the NOR tests revealed that Tg(*Dyrk1a*) deficits were still corrected 24 h, but not 48 h, after the last L41 treatment (Fig. 6B,D). Because L41 is essentially undetectable in brain extracts 2 h after the acute i.p. injection, it might be protected from degradation once bound to DYRK1A or it could have been metabolized to an unidentified, stable active inhibitor.

Overexpressed DYRK1A accumulates in cytoplasm and synapse: differential subcellular L41 distribution

We next investigated the subcellular distribution of DYRK1A in the brains of Tg(*Dyrk1a*) and wt animals (Fig. 7A,B). Brains were collected and cells dissociated and fractionated using two methods. The first allowed the separation of a cytosol+synaptosomes fraction from a nuclear fraction (Fig. 7A). The second separated a cytosol+nuclei fraction from a synaptosomal fraction (Fig. 7B). The purity of each fraction was evaluated by WB with specific markers: postsynaptic density protein 95 (PSD95; also known as DLG4) (cytosol+synaptosomes), histone H2B (nuclei), cyclin L1 (cytosol+nuclei), SYN1 and AMPA-selective glutamate receptor 1 (GLUR1; also known as GRIA1) (synaptosomal fraction) (Fig. 7A,B, top). DYRK1A expression levels were assessed following sodium dodecyl sulfate–polyacrylamide gel electrophoresis (SDS-PAGE) of the different cellular fractions, followed by WB, and normalization to the levels of β-actin (Fig. 7A,B, bottom). DYRK1A was detected in all fractions in both genotypes, but its expression was significantly higher (~1.5-fold), in the cytosol and synaptosomes of Tg(*Dyrk1a*) brains compared with those of wt brains. No differences in nuclear DYRK1A expression were seen between transgenic and wt animals. Brain DYRK1A overdosage in Tg(*Dyrk1a*) animals thus occurs in the cytosol and synaptosomes, but not in the nuclei. We are currently exploring the reasons for this differential distribution of excess DYRK1A.

We next measured L41 levels in nuclear and cytoplasmic fractions prepared from the brains of Tg(*Dyrk1a*) and wt animals which had been i.p. injected daily for 19 days with L41 (20 mg/kg) or vehicle (Fig. 7C,D). At the end of the treatments, brains were recovered and processed for L41 extraction and quantification by isobaric stable isotope chemical labelling, offline hydrophilic interaction chromatography (HILIC), followed by ultra-high precision liquid chromatography with electrospray ionization mass spectrometry (LC–MS). Results show essentially undetectable L41 in vehicle-treated animals, identical L41 levels in the brain nuclear fractions of Tg(*Dyrk1a*) and wt animals (Fig. 7C), and a significantly increased L41 level in the cytoplasmic fraction of Tg(*Dyrk1a*) brains compared with the cytoplasmic fraction of wt animals' brains (Fig. 7D). Thus, DYRK1A overexpression in the transgenic animals' brains appears to be limited to the cytoplasmic fraction, corresponding to the subcellular distribution of overexpressed DYRK1A (Fig. 7A,B). Accordingly, more L41 is detected in the cytoplasmic fraction from transgenic animals compared with their control littermates.

Phosphoproteomic effects of DYRK1A trisomy and L41 treatment reveal key synaptic and cytoskeletal components

To explore the mechanisms underlying the correcting effects of L41 on NOR cognitive deficits of transgenic models, we analysed the phosphoproteome of proteins isolated from the hippocampus, cortex and cerebellum of both Tg(*Dyrk1a*) and Ts65Dn models, along with their respective wt counterparts, and following treatment with vehicle or L41 (20 mg/kg, daily i.p. injection for 19 days) (Fig. 8). All tissue samples were processed for phosphoproteomics analysis based on the enrichment and separation of proteotypic phosphopeptides with HILIC (see Materials and Methods). In Tg(*Dyrk1a*) and Ts65Dn mice, the hippocampus, cortex and cerebellum yielded 1384, 1523 and 2004 peptides, respectively, corresponding to 886, 948 and 1229 proteins (Table 1; Tables S1-S13).

Among the peptides/proteins detected in this study, only 30% of the proteins and 20% of the peptides were significantly up- or downregulated in trisomic versus wt animals. Most peptides (80%) were phosphorylated on serine residues, whereas phosphorylation on threonine (15%) or tyrosine residues (5%) was less frequent.

Disease Models & Mechanisms (2018) 11, dmm035634. doi:10.1242/dmm.035634

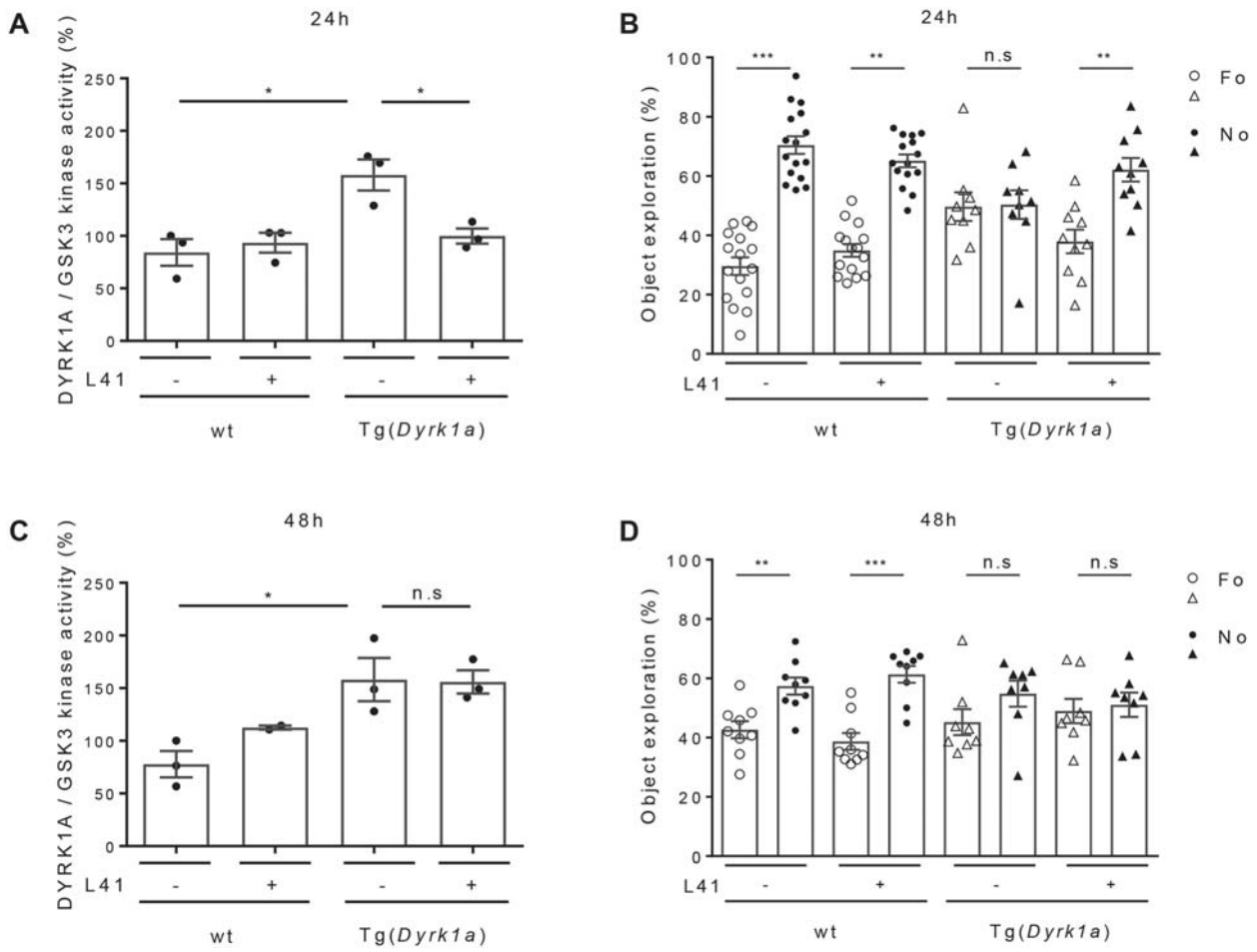

Fig. 6. Persistence of the L41 inhibitory effect on DYRK1A activity and rescue of NOR deficit. (A,C) DYRK1A and GSK-3α/β activities were measured after purification from the brains of wt (*n*=3), L41-treated wt (*n*=3), Tg(*Dyrk1a*) (*n*=3) and L41-treated Tg(*Dyrk1a*) (*n*=3) animals, 24 h (A) or 48 h (C) following the end of a 19 day L41 treatment. After 24 h (*P*=0.02), but not at 48 h (*P*=0.93), the DYRK1A catalytic activity of the treated Tg(*Dyrk1a*) mice brains was normalized compared with that of nontreated animals. (B,D) NOR tests were performed 24 h (B) or 48 h (D) after the last day of the 19 day L41 treatment. Although the rescuing effect was detectable 24 h after the last L41 treatment (*P*=0.01), no rescue was seen after a 48 h delay (*P*=0.72). n.s., not significant. **P*<0.05, ***P*<0.01, ****P*<0.001.

Few peptides (less than 5%) were phosphorylated on two amino acids. Very few phosphopeptides displayed the consensus DYRK1A phosphorylation sequence [R-P-x(1,3)-S/T-P] and most phosphopeptides were predicted to be phosphorylated by kinases from the CMGC (MAPK or GSK-3 protein) or AGC [MTOR or PKG (also known as PRKG1)] groups (data obtained with the PhosphoRS algorithm within the Proteome Discoverer software tool, version 1.4).

We selected the phosphopeptides displaying a trisomy-associated modulation (up- or downregulation) which was reverted by L41 treatment (down- or upregulation) (Fig. 8). These analyses were first run in each brain tissue and in each of the two models and their wt controls. We thus focused on proteins displaying an L41-reversible, trisomy-associated phosphorylation modulation. Based on these two criteria, 258 and 248 phosphoproteins were selected from Tg(*Dyrk1a*) and Ts65Dn hippocampus (Fig. 8A), respectively. Similarly, the Tg(*Dyrk1a*) and Ts65Dn cortex showed 238 and 223 dysregulated phosphoproteins, respectively (Fig. 8A). We found that 330 and 341 phosphoproteins in Tg(*Dyrk1a*) and Ts65Dn cerebellum, respectively, were altered by trisomy and L41 treatment (Fig. 8A). Among these phosphoproteins, 102, 88 and 124 were common to both transgenic models in the hippocampus, cortex and cerebellum, respectively (Tables S1-S12). These shared phosphoproteins were selected for DAVID cluster analysis (Tables S10-S12), which unravelled enrichment in synaptic, cytoskeletal and learning pathways (Fig. 8B; Fig. S4). ToppCluster analysis of the modulated phosphoproteins in each model and each brain region confirmed enrichment in synaptic transmission common to both models in the hippocampus and cortex, while cytoskeleton organization was enriched in both models for all three brain regions (Fig. 8B; Tables S11-S13).

We also compared, in each model, the phosphoproteins subsets of all three brain areas (Fig. 8C). In Tg(*Dyrk1a*), only 16 phosphoproteins were commonly modulated in the three brain substructures (Fig. 8C, left), while only 22 responded to these criteria in Ts65Dn (Fig. 8C, centre). Among these 16 and 22 phosphoproteins shared by the three brain regions, only five were common to both DS models (Fig. 8D): the microtubule-associated proteins MAP1A, MAP1B and MAP2, and presynaptic components piccolo (PCLO) and SYN1. All phosphosites modulated by both trisomy and L41 treatment, for each of the five proteins, are schematized in Fig. S5. They illustrate the complexity of the phosphoproteomics consequences of a single gene trisomy [Tg(*Dyrk1a*)] or a partial chromosome 16 trisomy (Ts65Dn) and the complexity resulting from the treatment with a single

Disease Models & Mechanisms (2018) 11, dmm035634. doi:10.1242/dmm.035634

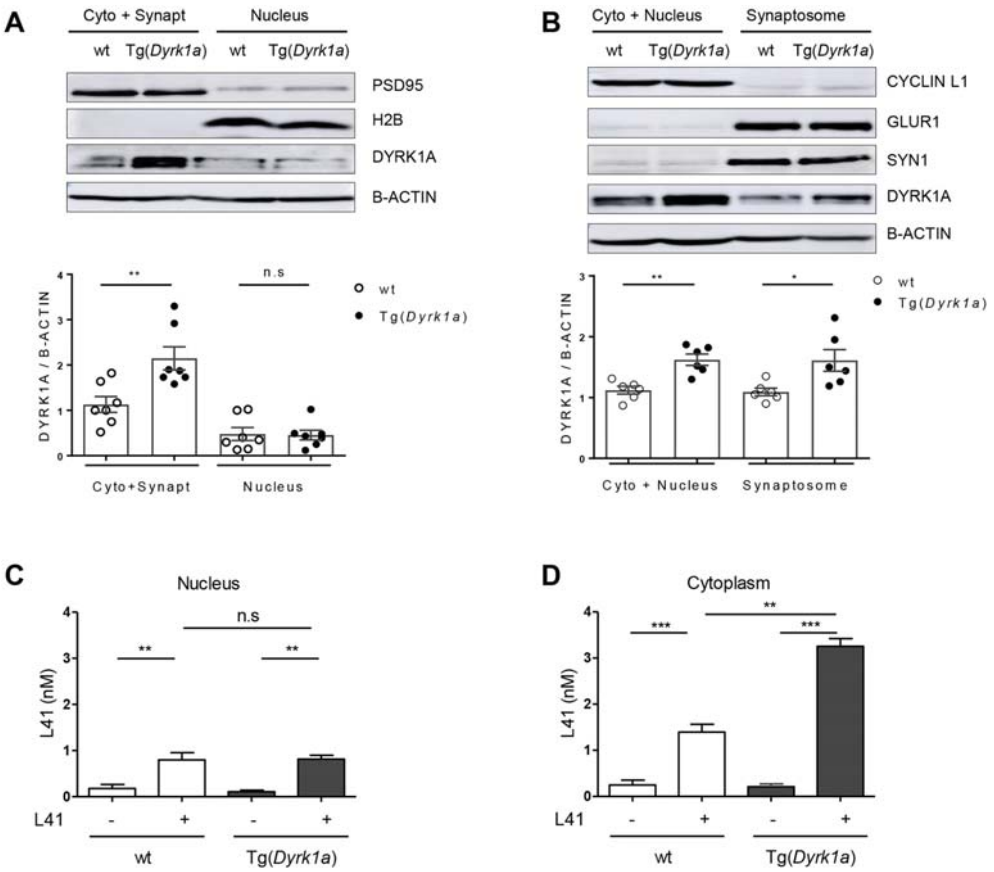

Fig. 7. DYRK1A and L41 subcellular localization. (A,B) Wt or Tg(*Dyrk1a*) brains were fractionated by two methods and the expression of DYRKA was estimated by WB following SDS-PAGE. Reference subcompartment-specific proteins were detected by WB. (A) DYRK1A expression in cytoplasm+synaptosomes and in nuclear fractions [wt, *n*=6; Tg(*Dyrk1a*), *n*=6]. DYRK1A overexpression is observed in the cytoplasm+synaptosomes fraction (*P*=0.006), but not in the nuclear fraction (*P*=0.9). WB of specific markers validates the purity of fractions: PSD95 (95 kDa, cytoplasmic+synaptosomal marker), H2B (17 kDa, nuclear marker), β-actin (42 kDa, housekeeping protein). (B) DYRK1A expression in cytoplasm+nuclei and in synaptosomal fractions [wt, *n*=7; Tg(*Dyrk1a*), *n*=7]. DYRK1A was overexpressed in both cytoplasmic+nuclear (*P*=0.001) and synaptosomal (*P*=0.02) fractions. Fractionation was confirmed by WB of specific compartment markers: cyclin L1 (55 kDa, cytoplasmic+nuclear marker), GLUR1 (100 kDa, postsynaptic marker), SYN1 (74 kDa, presynaptic marker), β-actin (42 kDa, housekeeping protein). (C,D) L41 subcellular levels. L41 was more highly detected in the brain nuclear (C) and cytoplasmic (D) compartments in L41-treated wt (*n*=5) and Tg(*Dyrk1a*) (*n*=2) mice compared with nontreated wt (*n*=5) and nontreated Tg(*Dyrk1a*) (*n*=5) mice. L41 distribution was not significantly different between the brain nuclear fractions of treated wt and Tg mice. In contrast, the L41 level was increased in the cytoplasm of treated Tg mice brain compared with the cytoplasm of control wt mice brain (*P*=0.002). n.s., not significant. **P*<0.05, ***P*<0.01, ****P*<0.001.

pharmacological agent. Among these five proteins, we looked for the residues with increased phosphorylation when DYRK1A was overexpressed, and with reduced phosphorylation when DYRK1A was inhibited by L41, and also matching the consensus DYRK1A phosphorylation sequence (Himpel et al., 2000). Based on these criteria, serine 551 of SYN1 was selected for further study.

DYRK1A interacts with SYN1 and other proteins implicated in synaptic functions

To investigate potential interactions between DYRK1A and SYN1, co-immunoprecipitation (co-IP) experiments were carried out with adult mouse brain lysates (Fig. 9A) using antibodies directed against SYN1 or DYRK1A (negative control, GAPDH). As expected, DYRK1A and SYN1 were found in their respective immunoprecipitates (IPs). SYN1 was detected in DYRK1A IPs and DYRK1A was detected in SYN1 IPs (Fig. 9A), suggesting that these proteins form a direct or indirect complex in brain extracts. Calmodulin-dependent kinase 2A (CAMK2A) was present in SYN1 IPs, as expected from previous results (Llinás et al., 1985; Benfenati et al., 1992) and from its role in presynaptic vesicle pool release (Cesca et al., 2010). CAMK2A was also detected in DYRK1A IPs, suggesting the possibility of a DYRK1A/SYN1/CAMK2A complex, although separate DYRK1A/CAMK2A and SYN1/CAMK2A complexes are possible.

To see whether DYRK1A directly phosphorylates SYN1, we ran *in vitro* kinase assays using recombinant DYRK1A and various SYN1-derived peptides, including Ser551, as potential substrates, or Woodtide as a reference substrate (Fig. 9B,C). Recombinant DYRK1A displayed similar activity towards SYN1-tide or SYN1-S553A-tide compared with Woodtide. In contrast, no significant phosphorylation could be measured with the SYN1-S551A peptide. This confirms that DYRK1A is able to phosphorylate SYN1 on its S551 residue, but not on the nearby Ser553 site. The Ser551 site matches with the consensus DYRK1A phosphorylation site (Fig. 9B).

DISCUSSION

Rescue of cognitive deficits by pharmacological inhibition of excess DYRK1A

In this study, we show that trisomy is associated with an increase in DYRK1A expression and catalytic activity, and that a class of

Disease Models & Mechanisms (2018) 11, dmm035634. doi:10.1242/dmm.035634

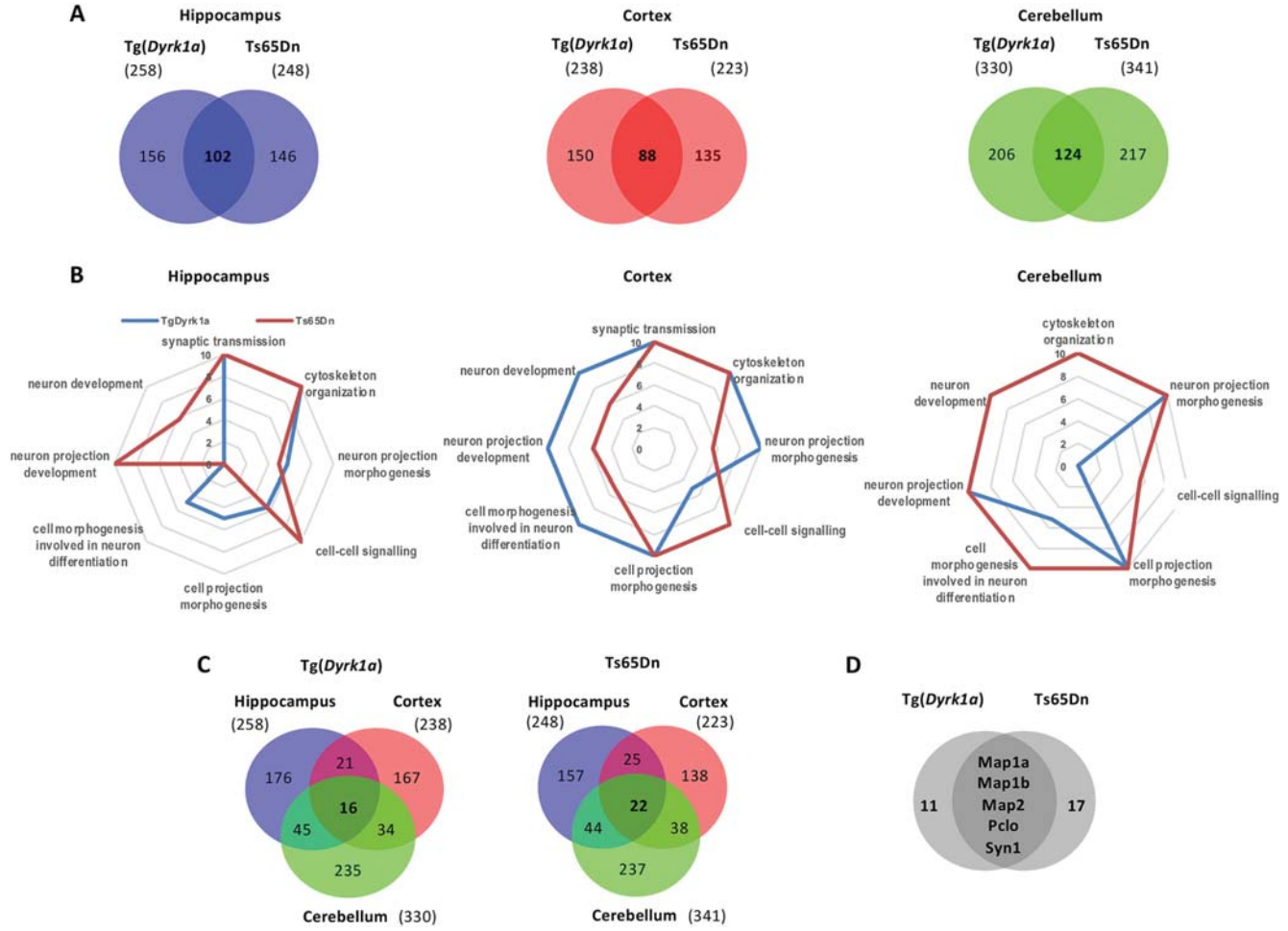

Fig. 8. Phosphoproteomic analysis of Tg(*Dyrk1a*) and Ts65Dn mice brains following exposure to L41. Phosphoproteins, in each brain substructure, that are both up- or downregulated by trisomy and, respectively, down- and upregulated by L41 treatment were selected for analysis. (A) Venn diagrams comparing the two transgenic models versus wt and L41 treatment, at tissue level. 102, 88 and 124 modified phosphoproteins were common to the two models in the hippocampus, cortex and cerebellum, respectively. Numbers in parentheses indicate dual modulated phosphoproteins in each model and each tissue. (B) Biological processes enrichment deregulated by the phosphoproteins which are modulated one way in both Tg(*Dyrk1a*) and Ts65Dn mice and affected by L41 treatment in the opposite way. Represented here are those common to both models and to the three brain tissues. DAVID and ToppCluster analyses were performed in the hippocampus, cortex and cerebellum separately. Enriched classification is determined by the –log(*P*-value). Synaptic transmission, common to the hippocampus and cortex, and cytoskeleton organization, common to the three brain regions, are the processes most modified by trisomy and sensitive to L41. (C) Venn diagrams illustrate the number of dually modulated phosphoproteins in each model and in each tissue, and the numbers shared by different brain areas. 16 and 22 proteins were shared by all three tissues in Tg(*Dyrk1a*) and Ts65Dn mice, respectively. (D) Venn diagram comparison of these 16 and 22 phosphoproteins revealed that five are shared by both models.

synthetic DYRK1A inhibitors, the leucettines, exemplified by L41, is able to cross the blood brain barrier and selectively inhibit the excess DYRK1A linked to trisomy. Why only this fraction of overexpressed DYRK1A is inhibited, and most native, basal DYRK1A is not, remains a mystery. This effect could be linked to the accumulation of excess DYRK1A and L41 in specific cellular compartments and not in others, as shown in Fig. 7. Intriguingly, a similar sensitivity to inhibition of excess DYRK1A compared with ‘normal’ DYRK1A was observed with EGCG. This finding is encouraging in terms of potential therapeutic implications, as complete inhibition of DYRK1A is not desired. Intracellular DYRK1A has been described in both nuclear and cytoplasm compartments (Martí et al., 2003). Our results indicate that it is also present in synaptosomes, which might have consequences on the regulation of synaptic vesicles trafficking (see below).

We here demonstrate the rescuing effect of synthetic DYRK1A inhibitors, leucettines L41 and L99, on deficient recognition memory of three different trisomic mouse models with increasing genetic complexity, Tg(*Dyrk1a*), Ts65Dn and Dp1Yey. These beneficial behavioural effects directly correlate with inhibition of excess DYRK1A activity. There is also a strong coincidence with the duration of the drug treatment (Figs 2A and 5), the potency of the leucettine analogues (Figs 2B and 5) and the duration of the drug-free period following the last injection (Fig. 6). Finally, behavioural correcting benefits detected in the NOR test (Figs 2 and 6) correlate with remodelling of brain functional connectivity detected by fMRI (Fig. 3). However, we observed that working and spatial memories impaired in the Tg(*Dyrk1a*) mice were insensitive to L41 treatment, as assessed in the Y-maze and place object location tasks, respectively. This indicates a specific action of DYRK1A inhibition on molecular pathways specifically related to recognition memory. Our findings further strengthen the essential role of DYRK1A in intellectual phenotypes associated with DS. Leucettine derivatives should thus

Disease Models & Mechanisms (2018) 11, dmm035634. doi:10.1242/dmm.035634

Table 1. Summary of phosphoproteomic analyses

Model	Tg(*Dyrk1a*)			Ts65Dn			Common		
Brain area	Hippocampus	Cortex	Cerebellum	Hippocampus	Cortex	Cerebellum	Hippocampus	Cortex	Cerebellum
Total protein number	886	948	1229	886	948	1229	–	–	–
Total peptide number	1384	1523	2004	1384	1523	2004	–	–	–
Modulated proteins, trisomic vs wt	275	256	364	257	230	365	–	–	–
Modulated peptides, trisomic vs wt	333	296	437	311	270	422	–	–	–
Modulated proteins, trisomic, L41 vs vehicle	267	240	344	253	228	355	34	38	59
Modulated peptides trisomic, L41 vs vehicle	321	275	403	307	265	410	40	38	63
Phospho-Ser peptides	265	221	333	246	205	320	33	29	51
Phospho-Thr peptides	39	44	58	53	42	75	6	6	11
Phospho-Tyr peptides	17	10	12	8	18	15	1	3	1
Phospho-Ser and phospho-Thr peptides	18	19	23	10	6	24	–	–	–
Phospho-Ser and phospho-Tyr peptides	5	1	4	2	3	4	–	–	–
Phospho-Thr and phospho-Tyr peptides	6	1	4	7	4	2	–	–	–
DYRK1A phosphorylation sites	1	7	8	6	3	6	–	–	–
Other kinases' phosphorylation sites	279	251	383	263	223	351	–	–	–

be investigated further as drug candidates to improve cognitive functions of DS patients.

L41 treatment in DYRK1A-overexpressing mice triggers remodelling of brain FC pathways

Brain rsfMRI in Dp1Yey mice revealed global resilience of functional cerebral circuitry after L41 administration. Notably, L41 corrected the abnormal DMN patterns found in Dp1Yey mice, but also acted on connectivity of key brain areas associated with cognitive and memory processing (PFC, ACA, PERI, HF). DMN (Raichle, 2015) – previously described as a highly active circuitry during rest – and preserved across species (Stafford et al., 2014), was shown to be vulnerable to various neuropathological conditions (Hawellek et al., 2011; Raichle, 2015; Zhou et al., 2017), including DS (Anderson et al., 2013; Pujol et al., 2015). The core area of this network in mice is the RSP (associated

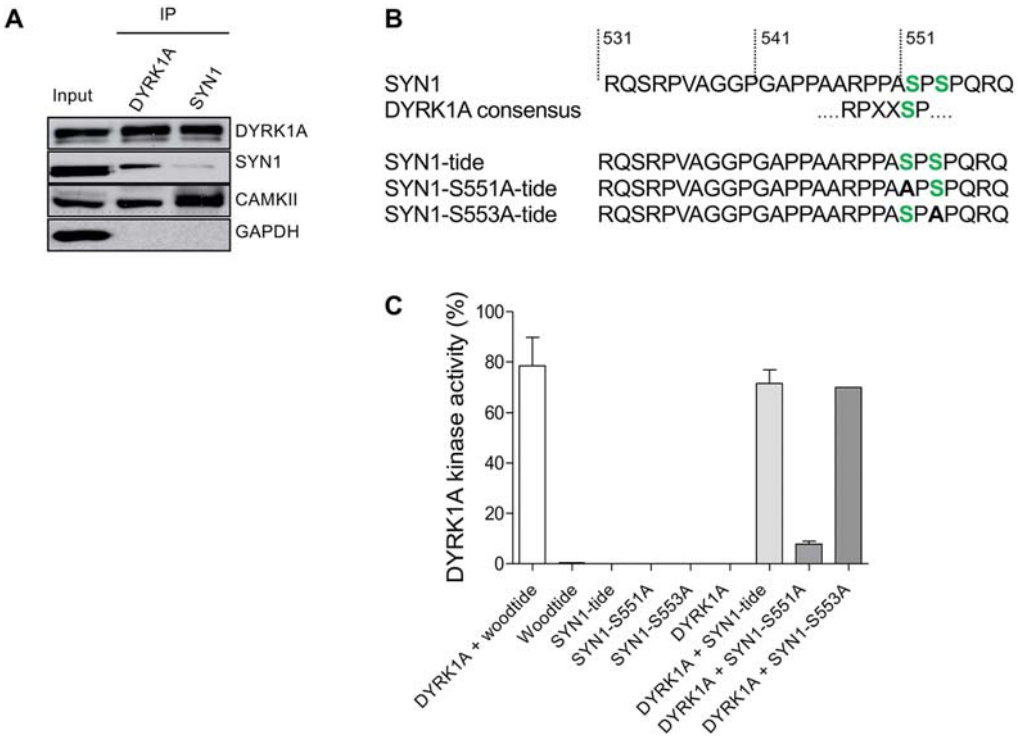

Fig. 9. Direct interaction of DYRK1A and SYN1, phosphorylation of SYN1 by DYRK1A. (A) DYRK1A and SYN1 were immunoblotted following immunoprecipitation from wt mice brain extracts. DYRK1A or SYN1 present in the starting material (Input) were recovered in the IPs. SYN1 (74 kDa) was present in the DYRK1A IP and DYRK1A (85 kDa) was detected in the SYN1 IP, suggesting that these two proteins interact directly. Positive control of the SYN1 IP was performed using an anti-CAMKII antibody. As expected, CAMKII (50 kDa) was present in the SYN1 IP. DYRK1A IP also brought down CAMKII, suggesting complexes between SYN1, CAMKII and DYRK1A. (B) Sequence of SYN1 in the vicinity of Ser551 matches with the consensus DYRK1A phosphorylation site. Based on this sequence, three peptides were synthesized and used as potential substrates: SYN1, SYN1-S551A and SYN1-S553A. (C) Kinase activity of recombinant DYRK1A towards the three different SYN1peptides. SYN1 and SYN1-S553A peptides were phosphorylated at the same level as Woodtide by recombinant DYRK1A (71.7%±5.2%, 70.1% and 78.4%±11.4%, respectively). No significant catalytic activity was measured with the SYN1-S551A peptide (7.9%±1.2%).

with the posterior cingulate/precuneus cortex in humans) (Hübner et al., 2017; Sforazzini et al., 2014). Our analysis unravelled increased local connectivity around the RSP in DS mice, but strongly reduced long-range communication with frontocortical brain regions (ACA, PFC; Fig. S3), when compared with wt animals. This short-range stronger connectivity is not limited to the RSP, but represented a common feature for other investigated brain regions (ACA, PERI, HF) of Dp1Yey mice. Such a pattern of increased local, short-range brain communication was described as a cardinal feature of FC in DS patients (Anderson et al., 2013; Pujol et al., 2015; Vega et al., 2015). Indeed, DS human brains are characterized by simplified network structure, organized by local connectivity (Anderson et al., 2013; Pujol et al., 2015; Vega et al., 2015) and impaired efficiency to integrate information from distant connections.

Dp1Yey mouse brains additionally displayed features of higher negative functional correlations as compared with the wt vehicle group and, more obviously, a reversed correlation pattern (switch from positive to negative correlations) between the RSP and frontal cortical areas in the DS model. This feature, attenuated or corrected following L41 treatment, could eventually be discussed in the context of L41 regulation of inhibition/excitation ratios, imbalanced in DYRK1A-overexpressing mice (Souchet et al., 2014). Indeed, increased number and signal intensity from neurons expressing GAD67 (also known as GAD1), an enzyme that synthesizes GABA, indicating inhibition pathway alterations, was quantified in three different DS models (Souchet et al., 2014), including Dp1Yey. Pharmacological correction of inhibition/excitation was achieved in the Tg(*Dyrk1a*) DS mouse model (Souchet et al., 2015) by EGCG treatment. We can speculate on a similar effect of L41 on inhibition/excitation balance, and subsequent modulation of brain connectivity. Nevertheless, the brain synchrony modifications after L41 inhibition of excess DYRK1A activity in DS models might potentially reflect other molecular mechanisms and interactions at the synaptic and cytoskeletal level, as shown here, and subsequently underpin correction of cognitive and memory deficits of DS mice. Importantly, L41 had only limited effects on FC in wt animals, whereas in the Dp1Yey model it largely impacted the connectivity features, on distributed action sites, that coincide with alterations reported for brain anatomy in DS models, most notably, frontal and prefrontal cortical areas (ACA/PFA), the HF, PAL and TH. Volumetric MRI in DS mouse models, showed a general trend for smaller frontal lobes, hippocampal and cerebellar regions, but larger thalamic and hypothalamic areas (Powell et al., 2016; Roubertoux et al., 2017). Diffusion MRI also identified potential microstructural alterations in the above-mentioned areas and also the striatum (including the PAL) (Nie et al., 2015). Our rsfMRI study advances the current knowledge on the brain functional communication in DS mouse models, revealing targeted and effective action of L41 on brain circuitry, consistent with the profile of cognitive and novel object recognition memory improvements.

DYRK1A and SYN1

Phosphoproteomic analyses using ultra-high precision LC–MS analysis unravelled several clusters of neuronal phosphorylated proteins directly controlled by DYRK1A or clusters indirectly modulated in the trisomic condition and sensitive to L41 treatment. Five phosphoproteins were shared by Tg(*Dyrk1a*) and Ts65Dn mice and were present in three brain substructures (hippocampus, cortex, cerebellum) (Fig. 8). Furthermore, these phosphoproteins showed significant modulation in their phosphorylation levels in trisomic versus disomic animals and these modulations were sensitive, in the opposite direction, to L41 treatment. A few key pathways, including controlling synaptic vesicle (SV) transport, calcineurin NFAT signalling and cytoskeleton organization, were found to be directly affected by DYRK1A, or as a consequence of its kinase activity (Fig. S4), while others might represent indirect effects of the overdosage. Nevertheless, the immune response was found to be affected, correlating with several studies linking DYRK1A to inflammation. We here focused on SYN1 as it was the only protein that revealed a serine residue corresponding to the DYRK1A phosphorylation consensus sequence. SYN1 Ser551 was hyperphosphorylated following DYRK1A overexpression and dephosphorylated following L41 treatment. Representative annotated ultra-high resolution product ion spectrum of proteotypic peptide qSRPVAGGPGAPPAARPPAsPSPqR encoding the phosphorylated residue Ser551 is shown in Fig. S6.

Co-IP experiments showed that DYRK1A interacts, either directly or indirectly, with SYN1 (Fig. 9). SYN1 has been described to be involved in the reserve SV pool maintenance at the presynaptic bouton by tethering SVs to the actin cytoskeleton (Hilfiker et al., 2005; Benfenati et al., 1991). Phosphorylation of SYN1 by CAMKII leads to the release of SVs and allows them to move close to the active zone (Llinás et al., 1991). Neurotransmitter release at the active zone is thus strongly dependent on SYN1 phosphorylation. We showed that SYN1 was phosphorylated by DYRK1A on its S551 residue *in vitro* and *in vivo*, thus highlighting a novel role of DYRK1A in SYN1-dependent presynaptic vesicle trafficking. Besides its physiological role in synaptic plasticity regulation, SYN1 has been associated with epilepsy (Garcia et al., 2004; Fassio et al., 2011). Mutations in the phosphorylation domains of SYN1 essential for vesicle recycling control have been related to epilepsy (Fassio et al., 2011). In addition, mental retardation, autosomal dominant 7 (MRD7) patients with *Dyrk1a* haploinsufficiency display epilepsy seizures (Courcet et al., 2012; Møller et al., 2008; Oegema et al., 2010; Valetto et al., 2012; Yamamoto et al., 2011). Our results suggest that epileptic seizures observed in MRD7 patients could be induced by defects in SYN1 regulation.

DYRK1A, microtubule-binding proteins, PCLO and other synaptic targets

The other four proteins found in our phosphoproteomics study will be the object of another study but are briefly reviewed here. The detection of MAP1A, MAP1B and MAP2, all previously reported as DYRK1A substrates (Murakami et al., 2012; Scales et al., 2009), validated the power of our analysis and confirmed the role of DYRK1A in dendrite morphogenesis and microtubule regulation (Ori-McKenney et al., 2016). The last phosphoprotein, PCLO, is a cytoskeletal matrix protein associated with the presynaptic active zone (Cases-Langhoff et al., 1996), which acts as a scaffolding protein implicated in SV endocytosis and exocytosis (Garner et al., 2000; Fenster et al., 2003). The lack of PCLO in the human brain leads to a dramatic neuronal loss associated with pontocerebellar hypoplasia type III (Ahmed et al., 2015). Moreover, PCLO knockdown in cultured hippocampal neurons increases SYN1 dispersion out of the presynaptic terminal and SV exocytosis (Leal-Ortiz et al., 2008). It has been shown that PCLO modulates neurotransmitter release by regulating F-actin assembly (Waites et al., 2011). It clearly appears that PCLO acts upstream of SYN1 and regulates its role in vesicle recycling.

Taken together, our findings reveal SYN1 as a new direct substrate of DYRK1A, suggesting a novel role of this kinase in the regulation of SV release at the presynaptic terminal. Moreover, the

relatively safe and selective DYRK1A inhibitors, the leucettines, successfully correct recognition memory deficits associated with DS in three different mice models. Although the DYRK1A-dependent biological process which is rescued by these drugs still needs to be elucidated, leucettines and their analogues represent promising therapeutic drugs to enhance cognitive functions in DS patients.

DYRK1A, DS and AD

There is strong support for the involvement of DYRK1A in cognitive deficits associated with Alzheimer's disease (AD): (1) *DYRK1A* mRNA (Kimura et al., 2007) and DYRK1A protein (Ferrer et al., 2005) levels are increased in postmortem human AD brains compared with healthy brains; (2) calpain 1-induced cleavage of DYRK1A is observed in AD brains and associated with increased activity (Jin et al., 2015); (3) DYRK1A phosphorylates key AD players, such as amyloid precursor protein (Ryoo et al., 2008), presenilin 1 (Ryu et al., 2010), Tau (also known as MAPT) (Woods et al., 2001; Ryoo et al., 2007; Azorsa et al., 2010; Coutadeur et al., 2015; Jin et al., 2015), septin (Sitz et al., 2008) and neprylysin (Kawakubo et al., 2017); (4) DYRK1A regulates splicing of Tau mRNA (Shi et al., 2008; Wegiel et al., 2011; Yin et al., 2012, 2017; Jin et al., 2015); (5) DYRK1A inhibition corrects cognitive defects in 3xTG-AD (Branca et al., 2017), APP/PS1 (B. Souchet, unpublished) and Aβ25-35 peptide-injected wt mice (Naert et al., 2015), three widely used mice models of AD. These facts provide additional incentive to investigate the regulation and substrates of brain DYRK1A and to develop potent and selective DYRK1A inhibitors to treat cognitive deficits observed in different indications. DS patients display early symptoms of AD and show a high frequency of dementia at later age (Ballard et al., 2016). The triplication of APP located on the HSA21 is thought to contribute to amyloid plaques and neurofibrillary tangles, two causative factors in AD, that accumulate early in 30- to 40-year-old DS people (Head, et al., 2012a). These factors, associated with neuroinflammation and oxidative damage also diagnosed in both AD and DS individuals, lead to precocious dementia observed from age 30 to 39 (Head et al., 2012b). Studying DS will have an impact on the understanding of AD and, reciprocally, DYRK1A is clearly a common factor between the two diseases.

MATERIALS AND METHODS

Animal models, treatment and behaviour assessment

Tg(*Dyrk1a*) mutant mice and Dp1Yey models were maintained on the C57BL/6J genetic background. Ts(17^{16})65Dn trisomic mice were obtained from The Jackson Laboratory and kept on the C57BL/6J×C3B, a congenic sighted line for the BALB/c allele at the *Pde6b* locus (Hoelter et al., 2008). The local ethics committee, Com'Eth (no. 17), approved all mouse experimental procedures, under the accreditation number APAFIS #5331 and #3473, with Y.H. as the principal investigator.

Behavioural studies were conducted in 12- to 20-week-old male animals. All assessments were scored blind to genotype and treatment, as recommended by the ARRIVE guidelines (Karp et al., 2015; Kilkenny et al., 2010). Leucettine L41 was prepared at 40 mg/ml in dimethyl sulfoxide (DMSO), aliquoted and stored below −20°C. The final formulation was prepared just prior to use as a 2 mg/ml solution diluted in PEG300/water (50/45), to reach a final DMSO/PEG300/water 5/50/45 (v/v/v) mix. Treated animals received a daily dose (5, 12 or 19 days) of this formulation by i.p. injection of 20 mg/kg/day. Nontreated animals received the same formulation without L41.

The NOR task is based on the innate tendency of rodents to differentially explore a novel object over a familiar one (Ennaceur and Delacour, 1988). Day 1 was a habituation session. Mice freely explored the apparatus, a white circular arena (53 cm diameter) placed in a dimly lit testing room (40 lux). On day 2, the acquisition phase, mice were free to explore two identical objects for 10 min. Mice were then returned to their home cage for a 24 h retention interval. To test their memory, on day 3, one familiar object (already explored during the acquisition phase) and one novel object were placed in the apparatus and mice were free to explore the two objects for a 10 min period. Between trials and subjects, the different objects were cleaned with 50° ethanol to reduce olfactory cues. To avoid a preference for one of the objects, the new object was different for different animal groups and counterbalanced between genotype and treatment as well as for location of novel and familiar objects (left or right). Object exploration was manually scored and defined as the orientation of the nose to the object at a distance <1 cm. For the retention phase, the percent of time spent exploring familiar versus novel objects was calculated to assess memory performance.

rsfMRI

rsfMRI was performed on 26 animals separated into four groups: wt, vehicle treated; wt, L41 treated; Dp1Yey, vehicle treated; Dp1Yey, L41 treated. rsfMRI was carried under medetomidine sedation during scanning [subcutaneous bolus injection, 0.3 mg/kg in 100 µl 0.9% NaCl solution right before the scan followed by continuous subcutaneous infusion of medetomidine (0.6 mg/kg, 200 µl/h)]. Physiological parameters were continuously monitored. rsfMRI data were collected using a 7 T small bore animal scanner and a mouse head adapted cryocoil (Biospec 70/20 and MRI CryoProbe, Bruker, Germany). The whole brain was examined [24 slices; 150×150×700 μm^3 spatial resolution) using single shot gradient echo EPI (echo time/repetition time=10 ms/1700 ms)] and 200 volumes were recorded. The preprocessing included motion correction, data co-registration with Allen Mouse Brain Atlas (mouse.brain-map.org), detrending, band pass filtering (0.01-0.1 Hz) and regression of ventricular signal. For seed-based correlation analysis, the functional connectivity of several brain areas was mapped: RSP to map the default mode network, CA1, DG, PERI and anterior cingulate area (ACC). Correlation coefficients were then computed (two-tailed Student's *t*-test, $P<0.001$) between the seed region and the averaged BOLD signal time series of the remaining whole brain for each group and were converted and mapped to z-values using Fisher's r-to-z transformation.

DYRK1A and GSK-3β protein levels

Brains were obtained from mice and snap-frozen until further use. Then tissues were weighed, homogenized and sonicated in 1 ml lysis buffer (60 mM β-glycerophosphate, 15 mM p-nitrophenylphosphate, 25 mM Mops pH 7.2, 15 mM EGTA, 15 mM $MgCl_2$, 2 mM dithiothreitol, 1 mM sodium orthovanadate, 1 mM sodium fluoride, 1 mM phenylphosphate disodium and protease inhibitor cocktail) per g of material. Homogenates were centrifuged for 15 min at 17,000 ***g*** and 4°C. The supernatant was recovered and assayed for protein content (Bio-Rad, France). The proteins were separated by 10% NuPAGE pre-cast Bis-Tris polyacrylamide mini gel electrophoresis (Invitrogen, France) with MOPS-SDS running buffer. Proteins were transferred to 0.45-µm nitrocellulose filters (Schleicher and Schuell, Germany). They were blocked with 5% low-fat milk in Tris-buffered vehicle/Tween 20, and incubated overnight at 4°C with antibodies. Anti-DYRK1A (H00001859-M01; 1:1000) and anti-GSK-3α/β (KAM-ST002E; 1:1000) were obtained from Interchim (France) and Stressgen (France), respectively. Appropriate secondary antibodies conjugated to horseradish peroxidase (Bio-Rad) were added to visualize the proteins using the enhanced chemiluminescence reaction (ECL, Amersham, France).

Protein kinase assays

Protein kinase assays to measure the catalytic activity of DYRK1A in the brains of the animals treated with or without drugs were performed as follows: frozen half brains were homogenized in lysis buffer (1.2 ml/half brain) using Precellys® homogenizer tubes. After centrifugation at 2800 ***g*** for 2×15 s, 1 mg brain extract was incubated with 2 µg DYRK1A (H00001859 M01, Interchim) or GSK3-β (MBS8508391, Emelca Bioscience, France) antibodies at 4°C for 1 h under gentle rotation. Then, 20 µl protein G agarose beads (Thermo Fisher Scientific, France), previously washed three times with bead buffer (50 mM Tris pH 7.4, 5 mM NaF, 250 mM NaCl,

5 mM EDTA, 5 mM EGTA, 0.1% Nonidet P-40 and protease inhibitor cocktail from Roche, France), were added to the mix and gently rotated at 4°C for 30 min. After a 1 min spin at 10,000 ***g*** and removal of the supernatant, the pelleted immune complexes were washed three times with bead buffer, and a last time with Buffer C (60 mM β-glycerophosphate, 30 mM p-nitrophenolphosphate, 25 mM Mops pH 7.2, 5 mM EGTA, 15 mM $MgCl_2$, 2 mM dithiothreitol, 0.1 mM sodium orthovanadate, 1 mM phenylphosphate, protease inhibitor cocktail). DYRK1A or GSK-3 immobilized on beads were assayed in buffer C as described in the Supplementary Materials and Methods with Woodtide (KKISGRLSPIMTEQ) (1.5 µg/assay) or GSK3-tide (YRRAAVPPSPSLSRHSSPHQpSED-EEE, where pS stands for phosphorylated serine) as substrates.

Protein kinase assays to evaluate SYN1 phosphorylation by DYRK1A were performed with 50 ng recombinant DYRK1A protein (PV3785, Thermo Fisher Scientific) and 0.98 mM Woodtide, and three peptides derived from the SYN1 putative DYRK1A phosphorylation site (Fig. 9C). Kinase activity was then measured as described in the Supplementary Materials and Methods.

The selectivity of the three leucettines used in this study was evaluated in a panel of 16 recombinant protein kinases assayed as described in the Supplementary Materials and Methods.

Subcellular fractionation

Nuclear, cytosolic and synaptosomal subcellular fractionation of brain tissue was performed with the Syn-PER™ and ProteoExtract® Tissue Dissociation Buffer Kit and Subcellular Proteome Extraction Kit following the instructions of the manufacturer. Fractions were analysed by SDS-PAGE and WB with specific antibodies.

Phosphoproteomics results analysis

Gene ontology enrichment analyses of phosphoproteins that are modulated (up- or downregulated) in Tg(*Dyrk1a*) or Ts65Dn mice versus wt and also modulated in the opposite manner (down- or upregulated) by the L41 treatment, were conducted using ToppCluster (Bonferroni correction, *P*-value cutoff 0.05). Only biological processes common to the three brain regions and both models are presented (complete biological processes are listed in Tables S11-S13).

DYRK1A substrates and their respective phosphorylation sites were identified in the phosphoproteome based on the DYRK1A phosphorylation consensus sequence R-P-x(1,3)-S/T-P (Himpel et al., 2000). Protein-protein interactions of each substrate were generated with STRING web server application. Biological process enrichments of each cluster were assessed by using ToppCluster web server application. Phospho-network was mapped with the Cytoscape tool. See Supplementary Materials and Methods for details.

Immunoprecipitation and immunoblotting

All immunoprecipitations were performed on fresh half brains of 3-month-old wt male mice. Brains were dissected and lysed in 1.2 ml RIPA lysis buffer (Santa-Cruz Biotechnology, France) using Precellys® homogenizer tubes. After centrifugation at 2800 ***g*** for 2×15 s, 1 ml brain extract was incubated with 2 µg of antibody of interest at 4°C for 1 h under gentle rotation. An aliquot of the remaining supernatant was kept for further immunoblotting as homogenate control. Then, 20 µl protein G agarose beads, previously washed three times with bead buffer, were added to the mix and gently rotated at 4°C for 30 min. After a 1 min spin at 10,000 ***g*** and removal of the supernatant, the pelleted immune complexes were washed three times with bead buffer before WB analysis with appropriate antibodies directed against DYRK1A (H00001859 M01, Interchim; 1:1000), PSD95 (ab18258, Abcam, France; 1:1000), SYN1 (ab64581, Abcam; 1:1000), CAMK2A (PA5-14315, Thermo Fisher Scientific; 1:1000) and GAPDH (MA5-15738, Thermo Fisher Scientific; 1:3000). Immunoblots were revealed with Clarity Western ECL Substrate (Bio-Rad).

Competing interests

L.M. is founder, CEO and CSO of ManRos Therapeutics, which licensed the patent on leucettines and develops these as DS/AD drug candidates. L.M., F.C. and J.-P.B. are co-inventors on the leucettine patent.

Author contributions

Conceptualization: T.L.N., A.D., S.D.G., L.M., Y.H.; Methodology: T.L.N., A.D., N.L., B.V., M.K., A.E.M., L.-A.H., E.L., J.-P.B., F.C., S.D.G.; Software: M.K., A.E.M., L.-A.H., S.D.G.; Validation: T.L.N., B.V., L.M.; Formal analysis: T.L.N., A.M., M.K., A.E.M., L.-A.H., S.D.G.; Investigation: T.L.N., A.D., A.M., N.L., B.V., G.P., M.K., A.E.M., J.-P.B., F.C., S.D.G.; Resources: A.M., E.L., J.-P.B., F.C.; Data curation: A.M., M.K., A.E.M., L.-A.H., S.D.G.; Writing - original draft: T.L.N., L.M.; Writing - review & editing: T.L.N., S.D.G., L.M., Y.H.; Supervision: S.D.G., L.M., Y.H.; Project administration: L.M., Y.H.; Funding acquisition: L.M., Y.H.

Funding

This work was supported by Fonds Unique Interministériel (TRIAD project; L.M., Y.H., J.-P.B.), Conseil Régional de Bretagne (L.M., Y.H., J.-P.B.), Fondation Jérôme Lejeune (L.M.), Seventh Framework Programme (BlueGenics; L.M.), Agence Nationale de la Recherche (Programme Investissements d'Avenir; ANR-10-IDEX-0002-02, ANR-10-LABX-0030-INRT, ANR-10-INBS-07 PHENOMIN to Y.H.) and CIFRE (T.L.N.).

Supplementary information

Supplementary information available online at
http://dmm.biologists.org/lookup/doi/10.1242/dmm.035634.supplemental

References

Ahmed, M. Y., Chioza, B. A., Rajab, A., Schmitz-Abe, K., Al-Khayat, A., Al-Turki, S., Baple, E. L., Patton, M. A., Al-Memar, A. Y., Hurles, M. E. et al. (2015). Loss of PCLO function underlies pontocerebellar hypoplasia type III. *Neurology* **84**, 1745.

Ahn, K.-J., Jeong, H. K., Choi, H.-S., Ryoo, S.-R., Kim, Y. J., Goo, J.-S., Choi, S.-Y., Han, J.-S., Ha, I. and Song, W.-J. (2006). DYRK1A BAC transgenic mice show altered synaptic plasticity with learning and memory defects. *Neurobiol. Dis.* **22**, 463-472.

Altafaj, X., Dierssen, M., Baamonde, C., Martí, E., Visa, J., Guimerà, J., Oset, M., González, J. R., Flórez, J., Fillat, C. et al. (2001). Neurodevelopmental delay, motor abnormalities and cognitive deficits in transgenic mice overexpressing Dyrk1A (Minibrain), a murine model of Down's syndrome. *Hum. Mol. Genet.* **10**, 1915-1923.

Altafaj, X., Martín, E. D., Ortiz-Abalia, J., Valderrama, A., Lao-Peregrín, C., Dierssen, M. and Fillat, C. (2013). Normalization of Dyrk1A Expression by AAV2/1-shDyrk1A attenuates hippocampal-dependent defects in the Ts65Dn mouse model of Down syndrome. *Neurobiol. Dis.* **52**, 117-127.

Alvarez, M., Altafaj, X., Aranda, S. and de la Luna, S. (2007). DYRK1A autophosphorylation on serine residue 520 modulates its kinase activity via 14-3-3 binding. *Mol. Biol. Cell* **18**, 1167-1178.

Anderson, J. S., Nielsen, J. A., Ferguson, M. A., Burback, M. C., Cox, E. T., Dai, L., Gerig, G., Edgin, J. O. and Korenberg, J. R. (2013). Abnormal brain synchrony in Down syndrome. *NeuroImage* **2**, 703-715.

Arron, J. R., Winslow, M. M., Polleri, A., Chang, C.-P., Wu, H., Gao, X., Neilson, J. R., Chen, L., Heit, J. J., Kim, S. K. et al. (2006). NFAT dysregulation by increased dosage of DSCR1 and DYRK1A on chromosome 21. *Nature* **441**, 595-600.

Azorsa, D. O., Robeson, R. L. H., Frost, D., Meec hoovet, B., Brautigam, G. R., Dickey, C., Beaudry, C., Basu, G. D., Holz, D. R., Hernandez, J. A. et al. (2010). High-content siRNA screening of the kinome identifies kinases involved in Alzheimer's disease-related tau hyperphosphorylation. *BMC Genomics* **11**, 25.

Ballard, C., Mobley, W., Hardy, J., Williams, G. and Corbett, A. (2016). Dementia in Down's syndrome. *Lancet Neurol.* **15**, 622-636.

Benfenati, F., Valtorta, F. and Greengard, P. (1991). Computer modeling of Synapsin I binding to synaptic vesicles and F-actin: implications for regulation of neurotransmitter release. *Proc. Natl Acad. Sci. USA* **88**, 575-579.

Benfenati, F., Valtorta, F., Rubenstein, J. L., Gorelick, F. S., Greengard, P. and Czernik, A. J. (1992). Synaptic vesicle-associated Ca2+/Calmodulin-dependent protein kinase II is a binding protein for synapsin I. *Nature* **359**, 417-420.

Branca, C., Shaw, D. M., Belfiore, R., Gokhale, V., Shaw, A. Y., Foley, C., Smith, B., Hulme, C., Dunckley, T., Meechoovet, B. et al. (2017). Dyrk1 inhibition improves Alzheimer's disease-like pathology. *Aging Cell.* **16**, 1146-1154.

Cases-Langhoff, C., Voss, B., Garner, A. M., Appeltauer, U., Takei, K., Kindler, S., Veh, R. W., De Cmilli, P., Gundelfinger, E. D. and Garner, C. C. (1996). Piccolo, a novel 420 kDa protein associated with the presynaptic cytomatrix. *Eur. J. Cell Biol.* **10**, 214-223.

Cesca, F., Baldelli, P., Valtorta, F. and Benfenati, F. (2010). The synapsins: key actors of synapse function and plasticity. *Prog. Neurobiol.* **91**, 313-348.

Chen, C.-K., Bregere, C., Paluch, J., Lu, J. F., Dickman, D. K. and Chang, K. T. (2014). Activity-dependent facilitation of synaptojanin and synaptic vesicle recycling by the minibrain kinase. *Nat. Commun.* **5**, ncomms5246.

Courcet, J.-B., Faivre, L., Malzac, P., Masurel-Paulet, A., Lopez, E., Callier, P., Lambert, L., Lemesle, M., Thevenon, J., Gigot, N. et al. (2012). The DYRK1A gene is a cause of syndromic intellectual disability with severe microcephaly and epilepsy. *J. Med. Genet.* **49**, 731-736.

Coutadeur, S., Benyamine, H., Delalonde, L., de Oliveira, C., Leblond, B., Foucourt, A., Besson, T., Casagrande, A.-S., Taverne, T., Girard, A. et al. (2015). A novel DYRK1A (Dual Specificity Tyrosine Phosphorylation-Regulated Kinase 1A) inhibitor for the treatment of Alzheimer's disease: effect on tau and amyloid pathologies in vitro. *J. Neurochem.* **133**, 440-451.

de la Torre, R., De Sola, S., Pons, M., Duchon, A., de Lagran, M. M., Farré, M., Fitó, M., Benejam, B., Langohr, K., Rodriguez, J. et al. (2014). Epigallocatechin-3-gallate, a DYRK1A inhibitor, rescues cognitive deficits in Down syndrome mouse models and in humans. *Mol. Nutr. Food Res.* **58**, 278-288.

de la Torre, R., de Sola, S., Hernandez, G., Farré, M., Pujol, J., Rodriguez, J., Espadaler, J. M., Langohr, K., Cuenca-Royo, A., Principe, A. et al. (2016). Safety and efficacy of cognitive training plus epigallocatechin-3-gallate in young adults with Down's syndrome (TESDAD): a double-blind, randomised, placebo-controlled, phase 2 trial. *Lancet Neurol.* **15**, 801-810.

Debdab, M., Carreaux, F., Renault, S., Soundararajan, M., Fedorov, O., Filippakopoulos, P., Lozach, O., Babault, L., Tahtouh, T., Baratte, B. et al. (2011). Leucettines, a class of potent inhibitors of cdc2-like kinases and dual specificity, tyrosine phosphorylation regulated kinases derived from the marine sponge Leucettamine B: modulation of alternative pre-RNA splicing. *J. Med. Chem.* **54**, 4172-4186.

Di Vona, C., Bezdan, D., Islam, A. B. M. M. K., Salichs, E., López-Bigas, N., Ossowski, S. and de la Luna, S. (2015). Chromatin-wide profiling of DYRK1A reveals a role as a gene-specific RNA polymerase II CTD kinase. *Mol. Cell* **57**, 506-520.

Duchon, A. and Herault, Y. (2016). DYRK1A, a dosage-sensitive gene involved in neurodevelopmental disorders, is a target for drug development in Down syndrome. *Front. Behav. Neurosci.* **10**, e54285.

Duchon, A., Raveau, M., Chevalier, C., Nalesso, V., Sharp, A. J. and Herault, Y. (2011). Identification of the translocation breakpoints in the Ts65Dn and Ts1Cje mouse lines: relevance for modeling Down syndrome. *Mamm. Genome* **22**, 674.

Ennaceur, A. and Delacour, J. (1988). A new one-trial test for neurobiological studies of memory in rats. 1: behavioral data. *Behav. Brain Res.* **31**, 47-59.

Fassio, A., Patry, L., Congia, S., Onofri, F., Piton, A., Gauthier, J., Pozzi, D., Messa, M., Defranchi, E., Fadda, M. et al. (2011). SYN1 loss-of-function mutations in autism and partial epilepsy cause impaired synaptic function. *Hum. Mol. Genet.* **20**, 2297-2307.

Fenster, S. D., Kessels, M. M., Qualmann, B., Chung, W. J., Nash, J., Gundelfinger, E. D. and Garner, C. C. (2003). Interactions between Piccolo and the actin/dynamin-binding protein Abp1 link vesicle endocytosis to presynaptic active zones. *J. Biol. Chem.* **278**, 20268-20277.

Ferrer, I., Barrachina, M., Puig, B., Martínez de Lagrán, M., Martí, E., Avila J. and Dierssen, M. (2005). Constitutive Dyrk1A is abnormally expressed in Alzheimer disease, Down syndrome, Pick disease, and related transgenic models. *Neurobiol. Dis.* **20**, 392-400.

Freund, T. F., Katona, I. and Piomelli, D. (2003). Role of endogenous cannabinoids in synaptic signaling. *Physiol. Rev.* **83**, 1017-1066.

Garcia, C. C., Blair, H. J., Seager, M., Coulthard, A., Tennant, S., Buddles, M., Curtis, A. and Goodship, J. A. (2004). Identification of a mutation in Synapsin I, a synaptic vesicle protein, in a family with epilepsy. *J. Med. Genet.* **41**, 183-186.

García-Cerro, S., Martínez, P., Vidal, V., Corrales, A., Flórez, J., Vidal, R., Rueda, N., Arbonés, M. L. and Martínez-Cué, C. (2014). Overexpression of Dyrk1A is implicated in several cognitive, electrophysiological and neuromorphological alterations found in a mouse model of Down syndrome. *PLoS ONE* **9**, e106572.

Garner, C. C., Kindler, S. and Gundelfinger, E. D. (2000). Molecular determinants of presynaptic active zones. *Curr. Opin. Neurobiol.* **10**, 321-327.

Graaf, K. d., Hekerman, P., Spelten, O., Herrmann, A., Packman, L. C., Büssow, K., Müller-Newen, G. and Becker, W. (2004). Characterization of Cyclin L2, a novel cyclin with an arginine/serine-rich domain phosphorylation by DYRK1A and colocalization with splicing factors. *J. Biol. Chem.* **279**, 4612-4624.

Grau, C., Arató, K., Fernández-Fernández, J. M., Valderrama, A., Sindreu, C., Fillat, C., Ferrer, I., de la Luna, S. and Altafaj, X. (2014). DYRK1A-mediated phosphorylation of GluN2A at Ser1048 regulates the surface expression and channel activity of GluN1/GluN2A receptors. *Front. Cell. Neurosci.* **8**, 331.

Guedj, F., Sébrié, C., Rivals, I., Ledru, A., Paly, E., Bizot, J. C., Smith, D., Rubin, E., Gillet, B., Arbones, M. et al. (2009). Green tea polyphenols rescue of brain defects induced by overexpression of DYRK1A. *PLoS ONE* **4**, e4606.

Guedj, F., Pereira, P. L., Najas, S., Barallobre, M.-J., Chabert, C., Souchet, B., Sebrie, C., Verney, C., Herault, Y., Arbones, M. et al. (2012). DYRK1A: a master regulatory protein controlling brain growth. *Neurobiol. Dis.* **46**, 190-203.

Gupta, M., Dhanasekaran, A. R. and Gardiner, K. J. (2016). Mouse models of Down syndrome: gene content and consequences. *Mamm. Genome* **27**, 538-555.

Hawellek, D. J., Hipp, J. F., Lewis, C. M., Corbetta, M. and Engel, A. K. (2011). Increased functional connectivity indicates the severity of cognitive impairment in multiple sclerosis. *Proc. Natl Acad. Sci. USA* **108**, 19066-19071.

Head, E., Powell, D., Gold, B. T. and Schmitt, F. A. (2012a). Alzheimer's disease in Down syndrome. *Eur. J. Neurodegener. Dis.* **1**, 353-364.

Head, E., Silverman, W., Patterson, D. and Lott, I. T. (2012b). Aging and Down syndrome. *Curr. Gerontol. Geriatr. Res.* **2012**, 412536.

Hilfiker, S., Benfenati, F., Doussau, F., Nairn, A. C., Czernik, A. J., Augustine, G. J. and Greengard, P. (2005). Structural domains involved in the regulation of transmitter release by synapsins. *J. Neurosci.* **25**, 2658-2669.

Himpel, S., Tegge, W., Frank, R., Leder, S., Joost, H.-G. and Becker, W. (2000). Specificity determinants of substrate recognition by the protein kinase DYRK1A. *J. Biol. Chem.* **275**, 2431-2438.

Hoelter, S. M., Dalke, C., Kallnik, M., Becker, L., Horsch, M., Schrewe, A., Favor, J., Klopstock, T., Beckers, J., Ivandic, B. et al. (2008). "Sighted C3H" mice - a tool for analysing the influence of vision on mouse behaviour? *Front. Biosci.* **13**, 5810-5823.

Hübner, N. S., Mechling, A. E., Lee, H.-L., Reisert, M., Bienert, T., Hennig, J., von Elverfeldt, D. and Harsan, L.-A. (2017). The connectomics of brain demyelination: functional and structural patterns in the cuprizone mouse model. *Neuroimage* **146**, 1-18.

Jiang, X., Liu, C., Yu, T., Zhang, L., Meng, K., Xing, Z., Belichenko, P. V., Kleschevnikov, A. M., Pao, A., Peresie, J. et al. (2015). Genetic dissection of the Down syndrome critical region. *Hum. Mol. Genet.* **24**, 6540-6551.

Jin, N., Yin, X., Gu, J., Zhang, X., Shi, J., Qian, W., Ji, Y., Cao, M., Gu, X., Ding, F. et al. (2015). Truncation and activation of dual specificity tyrosine phosphorylation-regulated kinase 1A by calpain I. *J. Biol. Chem.* **290**, 15219-15237.

Karp, N. A., Meehan, T. F., Morgan, H., Mason, J. C., Blake, A., Kurbatova, N., Smedley, D., Jacobsen, J., Mott, R. F., Iyer, V. et al. (2015). Applying the ARRIVE guidelines to an in vivo database. *PLoS Biol.* **13**, e1002151.

Kawakubo, T., Mori, R., Shirotani, K., Iwata, N. and Asai, M. (2017). Neprilysin Is suppressed by dual-specificity tyrosine-phosphorylation regulated kinase 1A (DYRK1A) in Down-syndrome-derived fibroblasts. *Biol. Pharm. Bull.* **40**, 327-333.

Khan, N., Afaq, F., Saleem, M., Ahmad, N. and Mukhtar, H. (2006). Targeting multiple signaling pathways by green tea polyphenol (−)-epigallocatechin-3-gallate. *Cancer Res.* **66**, 2500-2505.

Kilkenny, C., Browne, W. J., Cuthill, I. C., Emerson, M. and Altman, D. G. (2010). Improving bioscience research reporting: the ARRIVE guidelines for reporting animal research. *PLoS Biol.* **8**, e1000412.

Kim, H., Lee, K.-S., Kim, A.-K., Choi, M., Choi, K., Kang, M., Chi, S.-W., Lee, M.-S., Lee, J.-S., Lee, S.-Y. et al. (2016). A chemical with proven clinical safety rescues down-syndrome-related phenotypes in through DYRK1A inhibition. *Dis. Model. Mech.* **9**, 839-848.

Kimura, R., Kamino, K., Yamamoto, M., Nuripa, A., Kida, T., Kazui, H., Hashimoto, R., Tanaka, T., Kudo, T., Yamagata, H. et al. (2007). The DYRK1A gene, encoded in chromosome 21 Down syndrome critical region, bridges between β-amyloid production and tau phosphorylation in Alzheimer disease. *Hum. Mol. Genet.* **16**, 15-23.

Korte, G., Dreiseitel, A., Schreier, P., Oehme, A., Locher, S., Geiger, S., Heilmann, J. and Sand, P. G. (2010). Tea Catechins' affinity for human cannabinoid receptors. *Phytomedicine* **17**, 19-22.

Leal-Ortiz, S., Waites, C. L., Terry-Lorenzo, R., Zamorano, P., Gundelfinger, E. D. and Garner, C. C. (2008). Piccolo modulation of Synapsin1a dynamics regulates synaptic vesicle exocytosis. *J. Cell Biol.* **181**, 831.

Li, Z., Yu, T., Morishima, M., Pao, A., LaDuca, J., Conroy, J., Nowak, N., Matsui, S.-I., Shiraishi, I. and Yu, Y. E. (2007). Duplication of the entire 22.9 Mb human chromosome 21 syntenic region on mouse chromosome 16 causes cardiovascular and gastrointestinal abnormalities. *Hum. Mol. Genet.* **16**, 1359-1366.

Litovchick, L., Florens, L. A., Swanson, S. K., Washburn, M. P. and DeCaprio, J. A. (2011). DYRK1A protein kinase promotes quiescence and senescence through DREAM complex assembly. *Genes Dev.* **25**, 801-813.

Llinás, R., McGuinness, T. L., Leonard, C. S., Sugimori, M. and Greengard, P. (1985). Intraterminal injection of Synapsin I or Calcium/Calmodulin-dependent protein kinase II alters neurotransmitter release at the squid giant synapse. *Proc. Natl. Acad. Sci. USA* **82**, 3035.

Llinás, R., Gruner, J. A., Sugimori, M., McGuinness, T. L. and Greengard, P. (1991). Regulation by Synapsin I and Ca(2+)-Calmodulin-dependent protein kinase II of the transmitter release in squid giant synapse. *J. Physiol.* **436**, 257.

Mao, J., Maye, P., Kogerman, P., Tejedor, F. J., Toftgard, R., Xie, W., Wu, G. and Wu, D. (2002). Regulation of Gli1 transcriptional activity in the nucleus by Dyrk1. *J. Biol. Chem.* **277**, 35156-35161.

Marchal, J. P., Maurice-Stam, H., Houtzager, B. A., Rutgers van Rozenburg-Marres, S. L., Oostrom, K. J., Grootenhuis, M. A. and van Trotsenburg, A. S. P. (2016). Growing up with Down syndrome: development from 6 months to 10.7 years. *Res. Dev. Disabil.* **59**, 437-450.

Martí, E., Altafaj, X., Dierssen, M., de la Luna, S., Fotaki, V., Alvarez, M., Pérez-Riba, M., Ferrer, I. and Estivill, X. (2003). Dyrk1A expression pattern supports specific roles of this kinase in the adult central nervous system. *Brain Res.* **964**, 250-263.

Martínez de Lagrán, M., Altafaj, X., Gallego, X., Martí, E., Estivill, X., Sahún, I., Fillat, C. and Dierssen, M. (2004). Motor phenotypic alterations in TgDyrk1a transgenic mice implicate DYRK1A in Down syndrome motor dysfunction. *Neurobiol. Dis.* **15**, 132-142.

Møller, R. S., Kübart, S., Hoeltzenbein, M., Heye, B., Vogel, I., Hansen, C. P., Menzel, C., Ullmann, R., Tommerup, N., Ropers, H.-H. et al. (2008). Truncation of the Down syndrome candidate gene DYRK1A in two unrelated patients with microcephaly. *Am. J. Hum. Genet.* **82**, 1165-1170.

Morris, A. F., Vaughan, S. E. and Vaccaro, P. (1982). Measurements of neuromuscular tone and strength in Down's syndrome children. *J. Intellect. Disabil. Res.* **26**, 41-46.

Murakami, N., Bolton, D. C., Kida, E., Xie, W. and Hwang, Y.-W. (2012). Phosphorylation by Dyrk1A of clathrin coated vesicle-associated proteins: identification of the substrate proteins and the effects of phosphorylation. *PLoS ONE* **7**, e34845.

Naert, G., Ferré, V., Meunier, J., Keller, E., Malmström, S., Givalois, L., Carreaux, F., Bazureau, J.-P. and Maurice, T. (2015). Leucettine L41, a DYRK1A-preferential DYRKs/CLKs inhibitor, prevents memory impairments and neurotoxicity induced by oligomeric Aβ25–35 peptide administration in mice. *Eur. Neuropsychopharmacol.* **25**, 2170-2182.

Nakano-Kobayashi, A., Awaya, T., Kii, I., Sumida, Y., Okuno, Y., Yoshida, S., Sumida, T., Inoue, H., Hosoya, T. and Hagiwara, M. (2017). Prenatal neurogenesis induction therapy normalizes brain structure and function in Down syndrome mice. *Proc. Natl Acad. Sci. USA* **114**, 10268-10273.

Nguyen, T. L., Fruit, C., Hérault, Y., Meijer, L. and Besson, T. (2017). Dual-specificity tyrosine phosphorylation-regulated kinase 1A (DYRK1A) inhibitors: a survey of recent patent literature. *Expert Opin. Ther. Patents* **27**, 1183-1199.

Nie, X., Hamlett, E. D., Granholm, A.-C., Hui, E. S., Helpern, J. A., Jensen, J. H., Boger, H. A., Collins, H. R. and Falangola, M. F. (2015). Evidence of altered age-related brain cytoarchitecture in mouse models of Down syndrome: a diffusional kurtosis imaging study. *Magn. Reson. Imaging* **33**, 437-447.

Oegema, R., de Klein, A., Verkerk, A. J., Schot, R., Dumee, B., Douben, H., Eussen, B., Dubbel, L., Poddighe, P. J., van der Laar, I. et al. (2010). Distinctive phenotypic abnormalities associated with submicroscopic 21q22 deletion including DYRK1A. *Mol. Syndromol.* **1**, 113.

Olmos-Serrano, J. L., Tyler, W. A., Cabral, H. J. and Haydar, T. F. (2016). Longitudinal measures of cognition in the Ts65Dn mouse: refining windows and defining modalities for therapeutic intervention in Down syndrome. *Exp. Neurol.* **279**, 40-56.

Ori-McKenney, K. M., McKenney, R. J., Huang, H. H., Li, T., Meltzer, S., Jan, L. Y., Vale, R. D., Wiita, A. P. and Jan, Y. N. (2016). Phosphorylation of β-Tubulin by the Down syndrome kinase, Minibrain/DYRK1a, regulates microtubule dynamics and dendrite morphogenesis. *Neuron* **90**, 551.

Pons-Espinal, M., Martinez de Lagran, M. and Dierssen, M. (2013). Environmental enrichment rescues DYRK1A activity and hippocampal adult neurogenesis in TgDyrk1A. *Neurobiol. Dis.* **60**, 18-31.

Powell, N. M., Modat, M., Cardoso, M. J., Ma, D., Holmes, H. E., Yu, Y., O'Callaghan, J., Cleary, J. O., Sinclair, B., Wiseman, F. K. et al. (2016). Fully-automated μMRI morphometric phenotyping of the Tc1 mouse model of Down syndrome. *PLoS ONE* **11**, e0162974.

Pujol, J., del Hoyo, L., Blanco-Hinojo, L., de Sola, S., Macià, D., Martínez-Vilavella, G., Amor, M., Deus, J., Rodríguez, J., Farré, M. et al. (2015). Anomalous brain functional connectivity contributing to poor adaptive behavior in Down syndrome. *Cortex* **64**, 148-156.

Raichle, M. E. (2015a). The brain's default mode network. *Annu. Rev. Neurosci.* **38**, 433-447.

Reeves, R. H., Irving, N. G., Moran, T. H., Wohn, A., Kitt, C., Sisodia, S. S., Schmidt, C., Bronson, R. T. and Davisson, M. T. (1995). A mouse model for Down syndrome exhibits learning and behaviour deficits. *Nat. Genet.* **11**, 177-184.

Roubertoux, P. L., Baril, N., Cau, P., Scajola, C., Ghata, A., Bartoli, C., Bourgeois, P., Christofaro, J., Tordjman, S. and Carlier, M. (2017). Differential brain, cognitive and motor profiles associated with partial trisomy. modeling Down syndrome in mice. *Behav. Genet.* **47**, 305-322.

Ryoo, S.-R., Jeong, H. K., Radnaabazar, C., Yoo, J.-J., Cho, H.-J., Lee, H.-W., Kim, I.-S., Cheon, Y.-H., Ahn, Y. S., Chung, S.-H. et al. (2007). DYRK1A-mediated hyperphosphorylation of Tau a functional link between down syndrome and Alzheimer disease. *J. Biol. Chem.* **282**, 34850-34857.

Ryoo, S.-R., Cho, H.-J., Lee, H.-W., Jeong, H. K., Radnaabazar, C., Kim, Y.-S., Kim, M.-J., Son, M.-Y., Seo, H., Chung, S.-H. et al. (2008). Dual-Specificity tyrosine(Y)-phosphorylation regulated kinase 1A-mediated phosphorylation of amyloid precursor protein: evidence for a functional link between Down syndrome and Alzheimer's disease. *J. Neurochem.* **104**, 1333-1344.

Ryu, Y. S., Park, S. Y., Jung, M.-S., Yoon, S.-H., Kwen, M.-Y., Lee, S.-Y., Choi, S.-H., Radnaabazar, C., Kim, M.-K., Kim, H. et al. (2010). Dyrk1A-mediated phosphorylation of Presenilin 1: a functional link between Down syndrome and Alzheimer's disease. *J. Neurochem.* **115**, 574-584.

Scales, T. M. E., Lin, S., Kraus, M., Goold, R. G. and Gordon-Weeks, P. R. (2009). Nonprimed and DYRK1A-primed GSK3β-phosphorylation sites on MAP1B regulate microtubule dynamics in growing axons. *J. Cell Sci.* **122**, 2424-2435.

Sforazzini, F., Schwarz, A. J., Galbusera, A., Bifone, A. and Gozzi, A. (2014). Distributed BOLD and CBV-weighted resting-state networks in the mouse brain. *Neuroimage* **87**, 403-415.

Shi, J., Zhang, T., Zhou, C., Chohan, M. O., Gu, X., Wegiel, J., Zhou, J., Hwang, Y.-W., Iqbal, K., Grundke-Iqbal, I. et al. (2008). Increased dosage of Dyrk1A alters alternative splicing factor (ASF)-regulated alternative splicing of tau in Down syndrome. *J. Biol. Chem.* **283**, 28660-28669.

Sitz, J. H., Baumgärtel, K., Hämmerle, B., Papadopoulos, C., Hekerman, P., Tejedor, F. J., Becker, W. and Lutz, B. (2008). The down syndrome candidate dual-specificity tyrosine phosphorylation-regulated kinase 1A phosphorylates the neurodegeneration-related Septin 4. *Neuroscience* **157**, 596-605.

Smith, D. J., Stevens, M. E., Sudanagunta, S. P., Bronson, R. T., Makhinson, M., Watabe, A. M., O'Dell, T. J., Fung, J., Weier, H.-U. G., Cheng, J.-F. et al. (1997). Functional screening of 2 Mb of human chromosome 21q22.2 in transgenic mice implicates minibrain in learning defects associated with Down syndrome. *Nat. Genet.* **16**, 28-36.

Smith, B., Medda, F., Gokhale, V., Dunckley, T. and Hulme, C. (2012). Recent advances in the design, synthesis, and biological evaluation of selective DYRK1A inhibitors: a new avenue for a disease modifying treatment of Alzheimer's? *ACS Chem. Neurosci.* **3**, 857-872.

Soppa, U., Schumacher, J., Ortiz, V. F., Pasqualon, T., Tejedor, F. and Becker, W. (2014). The Down syndrome-related protein kinase DYRK1A phosphorylates p27Kip1 and Cyclin D1 and induces cell cycle exit and neuronal differentiation. *Cell Cycle* **13**, 2084-2100.

Souchet, B., Guedj, F., Sahún, I., Duchon, A., Daubigney, F., Badel, A., Yanagawa, Y., Barallobre, M. J., Dierssen, M., Yu, E. et al. (2014). Excitation/inhibition balance and learning are modified by Dyrk1a gene dosage. *Neurobiol. Dis.* **69**, 65-75.

Souchet, B., Latour, A., Gu, Y., Daubigney, F., Paul, J.-L., Delabar, J.-M. and Janel, N. (2015). Molecular rescue of DYRK1A overexpression in cystathionine beta synthase-deficient mouse brain by enriched environment combined with voluntary exercise. *J. Mol. Neurosci.* **55**, 318-323.

Stafford, J. M., Jarrett, B. R., Miranda-Dominguez, O., Mills, B. D., Cain, N., Mihalas, S., Lahvis, G. P., Lattal, K. M., Mitchell, S. H., David, S. V. et al. (2014). Large-scale topology and the default mode network in the mouse connectome. *Proc. Natl Acad. Sci. USA* **111**, 18745-18750.

Stotani, S., Giordanetto, F. and Medda, F. (2016). DYRK1A inhibition as potential treatment for Alzheimer's disease. *Future Med. Chem.* **8**, 681-696.

Sureshbabu, R., Kumari, R., Ranugha, S., Sathyamoorthy, R., Udayashankar, C. and Oudeacoumar, P. (2011). Phenotypic and dermatological manifestations in Down syndrome. *Dermatol. Online J.* **17**, 3. http://escholarship.org/uc/item/8jx5f2v2

Tahtouh, T., Elkins, J. M., Filippakopoulos, P., Soundararajan, M., Burgy, G., Durieu, E., Cochet, C., Schmid, R. S., Lo, D. C., Delhommel, F. et al. (2012). Selectivity, cocrystal structures, and neuroprotective properties of leucettines, a family of protein kinase inhibitors derived from the marine sponge alkaloid leucettamine B. *J. Med. Chem.* **55**, 9312-9330.

Thomazeau, A., Lassalle, O., Iafrati, J., Souchet, B., Guedj, F., Janel, N., Chavis, P., Delabar, J. and Manzoni, O. J. (2014). Prefrontal deficits in a murine model overexpressing the Down syndrome candidate gene Dyrk1a. *J. Neurosci.* **34**, 1138-1147.

Valetto, A., Orsini, A., Bertini, V., Toschi, B., Bonuccelli, A., Simi, F., Sammartino, I., Taddeucci, G., Simi, P. and Saggese, G. (2012). Molecular cytogenetic characterization of an interstitial deletion of chromosome 21 (21q22.13q22.3) in a patient with dysmorphic features, intellectual disability and severe generalized epilepsy. *Eur. J. Med. Genet. Epilepsy Genet.* **55**, 362-366.

Vega, J. N., Hohman, T. J., Pryweller, J. R., Dykens, E. M. and Thornton-Wells, T. A. (2015). Resting-state functional connectivity in individuals with Down syndrome and williams syndrome compared with typically developing controls. *Brain Connectivity* **5**, 461-475.

Waites, C. L., Leal-Ortiz, S. A., Andlauer, T. F. M., Sigrist, S. J. and Garner, C. C. (2011). Piccolo regulates the dynamic assembly of presynaptic F-actin. *J. Neurosci.* **31**, 14250.

Walte, A., Rüben, K., Birner-Gruenberger, R., Preisinger, C., Bamberg-Lemper, S., Hilz, N., Bracher, F. and Becker, W. (2013). Mechanism of dual specificity kinase activity of DYRK1A. *FEBS J.* **280**, 4495-4511.

Wegiel, J., Kaczmarski, W., Barua, M., Kuchna, I., Nowicki, K., Wang, K.-C., Wegiel, J., Yang Ma, S., Frackowiak, J., Mazur-Kolecka, B. et al. (2011). The link between DYRK1A overexpression and several-fold enhancement of neurofibrillary degeneration with 3-repeat tau protein in Down syndrome. *J. Neuropathol. Exp. Neurol.* **70**, 36-50.

Wilson, R. I. and Nicoll, R. A. (2002). Endocannabinoid signaling in the brain. *Science* **296**, 678-682.

Woods, Y. L., Cohen, P., Becker, W., Jakes, R., Goedert, M., Wang, X. and Proud, C. G. (2001). The kinase DYRK phosphorylates protein-synthesis initiation factor eIF2Bepsilon at Ser539 and the microtubule-associated protein tau at Thr212: potential role for DYRK as a glycogen synthase kinase 3-priming kinase. *Biochem. J.* **355**, 609-615.

Yamamoto, T., Shimojima, K., Nishizawa, T., Matsuo, M., Ito, M. and Imai, K. (2011). Clinical manifestations of the deletion of Down syndrome critical region including DYRK1A and KCNJ6. *Am. J. Med. Genet. A* **155**, 113-119.

Disease Models & Mechanisms (2018) 11, dmm035634. doi:10.1242/dmm.035634

Yang, C. S., Wang, X., Lu, G. and Picinich, S. C. (2009). Cancer prevention by tea: animal studies, molecular mechanisms and human relevance. *Nat. Rev. Cancer* **9**, 429-439.

Yin, X., Jin, N., Gu, J., Shi, J., Zhou, J., Gong, C.-X., Iqbal, K., Grundke-Iqbal, I. and Liu, F. (2012). Dual-specificity tyrosine phosphorylation-regulated kinase 1A (Dyrk1A) modulates serine/arginine-rich protein 55 (SRp55)-promoted Tau exon 10 inclusion. *J. Biol. Chem.* **287**, 30497-30506.

Yu, T., Liu, C., Belichenko, P., Clapcote, S. J., Li, S., Pao, A., Kleschevnikov, A., Bechard, A. R., Asrar, S., Chen, R. et al. (2010). Effects of individual segmental trisomies of human chromosome 21 syntenic regions on hippocampal long-term potentiation and cognitive behaviors in mice. *Brain Res.* **1366**, 162-171.

Zhou, Y., Friston, K. J., Zeidman, P., Chen, J., Li, S. and Razi, A. (2018). The hierarchical organization of the default, dorsal attention and salience networks in adolescents and young adults. *Cereb. Cortex* **28**, 726-737.

Common functional networks in the mouse brain revealed by multi-centre resting-state fMRI analysis

Joanes Grandjean[a], Carola Canella[b,c], Cynthia Anckaerts[d], Gülebru Ayrancı[e], Salma Bougacha[f,g], Thomas Bienert[j], David Buehlmann[h], Ludovico Coletta[b,c], Daniel Gallino[e], Natalia Gass[i], Clément M. Garin[f,g], Nachiket Abhay Nadkarni[f,g], Neele Hübner[j], Meltem Karatas[k], Yuji Komaki[l,m], Silke Kreitz[n], Francesca Mandino[a,o], Anna E. Mechling[j], Chika Sato[p], Katja Sauer[n], Disha Shah[d,q], Sandra Strobelt[n], Norio Takata[l,r], Isabel Wank[n], Tong Wu[s,t], Noriaki Yahata[p], Ling Yun Yeow[a], Yohan Yee[u], Ichio Aoki[p], M. Mallar Chakravarty[e], Wei-Tang Chang[a], Marc Dhenain[f,g], Dominik von Elverfeldt[j], Laura-Adela Harsan[k], Andreas Hess[n], Tianzi Jiang[s,v], Georgios A. Keliris[d], Jason P. Lerch[u], Hideyuki Okano[m,w], Markus Rudin[h], Alexander Sartorius[i], Annemie Van der Linden[d], Marleen Verhoye[d], Wolfgang Weber-Fahr[i], Nicole Wenderoth[x], Valerio Zerbi[x], Alessandro Gozzi[b]

a Singapore Bioimaging Consortium, Agency for Science, Technology and Research, 11 Biopolis Way, Singapore 138667, Singapore
b Functional Neuroimaging Laboratory, Istituto Italiano di Tecnologia, Centre for Neuroscience and Cognitive Systems @ UNITN, 38068 Rovereto, Italy
c CIMeC, centre for Mind/Brain Sciences, University of Trento, 38068 Rovereto, Italy
d Bio-Imaging Lab, University of Antwerp, CDE, Universiteitsplein 1, 2610 Antwerp, Belgium
e Douglas Mental Health University Institute & Departments of Psychiatry and Biological and Biomedical Engineering, McGill University, Montreal, Quebec, Canada.
f Commissariat à l'Énergie Atomique et aux Énergies Alternatives (CEA), Direction de la Recherche Fondamentale (DRF), Institut François Jacob, MIRCen, Fontenay aux roses, France
g Centre National de la Recherche Scientifique (CNRS), Université Paris-Sud, Université Paris-Saclay UMR 9199, Neurodegenerative Diseases Laboratory, Fontenay-aux-Roses, France
h Institute for Biomedical Engineering, University and ETH Zürich, Wolfgang-Pauli-Str. 27, 8093 Zürich, Switzerland, & Institute of Pharmacology and Toxicology, University of Zürich, Winterthurerstrasse 190, 8057 Zürich, Switzerland
i Department of Neuroimaging, Central Institute of Mental Health, Medical Faculty Mannheim, University of Heidelberg, Mannheim, Germany
j Department of Radiology, Medical Physics, Medical Center – University of Freiburg, Faculty of Medicine, University of Freiburg, Killianstr. 5a, 79106 Freiburg, Germany; BrainLinks-BrainTools Cluster of Excellence, University of Freiburg, Georges-Köhler-Allee 80, 79110 Freiburg, Germany
k Department of Biophysics and Nuclear Medicine, University Hospital Strasbourg, 67000 Strasbourg, France
l Central Institute for Experimental Animals (CIEA), 3-25-12, Tonomachi, Kawasaki, Kanagawa 210-0821, Japan
m Department of Physiology, Keio University School of Medicine, 35 Shinanomachi, Shinjuku, Tokyo 160-8582, Japan
n Institute of Experimental and Clinical Pharmacology and Toxicology, Friedrich-Alexander University Erlangen-Nürnberg (FAU), Fahrstraße 17, 91054, Erlangen, Germany
o Faculty of Life Sciences, University of Manchester, Manchester, United Kingdom
p Functional and Molecular Imaging Team, Department of Molecular Imaging and Theranostics, National Institute of Radiological Sciences, National Institutes for Quantum and Radiological Science and Technology, Anagawa 4-9-1, Inage, Chiba-city, Chiba 263-8555, Japan
q Laboratory for the Research of Neurodegenerative Diseases, VIB center for Brain and Disease Research, KU Leuven, O&N4 Herestraat 49 box 602, 3000 Leuven, Belgium
r Department of Neuropsychiatry, Keio University School of Medicine, 35 Shinanomachi, Shinjuku, Tokyo 160-8582, Japan
s Queensland Brain Institute, The University of Queensland, Brisbane, Queensland, Australia
t Centre for Medical Image Computing, Department of Computer Science, & Max Planck University College London Centre for Computational Psychiatry and Ageing Research, University College London, London, UK
u Hospital for Sick Children and Department of Medical Biophysics, The University of Toronto, Toronto, Ontario, Canada
v Brainnetome Centre, Institute of Automation, Chinese Academy of Sciences, Beijing & Key Laboratory for NeuroInformation of the Ministry of Education, School of Life Science and Technology, University of Electronic Science and Technology of China, Chengdu 625014, China
w Laboratory for Marmoset Neural Architecture, RIKEN Brain Science Institute, Wako, Saitama 351-0198, Japan
x Neural Control of Movement Lab, Department of Health Sciences and Technology, ETH Zürich, Winterthurerstrasse 190, 8057 Zurich, Switzerland

Corresponding author
Joanes Grandjean, PhD
Singapore Bioimaging Consortium (SBIC)
11 Biopolis Way
#01-02 Helios Building
Singapore 138667
Tel: +65 91434319
Fax: +65 6478 9957
Joanes_Grandjean@sbic.a-star.edu.sg

Abstract

Preclinical applications of resting-state functional magnetic resonance imaging (rsfMRI) offer the possibility to non-invasively probe whole-brain network dynamics and to investigate the determinants of altered network signatures observed in human studies. Mouse rsfMRI has been increasingly adopted by numerous laboratories world-wide. Here we describe a multi-centre comparison of 17 mouse rsfMRI datasets via a common image processing and analysis pipeline. Despite prominent cross-laboratory differences in equipment and imaging procedures, we report the reproducible identification of several large-scale resting-state networks (RSN), including a murine default-mode network, in the majority of datasets. A combination of factors was associated with enhanced reproducibility in functional connectivity parameter estimation, including animal handling procedures and equipment performance. Our work describes a set of representative RSNs in the mouse brain and highlights key experimental parameters that can critically guide the design and analysis of future rodent rsfMRI investigations.

Introduction

The brain is the most complex organ, consisting of 86 billion neurons (Azevedo et al., 2009), each forming on average 7000 synapses. Approaching the complexity of the brain is rendered difficult due to the limited access to the tissue and the imperative for minimally invasive procedures in human subjects. Resting-state functional magnetic resonance imaging (rsfMRI) has gained attention within the human neuroimaging community due to the possibility to interrogate multiple resting-state networks (RSNs) in parallel with a relatively high spatial and temporal resolution (Biswal et al., 1995, 2010; Fox and Raichle, 2007). Functional connectivity (FC), i.e. the statistical dependence of two or more time series extracted from spatially defined regions in the brain (Friston, 2011), is the principal parameter estimated from rsfMRI studies. The importance of FC to neuroscience research can be understood through its widespread use to describe functional alterations in psychiatric and neurological disorders, e.g. for review (Buckner et al., 2008; Greicius, 2008). However, despite an extensive characterization of the functional endophenotype associated with diseased states, limitations with respect to invasiveness and terminal experiments generally preclude the establishment of detailed mechanisms in humans, as can be achieved with animal models.

Since its onset in 2011 (Jonckers et al., 2011), mouse rsfMRI has developed in a number of centres and has grown to become a routine method with a number of applications, reviewed in (Chuang and Nasrallah, 2017; Gozzi and Schwarz, 2016; Hoyer et al., 2014; Jonckers et al., 2015, 2013; Pan et al., 2015). Prominently, mouse rsfMRI has been used to investigate an extensive list of models, including Alzheimer's disease (Grandjean et al., 2014b, 2016b, Shah et al., 2013, 2016c; Wiesmann et al., 2016; Zerbi et al., 2014), motor (DeSimone et al., 2016; Li et al., 2017), affective (Grandjean et al., 2016a), autism spectrum (Bertero et al., 2018; Haberl et al., 2015; Liska et al., 2018; Liska and Gozzi, 2016; Michetti et al., 2017; Sforazzini et al., 2016; Zerbi et al., 2018; Zhan et al., 2014), schizophrenia (Errico et al., 2015; Gass et al., 2016), pain (Buehlmann et al., 2018; Komaki et al., 2016), reward (Charbogne et al., 2017; Mechling et al., 2016), and demyelinating disorders (Hübner et al., 2017). Another application of mouse rsfMRI is the elucidation of large-scale functional alterations exerted by pharmacological agents (Razoux et al., 2013; Shah et al., 2016a, 2015). Finally, the method has been used to address fundamental questions. These include the investigation of the structural basis underlying FC (Bergmann et al., 2016; Grandjean et al., 2017b; Hübner et al., 2017; Schroeter et al., 2017; Sforazzini et al., 2016; Stafford et al., 2014), the nature of the dynamical event encoded in the resting-state signal (Belloy et al., 2018a, 2018b; Bukhari et al., 2018; Grandjean et al., 2017a;

Sethi et al., 2017), as well as strain (Jonckers et al., 2011; Schroeter et al., 2017; Shah et al., 2016b), and the impact of sedation or awake conditions on the underlying signal and connectivity patterns (Bukhari et al., 2017; Grandjean et al., 2014a; Jonckers et al., 2014; Wu et al., 2017; Yoshida et al., 2016). This body of work obtained mainly over the past 5 years reflects the growth and interest into this modality as a translational tool to understand mechanisms underlying RSNs organisation in the healthy and diseased states, with the promise to highlight relevant targets in the drug development process and to advance fundamental knowledge in neuroscience.

Despite a growing interest in the field, rsfMRI studies in animals have been inherently difficult to compare. On top of centre-related contributions analogous to those observed in human studies (Jovicich et al., 2016), comparisons in rodents are further confounded by greater variability in preclinical equipment (e.g. field strength, hardware design), animal handling protocols and sedation regimens employed to control for motion and stress. Discrepancies between reports, such as the anatomical and spatial extent of a rodent homologue of the human default-mode network (DMN) (Becerra et al., 2011; Gozzi and Schwarz, 2016; Guilfoyle et al., 2013; Hübner et al., 2017; Liska et al., 2015; Lu et al., 2012; Sforazzini et al., 2014; Stafford et al., 2014; Upadhyay et al., 2011), or the organisation of murine RSNs (Jonckers et al., 2011), have stark consequences for the interpretations of the results. To meet a growing need to establish standards and points of comparison in rodent fMRI, we carried out a multi-centre comparison of mouse rsfMRI datasets. Multiple datasets representative of the local centre acquisitions were analysed with a common preprocessing pipeline and examined with seed-based analysis (SBA) and independent component analysis (ICA), two common brain mapping methods used to investigate RSNs. The aims of our work were to identify representative mouse RSNs, to establish a set of reference pre-processing and analytical steps and good-practices, and to highlight protocol requirements enabling more sensitive and specific FC detection in the mouse brain.

Results

Dataset description and preprocessing validation

A total of 17 datasets were included in this study. Dataset selection was restricted to 15 gradient-echo echo planar imaging acquired on C57Bl/6J mice, any gender, any age, any sedation protocol (**Supplementary table 1)**. Cortical signal-to-noise ratio (SNR) ranged from 17.04 to 448.56, while temporal SNR (tSNR) ranged from 8.11 to 112.68 (**Supplementary figure 1ab**). A comparison between SNR and tSNR indicated a positive association between the two measures (pearson's r = 0.75, t = 18.30, df = 253, p = 2.2e-16). Due to the lack of orthogonality between the two factors, only SNR was considered in the remaining of the analysis. Mean framewise displacement (FWD) ranged 0.0025 mm to 0.15 mm (**Supplementary figure 1c**). A summary of representative estimated motion parameters is shown in the supplementary material (**Supplementary figure 2**). Each preprocessing output was visually inspected. Automatic brain extraction generated plausible brain masks. Normalisation was carried out to the Allen Institute for Brain Science (AIBS) template (**Supplementary figure 3**). Spatial coverage along the anterior-posterior axis varied across datasets. The following analysis is thus restricted to areas fully covered by all scans, corresponding to approximately 2.96 and -2.92 mm relative to Bregma. Moreover, distortions made it impossible to cover the amygdala region in full. No marked differences in the performance of each preprocessing steps were identified between datasets. The brain masked, spatially smoothed, temporally filtered, and normalized scans were further processed as follows.

Vascular and ventricle signal regression enhances functional connectivity specificity

Denoising procedures are an integral step in all FC analyses relying on rsfMRI acquisitions. Nuisance signal originates from multiple sources, including physiological and equipment related noise (Murphy et al., 2013). No consensus exists both in human and rodent fMRI fields regarding optimal noise removal procedures. In this study the following six nuisance regression models were designed and compared with the aim to select one model based on objective criteria for the remaining of the analysis. The first nuisance model includes only motion correction and parameter regression (MC). Global signal regression (GSR) was added to the motion parameter in a second model. Signal from either white-matter (WM), ventricle (VEN), or vascular (VASC) masks (**Supplementary figure 4bcd**) were combined with motion parameters in additional regression models. Finally, based on results obtained with these approaches, a combination (VV) model including VEN and VASC signal regression was included for the comparison. The effectiveness of nuisance regression models and the specificity of the resulting

networks at the subject level were assessed based on the outcome of a SBA using the anterior cingulate area (ACA, **Supplementary figure 4a**) as seed region. This seed was selected as a central node of the putative rodent DMN (Gozzi and Schwarz, 2016).

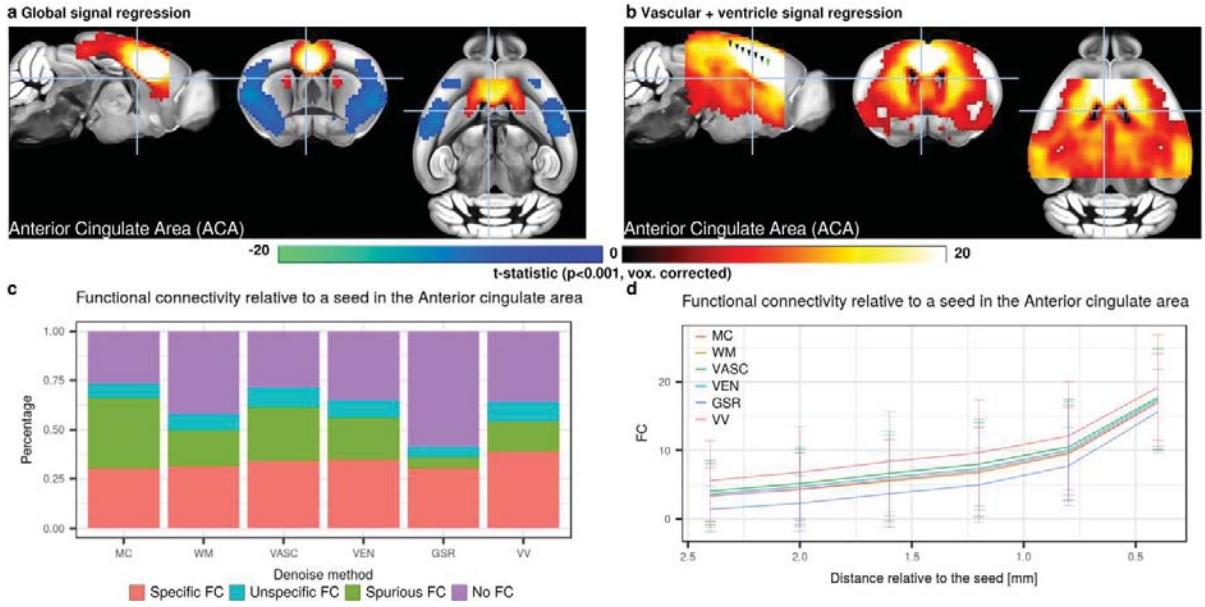

Figure 1 I *Denoising strategies and their impact on functional connectivity (FC) specificity.* ***a-b,*** *Seed-based analysis for a seed in the anterior cingulate area (ACA) following either global signal regression (GSR,* ***a****) or vascular+ventricle signal regression (VV,* ***b****). The spatial maps obtained lead to a set of regions for which the BOLD signals were positively associated to the BOLD signal of the ACA. These included the prefrontal cortex, retrosplenial area (RSP), dorsal striatum. Under VV, the connectivity profile extended to peri-hippocampal areas. Significant anti-correlation (negative t-statistic, blue) are also present in the primary somatosensory areas (SSp) under GSR but not VV condition. Individual scans were classified as presenting "Specific", "Unspecific", "Spurious", or "No" FC relative to the ACA seed (****c****, see* ***Supplementary figure 5*** *for details). Comparison of each FC category depending on the denoising strategies revealed that motion correction and GSR lead to lowest percentage of "specific FC" at 30%, while that percentage was highest under VV condition (38%). FC as a function of distance to the ACA seed indicates comparable rate of decline between denoising strategies (****d****). Green arrowhead indicates the position of the ACA seed, black arrowheads indicate ROIs spaced 0.4 mm apart. Voxelwise corrected t-statistic for one-sample t-tests (p<0.001, corrected) are shown as a colour-coded overlay on the AIBS reference template. Descriptive statistics are shown as mean ± 1 standard deviation.*

The statistical maps of the one-sample t-test across all individual maps following GSR (**Figure 1a**) indicated positive FC along rostro-caudal axis, through the ACA and extending to the retrosplenial area (RSP), with anti-correlations in adjacent primary somatosensory areas (SSp). Comparatively, in the VV nuisance model, a more extended network was revealed to include posterior parietal cortical areas (**Figure 1b**), while anti-correlations in the SSp did not reach statistical significance. To assess the specificity of the obtained functional networks, subject-level FC parameter (z-statistic) were extracted from ROIs located in the RSP and left SSp. The former was defined as a specific ROI, i.e. a ROI where positive FC is expected, while the latter was defined as a non-specific ROI, i.e. a ROI where low or negative FC is expected. The decision to consider these two areas as belonging to separable network systems reflects several lines of converging evidence: a) these regions are not linked by major white matter bundles or direct axonal projections in the mouse brain (Oh et al., 2014), b) they reflect separable electrophysiological signatures in mammals (Popa et al., 2009) c) they belong to separable functional communities (Liska et al., 2015) and are similarly characterized by the absence of significant positive correlation in corresponding human RSN (Fox et al., 2005).

Detailed FC within the specific ROI for the GSR and VV nuisance model are shown as a function of FC within the corresponding non-specific ROI at the single-subject level (**Supplementary figure 5**). In the VV condition, 98/255 (i.e. 38%) of individual scans fell into the "specific FC" category while both MC and GSR reach lowest percentage (30%) of scans exhibiting "specific FC" relative to the ACA seed (**Figure 1c**). Out of the 98/255 scans categorised as presenting "specific FC" relative to the ACA seed, up to 14/15 scans originated from the same dataset (median = 6/15). Two datasets did not contain scans that met the definition. Correspondingly, the 98 scans were also unevenly distributed according to the different acquisition parameters, including field strength (4.7T N = 1/15, 7T N = 41/120, 9.4T N = 38/90, 11.7T = 18/30, X^2 = 13.76, df = 3, p-value = 0.0032), coil type (room-temperature N = 26/105, cryoprobe N = 72/150, X^2 = 13.13, df = 1, p-value = 0.00029), breathing condition (free-breathing N = 58/180, ventilated N = 40/75, X^2 = 9.10, df = 1, p-value = 0.0026), and sedation condition (awake N = 7/15, isoflurane/halothane N = 18/90, medetomidine N = 26/75, medetomidine+isoflurane N = 47/75, X^2 = 32.42, df = 3, p-value = 4.28e-07). Hence, scans presenting "specific FC" patterns were more often found in datasets acquired at higher field strengths, with cryoprobes, in ventilated animals, and under medetomidine+isoflurane combination sedation.

To test how FC is affected as a function of distance to the seed and nuisance model, FC in the ACA and RSP along the anterior - posterior axis was extracted (**Figure 1d**). Comparable rate of decrease was observed in all conditions, with GSR displaying an overall decrease of FC throughout. This is consistent with the overall decrease in FC induced by GSR relative to VV in the specificity analysis (**Supplementary figure 5**). In summary, the VV nuisance model enhanced specificity of SBA-derived DMN, as indicated by higher incidence of scans in the "specific FC" category. Based on this criterion, this nuisance model was used in all the subsequent analyses.

Seed-based analysis identifies common and reproducible murine resting-state networks

We sought to identify common murine RSNs by means of SBA and to compare reproducibility across datasets. Seeds positioned in representative anatomical regions of the left hemisphere (**Supplementary figure 4a**) were used to reveal the spatial extent of previously described mouse resting-state networks. The seeds were selected to represent different cortical (somatosensory, motor, high order processing), as well as subcortical systems (striatum, hippocampal formation, thalamus). To obtain high-specificity and high-confidence group-level SBA maps, we first probed only the 98/255 scans listed as containing "specific FC" in the previous analysis. We next extended these analyses to include all the 255/255 scans (**Supplementary figure 7**). For datasets comparisons, all 15 scans from each dataset were included to reflect inter-dataset variability in the incidence maps.

All group-level SBA maps exhibited a strong bilateral and homotopic extension (**Figure 2a, Supplementary figure 6**). A seed in the ACA revealed a network involving the prefrontal cortex, RSP, dorsal striatum, dorsal thalamus and peri-hippocampal areas. This recapitulates anatomical features reminiscent of the human, primate and rat DMN (Gozzi and Schwarz, 2016; Hutchison and Everling, 2012; Sforazzini et al., 2014; Stafford et al., 2014). Comparable regions were observed with a seed in the RSP, a region evolutionarily related to the posterior cingulate cortex found in the human DMN (**Supplementary figure 6**). The anterior insular seed was found to co-activate with the dorsal cingulate and the amygdalar areas, corresponding to the putative rodent salience network (Gozzi and Schwarz, 2016), while the primary somatomotor region (MO) defined a previously described latero-cortical network that appears to be antagonistic to midline DMN regions, and that has been for this reason postulated to serve as a possible rodent homologous of the primate task-positive network (**Figure 2a**)(Liska et al., 2015;

Sforazzini et al., 2014). Corresponding network across all scans (255/255) recapitulated features identified in the 98/255 scans listed as containing "specific FC", but appeared to be characterized by much lower spatial specificity (**Supplementary figure 7**). Maps derived from individual datasets revealed that 70% (12/17) of the datasets presented the features listed above (**Figure 2b**, **Supplementary figure 8**). Incidence maps indicate, on a voxel basis, the percentage of the dataset presenting a significant FC. They confirmed the different extent of network detection in the different dataset. In summary, this analysis revealed the commonly shared spatial extent of mouse RSNs derived from SBA but also indicates that a small subset of the datasets failed to present these features with sufficient sensitivity or specificity.

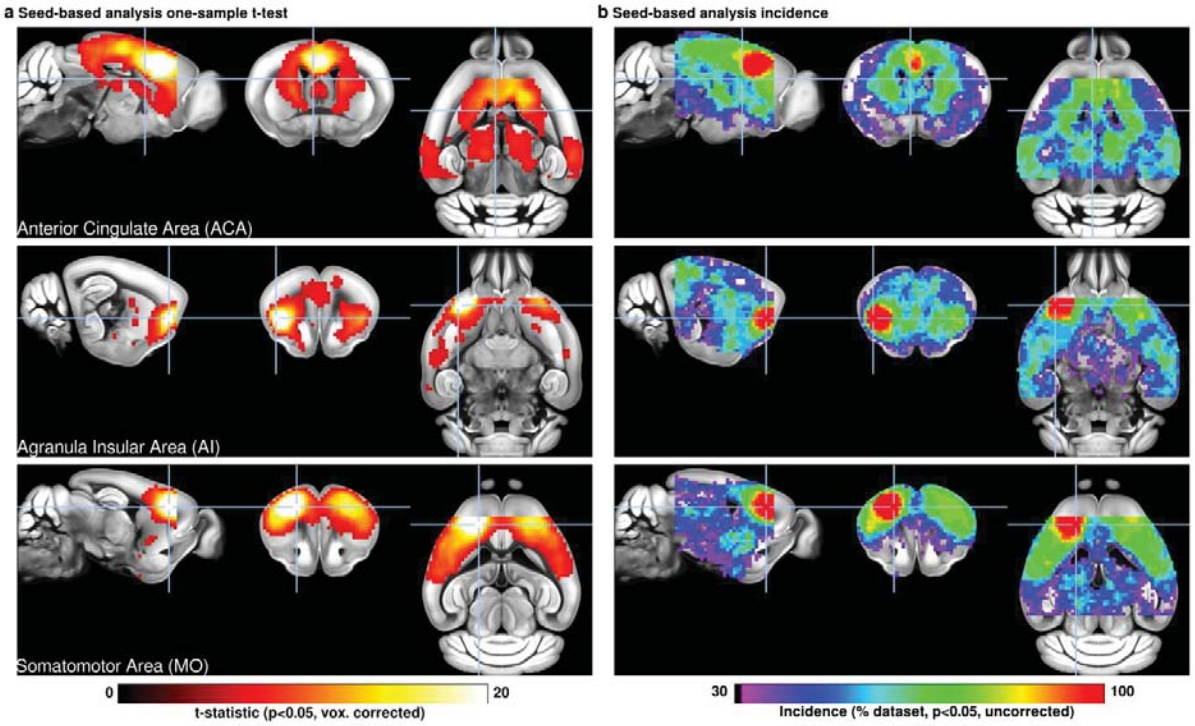

Figure 2 I *Seed-based analysis (SBA) for 3 selected seeds positioned on the left hemisphere. One-sample t-test maps of individual maps reveal the full extent of SBA-derived resting-state networks in the mouse brain across 98/255 scans that presented "specific FC" following vascular+ventricle signal regression. Functional connectivity (FC) relative to a seed located in the anterior cingulate area reveals the extent of the murine default-mode network, including the dorsal caudoputamen, dorsal thalamus, and peri-hippocampal areas. The seed in the insular area reveals significant FC in dorsal cingulate and amygdalar areas, corresponding to areas previously associated with the human salience network. Inter-hemispheric homotopic FC is found relative to the MO seed, together with lateral striatal FC. Incidence maps, indicating the*

*percentage of dataset presenting significant FC in one-sample t-test (p<0.05, uncorrected), reveal that 12/17 of datasets recapitulated the features stated above. Out of these, 5 were not considered to overlap specifically (**Supplementary figure 6**). Voxelwise corrected t-statistic for one-sample t-tests and incidence maps are shown as a colour-coded overlay on the AIBS reference template.*

Sedation protocol and SNR affect connectivity strength

The datasets analysed here were acquired at varying field strengths, coil designs, EPI sequence parameters, animal handling, and with different anesthesia protocols, i.e. either awake or sedated states. Hence the acquisitions were not purposefully balanced to test for specific effects. To identify factors associated with FC strength, a simplified linear model was designed including the following explanatory factors: sedation and breathing conditions, SNR, and motion (mean framewise displacement). Limitations in orthogonality and representation of specific acquisition factors such as field strength, coil design, EPI sequence parameters, number of volumes, gender and age precluded a more extensive model.

Individual-level FC values (z-statistic) were extracted from SBA maps estimated from the ACA seed using a ROI located in the RSP and shown as a function of different acquisition parameters (**Figure 3**). Sedation protocol ($F_{(247, 251)}$ = 18.29, p = 3.5e-13) and SNR ($F_{(247, 248)}$ = 12.39, p = 5.1e-4) were significantly associated with FC, while the remaining factors, breathing condition ($F_{(247, 248)}$ = 3.48, p = 0.063) and motion ($F_{(247, 248)}$ = 0.082, p = 0.77) were not. The awake and medetomidine+isoflurane combination led to higher FC compared to the other two sedation categories. With respect to SNR, high FC values started to be observed at SNR > 50, suggesting that lower SNR may not be sufficient to detect relevant fluctuations. Interestingly, these effects were found consistently across the different ROI pairs considered (**Supplementary table 2**), thus confirming the importance of sedation conditions and SNR, and suggesting that breathing conditions impact mildly FC sensitivity.

These animal handling conditions and sedation protocols highlighted here may not be applicable to all studies or laboratories due to local legislation, equipment availability, or technical knowledge. Distributions of FC values may hence provide useful reference points. Connectivity strength between the ACA and RSP, representing a central feature of the rodent DMN, reached z = 2.77, 5.71, and 10.46 at the 50^{th}, 75^{th}, and 95^{th} percentile respectively (Pearson's r = 0.15, 0.26, 0.43, when SBA is carried out with a correlation analysis instead of a

general linear model). Additional SBA parameter distributions are provided for other ROI pairs in **Supplementary table 2**. The parameters of the acquisitions featured in this analysis offer an objective criterion to evaluate and compare sensitivity to FC in a new dataset or in previous publications, insofar comparable metrics are available.

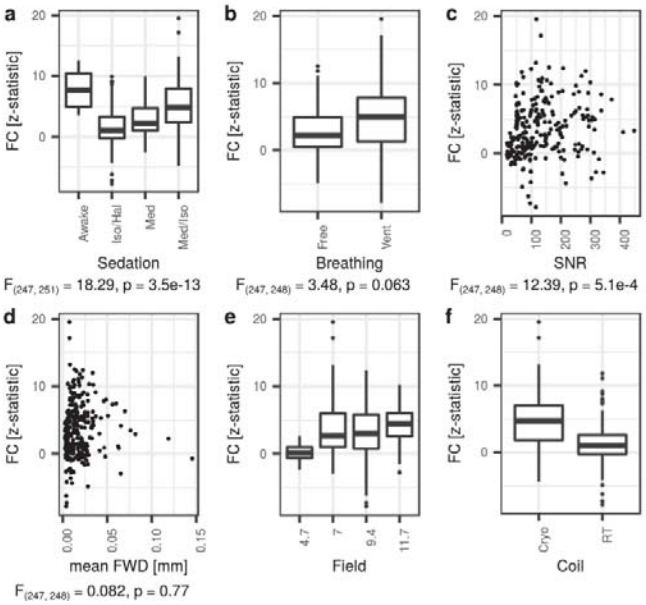

Figure 3 I *Functional connectivity (FC) in the retrosplenial cortex relative to a seed located in the anterior cingulate area, as a function of acquisition parameters. A statistically significant association was determined between sedation effect and FC (**a**, $F_{(247, 251)}$ = 18.29, p = 3.5e-13) and between SNR and FC (**c**, $F_{(247,248)}$ = 12.39, p = 5.1e-4). Neither breathing condition nor motion effects were significant with FC (**b**, **d**). Due to limitations in the representation of each level within a factor, coil design (**e**) and magnetic field (**f**) were omitted from the final statistical model. Free = Free-breathing, Vent = Mechanically ventilated, Cryo = cryoprobe, RT = room-temperature.*

Network-specific functional connectivity is found in all datasets

Evidence for robust distal FC could not be established in all datasets with SBA. To investigate the presence of network-specific FC also in datasets characterized by weaker long range connectivity, a dual regression combined with group-level ICA (drICA) approach was undertaken (Filippini et al., 2009). To obtain an enriched data-driven reference atlas, a group ICA atlas was generated out of the 98 “specific FC” scans selected in the SBA above, using 20

dimensions. The atlas revealed 9 cortical components (**Figure 4a, Supplementary figure 9, Supplementary table 3**), 5 overlapping with the latero-cortical network (somatomotor area (MO) and 4 SSp areas), 3 overlapping with elements of the DMN (prefrontal, cingulate/RSP, and temporal associative areas) and 1 overlapping with the insular area (AI). Additionally, 5 sub-cortical components were revealed, overlapping with the nucleus accumbens (ACB), caudoputamen (CP), pallidum (PAL), hippocampal region (HIP), and thalamus (TH) (**Supplementary figure 10**). The components recapitulate many of the features identified with SBA (**Figure 4b**), namely a strong emphasis on homotopic bilateral organization. The components identified here also presented strong similarities to a previous analysis (Zerbi et al., 2015). Due to uneven brain coverages across datasets, rostral and caudal RSNs could not be examined, including olfactory, auditory, and visual networks. To obtain individual-level representation of these components, a dual regression approach was implemented using the reference ICA identified above. These group-level ICA were used as masks to extract time series which were then regressed into individual scans using a general linear model. To investigate specificity relative to a DMN-related component, FC relative to the cingulate/RSP component was extracted from the ACA ROI (Specific ROI, z = 8.33, 14.41, and 22.32, 50^{th}, 75^{th}, and 95^{th} percentiles) and SSp ROI (Unspecific ROI). “Specific FC” was determined in 79% (201/255) of the scans, “Unspecific FC” in 16%, “Spurious FC” in 1.5%, and “No FC” in 3.1% (**Figure 4c**). “Specific FC” in 15/15 scans was determined in 2 datasets (Median = 12/15). The “Specific FC” category was also more evenly distributed relative to acquisition protocols and equipments: Field strength (4.7T N = 14/15, 7T N = 89/120, 9.4T N = 73/90, 11.7T N = 25/30, X^2 = 4.01, df = 3, p-value = 0.25), coil type (room-temperature N = 88/105, cryoprobe N = 113/150, X^2 = 2.17, df = 1, p-value = 0.14), breathing condition (free-breathing N = 138/180, ventilated N = 63/75, X^2 = 1.29, df = 1, p-value = 0.25), and sedation condition (awake N = 13/15, isoflurane/halothane N = 65/90, medetomidine N = 55/75, medetomidine+isoflurane N = 68/75, X^2 = 10.56, df = 3, p-value = 0.014). Importantly, statistical inference revealed that significant within-component FC could be established in 17/17 datasets for all 14 components (**Figure 4d**, **Supplementary figure 11, Supplementary figure 12**). This suggests that network-specific inferences can be probed in all rsfMRI datasets, and that drICA is a powerful approach enabling robust FC detection in all datasets, including those that may not robustly exhibit distal connectivity patterns.

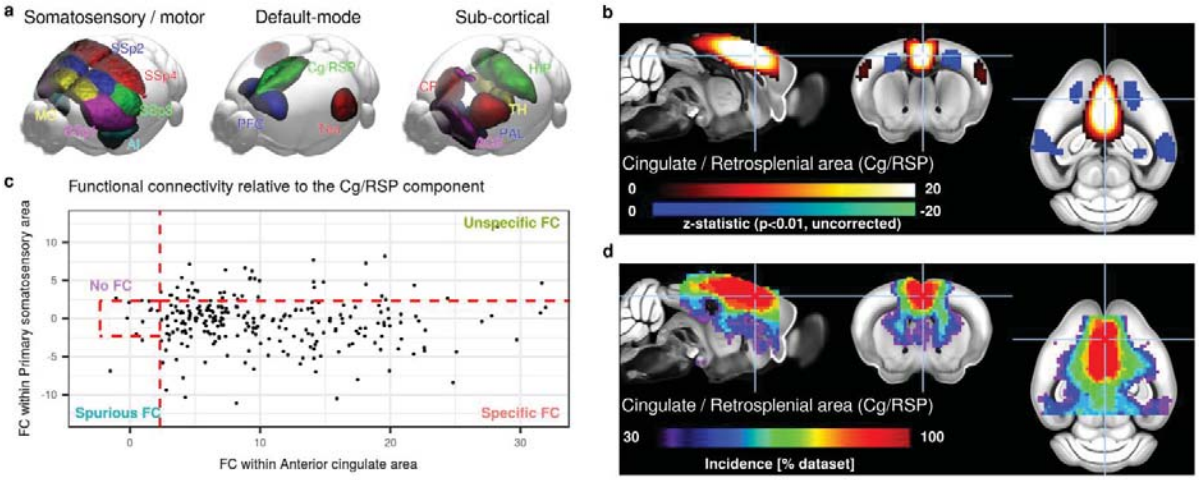

Figure 4 I *Group-level independent component analysis (ICA) estimated across 98/255 "specific FC" scans reveals canonical murine components (**a**). All components presented a marked bilateral organisation. Nine components were found to overlap principally with the isocortex including regions attributed to latero-cortical, salience and DMN networks by SBA, 3 components overlapped with the striatum, one with the hippocampal areas, and one with the thalamus. Detailed representations of the Cingulate / Retrosplenial area component (Cg/RSP **b**). Remaining components are presented in **Supplementary figure 9, 10**. FC relative to Cg/RSP is found specifically in the anterior cingulate area but not in the primary somatosensory in 79% of the individual scans following dual-regression (**c**). One-sample t-test within datasets indicates 100% of datasets presented significant FC ($p < 0.05$, uncorrected) within the Cg/RSP component. Incidence for the remaining components are presented in **Supplementary figure 11, 12**. AI = insular area, MO = somatomotor area, SSp = primary somatosensory area, PFC = prefrontal cortex, Cg/RSP = cingulate + retrosplenial area, Tea = temporal associative area, CP = caudoputamen, ACB = nucleus accumbens, PAL = pallidum, HIP = hippocampal region, TH = thalamus.*

Discussion

Rodent rsfMRI has been a growing research field in neuroscience over the past 10 years (Chuang and Nasrallah, 2017; Gozzi and Schwarz, 2016; Hoyer et al., 2014; Jonckers et al., 2015, 2013; Pan et al., 2015). The fast-paced development of the field has yielded a number of exciting results, yet the comparability of these findings remains unclear. The results presented here indicate that, despite major differences in cross-site equipment, scan conditions, sedation protocols and experience in the implementation of these procedures, mouse rsfMRI networks converge toward spatially defined motifs encompassing previously described neuroanatomical

systems of the mouse brain. Importantly, we also highlight the possibility to use rsfMRI to probe distributed network systems of high translational relevance, including a rodent DMN, salience network, and latero-cortical network. While not reliably identified in all datasets and scan conditions, these large-scale networks were found to colocalize into well delineated boundaries in the majority of scans and datasets respectively, recapitulating previous descriptions in rodents (Gozzi and Schwarz, 2016; Lu et al., 2012; Sforazzini et al., 2014; Stafford et al., 2014), monkeys (Hutchison and Everling, 2012) and humans (Buckner et al., 2008).

Interestingly, most (70%) of the datasets converged toward spatially defined common RSN when long-range FC relative to a seed was assessed. When the analysis was restricted to local connectivity, all datasets converged. These results indicate that group-level, or second-level inferences, may be assessed irrespective of acquisition protocol or animal handling procedures in all datasets using robust analysis strategies. At the subject level, “specific FC” relative to the DMN was found in 38% of the scans, indicating that first-level inference on long-range FC is within reaches in some, but not all datasets. Sedation and equipment performance leading to increased SNR were the major factors associated with both FC sensitivity and specificity, together with breathing conditions. Awake animals presented higher FC overall, however datasets acquired with medetomidine+isoflurane combination together with mechanical ventilation were associated with greater specificity within elements of the DMN. Importantly, the results converged irrespective of sedation or awake protocols. This underlines that all datasets should be examined with the same expectations and criteria to further enhance results comparability. Hence, the set of standards provided here (e.g. spatial maps and FC parameter distributions), will allow the calibration of future multi-centre projects and assist in designing meta-analysis and replication studies, the gold standards in evidence-based research.

In addition to acquisition procedures, the adoption of analysis standards must be encouraged. A MRI template (Dorr et al., 2008) transformed into the AIBS standard space provides a common space that extends beyond animal MRI studies, including the seamless implementation of AIBS resources (Bergmann et al., 2016; Grandjean et al., 2017b; Oh et al., 2014; Richiardi et al., 2015; Stafford et al., 2014). Moreover, analysis based on robust methods (Zuo and Xing, 2014), such as drICA (Filippini et al., 2009), together with considerations for statistical analysis (Eklund et al., 2016), and sharing datasets on online repositories (Nichols et al., 2017) provide a comprehensive evidence-based roadmap to improve the comparability of acquisitions carried out between centres and enhance the robustness and reproducibility of future results. In

particular, all the dataset analyzed in the context of this study will be shared and therefore provide references for scientists developing customized rsfMRI protocols.

Several major limitations within this study should be acknowledged. First and foremost, the lack of consensus quality assurance parameters for the estimation of FC led us to devise a strategy to examine FC specificity. Because this study grouped together a set of existing scans, factors were not entirely orthogonal and it was not possible to model a number of potentially relevant effects impacting FC metrics, such as specific sequence parameters (e.g. number of volumes), as well as biologically relevant factors including sex, age, and mouse strain. Finally, lack of distal FC in some datasets could not be attributed to specific animal handling protocols or equipment performance. This indicates that additional experimental factors not considered here may be better predictors estimating this particular kind of FC. For example, the implementation of procedures to control the arterial level of carbon dioxide may be critical to prevent hypercapnic conditions, a feature that is associated with reduced FC connectivity (Biswal et al., 1997) and that is often observed in freely breathing anesthetized rodents. Despite these limitations, the work presented here is likely to enhance the true scientific value of mouse rsfMRI by establishing standards and how to attain them. With these, the field is set to meet its goals toward the establishments and understanding of the cellular and molecular mechanisms of large-scale brain functional reorganisation in the healthy and diseased brain.

Material and methods

Comparison dataset acquisition

All animal experiments were carried out with explicit permits from local regulatory bodies. Seventeen datasets, consisting of 15 individual pre-acquired rsfMRI scans each, were acquired with parameters reflecting each centre standards. A summary of equipment, acquisition parameters, and animal handling procedures is listed in **Supplementary table 1**. Scans were acquired on dedicated Bruker magnets operating at 4.7T (N = 1 dataset), 7T (N = 8), 9.4T (N = 6), 11.7T (N = 2), with either room-temperature coils (N = 7) or cryoprobes (N = 10). Gradient-echo echo planar imaging (EPI) sequences were used to acquire all datasets, with repetition time (TR) ranging 1000 - 2000 ms, echo time (TE) 10 - 25 ms, and number of volume 150 - 1000. Acquisitions were performed on awake (N = 1) or anesthetized C57Bl/6J mice (both male and female) with either isoflurane 1-1.25% (N = 5), halothane 0.75% (N = 1), medetomidine 0.1-0.4 mg/kg bolus and 0.2-0.8 mg/kg/h infusion (N = 5), or a combination of isoflurane 0.2-0.5% and medetomidine 0.05-0.3 mg/kg bolus and 0-0.1 mg/kg/h infusion (N = 5). Awake mice were fitted with a non-magnetic head implant to fix the heads to a compatible cradle (Yoshida et al., 2016). Animals were either freely-breathing (N = 12) or mechanically ventilated (N = 5). Datasets are publicly available in BIDS format on openneuro.org (project ID : Mouse_rest_multicentre, https://openneuro.org/datasets/ds001720).

Data preprocessing

Volumes were analysed in their native resolution. Firstly, image axes were reoriented into LPI orientation (*3dresample*, Analysis of Functional NeuroImages, AFNI_16.1.26, https://afni.nimh.nih.gov) (Cox, 1996). Temporal spikes were removed (*3dDespike*), followed by motion correction (*3dvolreg*). Brain masks (*RATS_MM,* https://www.iibi.uiowa.edu) (Oguz et al., 2014) were estimated on temporally averaged EPI volume (*fslmaths*). Motion outliers were detected based on relative framewise displacement estimated during motion correction. Volumes with spikes or framewise displacement greater than 0.100 mm, corresponding to approximately 0.5 voxel of the average in-plane resolution, were labelled in a confound file to be excluded from later seed-based analysis and dual-regression. Linear affine parameters and nonlinear deformations with greedy SyN diffeomorphic transformation (*antsIntroduction.sh*) were estimated relative to a reference T2 MRI template (Dorr et al., 2008) registered into the AIBS Common Coordinate Framework (CCF v3, http://www.brain-map.org/) resampled to 0.200 mm^3. Normalisation to AIBS space was carried out on brain masked EPI directly using ANTS (Advanced Normalization Tools, http://picsl.upenn.edu/software/ants/) (Avants et al., 2014,

2011). Anatomical scans corresponding to each EPI acquisition were not available in all cases. Despite this limitation, plausible registrations of murine EPI directly onto a T2 MRI template were rendered possible due to the relatively simple structure of the lissencephalic cerebrum and high EPI quality. Individual registered brain mask were multiplied (*fslmaths*) to obtain a study mask. The analysis was bounded within this study mask, i..e the brain areas covered by all individual scans. References to anatomical areas are made with respect to the AIBS atlas. All brain masks and registrations were visually inspected and considered plausible.

Six different denoising approaches were applied: i) 6 motion parameters regression (MC), or the following together with motion parameters, ii) white matter (WM), iii) ventricle (VEN), iv) vascular (VASC), v) vascular + ventricle (VV), or vi) global (GSR) signal regression. White matter and ventricle masks were adapted from the AIBS atlas (**Supplementary figure 4cd**), a vascular mask was obtained by averaging and thresholding hand-selected individual-level independent components registered to AIBS space (**Supplementary figure 4b**). Inverse transformations were applied to each mask. Average time series within masks were extracted (*fslmeants*) and regressed out (*fsl_regfilt*). Finally, spatial smoothing was applied with a isotropic 0.45 mm kernel (*3dBlurInMask*), and bandpass filtering was applied between 0.01 - 0.1 Hz (*3dBandpass*). The smoothing kernel was selected to correspond approximately to 1.5 x voxel dimension of the lowest in-plane resolution. The bandpass filter was applied to all datasets to enhance comparability between datasets, despite indications that medetomidine leads to a shift in resting fluctuation frequencies (Grandjean et al., 2014a; Kalthoff et al., 2013; Paasonen et al., 2018). The denoised and filtered individual scans were normalised to AIBS reference space (*WarpTimeSeriesImageMultiTransform*).

Noise was estimated by extracting the signal standard deviation from manually defined regions-of-interest (ROIs) in the upper corners of at least 3 slices, carefully avoiding ghosting artefacts or tissues (brain or otherwise). Mean signal was extracted from the 20th acquisition volume using a cortical mask spanning over the whole isocortex (defined by AIBS atlas) and registered in individual spaces to estimate signal-to-noise ratio (SNR). The same cortical mask was used to extract standard deviation of temporal signals to estimate temporal SNR (tSNR).

Seed-based analysis and independent component analysis

Seeds on the left hemisphere were defined in AIBS space based on the AIBS atlas using 0.300 mm^3 spheres, corresponding to 27 voxels (**Figure S1a**). Mean BOLD signal time series within a

seed were extracted (*fslmeants*) and regressed into individual scans to obtain z-statistic maps (*fsl_glm*). Multi-session temporal concatenation ICA was carried out using MELODIC (Multivariate Exploratory Linear Optimized Decomposition into Independent Components, v3.14) using 20 components. Group-level component classification was adapted on a set of rules defined in (Zerbi et al., 2015). The following were considered plausible resting-state networks: (i) components with either bilateral organisation or (ii) unilateral components with a corresponding separate contralateral component, (iii) minimal crossing of relevant brain boundaries such as white matter tracts, (iv) spatial extent covering more than one slice. The following were considered as implausible resting-state networks: (i) components overlapping mainly with either white matter, ventricle, or vascular masks (**Supplementary figure 4bcd**), (ii) components mainly localised on brain edges. Dual-regression was carried out using the eponymous FSL function to obtain individual-level representations of 14 selected plausible group-level components (Filippini et al., 2009).

Statistical analysis and data representation

Voxelwise statistics were carried out in FSL using either non-parametric permutation tests (*randomise*) for across datasets one-sample t-tests using 5000 permutations and voxelwise correction, or uncorrected parametric one-sample t-tests for within-dataset comparisons (*fsl_glm*). Voxelwise statistical maps are shown as colour-coded t-statistics overlays on the ABI template resampled at 25µm^3 isotropic using MRIcron (Rorden et al., 2007). Statistical analysis carried out on parameters extracted from ROIs was performed in R (v3.4.4, “Someone to Lean on”, R Foundation for Statistical Computing, Vienna, Austria, https://R-project.org) using a linear model (*lm*). A simplified model was designed including the following fixed effects: breathing conditions (2 levels: ventilated or free-breathing), sedation conditions (4 levels: awake, isoflurane/halothane, medetomidine, medetomidine + isoflurane combination), SNR (continuous variable), mean FWD (continuous variable). Interactions effects between these factors were not modeled. Fixed effects significance was tested using likelihood ratio test. Scan parameter occurrence rates were assessed with Chi-square test (*chisq.test*). Residual analysis was performed with QQ-plots to inspect normal distribution, Tukey–Anscombe plots for the homogeneity of the variance and skewness, and scale location plots for homoscedasticity (i.e., the homogeneity of residual variance). The assumption of normality of the residuals was considered plausible in all statistical tests. Plots were generated using ggplot2 (v2.1.0) package for R. Significance level was set at $p<=0.05$ one-tailed with family-wise error correction at a

voxelwise level, unless specified otherwise. Descriptive statistics are given as mean ± 1 standard deviation.

Acknowledgements

This work was supported by the Singapore Bioimaging Consortium (SBIC), A*STAR, Singapore. AG acknowledges funding from the Simons Foundation (SFARI 314688 and 400101), the Brain and Behavior Foundation (2017 NARSAD independent Investigator Grant) and the European Research Council (ERC, G.A. 802371). This work was also supported by the JSPS KAKENHI Grant Number 16K07032 to NT, Brain/MINDS, the Strategic Research Program for Brain Sciences (SRPBS) from the Ministry of Education, Culture, Sports, Science, and Technology of Japan (MEXT) and Japan Agency for Medical Research and Development (AMED) to NT and HO. It was further supported as part of the Excellence Cluster 'BrainLinks-BrainTools' by the German Research Foundation, grant EXC1086. AH acknowledges funding from the German BMBF (NeuroImpa, 01EC1403C and NeuroRad 02NUK034D). MD acknowledges funding from France-Alzheimer Association, Plan Alzheimer Foundation and the French Public Investment Bank's "ROMANE" program. This work was also supported by the Fund for Scientific Research Flanders (FWO) (grant agreements G057615N and 12S4815N - AvL), the Stichting Alzheimer Onderzoek (SAO-FRA, grant agreement 13026-AvL), the interdisciplinary PhD grant BOF DOCPRO 2014 - MV). The authors would like to thank Itamar Kahn, Eyal Bergmann and Daniel Gutierrez-Barragan for critically reading the manuscript.

Author Contributions

JG designed the study. Every author contributed to data acquisition. JG, CC and AG carried out the analysis. Every author participated in the preparation of the manuscript.

Competing interests statement

The authors have no conflicts of interest to declare.

References

Bergmann, E., Zur, G., Bershadsky, G., Kahn, I., 2016. The Organization of Mouse and Human Cortico-Hippocampal Networks Estimated by Intrinsic Functional Connectivity. Cereb. Cortex 26, 4497–4512. doi:10.1093/cercor/bhw327resting state

Avants, B.B., Tustison, N.J., Song, G., Cook, P.A., Klein, A., Gee, J.C., 2011. A reproducible evaluation of ANTs similarity metric performance in brain image registration. Neuroimage 54, 2033–2044. doi:10.1016/j.neuroimage.2010.09.025

Avants, B.B., Tustison, N.J., Stauffer, M., Song, G., Wu, B., Gee, J.C., 2014. The Insight ToolKit image registration framework. Front. Neuroinformatics 8, 44. doi:10.3389/fninf.2014.00044

Azevedo, F.A.C., Carvalho, L.R.B., Grinberg, L.T., Farfel, J.M., Ferretti, R.E.L., Leite, R.E.P., Jacob Filho, W., Lent, R., Herculano-Houzel, S., 2009. Equal numbers of neuronal and nonneuronal cells make the human brain an isometrically scaled-up primate brain. J. Comp. Neurol. 513, 532–541. doi:10.1002/cne.21974

Becerra, L., Pendse, G., Chang, P.-C., Bishop, J., Borsook, D., 2011. Robust reproducible resting state networks in the awake rodent brain. PLoS ONE 6, e25701. doi:10.1371/journal.pone.0025701

Belloy, M.E., Naeyaert, M., Abbas, A., Shah, D., Vanreusel, V., van Audekerke, J., Keilholz, S.D., Keliris, G.A., Van der Linden, A., Verhoye, M., 2018a. Dynamic resting state fMRI analysis in mice reveals a set of Quasi-Periodic Patterns and illustrates their relationship with the global signal. Neuroimage 180, 463–484. doi:10.1016/j.neuroimage.2018.01.075

Belloy, M.E., Shah, D., Abbas, A., Kashyap, A., Roßner, S., Van der Linden, A., Keilholz, S.D., Keliris, G.A., Verhoye, M., 2018b. Quasi-Periodic Patterns of Neural Activity improve Classification of Alzheimer's Disease in Mice. Sci. Rep. 8, 10024. doi:10.1038/s41598-018-28237-9

Bergmann, E., Zur, G., Bershadsky, G., Kahn, I., 2016. The Organization of Mouse and Human Cortico-Hippocampal Networks Estimated by Intrinsic Functional Connectivity. Cereb. Cortex 26, 4497–4512. doi:10.1093/cercor/bhw327

Bertero, A., Liska, A., Pagani, M., Parolisi, R., Masferrer, M.E., Gritti, M., Pedrazzoli, M., Galbusera, A., Sarica, A., Cerasa, A., Buffelli, M., Tonini, R., Buffo, A., Gross, C., Pasqualetti, M., Gozzi, A., 2018. Autism-associated 16p11.2 microdeletion impairs prefrontal functional connectivity in mouse and human. Brain 141, 2055–2065. doi:10.1093/brain/awy111

Biswal, B., Hudetz, A.G., Yetkin, F.Z., Haughton, V.M., Hyde, J.S., 1997. Hypercapnia reversibly suppresses low-frequency fluctuations in the human motor cortex during rest using echo-

planar MRI. J. Cereb. Blood Flow Metab. 17, 301–308. doi:10.1097/00004647-199703000-00007

Biswal, B., Yetkin, F.Z., Haughton, V.M., Hyde, J.S., 1995. Functional connectivity in the motor cortex of resting human brain using echo-planar MRI. Magn. Reson. Med. 34, 537–541. doi:10.1002/mrm.1910340409

Biswal, B.B., Mennes, M., Zuo, X.-N., Gohel, S., Kelly, C., Smith, S.M., Beckmann, C.F., Adelstein, J.S., Buckner, R.L., Colcombe, S., Dogonowski, A.-M., Ernst, M., Fair, D., Hampson, M., Hoptman, M.J., Hyde, J.S., Kiviniemi, V.J., Kötter, R., Li, S.-J., Lin, C.-P., Milham, M.P., 2010. Toward discovery science of human brain function. Proc Natl Acad Sci USA 107, 4734–4739. doi:10.1073/pnas.0911855107

Buckner, R.L., Andrews-Hanna, J.R., Schacter, D.L., 2008. The brain's default network: anatomy, function, and relevance to disease. Ann. N. Y. Acad. Sci. 1124, 1–38. doi:10.1196/annals.1440.011

Buehlmann, D., Grandjean, J., Xandry, J., Rudin, M., 2018. Longitudinal resting-state functional magnetic resonance imaging in a mouse model of metastatic bone cancer reveals distinct functional reorganizations along a developing chronic pain state. Pain 159, 719–727. doi:10.1097/j.pain.0000000000001148

Bukhari, Q., Schroeter, A., Cole, D.M., Rudin, M., 2017. Resting State fMRI in Mice Reveals Anesthesia Specific Signatures of Brain Functional Networks and Their Interactions. Front. Neural Circuits 11, 5. doi:10.3389/fncir.2017.00005

Bukhari, Q., Schroeter, A., Rudin, M., 2018. Increasing isoflurane dose reduces homotopic correlation and functional segregation of brain networks in mice as revealed by resting-state fMRI. Sci. Rep. 8, 10591. doi:10.1038/s41598-018-28766-3

Charbogne, P., Gardon, O., Martín-García, E., Keyworth, H.L., Matsui, A., Mechling, A.E., Bienert, T., Nasseef, T., Robé, A., Moquin, L., Darcq, E., Ben Hamida, S., Robledo, P., Matifas, A., Befort, K., Gavériaux-Ruff, C., Harsan, L.-A., von Elverfeldt, D., Hennig, J., Gratton, A., Kieffer, B.L., 2017. Mu Opioid Receptors in Gamma-Aminobutyric Acidergic Forebrain Neurons Moderate Motivation for Heroin and Palatable Food. Biol. Psychiatry 81, 778–788. doi:10.1016/j.biopsych.2016.12.022

Chuang, K.-H., Nasrallah, F.A., 2017. Functional networks and network perturbations in rodents. Neuroimage 163, 419–436. doi:10.1016/j.neuroimage.2017.09.038

Cox, R.W., 1996. AFNI: software for analysis and visualization of functional magnetic resonance neuroimages. Comput. Biomed. Res. 29, 162–173. doi:10.1006/cbmr.1996.0014

DeSimone, J.C., Febo, M., Shukla, P., Ofori, E., Colon-Perez, L.M., Li, Y., Vaillancourt, D.E.,

2016. In vivo imaging reveals impaired connectivity across cortical and subcortical networks in a mouse model of DYT1 dystonia. Neurobiol. Dis. 95, 35–45. doi:10.1016/j.nbd.2016.07.005

Dorr, A.E., Lerch, J.P., Spring, S., Kabani, N., Henkelman, R.M., 2008. High resolution three-dimensional brain atlas using an average magnetic resonance image of 40 adult C57Bl/6J mice. Neuroimage 42, 60–69. doi:10.1016/j.neuroimage.2008.03.037

Eklund, A., Nichols, T.E., Knutsson, H., 2016. Cluster failure: Why fMRI inferences for spatial extent have inflated false-positive rates. Proc Natl Acad Sci USA 113, 7900–7905. doi:10.1073/pnas.1602413113

Errico, F., D'Argenio, V., Sforazzini, F., Iasevoli, F., Squillace, M., Guerri, G., Napolitano, F., Angrisano, T., Di Maio, A., Keller, S., Vitucci, D., Galbusera, A., Chiariotti, L., Bertolino, A., de Bartolomeis, A., Salvatore, F., Gozzi, A., Usiello, A., 2015. A role for D-aspartate oxidase in schizophrenia and in schizophrenia-related symptoms induced by phencyclidine in mice. Transl. Psychiatry 5, e512. doi:10.1038/tp.2015.2

Filippini, N., MacIntosh, B.J., Hough, M.G., Goodwin, G.M., Frisoni, G.B., Smith, S.M., Matthews, P.M., Beckmann, C.F., Mackay, C.E., 2009. Distinct patterns of brain activity in young carriers of the APOE-epsilon4 allele. Proc Natl Acad Sci USA 106, 7209–7214. doi:10.1073/pnas.0811879106

Fox, M.D., Raichle, M.E., 2007. Spontaneous fluctuations in brain activity observed with functional magnetic resonance imaging. Nat. Rev. Neurosci. 8, 700–711. doi:10.1038/nrn2201

Fox, M.D., Snyder, A.Z., Vincent, J.L., Corbetta, M., Van Essen, D.C., Raichle, M.E., 2005. The human brain is intrinsically organized into dynamic, anticorrelated functional networks. Proc Natl Acad Sci USA 102, 9673–9678. doi:10.1073/pnas.0504136102

Friston, K.J., 2011. Functional and effective connectivity: a review. Brain Connect. 1, 13–36. doi:10.1089/brain.2011.0008

Gass, N., Weber-Fahr, W., Sartorius, A., Becker, R., Didriksen, M., Stensbøl, T.B., Bastlund, J.F., Meyer-Lindenberg, A., Schwarz, A.J., 2016. An acetylcholine alpha7 positive allosteric modulator rescues a schizophrenia-associated brain endophenotype in the 15q13.3 microdeletion, encompassing CHRNA7. Eur. Neuropsychopharmacol. 26, 1150–1160. doi:10.1016/j.euroneuro.2016.03.013

Gozzi, A., Schwarz, A.J., 2016. Large-scale functional connectivity networks in the rodent brain. Neuroimage 127, 496–509. doi:10.1016/j.neuroimage.2015.12.017

Grandjean, J., Azzinnari, D., Seuwen, A., Sigrist, H., Seifritz, E., Pryce, C.R., Rudin, M., 2016a.

Chronic psychosocial stress in mice leads to changes in brain functional connectivity and metabolite levels comparable to human depression. Neuroimage 142, 544–552. doi:10.1016/j.neuroimage.2016.08.013

Grandjean, J., Derungs, R., Kulic, L., Welt, T., Henkelman, M., Nitsch, R.M., Rudin, M., 2016b. Complex interplay between brain function and structure during cerebral amyloidosis in APP transgenic mouse strains revealed by multi-parametric MRI comparison. Neuroimage 134, 1–11. doi:10.1016/j.neuroimage.2016.03.042

Grandjean, J., Preti, M.G., Bolton, T.A.W., Buerge, M., Seifritz, E., Pryce, C.R., Van De Ville, D., Rudin, M., 2017a. Dynamic reorganization of intrinsic functional networks in the mouse brain. Neuroimage 152, 497–508. doi:10.1016/j.neuroimage.2017.03.026

Grandjean, J., Schroeter, A., Batata, I., Rudin, M., 2014a. Optimization of anesthesia protocol for resting-state fMRI in mice based on differential effects of anesthetics on functional connectivity patterns. Neuroimage 102 Pt 2, 838–847. doi:10.1016/j.neuroimage.2014.08.043

Grandjean, J., Schroeter, A., He, P., Tanadini, M., Keist, R., Krstic, D., Konietzko, U., Klohs, J., Nitsch, R.M., Rudin, M., 2014b. Early alterations in functional connectivity and white matter structure in a transgenic mouse model of cerebral amyloidosis. J. Neurosci. 34, 13780–13789. doi:10.1523/JNEUROSCI.4762-13.2014

Grandjean, J., Zerbi, V., Balsters, J.H., Wenderoth, N., Rudin, M., 2017b. Structural Basis of Large-Scale Functional Connectivity in the Mouse. J. Neurosci. 37, 8092–8101. doi:10.1523/JNEUROSCI.0438-17.2017

Greicius, M., 2008. Resting-state functional connectivity in neuropsychiatric disorders. Curr. Opin. Neurol. 21, 424–430. doi:10.1097/WCO.0b013e328306f2c5

Guilfoyle, D.N., Gerum, S.V., Sanchez, J.L., Balla, A., Sershen, H., Javitt, D.C., Hoptman, M.J., 2013. Functional connectivity fMRI in mouse brain at 7T using isoflurane. J. Neurosci. Methods 214, 144–148. doi:10.1016/j.jneumeth.2013.01.019

Haberl, M.G., Zerbi, V., Veltien, A., Ginger, M., Heerschap, A., Frick, A., 2015. Structural-functional connectivity deficits of neocortical circuits in the Fmr1 (-/y) mouse model of autism. Sci. Adv. 1, e1500775. doi:10.1126/sciadv.1500775

Hoyer, C., Gass, N., Weber-Fahr, W., Sartorius, A., 2014. Advantages and challenges of small animal magnetic resonance imaging as a translational tool. Neuropsychobiology 69, 187–201. doi:10.1159/000360859

Hübner, N.S., Mechling, A.E., Lee, H.-L., Reisert, M., Bienert, T., Hennig, J., von Elverfeldt, D., Harsan, L.-A., 2017. The connectomics of brain demyelination: Functional and structural

patterns in the cuprizone mouse model. Neuroimage 146, 1–18. doi:10.1016/j.neuroimage.2016.11.008

Hutchison, R.M., Everling, S., 2012. Monkey in the middle: why non-human primates are needed to bridge the gap in resting-state investigations. Front. Neuroanat. 6, 29. doi:10.3389/fnana.2012.00029

Jonckers, E., Delgado y Palacios, R., Shah, D., Guglielmetti, C., Verhoye, M., Van der Linden, A., 2014. Different anesthesia regimes modulate the functional connectivity outcome in mice. Magn. Reson. Med. 72, 1103–1112. doi:10.1002/mrm.24990

Jonckers, E., Shah, D., Hamaide, J., Verhoye, M., Van der Linden, A., 2015. The power of using functional fMRI on small rodents to study brain pharmacology and disease. Front. Pharmacol. 6, 231. doi:10.3389/fphar.2015.00231

Jonckers, E., Van Audekerke, J., De Visscher, G., Van der Linden, A., Verhoye, M., 2011. Functional connectivity fMRI of the rodent brain: comparison of functional connectivity networks in rat and mouse. PLoS ONE 6, e18876. doi:10.1371/journal.pone.0018876

Jonckers, E., Van der Linden, A., Verhoye, M., 2013. Functional magnetic resonance imaging in rodents: an unique tool to study in vivo pharmacologic neuromodulation. Curr. Opin. Pharmacol. 13, 813–820. doi:10.1016/j.coph.2013.06.008

Jovicich, J., Minati, L., Marizzoni, M., Marchitelli, R., Sala-Llonch, R., Bartrés-Faz, D., Arnold, J., Benninghoff, J., Fiedler, U., Roccatagliata, L., Picco, A., Nobili, F., Blin, O., Bombois, S., Lopes, R., Bordet, R., Sein, J., Ranjeva, J.-P., Didic, M., Gros-Dagnac, H., PharmaCog Consortium, 2016. Longitudinal reproducibility of default-mode network connectivity in healthy elderly participants: A multicentric resting-state fMRI study. Neuroimage 124, 442–454. doi:10.1016/j.neuroimage.2015.07.010

Kalthoff, D., Po, C., Wiedermann, D., Hoehn, M., 2013. Reliability and spatial specificity of rat brain sensorimotor functional connectivity networks are superior under sedation compared with general anesthesia. NMR Biomed. 26, 638–650. doi:10.1002/nbm.2908

Komaki, Y., Hikishima, K., Shibata, S., Konomi, T., Seki, F., Yamada, M., Miyasaka, N., Fujiyoshi, K., Okano, H.J., Nakamura, M., Okano, H., 2016. Functional brain mapping using specific sensory-circuit stimulation and a theoretical graph network analysis in mice with neuropathic allodynia. Sci. Rep. 6, 37802. doi:10.1038/srep37802

Li, Q., Li, G., Wu, D., Lu, H., Hou, Z., Ross, C.A., Yang, Y., Zhang, J., Duan, W., 2017. Resting-state functional MRI reveals altered brain connectivity and its correlation with motor dysfunction in a mouse model of Huntington's disease. Sci. Rep. 7, 16742. doi:10.1038/s41598-017-17026-5

Liska, A., Bertero, A., Gomolka, R., Sabbioni, M., Galbusera, A., Barsotti, N., Panzeri, S., Scattoni, M.L., Pasqualetti, M., Gozzi, A., 2018. Homozygous Loss of Autism-Risk Gene CNTNAP2 Results in Reduced Local and Long-Range Prefrontal Functional Connectivity. Cereb. Cortex 28, 1141–1153. doi:10.1093/cercor/bhx022

Liska, A., Galbusera, A., Schwarz, A.J., Gozzi, A., 2015. Functional connectivity hubs of the mouse brain. Neuroimage 115, 281–291. doi:10.1016/j.neuroimage.2015.04.033

Liska, A., Gozzi, A., 2016. Can mouse imaging studies bring order to autism connectivity chaos? Front. Neurosci. 10, 484. doi:10.3389/fnins.2016.00484

Lu, H., Zou, Q., Gu, H., Raichle, M.E., Stein, E.A., Yang, Y., 2012. Rat brains also have a default mode network. Proc Natl Acad Sci USA 109, 3979–3984. doi:10.1073/pnas.1200506109

Mechling, A.E., Arefin, T., Lee, H.-L., Bienert, T., Reisert, M., Ben Hamida, S., Darcq, E., Ehrlich, A., Gaveriaux-Ruff, C., Parent, M.J., Rosa-Neto, P., Hennig, J., von Elverfeldt, D., Kieffer, B.L., Harsan, L.-A., 2016. Deletion of the mu opioid receptor gene in mice reshapes the reward-aversion connectome. Proc Natl Acad Sci USA 113, 11603–11608. doi:10.1073/pnas.1601640113

Michetti, C., Caruso, A., Pagani, M., Sabbioni, M., Medrihan, L., David, G., Galbusera, A., Morini, M., Gozzi, A., Benfenati, F., Scattoni, M.L., 2017. The Knockout of Synapsin II in Mice Impairs Social Behavior and Functional Connectivity Generating an ASD-like Phenotype. Cereb. Cortex 27, 5014–5023. doi:10.1093/cercor/bhx207

Murphy, K., Birn, R.M., Bandettini, P.A., 2013. Resting-state fMRI confounds and cleanup. Neuroimage 80, 349–359. doi:10.1016/j.neuroimage.2013.04.001

Nichols, T.E., Das, S., Eickhoff, S.B., Evans, A.C., Glatard, T., Hanke, M., Kriegeskorte, N., Milham, M.P., Poldrack, R.A., Poline, J.-B., Proal, E., Thirion, B., Van Essen, D.C., White, T., Yeo, B.T.T., 2017. Best practices in data analysis and sharing in neuroimaging using MRI. Nat. Neurosci. 20, 299–303. doi:10.1038/nn.4500

Oguz, I., Zhang, H., Rumple, A., Sonka, M., 2014. RATS: Rapid Automatic Tissue Segmentation in rodent brain MRI. J. Neurosci. Methods 221, 175–182. doi:10.1016/j.jneumeth.2013.09.021

Oh, S.W., Harris, J.A., Ng, L., Winslow, B., Cain, N., Mihalas, S., Wang, Q., Lau, C., Kuan, L., Henry, A.M., Mortrud, M.T., Ouellette, B., Nguyen, T.N., Sorensen, S.A., Slaughterbeck, C.R., Wakeman, W., Li, Y., Feng, D., Ho, A., Nicholas, E., Zeng, H., 2014. A mesoscale connectome of the mouse brain. Nature 508, 207–214. doi:10.1038/nature13186

Paasonen, J., Stenroos, P., Salo, R.A., Kiviniemi, V., Gröhn, O., 2018. Functional connectivity

under six anesthesia protocols and the awake condition in rat brain. Neuroimage 172, 9–20. doi:10.1016/j.neuroimage.2018.01.014

Pan, W.-J., Billings, J.C.W., Grooms, J.K., Shakil, S., Keilholz, S.D., 2015. Considerations for resting state functional MRI and functional connectivity studies in rodents. Front. Neurosci. 9, 269. doi:10.3389/fnins.2015.00269

Popa, D., Popescu, A.T., Paré, D., 2009. Contrasting activity profile of two distributed cortical networks as a function of attentional demands. J. Neurosci. 29, 1191–1201. doi:10.1523/JNEUROSCI.4867-08.2009

Razoux, F., Baltes, C., Mueggler, T., Seuwen, A., Russig, H., Mansuy, I., Rudin, M., 2013. Functional MRI to assess alterations of functional networks in response to pharmacological or genetic manipulations of the serotonergic system in mice. Neuroimage 74, 326–336. doi:10.1016/j.neuroimage.2013.02.031

Richiardi, J., Altmann, A., Milazzo, A.-C., Chang, C., Chakravarty, M.M., Banaschewski, T., Barker, G.J., Bokde, A.L.W., Bromberg, U., Büchel, C., Conrod, P., Fauth-Bühler, M., Flor, H., Frouin, V., Gallinat, J., Garavan, H., Gowland, P., Heinz, A., Lemaître, H., Mann, K.F., IMAGEN consortium, 2015. BRAIN NETWORKS. Correlated gene expression supports synchronous activity in brain networks. Science 348, 1241–1244. doi:10.1126/science.1255905

Rorden, C., Karnath, H.-O., Bonilha, L., 2007. Improving lesion-symptom mapping. J. Cogn. Neurosci. 19, 1081–1088. doi:10.1162/jocn.2007.19.7.1081

Schroeter, A., Grandjean, J., Schlegel, F., Saab, B.J., Rudin, M., 2017. Contributions of structural connectivity and cerebrovascular parameters to functional magnetic resonance imaging signals in mice at rest and during sensory paw stimulation. J. Cereb. Blood Flow Metab. 37, 2368–2382. doi:10.1177/0271678X16666292

Sethi, S.S., Zerbi, V., Wenderoth, N., Fornito, A., Fulcher, B.D., 2017. Structural connectome topology relates to regional BOLD signal dynamics in the mouse brain. Chaos 27, 047405. doi:10.1063/1.4979281

Sforazzini, F., Bertero, A., Dodero, L., David, G., Galbusera, A., Scattoni, M.L., Pasqualetti, M., Gozzi, A., 2016. Altered functional connectivity networks in acallosal and socially impaired BTBR mice. Brain Struct. Funct. 221, 941–954. doi:10.1007/s00429-014-0948-9

Sforazzini, F., Schwarz, A.J., Galbusera, A., Bifone, A., Gozzi, A., 2014. Distributed BOLD and CBV-weighted resting-state networks in the mouse brain. Neuroimage 87, 403–415. doi:10.1016/j.neuroimage.2013.09.050

Shah, D., Blockx, I., Guns, P.-J., De Deyn, P.P., Van Dam, D., Jonckers, E., Delgado Y

Palacios, R., Verhoye, M., Van der Linden, A., 2015. Acute modulation of the cholinergic system in the mouse brain detected by pharmacological resting-state functional MRI. Neuroimage 109, 151–159. doi:10.1016/j.neuroimage.2015.01.009

Shah, D., Blockx, I., Keliris, G.A., Kara, F., Jonckers, E., Verhoye, M., Van der Linden, A., 2016a. Cholinergic and serotonergic modulations differentially affect large-scale functional networks in the mouse brain. Brain Struct. Funct. 221, 3067–3079. doi:10.1007/s00429-015-1087-7

Shah, D., Deleye, S., Verhoye, M., Staelens, S., Van der Linden, A., 2016b. Resting-state functional MRI and [18F]-FDG PET demonstrate differences in neuronal activity between commonly used mouse strains. Neuroimage 125, 571–577. doi:10.1016/j.neuroimage.2015.10.073

Shah, D., Jonckers, E., Praet, J., Vanhoutte, G., Delgado Y Palacios, R., Bigot, C., D'Souza, D.V., Verhoye, M., Van der Linden, A., 2013. Resting state FMRI reveals diminished functional connectivity in a mouse model of amyloidosis. PLoS ONE 8, e84241. doi:10.1371/journal.pone.0084241

Shah, D., Praet, J., Latif Hernandez, A., Höfling, C., Anckaerts, C., Bard, F., Morawski, M., Detrez, J.R., Prinsen, E., Villa, A., De Vos, W.H., Maggi, A., D'Hooge, R., Balschun, D., Rossner, S., Verhoye, M., Van der Linden, A., 2016c. Early pathologic amyloid induces hypersynchrony of BOLD resting-state networks in transgenic mice and provides an early therapeutic window before amyloid plaque deposition. Alzheimers Dement 12, 964–976. doi:10.1016/j.jalz.2016.03.010

Stafford, J.M., Jarrett, B.R., Miranda-Dominguez, O., Mills, B.D., Cain, N., Mihalas, S., Lahvis, G.P., Lattal, K.M., Mitchell, S.H., David, S.V., Fryer, J.D., Nigg, J.T., Fair, D.A., 2014. Large-scale topology and the default mode network in the mouse connectome. Proc Natl Acad Sci USA 111, 18745–18750. doi:10.1073/pnas.1404346111

Upadhyay, J., Baker, S.J., Chandran, P., Miller, L., Lee, Y., Marek, G.J., Sakoglu, U., Chin, C.-L., Luo, F., Fox, G.B., Day, M., 2011. Default-mode-like network activation in awake rodents. PLoS ONE 6, e27839. doi:10.1371/journal.pone.0027839

Wiesmann, M., Zerbi, V., Jansen, D., Haast, R., Lütjohann, D., Broersen, L.M., Heerschap, A., Kiliaan, A.J., 2016. A Dietary Treatment Improves Cerebral Blood Flow and Brain Connectivity in Aging apoE4 Mice. Neural Plast. 2016, 6846721. doi:10.1155/2016/6846721

Wu, T., Grandjean, J., Bosshard, S.C., Rudin, M., Reutens, D., Jiang, T., 2017. Altered regional connectivity reflecting effects of different anaesthesia protocols in the mouse brain.

Neuroimage 149, 190–199. doi:10.1016/j.neuroimage.2017.01.074

Yoshida, K., Mimura, Y., Ishihara, R., Nishida, H., Komaki, Y., Minakuchi, T., Tsurugizawa, T., Mimura, M., Okano, H., Tanaka, K.F., Takata, N., 2016. Physiological effects of a habituation procedure for functional MRI in awake mice using a cryogenic radiofrequency probe. J. Neurosci. Methods 274, 38–48. doi:10.1016/j.jneumeth.2016.09.013

Zerbi, V., Grandjean, J., Rudin, M., Wenderoth, N., 2015. Mapping the mouse brain with rs-fMRI: An optimized pipeline for functional network identification. Neuroimage 123, 11–21. doi:10.1016/j.neuroimage.2015.07.090

Zerbi, V., Ielacqua, G.D., Markicevic, M., Haberl, M.G., Ellisman, M.H., A-Bhaskaran, A., Frick, A., Rudin, M., Wenderoth, N., 2018. Dysfunctional Autism Risk Genes Cause Circuit-Specific Connectivity Deficits With Distinct Developmental Trajectories. Cereb. Cortex 28, 2495–2506. doi:10.1093/cercor/bhy046

Zerbi, V., Wiesmann, M., Emmerzaal, T.L., Jansen, D., Van Beek, M., Mutsaers, M.P.C., Beckmann, C.F., Heerschap, A., Kiliaan, A.J., 2014. Resting-state functional connectivity changes in aging apoE4 and apoE-KO mice. J. Neurosci. 34, 13963–13975. doi:10.1523/JNEUROSCI.0684-14.2014

Zhan, Y., Paolicelli, R.C., Sforazzini, F., Weinhard, L., Bolasco, G., Pagani, F., Vyssotski, A.L., Bifone, A., Gozzi, A., Ragozzino, D., Gross, C.T., 2014. Deficient neuron-microglia signaling results in impaired functional brain connectivity and social behavior. Nat. Neurosci. 17, 400–406. doi:10.1038/nn.3641

Zuo, X.-N., Xing, X.-X., 2014. Test-retest reliabilities of resting-state FMRI measurements in human brain functional connectomics: a systems neuroscience perspective. Neurosci. Biobehav. Rev. 45, 100–118. doi:10.1016/j.neubiorev.2014.05.009

Université de Strasbourg

Meltem KARATAŞ

École Doctorale des Sciences de la Vie et de la Santé STRASBOURG

Analyse longitudinale des réseaux cérébraux par Imagerie de Résonance Magnétique (IRM) dans un modèle murin de dépression induite par la douleur neuropathique

Résumé

Les douleurs chroniques développent souvent des troubles de l'anxiété et des états dépressifs. Malgré des recherches cliniques considérables, les mécanismes sous-jacents à cette comorbidité restent inconnus. Nous avons mené une étude d'imagerie non-invasive, par Imagerie de Résonance Magnétique (IRM), pour étudier les changements dans la connectivité structurelle et fonctionnelle dans un modèle murin de dépression induite par la douleur neuropathique. Nous avons utilisé deux méthodes d'IRM pour étudier les voies fonctionnelles de communication (en utilisant l'imagerie fonctionnelle de repos-IRMfr) ainsi que leurs substrats microstructuraux (imagerie du tenseur de diffusion) de manière longitudinale. Les résultats obtenus dans le cadre de ce projet démontrent des modifications structurels et fonctionnels remarquables des réseaux cérébraux suite à l'induction de la douleur neuropathique et à l'émergence de comportements dépressifs. En combinant un modèle animal pertinent et l'IRM cérébrale in-vivo nous avons identifié la signature de la dépression induite par la douleur et son évaluation longitudinale sur la connectivité cérébrale, impliquant des altérations dans le cadre des circuits de la récompense, avec un impact majeur sur la connectivité des deux centres : le CCA et l'ATV. Les résultats principales d'IRLfr montrent une modification considérable dans les réseaux englobant le MPD et le circuit de récompense, qui sont impliqués à la fois dans les pathologies de la douleur chronique et de la dépression. Il est maintenant nécessaire d'étudier la relation causale entre la dépression induite par la douleur et ses changements fonctionnels qui font partie de la perspective long-termes de ce projet.

Mots-clés : douleur neuropathique, dépression, modèle murin, IRM, connectivité cérébrale

Abstract

Chronic pain conditions frequently lead to anxiety and depressive disorders. Despite considerable clinical research, the mechanisms underlying this comorbidity remain elusive. We conducted a non-invasive brain imaging study to investigate changes in structural and functional connectivity in a mouse model of neuropathic pain-induced depression. We employed two methods of magnetic resonance imaging (MRI) to investigate functional communication pathways (using resting state functional MRI-rs-fMRI) as well as their microstructural substrates (diffusion MRI) in longitudinal manner. Brain networks demonstrate remarkable structural and functional modifications following the induction of neuropathic pain and the emergence of depressive phenotype. Combining a relevant preclinical model and in vivo brain MRI, we identified a brain connectivity signature of pain-induced depression and its evolution over time, involving alterations in reward circuits, with a major impact of the two centers: ACA and VTA. The main results of functional imaging reveal considerable changes in the networks encompassing the reward circuit and DMN, which are known to be involved in both chronic pain pathologies and major depression. The long-term perspective of this project is to investigate the causal relationship between pain and depression, reaching a mechanistic explanation for the comorbidity.

Keywords: neuropathic pain, depression, mouse model, MRI, brain connectivity